SKA-India Science Book: Version 2

April 06, 2016

Contents

All the figures are printed in black and white. The original colour versions are available online on the SKA-India website.

Credits: cover picture `www.DGanesh.com`

Indian initiatives in science with the SKA

T. Roy Choudhury*[1] and Yashwant Gupta[1]

[1] *National Centre for Radio Astrophysics, TIFR, Pune 411007, India*

Indian has been associated with the Square Kilometre Array (SKA), a international mega-project to build the world's largest telescope, from the beginning. The association has been strengthened recently when India joined the SKA Organisation as a full member. The first phase of the SKA, called the SKA-1, is currently in the design phase with construction expected to start within the next couple of years, i.e., around 2018. Early science is expected to be possible from around 2022 or so. So it is natural that Indian scientists are looking to enhance their scientific contribution to the SKA, and also to build up a base of astronomers that will be prepared to use the SKA when it is ready.

SKA-related initiatives in India are overseen by the "SKA-India Consortium" which has over a dozen member organisations from all over the country. In particular, the science initiatives in different areas are coordinated by the SKA-India Science Working Groups (SWGs), somewhat in line with what is being done by the SKA Office for the international science community. These Indian SWGs have been instrumental in creating awareness related to the SKA within the Indian scientists by organising talks, workshops, meetings etc. The number of scientists interested in the SKA has grown substantially over the last couple of years. The SWGs have not only been able to attract radio astronomers, but also astronomers working in other wave bands and theoreticians interested in model building and signal predictions.

The capabilities of SKA-1 will be phenomenal, for a variety of science goals and applications, and will far surpass that of any existing or planned radio astronomy facility. The goals cover a wide range of research areas starting from understanding the formation of stars using hyperfine transition of neutral hydrogen to testing Einstein's theory of general relativity using pulsars to detailed understanding of some of the early phases in the life of the Universe. At present, the international community is busy in developing up the so-called "Key Science Projects" (KSPs), i.e., large scale collaborative projects addressing key scientific questions.

Keeping in line with the above, the Indian astronomers too are looking to build up their science cases so that they are in positions to play significant roles in the appropriate KSPs of interest. The first task along these lines has been to prepare a set of articles highlighting the science areas which Indians are interested in, and also to provide initial plans for what they would want to do with the SKA. The first collection of the articles was published as a booklet during the workshop on "Indian Participation in the SKA" held in NCRA-TIFR, Pune on February 16, 2015. Over the last one year these articles have been refined and more material added to produce the next version of the booklet, which we call the *"SKA-India Science Book: Version 2"*.

As one will see, the science book contains articles covering a wide range of science areas, almost all areas that are being explored by the SKA international community. The areas cover nearby objects like neutron stars as well as distant ones like galaxy clusters, AGNs and the first stars. One would find a wide variety in terms of the techniques too. On the one hand, there are articles exploring possibilities of conducting immediate observations using the SKA pathfinders (e.g., uGMRT), and extending these to the future with the SKA. On the other hand, there are articles describing theoretical models and making predictions for the SKA. There are also plans of coordinating with observations in other wave bands, as well as gravitational waves. Such a coordination between astronomers from different backgrounds is crucial in making full use of a facility as advanced as the SKA.

We hope the present set of articles would provide a clear direction, both to the international as well as the Indian community, regarding the SKA-related science areas of current interest within India. We

*tirth@ncra.tifr.res.in

also hope that these will enthuse more astronomers to get involved with the SKA, thus allowing the community to explore subjects beyond what has been covered in the present booklet.

We would like to thank all members of the SKA-India community who have contributed their time and effort enthusiastically to this collection of articles, and look forward to continued and increased participation from the Indian astronomy community in these endeavours.

Neutron Star Physics in the SKA Era: An Indian Perspective

Sushan Konar*[1], Manjari Bagchi[2], Debades Bandyopadhyay[3], Sarmistha Banik[4], Dipankar Bhattacharya[5], Sudip Bhattacharyya[6], R. T. Gangadhara[7], A. Gopakumar[6], Yashwant Gupta[1], B. C. Joshi[1], Yogesh Maan[1], Chandreyee Maitra[8], Dipanjan Mukherjee[9], Archana Pai[10], Biswajit Paul[11], Alak K. Ray[6], and Firoza K. Sutaria[7]

[1] *NCRA-TIFR, Pune*
[2] *IMSc, Chennai*
[3] *SINP, Kolkata*
[4] *BITS-Pilani, Hyderabad*
[5] *IUCAA, Pune*
[6] *TIFR, Mumbai*
[7] *IIAp, Bangalore*
[8] *CEA, Saclay*
[9] *RSAA-ANU, Canberra*
[10] *IISER, Thiruvananthapuram*
[11] *RRI, Bangalore*

Abstract

It is an exceptionally opportune time for Astrophysics when a number of next-generation mega-instruments are poised to observe the universe across the entire electromagnetic spectrum with unprecedented data quality. The Square Kilometre Array (SKA) is undoubtedly one of the major components of this scenario. In particular, the SKA is expected to discover tens of thousands of new neutron stars giving a major philip to a wide range of scientific investigations. India has a sizeable community of scientists working on different aspects of neutron star physics with immediate access to both the uGMRT (an SKA pathfinder) and the recently launched X-ray observatory Astrosat. The current interests of the community largely centre around studies of - a) *the neutron star equation of state*, b) *the evolution of neutron stars in binaries*, c) *the magnetic fields of the neutron stars*, d) *the radio pulsar emission mechanism*, and e) *the radio pulsars as probes of gravitational physics*. This article summarizes the science goals of the Indian neutron star community in the SKA era, with significant focus on coordinated efforts among the SKA and other existing/upcoming instruments.

1 Introduction

Since the first detection of a neutron star (NS) as a radio pulsar (Hewish et al. 1968), we now have some $\sim$ 2500 objects detected with diverse characteristic properties across almost the entire electromagnetic spectrum (Manchester et al. 2005). A consequence of this is the emergence of a large number of distinct observational classes. Over the years, the study of this huge variety of neutron stars has mainly been focused into three primary areas - i) to understand the evolutionary (or otherwise) connection between the distinct observational classes, ii) to understand the physical processes relevant in and around a neutron star and iii) to use the neutron stars as tools to understand certain aspects of fundamental physics.

All of these areas are expected to receive a tremendous boost with the advent of new generation instruments. In particular, because neutron star astronomy depends greatly on radio observations, the SKA era would be of paramount importance. Potential applications include pulsar search and survey,

*sushan@ncra.tifr.res.in

pulsar magnetospheric studies, characterisation of transient objects (like RRATs) identification of gravitational wave candidates, and so on. These will provide new insights and results in topics of fundamental importance. The combination of the high spectral, time and spatial resolution and the unprecedented sensitivity of the SKA will radically advance our understanding of basic physical processes operative in the vast population of neutron stars and provide a solid foundation for the future advancement of the field. The extent of such impact has recently been discussed in great detail in the international neutron star community (Tauris et al. 2015; Watts et al. 2015; Keane et al. 2015; Shao et al. 2015; Hessels et al. 2015; Karastergiou et al. 2015; Eatough et al. 2015; Gelfand et al. 2015; Antoniadis et al. 2015). In this document we focus on the areas of particular interest to the Indian scientists working in different areas of neutron star physics.

2 The Generation : NS - SNR associations

Canonically neutron stars are created as end products of core collapse supernovae (CC-SNe). To date only 79 of them have been spatially associated with supernovae remnants (SNR). While in most cases, the spin down ages of the pulsars match well with the life time of the SNRs, there exist several objects of comparable age, for which no SNRs have been detected in any electromagnetic band. This could be a selection effect, caused by the sensitivity limitations of the (multi-waveband) instruments, or it could be due to factors controlling the temporal and spatial evolution and emissivity of the SNRs. As the supernova shock propagates through the interstellar medium (ISM), forming an SNR, its life time dominated by the following four distinct phases.

1. The free expansion phase - This may last for several hundred years and is dominated by thermal emission, wherein the mass of the swept up ISM dust and gases is very small compared to the mass of the ejecta ($M_{\rm ISM} \ll M_{\rm ejecta}$), with the temperature of the fast moving medium being in the range $T \sim 10^6 - 10^7$ K (Chevalier 1977).

2. The adiabatic (Sedov–Taylor) expansion phase - This is reached when $M_{\rm ISM} \simeq M_{\rm ejecta}$, and in this phase the cooling ejecta also emits X-ray lines and thermal bremsstrahlung in the entire electromagnetic band from the radio to the X-rays.

3. The "snow-plow" phase - This is dominated by radiative cooling, and is reached when $M_{\rm ISM} \gg M_{\rm ejecta}$, and $T \leq 10^5$ K, leading to optical and UV line emission. This phase continues for $\sim 10^5$ year, leading to

4. The final mixing of the ISM and the ejecta such that the shell breaks up in clumps (possibly due to Rayleigh–Taylor and Kelvin–Helmholtz instabilities) and disperses the SN-provender's material, and the energy of the shock is dissipated in the ISM.

The duration for which the SNR remains in each phase, and its spectra, are determined by strength of the SNe shock, the $M_{\rm ejecta}$, the density of the CSM (all of which in turn depend on the properties of the progenitor), and also on the mass and thermodynamic properties of the ISM.

In the absence of a central compact object (CCO), SNRs are mostly identified by their morphology (shell-like, plerionic, or composite structure) and the presence of non-thermal (synchrotron) emission, emitted mainly by highly relativistic electrons accelerated by magnetic fields trapped in the remnant, along with some diffuse emission from thermal bremsstrahlung processes. While the reverse shock in a young SNR serves as a good accelerator, in older SNRs, the radio morphology (mainly filamentary emission) and luminosity also trace out regions of turbulence induced amplification of magnetic fields in the SNRs, caused by interaction with the ISM clouds. Further, the spectral index of the synchrotron emission (especially early in the lifetime of the SNR), can be changed significantly by the high energy cosmic rays (mainly protons) in the presence of strong magnetic fields (Jun & Jones 1999).

There exist several radio pulsars (PSR) with spin down ages below $\tau \simeq 10^4$ year, with magnetic field in the range of $10^{12} < \mathbf{B}_{\rm surf} \simeq 10^{14}$ G (i.e. from "ordinary" pulsars to magnetars), which have no

observational evidence of any associated SNRs (see table [1]). Likewise, while the presence of a CCO would confirm a CC-SNe, its absence in an SNR may also be because of a high kick velocity imparted to the CCO at birth, or because the emission is beamed away from us, with any thermal radiation being below the detection threshold of instruments in appropriate wavebands (young CCOs emit thermally in the 0.2-10 keV band). For example, the nearest, recent SNR, SN1987A, shows no CCO but VLA observations do show some evidence of a PWN 4. Finally, the paucity of SNR-PSR associations may simply be because (a) the canonical "age" of SNRs is being grossly over-estimated, and/or (b) the pulsar velocities at birth may have been severely under-estimated. All of these then raise important questions about galactic rate of supernovae across types, the poorly understood physics of supernovae and neutron star (or magnetar) formation, and SNe shock-ISM interaction. The high spatial resolution of SKA, and its higher sensitivity should be able to answer at least some of these, both by probing the structure of Galactic SNRs down to higher resolution and faintness, and by discovering new SNRs which may have been missed out due to limits on the current surveys.

The neutron stars associated with the CC-SNe fall into two categories; the pulsar wind nebula (PWN) and the Central Compact objects (CCO). In young pulsars, the rapid rotation and large magnetic fields ($B \geq 10^{12}$ G) accelerate particles and produce energetic winds, resulting in spin-down of the neutron star. Confinement of the pulsar winds in the surrounding medium generates luminous PWN seen all across the electromagnetic spectrum, shining most prominently in radio and X-rays. First proposed by Rees (1974), morphology of the PWNe can provide crucial information on the properties of the outflow, the interacting ambient medium and the geometry of the pulsar powering it (see (Gaensler & Slane 2006), and references therein). In the innermost regions, relativistic outflows in the form of torus and jets are formed; the geometry of which reveals the orientation of the pulsar spin axes and can provide information on the formation of kicks imparted in the moments following their formation. The larger-scale structures of the PWN provide insights on the ambient magnetic field and signatures of interaction with the supernova ejecta. The evolution of a PWN inside an SNR follows three important evolutionary phases: an initial free-expansion in the supernova ejecta, the collision between the PWN and SNR reverse shock, which crushes the PWN subjecting it to various instabilities, and eventually subsonic re-expansion of the PWN in the shock heated ejecta (Gelfand et al. 2007) and references therein). An additional later phase might also be identified, when the pulsar's motion becomes supersonic at it approaches the shell of the supernova remnant and it acquires a bow-shock morphology (van der Swaluw, Downes, & Keegan 2004).

CCOs are X-ray point-like sources found at the centre of supernova remnants (Pavlov 2005). They have a purely thermal X-ray spectrum with KT $\sim$ 0.2–0.5 keV and luminosity $\sim 10^{33} - 10^{34}$ erg s^{-1}. No radio/Gamma-ray counterparts have been found. There is also no evidence of an extended nebular emission surrounding these objects.

3 The Population

3.1 Classification

Even though some 2500 neutron stars with diverse characteristic properties have been observed, interestingly the processes responsible for the generation of the observed emitted energy are basically of three types. This leads to a simple classification of the neutron stars according to the nature of energy generation in them (Konar 2013). Primarily, we have - the rotation powered pulsars (RPP) powered by the loss of rotational energy due to magnetic braking; and the accretion powered pulsars (APP) where material accretion from a companion gives rise to energetic radiation. Then there is the new class of internal energy powered neutron stars (IENS) (for want of a better name) where the emission is suspected to come from their internal reservoir of energy (be it that of a very strong magnetic field or the residual heat of a young neutron star) (Kaspi 2010).

1. **Rotation Powered Pulsars (RPP) :** - As of now, there are about three types that fall into these category.

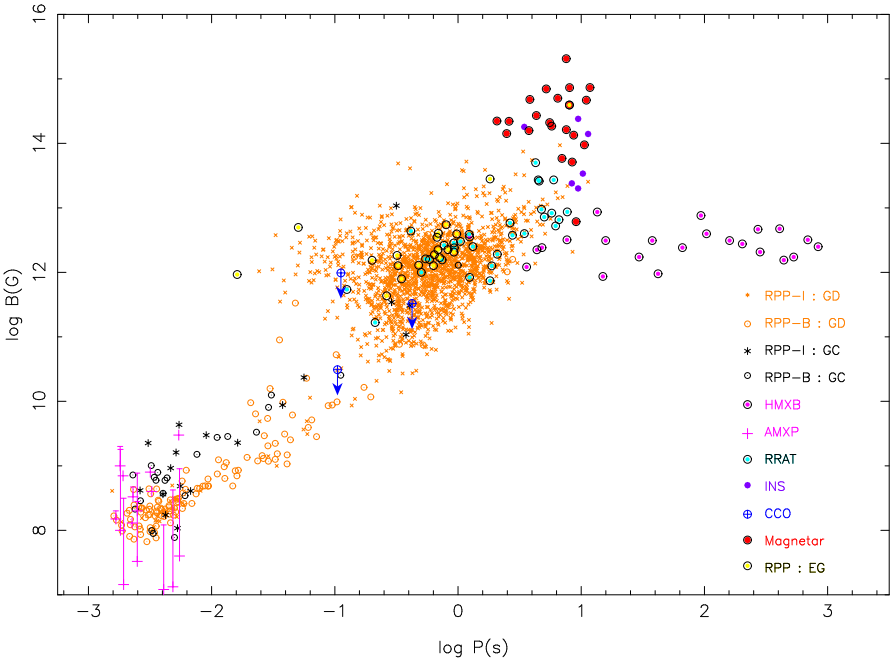

Figure 1: Different observational classes of neutron stars (with some measurement/estimate of the magnetic fields) in the $P - B$ plane.
Data : RPP - ATNF pulsar catalogue, RRAT - `http://astro.phys.wvu.edu/rratalog/`, Magnetar - `http://www.physics.mcgill.ca/ pulsar/magnetar/main.html`, AMXP - Patruno & Watts (2012), Mukherjee et al. (2015); HMXB - Caballero & Wilms (2012), INS - Haberl (2007), Kaplan & van Kerkwicjk (2009); CCO - Halpern & Gotthelf (2010), Ho (2013);
Legends : I/B - isolated/binary, GC - globular cluster, GD - galactic disc, EG - extra-galactic objects

(a) These are mainly the classical radio pulsars (**PSR** - $P \sim 1$ s, $B \sim 10^{11} - 10^{13.5}$ G), powered by the loss of rotational energy due to magnetic braking.

(b) Among the current sample of 2000+ radio pulsars known primarily in our Galaxy, millisecond radio pulsars (**MSRP** - $P \lesssim 20$ ms, $B \lesssim 10^{10}$ G) now number almost 200 (Lorimer 2009). This famous (and initially the only) sub-class of RPPs, have different evolutionary histories, involving long-lived binary systems and a 'recycling' accretion episode reducing both the spin-period and the magnetic field (Tauris 2011).

(c) The mildly recycled pulsars (**MRP**), defined as objects with $P \sim 20-100$ ms and $B_p < 10^{11}$ G. The rotating radio transients (**RRAT**) are also likely to be a sub-class of RPPs; suspected to be extreme cases of nulling/intermittent pulsars.

2. **Accretion Powered Pulsars (APP) :** - Depending on the mass of the donor star these are classified as High-Mass X-ray Binaries (HMXB) or Low-Mass X-Ray Binaries (LMXB).

   (a) Neutron stars in HMXBs typically have $B_p \sim 10^{12}$ G and O or B type companions and mostly show up as an X-ray pulsars (**XRP**) (Caballero & Wilms 2012).They have a hard X-ray spectrum (KT $>$ 15 keV). The spectrum exhibits possible signatures of interaction of the accreted material with the strong magnetic field of the neutron star in the form of Comptonisation, and the presence of broad absorption lines known as Cyclotron Resonance Scattering Features (CRSF). CRSFs are found in more than 20 XRPs, and is a direct tracer of the magnetic field strength of the neutron star from the 12-B-12 rule: $E_c = 11.6$ keV $\times \frac{1}{1+Z} \times \frac{B}{10^{12}}$ G; E_c being the centroid energy, z the gravitational red-shift and B the magnetic field strength of the neutron star.

   (b) LMXBs, on the other hand, harbour neutron stars with magnetic fields significantly weakened ($B \lesssim 10^{11}$ G) through an extended phase of accretion. Physical process taking place in such accreting systems are manifested as - thermonuclear X-ray bursts; accretion-powered millisecond-period pulsations; kilohertz quasi-periodic oscillations; broad relativistic iron lines; and quiescent emissions (Bhattacharyya 2010). These have given rise to two exciting observational classes in recent times - the accreting millisecond X-ray pulsars (**AMXP**) and the accreting millisecond X-ray bursters (**AMXB**).

3. **Internal Energy Powered Neutron Stars :** - The connecting link between these classes is the fact that the mechanism of energy generation is not obvious for any of them. For most part it is suspected that the decay of a strong magnetic field or residual cooling might be responsible for the observed emission.

   (a) **Magnetars** are thought to be young, isolated neutron stars and they shine because of the decay of their super-strong magnetic fields and are actually related to soft gamma ray repeaters (**SGR**) and anomalous X-ray pulsars (**AXP**). It is believed that the main energy source of these objects is the decay of super-strong magnetic fields (magnetar model) (Thompson & Duncan 1996).

   (b) The handful of X-ray bright compact central objects (**CCO**) are characterised by absence both of associated nebulae and of counterparts at other wavelengths and exceptionally low magnetic fields ($B \sim 10^{10}$ G). It has been suggested that a regime of hypercritical accretion immediately after the birth of the neutron star could bury the original field to deeper regions of the crust (Viganò & Pons 2012).

   (c) The seven isolated neutron stars (**INS**), popularly known as *Magnificent Seven*, are optically faint, have blackbody-like X-ray spectra ($T \sim 10^6$ K), relatively nearby and have long spin-periods ($P \sim -10$ s). They are probably like ordinary pulsars but a combination of strong magnetic field and spatial proximity make them visible in X-rays.

One of the prime challenges of neutron star research has always been to find a unifying theme to explain the menagerie presented by the disparate observational classes (shown in Fig.1]) of the neutron stars. The magnetic field, ranging from 10^8 G in MSRPs to 10^{15} G in magnetars, has been central to this theme. It plays an important role in determining the evolution of the spin, the radiative properties and

the interaction of a neutrons star with its surrounding medium. Consequently, it is the evolution of the magnetic field which link these classes.

Some of the evolutionary pathways have now become well established through decades of investigation by a number of researchers. For example, the connection between the ordinary radio pulsars with their millisecond cousins via binary processing is now an established evolutionary pathway (Bhattacharya 2002; Konar 2013; Konar, Mukherjee, & Bhattacharya 2016). On the other hand, to understand the connection between different types of isolated neutron stars a detailed theory of magneto-thermal evolution is being developed only in the last few years (see Pons, Miralles, & Geppert (2009); Kaspi (2010); and Vigano (2013) for details of these model and other references). Therefore, it appears that a scheme of grand unification, encompassing all the varieties, has started to emerge now. And it is expected that in the SKA era important gaps in this unification scheme could be filled.

3.2 Radio Pulsars : Statistical Studies

Timing irregularities seen in radio pulsar rotation rates are of two kinds - a) timing noise : continuous, noise-like fluctuations; and b) glitches. The abrupt cessation of pulsed radio emission for several pulse periods, observed in some hundred odd pulsars, is known as the phenomenon of nulling. The nature and degree of this nulling varies from one pulsar to the other. We undertake a comprehensive statistical study of these pulsars.

In the second part, we also include the intermittent pulsars and the RRATs in our study. Recently, it has been suggested that there may exist a trend for nulling activity, going from ordinary nulling pulsars to intermittents to RRATs. Here we try to quantify the nulling behaviour to check for any difference between these different classes of pulsars. With that aim we find the proximity of a given object to the death-line. We find that for any assumed death-line the statistical distribution of q d for ordinary nulling pulsars is very different from that of the RRATs. A number of scenarios were proposed to explain the new observational class of RRATs. Assuming them to be a completely separate population of neutron stars leads to the conclusion that in such a situation the inferred number of Galactic neutron stars would be totally at variance with the Galactic supernova rates (Keane et al. 2010). They have also been conjectured to be part of the normal pulsar intermittency spectrum - the case of extreme nulling, which have been shown not to hold much promise recently (Konar, Gupta, & Agarwal 2016).

A glitch is a timing irregularity of radio pulsars, marked by a sudden increase in the spin-frequency ν which may sometimes be followed by a relaxation towards its unperturbed value. These are probably caused by sudden and irregular transfer of angular momentum to the solid crust of the neutron star by a super-fluid component rotating faster; or by the crust quakes. It has been suggested that the bimodality seen within the range of glitch values actually pertain to these two separate mechanisms (Yu et al. 2013). Our statistical analysis supports the conjecture that there exist more than one glitch mechanism corresponding to different intrinsic energies. We suggest that mechanisms responsible for glitches are perhaps different for different energy regimes, originating in different regions of the star (Konar & Arjunwadkar 2014).

3.3 Radio Pulsars : Synthesis Studies

Population synthesis study is the effort to understand the cumulative properties of neutron stars in different 'classes' and to reveal the underlying physics behind such observed properties. One simple method of population synthesis study is the so called 'snapshot' method where people study the observed properties of one or more 'classes' or 'sub-classes' (Hui, Cheng, & Taam 2010; Konar 2010; Papitto et al. 2014). This method is not always sufficient to reveal the true characteristics of a 'class' of neutron stars, mainly because of our limitations in observing neutron stars. So the detailed 'full dynamical' method becomes unavoidable (Bhattacharya et al. 1992; Faucher-Giguère & Kaspi 2006; Story, Gonthier, & Harding 2007; Ridley & Lorimer 2010). In this method, one first chooses a set of initial parameters for the objects belonging to the 'class' or 'classes' under investigation (Monte-Carlo simulations), then model

the evolution of the objects with chosen parameters, as well as their observability, i.e. the probability of detection. Finally one justifies the choice of initial parameters, evolutionary models, etc., by comparing the 'observable' properties of the synthetic set of objects with the observed properties of such objects. This method sometime reveals interesting properties of the objects under investigation, e.g., the study by Bhattacharya et al. (1992) first established the fact that the magnetic field of isolated rotation powered radio pulsars does not decay. Sometimes, methods intermediate between the 'snapshot' approach and the 'full dynamical' approach have been used (Lorimer et al. 1993; Hansen & Phinney 1997; Bagchi, Lorimer, & Chennamangalam 2011; Gullón et al. 2014). Note that, because of the complexity of the 'full dynamical' approach and uncertainties in initial conditions, this method is more popular to study isolated radio pulsars with the initial point of the evolution started at the birth of the neutron stars. In principle, one can perform the study starting from the zero age main sequence phase of the progenitor of the neutron star, as theory of evolution of massive stars is well known. Similarly, there are many studies on evolution and formation of neutron stars in binaries (Bhattacharya & van den Heuvel 1991; Verbunt 1993; Portegies Zwart & Yungelson 1998; Dewi, Podsiadlowski, & Sena 2006; Belczynski et al. 2008; Kiel et al. 2008; Tauris et al. 2013), where the evolution and detectability of binary radio pulsars had not been studied. Thus population synthesis remains an open avenue, which is likely to shed more light on the physics of different sub-classes of rotation powered pulsars (for example, the RRATs) which are yet to be understood properly. Population synthesis will be useful for other areas of research as well, including gravitational wave astronomy, short GRBs etc. Moreover, there is enough scope of employing population synthesis methods to other 'classes' of neutron stars, e.g., APPs.

It is expected that the SKA will lead to discoveries of more RPPs (Smits et al. 2009; Smits et al. 2011). This larger data set will enable us to test existing and future population synthesis studies better. Also, due to its higher sensitivity and execution of motivated pulsar surveys, SKA might discover expected sub-classes of RPPs including pulsars with stellar mass black hole (BH) companions, companions, galactic centre pulsars, etc., and probably even some unexpected/unknown sub-classes. Presently, GMRT is being widely used for pulsar surveys and will be used for such purposes in the near future. Lessons learnt from GMRT pulsar surveys will help to devise efficient pulsar surveys using the SKA.

3.4 Black-widows & Redbacks : super-Jupiter companions

Observation of molecular lines in the ablated wind of super-Jupiter companions of black-widow and/or redback pulsars can provide an interesting line of investigation into the physics of these systems. The first black-widow pulsar observed is PSR B1957+20 (Fruchter, Stinebring, & Taylor 1988; Fruchter et al. 1990), a millisecond radio pulsar (P_{spin} = 6.2 ms) ablating its companion in a binary system (P_{orb} = 9.17 hr). It has been suggested (Kluzniak et al. 1988; Phinney et al. 1988) that strong gamma-ray irradiation from the millisecond pulsar drives the wind from the companion star and gives rise to a bow shock between the wind and pulsar magnetic field. The pulsar is likely to be left as an isolated millisecond pulsar after few times 10^8 yr. The observability of these binary pulsars in the black widow state implies that the lifetime of this transitory phase cannot be much shorter. Given the strong pulsar radiation and the relativistic electron-positron outflow ablating its companion to drive a comet-tail like wind, it is feasible to search for absorption lines in radio spectra.

Detection of OH line absorption through radio line spectroscopy in intra-binary space around a few millisecond pulsars has recently been suggested (Ray & Loeb 2015). A detection may lead to a better understanding of past evolutionary history of such systems as well as the composition of the companions themselves. The knowledge may help us to discern formation scenarios of ultra low mass companions of pulsars. Detection of OH lines would lead to constraints on the present state, e.g. the mass and radius of the companion. OH is usually formed by the dissociation of H_2O molecule, so it is often considered a proxy for water, the most sought after molecule in the exoplanet context. Black widow and redback pulsars have the characteristics that make them good targets for OH line detection observations since pulsar timing and optical observations allow us to determine their geometry, including the eclipsing region, well and their short orbital periods allow for repeated observations over many orbits within reasonable time-lines to build up gated exposure time on the radio pulses near eclipse ingress and egress. The geometry for a pulsar beam passing through the ablated wind of a companion orbiting a typical

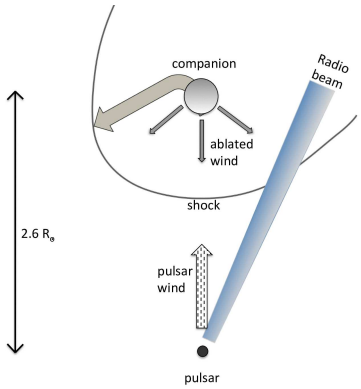

Figure 2: The geometry of a pulsar beam passing through the ablated wind from the super-Jupiter companion orbiting a black widow pulsar. The wind may be rich in Oxygen if the companion is the remnant of a star that has generated Carbon or Oxygen during its own evolutionary process.

black widow pulsar is shown in Fig. 2.

The intended targets would have to include *binary, millisecond* pulsars with high spin-down power and moderate radio flux densities, with ultra-low mass (or even comparable to Jupiter mass) companions in close orbits ($P_{orb} \sim 2 - 14$ hr). Their moderate mean flux densities and their small orbital dimensions would make them good targets for OH absorption studies against their pulsed flux. It has been argued that even with existing telescopes like GBT, Arecibo and Parkes it should be possible to detect the OH line from black-widow and redback pulsars (Ray & Loeb 2015). Such lines in absorption spectroscopy or maser emission in the (ISM) has already been detected for a few pulsars (Stanimirović et al. 2003; Weisberg et al. 2005; Minter 2008).

Future telescopes like the Square Kilometer Array (SKA) will have typically ten (SKA1-Mid) to hundred times (full SKA) flux sensitivity compared to GBT. With SKA-1 increased sensitivity in L-band (Band3) using low noise amplifiers, it will be possible to carry out such molecular line detections down to a pulsar mean flux density level of 0.7 mJy or lower, opening up several other known pulsar targets for similar studies. In addition, many newly discovered pulsar targets will become available for studies of composition of the winds from the companion.

4 The Evolution

4.1 In HMXBs

While the double neutron star (DNS) binaries and the yet to be discovered NS-BH binaries are the most promising candidates for the gravitational wave detectors, formation rates of such systems depend crucially on the formation, co-evolution, and survival rates of the massive binary stellar systems. One important phase of such binaries, in which their evolution can be measured with high accuracy is the HMXB phase in which one component has evolved to a compact star, most often a high magnetic field neutron star. The accreting neutron star in such a system is an X-ray pulsar that enables accurate measurement of the orbital parameters and its evolution. In almost all of the accreting X-ray pulsars with super-giant companion stars, the orbital evolution time scale is found to be short, less than a million year; suggesting a tidal force driven orbital evolution (Paul et al. 2011). The evolution of such systems, leading to the formation of DNS or NS-BH binaries in some of them therefore must account for the measured orbital decay rates of such systems. The orbital decay may lead to more compact configuration which will increase the survival rate during the second supernova explosion and the decay

may also lead to complete spiral-in which will lead to a single remnant. The orbital evolution of only a handful of such systems have been followed so far. Measurements of orbital decay of a large number of HMXBs are expected to be performed with Astrosat and other planned X-ray timing instruments. This would have an impact on the rate of DNS and NS-BH binary searches with the SKA and eventually have an impact on the event rate estimate of gravitational wave detectors.

4.2 In LMXBs, Transition Pulsars

MSRPs are thought to be spun up by a billion-year-long phase of angular momentum transfer in LMXBs (Alpar et al. 1982; Radhakrishnan & Srinivasan 1982). While this hypothesis is widely accepted, till recently, a direct connection between MSRPs and LMXBs was not established, because radio pulsations were not observed from an LMXB. This is very important to understand the binary evolution and accretion processes, because the extent of spinning up depends on (1) the evolution of accretion rate and structure due to the evolution of the binary properties, (2) whether accretion primarily happens via a geometrically thin accretion disk and hence transfers a large amount of angular momentum, (3) what fraction of the accreted matter leaves the system via jet and wind, (4) whether accretion happens continuously or intermittently, and so on. Observation of radio pulsation from an X-ray binary also gives us a unique opportunity to study how pulsar radiation and pulsar wind nebula affect the accretion process. Recently, three sources (PSR J1023+0038, PSR J1227-4853, PSR J1824-2452I) have shown transitions between the radio pulsar phase and the LMXB phase (Archibald et al. 2009; Roy et al. 2015; Papitto et al. 2013). Each of the three systems is a Redback system, that is a binary stellar system with an ms pulsar and a main-sequence star rotating around each other. These discoveries have confirmed that such sources can change between radio pulsar state and LMXB state back and forth. Moreover, various low-intensity X-ray states have recently been reported for these sources (Linares 2014). So, as mentioned earlier, the systems showing both radio pulsar and LMXB phases can be very useful to probe binary evolution, accretion-ejection mechanism, and so on. In order to achieve this, it is essential to discover as many such systems as possible, and study them in both radio and X-rays in various intensity states. So far, roughly 18 red-back systems are known. SKA will increase this number by at least a factor of a few (Keane et al. 2015). Moreover, the two phases may be discovered even from non-redback sources. The radio pulsation phase of this increased population should be observed and monitored with SKA. When the radio pulsation disappears, or when the source X-ray intensity increases as detected with X-ray monitors, X-ray pointed observations should be done. This way the above mentioned scientific problems can be addressed very effectively by observations with SKA and proposed X-ray observatories such as Astrosat and Athena.

4.3 Evolution of the magnetic fields

As mentioned in section 3.1, the evolution of magnetic field is one of the central ingredients in understanding the interconnections between different observational classes of the neutron stars. The evolution of the magnetic field in accreting neutron stars has been of sustained interest to a number of Indian scientists over the years. The following summarises the recent efforts in this area which is expected to get a fillip with the expected increase in the number of transient pulsars (like black-widow & redback, for example) and other categories in the SKA era.

In accreting neutron star binaries, matter is channelled along the magnetic field lines from the accretion disc to the poles forming an accretion column (Ghosh & Lamb 1978; Basko & Sunyaev 1976). The matter accumulated at the base of such accretion columns can significantly distort the local magnetic field due (Melatos & Phinney 2001; Payne & Melatos 2004; Mukherjee & Bhattacharya 2012). Understanding the evolution of the accretion mounds and its effect on the neutron star's magnetic field will help address several open questions, which can be broadly classified into two categories:

1. *Short term evolution of the accretion column:* The accreted matter will be confined by the magnetic field at the polar cap of the neutron star. However, beyond a threshold accreted mass,

pressure driven plasma instabilities will cause the matter to break out of the magnetic confinement and spread over the neutron star (Mukherjee, Bhattacharya, & Mignone 2013a; Mukherjee, Bhattacharya, & Mignone 2013b; Ferrigno et al. 2013). Such dynamic processes occurring over short time scales (local Aflven times and accretion time scales) will leave a significant imprint in the local magnetic field topology. The dynamics of the spreading of matter from accretion columns remains an unresolved question, both from observational and theoretical perspectives.

The local field topology can be directly probed from observations of cyclotron resonance scattering features (CRSF) from X-ray observations (Harding & Lai 2006). Distortions in the magnetic field is also expected to cause to complex line shapes in the CRSF profiles (Mukherjee & Bhattacharya 2012; Mukherjee, Bhattacharya, & Mignone 2013a). Due to limited capabilities of existing instruments, there have been only a few detections of asymmetric line profiles (Pottschmidt et al. 2005; Fürst et al. 2015). Future observations with Astrosat, NuStar and Hitomi is expected to constrain the physics of accretion columns further. Theoretical understanding of the interplay of radiation pressure and infalling matter and its effect on continuum radiation is also currently lacking. Such studies will help better constrain models of accretion columns which is currently used to model X-ray observations.

2. *Long term evolution of the magnetic field:* The low magnetic field strengths of millisecond pulsars have long been attributed to recycling due to accretion (Bisnovatyi-Kogan & Komberg 1974; Romani 1990). However, the exact mechanism of field decay is still unclear. Although diamagnetic screening due to field burial has been proposed (Melatos & Phinney 2001; Payne & Melatos 2004; Choudhuri & Konar 2002; Konar & Choudhuri 2004) as a possible mechanism, there is no clear consensus on whether large scale field burial is possible without re-emergence (Cumming, Zweibel, & Bildsten 2001) or if MHD instabilities (Mukherjee, Bhattacharya, & Mignone 2013a; Mukherjee, Bhattacharya, & Mignone 2013b) may inhibit deformation of field lines required to reduce the apparent dipole moment. Accretion enhanced ohmic decay of magnetic fields (Konar 1997; Konar & Bhattacharya 1997; Konar & Bhattacharya 1999) is another plausible mechanism that may reduce the magnetic fields to values observed for millisecond pulsars. However the current works do not address in detail the dynamics of spreading resulting from magnetic channelling of matter onto the neutron star, which needs to be addressed. Such studies will also help understand the evolution of magnetic field strength of accreting neutron stars from $\sim 10^{12}$ G to $\sim 10^{8}$ G in millisecond pulsars.

   Recently two accretion powered pulsars have shown evidences of long term evolution of the magnetic field through evolution of the CRSF centroid energy. Her X-1 has shown long term evolution of the CRSF independent to other observables both in the form of a sudden jump followed by a gradual decay (Staubert et al. 2014; Klochkov et al. 2015). 4U 1538-522 also shows signatures of an evolving CRSF energy (Hemphill et al. 2016).

5 The Interior

5.1 State of the matter

Shortly after the discovery of pulsars, the study of dense matter in the core of neutron stars had gained momentum (Glendenning 1996). The rapid accumulation of data on compact stars in recent years may shed light on the gross properties of cold dense matter far off normal nuclear matter density. Neutron star matter encompasses a wide range of densities, from the density of iron nucleus at the surface of the star to several times normal nuclear matter density in the core. Since the chemical potentials of nucleons and leptons increase rapidly with density in the interior of neutron stars, several novel phases with large strangeness fraction such as, hyperon matter, Bose-Einstein condensates of strange mesons and quark matter may appear there. It is to be noted that strange matter typically makes the equation of state (EoS) softer resulting in a smaller maximum mass for neutron stars than that for the nuclear EoS (Glendenning 1996).

Observed masses and radii of neutron stars are direct probes of compositions and EoS of the interior. The theoretical mass-radius relationship of compact stars could be directly compared with measured

masses and radii from various observations. Consequently, the composition and EoS of dense matter in neutron stars might be constrained. Neutron star masses have been estimated to very high degree of accuracy. This has been possible because post-Keplerian parameters such as time derivative of orbital period, advance of periastron, Shapiro delay, Einstein time delay etc. were measured in several binary pulsars. Currently the accurately measured highest neutron star mass is 2.01 ± 0.04 $M_\odot$ (Antoniadis et al. 2013). This puts a strong constraint on the EoS of neutron star matter. Those EoS which can not satisfy the 2 $M_\odot$ constraint, are ruled out (Banik, Hempel, & Bandyopadhyay 2014).

Unlike masses, radii of neutron stars have not been accurately measured yet. After the discovery of highly relativistic binary systems such as the double pulsar system, PSR J00737-3039, for which masses of both the pulsars are known accurately, it was argued that a precise measurement of moment of inertia (I) of one pulsar might overcome the uncertainties in the determination of radius (R) because dimensionally $I \propto MR^2$ (Lattimer & Schutz 2005). In relativistic binary systems, higher order post Newtonian (PN) effects could be measured. Furthermore, the relativistic spin-orbit (SO) coupling may manifest in an extra advancement of periastron above the PN contributions such that the total advance of periastron is $\dot{\omega} = \dot{\omega}_{1PN} + \dot{\omega}_{2PN} + \dot{\omega}_{SO}$ (Damour & Schafer 1988). The SO contribution has a small effect and could be measured when it is comparable to the 2PN contribution. The measurement of the SO effect leads to the determination of moment of inertia of a pulsar in the double pulsar system (Watts et al. 2015; Shao et al. 2015). With the present day timing accuracy for the pulsar A of PSR J0737-3039, the determination of moment of inertia at 10 percent level would take about 20 years.

This situation would change with the advent of the SKA. Substantial advancement in the timing precision is expected to come from the SKA. The high precision timing technique in the SKA would determine the moment of inertia of a pulsar earlier than that in the present day scenario. The accurate determination of masses and moments of inertia of pulsars in relativistic binary systems with the SKA leads to simultaneous knowledge about masses, radii and spin frequencies of pulsars which would be used to confront different theoretical models and constrain the EoS and compositions in neutron star interior or even yield the EoS in a model independent way by inverting the Tolman-Oppenheimer-Volkoff equation (Lindblom 1992). The EoS and compositions of dense matter extracted from neutron star observations are also important for the construction of EoS tables for CC-SNe simulations, neutron star mergers and understanding the appearance of strange matter in the early post bounce phase of a CC-SNe (Banik, Hempel, & Bandyopadhyay 2014).

The spin-off from the measurement of moment of inertia in the SKA era will be manifold. It was already predicted that the plot of moment of inertia versus rotational velocity (Ω) might reveal some interesting features of pulsars. It was shown that after the initial spin down of a pulsar along a supra-massive sequence, there was a spin up followed by another spin down in the I vs. Ω plane (Weber 1999; Zdunik et al. 2004; Banik et al. 2004). This is known as the back bending (S-shaped curve in the plot) phenomenon. This phenomenon was attributed to the strong first order phase transition from nuclear matter to some exotic (hyperon, kaon condensed or quark) matter. The SKA might provide an opportunity to investigate the back bending phenomenon and the existence of exotic matter in pulsars.

Another interesting possibility is the presence of super-fluidity in neutron star matter. Generally it is inferred that pulsar glitches are the manifestation of super-fluid neutron matter in neutron stars (Andersson et al. 2012). Recently, it has been argued whether the moment of inertia of the super-fluid reservoir in the inner crust is sufficient to explain the latest observational data of pulsar glitches or not (Andersson et al. 2012; Chamel 2013). When the entrainment effect which couples the neutron super-fluid with the crust, is taken into account, a larger angular momentum reservoir is needed for observed glitches (Andersson et al. 2012). Consequently, the required super-fluid moment of inertia exceeds that of the super-fluid crust. This indicates that some part of the super-fluid core would contribute to pulsar glitches. It would be worth investigating the super-fluidity in neutron stars in general and the super-fluid moment of inertia fraction for pulsar glitches in particular using the precision pulsar timing technique of the SKA.

The Indian Neutron Star Community has tremendous expertise in theoretical modelling of the EoS of dense matter and mass-radius relationships of (non)rotating neutron stars and will contribute immensely in the science programme of the SKA.

5.2 EOS constraints from thermonuclear bursts

Thermonuclear X-ray bursts are observed from neutron star low-mass X-ray binaries. These bursts originate from intermittent unstable thermonuclear burning of accumulated accreted matter on the neutron star surface (Strohmayer & Bildsten 2006). Thermonuclear bursts provide the following methods to measure neutron star parameters, and hence to constrain the theoretically proposed equation of state models of neutron star cores (see Bhattacharyya (2010) and references therein). (1) Continuum spectrum method: fitting of the continuum burst spectrum with an appropriate model can be useful to measure the neutron star radius. (2) Spectral line method: atomic spectral line observed from the surface of a neutron star provides a clean method to measure the neutron star radius to mass ratio (Bhattacharyya, Miller, & Lamb 2006). However, so far a reliable detection of such a line has not been done. (3) Photospheric radius expansion burst method: a strong burst, which shows an expansion of the photosphere, can be used to constrain the mass-radius space of neutron stars (Özel 2006). (4) Burst oscillation method: intensity variation during thermonuclear X-ray bursts, i.e., burst oscillation, provides the neutron star spin frequency with an accuracy usually much better than 1% (Chakrabarty et al. 2003). The fitting of phase-folded burst oscillation light curves with an appropriate relativistic model can be useful to measure neutron star mass and radius (Bhattacharyya et al. 2005; Lo et al. 2013). (5) Millihertz (mHz) quasi-periodic oscillation (QPO) method: mHz QPO, which originates from marginally stable thermonuclear burning on neutron stars, can be used to measure the stellar surface gravity, and hence to constrain the mass-radius space of neutron stars (Heger, Cumming, & Woosley 2007). Given the systematic uncertainties in measurements, a joint application of some of these methods can be very useful to constrain neutron star parameters. Burst properties can be studied with current and future X-ray instruments, including those of the upcoming Astrosat. In its time, only the LAXPC instrument of Astrosat will have the capability to detect burst oscillations. The above mentioned methods will be complementary to the capability of SKA to measure neutron star parameters (Watts et al. 2015).

6 The Magnetosphere

6.1 Radio Pulsars

A majority of the known neutron stars are radio pulsars, and have been detected via their radio emission. Soon after the discovery of the first pulsar (Hewish et al. 1968), it became clear that the pulsed nature of the received signal is likely due to a misalignment of the rotation and the magnetic axes of the pulsar (Radhakrishnan & Cooke 1969). Yet, a complete understanding of the underlying physical mechanisms responsible for the radio emission is far from complete.

The key to the pulsar puzzle lies in a critical understanding of the emission region geometry through a comparison of the high time resolution pulse data and high-sensitivity precision polarimetry with quantitative theoretical predictions. One of the limitations has been the lack of precision data. The radio emission region of a pulsar is small and it is at an altitude of a few hundred kilometers depending on field geometry. It is thought that the radio-loud regions in pulsar magnetosphere are ruled by plasma electrodynamics in a rotating system. The magnetic field is strong enough to constrain the plasma flow to one dimension, and quantise the gyro-motion. The induced electric field is strong enough to accelerate charges to very high Lorentz factors. A relativistic plasma within this system emits coherent radiation as a by-product of pair creation and plasma dynamics. Although this hypothesis has gained wide acceptance, it must be tested by measurements using the widest possible bandwidths, the highest possible time resolution and the best possible sensitivity of the proposed SKA. An extreme antithetical model is one in which the emission is infinitely beamed radiating tangentially to the local magnetic field lines (Gangadhara 2004).

The sensitivities and the ranges of operating frequencies of the present instruments are such that these are sufficient only for certain specific magnetospheric studies. But there exist other areas of investigation which are possible only with sufficient increase in sensitivity that will be facilitated by SKA. A subset of studies related to the pulsar emission mechanism, broadly divided on the basis of the timescales involved

and the extents of the emission regions, are discussed below.

1. *Phenomena at single pulse timescales:* There are primarily 3 kinds of intriguing phenomena observed in single pulse sequences of a significant number of pulsars — pulse-nulling, sub-pulse drifting and mode-changing. Nulling is an interesting phenomenon wherein the pulse suddenly disappears, implying possibly a complete cessation of emission or emitted flux density below the detection sensitivity of current generation telescopes. Recent studies exploiting simultaneous multi-frequency observations using different telescopes suggest that the magnetospheric changes responsible for observed nulling occur at a global scale (Gajjar et al. 2014). Detecting nulls with duration of one or only a few pulse periods has been possible only for bright pulsars. The high sensitivity of SKA will help in (1) detection of any faint emission during the apparent nulls, and (2) studying the nulling properties of faint pulsars. The increased sensitivity will also help in studying the emission properties of pulsars when the transition from one profile mode to the other takes place. Both these aspects will provide crucial inputs to modelling of physical theories explaining these phenomena.

   Sub-pulse drifting or sub-pulse modulation involves intriguing modulations in single pulse components, which indicate towards physical processes occurring at a range of timescales — from a few milliseconds to a few hundreds of seconds. A phenomenological model (carousel model) to explain sub-pulse drifting was suggested (Ruderman & Sutherland 1975) at a very early stage. The carousel model was modified to address some of the observed inconsistencies (Gil & Sendyk 2000). Significant observational advances have also been made in this direction. Several pulsars have been studied in detailed, with some studies providing strong support to the above carousel model (Vivekanand & Joshi 1999; Deshpande & Rankin 1999; Deshpande & Rankin 2001; Asgekar & Deshpande 2005) while the others indicating towards inconsistencies in the model (Edwards, Stappers, & van Leeuwen 2003; Maan & Deshpande 2014). Some other models also have been proposed (Clemens & Rosen 2004; Clemens & Rosen 2008; Jones 2013; Jones 2014) to explain the sub-pulse modulation in pulsars. Further observational progress on this front, like systematic tests of various proposed models, requires high sensitivity and good quality full-polarimetric measurements of pulsars at wide range of frequencies. Such measurements are possible with the existing telescopes only for a sample of bright pulsars. SKA will make it possible to extend these studies to even the fainter pulsars, and hence, aid in developing a robust physical model applicable to majority of pulsars.

2. *Phenomena at micro- and nano-second timescales:* Micro-structures (less-ordered intensity variations with time-scales 1 to 500 μs) are seen in nearly all bright pulsars, but no consensus has been reached as to their origins It is suspected that these are tied to plasma dynamics within the emission regions. Detection and study of micro-structures obviously needs detection of single pulses with sufficiently high signal to noise ratios (S/N).

   Giant pulse (GP) emissions – a phenomenon currently known to be exhibited by only about a dozen radio pulsars (out of nearly 2500 known) – are short-duration (sometimes as short as a few nanoseconds) burst-like sporadic increases of individual pulse intensities (Hankins et al. 2003). The peak flux densities of GPs can exceed those of regular individual pulses by factors of hundreds or even thousands. Although several mechanisms have been proposed for the observed GP emission, there is no satisfactory answer for a question as simple as following: what are the identifying characteristics of the pulsars that emit giant pulses?

   Large bandwidths are required to separate intrinsic frequency structure from that imposed by propagation through the inhomogeneous interstellar medium, i.e., interstellar scattering. New technology in the form of low-noise decade-bandwidth dual-polarisation antenna feeds and associated low-noise amplifiers are required as well as data recording systems fast enough to sample these bandwidths. The increased sensitivity facilitated by SKA will help in detection and study of microstructures as well as giant pulses from a statistically large number of pulsars. The purity of the polarisation measurements of such detections will also provide crucial help in localising the physical emission regions, and hence, in understanding the emission mechanism of these features.

3. *Ultra-wide bandwidth, ultra-high time resolution observations* are critical, because models diverge in what they predict for short time scales and fundamental emitter bandwidths. The emission changes

within one rotation period, so we must have the *highest possible sensitivity* to see individual "pulses". We need radio observations which can resolve the dynamic time-scales of the plasma (on the order of $\sim 10^{-7}$ to 10^{-5} s), the intrinsic plasma-turbulent time scales (as short as $\sim 10^{-9}$ s), and reveal the intrinsic bandwidths of the emission.

4. *Motion of emission point:* With the advent of long baseline interferometry it is possible to measure the astrometric motion of pulsar emission point with respect to rotation phase (Pen et al. 2014). The relativistic effects such as aberration and retardation (A/R) effects indeed change the locations of emission point coordinates (Gangadhara & Gupta 2001; Gupta & Gangadhara 2003; Gangadhara 2005), and they are much effective in millisecond pulsars compared to the normal ones. To resolve the emission region of a pulsar would require nano- or picoarcsecond imaging, which is challenging to achieve with the existing telescopes.

5. *Polarimetry:* Resolution of single pulses to the micro-structure level with full Stokes polarisation is required to advance our understanding of the pulsar radio emission mechanism and the propagation effects in the pulsar magnetosphere. Wave polarisation provides almost all information about the emission geometry and reflects the physics of the emission and/or propagation directly. High sensitivity is absolutely a key because useful polarimetry requires that the received signal level S substantially exceed the noise level N, e.g., $S/N \gg 1$. What determines the linear and circular polarisation of a signal? What causes the rapid orthogonal mode transitions in linear polarisation, and the rapid sign changes of circular polarisation? Are these a signature of the emission process, or a result of propagation in the pulsar magnetosphere? Although calibration techniques for accurate polarimetry are now well known, attention must be paid to the polarisation characteristics of new wide-band feed systems to assure that they can be accurately and unambiguously calibrated. To take advantage of these wide bands we will need fast digital "backend" data acquisition systems with high dynamic range to allow interference excision without corrupting pulsar signals in interference-free bands.

6. *Pulsar Emission Physics:* The SKA is expected to greatly help us to address some of the key problems in pulsar physics.

   - *How can we construct the 3D structure of pulsar emission beam?* Currently the 3D structure of pulsar emission is not clear whether it is conal or patchy. There are arguments for concentric rings near and around the magnetic field axis (Rankin 1983; Rankin 1993; Gangadhara & Gupta 2001; Mitra & Rankin 2002) or random locations in the beam rather than in some coherent conal structure (Lyne & Manchester 1988). Gangadhara & Gupta (2001) have further showed that at any given radio frequency the emissions close to magnetic axis comes from lower altitude compared to the conal emissions. The individual pulses that build the stable profile show enormous diversity in their overall characteristics. One needs to understand how the single pulses averaged to a stable mean profile. Deduction of 3D structure of the pulsar radio beam and how it forms from individual pulses, comprises a major step in revealing the pulsar radio emission mechanism. One has to study in a large survey the beam shapes of young and old pulsars to resolve this issue.
   - *Modelling of polarisation of pulsar profiles* - Both the emission process and the viewing geometry set the polarisation state of the pulsar radio emission, which is expected to be further modified by the propagation effects in pulsar magnetosphere. Gangadhara (2010) has developed a polarisation model of pulsars based on curvature emission, and shown how the S-type polarisation angle swing correlates with the sense of circular polarisation. Further, Kumar and Gangadhara (2012b, 2012a, 2013) generalised the polarisation model to include aberration-retardation and polar cap currents. Propagation effects have been observed, the most prominent being orthogonal modes of polarisation, which are generated in the magnetospheric plasma. Understanding the nature and origin of orthogonal polarisation modes in magnetospheric plasma is crucial in understanding pulsar emission physics. The observing capabilities of SKA is expected to resolve the issue of the origin of orthogonal polarisation modes: intrinsic to the emission process or generated by the propagation effects.

7. *Continuous/unpulsed/off-pulse Emission :* Presence of a continuous emission component, i.e., emission in the off-pulse regime or far from the main pulse in the profile, has been long looked for. It is

only recently that such emissions have been made from the pulsars B0525+21 and B2045−16 (Basu, Athreya, & Mitra 2011). A magnetospheric origin of such off-pulse emission raises questions about the location of the emission region. These detections have been possible due to the availability of a fast sampling time ($\sim$ 125 ms) in the interferometric mode of the GMRT. GMRT's fast sampling time is adequate to resolve the off-pulse emission only for a handful of pulsars, that too very coarsely. The strength of the off-pulse emission has also been found to be only about 1% of that of the main pulse, demanding a very high sensitivity instrument. The SKA, with its high sensitivity, possible gating in 100 bins across the pulsar period and large frequency coverage will be an ideal and much awaited telescope to carry out the off-pulse emission searches and studies.

Apart from the known emission components detailed above, very faint radio emission from a some of the gamma-ray pulsars, earlier considered to be *radio-quiet*, have been detected. Two of these gamma-ray pulsars, J0106+4855 and J1907+0602, have been found to emit in radio with L-band flux densities below 10 μJy (Pletsch et al. 2012; Abdo et al. 2010). Furthermore, another gamma-ray pulsar, J1732−3131, has been found to emit at low radio frequencies (Maan, Aswathappa, & Deshpande 2012; Maan & Aswathappa 2014; Maan et al. 2016) with an upper limit on its flux density at L-band being 50 μJy. Unusual radio emission from these gamma-ray pulsars might also be detected in the form of "giant-pulses" or bursty emission (Maan 2015). Detection of such faint or bursty radio emission from these pulsars might suggest presence of radio emission from all the gamma-ray pulsars that is below the detection sensitivity of current telescopes. The upcoming telescopes SKA and FAST, with their unprecedented sensitivities, might uncover such faint emission from these pulsars, and hence, a new class of faint radio pulsars. Detection of the faint emission with polarimetric information will also play a crucial role in understanding the location of the gamma-ray emission regions relative to the radio emission regions.

6.2 Fast Radio Bursts

Fast radio bursts (FRB) are a recently discovered (Lorimer et al. 2007; Thornton et al. 2013; Spitler et al. 2014a; Ravi, Shannon, & Jameson 2015) class of radio transients which are of very short duration ($\sim$ millisecond), show characteristics of propagation through cold, diffuse plasma, and likely originate at cosmological distances. There are different hypotheses for creation mechanism of FRBs, including super-conducting strings (Vachaspati 2008; Yu et al. 2014), merger of binary white dwarfs (Kashiyama, Ioka, & Mészáros 2013) or neutron stars (Totani 2013), collapse of supra-massive neutron stars (Falcke & Rezzolla 2014), exploding black holes (Barrau, Rovelli, & Vidotto 2014), dark matter induced collapse of neutron stars (Fuller & Ott 2015), and many others. None of the above hypotheses is established beyond doubt, and the understanding of the physical origin of FRBs remains as an open challenge. Moreover, discovery of more FRBs might lead to better understanding of the intergalactic medium (Zheng et al. 2014).

A theoretical understanding of FRBs, supplemented by a search for new FRBs in existing pulsars surveys, is of significant recent interest. Already, the Parkes FRB triggers are being investigated with the GMRT for their afterglow emissions. Moreover, there is an ongoing project to develop a transient detection system at GMRT (Bhat et al. 2013), which might be very successful to detect FRBs. More details on FRBs and description of activities and interests among Indian researchers can be found in the write-up presented by the 'Transient Science Working Group'.

7 Gravitational Physics : Pulsar probes

Two key Science goals of the SKA involve exploring the nature of relativistic gravity and to directly detect nano-Hertz gravitational waves, predicted in general relativity. At present, Pulsars in binary systems are extremely successful in testing general relativity in the strong field regime (Stairs 2003; Stairs 2004; Kramer et al. 2006; Stairs 2010). These pulsar binaries usually include neutron star-white dwarf (NS-WD) and neutron star-neutron star (NS-NS) systems. Unfortunately, neutron star-black hole (NS-BH) binaries are yet to be discovered, although different studies on such possible binaries in the Galactic disk

(Pfahl, Podsiadlowski, & Rappaport 2005; Kiel & Hurley 2009), globular clusters (Sigurdsson 2003), and near the Galactic centre (Faucher-Giguère & Loeb 2011) have been presented. If NS-BH binaries have small orbital periods (around a day), as predicted (Pfahl, Podsiadlowski, & Rappaport 2005; Kiel & Hurley 2009), these might lead to superior tests of general relativity, provided technical difficulties can be overcome. These systems might also help to determine the spin parameter of the BH and test the validity of the *Cosmic Censorship Conjecture* and to test the *BH no-hair theorem* (Shao et al. 2015). As NS-BH binaries are also important sources for gravitational waves for Advanced LIGO, understanding of the properties of these systems from pulsar data analysis will help the gravitational wave community to build better waveform templates.

The orbital dynamics of pulsars in binary systems are generally described in terms of five Keplerian and eight post-Keplerian parameters (Damour & Deruelle 1986; Kopeikin 1994; Lorimer & Kramer 2004). The leading order expressions under general relativity have been used for the post-Keplerian parameters. Measurements of these post-Keplerian parameters (through pulsar timing analysis) lead to the determination of the masses of the pulsar and the companion. For a NS-BH binary, the values of these post-Keplerian parameters will be larger, e.g., the Shapiro range parameter for a NS-BH binary is more than seven times larger than that for a NS-NS binary (Bagchi & Torres 2014). Such high values of these leading order post-Keplerian parameters for NS-BH systems imply that these terms will be measurable even with a shorter data span. Moreover, even the higher order terms might be significant, and if that is the case, one would need to incorporate these higher order terms while performing timing analysis to avoid obtaining inaccurate system parameters (Bagchi 2013; Bagchi & Torres 2014).

The central region of the galaxy has a dense population of visible stars. It is quite likely that compact objects, such as black holes (BHs) (Morris 1993; Freitag, Amaro-Seoane, & Kalogera 2006), neutron stars and Intermediate Mass Black Holes (IMBH) (Portegies Zwart et al. 2006) may also be present there. The discovery and timing of millisecond pulsars in the centre of our galaxy (hereafter GC) may allow us to detect long wavelength gravitational waves (GWs) emitted from the SGR A* region due to large mass black-holes orbiting the central super-massive black-hole (SMBH). This will allow us to "gravitationally probe" these crowded regions which are usually obscured in the electromagnetic channels (Kocsis, Ray, & Portegies Zwart 2012). The GW signal generated by a population of objects (the "foreground") is smooth if the average number per Δf frequency bin satisfies $\langle \Delta N \rangle \gg 1$. The GW spectrum becomes spiky (with $\langle \Delta N \rangle \leq 1$) above a critical frequency $f_{\rm res}$ that depends on the number of objects within 1pc of the GC and on the timing observation span. Sources within $r_{\rm res}$ generate distinct spectral peaks above frequency $f_{\rm res}$. These sources are *resolvable*. The GW spectrum transitions from continuous to discrete at higher frequencies inside the Pulsar Timing Array frequency band. If pulsars are observed repeatedly in time for an observation span $T = 10$ yr and with an interval $\Delta t = 1$ week, this can probe the range of GW frequencies: 3×10^{-9} Hz (3nHz) $<$ f $< 3 \times 10^{-6}$ Hz (3000nHz). The cosmological GW background from the whole population of massive black hole binaries (MBHBs) is actually an astrophysical "noise" for the purpose of measuring the GWs of objects orbiting SgrA*. The characteristic GW amplitudes (either of a stochastic background or of a resolvable source) can be translated into into a "characteristic timing residual" $\delta t_c(f)$ corresponding to a delay in the time of arrivals of pulses due to GWs, after averaging over the sky position and polarisation. The results of simulations are summarised in Fig 1. BHs in orbit around SMBH SgrA* generates a continuous GW spectrum with $f < 40$ nHz. A 100 ns - 10 μs timing accuracy with SKA will be sufficient to detect IMBHs (1000 $M_\odot$), if they exist, in a 3 yr observation if stable PSRs $0.1 - 1$ pc away from SgrA* are timed.

A large population of pulsars could be present inside the GC ((Pfahl & Loeb 2004)). The recent discovery of GC magnetar SGR J1745-29 in the X-ray bands with NuSTAR and subsequently in the $1.2 - 18.95$ GHz radio bands ((Bower et al. 2014), (Spitler et al. 2014b)) shows that the source angular sizes are consistent with scatter broadened size of SgrA* at each radio frequency. Additionally, pulse broadening timescale at 1 GHz ((Spitler et al. 2014b)) is several orders of magnitude lower than the scattering predicted by NE2001 model (Cordes & Lazio 2002). (Chennamangalam & Lorimer 2014) estimate an upper limit of ~ 950 potentially observable radio loud pulsars in GC. However, (Dexter & O'Leary 2014) point out that despite several deep radio surveys no ordinary pulsars have been detected very close to the GC and suggest an intrinsic deficit in the ordinary (i.e. slow) pulsar population. (Macquart & Kanekar 2015) distinguish two possible scattering scenarios affecting the search for millisecond pulsar search in the GC and suggest that in the weak scattering regime (if applicable for a large part of the

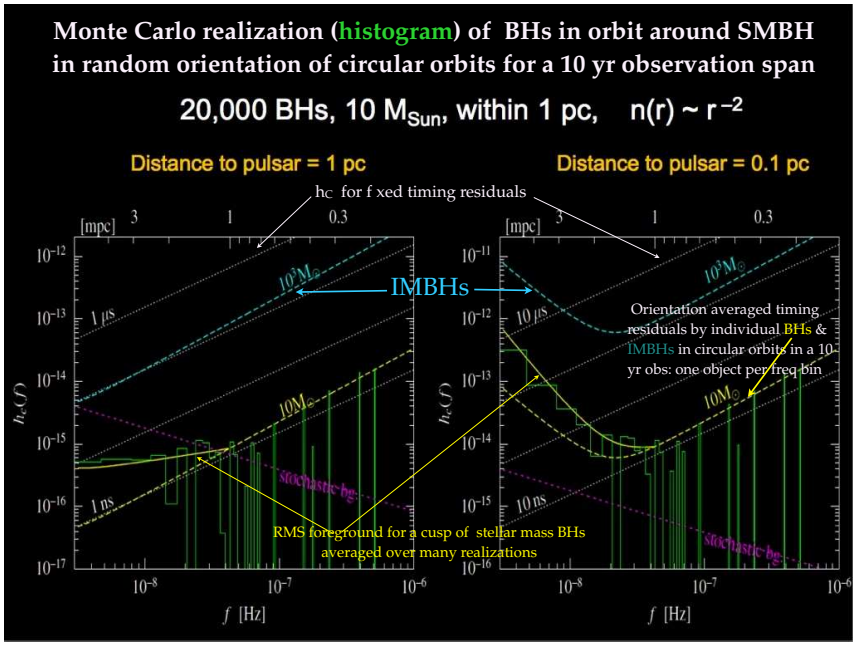

Figure 3: Detectable phase space of characteristic strain amplitude h_c and GW frequency f with pulsar timing with a probe pulsar at 1 pc (left) and 0.1 pc (right) from the Galactic Centre. Dotted white lines show the orientation-averaged h_c for fixed timing residuals measured from the probe pulsars. Yellow and cyan dashed lines show respectively the binary orientation-averaged timing residuals caused by individual stellar BHs and IMBHs on circular orbits around the SMBH in a 10 yr timing of the probe pulsar, assuming 1 object (source) per frequency bin. Green lines (histogram) show the timing residuals for a random realisation of 10 $M_\odot$ stellar BHs in the cluster (20,000 BHs within 1 pc with number density $\propto r^{-2}$). At high f, only few bins are occupied, generating a spiky signal. At lower f, many sources overlap to create a continuous spectrum. Magenta dashed lines show the cosmological stochastic GW background which can be much smaller, especially as f increases. For other (steeper) BH population density profiles or for BH orbits with isotropic thermal eccentricity distributions, see Kocsis et al (2012).

GC) a substantial fraction of the pulsars (> 1 mJy kpc^2 at 1.4 GHz) would be detected when observed with SKA-Mid in the X-band (~ 8 GHz) and possibly a smaller fraction even with EVLA and GBT at a less deep level. For the strong scattering regime however, the full high frequency (~ 25 GHz) capability of the SKA on the longer term will be necessary. The detection and long term accurate timing of stable millisecond pulsars near the GC will be of interest to the Indian partners of the SKA community from multiple perspectives of probing the contents of the galactic centre, detecting gravitational waves and tests of strong gravity.

A NS-BH system will be a very good tool to test the validity of non-conservative theories of gravity, which produce a self acceleration of the centre of mass of a binary (Bagchi & Torres 2014). Moreover, within the framework of general relativity and many other theories of gravity, any perturbation in the space-time (like rotating neutron stars or black holes, neutron stars with other compact objects as binary companions, etc.) produces ripples, i.e. gravitational waves. For the case of general relativity, the emission of the monopolar gravitational wave is forbidden by the conservation of mass and the emission of the dipolar gravitational wave is forbidden by the conservation of momentum. The quadrupolar emission remains as the lowest order mode of emission of gravitational waves under this theory. The existence of such emission has been established by measurement of the decrease of the orbital period of many NS-NS and NS-WD binaries. But there are many hypothetical alternative theories of gravity (like the 'scalar-tensor' theories) which allow emission of monopolar and dipolar gravitational waves. NS-BH systems will be better systems to detect such emissions as the combined effect of monopolar, dipolar and qudrupolar gravitational wave emission is much larger for such a system than that of NS-WD systems (Bagchi & Torres 2014). It will be interesting to probe the implications of employing adiabatic precessional equation for the orbital plane in the context of testing the *BH no-hair theorem*. It turns out that going beyond such an adiabatic approximation is relevant while constructing gravitational wave inspiral templates (Gopakumar & Schäfer 2011; Gupta & Gopakumar 2014). Going beyond the above adiabatic approximation can lead to certain quasi-periodic variations of angles that specify the orbit. This is qualitatively similar to quasi-periodic evolution of few Keplerian parameters while incorporating the effect of gravitational wave emission in a non-adiabatic manner as detailed in (Damour, Gopakumar, & Iyer 2004).

However, a NS-BH system will not be as good as a NS-WD system while trying to probe possible variation in the value of the gravitational constant G or to test strong equivalence principle (Bagchi & Torres 2014). Another interesting possibility will be to observe millisecond pulsar binaries whose companions are visible in the optical and near-infrared wavelengths with large telescopes like the Thirty Meter Telescope in the square kilometer array era. The combined optical and radio observations of such double spectroscopic binaries should eventually allow us to test 'scalar-tensor' relativity theories in certain interesting regime which are at present difficult to achieve (Khargharia et al. 2012).

On the gravitational wave aspect, we plan to pursue investigations that can provide constructs, relevant for analysing pulsar timing array data, that model gravitational waves from massive spinning black hole binaries in post-Newtonian eccentric (and hyperbolic) orbits. These investigations are expected to be influenced by (Damour, Gopakumar, & Iyer 2004; Tessmer & Gopakumar 2007; Gopakumar & Schäfer 2011; De Vittori et al. 2014) that provided accurate and effect prescription to construct post-Newtonian accurate gravitational wave templates compact binaries in non-circular orbits.

Super-massive Black Hole binaries (SMBHBs) are putative sources in nanoHertz gravitational wave astronomy. Incoherent superposition a large number of SMBHBs is expected to produce stochastic background signal for Pulsar Timing Arrays (PTA). Though it is unlikely to resolve the sources individually, such a possibility has been explored for $z<2$ (Sesana, Vecchio, & Colacino 2008; Ölmez, Mandic, & Siemens 2010; Ravi et al. 2012). The authors further study and show that with 100 pulsars, the SMBHBs can be located with 40 degree square (Sesana & Vecchio 2010). Pertaining to the early inspiral phase, the signal from such source is monochromatic in nature. The maximum likelihood approach has been further developed to explore the feasibility to localise the SMBHB source with a PTA (Babak & Sesana 2012). Recently, we have defined the figures of merit of PTA to quantify its efficiency and probe the angular resolution ability as well as the polarisation recovery of the underlying SMBHB source (Agarwal & Pai 2016). This work clearly demonstrates the idea of using PTA as a multi-detector network to detect gravitational waves from SMBHBs.

The fast spinning accreting neutron stars with an accretion mound are potential sources for the ground based gravitational wave detectors (Bildsten 1998). These sources are attractive due their spin frequency being several hundred hertz, a match with the GW detectors. At the same time, gravitational wave search from these sources are very computation intensive because its detection will require coherent analysis of data over a long period of time, a couple of years. One needs to know the spin and orbital parameters of the system and their evolution very accurately over this entire period. Otherwise, the parameters space for search is very large (Watts & Krishnan 2009) rendering it impossible and it will also reduce the significance of any detected signal. The spin and orbital evolution of a few accreting millisecond pulsars are known (Hartman et al. 2008), but unfortunately, these systems are transient, and therefore have lower average mass accretion rate, aka weak gravitation wave signal. Some transient sources, like EXO 0748-676, can however, be very potential candidate as they spend long periods in X-ray bright state and go into quiescence in between. If SKA finds radio pulsations from some of these sources in quiescence (same as the the transitional LMXBS), which will also help establish the orbital parameters, gravitation wave searches can be done over relatively smaller parameter ranges during their future X-ray bright states.

8 Multi-wavelength Studies

Observations with Astrosat will improve our understanding of neutron stars in X-ray binaries in several ways. The biggest advantage that Astrosat provides is in terms of large effective area of the LAXPC instrument, especially over a wide energy band extending upto 80 keV. Among the known and yet to be discovered LMXBs, Astrosat is likely to discover more accreting millisecond X-ray pulsars, the improved statistics will give better understanding of the mechanism and limits of the neutron star spin-up via accretion in LMXBs. Discovery of more pulsars in the process of spinning up in LMXBs, like the 11 Hz accreting pulsar in the globular cluster Terzan 5 will be additional support for the process of spinning up of neutron stars through their LMXB phase. Observations of the KHz quasi-periodic oscillations, thermonuclear burst oscillations, and thermonuclear burst spectroscopy are also likely to be significantly improved with Astrosat. All of these are very useful for understanding the EOS of neutron stars.

Astrosat will carry out a lot of study of the high magnetic field accreting neutron stars, more commonly known as accreting X-ray pulsars, most of which are found in HMXB systems. Different aspects of X-ray pulsar studies with Astrosat that are of wider interest are i) magnetic field configuration of the neutron stars, ii) possible alignment of the spin and magnetic axis, iii) magnetic field evolution in the accretion phase. Understanding of these will improve with Astrosat measurements of energy and intensity dependence of the pulse profiles of these systems and pulse phase dependence, luminosity dependence, and time dependence of the cyclotron line parameters of the X-ray pulsars. A type of relatively newly known accreting systems are the fast X-ray transients with super-giant companion stars. Though most of these systems are expected to harbour high magnetic field neutron stars, persistent X-ray pulsations have been detected in only three of these systems and cyclotron line has been detected in only one system. Astrosat observations are likely to bring more clarity to the nature of the compact objects in these systems and perhaps provide insight onto why accretion from wind in these systems give different X-ray features in the form of fast transient outbursts.

Though the immediate emphasis of this document has been the impact of SKA era on neutron star research and the immediate benefits of Astrosat, we need to remember that a large number of other high-sensitivity instruments (both in radio and higher energies) are also upcoming; many of which has active Indian participation (like, SKA, TMT, LIGO etc.). It is imperative that maximal advantage is taken of the science capabilities of these. In tables [2] & [3] we present a comprehensive list of such instruments and note down the particular kind of investigations that could be undertaken using them.

9 Summary

It is noted that the interests of the neutron star community in India correspond closely to the SKA science goals, in regard to the pulsar astronomy. We are now beginning to define theoretical calculations/simulations as well as observational projects, keeping in mind that the community can immediately make use of the recently launched X-ray instrument **Astrosat** and the upgraded GMRT (**uGMRT**) which has been given the **SKA pathfinder** status. Execution of these projects, theoretical as well as observational, would prepare the community to take appropriate use of the SKA capabilities in future.

References

Abdo A. A. et al., 2010, ApJ, 711, 64

Agarwal D., Pai A., 2016, *in prep.*

Alpar M. A., Cheng A. F., Ruderman M. A., Shaham J., 1982, Nature, 300, 728

Andersson N., Glampedakis K., Ho W. C. G., Espinoza C. M., 2012, Physical Review Letters, 109, 241103

Antoniadis J. et al., 2013, Science, 340, 448

Antoniadis J. et al., 2015, ArXiv e-prints

Archibald A. M. et al., 2009, Science, 324, 1411

Asgekar A., Deshpande A. A., 2005, MNRAS, 357, 1105

Babak S., Sesana A., 2012, Phys. Rev. D, 85, 044034

Bagchi M., 2013, MNRAS, 428, 1201

Bagchi M., Lorimer D. R., Chennamangalam J., 2011, MNRAS, 418, 477

Bagchi M., Torres D. F., 2014, J. Cosmology Astropart. Phys., 8, 55

Banik S., Hanauske M., Bandyopadhyay D., Greiner W., 2004, Phys. Rev. D, 70, 123004

Banik S., Hempel M., Bandyopadhyay D., 2014, ApJS, 214, 22

Barrau A., Rovelli C., Vidotto F., 2014, Phys. Rev. D, 90, 127503

Basko M. M., Sunyaev R. A., 1976, MNRAS, 175, 395

Basu R., Athreya R., Mitra D., 2011, ApJ, 728, 157

Belczynski K., Kalogera V., Rasio F. A., Taam R. E., Zezas A., Bulik T., Maccarone T. J., Ivanova N., 2008, ApJS, 174, 223

Bhat N. D. R. et al., 2013, ApJS, 206, 2

Bhattacharya D., 2002, Journal of Astrophysics and Astronomy, 23, 67

Bhattacharya D., van den Heuvel E. P. J., 1991, Phys. Rep., 203, 1

Bhattacharya D., Wijers R. A. M. J., Hartman J. W., Verbunt F., 1992, A&A, 254, 198

Bhattacharyya S., 2010, Advances in Space Research, 45, 949

Bhattacharyya S., Miller M. C., Lamb F. K., 2006, ApJ, 644, 1085

Bhattacharyya S., Strohmayer T. E., Miller M. C., Markwardt C. B., 2005, ApJ, 619, 483

Bildsten L., 1998, ApJ, 501, L89

Bisnovatyi-Kogan G. S., Komberg B. V., 1974, Soviet Ast., 18, 217

Bower G. C. et al., 2014, ApJ, 780, L2

Caballero I., Wilms J., 2012, Mem. Soc. Astron. Italiana, 83, 230

Chakrabarty D., Morgan E. H., Muno M. P., Galloway D. K., Wijnands R., van der Klis M., Markwardt C. B., 2003, Nature, 424, 42

Chamel N., 2013, Physical Review Letters, 110, 011101

Chennamangalam J., Lorimer D. R., 2014, MNRAS, 440, L86

Chevalier R. A., 1977, ARA&A, 15, 175

Choudhuri A. R., Konar S., 2002, MNRAS, 332, 933

Clemens J. C., Rosen R., 2004, ApJ, 609, 340

Clemens J. C., Rosen R., 2008, ApJ, 680, 664

Cordes J. M., Lazio T. J. W., 2002, ArXiv Astrophysics e-prints

Cumming A., Zweibel E., Bildsten L., 2001, ApJ, 557, 958

Damour T., Deruelle N., 1986, Ann. Inst. Henri Poincaré Phys. Théor., Vol. 44, No. 3, p. 263 - 292, 44, 263

Damour T., Gopakumar A., Iyer B. R., 2004, Phys. Rev. D, 70, 064028

Damour T., Schafer G., 1988, Nuovo Cimento B Serie, 101, 127

De Vittori L., Gopakumar A., Gupta A., Jetzer P., 2014, Phys. Rev. D, 90, 124066

Deshpande A. A., Rankin J. M., 1999, ApJ, 524, 1008

Deshpande A. A., Rankin J. M., 2001, MNRAS, 322, 438

Dewi J. D. M., Podsiadlowski P., Sena A., 2006, MNRAS, 368, 1742

Dexter J., O'Leary R. M., 2014, ApJ, 783, L7

Eatough R. P. et al., 2015, ArXiv e-prints

Edwards R. T., Stappers B. W., van Leeuwen A. G. J., 2003, A&A, 402, 321

Falcke H., Rezzolla L., 2014, A&A, 562, A137

Faucher-Giguère C.-A., Kaspi V. M., 2006, ApJ, 643, 332

Faucher-Giguère C.-A., Loeb A., 2011, MNRAS, 415, 3951

Ferrigno C., Farinelli R., Bozzo E., Pottschmidt K., Klochkov D., Kretschmar P., 2013, A&A, 553, A103

Freitag M., Amaro-Seoane P., Kalogera V., 2006, ApJ, 649, 91

Fruchter A. S. et al., 1990, ApJ, 351, 642

Fruchter A. S., Stinebring D. R., Taylor J. H., 1988, Nature, 333, 237

Fuller J., Ott C. D., 2015, MNRAS, 450, L71

Fürst F. et al., 2015, ApJ, 806, L24

Gaensler B. M., Slane P. O., 2006, ARA&A, 44, 17

Gajjar V., Joshi B. C., Kramer M., Karuppusamy R., Smits R., 2014, ApJ, 797, 18

Gangadhara R. T., 2004, ApJ, 609, 335

Gangadhara R. T., 2005, ApJ, 628, 923

Gangadhara R. T., 2010, ApJ, 710, 29

Gangadhara R. T., Gupta Y., 2001, ApJ, 555, 31

Gelfand J. D., Breton R. P., Ng C.-Y., Hessels J. W. T., Stappers B., Roberts M. S. E., Possenti A., 2015, ArXiv e-prints

Gelfand J. D., Gaensler B. M., Slane P. O., Patnaude D. J., Hughes J. P., Camilo F., 2007, ApJ, 663, 468

Ghosh P., Lamb F. K., 1978, ApJ, 223, L83

Gil J. A., Sendyk M., 2000, ApJ, 541, 351

Glendenning N., 1996, Compact Stars. Nuclear Physics, Particle Physics and General Relativity. Springer-Verlag, New York

Gopakumar A., Schäfer G., 2011, Phys. Rev. D, 84, 124007

Gullón M., Miralles J. A., Viganò D., Pons J. A., 2014, MNRAS, 443, 1891

Gupta A., Gopakumar A., 2014, Classical and Quantum Gravity, 31, 065014

Gupta Y., Gangadhara R. T., 2003, ApJ, 584, 418

Haberl F., 2007, Ap&SS, 308, 181

Halpern J. P., Gotthelf E. V., 2010, ApJ, 709, 436

Hankins T. H., Kern J. S., Weatherall J. C., Eilek J. A., 2003, Nature, 422, 141

Hansen B. M. S., Phinney E. S., 1997, MNRAS, 291, 569

Harding A. K., Lai D., 2006, Reports on Progress in Physics, 69, 2631

Hartman J. M. et al., 2008, ApJ, 675, 1468

Heger A., Cumming A., Woosley S. E., 2007, ApJ, 665, 1311

Hemphill P. B. et al., 2016, MNRAS

Hessels J. W. T. et al., 2015, ArXiv e-prints

Hewish A., Bell S. J., Pilkington J. D. H., Scott P. F., Collins R. A., 1968, Nature, 217, 709

Ho W. C. G., 2013, in IAU Symposium, Vol. 291, IAU Symposium, p. 101

Hui C. Y., Cheng K. S., Taam R. E., 2010, ApJ, 714, 1149

Jones P. B., 2013, MNRAS, 431, 2756

Jones P. B., 2014, MNRAS, 437, 4027

Jun B.-I., Jones T. W., 1999, ApJ, 511, 774

Kaplan D. L., van Kerkwijk M. H., 2009, ApJ, 692, L62

Karastergiou A. et al., 2015, ArXiv e-prints

Kashiyama K., Ioka K., Mészáros P., 2013, ApJ, 776, L39

Kaspi V. M., 2010, Proceedings of the National Academy of Science, 107, 7147

Keane E. F. et al., 2015, ArXiv e-prints

Khargharia J., Stocke J. T., Froning C. S., Gopakumar A., Joshi B. C., 2012, ApJ, 744, 183

Kiel P. D., Hurley J. R., 2009, MNRAS, 395, 2326

Kiel P. D., Hurley J. R., Bailes M., Murray J. R., 2008, MNRAS, 388, 393

Klochkov D., Staubert R., Postnov K., Wilms J., Rothschild R. E., Santangelo A., 2015, A&A, 578, A88

Kluzniak W., Ruderman M., Shaham J., Tavani M., 1988, Nature, 334, 225

Kocsis B., Ray A., Portegies Zwart S., 2012, ApJ, 752, 67

Konar S., 1997, Ph.D. thesis, JAP, Department of Physics Indian Institute of Science Bangalore, India and Astrophysics Group Raman Research Institute Bangalore, India

Konar S., 2010, MNRAS, 409, 259

Konar S., 2013, in Astronomical Society of India Conference Series, Vol. 8, Das S., Nandi A., Chattopadhyay I., ed, Astronomical Society of India Conference Series, p. 89

Konar S., Arjunwadkar M., 2014, ArXiv e-prints

Konar S., Bhattacharya D., 1997, MNRAS, 284, 311

Konar S., Bhattacharya D., 1999, MNRAS, 308, 795

Konar S., Choudhuri A. R., 2004, MNRAS, 348, 661

Konar S., Gupta Y., Agarwal D., 2016, *in prep.*

Konar S., Mukherjee D., Bhattacharya D., 2016, *in prep.*

Kopeikin S. M., 1994, ApJ, 434, L67

Kramer M. et al., 2006, Science, 314, 97

Kumar D., Gangadhara R. T., 2012a, ApJ, 754, 55

Kumar D., Gangadhara R. T., 2012b, ApJ, 746, 157

Kumar D., Gangadhara R. T., 2013, ApJ, 769, 104

Lattimer J. M., Schutz B. F., 2005, ApJ, 629, 979

Linares M., 2014, ApJ, 795, 72

Lindblom L., 1992, ApJ, 398, 569

Lo K. H., Miller M. C., Bhattacharyya S., Lamb F. K., 2013, ApJ, 776, 19

Lorimer D. R., 2009, in Astrophysics and Space Science Library, Vol. 357, Becker W., ed, Astrophysics and Space Science Library, p. 1

Lorimer D. R., Bailes M., Dewey R. J., Harrison P. A., 1993, MNRAS, 263, 403

Lorimer D. R., Bailes M., McLaughlin M. A., Narkevic D. J., Crawford F., 2007, Science, 318, 777

Lorimer D. R., Kramer M., 2004, Handbook of Pulsar Astronomy

Lyne A. G., Manchester R. N., 1988, MNRAS, 234, 477

Maan Y., 2015, ApJ, 815, 126

Maan Y., Aswathappa H. A., 2014, MNRAS, 445, 3221

Maan Y., Aswathappa H. A., Deshpande A. A., 2012, MNRAS, 425, 2

Maan Y., Deshpande A. A., 2014, ApJ, 792, 130

Maan Y., Naidu A., Joshi B. C., Roy J., Kale R., Krishnakumar A., Manoharan P., 2016, *in prep.*

Macquart J.-P., Kanekar N., 2015, ApJ, 805, 172

Manchester R. N., Hobbs G. B., Teoh A., Hobbs M., 2005, AJ, 129, 1993

Melatos A., Phinney E. S., 2001, PASA, 18, 421

Minter A. H., 2008, ApJ, 677, 373

Mitra D., Rankin J. M., 2002, ApJ, 577, 322

Morris M., 1993, ApJ, 408, 496

Mukherjee D., Bhattacharya D., 2012, MNRAS, 420, 720

Mukherjee D., Bhattacharya D., Mignone A., 2013a, MNRAS, 430, 1976

Mukherjee D., Bhattacharya D., Mignone A., 2013b, MNRAS, 435, 718

Mukherjee D., Bult P., van der Klis M., Bhattacharya D., 2015, MNRAS, 452, 3994

Ölmez S., Mandic V., Siemens X., 2010, Phys. Rev. D, 81, 104028

Özel F., 2006, Nature, 441, 1115

Papitto A. et al., 2013, Nature, 501, 517

Papitto A., Torres D. F., Rea N., Tauris T. M., 2014, A&A, 566, A64

Patruno A., Watts A. L., 2012, ArXiv e-prints, 0

Paul B., Raichur H., Jain C., James M., Devasia J., Naik S., 2011, in Astronomical Society of India Conference Series, Vol. 3, Astronomical Society of India Conference Series, p. 29

Pavlov G., 2005, in Neutron Stars at the Crossroads of Fundamental Physics

Payne D. J. B., Melatos A., 2004, MNRAS, 351, 569

Pen U.-L., Macquart J.-P., Deller A. T., Brisken W., 2014, MNRAS, 440, L36

Pfahl E., Loeb A., 2004, ApJ, 615, 253

Pfahl E., Podsiadlowski P., Rappaport S., 2005, ApJ, 628, 343

Phinney E. S., Evans C. R., Blandford R. D., Kulkarni S. R., 1988, Nature, 333, 832

Pletsch H. J. et al., 2012, ApJ, 744, 105

Pons J. A., Miralles J. A., Geppert U., 2009, A&A, 496, 207

Portegies Zwart S. F., Baumgardt H., McMillan S. L. W., Makino J., Hut P., Ebisuzaki T., 2006, ApJ, 641, 319

Portegies Zwart S. F., Yungelson L. R., 1998, A&A, 332, 173

Pottschmidt K. et al., 2005, ApJ, 634, L97

Radhakrishnan V., Cooke D. J., 1969, Astrophys. Lett., 3, 225

Radhakrishnan V., Srinivasan G., 1982, Current Science, 51, 1096

Rankin J. M., 1983, ApJ, 274, 333

Rankin J. M., 1993, ApJ, 405, 285

Ravi V., Shannon R. M., Jameson A., 2015, ApJ, 799, L5

Ravi V., Wyithe J. S. B., Hobbs G., Shannon R. M., Manchester R. N., Yardley D. R. B., Keith M. J., 2012, ApJ, 761, 84

Ray A., Loeb A., 2015, ArXiv e-prints

Rees M. J., Gunn J. E., 1974, MNRAS, 167, 1

Ridley J. P., Lorimer D. R., 2010, MNRAS, 404, 1081

Romani R. W., 1990, Nature, 347, 741

Roy J. et al., 2015, ApJ, 800, L12

Ruderman M. A., Sutherland P. G., 1975, ApJ, 196, 51

Sesana A., Vecchio A., 2010, Phys. Rev. D, 81, 104008

Sesana A., Vecchio A., Colacino C. N., 2008, MNRAS, 390, 192

Shao L. et al., 2015, ArXiv e-prints

Sigurdsson S., 2003, in Astronomical Society of the Pacific Conference Series, Vol. 302, Bailes M., Nice D. J., Thorsett S. E., ed, Radio Pulsars, p. 391

Smits R., Kramer M., Stappers B., Lorimer D. R., Cordes J., Faulkner A., 2009, A&A, 493, 1161

Smits R., Tingay S. J., Wex N., Kramer M., Stappers B., 2011, A&A, 528, A108

Spitler L. G. et al., 2014a, ApJ, 790, 101

Spitler L. G. et al., 2014b, ApJ, 780, L3

Stairs I. H., 2003, Living Reviews in Relativity, 6, 5

Stairs I. H., 2004, Science, 304, 547

Stairs I. H., 2010, in IAU Symposium, Vol. 261, Klioner S. A., Seidelmann P. K., Soffel M. H., ed, IAU Symposium, p. 218

Stanimirović S., Weisberg J. M., Dickey J. M., de la Fuente A., Devine K., Hedden A., Anderson S. B., 2003, ApJ, 592, 953

Staubert R., Klochkov D., Wilms J., Postnov K., Shakura N. I., Rothschild R. E., Fürst F., Harrison F. A., 2014, A&A, 572, A119

Story S. A., Gonthier P. L., Harding A. K., 2007, ApJ, 671, 713

Strohmayer T., Bildsten L., 2006, Lewin W. H. G., van der Klis M., ed, New views of thermonuclear bursts. p. 113

Tauris T. M., 2011, in Astronomical Society of the Pacific Conference Series, Vol. 447, Schmidtobreick L., Schreiber M. R., Tappert C., ed, Evolution of Compact Binaries, p. 285

Tauris T. M. et al., 2015, ArXiv e-prints

Tauris T. M., Sanyal D., Yoon S.-C., Langer N., 2013, A&A, 558, A39

Tessmer M., Gopakumar A., 2007, MNRAS, 374, 721

Thompson C., Duncan R. C., 1996, ApJ, 473, 322

Thornton D. et al., 2013, Science, 341, 53

Totani T., 2013, PASJ, 65, L12

Vachaspati T., 2008, Physical Review Letters, 101, 141301

van der Swaluw E., Downes T. P., Keegan R., 2004, A&A, 420, 937

Verbunt F., 1993, ARA&A, 31, 93

Viganò D., 2013, Ph.D. thesis, University of Alicante

Viganò D., Pons J. A., 2012, MNRAS, 425, 2487

Vivekanand M., Joshi B. C., 1999, ApJ, 515, 398

Watts A. et al., 2015, ArXiv e-prints

Watts A. L., Krishnan B., 2009, Advances in Space Research, 43, 1049

Weber F., ed, 1999, Pulsars as astrophysical laboratories for nuclear and particle physics

Weisberg J. M., Johnston S., Koribalski B., Stanimirović S., 2005, Science, 309, 106

Yu M. et al., 2013, MNRAS, 429, 688

Yu Y.-W., Cheng K.-S., Shiu G., Tye H., 2014, J. Cosmology Astropart. Phys., 11, 40

Zdunik J. L., Haensel P., Gourgoulhon E., Bejger M., 2004, A&A, 416, 1013

Zheng Z., Ofek E. O., Kulkarni S. R., Neill J. D., Juric M., 2014, ApJ, 797, 71

Table 1. Pulsars with no associated SNRs

	Name	Association	τ_s Yr	$\mathbf{B}_s$ G	$\dot{E}_{\rm rot}$ erg.s^{-1}
1	J1050-5953	XRS	2.68e+03	5.02e+14	5.6e+33
2	J1023-5746	GRS(F)	4.6e+03	6.62e+12	1.1e+37
3	J1838-0537	*	4.89e+03	8.39e+12	6.0e+36
4	J0100-7211	EXGAL:SMC,XRS	6.76e+03	3.93e+14	1.4e+33
5	J1357-6429	XRS:PWN	7.31e+03	7.83e+12	3.1e+36
6	B1610-50	*	7.42e+03	1.08e+13	1.6e+36
7	J1617-5055	GRS	8.13e+03	3.1e+12	1.6e+37
8	J1734-3333	*	8.13e+03	5.22e+13	5.6e+34
9	J1708-4008	XRS	8.9e+03	4.7e+14	5.8e+32
10	J1418-6058	GRS(F),GRS(H)	1.03e+04	4.38e+12	4.9e+36
11	J1301-6305	*	1.1e+04	7.1e+12	1.7e+36
12	J1809-1943	XRS(AXP)	1.13e+04	2.1e+14	1.8e+33
13	J1746-2850	*	1.27e+04	3.85e+13	4.2e+34
14	J1420-6048	GRS(F),GRS(H)	1.3e+04	2.41e+12	1.0e+37
15	J1413-6141	*	1.36e+04	9.88e+12	5.6e+35
16	J1826-1256	GRS(F),XRS(AXP),PWN	1.44e+04	3.7e+12	3.6e+36
17	J1702-4310	*	1.7e+04	7.42e+12	6.3e+35
18	J2021+3651	GRS,GRS(F)	1.72e+04	3.19e+12	3.4e+36
19	J2111+4606	GRS(F)	1.75e+04	4.81e+12	1.4e+36
20	J2004+3429	*	1.85e+04	7.14e+12	5.8e+35
21	B1046-58	GRS(F)	2.03e+04	3.49e+12	2.0e+36
22	B1737-30	*	2.06e+04	1.7e+13	8.2e+34
23	J1856+0245	GRS(H),XRS (AXP)	2.06e+04	2.27e+12	4.6e+36
24	J1935+2025	*	2.09e+04	2.23e+12	4.7e+36
25	B1823-13	GRS,XRS:PWN	2.14e+04	2.8e+12	2.8e+36
26	J1934+2352	*	2.16e+04	4.89e+12	9.1e+35
27	J1958+2846	GRS(F)	2.17e+04	7.94e+12	3.4e+35
28	J1838-0655	XRS (AXP), GRS(H)	2.27e+04	1.89e+12	5.5e+36
29	J1135-6055	*	2.3e+04	3.05e+12	2.1e+36
30	J1909+0749	*	2.47e+04	6.07e+12	4.5e+35
31	J1410-6132	*	2.48e+04	1.28e+12	1.0e+37
32	J1747-2958	GRS (PWN)	2.55e+04	2.49e+12	2.5e+36
33	B1727-33	*	2.6e+04	3.48e+12	1.2e+36
34	J2238+5903	GRS(F)	2.66e+04	4.02e+12	8.9e+35
35	J1821-1419	*	2.93e+04	3.89e+13	7.8e+33
36	J1841-0524	*	3.02e+04	1.03e+13	1.0e+35
37	J1524-5625	*	3.18e+04	1.77e+12	3.2e+36
38	J1112-6103	*	3.27e+04	1.45e+12	4.5e+36
39	J1718-3718	*	3.32e+04	7.47e+13	1.7e+33
40	J1837-0604	*	3.38e+04	2.11e+12	2.0e+36
41	J1833-0831	XRS (SGR)	3.49e+04	1.63e+14	3.1e+32
42	J0729-1448	*	3.52e+04	5.4e+12	2.8e+35
43	J1932+1916	*	3.54e+04	4.46e+12	4.1e+35
44	J1551-5310	*	3.68e+04	9.52e+12	8.3e+34
45	J1907+0918	*	3.8e+04	4.67e+12	3.2e+35
46	J1015-5719	*	3.86e+04	2.87e+12	8.3e+35
47	B1930+22	*	3.98e+04	2.92e+12	7.5e+35
48	J1044-5737	GRS(F)	4.03e+04	2.79e+12	8.0e+35
49	J1815-1738	*	4.04e+04	3.98e+12	3.9e+35
50	J1637-4642	*	4.12e+04	3.06e+12	6.4e+35
51	J1849-0001	XRS,GRS,GRS(H)	4.29e+04	7.49e+11	9.8e+36
52	J1745-2900	XRS (AXP)	4.31e+04	7.3e+13	1.0e+33
53	J1813-1246	GRS	4.34e+04	9.3e+11	6.2e+36
54	J0631+1036	GRS(F)	4.36e+04	5.55e+12	1.7e+35
55	J0940-5428	*	4.22e+04	1.72e+12	1.9e+36
56	J0631+1036	GRS(F)	4.36e+04	5.55e+12	1.7e+35
57	J1524-5706	*	4.96e+04	2.02e+13	1.0e+34
58	J1412-6145	*	5.06e+04	5.64e+12	1.2e+35
59	J1809-1917	XRS (PWN)	5.13e+04	1.47e+12	1.8e+36
60	J1737-3137	*	5.14e+04	8e+12	6.0e+34
61	J1838-0453	*	5.22e+04	6.72e+12	8.3e+34

Table 1 (cont'd)

62	J1055-6028	GRS	5.35e+04	1.74e+12	1.2e+36
63	J1702-4128	*	5.51e+04	3.12e+12	3.4e+35
64	J1422-6138	*	5.58e+04	5.81e+12	9.6e+34
65	J1841-0345	*	5.59e+04	3.48e+12	2.7e+35
67	J0633+0632	GRS(F)	5.92e+04	4.92e+12	1.2e+35
68	J1429-5911	GRS(F)	6.02e+04	1.9e+12	7.7e+35
69	J1406-6121	*	6.17e+04	3.45e+12	2.2e+35
70	J1938+2213	*	6.2e+04	2.69e+12	3.7e+35
71	J0248+6021	GRS(F)	6.24e+04	3.5e+12	2.1e+35
72	J1541-5535	*	6.25e+04	4.77e+12	1.1e+35
73	J1413-6205	GRS(F)	6.28e+04	1.76e+12	8.3e+35
74	J1806-2125	*	6.29e+04	7.74e+12	4.3e+34
75	J1105-6107	XRS	6.33e+04	1.01e+12	2.5e+36
76	J1459-6053	GRS(F)	6.47e+04	1.63e+12	9.1e+35
77	J1850-0026	*	6.75e+04	2.58e+12	3.3e+35
78	J0534-6703	EXGAL:LMC	6.78e+04	2.81e+13	2.8e+33
79	J0146+6145	XRS	6.91e+04	1.33e+14	1.2e+32
80	J1954+2836	GRS(F)	6.94e+04	1.42e+12	1.0e+36
81	J1636-4440	*	7.01e+04	3.14e+12	2.1e+35
82	J1857+0143	*	7.1e+04	2.11e+12	4.5e+35
83	J1601-5335	*	7.33e+04	4.29e+12	1.0e+35
84	J1828-1101	*	7.71e+04	1.05e+12	1.6e+36
85	J0901-4624	*	8e+04	6.29e+12	4.0e+34
86	B1727-47	*	8.04e+04	1.18e+13	1.1e+34
87	J1855+0527	*	8.26e+04	1.95e+13	3.9e+33
88	J1928+1746	*	8.26e+04	9.64e+11	1.6e+36
89	J1847-0130	*	8.33e+04	9.36e+13	1.7e+32
90	J1705-3950	*	8.34e+04	4.45e+12	7.4e+34
91	J1814-1744	*	8.46e+04	5.51e+13	4.7e+32
92	J1738-2955	*	8.58e+04	6.1e+12	3.7e+34
93	J1638-4608	*	8.56e+04	3.83e+12	9.4e+34
94	J1803-2149	GRS(F)	8.63e+04	1.46e+12	6.4e+35
95	B1916+14	*	8.81e+04	1.6e+13	5.1e+33
96	B0611+22	*	8.93e+04	4.52e+12	6.2e+34
97	J1718-3825	GRS(F),GRS(H)	8.95e+04	1.01e+12	1.3e+36
98	J1028-5819	GRS(F)	9e+04	1.23e+12	8.3e+35
99	J1913+0446	*	9.18e+04	2.15e+13	2.6e+33
100	J1558-5756	*	9.54e+04	1.46e+13	5.2e+33
101	J1531-5610	*	9.71e+04	1.09e+12	9.1e+35
102	J1909+0912	*	9.87e+04	2.86e+12	1.3e+35
103	J2216+5759	*	9.62e+04	5.44e+12	3.7e+34

*List of all pulsars with spin down ages $< 10^5$ year, with no associated supernova remnant. The list is in ascending order of age, and the surface magnetic field ($\mathbf{B}_{surf}$), and rotational energy ($\dot{E}_{\rm rot}$) of the pulsar are provided. Extragalactic sources, those associated with pulsar wind nebulae (PWN), magnetars (SGRs or AXPs) or any other spatially coincident X-ray source (XRS), or Gamma-ray source (GRS) discovered by Fermi (F) or Hess (H) is indicated. For further details of pulsar properties, associations and references, please see the ATNF pulsar catalogue.

Table 2. Pulsar studies with high sensitivity ***Radio Telescopes***

	Name & Location	Type	Operating Frequency†	Pulsar Studies*	Remarks
1	Arecibo Telescope, Puerto Rico	Single dish	0.3–10 GHz	1, 2, 3	The world's largest single-dish; 305 m
2	Parkes Radio Telescope, Australia	Single dish	0.7–26 GHz	1, 2, 3	64 m dish
3	GBT, Green Bank, USA	Single dish	0.29–115.3 GHz	2, 1, 3	World's largest (100 m) fully steerable single-dish
4	Effelsberg Telescope, Germany	Single dish	0.4–95 GHz	2, 1, 3	100 m dish
5	Lovell Telescope, England	Single dish	0.4–6 GHz	1, 2, 3	76 m dish
6	GMRT, Pune, India	Interferometer	150–1420 MHz	3, 1, 2	30 dishes (45 m); largest telescope at meter wavelengths, SKA pathfinder
7	Nancay Radio Telescope, France	Kraus-type design	1.1–3.5 GHz	1, 2	single-dish antenna equivalent to that of a 94-m-diameter parabolic dish
8	LOFAR, (mainly) Netherlands	Dipole array	10–240 MHz	3, 1, 2	Low frequency array of crossed-dipole antennas at 1.25 to 30m wavelengths
9	Ooty radio telescope, India	Cylindrical Paraboloid	326.5 MHz	3, 2	530 m × 30 m paraboloid
10	Gauribidanur telescope, India	Dipole Array	34 MHz	3, 1	640 dipoles in East-West direction (originally 1000 dipoles in in a "T" configuration)
11	LWA, Socorro, USA	Dipole array	10–88 MHz	3, 1	256 crossed-dipoles
12	UTR–2, Ukraine	T-shaped dipole array	8–40 MHz	3	Largest telescope at decametre wavelengths (collecting area 150,000 m^2)
13	MWA, Australia	Interferometric	80–300 MHz	3, 2, 1	128× 16-element cross-polar antennas
14	BSA, Pushchino, Russia	dipole array	100 MHz	3	16384 dipoles
15	DKR-1000, Pushchino, Russia	parabolic cylinder	30–120 MHz	3	1000 m × 40 m cylindrical paraboloids (East-West and North-South)
16	HartRAO, South Africa	Single dish	1.66–23 GHz	2	26 m dish
17	WSRT, Netherlands	Interferometer	0.3–8.5 GHz	2	14 dish × 25 ms

*Pulsar studies could be generally linked to primarily three observational kinds — 1: Pulsar searches; 2: Pulsar timing; and 3: Study of pulsar emission mechanisms and interstellar medium properties. The order as well as the main types of studies that have been (or potentially could be) carried out using a particular telescope, are subjective, and entirely a reflection of the author's perception.

†The operating frequency range is nominal, and the observing frequency range may vary depending on the receivers and back-end.

Table 3. Neutron Star studies with ***High-Energy Instruments****

	Mission	Launch Date	Status	Neutron Star Studies
1	Astrosat	current		cyclotron line, KHz QPOs with large area and broad energy coverage
2	Chandra	current		accurate position/identification, faint source flux measurement, high resolution spectroscopy
4	Fermi	current		frequency evolution, accretion torque, magnetar outbursts
5	Integral	current		HMXB outbursts, Cyclotron line evolution, Highly absorbed systems
6	MAXI	current		accreting NS systems, orbital coverage for spectral study of bright sources
7	NuStar	current		cyclotron line - new sources, spectral measurement
8	Suzaku	current		cyclotron line, broad band spectroscopy
9	Swift	current		super-giant Fast X-ray Transients, all sky monitoring in hard X-rays
3	XMM	current		iron line shape, high resolution and high throughput spectroscopy, M/R from line during bursts
10	Hitomi	current		highest resolution spectroscopy, plasma diagnostics, cyclotron lines, broadest band (NuStar++)
11	NICER	2017	approved	EOS, soft X-ray spectral and timing studies with large area
13	HXMT	2017	approved	
14	eXTP	2025	potential	soft X-ray imaging, polarimetry, perhaps EOS & strong gravity
15	Athena	2028	approved	
12	eRosita		approved	medium energy X-ray survey, new members/population of sources? More magnetars?
16	POLIX		approved	magnetic field structures, emission mechanism in accreting and young NS.

*Authentic list of current and past observatories are at `http://heasarc.gsfc.nasa.gov/docs/observatories.html`

Neutron stars in the light of SKA: Data, statistics, and science

Mihir Arjunwadkar*[1], Akanksha Kashikar[2], and Manjari Bagchi[3]

[1] *Centre for Modeling and Simulation, Savitribai Phule Pune University, Ganeshkhind, Pune 411007 India*
[2] *Department of Statistics, Savitribai Phule Pune University, Ganeshkhind, Pune 411007 India*
[3] *The Institute of Mathematical Sciences, Taramani, Chennai 600113 India*

Abstract

The square-kilometer array (SKA) is expected to enrich the neutron star (NS) catalogues by at least an order of magnitude over their current state. In this article, we present a meta-analysis (from a methodological viewpoint) of statistical analyses performed using existing NS data, with a two-fold goal. First, this should bring out how statistical models and methods are shaped and dictated by the science problem being addressed. Second, it is hoped that these analyses will provide useful starting points for deeper analyses involving richer data from SKA whenever it becomes available.

1 Introduction

The twenty-first century science has been aptly described as *large data sets, complex questions* science (Effron, 2011). Astronomy and astrophysics are no exceptions, with well-known examples including extensive sky surveys (Brunner et al., 2002) and observational cosmology (Hamilton, 2014). In the context of radio astronomy the square-kilometer array (SKA) is expected to enrich the neutron star (NS) physics by increasing the observed NS population by at least an order of magnitude over its current size. This would also imply discovery of new objects leading to better sampling of under-represented NS categories, precision measurements of intrinsic properties such as spin period and magnetic field, and high quality data on pulsar magnetospheric phenomena such as micro-structures, nulling, mode-changing, glitching, etc. On the one hand, this will present a unique opportunity to seek answers to interesting and fundamental questions about the extreme physics underlying these exotic objects in the universe. On the other hand, with an unprecedented increase in the data size and complexity great refinements in statistical and computational methods would be necessary. This article presents case studies intended to illustrate how statistical methods may be meaningfully devised or adopted in the light of appropriate questions.

Two important lessons have been learnt in the course of this work. First, the methodologies need to be tested on the available data to understand their limits and suitability keeping in mind that eventually the data volumes would become much larger. Second, it would be important to involve scientists from allied fields (eg. statistics and computer/computational science) for a fresher perspective on the handling of the data. We believe these lessons would be of significance in the large-data regime of the SKA era.

2 Neutron Star taxonomy

What different categories of NS objects are suggested by the available data? Data-driven taxonomy of NS objects is an imminent direction for methodological research in the light of SKA. Arguably, the most precise measurements available for NS are for the two fundamental intrinsic properties, namely, spin period and magnetic field. In principle, any other available measurements can also be used for this purpose. Such data-driven research can benefit immensely from the use of advanced statistical methods for data modeling, identifying potential outliers, clustering/classification together with investigation of the most typical or atypical elements in a class, density estimation, regression, statistical/machine learning etc. (Hastie et al., 2009; Wasserman, 2004, 2006).

*mihir.arjunwadkar@gmail.com

A work in progress (Kashikar et al., 2016) explores machine learning methods to categorize NS using their two fundamental intrinsic properties (spin period and magnetic field). Specifically, we have explored a few standard clustering methods such as hierarchical clustering, k-means, k-medoids, etc. Optimal number of clusters needs to be decided up-front in these approaches, and most methods for this purpose rely on different criteria that take into account the within-cluster and between-cluster variability of clustering (Hastie et al., 2009). For available NS data, the optimal number of clusters turns out to be 2 or 3, primarily separating regular pulsars from millisecond pulsars. However, the within-cluster variability is quite high. Further, because the two intrinsic properties are highly correlated positively, it turns out that clustering carried out using magnetic field *alone* provides nearly the same results. This suggests that additional information on other variables, possibly orthogonal to the two existing ones, should provide better classification. Supervised learning (i.e., classification) methods can be employed to assess the role of these variables in corroborating the existing (physics-based) classification. Our preliminary results (not shown) indicate that the existing NS groups are not linearly separable on the basis of these two variables alone: This again underscores the need for reliable data on other NS characteristics so as to improve data-driven classification. Unequal class sizes pose another challenge with these data. The performance of many supervised classification algorithms is adversely affected by variation in group sizes. Further, commonly used measures of misclassification such as accuracy fail to take into account the effect of unequal group sizes. For example, if 5 observations from a group of size 20 are misclassified, that results into a misclassification rate of 25% for that particular group. However, if the total number of observations is large, the overall misclassification rate reported to be low due to less misclassification in the bigger groups. Hence, while developing or adopting classification methods, this issue needs to be taken into consideration.

3 Radio Pulsar Statistics

3.1 Glitch : multiple populations?

Do the pulsar glitch data support the above view that there could be more than one mechanism responsible for producing glitches? What do the data say about the glitch distribution having more than one mode? These questions are addressed in (Konar and Arjunwadkar, 2014). Because the estimated error bars on glitch magnitudes are at least an order-of-magnitude smaller, we decided to ignore them and to consider the glitch magnitudes as well-determined, precise data. This can be thought of as a data-modeling assumption that simplifies the subsequent analysis, because if the glitch data were not so precise, then what may appear multimodal in one data set may not appear so in another.

Given the nature of the question, it was natural to consider formulating this problem as a statistical inference problem involving hypothesis tests where the null hypothesis is that of unimodality. The specific tests we applied to a recent version of a glitch data set (Espinoza et al., 2011) were the dip test (Hartigan and Hartigan, 1985), the Silverman test (Silverman, 1981; Hall and York, 2001), and the bimodality test (Holzmann and Vollmer, 2008). The individual p-values of all tests suggest strong evidence against the null hypothesis of unimodality. While applying a battery of hypothesis tests to a data set may not seem like a good statistical practice, this was done here for exploratory purposes only to arrive at tentative qualitative conclusions.

We also considered a more general scenario in which the data may be unimodal but has the structure suggestive of a mixture of multiple populations. This suggested modeling the glitch data using a mixture model; specifically, a mixture of Gaussian probability distributions (McLachlan and Peel, 2000) each representing one glitch mechanism. The Gaussianity assumption can be contested. For example, self-organized criticality considerations (see, e.g., Aschwanden (2011)), if applicable in the glitch context, may suggest a mixture of Pareto-like power-law distributions. It was used here only to see if there is enough structure to glitch data to support the multiple-populations view. Use of Gaussian mixtures, in particular, can lead to serious over-fitting and identifiability problems, which could invalidate an analysis or render it inconclusive. This pathology was avoided through judicious use of BIC-based model selection (Burnham and Anderson, 2002), and the results suggest structure in the glitch probability distribution which supports the multiple populations view.

3.2 Nulling fraction

Certain pulsars cease to emit pulses abruptly for one or more consecutive periods. this phenomenon is called *nulling* (Backer, 1970). The proportion of pulses not emitted, which is a gross measure of the extent of nulling, is called the *null fraction* (NF). The phenomenon of nulling, along with related phenomena such as mode-changing, intermittency, micro-structure, etc., are important for an understanding of the emission mechanisms operative in pulsars. The portions of a pulse with and without appreciable emission are called, respectively, the *on-pulse* and *off-pulse* parts. NF is conventionally estimated using pulse energy data, by matching off-pulse and on-pulse energy histograms (Ritchings, 1976). This approach, although simple and popular, relies on histograms and thereby on an *ad hoc* choice of the histogram bin width. Such *ad hoc* approaches that do not have firm grounding in statistical theory come with little or no formal guaranties (e.g., regarding their behaviour in the asymptotic regime, contamination in the data, etc.). Further, obtaining error bars in the form of valid confidence intervals is usually difficult in such approaches.

This problem of estimating NF together with valid confidence intervals is considered in Arjunwadkar et al. (2016), where we use Gaussian mixture models (McLachlan and Peel, 2000) to model the on-pulse energy distribution. This methodology comprises of Gaussian mixtures to model the pulse energy data, a robust multivariate method to identify outliers in the data, the EM algorithm to fit models to the data, BIC-based model selection (Burnham and Anderson, 2002) to choose an optimal mixture model, and two bootstrap prescriptions for computing confidence intervals on the null fraction (Wasserman, 2004). We have presented results on archival Giant Meterwave Radio Telescope (GMRT) data for a set of well-characterized pulsars to illustrate and validate the methodology.

A key feature of this methodology is the use of off-pulse energy distribution parameters to constrain the null-pulse Gaussian in the mixture model. Together with BIC-based model selection, this use of available information helps alleviate the identifiability and over-fitting problems notoriously associated with Gaussian mixtures. Compared to the conventional method, this methodology works well even for data with moderately low signal-to-noise ratio (SNR). Indeed, a companion paper (Rajwade et al., 2016) applies this methodology to investigate nulling in millisecond pulsars where the SNR is quite low.

This methodology can be criticized on two counts. First, the computational cost, which scales with the data size and the number of bootstrap replications, can be high especially for large data sets. (Thankfully, the bootstrap is a happily parallel computation.) Second, from a statistical modeling viewpoint, is such detailed model as a Gaussian mixture really necessary if the purpose is only to obtain NF? Perhaps not. Our hope is that, in future, such detailed modeling of the on-pulse energy distribution, which can be thought of as a probabilistic description of the emission profile of a pulsar, might turn out to be useful as device for characterizing or classifying pulsars.

3.3 Pulse micro-structure

Sufficiently bright single pulses from many pulsars, when observed with sufficient time resolution, show intensity fluctuations over longer timescales of the order of the pulse period, and shorter timescales of the order of tens of microseconds. The latter, which are quasi-periodic intensity variations, are called the *micro-structure* of a pulse (Craft et al., 1968). Individual single pulses show considerable variability over and above the average pulse profile on both timescales. The micro-structure timescale is characteristic to a pulsar. Both timescales (micro-structure and pulsar period) and their relationship to each other are important from the perspective of pulsar emissions mechanisms.

The problem of estimating the micro-structure timescale is considered in Mitra et al. (2015). The traditional device for extracting micro-structure timescales is the auto-correlation function (ACF), where timescales are estimated as minima or maxima in the ACF. The procedure is confounded by the fact that the ACF of a pulse is dominated by power at low frequencies; i.e., by the longer-timescale variations, which we refer to as the *envelope*. In this frequency-domain view, micro-structure corresponds to higher-frequency but low-power features in the power spectrum. Additional oscillations can result from the presence of noise in the pulse time series. To be able to estimate the micro-structure timescale using ACF, one therefore needs to isolate the micro-structure component from the noise and the envelope components. After considering many different methods both in the time and frequency domains, the strategy which worked best was as follows: First, obtain a model-independent smoothing spline fit with optimal smoothing; this gives a de-noised version of the pulse. Second, estimate the envelope using kernel

regression with a heuristic bandwidth which smoothens out the microstructure component completely. The difference in these two fits is taken to the microstructure component, which is used to estimate timescales via the ACF approach.

The strength of this approach is that it tries to neatly separate noise, envelope, and microstructure components of a pulse time series. Shortcomings of this approach are (a) that the envelope is obtained using a heuristic bandwidth obtained through trial-and-error; and (b) is that formal analysis of the behaviour of our complete prescription has not been done. Despite this, the approach is turning out to be useful in analyzing single pulses (see, e.g., Mitra et al. (2016)), and we hope that its limits of applicability as well as better alternatives will emerge with its continued use in the community.

3.4 Knowledge about pulsar spectral indices and luminosity distribution

It is a well-known fact that pulsars are not equally bright at different frequencies, and the frequency dependence of pulsar brightness is expressed with the equation $S_\nu \propto \nu^\alpha$ where S_ν is the flux density of the pulsar at the observing frequency ν, and α is known as the "spectral index. The value of α is different for different pulsars. But for most of them, it lies in the range of -1 to -2 implying that pulsars are in general brighter at lower frequencies. The distribution of spectral indices of all 330 pulsars (for which spectral indices have been estimated as of February 2016) has a mean of -1.67 and median -1.70. There are extreme examples like PSR J0711+0931 ($\alpha = -3.5$) and PSR J1740+1000 ($\alpha = 0.9$). There are also a few pulsars with almost flat spectrum, the values of α lying between $+0.30$ to -0.30. Some pulsars even show deviations from a single power law, and their luminosities peak at a particular values of the frequency, for some the peak is around 1 GHz (Kijak et al., 2007), while for some others the peak has been noticed around 100 MHz (Malofeev et al., 1994). The subset of 39 MSPs has less diverse values for the spectral index, the maximum value is -1.1 and the minimum is -2.9 while the mean being -1.86 and median -1.80. It is conventional to use $\alpha = -1.9$ for MSPs (Toscano et al., 1998; Bagchi et al., 2011). But there is not many extensive statistical analyses on the distribution of α, mostly because the dataset is not large enough. One exception is the recent study by Bates, Lorimer, Verbiest (Bates et al., 2013) who used a population synthesis technique and a likelihood analysis and concluded that the distribution of α from different pulsar surveys can be modelled by a Gaussian distribution with a mean of -1.4 and unit standard deviation. They also concluded that the high-frequency (> 2 GHz) surveys preferentially select flatter-spectrum pulsars and the opposite is true for lower-frequency (< 1 GHz) surveys, and hypothesized that many known pulsars which have been detected at high frequencies will have small, or positive, spectral indices. More data on pulsar spectral indices coming out of flux density measurements over a wide frequency range, followed by extensive statistical analysis will be useful to understand this diversity, and whether there is any relation between the spectral index and other properties of pulsars, eventually shedding more light into the difficult-to-grasp pulsar emission mechanism. SKA and its pathfinders (including uGMRT) can contribute significantly in this issue.

Then, there is the question on the distribution of pulsar luminosities (or 'pseudo-luminosities' $L_\nu = S_\nu d^2$ where d is the distance). During the last three decades of the last century, L_ν has been considered as a function of the spin period and the first time derivative of the spin period (see (Bagchi, 2013) for a recent review on all those spin dependent luminosity modelling). But afterwards, people started to use spin independent luminosity distribution functions. The most popular was the use of a 'power-law' or a 'broken power law'. The most extensive work in this line is the one by Lorimer et al. (1993) (Lorimer et al., 1993) who found that that the distribution of total galactic population of pulsars with $L_{400} > 10$ mJy kpc^2 could be expressed as $N(\geq L_{400}) = (7.34 \pm 1.06) \times 10^4 L_{400}^{-1}$ and the distribution of potentially observable pulsars with $L_{400} > 10$ mJy kpc^2 could be expressed as $N(\geq L_{400}) = (1.31 \pm 0.17) \times 10^4 L_{400}^{-1}$, in both of the cases $N(\geq L_{400})$ is the total number of pulsars having luminosities equal to or greater than L_{400}. Later, a long-normal distribution with mean -1.1 and standard deviation 0.9, has been preferred by different studies (Faucher-Gigure and Kaspi, 2006; Bagchi et al., 2011) employing simulations and Kolmogorov-Smirnov test to check the agreement between the simulated and the observed data, although the power-law models could not be ruled out.

3.5 Use of Bayes' theorem in pulsar astronomy

Bayesian statistics is becoming increasingly popular in pulsar astronomy, so in this section we would like to discuss about this. Bayes' theorem can be written as (Wall and Jenkins, 2003; Gregory, 2005):

$$p(\mathbf{\Theta}|\mathscr{D},\mathscr{M}) = \frac{p(\mathscr{D}|\mathbf{\Theta},\mathscr{M})p(\mathbf{\Theta}|\mathscr{M})}{p(\mathscr{D}|\mathscr{M})}, \quad (1)$$

where $\mathbf{\Theta}$ is a set of parameters, $\mathscr{D}$ is the data and $\mathscr{M}$ is a model describing the parameters. In this notation, $p(\mathbf{\Theta}|\mathscr{D},\mathscr{M})$ represents the probability of obtaining a set of parameter values given the data and the model, and is termed the *joint posterior probability density*. Similarly, $p(\mathscr{D}|\mathbf{\Theta},\mathscr{M})$ is the probability of having obtained the observed data, given the parameter values and the model, and is called the *likelihood*, and $p(\mathbf{\Theta}|\mathscr{M})$, the *a priori* probability dictated by the model, is called the *prior probability density*. The denominator, $p(\mathscr{D}|\mathscr{M})$ is termed the *evidence*, and is just a normalizing factor that can be dropped since when one is only interested in relative probabilities.

Notable applications of Bayes' theorem over the last tetrad of years include the prediction of observable population of pulsars in some of the Galactic globular clusters (Chennamangalam et al., 2013), in the Large Magellanic Cloud (Ridley et al., 2013) and close to the Galactic centre (Chennamangalam and Lorimer, 2014), all using the presently known population as the *prior*. Another example is the prediction of the Galactic neutron star−neutron star merger rate using the data of the double pulsar as a *prior* (Kim et al., 2015). Earlier, Bayesian analysis has been employed to understand the uncertainties in pulsar distance measurements due to Lutz-Kelker bias (Verbiest et al., 2010, 2012). It is obvious that improved *prior* improves Bayesian predictions within a particular model. Thus, there is enough scope to improve results of earlier studies as well as to study unexplored properties of pulsars using the present and upcoming data from uGMRT and other radio telescopes. These results will eventually be tested in the SKA era with much richer dataset.

Acknowledgements

MA would like to thank Sushan Konar and Dipanjan Mitra for useful discussions.

References

Arjunwadkar, M., Rajwade, K., and Gupta, Y.: 2016, *Under Preparation*

Aschwanden, M.: 2011, *Self-Organized Criticality in Astrophysics: The Statistics of Nonlinear Processes in the Universe*, Springer

Backer, D. C.: 1970, *Nature* **228**, 42

Bagchi, M.: 2013, *International Journal of Modern Physics D* **22(10)**, 1330021

Bagchi, M., Lorimer, D. R., and Chennamangalam, J.: 2011, *Monthly Notices of the Royal Astronomical Society* **418(1)**, 477

Bates, S. D., Lorimer, D. R., and Verbiest, J. P. W.: 2013, *Monthly Notices of the Royal Astronomical Society* **431(2)**, 1352

Brunner, R. J., Djorgovski, S. G., Prince, T. A., and Szalay, A. S.: 2002, in J. Abello, P. M. Pardalos, and M. G. C. Resende (eds.), *Handbook of massive data sets*, pp 931–979, Springer

Burnham, K. and Anderson, D.: 2002, *Model Selection and Multimodel Inference*, Springer, New York, USA

Chennamangalam, J. and Lorimer, D. R.: 2014, *Monthly Notices of the Royal Astronomical Society: Letters* **440(1)**, L86

Chennamangalam, J., Lorimer, D. R., Mandel, I., and Bagchi, M.: 2013, *Monthly Notices of the Royal Astronomical Society* **431(1)**, 874

Craft, H. D., Comella, J. M., and Drake, F. D.: 1968, *Nature* **218**, 1122

Effron, B.: 2011, in M. Lovric (ed.), *International Encyclopedia of Statistical Science*, pp vii–x, Springer-Verlag

Espinoza, C. M., Lyne, A. G., Stappers, B. W., and Kramer, M.: 2011, *Monthly Notices of the Royal Astronomical Society* **414**, 1679

Faucher-Gigure, C.-A. and Kaspi, V. M.: 2006, *The Astrophysical Journal* **643(1)**, 332

Gregory, P. C.: 2005, *Bayesian Logical Data Analysis for the Physical Sciences: A Comparative Approach with `Mathematica` Support*, Cambridge University Press

Hall, P. and York, M.: 2001, *Statistica Sinica* **11**, 515

Hamilton, J.-C.: 2014, *Studies in History and Philosophy of Science Part B: Studies in History and Philosophy of Modern Physics* **46(A)**, 70

Hartigan, J. and Hartigan, P.: 1985, *Annals of Statistics* **13**, 70

Hastie, T., Tibshirani, R., and Friedman, J.: 2009, *The Elements of Statistical Learning: Data Mining, Inference, and Prediction*, Springer, second edition

Holzmann, H. and Vollmer, S.: 2008, *AStA Advances in Statistical Analysis* **92(1)**, 57

Kashikar, A., Konar, S., and Arjunwadkar, M.: 2016, *(In progress)*

Kijak, J., Gupta, Y., and Krzeszowski, K.: 2007, *Astronomy and Astrophysics* **462**, 699

Kim, C., Perera, B. B. P., and McLaughlin, M. A.: 2015, *Monthly Notices of the Royal Astronomical Society* **448(1)**, 928

Konar, S. and Arjunwadkar, M.: 2014

Lorimer, D. R., Bailes, M., Dewey, R. J., and Harrison, P. A.: 1993, *Monthly Notices of the Royal Astronomical Society* **263(2)**, 403

Malofeev, V. M., Gil, J. A., Jessner, A., Malov, I. F., Seiradakis, J. H., Sieber, W., and Wielebinski, R.: 1994, *Astronomy and Astrophysics* 285

McLachlan, G. and Peel, D.: 2000, *Finite Mixture Models*, Wiley, New York, USA

Mitra, D., Arjunwadkar, M., and Rankin, J. M.: 2015, *The Astrophysical Journal* **806(2)**, 236

Mitra, D., Rankin, J. M., and Arjunwadkar, M.: 2016, *Submitted*

Rajwade, K., Arjunwadkar, M., Gupta, Y., and Kumar, U.: 2016, *Under Preparation*

Ridley, J. P., Crawford, F., Lorimer, D. R., Bailey, S. R., Madden, J. H., Anella, R., and Chennamangalam, J.: 2013, *Monthly Notices of the Royal Astronomical Society* **433(1)**, 138

Ritchings, R.: 1976, *Monthly Notices of the Royal Astronomical Society* **176**, 249

Silverman, B.: 1981, *Journal of the Royal Statistical Society, Series B* **43**, 97

Toscano, M., Bailes, M., Manchester, R. N., and Sandhu, J. S.: 1998, *The Astrophysical Journal* **506(2)**, 863

Verbiest, J. P. W., Lorimer, D. R., and McLaughlin, M. A.: 2010, *Monthly Notices of the Royal Astronomical Society* **405**, 564

Verbiest, J. P. W., Weisberg, J. M., Chael, A. A., Lee, K. J., and Lorimer, D. R.: 2012, *Astrophysical Journal* **755**, 39

Wall, J. V. and Jenkins, C. R.: 2003, *Practical Statistics for Astronomers*, Cambridge University Press

Wasserman, L.: 2004, *All of Statistics*, Springer, New York, USA

Wasserman, L.: 2006, *All of Nonparametric Statistics*, Springer, New York, USA

Interstellar medium and star formation studies with the Square Kilometre Array

P. Manoj*[1], S. Vig[2], Maheswar, G.[3], U. S. Kamath[4], and A. Tej[2]

[1] *Tata Institute of Fundamental Research, Homibhabha Rd, Mumbai 400 005*
[2] *Department of Earth and Space Science, Indian Institute of Space Science and Technology, Thiruvananthapuram 695 547, India*
[3] *Aryabhatta Research Institute of Observational Sciences, Manora Peak, Nainital, 263 129, India*
[4] *Indian Institute of Astrophysics, Sarjapur Road, Koramangala, Bangalore 560034, India*

Abstract

Stars and planetary systems are formed out of molecular clouds in the interstellar medium. Although the sequence of steps involved in star and planet formation are generally known, a comprehensive theory which describes the details of the processes that drive star and planet formation is still missing. The Square Kilometre Array (SKA), with its unprecedented sensitivity and angular resolution, will play a major role in filling these gaps in our understanding. In this article, we present a few science cases that the Indian star formation community is interested in pursuing with SKA, which include investigation of AU-sized structures in the neutral ISM, the origin of thermal and non-thermal radio jets from protostars, the accretion history of protostars, and formation of massive stars and their effect on the surrounding medium.

1 Introduction

The formation of stars and planetary systems out of interstellar clouds is one of the central problems in contemporary astrophysics. Multi-wavelength observational studies, augmented by theoretical and laboratory studies in the last three decades or so have been successful in providing a frame work to understand the formation of stars and planetary systems. In the current paradigm for low-mass star formation, the process begins with the gravitational collapse of a slowly rotating cloud core, leading to the formation of a central protostar surrounded by a rotating disk and an overlying envelope from which the material rains down onto the disk (see reviews: Shu et al., 1987a; McKee & Ostriker, 2007). Since the total angular momentum is conserved during the collapse, the high angular momentum material in the outer envelope first collapses to form a disk, before getting accreted onto the central protostar (Ulrich, 1976; Cassen & Moosman, 1981; Terebey et al., 1984). In the early embedded stages, the system drives powerful bipolar jets/outflows, the origin of which is not entirely understood. As the system evolves, the envelope dissipates either by draining onto the disk or cleared out by stellar winds and outflows, leaving behind a young pre-main sequence star surrounded by a disk. Planetary systems are formed out of such protoplanetary disks which are the natural byproducts of star formation process (e.g. Stahler & Palla, 2004; Hartmann, 2009). Although the different stages in the formation of star and planetary systems are broadly understood, the details of the various processes that drive star and planet formation is only poorly known. Several questions remain to be answered. How are molecular clouds formed out of neutral Interstellar medium (ISM) and how long do they last? What processes controls the efficiency of star formation in molecular clouds? What determines the final stellar mass? What drives the accretion in protostars? What is the launching mechanisms for the jets in young stars? How are they collimated and accelerated to such large distances? How are planetary systems formed out of protoplanetary disks in a few Myr timescale? What determines their architecture? What are the processes that dissipate protoplanetary disks in a few Myr? In addition, as opposed to low-mass star formation, there is no coherent picture yet for the formation of massive stars.

*manoj.puravankara@tifr.res.in

The Square Kilometre Array (SKA), with its unprecedented sensitivity and angular resolution, will play a major role in answering several of these questions. Below we discuss a few of problems in star and planet formation that SKA can directly address.

2 Investigation of the AU-sized structures in ISM: SKA-TMT Synergies

The 21-cm absorption observable in the spectra of bright continuum sources in the background are used to probe the properties of the cold atomic component of interstellar medium (ISM). Several interferometric studies of the bright extended sources have revealed the existence of structure in cold HI gas (Clark et al., 1962; Clark, 1965). Subsequently, over the past few decades, both observations and theory have provided ample evidence for the existence of structures in the ISM on scales from $\sim$1 kpc down to $\sim$1 pc (e.g., Dickey & Lockman, 1990). Adopting typical values of thermal pressure, temperature and observed column density of the cold neutral medium (CNM) as $P_{th} \sim 2250$ cm^{-3} K (Jenkins & Tripp, 2001), T$\sim$70 K (Heiles & Troland, 2003) and 5×10^{19} cm^{-2} (Heiles & Troland, 2003), the typical expected scale length for CNM feature is about 1 pc. Thus it came as a surprise when observers began to report structures on AU scales in several sightlines. These results were based on spatial mapping of the HI absorption-line profiles across extended extragalactic background sources (Dieter et al., 1976; Diamond et al., 1989; Davis et al., 1996; Faison & Goss, 2001), temporal and spatial variations of optical interstellar absorption lines (like NaI D and CaIIK) against binary stars (Meyer & Blades, 1996; Watson & Meyer, 1996), globular clusters (Meyer & Lauroesch, 1999), and the time variability of HI absorption profiles against high proper motion pulsars (Deshpande et al., 1992; Frail et al., 1994; Johnston et al., 2003). In addition to these, the presence of AU-sized structures in the ionized (Fiedler et al., 1987; Romani et al., 1987) and the molecular (Marscher et al., 1993) components of ISM, though not as prevalent as in CNM, has invoked further interest in the topic.

The thermal pressure calculated for the observed AU-sized structures, assuming them as blobs of HI gas having a spherical geometry, is found to be much higher than the hydrostatic equilibrium pressure of the ISM or the standard thermal pressure of the CNM (Heiles, 1997). Thus it is difficult to comprehend the existance of these sturctures in pressure equilibrium with other components of ISM. Also, such over-dense and over-pressured structures are expected to be short-lived yet are omnipresent in observations. Several explainations were proposed to reconcile the observations. Heiles (1997) suggested that the observed AU-sized structures are actually gas distribution in nonspherical geometries like curved filaments and/or sheets that happen to be aligned along the line of sight. On the other hand, Deshpande (2000) argued that the opacity fluctuations seen in the HI observations correspond to a natural extension of a hierarchical structure from large to small scales organized based on a single power law distribution. The scintillation phenomenon combined with the velocity gradient across the absorbing H I gas was suggested by Gwinn (2001) to explain the optical depth fluctuations seen especially in multi-epoch pulsar observations.

Apart from understanding the mechanisms involved in the formation and the physical properties of the AU-sized structures, one of the most important questions to address first is whether the structures detected in the radio and optical observations are same or different. To investigate this we required to make observations of same sightlines. With the future facilities like SKA and TMT, this study should be possible. It would also be important to make such study in locations which are diverse in physical properties to ascertain the effects of environment on the formation of AU-sized structures.

3 Jets and outflows from protostars

During the early stages of their formation, young stars drive powerful jets/outflows. They play a significant role in the evolution of a protostar as they transfer angular momentum from the young protostellar system to its environment, in the absence of which accretion cannot occur and a star cannot form. Jets are believed to drive the large scale outflows. The mechanism for the launch of jets, however, is far from certain although significant advances have been made through various numerical simulation(Zanni et al., 2007; Fendt, 2006; Ouyed & Pudritz, 1997). Most successful models of jet engines invoke magnetic fields for the launch and driving of jets. It is still not clear if the engine for jet launch is the interface between

the star's magnetosphere and disk (X-wind model, Shu et al., 2000) or a wide range of disk radii (disk or D-wind model, Konigl & Pudritz, 2000). In the X-wind model, jets are launched magneto-centrifugally from accretion disks when their inner edges interact with strongly magnetised stars. Disk-wind model on the other hand, explain jets as centrifugally driven winds in magnetised accretion disks, powered by accretion.

Protostellar jets are observed at multiple frequencies. Observations at different frequencies trace different locations and physical processes associated with jets/outflows. For example, CO observations at submillimeter/millimeter wavelengths trace the molecular gas entrained and swept-up by jets which provide a fossil record of the mass loss history of the protostar (Bontemps et al., 1996; Bachiller & Tafalla, 1999; Richer et al., 2000). Optical and near-IR forbidden lines such as [S II], [O III] and [Fe II] (e.g Bally et al., 2007; Nisini, 2009) probe fast (a few tens to few hundreds of km s^{-1}), highly collimated and partially ionised jets. Because of the large line-of-sight extinction towards protostars, these optical and IR lines are generally used to trace outer parts of the jets, farther out from the central engine, and in relatively evolved protostars with tenuous envelopes. Mid- and far-IR fine structure lines such [O I], [Fe II], [Si II], observed with Spitzer and Herschel, suffer relatively less extinction, and they trace hot gas that is currently being shocked in jets (e.g. Watson et al., in prep). The spatial resolution of Spitzer and Herschel, however, is relatively poor ($10''$ for [OI] at 63 μm) and cannot probe the innermost parts of the jet close to where it is launched. Despite the existence of a wealth of observational studies, the nature of the primary jets from protostars is far from clear. Several questions remain: Where and how are protostellar jets launched and accelerated? How are they collimated to such high degree? How does the jet propagation and interaction affect the surrounding medium? How do the jet properties evolve with system age? How long does jet production persist?

3.1 'Thermal' radio jets from protostars

Observations at cm wavelengths have revealed the presence of compact continuum emission centered on protostars which is often found to be elongated roughly in the direction of the large-scale jet/outflow, indicating that the cm emission traces the base of the jet very close to the driving source (e.g. Anglada, 1996; Reipurth et al., 2002, 2004). The cm flux density generally has a positive spectral index ($F_\nu \propto \nu^\alpha$; $\alpha \sim 0.6$ for winds or radio jets) and the emission is thought to be dominated by thermal free-free radiation from ionised gas (Reynolds, 1986; Curiel et al., 1989). Thus, cm emission from low-mass protostars traces collimated and ionised jets extending to a few hundred AUs from the exciting source and corresponding to material ejected from the protostars with dynamical ages of the order of a few years or less.

Unlike the near-infrared and optical, there have been relatively fewer studies of protostellar jets in the radio regime as the emission is relatively weak, of the order of few mJy. Most of the detection of the radio jets have been for low-mass protostars that are relatively nearby (Girart et al., 2002). In the case of massive protostars, only a handful of radio jets have been detected due to the observational difficulties encountered in studying the early phases of massive stars. Sensitive polarisation measurements at cm wavelengths using VLA of a jet GGD27-28 (Carrasco-González et al., 2010a) has shown that the magnetic field lines are parallel to the jet axis upto ~ 2500 AU and increases in intensity towards the centre. The investigation of radio jets is of significance from massive protostars as it can help us constrain the models of massive star formation as the location and timing of launch of jet can throw light on the massive star formation scenario vis-a-vis low mass star formation.

SKA will address some very fundamental questions linked to the origin and collimation of jets by probing radio emission from the jet very close to launch point from the central exciting object. At 1 GHz, SKA should be able to observe regions as close as 25-30 AU from the central protostar at 100 pc. Although radio emission detected from jets is very weak (mJy level), a sensitive interferometer like SKA will detect radio emission from nearly all jets and outflows in the solar neighbourhood, including that from low mass protostars.

3.2 Tracing mass accretion history from jets/outflows

Mass accretion in young stellar objects is thought to be highly time variable and episodic (e.g. Kenyon et al., 1990; Hartmann & Kenyon, 1996; Evans et al., 2009; Dunham & Vorobyov, 2012). While outbursts of varying intensities and frequencies have been observed in several young stars (e.g Herbig, 1977; Kenyon, 1995; Green et al., 2006; Fischer et al., 2012; Green et al., 2013; Audard et al., 2014), a detailed picture

of the time evolution of mass accretion from early protostellar phase to late pre-main sequence phase is still missing. This is primarily because, most of the commonly used direct observational tracers of mass accretion such as UV and optical continuum excess and emission lines of Hα, Paβ, Brγ fall at wavelengths $\lesssim 2$ μm (e.g. Calvet & Gullbring, 1998; Muzerolle et al., 1998a,b, 2001), and are heavily extinguished toward protostars which are deeply embedded in their natal core. Jets and outflows from embedded protostars, on the other hand, are more readily accessible to observations than the direct accretion tracers, particularly at far-IR, mm and radio wavelengths, where the line of sight extinction can be very low. Observations of protostellar jets and outflows at these wavelengths provide important diagnostics for the energetics of mass ejection and mass loss rates from protostars (e.g. Bachiller & Tafalla, 1999; Richer et al., 2000; Hollenbach et al., 1989; Reynolds, 1986). Moreover, mass accretion and ejection in protostars are thought to be strongly coupled. Theoretical models of mass ejection mechanisms from protostars predict a linear relation between mass loss rate from protostars, $\dot{M}_{\rm out}$, and mass accretion rate, $\dot{M}_{\rm acc}$, onto the protostar (Shu et al., 1994; Najita & Shu, 1994; Pelletier & Pudritz, 1992; Wardle & Koenigl, 1993; Matt & Pudritz, 2005, 2008). Thus, observed properties of mass ejection can be used to study the mass accretion history in protostars.

Observations of molecular outflows from protostars at (sub)mm wavelengths measures time-averaged flow energetic parameters, viz., the mechanical luminosity ($L_{\rm mech}$) and the momentum flux or outflow force ($F_{\rm CO}$). Since the observed molecular outflows are driven by protostellar jets, the measured $L_{\rm mech}$ and $F_{\rm CO}$ of the outflows are the rates at which kinetic energy and momentum are injected into the flow by the jets. These are time-averaged rates over the dynamical timescale of the observed molecular flow, which is typically in the range of 10^4−10^5 yr. Thus from (sub)mm CO observations we can obtain mass loss rates from protostars averaged over 10^4−10^5 yr. Observations of protostellar jets in the [O I] line at 63 μm provide mass loss rates averaged over the cooling timescale of ∼100 yr (e.g. Hollenbach, 1985; Watson, 1985, Manoj et al. in prep). On the other hand, the ionised jets observed at radio wavelengths have dynamical timescales of $\sim$ a few yr, thus measuring the instantaneous mass loss rates. With its high sensitivity and angular resolution, SKA will resolve 'thermal' jets from several hundreds of low-mass protostars in star forming regions within 500 pc from us, most of which has already been observed in (sub)mm CO lines and with *Herschel*. Thus, equipped with protostellar mass loss rates smoothed over a few yr, 100 yr and 10^4 yr, we will be able to study the detailed time evolution of mass ejection/accretion in protostars. Such a study will place strong constraints on the frequency, amplitude and duration of episodic accretion events in protostars during their early stages of evolution.

3.3 Non-thermal jets from protostars

Although the radio jets from protostars show positive spectral index, in a few cases the cm flux density in strong radio knots is found to have negative spectral slopes, indicative of non-thermal emission (e.g. Curiel et al., 1993; Wilner et al., 1999). Linearly polarised emission has been detected in some of them, confirming that the emission mechanism is non-thermal synchrotron emission (e.g. Carrasco-González et al., 2010b). This provides evidence for the presence of a population of electrons accelerated to relativistic energies. It is generally thought that the electrons are accelerated to such high velocities in strong and fast shocks (e.g. Carrasco-González et al., 2010b), but the exact mechanism is far from clear. Negative spectral indices at cm wavelengths are observed in only a few systems, and the polarisation measurements exist for even fewer. Linear polarisation measurements are difficult as polarised flux density is only a fraction (typically ∼10%) of the total emission and the total radio emission itself is very weak, particularly in low-mass protostars.

With the high senisitivity offered by SKA we will be able to detect the ionised jets in protostars across a wide frequency range (few GHz to MHz) and measure the spectral indices in a large number of sources to study the incidence of non-thermal emission. Follow-up linear polarisation measurements of sources which show negative spectral indices will allow us to infer the energy spectrum of the population of relativistic electrons and to study the details of particle acceleration mechanisms. In addition, such studies will also map the magnetic fields in protostellar jets, which will help address questions of collimation and acceleration of jets.

4 Formation of high-mass stars and their effect on the surrounding ISM

High-mass stars, with their radiative, mechanical and chemical feedback, play an important role in the dynamical and chemical evolution of the interstellar medium (ISM) and the galaxy. The outpouring of UV photons and the associated generation of HII regions, accompanied by strong stellar winds profoundly alter the surrounding ISM. Apart from this, massive stars down to ~ 8 $M_{\odot}$ evolve to become Type II Supernovae and hence inject energy and heavy elements to the ISM. However, the formation mechanism and the very early phases of evolution of this mass regime is still not well understood although the basic feature of the collapse of a rotating cloud core is applicable to all mass ranges. The question that arises is whether the formation mechanism of high-mass stars (greater than ~ 8 $M_{\odot}$) is just a scaled up version of the low mass regime or the processes involved are completely different. The formation scenario is expected to be different for the high-mass range because the accretion timescales become larger than the protostar contraction timescales implying that the star 'switches on' (i.e reaches the zero age main-sequence, ZAMS) while still accreting. This invokes the 'radiation-pressure' problem that inhibits further accretion onto the protostar (Kahn, 1974; Wolfire & Cassinelli, 1987) thereby questioning the very formation of higher mass stars which are observationally a reality. This implies that these stars accrete a significant fraction of mass while on the main-sequence.

Theoretically, there is still no general consensus on the processes in play during the initial stages of massive star formation. Monolithic collapse with scaled up parameters such as larger mass accretion rates and outflows have been proposed (Yorke & Sonnhalter, 2002). Another contender is the turbulent core model where massive stars form in gravitationally bound cores supported by turbulence and magnetic field (McKee & Tan, 2003). Alternative models called competitive accretion models have been proposed by Bonnell et al. (2004) where small stars form via gravitational collapse and then grow by gravitational accretion of gas that was initially unbound to the star. Observationally, factors that hinder the investigation of massive stars in their infancy include rarity of sources (owing to fast evolutionary time scales), formation in clustered environment, large distances, complex, embedded and influenced environment, as well as high extinction. Hence, observational studies to probe the various phases involved in high-mass star formation and the effect they have on the surrounding ISM are of crucial importance in validating the proposed theories.

4.1 Understanding the Early Phases

Initial studies on samples of young massive star forming regions were based on far-infrared colours of IRAS (Palla et al., 1991; Wouterloot et al., 1993; Palagi et al., 1993). This was used to recognise and understand sign-posts of massive star formation. In the last couple of decades, the importance of multiwavelength observations spanning a wide wavelength range has been realised in the investigation massive star forming regions. Along the lines of the well established phases of low-mass stars (Shu et al., 1987b), recently there have been a number of attempts to classify the evolutionary stage of massive star forming regions on the basis of signposts such as masers, near and mid- infrared emission, jets and outflows, shocked gas as well as the presence of radio emission (Molinari et al., 2008; Battersby et al., 2010; Sánchez-Monge et al., 2013; Giannetti et al., 2013). The early phases of massive star forming sites are characterised by presence of cold clumps detected in millimetre continuum and infrared emission, presence of water or methanol maser and low levels of radio continuum emission (Molinari et al., 2008; Sánchez-Monge et al., 2013). The earliest evolutionary phase is categorised as Type 1 with dominant millimetre emission and possibly located close to an infrared source, but not coincident with it. This corresponds to high-mass protostars embedded in dusty clumps, surrounded by infrared emission that could originate from more evolved, nearby lower mass stars. Regions associated with the Type 2 phase have both millimetre and infrared emission. These would be deeply embedded Zero Age Main Sequence (ZAMS) OB stars that are still undergoing accretion. And finally the Type 3 phase, where the associated regions show only infrared emission but are located near a millimetre source. These would represent ZAMS OB stars surrounded only by remnants of their parental clumps. Radio continuum emission at centimetre wavelengths has been detected mostly (72%) from Type 2 and Type 3 sources and only a small fraction (7%) from Type 1 sources (Sánchez-Monge et al., 2013). Battersby et al. (2010) have also examined massive star formation by investigating a number of infrared dark clouds and have described

an observational evolutionary sequence comprising of four stages: (i) quiescent clump, (ii) clump with signature of active star formation (maser, green fuzzy, or 24 μm emission), (iii) initiation of ultracompact HII region, and (iv) diffuse red clump, finally leading to formation of a young stellar stellar cluster. This clearly indicates the well-known premise that as evolution proceeds, the radio emission from ionised gas becomes stronger and expands as the newly formed massive star evolves. Hence, high-resolution radio continuum mapping holds the potential of unravelling the onset of Lyman continuum photon emission from massive stars, thus providing impetus for a rigorous study of the early phases of massive stars.

Ultra-compact (UC) HII regions are associated with the early phases of the massive stars soon after they are born and still deeply embedded in the prenatal cloud. These HII regions display a variety of radio morphologies. Studying these morphology holds the key to understanding the nature of the surrounding ISM during the formation of the star. Of special interest are the cometary morphologies seen in 20% of the UC HII regions (Wood & Churchwell, 1989). Reid & Ho (1985) first suggested that the cometary appearance of such HII regions is due to the relative motion of the star against the dense molecular material. This led to the bow-shock model by van Buren et al. (1990) which postulated the cometary HII regions as bow-shocks created by wind-blowing massive stars moving supersonically through molecular clouds. This is due to the balance between the stellar wind pressure and the ram pressure of the molecular material as the result of motion of the massive star. The bow-shock model makes specific predictions regarding the internal motions of ionised gas with respect to the nearby molecular material. The ionised material near the cometary head should be moving, on average, with the velocity of the star and further down towards the tail, velocity of the ionised gas should be slower, approaching that of the molecular cloud.

From among the UC HII regions, a distinct class of exceptionally small and dense objects are observed which are termed as Hyper-compact (HC) HII regions. These HC HII regions display broad radio recombination line profiles compared to the UC HII regions (Sewilo et al., 2004). The observed line profiles of the HC HII regions lie inbetween the massive YSOs with strong ionized stellar wind and the slow UC HII regions. Since the database of HC HII regions is very limited, morphologies of these objects are not studied in detail. Understanding the mechanisms responsible for the broad line profiles is of importance and crucially linked to the very early phase of high-mass star formation. High resolution radio recombination line studies would not only shed light on this but would also provide information on the morphology.

4.2 Triggered star formation in Molecular Clouds

As the star-forming nebula evolves, the OB stars contained within it can move far from their original birthplaces. Moreover, molecular clouds are clumpy and inhomogeneous on all scales. Therefore, displacement of the local gas and creation of non-spherical ionization fronts changes the overall structure of the GMC. Studies of individual UC HII regions show evidence for the evolutionary sequence of the associated nebulae. These regions can mutually interact and influence the future course of star formation in the entire molecular cloud. The W3/ W4/ W5 star-forming complexes are prime examples of how this can happen. This region contains some of the richest and well-studied populations of deeply embedded massive stars. It presents evidence of triggered star formation, wherein new generations of stars have been triggered by previous generations of OB stars. The presence of thousands of young, low-mass stars in this region demonstrates that the low-mass versus high-mass star formation scenarios need not necessarily work in isolation. The W4 region is the nearest example of a galactic superbubble powered by the winds of supernovae and massive OB stars. Isolated clouds seen near some GMCs could have been torn away from the parent GMC by the action of OB star winds.

It is known that significant fraction of the cluster population in a star forming region is confined to just a few rich clusters. Only a global view of the region, as opposed to studies of UC H II regions alone, would be able to tell us why and how these regions emerge from the molecular cloud. Another well studied object, W51, is a giant complex composed of several H II regions spread over an area of 1^o. It broadly comprises of four components, each having futher sub-components, with different properties related to star formation. Again, observations of the entire region would enable an overall understanding of such GMCs.

4.3 Mid-infrared Bubbles

An interesting manifestation of the interplay between the massive stars and the surrounding ISM is seen in the form of mid-infrared bubbles. The strong stellar winds emanating from high-mass stars interact with the ambient interstellar gas resulting in an expanding spherical system - a 'bubble'. The interior is filled with hot ($T \geq 10^6$K), shocked, and tenuous stellar wind. The swept-up interstellar gas is compressed into a thin spherical shell. When the dynamical pressure of the winds emanating from the early-type star falls to the value of the thermal pressure of the surrounding, a reverse shock slows down the wind. This shocked gas drives a strong shock into the ambient interstellar medium, sweeping it up resulting in the bubble. Catalogs of IR bubbles have been compiled by (Churchwell et al., 2006, 2007) and more recently by (Simpson et al., 2012, - The Milky Way Project). These are based on the *Spitzer* - GLIMPSE and MIPSGAL survey images. These bubbles are believed to be driven by a central massive star or stellar cluster since substantial UV radiation is required to excite the polycyclic aromatic hydrocarbons (PAHs) lines in the IRAC bands. Strong stellar winds from OB stars would result in an evacuated cavity around the central star. This is consistent with the observed morphology. A good correlation has also been seen between IR bubbles and HII regions (Churchwell et al., 2006, 2007; Deharveng et al., 2010). Populations of young stellar objects (YSOs) are seen towards the periphery of several bubbles suggesting triggered star formation (Deharveng et al., 2010). Hence, these objects provide an ideal database not only for probing high-mass star formation but also for understanding the proposed theories related to triggered or sequential star formation (Zinnecker & Yorke, 2007; Elmegreen & Lada, 1977). The two commonly accepted models for this are the collect and collapse ((CC) Elmegreen & Lada, 1977; Deharveng et al., 2010, and references therein) and radiatively driven implosion (RDI) ((RDI) Lefloch & Lazareff, 1994). Their association with massive star formation, the connection between initial and triggered star formation and preferred mechanism for sequential star formation (CC or RDI) are still some questions that remain unanswered.

High resolution radio continuum emission provides crucial information on the triggering source, ionization zone, variation of spectral indices in different zones of the bubble. The radio luminosity allows us to understand the dynamics of the stellar wind as well. Of further interest is the search for UC HII regions in the periphery of these bubbles that can shed light on the possibility of expanding HII regions triggering massive star formation. This aspect is still not clearly understood given that the feedback from the initial massive OB stars are known to influence the cloud and inhibit the next generation of star formation. Several studies like those by Hopkins et al. (2011), (Matzner, 2002), Dale & Bonnell (2011) make the scenario of sequential massive star formation complicated. This makes radio continuum observations of bubbles crucial.

4.4 Massive Star formation studies using GMRT and role of SKA

The Giant Metrewave Radio Telescope (GMRT) has given Indian astronomers opportunities to study massive star formation at low radio frequencies. A number of massive star forming regions have been explored in conjunction with infrared and submillimetre wavebands. Vig et al. (2006) investigated the radio morphology of IRAS 19111+1048, that indicates the presence of highly inhomogeneous medium in the neighbourhood of an ultracompact HII region. Twenty compact sources including one non-thermal source were detected here. The sources having near-infrared counterparts are found to have matching spectral types for a good fraction of radio sources. Comparative evolutionary stage of two star forming regions were estimated based on the multiwavelength information. However, not all compact radio sources are internally excited by an embedded ZAMS star. In cases such as IRAS 17258-3637 (Vig et al., 2014) and IRAS 06055+2039 (Tej et al., 2006), apart from the brightest compact source that represents the location of exciting star, several high density radio clumps have been detected that are likely to be externally ionised in a clumpy medium. Studies of young clusters in HII (Mallick et al., 2015) regions and sites of triggered star formation associated with expanding HII regions(Samal et al., 2014) have also been investigated using GMRT observations.

In star formation studies, a prominent advantage of GMRT has been in the simultaneous mapping of compact and diffuse emission as result of the antenna distribution in the hybrid array. While massive stars in earlier evolutionary stages have only compact emission, as they evolve into the surrounding parental cocoon of gas and dust, they ionise the ambient medium that gives rise to the nebulosity associated with it (Kim & Koo, 2001). The spectral indices of diffuse emission can provide information on the mechanism

of ionisation, thermal versus non-thermal. Spectral indices of diffuse emission extending upto 3 pc have been determined towards the cometary HII region IRAS 17256-3631 at low frequencies (Veena et al., 2016). It is interesting to note that non-thermal emission is seen prominently towards the tail region that is ionisation bounded. It has been proposed that the diffuse non-thermal emission corresponds to synchrotron radiation from electrons that are accelerated in the region of interaction between stellar wind and ambient cloud material (Garay et al., 1996).

With SKA, we will be able to examine various phases in the formation of massive stars when they start radiating. SKA can play a prominent role towards detecting the earliest HII regions, i.e hypercompact HII regions with its sensitivity and resolution. For instance, at a distance of 1 kpc, SKA should be able to resolve distances upto ~ 100 AU at 2 GHz. This should help understand the nature of hypercompact HII regions, i.e whether it is arising due to thermally evaporating flow from disks (Lugo et al., 2004) or gravitationally trapped ionised accretion flow (Keto, 2002). The kinematics of HII regions, investigated by mapping radio recombination lines, should help understand the properties, morphology of the HII region and give clues about HII region formation history including triggered star formation. The large field-of-view SKA (~ 1 sq deg at 1.4 GHz) would also enable in obtaining a global picture of GMCs and HII regions within them.

References

Anglada, G. 1996, in Astronomical Society of the Pacific Conference Series, Vol. 93, Radio Emission from the Stars and the Sun, ed. A. R. Taylor & J. M. Paredes, 3–14

Audard, M., Ábrahám, P., Dunham, M. M., Green, J. D., Grosso, N., Hamaguchi, K., Kastner, J. H., et al. 2014, Protostars and Planets VI, 387

Bachiller, R. & Tafalla, M. 1999, in NATO Advanced Science Institutes (ASI) Series C, Vol. 540, NATO Advanced Science Institutes (ASI) Series C, ed. C. J. Lada & N. D. Kylafis, 227

Bally, J., Reipurth, B., & Davis, C. J. 2007, Protostars and Planets V, 215

Battersby, C., Bally, J., Jackson, J. M., Ginsburg, A., Shirley, Y. L., Schlingman, W., & Glenn, J. 2010, ApJ, 721, 222

Bonnell, I. A., Vine, S. G., & Bate, M. R. 2004, MNRAS, 349, 735

Bontemps, S., André, P., Terebey, S., & Cabrit, S. 1996, A&A, 311, 858

Calvet, N. & Gullbring, E. 1998, ApJ, 509, 802

Carrasco-González, C., Rodríguez, L. F., Anglada, G., Martí, J., Torrelles, J. M., & Osorio, M. 2010a, Science, 330, 1209

—. 2010b, Science, 330, 1209

Cassen, P. & Moosman, A. 1981, Icarus, 48, 353

Churchwell, E., Povich, M. S., Allen, D., Taylor, M. G., Meade, M. R., Babler, B. L., Indebetouw, R., et al. 2006, ApJ, 649, 759

Churchwell, E., Watson, D. F., Povich, M. S., Taylor, M. G., Babler, B. L., Meade, M. R., Benjamin, R. A., Indebetouw, R., & Whitney, B. A. 2007, ApJ, 670, 428

Clark, B. G. 1965, ApJ, 142, 1398

Clark, B. G., Radhakrishnan, V., & Wilson, R. W. 1962, ApJ, 135, 151

Curiel, S., Rodriguez, L. F., Bohigas, J., Roth, M., Canto, J., & Torrelles, J. M. 1989, Astrophysical Letters and Communications, 27, 299

Curiel, S., Rodriguez, L. F., Moran, J. M., & Canto, J. 1993, ApJ, 415, 191

Dale, J. E. & Bonnell, I. 2011, MNRAS, 414, 321

Davis, R. J., Diamond, P. J., & Goss, W. M. 1996, MNRAS, 283, 1105

Deharveng, L., Schuller, F., Anderson, L. D., Zavagno, A., Wyrowski, F., Menten, K. M., Bronfman, L., et al. 2010, A&A, 523, A6

Deshpande, A. A. 2000, MNRAS, 317, 199

Deshpande, A. A., McCulloch, P. M., Radhakrishnan, V., & Anantharamaiah, K. R. 1992, MNRAS, 258, 19P

Diamond, P. J., Goss, W. M., Romney, J. D., Booth, R. S., Kalberla, P. M. W., & Mebold, U. 1989, ApJ, 347, 302

Dickey, J. M. & Lockman, F. J. 1990, ARA&A, 28, 215

Dieter, N. H., Welch, W. J., & Romney, J. D. 1976, ApJ, 206, L113

Dunham, M. M. & Vorobyov, E. I. 2012, ApJ, 747, 52

Elmegreen, B. G. & Lada, C. J. 1977, ApJ, 214, 725

Evans, N. J., Dunham, M. M., Jørgensen, J. K., Enoch, M. L., Merín, B., van Dishoeck, E. F., Alcalá, J. M., et al. 2009, ApJS, 181, 321

Faison, M. D. & Goss, W. M. 2001, AJ, 121, 2706

Fendt, C. 2006, ApJ, 651, 272

Fiedler, R. L., Dennison, B., Johnston, K. J., & Hewish, A. 1987, Nature, 326, 675

Fischer, W. J., Megeath, S. T., Tobin, J. J., Stutz, A. M., Ali, B., Remming, I., Kounkel, M., et al. 2012, ApJ, 756, 99

Frail, D. A., Weisberg, J. M., Cordes, J. M., & Mathers, C. 1994, ApJ, 436, 144

Garay, G., Ramirez, S., Rodriguez, L. F., Curiel, S., & Torrelles, J. M. 1996, ApJ, 459, 193

Giannetti, A., Brand, J., Sánchez-Monge, Á., Fontani, F., Cesaroni, R., Beltrán, M. T., Molinari, S., Dodson, R., & Rioja, M. J. 2013, A&A, 556, A16

Girart, J. M., Curiel, S., Rodríguez, L. F., & Cantó, J. 2002, Rev. Mexicana Astron. Astrofis., 38, 169

Green, J. D., Evans, II, N. J., Kóspál, Á., Herczeg, G., Quanz, S. P., Henning, T., van Kempen, T. A., et al. 2013, ApJ, 772, 117

Green, J. D., Hartmann, L., Calvet, N., Watson, D. M., Ibrahimov, M., Furlan, E., Sargent, B., & Forrest, W. J. 2006, ApJ, 648, 1099

Gwinn, C. R. 2001, ApJ, 561, 815

Hartmann, L. 2009, Accretion Processes in Star Formation: Second Edition (Cambridge University Press)

Hartmann, L. & Kenyon, S. J. 1996, ARA&A, 34, 207

Heiles, C. 1997, ApJ, 481, 193

Heiles, C. & Troland, T. H. 2003, ApJ, 586, 1067

Herbig, G. H. 1977, ApJ, 217, 693

Hollenbach, D. 1985, Icarus, 61, 36

Hollenbach, D. J., Chernoff, D. F., & McKee, C. F. 1989, in ESA Special Publication, Vol. 290, Infrared Spectroscopy in Astronomy, ed. E. Böhm-Vitense, 245–258

Hopkins, P. F., Quataert, E., & Murray, N. 2011, MNRAS, 417, 950

Jenkins, E. B. & Tripp, T. M. 2001, ApJS, 137, 297

Johnston, S., Koribalski, B., Wilson, W., & Walker, M. 2003, MNRAS, 341, 941

Kahn, F. D. 1974, A&A, 37, 149

Kenyon, S. J. 1995, in Revista Mexicana de Astronomia y Astrofisica, vol. 27, Vol. 1, Revista Mexicana de Astronomia y Astrofisica Conference Series, ed. S. Lizano & J. M. Torrelles, 237

Kenyon, S. J., Hartmann, L. W., Strom, K. M., & Strom, S. E. 1990, AJ, 99, 869

Keto, E. 2002, ApJ, 580, 980

Kim, K.-T. & Koo, B.-C. 2001, ApJ, 549, 979

Konigl, A. & Pudritz, R. E. 2000, Protostars and Planets IV, 759

Lefloch, B. & Lazareff, B. 1994, A&A, 289, 559

Lugo, J., Lizano, S., & Garay, G. 2004, ApJ, 614, 807

Mallick, K. K., Ojha, D. K., Tamura, M., Linz, H., Samal, M. R., & Ghosh, S. K. 2015, MNRAS, 447, 2307

Marscher, A. P., Moore, E. M., & Bania, T. M. 1993, ApJ, 419, L101

Matt, S. & Pudritz, R. E. 2005, ApJ, 632, L135

—. 2008, ApJ, 681, 391

Matzner, C. D. 2002, ApJ, 566, 302

McKee, C. F. & Ostriker, E. C. 2007, ARA&A, 45, 565

McKee, C. F. & Tan, J. C. 2003, ApJ, 585, 850

Meyer, D. M. & Blades, J. C. 1996, ApJ, 464, L179

Meyer, D. M. & Lauroesch, J. T. 1999, ApJ, 520, L103

Molinari, S., Faustini, F., Testi, L., Pezzuto, S., Cesaroni, R., & Brand, J. 2008, A&A, 487, 1119

Muzerolle, J., Calvet, N., & Hartmann, L. 1998a, ApJ, 492, 743

—. 2001, ApJ, 550, 944

Muzerolle, J., Hartmann, L., & Calvet, N. 1998b, AJ, 116, 2965

Najita, J. R. & Shu, F. H. 1994, ApJ, 429, 808

Nisini, B. 2009, Jets from Embedded Protostars, ed. K. Tsinganos, T. Ray, & M. Stute (Springer Heidelberg Dordrecht London New York), 215–224

Ouyed, R. & Pudritz, R. E. 1997, ApJ, 482, 712

Palagi, F., Cesaroni, R., Comoretto, G., Felli, M., & Natale, V. 1993, A&AS, 101, 153

Palla, F., Brand, J., Comoretto, G., Felli, M., & Cesaroni, R. 1991, A&A, 246, 249

Pelletier, G. & Pudritz, R. E. 1992, ApJ, 394, 117

Reid, M. J. & Ho, P. T. P. 1985, ApJ, 288, L17

Reipurth, B., Rodríguez, L. F., Anglada, G., & Bally, J. 2002, AJ, 124, 1045

—. 2004, AJ, 127, 1736

Reynolds, S. P. 1986, ApJ, 304, 713

Richer, J. S., Shepherd, D. S., Cabrit, S., Bachiller, R., & Churchwell, E. 2000, Protostars and Planets IV, 867

Romani, R. W., Blandford, R. D., & Cordes, J. M. 1987, Nature, 328, 324

Samal, M. R., Zavagno, A., Deharveng, L., Molinari, S., Ojha, D. K., Paradis, D., Tigé, J., Pandey, A. K., & Russeil, D. 2014, A&A, 566, A122

Sánchez-Monge, Á., Beltrán, M. T., Cesaroni, R., Fontani, F., Brand, J., Molinari, S., Testi, L., & Burton, M. 2013, A&A, 550, A21

Sewilo, M., Churchwell, E., Kurtz, S., Goss, W. M., & Hofner, P. 2004, ApJ, 605, 285

Shu, F., Najita, J., Ostriker, E., Wilkin, F., Ruden, S., & Lizano, S. 1994, ApJ, 429, 781

Shu, F. H., Adams, F. C., & Lizano, S. 1987a, ARA&A, 25, 23

—. 1987b, ARA&A, 25, 23

Shu, F. H., Najita, J. R., Shang, H., & Li, Z.-Y. 2000, Protostars and Planets IV, 789

Simpson, R. J., Povich, M. S., Kendrew, S., Lintott, C. J., Bressert, E., Arvidsson, K., Cyganowski, C., et al. 2012, MNRAS, 424, 2442

Stahler, S. W. & Palla, F. 2004, The Formation of Stars (WILEY-VCH Verlag GmbH & Co. KGaA, Weinheim)

Tej, A., Ojha, D. K., Ghosh, S. K., Kulkarni, V. K., Verma, R. P., Vig, S., & Prabhu, T. P. 2006, A&A, 452, 203

Terebey, S., Shu, F. H., & Cassen, P. 1984, ApJ, 286, 529

Ulrich, R. K. 1976, ApJ, 210, 377

van Buren, D., Mac Low, M.-M., Wood, D. O. S., & Churchwell, E. 1990, ApJ, 353, 570

Veena, V. S., Vig, S., Tej, A., Varricatt, W. P., Ghosh, S. K., Chandrasekhar, T., & Ashok, N. M. 2016, MNRAS, 456, 2425

Vig, S., Ghosh, S. K., Kulkarni, V. K., Ojha, D. K., & Verma, R. P. 2006, ApJ, 637, 400

Vig, S., Ghosh, S. K., Ojha, D. K., Verma, R. P., & Tamura, M. 2014, MNRAS, 440, 3078

Wardle, M. & Koenigl, A. 1993, ApJ, 410, 218

Watson, D. M. 1985, Physica Scripta Volume T, 11, 33

Watson, J. K. & Meyer, D. M. 1996, ApJ, 473, L127

Wilner, D. J., Reid, M. J., & Menten, K. M. 1999, ApJ, 513, 775

Wolfire, M. G. & Cassinelli, J. P. 1987, ApJ, 319, 850

Wood, D. O. S. & Churchwell, E. 1989, ApJ, 340, 265

Wouterloot, J. G. A., Brand, J., & Fiegle, K. 1993, A&AS, 98, 589

Yorke, H. W. & Sonnhalter, C. 2002, ApJ, 569, 846

Zanni, C., Ferrari, A., Rosner, R., Bodo, G., & Massaglia, S. 2007, A&A, 469, 811

Zinnecker, H. & Yorke, H. W. 2007, ARA&A, 45, 481

Explosive Transients: Transient Astronomy with SKA and its Precursors

Poonam Chandra*[1], G. C. Anupama[2], K. G. Arun[3], Shabnam Iyyani[4], Kuntal Misra[5], D. Narasimha[4], Alak Ray[4], L. Resmi[6], and Firoza Sutaria[2]

[1] *National Centre for Radio Astrophysics, TIFR, Ganeshkhind, Pune 411007*
[2] *Indian Institute of Astrophysics,II Block, Koramangala, Bangalore 560034*
[3] *Chennai Mathematical Institute, Siruseri, Tamilnadu 603103*
[4] *Tata Institute of Fundamental Research, Dr. Homi Bhabha Road, Colaba Mumbai 400005*
[5] *Aryabhatta Research Institute of Observational Sciences, Manora Peak, Nainital 263002*
[6] *Indian Institute of Space Science & Technology, Thiruvananthapuram 695547*

Abstract

With the high sensitivity and wide-field coverage of the SKA, very large samples of explosive transients are expected to be discovered. Radio wavelengths, especially in commensal survey mode, are particularly well suited for uncovering transient phenomena, as observations at radio wavelengths may suffer less obscuration than in other bands (e.g. optical/IR or X-rays) due to dust and other absorption. At the same time, multiwaveband information often provides critical source classification rapidly than possible with only radio band data. Therefore, multiwaveband observational efforts with wide fields of view will be the key to progress of transients astronomy from the middle 2020s offering unprecedented deep images and high spatial and spectral resolutions. Radio observations of gamma ray bursts (GRBs) with SKA will uncover not only much fainter bursts verifying claims of sensitivity limited population versus intrinsically dim GRBs, one will also discover the enigmatic population of orphan afterglows. Dust extinction causing the supernova rate problem is expected to be lifted in the SKA era. In addition, finally the debate of single degenerate scenario versus double degenerate scenario will be put to rest in thermonuclear supernovae since highly sensitive measurements will lead to very accurate mass loss estimation in these supernovae. One also expects to detect gravitationally lensed supernovae in far away Universe in the SKA bands. Radio counterparts of the gravitational waves are likely to become a reality once SKA comes online.

1 Introduction

Square kilometre Array (SKA) when ready will be world's largest radio telescope, to be built in Australia and S. Africa. It will be built in two phases. Phase I is expected to complete in 2020; Phase II will be completed in 2024. Phase I will have $\sim$ 10% of the total collecting area. SKA will have a range of detectors: from aperture arrays to dishes; and will span the frequency range from a few tens of megahertz to a few gigahertz. SKA will have unique combination of great sensitivity, wide field of view and unprecedented computing power. Exploration of the transient Universe is an exciting and fast-emerging area within radio astronomy. With its wider field of view and higher sensitivity, the SKA, holds great potential to revolutionize this relatively new and exciting field, thereby opening up incredible new science avenues in astrophysics.

1.1 Explosive Transients

Transient radio sources are compact sources and are locations of explosive or dynamic events. Transient phenomenon usually represent extremes of gravitational and magnetic fields, velocity, temperature, pressure and density. In terms of duration, radio transients phenomenon can be classified into two classes,

*poonam@ncra.tifr.res.in

long time variability (min-days) and bursting radio sky (msec-sec; Carilli, 2014). Transients in radio bands are mainly dominated by three kinds of emission mechanisms:
1:) **Incoherent synchrotron emission:** Transients with incoherent emission show relatively slow variability, and are limited by brightness temperature. These events are mainly associated with explosive events, such as Gamma Ray Bursts (GRBs), supernovae (SNe), X-ray binaries (XRBs), tidal disruption events (TDE) etc. Incoherent transients are mostly discovered in the images of the sky.
2:) **Non-thermal coherent emission**: Transients associated with coherent emission show relatively fast variability, high brightness temperature and often show high polarization associated with them, such as Fast Radio bursts (FRBs; Thornton et al., 2013), pulsars, flare stars etc. The coherent emission transients are discovered in time series observations. The short-duration transients are powerful probes of intervening media owing to dispersion, scattering and Faraday rotation.
3:) **Thermal emission**: These kind of emission is seen in slow transients like novae, symbiotic stars.

The dynamic radio sky is poorly sampled as compared to sky in X-ray and γ-ray bands. To search for transient phase space, one needs the combination of sensitivity, field of view and time on the sky. This has been difficult to realise simultaneously, hence there have been a very few comprehensive transient surveys in radio bands. In addition, the variation in time scales (nano seconds to minutes), and complex structures in frequency-time plane makes things further difficult. The advent of the multi-beam receivers placed on the single dish telescopes, such as Parkes and Arecibo has led us to detect new phenomena such as rotating radio transients (RRATs), FRBs etc. However, much larger FOV is required to discover more of such phenomena.

In India active research is going on in transient astronomy, especially in the fields of SNe, GRBs, Pulsars & related phenomenology, novae, X-ray binaries, TDEs, Galactic black hole candidates, and electromagnetic (EM) signatures in gravitational waves (GWs). Major observational facilities operated by National Centre for Radio Astrophysics (NCRA), Aryabhatta Research Institute of Observational Sciences (ARIES), Indian Institute of Astrophysics (IIA), Inter University Centre of Astronomy & Astrophysics (IUCAA) are widely used. Researchers also avail the wealth of archival data from high energy space missions like *RXTE*, *XMM Newton*, *SWIFT*, *Chandra* and *Fermi*. Groups are also working towards multimessenger astronomy mainly in the context of GWs. Indian Astronomers have access to several observational facilities, both presently existing and to come in the future (e.g., Pandey, 2013).

1.2 SKA, SKA precursors/pathfinders for transients

SKA has adopted transients as its key science goal as it is well in tune with the concept of SKA which is "The primary success metric for the SKA Observatory will be the significance of its role in making fundamental scientific discoveries and facilitating overall scientific progress, expressed as high impact, peer-reviewed scientific papers using SKA data". SKA will open up a new parameter space in the search for radio transients. Some of the basic questions to ask in context of SKA are the following: What do we know about the radio transient sky? How can we improve searches for radio transients? What successes do we expect from SKA pathfinders? How will SKA pathfinders improve our understanding of transients? To achieve the above goals, one needs the right combination of different technologies. Many of these technologies and ideas are being tested with the SKA pathfinders and precursors, such as ASKAP, MWA, LOFAR, uGMRT etc.. The use of widely distributed many small elements for the SKA means that one needs to take advantage of vast computing resources to be able to sample a larger fraction of the sky. Also the discovery of truly transient events relies on having excellent instantaneous sensitivity.

The SKA-International transient Science Working Group (SWG) is driven by key science of (i) FRB cosmology, (ii) Cosmic explosions and extreme astrophysics, (iii) black hole growth and feedback, (iv) Electromagnetic counterparts of GW transients. For SKA to be an optimal telescope for transient science, the international transient SWG has recommended mainly two changes to SKA Phase 1 design:

Commensal Transient Searches:
It is important to do near-real-time searching of all data for transient event. This will increase rate of events by at least one order of magnitude. Also the detection needs to be reported widely, globally and rapidly.

Rapid (robotic) Response to Triggers:
One may be able to detect very early-time radio emission (coherent or prompt synchrotron) if SKA has Robotic response to external alerts, allowing very rapid follow-up of high-priority events. For example,

the Arcminute Micro-kelvin Imager Large Array (AMI-LA) is world's first robotic automated radio telescope. Its response time to Swift triggers are only 30 seconds. AMI has provided the first millijansky-level constraints on prolonged radio emission from GRBs within the first hour post-burst (Staley et al., 2013).

Here it is important to note that multiwavelength observations of the sky are important for the detection and follow-up of transient sources, as they provide complementary views of the same phenomena. The SKA will be roughly contemporaneous with other International facilities like Large Synoptic Survey Telescope (LSST), Gaia, Thirty Meter Telescope (TMT) in optical/IR bands and next generation successors of Swift, Chandra and XMM-Newton in the gamma-ray and X-ray bands (such as SVOM (France-China), SMART-X (US) and ATHENA (ESA) missions). SKA is expected to increase number of transients at least by an order of magnitude. In optical bands, LSST, which will be contemporary of SKA, anticipates finding around 1 million transients per night. However, this rate is not known at the GHz bands. But it is estimated that around 1% of the mJy sources are variable (Frail et al., 2012). LOFAR has recently detected a transient at 10 Jy flux density level at 60 MHz band (Stewart et al., 2015). The transient does not repeat and has no counterpart. The nature of this transient is enigmatic. SKA-LOW will most likely detect 100s of such transients per day in MHz band. Frail et al. (2012) claims that with 10 μJy rms, one can expect around 1 transient per degree. This is achievable by SKA Phase 1 mid frequency.

2 Gamma Ray Bursts

Gamma Ray Bursts (GRBs) were serendipitously discovered in late 1960s by Vela military satellites. They are non-recurring bright flashes of γ-rays lasting from seconds to minutes with an average observed rate of around one burst per day. The energy isotropically released in γ-rays ranges from $\sim 10^{48}$ to $\sim 10^{54}$ ergs. The prompt emission in majority of cases is in γ-ray bands. In a few cases, optical prompt emission is detected. The prompt emission spectrum is mostly non-thermal, though presence of thermal or quasi-thermal components are seen in a handful of bursts (see Kumar & Zhang (2014) for a review). Afterglow emission following the burst in longer wavelengths and lasting for longer time was eventually discovered leading to the confirmation that the bursts are cosmological. GRBs are one of the furthest known objects so far, the redshift distribution ranges from 0.008 to ~ 9 as of now. We currently understand them as catastrophic events generating a central engine which launches an ultra-relativistic collimated outflow.

After nearly 4 decades of extensive research, even though our knowledge about GRBs have definitely enhanced, the very nature of the progenitor, and the radiation physics giving rise to the observed emission in both prompt as well afterglow is yet to be solved. This is mainly attributed to its nonrecurring behaviour, with the emission over only a short timescale resulting in unique and variable light curves. Some of the prominent questions that need to be answered are: what is the nature of the content of the outflow, is it baryonic dominated or Poynting flux?; what is the radiation physics: photospheric emission or non-thermal processes such as synchrotron emission or inverse Compton?; from where exactly in the outflow does the emission occur?; what are the microphysics involved in these radiation events?; what are the dynamics of the outflow resulting in these variable light curves?; how does the transition between the prompt and afterglow phase occur and what is its nature giving rise to the X-ray flares, plateaus, steep decay in flux observed in the early X-ray afterglow?; GRB are believed to be collimated jet emissions to reconcile with the observed energetics, however, this raises question as to why jet breaks are not observed in all afterglow observations?

Resolving the above queries would enable us to use GRB as an effective cosmological tool to probe the early universe. There are several theoretical models proposed for both prompt as well afterglow of GRBs which are sometimes equally consistent with the data. Therefore, we are at such a juncture where it is imperative for the forthcoming observations and studies of GRBs to be able to break the current degeneracy between existing models. Afterglow emission has always been instrumental in diagnosing burst physics like the energy in the explosion, structure of jet, nature of the ambient medium and the physics of relativistic shocks. In this direction, it is evidently clear that we require a multi-wavelength observational coverage of these events extending from gamma rays to radios, which can prove highly constraining for existing theoretical models. This in turn would then become effective in developing a global model connecting prompt to afterglow emission, which can also be adequately tested. SKA, with

its broad field of view and higher sensitivity would be able to play a key role in achieving this prospect as well as in resolving many of the above mentioned open questions.

The combination of high sensitivity, high angular resolution, quick slewing time and broad band frequency range of SKA will be extremely crucial for GRB science through radio observations.

2.1 Long versus Short GRBs

The histogram of GRB duration reveals a bimodal distribution (Kouveliotou et al., 1993): the long and the short bursts. In the BATSE burst population, bursts with duration less than 2 s were classified as short and those lasting for more than 2 s were classified as long. Apart from the duration, long and short bursts also show difference in the hardness of their γ-ray spectrum (Kouveliotou et al., 1993). The short bursts are typically harder than the long ones. Subsequently, long GRBs at lower redshifts are found to be associated with type Ib/c broad lined supernovae, thereby establishing their origin in the gravitational collapse of massive stars (Woosley & Bloom, 2006). No short burst has so far been found associated with supernovae. Further studies have revealed that the difference lies deeper than the prompt emission, and extends to the burst environment. In accordance with the massive star hypothesis, long GRBs are predominantly found in star forming regions of late type galaxies (Fruchter et al., 2006) while short bursts are seen in a variety of environments (Fong, Berger, & Fox, 2010). Distribution of the off-set of burst position from the photocentre of the host galaxy shows that short bursts typically are further away from the central regions of the galaxy compared to their longer cousins (Fong, Berger, & Fox, 2010). These evidences support a hypothesis that long bursts are possible end stages of massive stars ($M > 15M_{\odot}$) while short bursts are associated with older stellar populations like compact objects. Currently we believe that at least a fraction of short GRBs form due to the merger of compact object binaries (see Berger (2014) for a review). With the recent discovery of gravitational waves (GWs), a new era of Gravitational Wave Astronomy has begun which can shed more light into this model if short GRBs or their afterglows are observed in coincidence with double NS or NS-BH mergers. (See Sec 5 of SKA (2015) for capabilities of SKA to carry out electromagnetic follow up of GW events).

Recently a new class of GRBs, named ultra-long bursts (ULGRBs), are found to be lasting for several thousands of seconds (Levan, 2015). It is speculated that ULGRBs are arising from a different class of progenitors.

In the *S*wift era, almost 93% of GRBs have a detected X-ray afterglow, $\sim 75\%$ have detected optical afterglows while only 31% have radio afterglows (Chandra & Frail, 2012). The SKA, with its extreme sensitivity, will dramatically improve statistics of radio afterglows. Using numerical simulation of the forward shock, Burlon et al. (2015) predicts around $400 - 500$ radio afterglow detections per sr per yr in SKA-1 Mid bands. In X-ray and optical bands GRB, fireball is almost always optically thin. However, early evolution of low frequency (< 4 GHz) radio lightcurves is through the optically thick regime, the lightcurve peak corresponds to transition from optically thick to thin regime. Hence, radio frequencies are unique in probing the evolution of the self-absorption frequency, ν_a, which in turn can constrain the physical parameters such as density of the environments etc.. Tracing the evolution of ν_a will also help in scrutinizing basic assumptions in the standard fireball model, especially of the time-invariant shock microphysics. SKA can densely sample the lightcurves of long as well as short GRBs at different frequencies, towards this understanding. Thus radio emission from long versus short GRBs will reveal the difference in the environments of these two classes of GRBs. However, Hancock et al. (2013) has claimed that undetected afterglows are intrinsically dim rather than sensitivity limited. SKA will be very crucial in lifting this degeneracy.

In the absence of γ-ray trigger, either due to the jet pointing away from earth or due to unavailability of a dedicated triggering instrument, orphan radio afterglows can be detected by SKA owing to its high sensitivity. Burlon et al. (2015) predicts $300 - 400$ orphan afterglows per all sky per week. Orphan afterglow detection rates will help in drawing indirect limits of jet structure.

2.2 Unveiling the GRB Reverse Shock with SKA

According to the standard model, a central engine, perhaps a black-hole torus system or a millisecond magnetar, formed during either the gravitational collapse of a massive star (for long GRBs) or the merger of a double compact object binary (short bursts), launches an ultra-relativistic jet. The jet energy could either be in the bulk kinetic energy of its baryonic content or in magnetic fields (Poynting

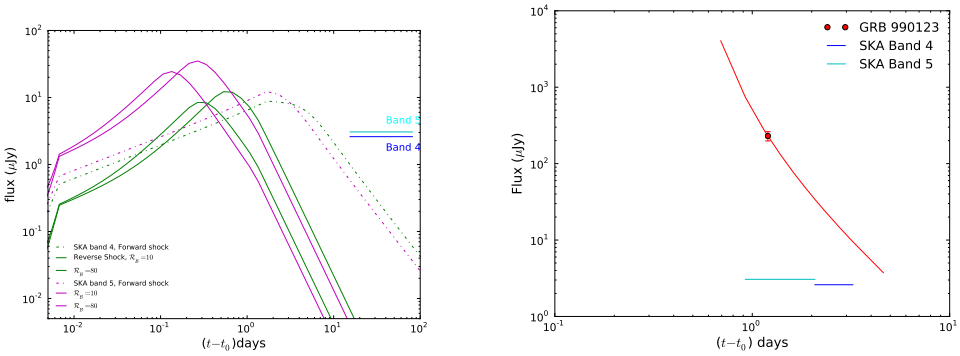

Figure 1: (Left): Reverse and forward shock predictions in SKA-1 Mid Band-4 (4 GHz) and Band-5 (9.2 GHz) for standard parameters (energy in explosion $E_{\rm iso} = 10^{52}$ergs; ambient medium density $n_0 = 0.1$ atom/cc; initial bulk Lorentz factor $\eta = 100$; energy content in forward and reverse shock electron populations, $\epsilon_e = 0.1$; energy content in forward shock magnetic field $\epsilon_B = 10^{-5}$). The burst is assumed to be at a redshift of 2. Reverse shock lightcurve strongly depends on the ratio $\mathcal{R}_\mathcal{B}$ of reverse to forward shock magnetic field energy density, in turn the magnetization of the ejecta. 3σ flux limits for SKA-Mid Band-4 and Band-5 for a 2hr on source integration are also shown for comparison. (Right): Radio flare of GRB990123 in VLA 8 GHz scaled to different redshifts. 3σ limits of SKA1-Mid Band-4 and Band-5 are plotted in the relevant redshift ranges.

Flux Dominated Outflow). Prompt emission arises due to internal dissipation of the outflow energy. The remaining energy gets dissipated in the medium surrounding the burst ensuing longer wavelength afterglow emission. However, in majority of GRBs, the early afterglow is influenced by continuous energy supply from the central engine.

The external energy dissipation happens through a forward and reverse shock system. The forward shock runs into the ambient medium and the reverse shock runs into the ejected material. Emission from the reverse shock is seen in the early optical (Sari & Piran, 1999) and radio afterglows (Laskar et al., 2013). Early afterglow is one of the main tools for probing the central engine. Particularly, the reverse shock emission can shed light into the magnetization of the ejecta which is an important parameter in knowing the jet launching mechanism.

There have been several observational as well as theoretical studies of radio reverse shock emission in the literature. The first detection of a radio flare, expected to be originating from the reverse shock, was for GRB990123. In recent times, deep and fast monitoring campaigns of radio reverse shock emission could be achieved using JVLA (Chandra & Frail, 2012; Laskar et al., 2013) for a number of bursts. Reverse shock emission is brighter in higher radio frequencies where self-absorption effects are relatively lesser. Gao et al. (2013); Kopac et al. (2015) and Resmi & Zhang (2016) have done comprehensive analytical and numerical calculations of radio reverse shock emission. Figure-1 (left) compares theoretical predictions of reverse shock emission from Resmi & Zhang (2016). The lightcurves are calculated by assuming a Newtonian reverse shock (thin shell regime) and ultra-relativistic forward shock system in a constant density ambient medium. Difference in ejecta magnetization is reflected in the RS lightcurve peak time. Radio afterglow monitoring campaigns in higher SKA bands will definitely be useful in exploring reverse shock characteristics. In Figure-1 (right) we look into the detectability of GRB990123 had it been at higher redshifts. The 8 GHz peak flux and corresponding $t_{\rm obs}$ are scaled accordingly. Accounting for cosmological k-correction, the flux will correspond to SKA1-Mid Band-4 and Band-5 as the redshift changes. SKA1-Mid will be able to detect a bright radio flare like GRB990123 even if it happens at a redshift of ~ 10.

2.3 Late afterglow and calorimetry with SKA

Longevity is the highest advantage of radio bands in studying GRB afterglows. While X-ray and optical afterglows stay above detection limits only for weeks or months, radio afterglows of nearby bursts can

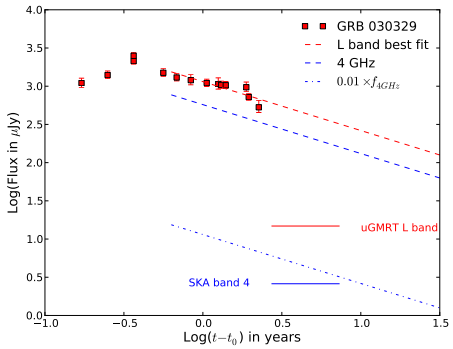

Figure 2: GMRT L-band lightcurve of GRB030329. Best power-law fit to late time L-band data is shown as dashed red line. A spectral factor assuming index -0.5 is used to obtain the 4 GHz extrapolation (blue dashed line). uGMRT and SKA Band-4 flux limits are for 2hr on source time. The dash-dot line correspond to a burst 100 times fainter than GRB030329 in 4GHz.

be detected upto years (Frail, Waxman, & Kulkarnii, 2000; Resmi et al., 2005). A couple of very bright afterglows have been observed in time scale of several years by VLA and GMRT. GRB 030329 is the longest observed afterglow, in a campaign made possible through GMRT low frequency capabilities even when the afterglow had gone below detection limits in higher frequencies. In figure-2 we plot the first two years of observations of GRB030329 radio afterglow in GMRT L band.

The longevity of radio afterglows make them interesting laboratories to study the dynamics and evolution of relativistic shocks. Fireball transition into non-relativistic regime can be probed through low frequency radio bands Frail, Waxman, & Kulkarnii (2000); van der Horst et al. (2008) This regime is largely unexplored due to limited number of bursts in past that stayed above detection limit beyond sub-relativistic regime. Several numerical calculations exist for the afterglow evolution starting from the relativistic phase and ending in the deep non-relativistic phase (van Eerten & MacFadyen, 2012; De Colle et al., 2012). SKA with its microJansky level sensitivity will be able to extend the current limits of afterglow longevity. This will provide us with an unprecedented opportunity to study the deep non-relativistic regime of afterglow dynamics and thereby will be able to refine our understanding of relativistic to non-relativistic transition of the blastwave and changing shock microphysics in the GRBs. In the SKA era, these predictions can be tested against observations. Late afterglow phase where the fireball is both sub-relativistic and nearly spherical, calorimetry can be employed to obtain the burst energetics. These estimates will be free of relativistic effects and collimation corrections.

2.4 Connecting prompt and afterglow Physics

GRB prompt spectra in general look non-thermal in nature, and is generally modelled using a Band function, which is a phenomenological function of two power laws smoothly joined at a peak parameterised as E_{peak} Band et al. (1993). However, the study of GRB spectra using non-thermal models pointed out several spectral features as well as questions such as how can sub peak spectra be both hard as well as soft? (Preece et al., 1998; Goldstein et al., 2013); why is the E_{peak} of the Band function fits clustered in a narrow energy range (Gruber et al., 2014; Goldstein et al., 2013); what drives the hardness-intensity correlation characteristic of each burst? (Amati et al., 2002; Lu , Hou, & Liang, 2010; Amati, Frontera, & Guidorzi, 2009) and more importantly, what gives rise to the observed high radiation efficiency in gamma rays? (Cenko et al., 2010; Racusin et al., 2011). Pure non-thermal models faced difficulty in addressing these questions, which evoked the idea of the presence of thermal component, which is inherent in the standard fireball model, along with non-thermal component in the spectrum. BATSE spectral analysis was limited due to its insufficient energy window (20 -2000 keV) in determining the overall shape of the GRB spectrum. The Swift hard X-ray detector BAT, however, is not very sensitive above about 150 keV (Meegan et al., 2009; Band, 2006) and hence cannot measure the prompt X-ray/ gamma-ray spectrum accurately (majority of GRBs have their peak energy around 250 keV). However, this drawback was

overcome by the launch of Fermi in 2008, providing observation over a broad energy range of nearly 7 orders of energy, 8 keV - 300 GeV, made possible by two main instruments onboard: Gamma ray burst monitor (GBM) Meegan et al. (2009) and Large Area Telescope (LAT) Atwood et al. (2009). Some of the key observations by Fermi had been: i) the delayed onset of high energy emission for both long and short GRBs Abdo et al. (2009a,c, 2209b), ii) LAT emission tends to last longer Ackermann et al. (2013), iii) very high Lorentz factors (~ 1000) are inferred for the detection of LAT high energy photons Abdo et al. (2009a), iv) several bright bursts show a significant detection of multiple emission components such as thermal component Guiriec et al. (2011); Axelsson et al. (2012); Burgess et al. (2014), power law Abdo et al. (2209b) or spectral cut off at high energies Ackermann et al. (2011), in addition to the traditional Band function, iv) interestingly, the Band function is found to have a different spectral shape in these multi-component fitting Guiriec et al. (2013) and v) recently, it was shown by Axelsson & Borgonovo (2015) that 78% of long GRBs and 85% of short GRBs have spectra with spectral width at full width half maximum of the νF_ν peak, that is much narrower than optically thin synchrotron emission, but still broader than a blackbody.

Theoretical models of photospheric emission have currently become the pivot of the study of prompt emission in GRBs. The time resolved analysis of the spectrum enables us to follow the dynamic spectral evolution as well that in these outflow parameters with time, which is crucial to our understanding of how progenitor evolves within the burst Iyyani et al. (2013, 2015, 2016).

While Swift and Fermi satellites have enriched our understanding of the GRBs by wide band spectral measurement during the prompt emission by the Fermi satellite and quick localisation, follow up observation and the consequent redshift measurement by the Swift satellite (Gehrels et al., 2009; Gehrels & Mészáros, 2012). But currently good spectral and timing measurement from early prompt phase to late afterglow is available for a few sources and they are particularly lacking for the SHBs. Some of the key problems that can be addressed by the observation of the radio afterglows by SKA in connection with the prompt emission would be the following: i) The connection of LAT detected GRBs with delayed high energy emission with afterglow parameters and comparing the Lorentz factor estimation with both LAT detected GeV photons as well as from the afterglow physics Kidd & Troja (2014). If the photosphere emission is detected in the prompt phase, this will also give an estimate of the dynamics of the outflow Iyyani et al. (2013). This effort would enable to constrain the Lorentz factor of the outflow which is one of the key dynamic parameters directly connected to the progenitor. ii) Evaluating the connection as well as comparison between non-thermal emission of both the prompt as well as afterglow emission. This would enable to constrain the microphysics of the shocks accelerating electrons to ultra-relativistic energies eventually producing the observed radiation. iii) Detailed modelling of the afterglow observation of both long and short GRBs, will enhance our knowledge about the circumstellar as well as interstellar medium surrounding the progenitors. This will provide information about the host galaxy and the environment which will be crucial in assessing the various proposed progenitor models for these bursts.

SKA with its finer sensitivity would play a key role in constraining the energetics of GRBs which is crucial in estimating the radiation efficiency of the prompt emission of GRBs. This would include the crucial detection of jet breaks in radios as well as in constraining the dynamics of the outflow parameters. This would also strengthen our understanding of the hardness - intensity correlation Amati et al. (2002) which can eventually enable us to adopt GRBs as standard candles to probe cosmology. Till to date GRB is the most distant event probed by any astronomical observatory at a photometric redshift estimate of $z = 9.4$ detected for the burst GRB 090429B Cucchiara et al. (2011). In co-ordination with both space as well as ground based observatories in other wavelengths, SKA observations can be crucial in studying the timing of the onset of emission in various wavelengths which can throw light on the issue of where in the outflow does the emission occurs. There have been several detections of thermal component in early X-ray afterglow Campana et al. (2006); Starling et al. (2012); Friis & Watson (2013) . It would be interesting to find the component in longer wavelengths extending till radios which can then prove highly constraining in assessing its connection to the observed prompt thermal emission or whether it has a completely different origin.

The recently launched Astrosat satellite (Singh et al., 2014) carries a suite of instruments for multi-wavelength studies and the Cadmium Zinc Telluride Imager (CZTI) can act as a monitor above about 80 keV (Rao, 2015; Bhalerao et al., 2015). CZTI, along with Swift, can provide prompt spectroscopy and CZTI can localise Fermi detected GRBs correct to a few degrees. Further, for bright GRBs it can provide time resolved polarisation measurements. Hence, for a few selected bright GRBs, CZTI, in conjunction with other operational satellites, can provide wide band spectra-polarimetric information

and if followed up by other ground based observatories like SKA pathfinder uGMRT, we can have a complete observational picture of a few bright GRBs from early prompt phase to late afterglow. This will provide us with a comprehensive picture of GRBs, thus enabling a good understanding of the emission mechanisms.

3 Supernovae

Supernovae (SNe) are explosive events with two basic types: 1. thermonuclear Supernovae (SNe-Ia), caused by the explosion of a massive white dwarf in a binary system. Their optical spectra are characterized by the absence of H lines and the presence of Si II absorption line; 2. Core-Collapse Supernovae, which mark the end of the life of massive stars. Their classification is based on the observed spectra. Presence or absence of Hydrogen lines classify them as Type II versus Type I. In Type I SNe, presence or absence of silicon lines categorize them between Type Ia versus Type Ib/c. Further Type Ib and Ic are classified based on the presence and absence of Helium lines, respectively. Amongst Type II SNe, the varied nature of light curves classify them into Type IIP, IIL and IIn.

The physical processes driving the radio emission, and its temporal and spectral properties, turns to be not only a characteristic of these explosive events itself, but of the pre-explosive evolutionary history of their precursor (progenitor) as well. Typically, there is almost no thermal radio emission in these events. A common property of all explosive transients which show up in the radio is the presence of some amount of circumstellar medium (CSM), either or diffuse, in the vicinity of the progenitor, and the synchrotron emission is often successfully modelled as being produced by the interaction of the explosion shock with this material. Incoherent radio emission has been detected from various types of core-collapse supernovae, which includes SNe-Ib (e.g. PS15bgt Kamble et al., 2015), SNe-Ic (e.g. SN 2012ap, Chakraborti et al., 2015), SNe-IIn, E.G. SN 1995N (Chandra et al., 2009), SN 2006jd(Chandra et al., 2012), SN 2010jl(Chandra et al., 2015), and SNe-IIP SNe, e.g. SN 2004et,][] (Misra et al., 2007), 2011ja (Chakraborti et al., 2013), 20012aw (Yadav et al., 2014; Chakraborti et al., 2016). As a survey instrument, SKA will be contemporaneous with LSST and WISE, thus opening a radio vista in to the statistical properties of a dynamic universe, while as a follow-up instrument, its high sensitivity and resolution will answer several crucial questions about the nature and origins of various SNe, both in the early and in the present Universe.

3.1 Radio view of Core Collapse Supernovae

In supernovae, radio emission arises from shock interaction with the surrounding circumstellar medium (CSM), which provides an important probe to see their last evolution stage. Since radio-SNe can show both early and late radio emission, the most probable model would be that the emission itself comes from relativistic electrons trapped in shocked CSM (early emission) or from the reverse shock itself, as it propagates inwards in to the SNe ejecta (late emission)(Chevalier, 1998) Therefore, radio SNe probe the dynamics of the SN ejecta, the progenitor structure, and the CSM. Since SSA necessarily requires the presence of a magnetic field in the emitting region, radio spectra also provide insight in to the nature of the CSM field, as well as in to the generation/disruption of fields in the SNe-ejecta. In addition, signatures in the multifrequency radio light curves give concurrent information about how the shock accelerated electrons cool in the presence of a long lasting optical emission from the SN through Inverse Compton (IC) cooling or instead, whether synchrotron cooling dominates over IC cooling (Chevalier, 2006). Compton cooling of electrons could keep the radio light curve relatively flat in the optically thin regime, whereas synchrotron cooling of electrons will be important if the magnetic field is efficiently built up in the explosion. Radio light curves around 100 days can indicate whether Compton cooling dominates over synchrotron cooling (Fig. 5 of Chevalier, 2006).

Radio data of a few type IIP SNe show long periods of radio brightness (e.g. beyond 100 days as in SN 2004et, Fig/ 3). Radio data on SN 2012aw shows the rapid evolution of the radio spectrum between 30 to 70 days and a signature of cooling at higher frequencies (Chevalier, 2006). Early observations at high frequencies are critical to the issue of IC cooling of radio emitting electrons. A fraction of type IIP supernovae e.g. 2011ja (Chakraborti et al., 2013) may happen inside circumstellar bubbles blown by hot progenitor or with complex circumstellar environments set up by variable winds.

SNe IIn are most complex in terms of stellar evolution. They encompass objects of different stellar

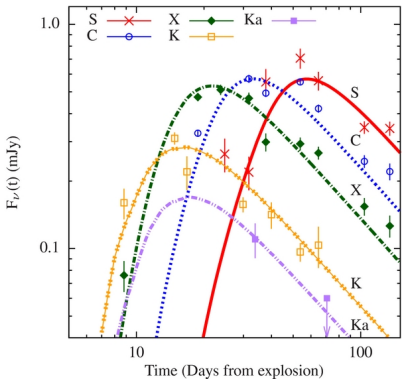

Figure 3: Radio observations of SN 2012aw. The bands are as follows: S (3.0 GHz), C (5.0 GHz), X (8.5 GHz), K (21.0 GHz), and Ka (32.0 GHz) (Yadav et al., 2014).

evolution and mass loss history. Some SNe IIn, like SN 2005gl, appear to have a luminous blue variable (LBV) star as their progenitor (Gal-Yam et al., 2007). A special class of SNe IIn is characterized by spectral similarities to SNe Ia at peak light, but later shows SN IIn properties, e.g., SNe 2002ic and 2005gj. Some SNe IIn appear to be related to SNe Ib/c. Most recently SN 2009ip is the unique Type IIn SN to have both a massive blue progenitor and LBV like episodic ejections (Mauerhan et al., 2013; Margutti et al., 2013). A challenging problem in SNe IIn is that neither their evolutionary status, nor the origin of the tremendous mass loss rates of their pre-SN progenitor stars is known. The estimated mass-loss rates of SN IIn progenitors are much higher than those of usual massive stars ($10^{-4} - 10^{-1}$ $M_\odot$ yr^{-1}). Thus SN IIn progenitors must have enhanced mass loss shortly before their explosions. Thus to unveil the nature of the mysterious SN IIn progenitors and mass loss related to them, we need to know the properties of the SN ejecta and dense CSM related to them.

Some SNe-Ib/Ic have been associated with long duration GRBs. However, as the cases of SN2009bb and SN 2012ap have shown, there may be a class of stellar explosions which bridge the continuum between jetted relativistic events like GRBs and the more spherically symmetric non-relativistic "garden variety" supernovae, without high energy counterparts. These recently discovered radio bright hypernovae (R-HNe) raise important questions about the nature of their central driving engines. The possibilities include: (a) relativistic jets which are formed deep inside the progenitor stars (and whose emergence is suppressed) (Margutti et al., 2014a); (b) quasi spherical magnetized winds from fast-rotating magnetars, leading to asymmetric explosions, and (c) re-energising of the shock, as the inner,slower moving shells successively catch up with the shocked region and refresh it (Nakauchi et al., 2015, and references therein) . The explosion geometry is is asymmetrical in the former two cases, and symmetrical in the case of the refreshed shock. Few radio hypernovae have been detected so far, and again, a radio survey like SKA would be the best option to increase the statistics for these events.

Typically, in SNe, spectral radio luminosity $L_R \simeq 10^{33}$ to 10^{38} erg s^1 at 5 GHz, making them fainter by a factor of$\sim 10^4$ in the radio than in the optical. However, there is much diversity in the radio light curves, in the temporal evolution of the radio "spectra", and in the onset of radio emission in different bands, as even across the same sub-class, there are both radio-bright and radio-suppressed events. The latter may partly be a selection effect, which could be resolved with the high sensitivity of the SKA.

Radio lightcurves are crucial to understand the history of the progenitor star. However, currently only $\sim$ 10% of the discovered core-collapse SNe show radio emission. Only the radio-brightest SNe are detected, and systematic searches of radio emission from core-collapse supernovae (CCSNe) are still lacking, and only targeted searches of radio emission from just some of the optically discovered CCSNe in the local universe have been carried out. And this in spite of optical searches missing a significant fraction of CCSNe. This is because the optically dim SNe are missing due to either being intrinsically faint or due to dust obscuration in the host galaxy. Therefore, radio supernova searches are much more promising for yielding the complete, unobscured star-formation rates in the local universe. As an obvious consequences of the increasing sensitivity of SKA, it will be possible to study a larger number of SNe (from current 2 radio detections/yr up to 50 detections/yr with SKA). We would also be able to follow-up

each of them for a longer time. The SKA1-mid will be able to detect many such dust obscured SNe, especially for those located in the innermost regions of host galaxies. Also the detection of intrinsically dim ones will also benefit from SKA1. The detection rate will provide unique information about the current star formation rate and the initial mass function. The commensal, wide-field, blind transient survey observations would result in an essentially complete census of all CCSNe in the local universe, as well as an accurate determination of the true volumetric CCSN rate. The best option is likely to be that of using SKA1 at a frequency of 1.7 GHz, angular resolution 1", FoV 18 deg^2, good sensitivity 3.7 uJy/beam. With an improved sensitivity level of 1 uJy, one can detect the brightest of radio SNe, such as the Type IIn SN 1988Z at the cosmologically interesting distance of z=1.

3.2 Unveiling thermonuclear Supernovae with SKA

Despite their great cosmological importance, the exact nature of progenitors of SN-Ia remains unknown. While the canonical model is that the SNe itself is caused by thermonuclear explosion of a CO WD, initiated by accretion from a secondary, the nature of the secondary itself is still debatable. In the singly degenerate (SD) progenitor scenario, the H- and/or He-rich secondary could be a non-degenerate star which is either MS, immediately post-MS, or even a late evolved red-giant, while in the double degenerate (DD) scenario it could be another WD in close contact binary, which merges in to the degenerate SNe progenitor, leading to the thermonuclear runaway reaction. Despite the very large number of optical observations of bright, nearby, SNe-Ia, which track the evolution of the SNe from shock outburst to nebular stage, the exact model has not yet been confirmed. Population synthesis studies of SD and DD models (Claeys et al., 2014; Rutter et al., 2009) suggests that the DD channel is the most probable one, with multiple possible evolutionary sequences, leading to the formation of the close DD system. In any case, it is to be expected that mass loss would have occurred from the progenitor(s) prior to explosion, via stellar winds, Roche-Lobe overflow (RLOW), or in the common envelope (CE) phase, and a shock-CSM interaction should produce radio emission, with the low frequencies (e.g.) SKA bands reaching peak luminosity at a later time. This implies that the temporal, spectral and flux evolution of the radio emission would serve as a trace of the physical properties of SNe shock and CSM interaction.

To date, no SNe-Ia has been detected in the radio, though this could also be a selection effect, in that few bright SNe-Ia have been followed up in the radio band, immediately post-shock, and because a less massive and/or dense CSM would mean that the radio flux density would lie below the detection threshold of the current generation of radio telescopes. E.g. for the nearby SN-Ia SN2014J (at 3.5 Mpc), only an upper limits on flux density in the eMERLIN (37.2 and 40.8 μJy at 1.55 and 6.17 GHz respectively), JVLA (12.0 and 24.0 μJy at 5.5 and 22 GHz respectively) and eEVN (28.5 μJy 1.66 GHz) are known, for epochs spanning up to 35 days post explosion (Pérez-Torres et al. , 2014) – this lack of prompt emission appears to be consistent with the DD progenitor model. Thus, for nearby type-Ia SNe ($\simeq 2$ such events are detect each year at $V_{peak} < 13$), even a non-detection of radio emission in the SKA bands would set tight constraints on the mass loss history of the progenitor system, and hence on the theoretical model. It is also to be noted that SNe of all kinds, whose optical emission is shrouded by dust, would nevertheless be visible in the SKA bands, and therefore a survey of transient SKA sources would further constrain supernova rates as a function of various galactic properties.

In addition, Supernova explosion triggers shock wave which expels and heats the surrounding CSM and ISM, so forms supernova remnant (SNR). It is expected that more SNRs will be discovered by the SKA. This may decrease the great number discrepancy between the expected and observed. Several Supernova remnants have been confirmed to accelerate protons, main component of cosmic rays, to very high energy by their shocks. The cosmic ray origin will hopefully be solved by combining the low frequency (SKA) and very high frequency (Cherenkov Telescope Array: CTA) bands' observations.

3.3 Gravitational Lensing of Transient Events

Time delay between multiple images of a Gravitationally lensed source is a powerful diagnostic of the Physics of the source and Cosmology. Time delay in lensing is the only direct observable that gives the Physical Scale of the system. Rich Galaxy clusters at intermediate redshift (order 0.2 to 1) are powerful lenses. In the central region, multiple images are linearly magnified (according to certain characteristic way) upto a factor of 100, and so, background galaxies at redshift of the order of 1 to 3 are elongated into giant arcs of 10 - 30 arcseconds. (This is an important channel to possibly detect even galaxies in

forming at redshifts of more than 6) There are more than 100 highly magnified lensed galaxies recorded and the number is increasing with more and more systematic surveys.

If a supernova or GRB occurs in one such galaxy, it will appear in one of the images first then in the other two images (or three, if magnification is sufficient for detection) at time lag of week to year scale. (This was pointed out by Schneider & Wagoner (1987); Narasimha & Chitre (1989). Position of the event and information about which image will have the event seen first can be unambiguously determined from optical observation of the system and lens model constructed from it. Multifrequency observations, specially optical and radio will be valuable in this respect.

Detecting the event in one image (even partially) allows an observer to plan and monitor the event in other images. This helps to test many aspects of the event itself with elaborate multifrequency observations. The subsequent refined models (specifically time delay measurements are important cosmological probe (specifically Hubble Constant and dark energy, Dev et al., 2004). Metcalf & Silk (2007) pointed out that the supernova data favour dark matter made of microscopic particles (such as the lightest supersymmetric partner) over macroscopic compact objects (MCOs).

Since there are more than 100 potential targets, we expect one year of careful monitor to register one usable event. uGMRT and SKA can organise such a programme and look for these events.

4 Novae Outbursts

Novae form an important sub-class of transients in our Galaxy as well as in other galaxies. A nova outburst is triggered by runaway thermonuclear burning on the surface of an accreting white dwarf in an interacting binary system. With outburst energy in the range of 10^{38} to 10^{43} ergs, these events are amongst the energetic explosive ones. At an estimated rate of 30 novae per year (2002), these events are fairly frequent. Although the current observed rate is much lower than estimated, future deep surveys by facilities such as the LSST are expected to increase the number of observed events. Nova systems serve as valuable astrophysical laboratories in the studies of physics of accretion onto compact, evolved objects, and thermonuclear runaways on semi-degenerate surface which give insight into nuclear reaction networks. They also contribute to enriching the ISM with heavy isotopes of ^{13}C, ^{15}N, ^{22}Na and ^{26}Al. In addition, if the mass ejected during a nova outburst is less than that accreted since the last outburst, there is the possibility of the WD growing in mass, making (at least some) of these systems interesting candidates for SNe Ia progenitors. However, despite their astrophysical significance as nearby laboratories, many aspects of these relatively common stellar explosions remain poorly understood. Although much of our current understanding of these systems has come from the optical observations, multi-waveband observations have augmented and enhanced our understanding. Radio observations play a key role in addressing some of the puzzling aspects of accretion, outburst and interaction with the environment.

Radio emission from novae typically lasts longer than the optical emission, on timescales of years, rather than months. Observations at different epochs yield information on different aspects of the nova outburst. While the very early phase observations provide information regarding the distance to the nova, as the nova evolves, the observations provide clues to the mass of the ejecta. The mass of ejecta is a fundamental prediction of nova models, and thereby provides a direct test of nova theory. The primary mechanism of radio emission is thermal bremsstrahlung from the warm ejecta. In addition, in the case of novae in dense environment, the interaction of the nova ejecta with the environment gives rise to a shock, which in turn may give rise to a non-thermal, synchrotron emission component, like in the case of GK Per (Seaquist et al. , 1989; Anupama & Kantharia , 2005), RS Oph (Hjellming et al. , 1986; Taylor et al. , 1989; OBrien et al., 2006; Kantharia et al. , 2007; Rupen et al., 2008; Sololoski et al., 2008; Eyres et al., 2009) and V745 Sco (Kantharia et al., 2016). The *Fermi* detection of recent novae such as V407 Cyg 2010, V959 Mon 2012, V1324 Sco 2012, V339 Del 2013 and V745 Sco has revealed that shock interaction with the dense environment can also lead to GeV gamma ray emission.

Previous radio observations of nova outbursts have illustrated the unique insights into nova explosions these observations bring. Since radio emission traces the thermal free-free emission, by extension it traces the bulk of the ejected mass. In addition, radio observations are not subject to the many complex opacity and line effects that optical observations both benefit and suffer from. Thus, in addition to being relatively easier to interpret, radio observations can also probe how the ejecta profile and dynamic mass loss evolve with time. Radio observations of novae will thus illuminate the many multi-wavelength

complexities observed in novae and test models of nova explosions.

SKA and its precursors will be very well placed to study novae at various epochs of the outburst. While the thermal emission from most novae have been well observed in the higher (> 1 GHz) frequencies, the sensitivities of the existing facilities are not well suited to detect thermal emission at < 1 GHz. The improved sensitivity of SKA at the lower frequencies will enable detection of the thermal emission at these frequencies, providing a better understanding of the evolution of the physical conditions in the nova ejecta. Also, the < 1 GHz frequencies are ideal to observe the non-thermal emission from novae, especially from the recurrent nova systems (see Kantharia et al., 2016). A sensitivity limit of 1 mJy can detect radio emission at < 1 GHz upto a distance of 10 kpc, if the non-thermal luminosity of the nova system is 10^{13} W Hz^{-1} (Kantharia, 2012). An important motivation for studying the non-thermal radio emission from recurrent novae is to interrogate possible evolutionary connection to the lack of detectable radio emission from type Ia supernova systems. As has been shown by Kantharia et al. (2016) for the recurrent novae RS Oph and V745 Sco, changes are observed in circumstellar material with subsequent outbursts. Observations of future outbursts will establish if these changes are evolutionary, and also their impact on the evolution of the binary system itself.

5 Multi-messenger Astronomy with SKA: Gravitational Wave perspective

Electromagnetic counterparts of gravitational waves (GWs) are another important class of transients relevant to SKA science. Laser Interferometric Gravitational wave observatory (LIGO) recently reported the first detection of a binary black hole merger (Abbott et al., 2016a), opening a new observational window to the universe through GWs.

This binary black hole event (named as GW150914) was followed up electromagnetically (Abbott et al., 2016) and in neutrinos (Adriań-Martińez et al, 2016) using various observational facilities in the world. Though no electromagnetic counterparts associated with GW150914 were reported, this sets milestone in the field of multi-messenger astronomy where a real GW signal was followed up various electromagnetic (EM) bands. It is worth noting that the above mentioned follow ups included radio follow ups by LOFAR, MWA and ASKAP which demonstrates the capabilities of radio telescopes to carry out searches for EM counterparts of GW events. The LIGO configuration which lead to the detection of GW150914 is going to evolve to much better sensitivities which will bring the detection of NS-NS and NS-BH binaries within its reach and more GW detectors are going to come online in the next few years which will considerably improve the source localization.

Phenomenon such as short GRBs and (a sub-population), FRBs have been proposed to be associated with NS-NS or NS-BH mergers. The science potential ranges from detecting radio afterglows associated with short GRBs coincident with GW observations of NS-NS or NS-BH binaries (hence directly confirming the compact binary progenitor of short GRBs), detecting orphan afterglows associated with some of the NS-NS or NS-BH mergers which might have produced a GRB which was pointed away from us and hence missing it, to somewhat speculative scenario of FRBs being detected in coincidence with GW observations (if a sub-population of the FRBs is produced due to mergers of NSs). Such joint observations can shed light on various aspects of the phenomenon including possible constraints on the models of GRB jets (Arun et al., 2014).

One of the interesting prospects of SKA for multi-messenger astronomy lies in the radio follow up of GW triggers using the second or third generation gravitational detectors detectors that may be operational at the time of SKA. The network of GW detectors by the time SKA comes online, may have the capability to localize the source to within few square degree which makes efficient follow up of the source much simpler. The FOVs of ASKAP (30 sq degree), SKA-1 survey (18 sq degree) and SKA-low (27 sq degree) (see Table 1 of SKA, 2015) suits requirements for the EM follow up of GW triggers using a network of interferometers which will localize the sources within a few sq degrees to a few tens of sq degrees (see Table 3 of Fairhurst (2011) for instance), depending on the nature of the compact binary. The very fact that ASKAP took part in the radio follow up search of GW150914, shows the preparedness of SKA-like detectors to take part in such follow up efforts. The science returns from such joint radio-GW observations are enormous. It is clear that ASKAP will continue to play a crucial role in the follow up of GW triggers in the upcoming science runs of LIGO. It is interesting to note that SKA will be one of the unique instruments which by itself will be searching for Gravitational Waves

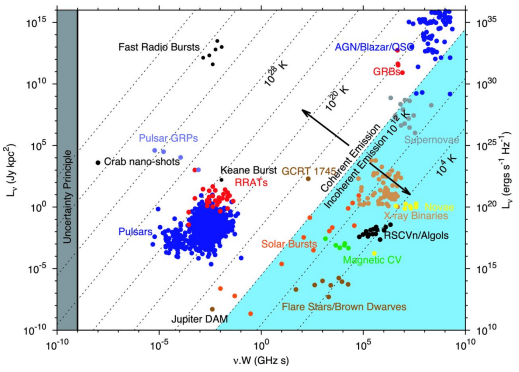

Figure 4: Parameter space for transient sources. This allows one to identify the sources of coherent radio emission (pulsars, fast radio bursts, certain emission from Jupiter and the Sun, etc.) for comparison with the more slowly varying synchrotron transients (Pietka et al., 2015).

(from supermassive BH binaries) in the pulsar timing array mode and also looking for electromagnetic counterparts to ground-based GW detector triggers. Hence multi-messenger astronomy associated with these systems is going to be very exciting.

6 Discussion and Conclusions

With the high sensitivity and wide-field coverage of the SKA, very large samples of explosive transients are expected to be discovered. A major fraction of these will be TDE events followed by type II SNe and orphan afterglows of GRBs and relativistic supernovae. Even at the ASKAP (precursor) stage, VAST-Wide surveys conducted at 1.2 GHz band for about 10,000 square degrees every fortnight will typically be expected to yield some 32 type II SNe, 82 Swift 1644+57 TDE events, 8 orphan afterglows (Frail et al., 2012). The large number of such newly discovered sources will be a rich harvest, among which there will be quite a few that will have characteristics (such as radio brightness, counterparts at other wavebands or other physical characteristics like outflow properties) that will make it possible to follow them up intensively with high cadence. Not only will these new discoveries trace out well-populated areas of phase space of explosions see Fig. 4, but quite likely, they will provide hitherto unknown linkages that will clarify or strengthen suspected unity among diversity (Pietka et al., 2015). Radio wavelengths are particularly well suited for uncovering such phenomena in synoptic surveys, since observations at radio wavelengths may suffer less obscuration than in other bands (e.g. optical/IR or X-rays) due to dust and other absorption. At the same time a multiwaveband approach is a "force-multiplier", since source identification becomes more secure and multiwaveband information often provides critical source classification rapidly than possible with only radio band data. Therefore, multiwaveband observational efforts with wide fields of view will be the key to progress of transients astronomy from the middle 2020s offering unprecedented deep images and high spatial and spectral resolutions. Indian astronomers with wide-ranging experience of low frequency radio astronomy in a variety of astronomical phenomena and targets would be particularly well-placed to pursue time critical transient objects with SKA and observatories at other bands.

Our strategy will also include to develop tools with machine learning capabilities to automatically and rapidly classify the transient events expected in the SKA era and follow up a few of these intensively and with multiwaveband coverage through other large facilities that India will likely have access to. These exceptional few objects have the potentials for discovery of major underlying physical processes and trends. For example the abundance of relativistic SNe without GRB counterparts, and luminous TDE events will have implications among other things on the sources of Ultra High Energy Cosmic Rays within the Greisen-Zatsepin-Kuzmin (GZK) cutoff distance from the Earth (Chakraborti et al., 2011).

The SKA will be a premier instrument for transient science. This strength of the science case will continue to increase as more and more class of transients are discovered with current surveys, including uGMRT, ASKAP, MWA etc. There is much development going on in hardware, software, simulation and

data analysis techniques, all to improve the chances of detecting transients. All of the next generation telescopes are including the transient science case as one of the core goals, and this is also being reflected in developments at nearly all other wavelengths.

References

Abbott et al. 2016, Phys. Rev. Lett. 116, 061102

Abbott et al. 2016, arXiv:1602.08492.

Abdo, A. A., Ackermann, M., & et al. 2009a, Nature, 462, 331

Abdo, A. A., Ackermann, M., & et al. 2009b, ApJL, 706, L138

Abdo, A. A., Ackermann, M., & et al. 2009c, Science, 323, 1688

Ackermann, M., Ajello, M., & et al. 2011, ApJ, 729, 114

Ackermann, M., Ajello, M., & et al. 2013, ApJS, 209, 11

Adriń-Martńez et al. 2016, arXiv:1602.05411

Amati, L., Frontera, F., & Guidorzi, C. 2009, A&A, 508, 173

Amati, L., Frontera, F., & et al. 2002, A&A, 390, 81

Anupama G.C., Kantharia N.G., 2005, A&A, 435, 167

Arun et al. 2014, Phys. Rev. D 90, 024060 .

Atwood, W. B., Abdo, A. A., Ackermann, M., et al. 2009, ApJ 697, 1071

Axelsson, M., Baldini, L., & et al. 2012, ApJ, 757, L31

Axelsson, M., & Borgonovo, L. 2015, MNRAS, 447, 3150

Band, D., Matteson, J., & et al. 1993, ApJ, 413, 281

Band, D. L. 2006, ApJ, 644, 378

Berger, E. 2014, Ann. Rev. Astron. Astrophys., 52, 43

Bhalerao, V., Bhattacharya, D., Rao, A. R., & Vadawale, S. 2015, GRB Coordinates Network, 18422, 1

Burgess, J. M., Preece, R. D., & et al. 2014, ApJ, 784, 17

Burlon, D., Ghirlanda, G., van der Horst, A., Murphy, T., Wijers, R., Gaensler, B., Ghisellini, G., & Prandoni, I. 2015, PoS, AASKA14, 052

Campana, S., Mangano, V., & et al. 2006, Nature, 442, 1008

Carilli, C. L. 2014, arXiv:1408.5317

Cenko, S. B., Frail, D. A., & et al. 2010, ApJ, 711, 641

Chakraborti, S., Ray, A., Soderberg, A. M., Loeb, A., & Chandra, P. 2011, Nature Communications, 2, 175

Chakraborti, S., Ray, A., Smith, R., et al. 2013, ApJ, 774, 30

Chakraborti, S. et al., 2015, ApJ, 805, 187.

Chakraborti, S., Ray, A., Smith, R., et al. 2016, ApJ, 817, 22

Chandra, P. et al. 2009, ApJ 690, 1839

Chandra, P. et al. 2012, ApJ 755, 110

Chandra, P., & Frail, D. A. 2012, Astrophys.J., 746, 156

Chandra, P. et al. 2015, ApJ 810, 32

Chevalier, R. A. 1998, ApJ, 499, 810

Chevalier, R. 2006, Bulletin of the American Astronomical Society, 38, 43.04

Claeys, J. S. W., Pols, O. R., Izzard, R. G., Vink, J., & Verbunt, F. W. M. 2014, A&A, 563, AA83

Cucchiara, A., et al. 2011, ApJ, 736, 7

De Colle, F., Ramirez-Ruiz, E., Granot, J., & Lopez-Camara, D. 2012, Astrophys. J., 751, 57

Dev, A., Jain, D., & Alcaniz, J. S. 2004, A & A, 417, 847

Eyres, S. P. S., O'Brien, T. J., Beswick, R., et al. 2009, MNRAS, 395, 1533

Fairhurst, S, Class.Quant.Grav.28:105021, (2011)

Fong, W.-f., Berger, E., & Fox, D. B. 2010, Astrophys. J., 708, 9

Frail, D. A., Waxman, E., & Kulkarni, S. R. 2000, Astrophys. J., 537, 191

Frail, D. A., Kulkarni, S. R., Ofek, E. O., Bower, G. C., & Nakar, E. 2012, ApJ, 747, 70

Friis, M., & Watson, D. 2013, ApJ, 771, 15

Fruchter, A. S., et al. 2006, Nature, 441, 463

Gal-Yam, A., Leonard, D. C., Fox, D. B., et al. 2007, ApJ, 656, 372

Gao, H., Lei, W.-H., Zou, Y.-C., Wu, X.-F., & Zhang, B. 2013, New Astron.Rev., 57, 141

Gehrels, N., Ramirez-Ruiz, E., & Fox, D. B. 2009, ARA&A, 47, 567

Gehrels, N., & Mészáros, P. 2012, Science, 337, 932

Godfrey et al., 2011, arXiv:1111.6398

Goldstein, A., Preece, R. D., & et al. 2013, ApJS, 208, 21

Gruber, D., Goldstein, A., & et al. 2014, ApJS, 211, 12

Guiriec, S., Connaughton, V., & et al. 2011, ApJL, 727, L33

Guiriec, S., Daigne, F., & et al. 2013, ApJ, 770, 32

Hancock, P. J., Gaensler, B. M., & Murphy, T. 2013, ApJ, 776, 106

Hjellming R. M., van Gorkom J. H., Seaquist E. R., Taylor A. R., Padin S., Davis R. J., Bode M. F., 1986, ApJ, 305, L71

Iyyani, S., Ryde, F., & et al. 2013, MNRAS, 433, 2739

Iyyani, S., et al. 2015, MNRAS, 450, 1651

Iyyani, S., Ryde, F., Burgess, J. M., Pe'er, A., & Bégué, D. 2016, MNRAS, 456, 2157

Kamble, A. et al., 2015, ATel, 7845,1K

Kantharia N. G., Anupama G. C., Prabhu T. P., Ramya S., Bode M. F., Eyres S. P. S., OB́rien T. J., 2007, ApJ, 667, L171

Kantharia N.G. 2012, BASI, 40, 311

Kantharia N.G., Dutta, P., Roy, N., Anupama, G.C., Ishwara-Chandra, C.H., Chitale, A., Prabhu, T.P., Banerjee, D.P.K., Ashok, N.M., 2016, MNRAS, 456, L49

Kidd, L., & Troja, E. 2014, in American Astronomical Society Meeting Abstracts, Vol. 223, American Astronomical Society Meeting Abstracts #223, 352.14

Kopac, D., et al. 2015, Astrophys. J., 806, 179

Kouveliotou, C., Meegan, C. A., Fishman, G. J., Bhyat, N. P., Briggs, M. S., Koshut, T. M., Paciesas, W. S., & Pendleton, G. N. 1993, Astrophys. J., 413, L101

Kumar, P., & Zhang, B. 2014, Phys.Rept., 561, 1

Laskar, T., et al. 2013, Astrophys. J., 776, 119

Levan, A. J. 2015, JHEAp, 7, 44

Lu, R.-J., Hou, S.-J., & Liang, E.-W. 2010, ApJ, 720, 1146

Margutti, R., Soderberg, A. M., Wieringa, M. H., et al. 2013, ApJ, 778, 18

Margutti, R., et al. 2014, ApJ, 797, 107

Mauerhan, J. C. et al. 2013, MNRAS 430, 1801

Meegan, C., Lichti, G., Bhat, P. N., et al. 2009, ApJj, 702, 791-804

Metcalf, R. B., & Silk, J. 2007, Physical Review Letters, 98, 071302

Misra, K., Pooley, D., Chandra, P., et al. 2007, MNRAS, 381, 280

Pietka, M., Fender, R. P., & Keane, E. F. 2015, MNRAS 446, 3687

Nakauchi, D., Kashiyama, K., Nagakura, H., Suwa, Y., & Nakamura, T. 2015, ApJ, 805, 164

Narasimha, D., & Chitre, S. M. 1989, AJ, 97, 327

O'Brien, T. J., Bode, M. F., Porcas, R. W., et al. 2006, Nature, 442, 279

Pandey, S. B. 2013, Journal of Astrophysics and Astronomy, 34, 157

Pérez-Torres, M. A., Lundqvist, P., Beswick, R. J., et al. 2014, ApJ 792, 38

Preece, R. D., Briggs, M. S., & et al. 1998, ApJL, 506, L23

Racusin, J. L., Oates, S. R., & et al. 2011, ApJ, 738, 138

Rao, A. R. 2015, Astronomical Society of India Conference Series, 12,

Resmi, L., Ishwara-Chandra, C. H., Castro-Tirado, A. J., et al. 2005, Astron. Astrophys., 440, 477

Resmi, L., & Zhang, B., submitted

Rupen M. P., Mioduszewski A. J., Sokoloski J. L., 2008, ApJ, 688, 559

Rutter et al. 2009, ApJ, 699, 2026

Sari, R., & Piran, T. 1999, Astrophys. J., 517, L109

Schneider, P., & Wagoner, R. V. 1987, ApJ, 314, 154

Seaquist E. R., Bode, M. F., Frail, D. A., et al. 1989, ApJ, 344, 805

SKA-TEL-SKO-DD-001

Sokoloski J. L., Rupen M. P., Mioduszewski J., 2008, ApJ, 685, L137

Singh, K. P., Tandon, S. N., Agrawal, P. C., et al. 2014, Proceedings of the SPIE, 9144, 91441S

Staley, T. D., Titterington, D. J., Fender, R. P., et al. 2013, MNRAS, 428, 3114

Starling, R. L. C., Page, K. L., & et al. 2012, MNRAS, 427, 2950

Stewart et al. 2015, in preparation

Taylor A. R., Davis R. J., Porcas R. W., Bode M. F., 1989, MNRAS, 237, 81

Thornton, D., Stappers, B., Bailes, M., et al. 2013, Science, 341, 53

van der Horst, A. J., et al. 2008, Astron. Astrophys., 480, 35

van Eerten, H. J., & MacFadyen, A. I. 2012, Astrophys. J., 747, L30

Woosley, S. E., & Bloom, J. S. 2006, Ann. Rev. Astron. Astrophys., 44, 507

Yadav, N., Ray, A., Chakraborti, S., et al. 2014, ApJ, 782, 30

Fast Transients with the SKA and its pathfinders : An Indian Perspective

Yashwant Gupta*[1], Poonam Chandra[1], Manjari Bagchi[2], Niruj Mohan Ramanujam[1], Yogesh Maan[1], Avinash A. Deshpande[3], and Siddharth Bhattacharyya[4]

[1] *NCRA-TIFR, Pune, India*
[2] *Institute of Mathematical Sciences, Chennai, India*
[3] *Raman Research Institute, Bangalore, India*
[4] *Indian Institute of Technology, Kharagpur, India*

1 The Transient Sky : an introduction

Exploration of transient phenomena in the Universe is an exciting and rapidly growing area of radio astronomy. Transient radio sources are expected to be compact and are usually associated with explosive or dynamic events, an allow interesting new regimes of physics to be probed. The time scales for transient phenomena range from several months down to microseconds (or shorter). Short duration (< 5s) transients are perhaps the most exciting variety of transient events, and also the most difficult to observe and localise in the sky. The dynamic radio sky remains poorly sampled as compared to sky in X-ray and γ-ray bands. This is because currently it is difficult to obtain both high time resolution and wide fields of view (FoVs) simultaneously. This is where the SKA, with its wide field of view and high sensitivity, is expected to open up a new parameter space in the search for radio transients.

1.1 Fast Transients: an overview

Short time scale (<5s) radio transients probe high brightness temperature emission, likely associated with extreme states of matter, and may throw light on physics of strong gravitational fields. They are also powerful probes of intervening media owing to dispersion, scattering and Faraday rotation. The latest class of fast radio transients are the mysterious Fast Radio Bursts (FRBs), which are characterised by their short durations ($\sim$ millisecond) and high values of the dispersion measure (DM, $\sim$ 400-1600). Although the first FRB was discovered as far back as 2007 (Lorimer et al., 2007), the next discoveries had to wait till 2013 (Thornton et al., 2013). The total number known today stands at 17, with all of them except one (Spitler et al., 2016), reported to have been detected only once. However, the expected rates of detectable FRBs are quite large (10^4 sky^{-1} day^{-1}), and hence there is significant potential for enhanced detections. Most of the presently known FRBs have been detected with the Parkes radio telescope, one with Green Bank telescope and another with Arecibo. An exhaustive catalogue of presently known FRBs is maintained by the radio pulsar group at the Swinburne University (http://astronomy.swin.edu.au/pulsar/frbcat/).

Because of the large values of DM, FRBs are believed to be of extra-galactic origin. If FRBs are indeed extra-galactic, then their study will help us to understand properties of ionised inter-galactic medium (IGM). None of the FRBs observed so far have not been identified with any specific host, except the recent, controversial claim of identification of the host galaxy of FRB 150418 (Keane et al., 2016; Williams and Berger, 2016).

The understanding of the physical origin of FRBs remains as an open challenge, and there exist a number of different hypothesis including flaring stars in the Galaxy (Loeb et al., 2014), magnetars close to the Galactic centre (Pen and Connor, 2015), collisions between neutron stars and asteroids (Geng

*ygupta@ncra.tifr.res.in

and Huang, 2015), dark matter induced collapse of neutron stars (Fuller and Ott, 2015), cosmic strings Yu et al. (2014); Vachaspati (2008), mergers of binary white dwarfs (Kashiyama et al., 2013), mergers of two neutron stars (Totani, 2013), axion stars (Iwazaki, 2015), collapse of supra-massive neutron stars into a black holes (Falcke and Rezzolla, 2014), white holes (Barrau et al., 2014), etc.

2 Fast Transients with the SKA : Long-term Prospects

In order to improve our understanding of the nature and origin of FRBs, and to use them as effective probes of interesting physics, it is important to increase the sample size by a significant amount. Whereas different efforts are underway with existing facilities, the SKA is expected to provide the most important boost. The higher sensitivity, coupled with the wide field of view, and sophisticated real-time processing techniques at high time resolutions make it very favourable for such discoveries. This increased sample, with possibilities for estimation of the spectral index, and of detection in polarised emission, alongwith rapid follow-up in other wavelengths, will be highly valuable in our aim to validate and/or rule out one or more of the competing theories for the origin of FRBs.

Moreover, the detection and localization of thousands of coherent bursts at cosmological distances will directly locate the missing baryons in intergalactic space that constitute at least 50% of the present-day Universe's baryonic content and determine their association with galaxy and cluster halos. As cosmological rulers, these bursts measure the curvature of the Universe and can help determine the dark energy equation of state at redshifts ≥ 2.

The scattering mechanism in the IGM is still an open challenge, and the redshift distribution of a large sample of FRBs, coupled with better understanding of the spectrum and the source mechanism, will guide us to determine better the scattering model for the IGM.

The SKA can achieve this with a design that has a wide field of view, a substantial fraction of its collecting area in a compact configuration (80% within a 3 km radius), and a capacity to process high time resolution (1 ms) signals. High precision cosmology with FRBs is a very important field. SKA1 Low and SKA1 Mid will both be extremely instrumental for such studies.

3 Fast Transients in the Indian context : present scenario and future plans

There is significant interest among Indian researchers to work on FRBs, in areas of both observations and theory. Of specific interest have been studies about the potential of detecting FRBs at low radio frequencies, as well as pilot experiments for the same. Some of the recent efforts, ongoing activities and future plans are highlighted below.

Though most of the FRBs have been detected at relatively higher radio frequencies (around 1.4 GHz), there is significant interest to look at the possibilities of FRB detections at low frequencies. These cover both theoretical studies and experiments. Given a significant number of low frequency facilities available in the country (GBD, ORT, GMRT), and the potential of SKA Low in the future, these studies are very important.

In a recent publication (Bera et al., 2016), Bera and colleague have developed a general formalism for FRB detection by any radio telescope, and have shown that the detection rate of FRBs at low frequencies can be quite appreciable. In particular, they calculate the rate for the Ooty Wide Field Array, which is currently under development and will operate at a frequency of 327 MHz, to be $\sim 10^3$ events per day, for an assumed spectral index of $\alpha = -1.4$. This makes searching for FRBs with the SKA Low an interesting prospect. In particular, constraints on the value of the spectral index for FRBs can best be obtained by such low frequency observations. Furthermore, Manjari Bagchi is interested in theoretical understanding of FRBs, as well in searching for new FRBs in the pulsar surveys she is involved at present and will be in the future.

Avinash Deshpande has proposed a broadband Indian Sky Watch Array Network (SWAN). This Indian-SWAN initiative is a proposed competitive coordinated network with nominally 1000 sq. m. array area at each location and operation spanning a decade in frequency : 50 to 500 MHz. The main objective is to facilitate and conduct searches and studies of fast (typically of sub-second duration) and slow transient radio radiation originating from astronomical sources. The proposed Indian-SWAN

is optimized to search for a large volume of the space with required sensitivity to detect FRB signals routinely, enabling a proper, detailed study to be carried out. Deshpande is also involved in a project in which more than 1000 hours of observations covering the entire Arecibo sky have been made using the ALFA in Meridian nodding mode, as a part of the GALFACTS continuum Full Stokes (polarization) imaging project. ALFA is a L-band, seven pixel, system with 300 MHz BW. One of the data streams resulting from these observations was designed to enable search for fast transients, with spectral resolution of about 1 MHz, and time resolution of 1 ms.

In addition, Avinash Deshpande and Yogesh Maan have been conducting a sky curvey at 35 MHz from Gauribidanur, covering the full visible sky, providing data on 3000 fields observed for 20 minutes each, with raw voltages recorded across a 1 MHz bandwidth. These data have also been used for searches of radio counterparts of the FERMI-LAT detections. Yogesh Maan is also carrying out a search for fast transients towards several selected directions at the very low frequency of 35 MHz, using the Gauribidanur radio telescope. So far, this search has resulted in the potential discovery of a few radio bursts at very low dispersion measures, and that of a nearby pulsar (Maan, 2015).

At the GMRT, there are a couple of different programs related to fast transients. Poonam Chandra and colleagues have been trying an interesting experiment where they "shadow" the FRB program at Parkes with lower frequency observations with the GMRT, with the hope of being able to detect a FRB afterglow, following a trigger from a higher frequency detection at Parkes.

There is also an ongoing program to develop a dedicated pipeline at the GMRT, for real-time detection of fast transients. This pipeline is intended to run both as a stand-alone program as well as in piggyback mode simultaneously with other, possibly imaging, observations at the observatory. The concept for this pipeline, outlined in (Bhat et al., 2013), is particularly well suited to multi-element telescopes like the GMRT, and will be easily extendable to the SKA mid : it splits the array into multiple sub-array (upto 4 or 5 is found to be optimal) and produces incoherently summed outputs for each sub-array, which are first individually searched for transient signals over a range of DMs and different pulse widths, to produce a list of possible detections for each sub-array. These are then passed through a coincidence filter, which (a) rejects false positives due to to noise fluctuations in individual sub-arrays and (b) rejects a lot of the RFI that is not correlated across the different sub-arrays. The false positive rejection allows much lower than normal detection thresholds to be set, which adequately compensate the loss in sensitivity of splitting the array into multiple, incoherently summed sub-arrays.

An off-line version of this pipeline has been extensively tested on recorded data (Bhat et al., 2013), to verify the concepts described above. A real-time version is under final stages of testing. This pipeline runs on the 32 MHz bandwidth data produced by the existing GMRT software back-end (Roy et al., 2010), for which its performance has been tuned to be well within real time. The implementation utilises the power of GPUs for accelerated computing. At present, work is on to adapt it for the full 400 MHz bandwidth data that the wide-band back-end of the upgraded GMRT (uGMRT) will deliver by the end of 2017. We will need to modify parts of the pipeline so that it continues to perform within real time for this configuration as well. The wide-band correlator will be able to produce 4 incoherent array beams, by dividing the 30 antennas into four different groups. Niruj Mohan Ramanujan and Yashwant Gupta, alongwith the digital back-end team members, are presently leading the effort on this work at NCRA. The aim would be to configure this as a SKA pathfinder project on the uGMRT for fast transients.

The above initiatives bring out the strong interest and skill sets of the Indian astronomy community in the area of fast transients, with an exciting set of ongoing activities and plans that would help build up the group's active participation in the SKA.

4 Summary

It is clear that the rapidly growing field of fast transients will be a significant area of research with the SKA. The Indian community, with significant interests in different aspects of studies of fast transients, ranging from theory and modeling to ongoing and planned experiments with various radio astronomy facilities in the country and abroad, is well positioned to make a significant impact in this exciting branch of astronomy.

References

Barrau A., Rovelli C., Vidotto F., 2014, PhRvD, 90l7503.

Bera A., Bhattacharyya S., Bharadwaj S., Chengalur J. N. & Bhat N. D. R. 2016, doi (10.1093/mnras/stw177).

Bhat N. D. R., Chengalur J. N., Cox P. J., et al., 2013, ApJS, 206, 2.

Falcke H., Rezzolla L., 2014, A&A, 562, 137F.

Fuller J., Ott C. D., 2015, MNRAS, 450L, 71.

Geng J. J., Huang Y. F., 2015, ApJ, 809, 24.

Iwazaki A., 2015, PhRvD, 91b3008.

Kashiyama K., Ioka K., Mészáros P., 2013, ApJ, 776L, 39.

Keane E. F., Johnston S., Bhandari S., et al., 2016, Nature 530, 453.

Loeb A., Shvartzvald Y., Maoz D., 2014, MNRAS, 439L, 46.

Lorimer D. R., Bailes M., McLaughlin M. A., Narkevic D. J., Crawford F., 2007, Science, 318, 777.

Maan, Y., 2015, ApJ, 815, 126.

Pen U. L., Connor L., 2015, ApJ, 807, 179.

Roy, J., Gupta, Y., Pen, U., et al., 2010, ExA, 28, 25.

Spitler L. G., Scholz, P., Hessels, J.W., et al, 2016, Nature, 531, 202.

Thornton D., Stappers, B., Bailes, M., et al, 2013, Science, 341, 53.

Totani T., 2013, PASJ, 65L, 12.

Vachaspati T., 2008, PhRvL, 101n1301.

Williams P. K. G., Berger E., arXiv:1602.08434.

Yu Y. W., Cheng K. S., Shiu G., Tye H., 2014, JCAP, 11, 040.

Clusters of galaxies and the cosmic web with SKA

Ruta Kale*[1], K. S. Dwarakanath[2], Dharam Vir Lal[1], Joydeep Bagchi[3], Surajit Paul[4], Siddharth Malu[5], Abhirup Datta[5], Viral Parekh[2], and Prateek Sharma[6]

[1] *National Centre for Radio Astrophysics, T. I. F. R., Pune*
[2] *Raman Research Institute, Bangalore*
[3] *Inter University Centre for Astronomy and Astrophysics, Pune*
[4] *Savitribai Phule Pune University, Pune*
[5] *Indian Institute of Technology, Indore*
[6] *Indian Institute of Science, Bangalore*

Abstract

The intra-cluster and inter-galactic media that pervade the large scale structure of the Universe are known to be magnetised at sub-micro Gauss to micro Gauss levels and to contain cosmic rays. The acceleration of cosmic rays and their evolution along with that of magnetic fields in these media is still not well understood. Diffuse radio sources of synchrotron origin associated with the ICM such as radio halos, relics and mini-halos are direct probes of the underlying mechanisms of cosmic ray acceleration. Past studies with radio telescopes such as the Giant Metrewave Radio Telescope, the Very Large Array and the Westerbork Synthesis Radio Telescope have led to the discoveries of about 80 such sources and made detailed studies in the frequency range 0.15 - 1.4 GHz of a handful of these possible. These studies have revealed scaling relations between the thermal and the non-thermal properties of clusters and favour the role of shocks in the formation of radio relics and of turbulent re-acceleration in the formation of radio halos and mini-halos. The radio halos are known to occur in merging clusters and mini-halos are detected in about half of the cool-core clusters. Due to the limitations of current radio telescopes, low mass galaxy clusters and galaxy groups remain unexplored as they are expected to contain much weaker radio sources. Distinguishing between the primary and the secondary models of cosmic ray acceleration mechanisms requires spectral measurements over a wide range of radio frequencies. Simulations have also predicted weak diffuse radio sources associated with filaments connecting galaxy clusters.

The Square Kilometer Array (SKA) is a next generation radio telescope that will operate in the frequency range of 0.05 - 20 GHz with unprecedented sensitivities and resolutions. The expected detection limits of SKA will reveal a few hundred to thousand new radio halos, relics and mini-halos providing the first large and comprehensive samples for their study. The wide frequency coverage along with sensitivity to extended structures will be able to constrain the cosmic ray acceleration mechanisms. The higher frequency (> 5 GHz) observations will be able to use the Sunyaev-Ze'ldovich effect to probe the ICM pressure in addition to the tracers such as lobes of head-tail radio sources. The SKA also opens prospects to detect the "off-state" or the lowest level of radio emission from the ICM predicted by the hadronic models and the turbulent re-acceleration models.

1 Overview

The Square Kilometer Array (SKA) is the next generation radio telescope that will probe the fundamental physics of formation and evolution of galaxies up to large scale structures in the Universe. The SKA has a low frequency component (SKA1-low) that will be built in Australia and a high frequency component (SKA1-mid) to be built in South Africa. This document gives an overview of the scientific interests of the Continuum Science Working Group members of SKA India in the field of galaxy clusters and the cosmic web.

*ruta@ncra.tifr.res.in

Table 1: Sensitivities of SKA1 as of Nov. 2015.

	ν GHz	BW MHz	rms μJy b^{-1} hr$^{-1/2}$	θ_b arcsec
SKA1-mid	1.67	770	0.75	0.25
SKA1-low	0.11	300	3.36	7

2 Current SKA1 parameters

A brief description of the currently planned SKA1-mid and the SKA1-low telescopes is provided below. The complete details can be found in the SKA document released in November 2015 [1].

2.1 SKA1-mid (0.35 - 13.6 (20) GHz)

The SKA1-Mid telescope is proposed to be a mixed array of 133 15-m SKA1 dishes and 64 13.5-m diameter dishes from the MeerKAT telescope. The antennas will be arranged in a moderately compact core with a diameter of ∼1 km, a further 2-dimensional array of randomly placed dishes out to ∼3 km radius, thinning at the edges. Three spiral arms will extend to a radius of ∼80 km from the centre.
The dishes will be capable of operations up to at least 20 GHz, although initially equipped to observe only up to 13.8 GHz for SKA1. MeerKAT dishes are expected to be equipped with a front-end equivalent to SKA Band 2 (0.95 - 1.76 GHz), a UHF front-end that overlaps with Band 1 (0.3 - 1 GHz), and an X-band front-end (8 - 14.5 GHz). Band 2 (0.95 - 1.76 GHz), 5 (4.6 - 13.8 GHz) and 1 (0.35 - 1.05 GHz) will be constructed in priority order as written and the sensitivity at a fiducial frequency of 1.67 GHz is given in Tab. 1.

2.2 SKA1-low (0.05 - 0.35 GHz)

SKA1-low telescope receptors will consist of an array of ∼131,000 log-periodic dual-polarised antenna elements. Many of the antennas will be arranged in a very compact configuration (the 'core') with a diameter of ∼1 km, the rest of the elements will be arranged in stations a few 10s of metres in diameter. The stations will be distributed over a 40-km radius region lying within Boolardy Station, most likely organised into spiral arms with a high degree of randomisation.
The antenna array will operate from 50 MHz to ∼350 MHz.
The antenna elements will be grouped into ∼512 stations, whose antennas will be beam-formed to expose a field-of-view of ∼20 deg^2. The expected sensitivity at a fiducial frequency of 0.11 GHz is given in Tab. 1.

3 Introduction: Galaxy clusters, groups and superclusters

The theorized large scale structure of the Universe evolving through initial density fluctuations (e.g. Zel'dovich, 1970) has been observed to be a network of filaments and sheets of matter (Spergel et al., 2003), interwoven like a 'web' (Bond et al., 1996) and has been reproduced by cosmological simulations (e.g. Springel et al., 2005). Galaxy clusters are the nodes of the 'web' having typical masses $\sim 10^{14-15}$ M$_\odot$ and containing hundreds to thousands of galaxies moving with velocities $\sim 700 - 1000$ km s^{-1} (e.g. Girardi et al., 1993). Diffuse thermal gas of temperature $\sim 10^{7-8}$ K (a few keV) at cluster cores emits thermal Bremsstrahlung making clusters extended, soft X-ray emitting sources (e.g. Felten et al., 1966; Mitchell and Culhane, 1977). This thermal plasma also contains relativistic particles (GeVs) and magnetic fields ($\sim 0.1 - 5\mu$G) and is collectively termed as the intra-cluster medium (ICM). Smaller, less massive ($< 10^{14}$ M$_\odot$) bound systems of galaxies that are found around galaxy clusters and in filaments are termed as galaxy groups. Loosely bound complexes of a number of galaxy clusters and groups are termed as superclusters.

[1] SKA-TEL-SKO-0000308_SKA1_System_Baseline_v2_DescriptionRev01-part-1-signed.pdf. Note that the "SKA1-SUR" for which predictions can be found in the articles in AASKA 2014 book has been deferred.

3.1 Generation and evolution of cosmic rays

The detectable radio emission from extragalactic sources in and around galaxy clusters is mainly of synchrotron origin. Therefore it is a direct probe of processes that govern the generation and evolution of relativistic particles and magnetic fields in the galaxies themselves and in the diffuse media surrounding them. The variety of radio sources in galaxy clusters can be classified into two broad categories:

i. those associated with individual galaxies in the cluster, and,

ii. those associated with the ICM.

Starbursts (supernovae), active galactic nuclei (AGN) and radio galaxies belong to class (i). These can be compact radio sources or extended sources, but showing obvious association with individual galaxies in the cluster. The class (ii) sources are diffuse extended sources with sizes typically $\gtrsim 100$ kpc and show no obvious association with individual galaxies. In this work we will focus mainly on class (ii) sources that are probes of the cosmic ray content and magnetic field in the ICM.

The cosmic rays once produced, will lose energy primarily by synchrotron emission and inverse Compton (IC) scattering of the Cosmic Microwave Background (CMB) photons. The synchrotron losses depend on the energy and magnetic field whereas the IC-losses depend on the energy density of the CMB photons and thus, will scale with redshift as $(1+z)^4$. Relativistic protons of energy 1GeV -1 TeV at cluster cores have radiative lifetimes of several Gyrs but that of the relativistic electrons are about 0.01 - 0.1 Gyrs. The distances over which the cosmic rays can travel within their radiative lifetimes is important to understand the observed source sizes. The dispersal of cosmic rays from their source into the ICM depends on the diffusivity of the ICM. The diffusion time, τ_{diff} taken by cosmic rays to diffuse to distances of Mpc assuming an optimistic spatial diffusion coefficient is several Gyrs (Brunetti and Jones, 2014). This implies that cosmic rays once produced will be confined to the cluster and need to be produced $in-situ$ in the ICM in the case of sources of sizes of 100s of kpc.

The primary models for the in-situ generation of cosmic ray electrons (CRes) are based on (re-)acceleration of electrons via shocks and turbulence and the secondary models are based on hadronic collisions (see Brunetti and Jones, 2014, for a review). The secondary models predict a population of relativistic protons (CRp) to accumulate in clusters over its formation that results in relativistic electrons via the collisions of CRps and thermal protons (e.g. Dennison, 1980; Blasi and Colafrancesco, 1999). An associated gamma ray flux is expected but has not been detected so far; stringent upper limits exist based on the Fermi Gamma Ray observatory (e.g. Ackermann et al., 2010; Brunetti et al., 2012; Ackermann et al., 2014). In the primary models, shocks in the ICM and turbulence are the drivers behind the acceleration of particles and thus are invoked in merging galaxy clusters. Radio observations provide the means to distinguish between the roles of these processes in the generation of synchrotron emission from the ICM.

4 Diffuse synchrotron radio emission from the ICM

Cluster-wide non-thermal radio emission has been a topic of study for nearly half a century since its discovery in the Coma cluster (Large et al., 1959; Willson, 1970). Over the last few decades, a large number of galaxy clusters were imaged at radio wavelengths ($20-200$ cm) using a variety of synthesis radio telescopes like the Very Large Array (VLA), the Westerbork Synthesis Radio Telescope (WSRT) and the Giant Metrewave Radio Telescope (GMRT). A large variety in the size, morphology and spectrum of these sources has been found. Based on the properties of the radio sources and the host cluster, the sources have been classified into three [2] main classes (e.g. Feretti et al., 2012):

- *Radio halos* – extended sources of sizes $\sim$ Mpc, nearly co-spatial with X-ray emission from the central regions of clusters.

- *Radio relics* – elongated, filamentary or sometimes arc-like sources of few hundred to $1-2$ Mpc on the longer sides, found at the peripheries of clusters.

[2] A fourth class of diffuse radio emission are the so-called "radio phoenixes" which are smaller scale sources that have been proposed to be fading and/or re-accelerated remnants of radio galaxy lobes; these are not discussed in this work.

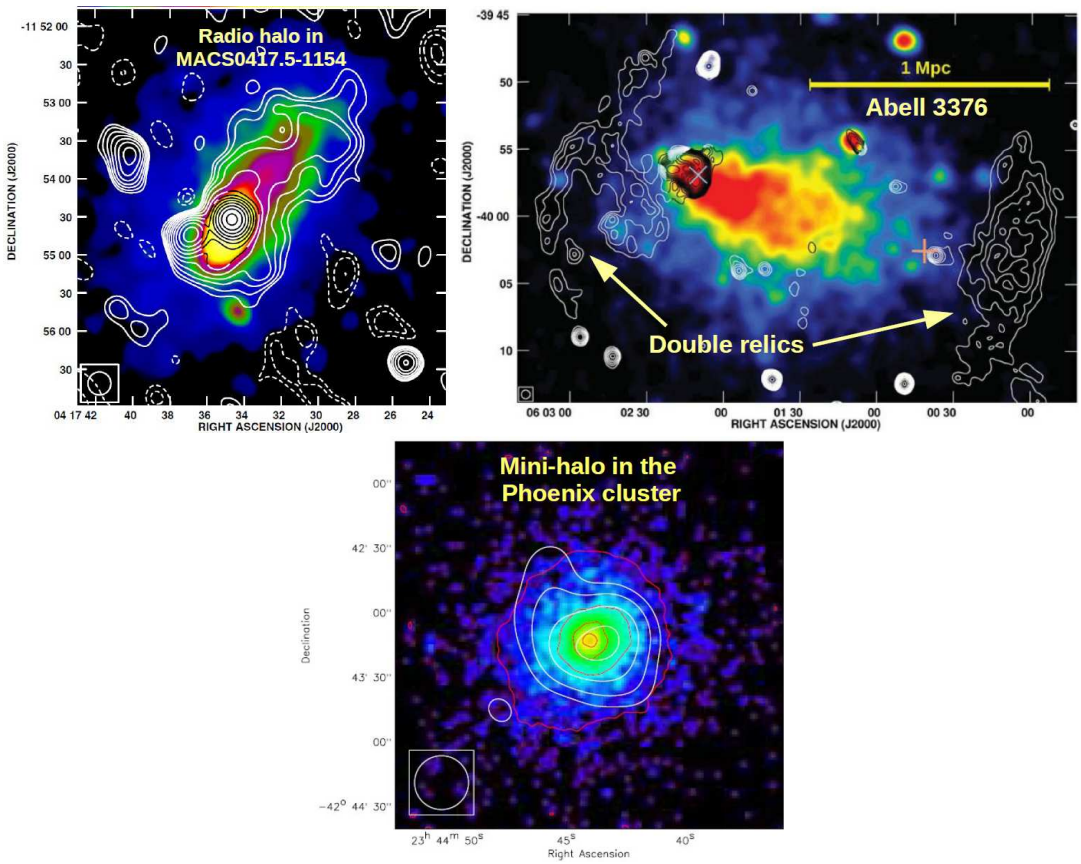

Figure 1: Examples of diffuse radio emission in clusters discussed in this chapter. The X-ray images are shown in colour scale and radio images in white contours are overlaid. Top left: Radio halo in the cluster MACS0417.5-1154. Image adapted from (Dwarakanath et al., 2011). Top right: Double radio relics in the cluster A3376. Image adapted from (Kale et al., 2012). Bottom: Radio mini-halo in the Phoenix cluster. Red contours show the X-ray emission. Image adapted from (van Weeren et al., 2014a).

- *Radio mini-halos* – extended sources of regular morphologies with sizes ∼100 - 500 kpc, surrounding central elliptical galaxies in cool-core clusters.

Illustrative examples of these sources are shown in Fig. 1. The common components of the ICM which lead to these sources are the relativistic electrons and magnetic fields.

The radio spectra of these sources are typically described by a power-law, $S_\nu \propto \nu^{-\alpha}$, where S_ν is the flux density at frequency ν and α is the spectral index. The spectral index, α is related to the injection spectral index, δ of the electron energy distribution, $N(E)dE = N_0 E^{-\delta} dE$ through, $\delta = 2\alpha + 1$ (see textbooks such as Padmanabhan (2000) for details). The spectra originating as a power-laws in the case of standard models of particle acceleration can be affected by the effects of overlapping regions of different magnetic fields, age of the electron population, energy losses by other mechanisms such as the IC losses and continuous or intermittent acceleration mechanism. Radio observations over a large range of frequencies are required to study the spectral properties of radio halos, relics and mini-halos and infer the state of the relativistic electron population and magnetic fields.

The sizes of several hundreds of kiloparsecs in the case of the radio halos imply the role of in-situ mechanisms of cosmic ray production in the ICM. The primary electron model invokes re-acceleration of electrons from the thermal pool or fossil mildly relativistic electrons via MHD turbulence injected by cluster mergers (Petrosian, 2001; Brunetti et al., 2001; Petrosian and East, 2008; Brunetti and Lazarian, 2016). The secondary or hadronic model invokes collisions between relativistic protons and thermal protons for producing relativistic electrons in the ICM as secondary products along with associated gamma rays (e.g. Dennison, 1980; Blasi and Colafrancesco, 1999). Based on the upper limits on the gamma ray fluxes from clusters, simulations show that the relativistic electrons produced via hadronic models alone are insufficient to explain the radio halos (e.g. Donnert et al., 2013) but can contribute to forming what are called 'off-state' radio halos in low mass clusters and relaxed clusters (Brunetti, 2011; Brown et al., 2011).

The radio emission in relics shows another mode of acceleration of mildly relativistic electrons to ultra relativistic energies via acceleration by shocks. In the large scale structure there are shocks in the filaments that have Mach numbers of 100s and near cluster peripheries shocks of Mach numbers of a few (1.5 -4) are found (Miniati et al., 2000; Kang, 2003). Diffusive shock acceleration (DSA) has been the proposed model for producing relativistic electrons at the shocks in sources such as the radio relics (e.g. Enßlin et al., 1998).

Mini-halos are diffuse sources around the central dominant galaxy in relaxed clusters. The secondary electron model and/or re-acceleration of fossil relativistic electrons by turbulence in the cool core produced due to the infall of subclusters inducing sloshing motions have been considered for producing the relativistic electrons responsible for the mini-halos (e.g. Gitti et al., 2002; Pfrommer and Enßlin, 2004; Fujita et al., 2007; Keshet and Loeb, 2010; ZuHone et al., 2013). A connection between cold-fronts and the mini-halos has also been found (Mazzotta and Giacintucci, 2008; Hlavacek-Larrondo et al., 2013; Giacintucci et al., 2014b,a). The connection between the central galaxy and the mini-halo and the role of external interaction with the cool-core are open questions being addressed using new radio observations and simulations.

4.1 Past studies

4.1.1 Radio surveys

The radio observations in the past couple of decades have provided a glimpse of the properties and occurrence rates of the diffuse radio sources in galaxy clusters. The initial discoveries of the radio halos and relics came mainly from the inspection of all sky radio surveys such as the NRAO VLA Sky Survey (NVSS,Condon et al. (1998)). It is a survey at 1.4 GHz carried out using the Very Large Array (VLA) in D configuration (27 antennas in 1 km^2 area) providing images of the sky with rms sensitivity of 0.45 mJy beam^{-1} where beam= $45'' \times 45''$. A number of radio halos and relics in clusters at redshifts < 0.2 were discovered using NVSS and subsequently confirmed with deep follow-up observations (e.g. Giovannini et al., 1999; Bagchi et al., 2002).

The low surface brightnesses, $\sim 0.2 - 1\mu$Jy arcsec^{-2} at 1.4 GHz of radio halos, relics and mini-halos and their extents of several arcminutes to a degreee make them a challenge for imaging with radio telescopes. Aperture synthesis radio telescopes require a combination of short and long baselines to effectively image the extended sources and to separate out the contamination by discrete compact

sources. A low frequency aperture synthesis telescope providing the necessary combination of short and long baselines with sufficient sensitivity to detect faint structures is ideal to carry out tailored surveys of galaxy clusters.

In the past decade systematic surveys of galaxy clusters at low radio frequencies (<GHz) have been taken up mainly with the Giant Metrewave Radio Telescope due to its suitable configuration and sensitivity to extended emission. The "GMRT Radio Halo Survey" (GRHS) and its extension, the "Extended GMRT Radio Halo Survey" carrried out at 610 MHz, are a systematic deep radio survey of 64 most X-ray luminous ($L_{\rm X[0.1-2.4keV]} > 5 \times 10^{44}$ erg s^{-1}) galaxy clusters in the redshift range 0.2 - 0.4. In the GRHS+EGRHS about sample 22% galaxy clusters contain radio halos, 16% contain mini-halos and 5% contain radio relics (Venturi et al., 2007, 2008; Kale et al., 2013, 2015). Moreover, the upper limits on the non-detections have showed that there is a bimodality in the clusters such that the detections and non-detections are well separated implying "radio bright" and "radio quiet" [3] clusters in the $P_{\rm 1.4GHz} - L_X$ plane . Apart from X-ray flux-limited samples of galaxy clusters that have been explored so far, with the telescopes such as the Planck, the South Pole Telescope and the Atacama Cosmology Telescope that detect clusters using the Sunyaev- Ze'ldovich effect, mass limited samples can now be explored. Radio surveys of complete mass limited samples are ongoing and will provide results in the coming years (Basu, 2012; Cuciti et al., 2015; Bonafede et al., 2015).

4.1.2 Radio halos and relics

The observations of radio halos and relics provide the constraints for the particle acceleration mechanisms. The Very Lage Array (VLA) in C and D configurations, the Westerbork Synthesis Radio Telescope (WSRT) and the Giant Metrewave Radio Telescope (GMRT) have provided the most sensitive measurements of the diffuse radio emission in galaxy clusters in the last two decades. Spectral index distribution across the extents of radio halos is essential to trace the in-situ acceleration mechanisms and the ageing of the electrons. For this measurement, matched arrays at multiple frequencies are needed and were achieved using a combination of telescopes. The first spectral index maps of radio halos were made with the VLA and the WSRT (e.g. Giovannini et al., 1993; Feretti et al., 2004). A spectral index study of the radio halo and relic in the cluster A2256 was carried out with a combination of the GMRT at 150 MHz, the WSRT at 350 MHz and the VLA at 1400 MHz (Kale and Dwarakanath, 2010). A spectral steepening in the halo at lower frequencies was found in the above observations for the first time and was interpreted in terms of the two epochs of particle acceleration driven by two mergers. Deeper studies with the Karl G. Jansky VLA (JVLA) have further shed light on the spectral properties of the radio relics (Owen et al., 2014; Trasatti et al., 2015). The follow-up of MACS (Massive Cluster Survey,(Ebeling et al., 2010)) clusters with the GMRT have led to the discovery of a halos, relics and mini-halos in couple of clusters and a number of other diffuse sources (Dwarakanath et al., 2011; Pandey-Pommier et al., 2013, 2015, Parekh et al. 2016, submitted; Pandey-Pommier et al. submitted). The MACS clusters have also been observed at 2 - 24 GHz with the ATCA to study the non-thermal and thermal pressures using diffuse emission and the Sunyaev Ze'ldovich effect (SZe) (, Malu et al. 2016, in prep.).

The Sunyaev-Ze'ldovich effect has emerged as a promising probe of discovering new clusters in the past few years. The Planck satellite, the South Pole Telescope and the Atacama Cosmology Telescope have all led to discoveries of new clusters (Planck Collaboration et al., 2011, 2014; Reichardt et al., 2013; Lindner et al., 2015). The first system of radio halo and relic was discovered in a massive new Planck cluster by (Bagchi et al., 2011) and were followed by discoveries in other clusters (e.g. Giacintucci et al., 2013; Bonafede et al., 2015). These newly discovered clusters have flatter entropy profiles at the cores and are more likely to be disturbed given the fact that these were missed in the X-ray flux limted catalogues due to their more disturbed morphology. Thus a search for new radio halos and relics in these clusters is on and is furthering the understanding the role of mass and the dynamical state of the cluster in the generation of radio halos and relics.

Spectral and polarization studies of relics are essential to distinguish between the models for their origin. The prototype of cluster peripheral double relics in the cluster A3376 were discovered and proposed to be the signatures of cluster merger shocks (Bagchi et al., 2006). The spectral and polarization study of the A3376 double radio relics led to the observational evidence of its connection to merger shocks (Kale et al., 2012). The low frequency GMRT observations have been crucial in the discoveries of new radio relics (van Weeren et al., 2010, 2011; de Gasperin et al., 2015) and radio halos (e.g.

[3]This terminology is not connected in any way to the one used in the context of radio galaxies.

Giacintucci et al., 2013; van Weeren et al., 2014b; Pandey-Pommier et al., 2015). The first among the class of "ultra-steep spectrum" radio halos predicted by the turbulent reacceleration model was found in the cluster A520 using the GMRT (Brunetti et al., 2008).

Bagchi et al. (2002) discovered the diffuse radio emission associated in a complex system of merging groups of galaxies ZWCl 2341.1+0000 in 1.4 GHz NVSS survey, and concluded that this emission was the first evidence of cosmic-ray particle acceleration taking place at magnetized cosmic shocks in a highly filamentary environment that is likely in the process of ongoing structure formation. In recent years more observations of this unusual and highly filamentary merging structure and a few other systems have revealed some intriguing details which brought to light some unusual aspects of particle acceleration and radio halo and relic formation in elongated, filamentary structures:

a. The unusually flat radio spectra of the peripheral double relics ($\alpha < 0.5$) implies high Mach number for the shocks, in contradiction with Mach number estimated from X-ray observations (Bagchi et al., 2002; Ogrean et al., 2014).

b. It is suggested that relics and radio halo in ZWCl 2341.1+0000 highlight the shortcomings or failure of DSA theory in explaining the particle injection spectrum in low mass, less energetic filamentary structures of the cosmic-web (Ogrean et al., 2014). Possibly our understanding of the origin of radio relics is incomplete, and that non-linear effects are required to explain particle acceleration at weak shocks.

c. If radio relics result from particle (re-)acceleration at shock fronts, then this shock should span the whole length of the radio relic it traces. Yet in ZWCL 2341.1+000, this expectation is not met, where the SE shock front was found to subtend an arc that is only about a third of the length of the arc subtended by the radio relic; the result was confirmed with a confidence level of $\sim 90\%$ by (Ogrean et al., 2014). Again this result is at odds with the standard DSA theory and needs more investigation with deeper radio observations and modeling.

The GMRT observations at multiple low frequency bands have been used to distinguish between merger shock related relics and adiabatically compressed lobes of radio galaxies. The adiabatic compression model proposed by Enßlin and Gopal-Krishna (2001) was used to model the spectra of the diffuse emission in A754 and the relics of double radio galaxies (Dwarakanath and Kale, 2009; Kale and Dwarakanath, 2009). In a multi-wavelength study of radio relics A4038, A1664 and A786, it was found that these are relics not associated with shocks but are adiabatically compressed or fading remnants of radio galaxy lobes (Kale and Dwarakanath, 2012). The GMRT low frequency observations revealed that the radio relic in A4038 is extended to over 100 kpc and what was seen earlier from observations at frequencies 1.4 GHz was only the brightest portion.

4.1.3 Mini-halos

Radio mini-halos are diffuse sources, typically of sizes 100 - 500 kpc that surround the central galaxies in cool-core clusters. The central galaxy always has associated compact source at its centre but is not connected to the surrounding diffuse mini-halo with jets but may have a role in injecting the seed relativistic electrons (e.g. Giacintucci et al., 2014b). The secondary electrons due to hadronic collisions may play a role in generating the seed electrons that form the mini-halo but are shown to be insufficient to power the mini-halo (ZuHone et al., 2014). It has been proposed that the MHD turbulence in the cool-core, generated via cooling flow or sloshing cores can lead to re-acceleration of relativistic electrons (e.g. Gitti et al., 2002; Mazzotta and Giacintucci, 2008).

As of now the number count of mini-halos is still limited to about 22 (Giacintucci et al., 2014b, Pandey-Pommier et al. 2016, submitted). About 50% of the cool-core subsample of the clusters in the Extended GMRT Radio Halo Survey were found to host a mini-halo and a scaling between their radio power and the X-ray luminosity was explored (Kale et al., 2013). The cooling at the centres and the mini-halos may be connected through scaling relations, but these have not been established due to the lack of statistical samples (e.g. Bravi et al., 2016).

Low mass clusters have not been surveyed to search for mini-halos; however there are cases such as the diffuse mini-halo like radio source in the cluster MRC0116+111 which may be remnants of the radio mode activity of the central galaxy (Bagchi et al., 2009).

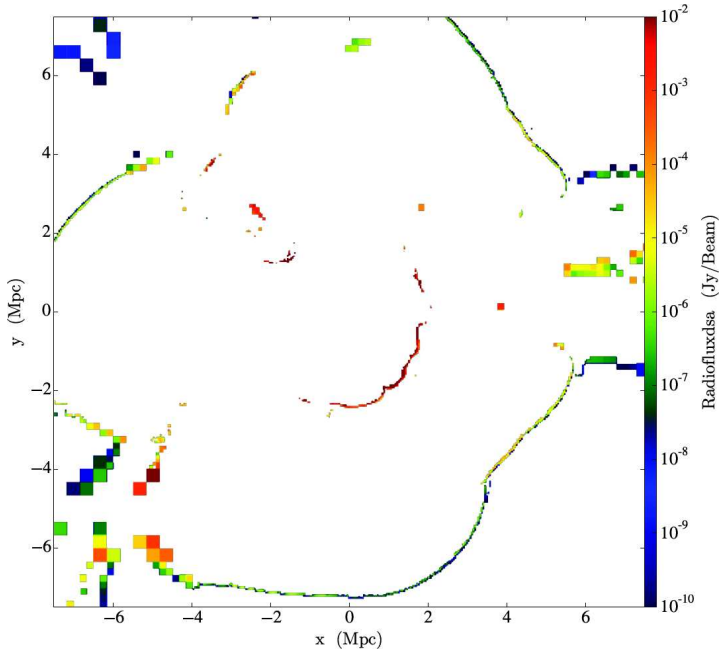

Figure 2: Computed DSA radio flux for 15 Mpc^2 h^{-1} cosmological simulated area at redshift z=0.06 (Paul et al. 2016, in prep.).

4.2 Simulations

Cosmological simulations using computations performed with the grid-based, adaptive mesh refinement hydrodynamical code *ENZO* show that turbulence in clusters can be sustained on timescales exceeding a Gyr and the breaking of shocks at inflowing filaments around the cluster can produce notches in the radio relics (Paul et al., 2011). Simulations including magnetic field evolution along with the structure formation and radiative cooling can provide predictions for the radio emission from the large scale structure based on the recipes for production of relativistic electrons (Hoeft and Brüggen, 2007; Donnert et al., 2013; Vazza and Brüggen, 2014; Vazza et al., 2015b). A saturation of magnetisation can be achieved in a fully turbulent medium and there is near equipartition between the magnetic field and kinetic energy densities (e. g. Subramanian et al., 2006; Iapichino and Brüggen, 2012). Magnetic field can be evolved in the simulation using the estimate of turbulence and a scaling between turbulent and magnetic energies. This has been implemented by Paul et al. (2016, in prep.) in the case of Coma and shows agreement with the observed magnetic field profiles (Bonafede et al., 2010) based on Faraday rotation of background sources. Radio mini-halos due to electron reacceleration by minor merger driven turbulence has been simulated by ZuHone et al. (2013). Implementation of diffusive shock acceleration and turbulent acceleration to accelerate cosmic rays is being used to predict synchrotron emission that will be observable with the SKA. Predictions by Paul et al. (2016, in prep.) indicate that the estimate of surface brightness at 1.4 GHz with a beam of $20''$ is about 10^{-8}Jy beam^{-1} from the filaments if only turbulent reacceleration is considered and in the range 10^{-6} Jy beam^{-1} if DSA is also included and denser regions such as groups and cluster outskirts are considered (Fig. 2). The uncertainties such as efficiency of turbulent reacceleration and magnetization in the large scale structure remain and will be constrained by deeper observations that will be made possible by the SKA.

4.3 Prospects for the SKA

In this section we discuss the numerous possibilities of studying diffuse radio emission from galaxy clusters opened by SKA, thanks to its unprecedented sensitivity.

4.3.1 Deep continuum and polarization imaging of halos, mini-halos and relics

Radio halos, relics and mini-halos in general have low surface brightness ($\sim 1\mu$Jy arcsec^{-2} at 1.4 GHz) and among these, radio halos have the lowest brightness levels. The average surface brightness of the known radio halos at 1.4 GHz is $\sim 0.25\mu$Jy arcsec^{-2} (inferred using the data in Feretti et al., 2012). The SKA1-low will achieve a resolution of $7'' \times 7''$ at 110 MHz (Tab. 1). In order to map the extended sources, the images are produced at a lower resolution than the best offered by the telescope configuration. Therefore we assume a canonical resolution of $10'' \times 10''$ for multi-wavelength observations of diffuse radio sources with the SKA1-low and SKA1-mid and discuss the predictions.

The currently prevalent models of turbulent re-acceleration for radio halos predict that the spectra change from a power-law to an exponential decay beyond a certain critical frequency (Brunetti and Jones, 2014). Assuming the critical frequency to be 1.4 GHz, the spectrum corresponding to the mean value of surface brightnesses of known halos is plotted in Fig. 3. The rms confusion at cm wavelengths assuming a Gaussian beam is approximated as (Condon, 2002),

$$\left(\frac{\sigma_c}{\text{mJy beam}^{-1}}\right) \approx 0.2 \left(\frac{\nu}{\text{GHz}}\right)^{-0.7} \left(\frac{\theta_b}{\text{arcmin}}\right)^2. \quad (1)$$

The expected rms confusion at the four frequencies of 0.15, 0.6, 1.4 and 5 GHz (Fig. 3) are shown in comparison to the radio halo spectra. It is clear from this figure that most of the known halos can be imaged up to 5 GHz if the cut-off frequency is ~ 1.4 GHz, but, only up to 2 GHz, if the cut-off occurs earlier. The surface brightnesses of diffuse sources are not uniform. The profiles of radio halos show that the central regions are the brightest with a gradual fall towards the edges. With SKA1-low and SKA1-mid , the known radio halos, relics and mini-halos can be imaged to a factor of a few deeper. The profiles of the radio halos in the outskirts of the clusters will provide clues to the underlying cosmic ray and magnetic field profile with implications to the proposed models for the generation of radio halos. It will be possible to reliably map spectral indices over the extent of the radio halos. This will lead to constraints on the in-situ acceleration mechanisms at work in the cluster. The case of radio halos discussed here is an illustration of the weakest of the diffuse radio sources in clusters. Radio relics and mini-halos being a few times brighter in surface brightness will be imaged in detail leading clues to their origin and evolution.

Furthermore, polarization is a direct probe of the magnetic field in the plane of the sky and complements the line of sight magnetic field estimated via Faraday rotation of the plane of polarization of background sources. Through polarization observations coherence lengths of magnetic field can be inferred and that is used to refine the simulations. Radio halos typically have low polarized emission fraction $< 5\%$ or so (Feretti et al., 2012). Polarization detection claimed in the radio halo of the cluster A2255 but it is likely due to polarized filament in the periphery of the cluster seen projected on the cluster (Govoni et al., 2005; Pizzo et al., 2011). Radio mini-halos are at cluster centres and thus depolarization is expected due to the ICM and hence little is known about their polarization properties. Radio relics are known to be polarized up to $10 - 30\%$, as expected based on their origin in shock acceleration (see Feretti et al., 2012; Brunetti and Jones, 2014, for reviews). SKA1-mid sensitivities will allow to probe the polarization properties of these sources to much deeper levels than currently possible and provide important constraints on magnetic fields in clusters of galaxies.

4.3.2 Constraining high frequency spectra of radio halos, relics and mini-halos

The spectra of radio halos, relics and mini-halos are important to constrain models proposed to explain them. The turbulent reacceleration model predicts that the spectra will steepen exponentially beyond a break frequency decided by the turbulent energy budget in the cluster (Cassano and Brunetti, 2005; Cassano et al., 2006). A handful of sources have been imaged at more than three frequency bands below 1 GHz (Feretti et al., 2012) and at frequencies higher than a GHz, the spectra are largely unknown. Recently two relics were imaged in the frequency range 0.15 - 30 GHz using a number of radio telescopes and its spectrum shows departure from the expectations from the Diffuse Shock Acceleration (DSA) model (Stroe et al., 2016) but theoretical works argue that DSA can explain it under certain condition of a shock passing through a cloud of fossil population of relativistic electrons (Kang and Ryu, 2016). It is important to probe the spectra of these diffuse sources at >GHz frequencies to locate the spectral breaks in them and to test the models.

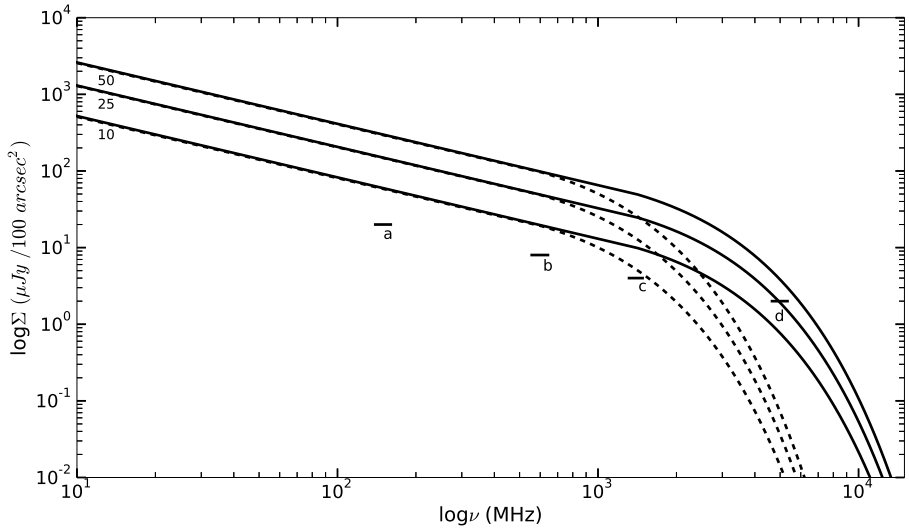

Figure 3: Surface brightness of radio halos as a function of frequency. The lines indicate the expected spectra for radio halos that are a combination of a power-law and an exponential decay. The critical frequency where the exponential decay starts is 1.4 GHz (solid lines) and 0.6 GHz (dashed lines), respectively. The three sets of spectra are for three different surface brightness values, 10, 25 and 50 μJy (100 arcsec)$^{-2}$ for the halos at 1.4 GHz. The short horizontal lines indicate the expected confusion limits (μJy (100 arcsec)$^{-2}$) at the respective frequencies.

Characterisation of galaxy clusters at > 10 GHz is hampered by the presence of the Sunyaev Ze'ldovich effect (SZE). The distortion of the spectrum of the CMB spectrum due to inverse Compton scattering of the CMB photons by the thermal electrons in the ICM is known as the SZE (Sunyaev and Zeldovich, 1972). At frequencies in the range of tens of GHz, the CMB produces a negative signal that can be mixed with the positive radio emission due to radio halos. It is possible to model the signal due to SZE as it has a ν^2 dependence and study the radio emission. Studies with ATCA at frequencies 9 and 18 GHz have shown that radio halos such as that in the Bullet cluster can be detected, though mixed with the SZE (Malu et al., 2010; Malu and Subrahmanyan, 2011).

Observations at matched resolution at high and low frequencies are needed to accurately study the radio halos and the SZE at GHz frequencies. We discuss the expectations for SKA1-mid using the Fig. 3. It can be seen that most of the known halos can be imaged up to 5 GHz if the cut-off frequency is $\sim$ 1.4 GHz, but, only up to 2 GHz, if the cut-off occurs at lower frequencies. However the spectra above 2 GHz for the radio halos, relics and mini-halos are largely unknown except in a few cases and presents an obvious niche for new observations.

4.3.3 Search for new radio halos, relics and mini-halos

The all-sky continuum surveys and targeted surveys of complete samples of clusters with the SKA will open windows to discover 100s to 1000s of new radio halos, relics and mini-halos. The statistical occurrence of the diffuse radio sources is critical to study their origin and evolution in the context of the evolution of the clusters themselves. Current telescopes have allowed a limited number of statistical studies owing to the long observations needed to image with high sensitivity (Venturi et al., 2007, 2008; Kale et al., 2013, 2015; Cuciti et al., 2015; Bonafede et al., 2015).

The prospects with the SKA to search for such sources in blind surveys and with targeted observations are promising. From Fig. 3 it is seen that SKA1-low will detect new radio halos as it will reach much better sensitivities than the current instruments. Based on the turbulent acceleration models, it has been predicted that about 2600 new radio halos will be discovered in a survey that can reach rms 20μJy beam^{-1} with a beam $\sim 10''$ at 120 MHz (Cassano et al., 2015). From the studies of the known radio

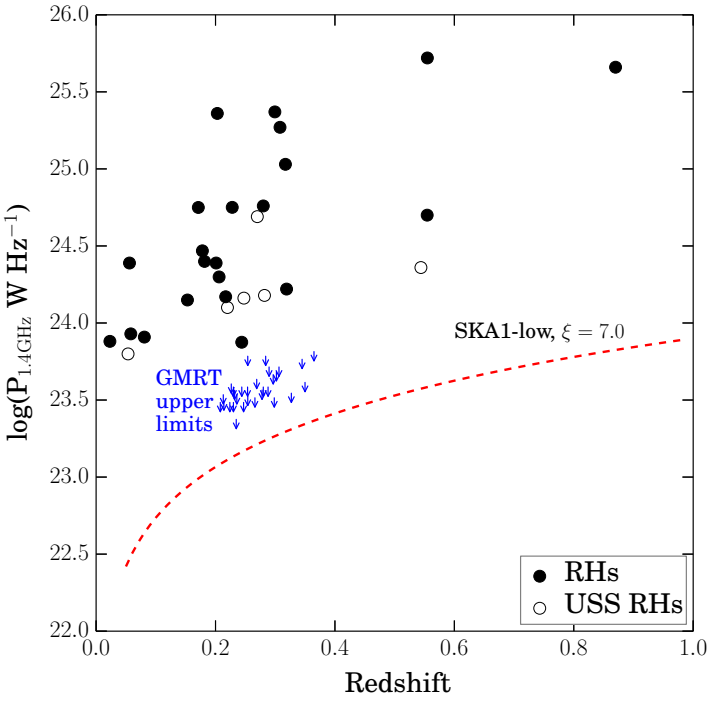

Figure 4: The expected detection thresholds for SKA1-low in comparison to the known radio halos. The known halos from literature and the GMRT upper limits are from Kale et al. (2015).

halos it has been inferred that about 58% of the flux density of the radio halo is contained within half its radius (Brunetti et al., 2007). A minimum detectable flux density of a radio halo, f_{min} can be inferred if it is assumed that a radio halo is detectable when the integrated flux density within half its size gives a signal to noise ratio, ξ (Cassano et al., 2015). It means that $f_{min}(< 0.5\theta_H) \simeq \xi\sqrt{N_b}F_{rms}$, where N_b is the number of independent beams within $0.5\theta_H$. It is found that,

$$f_{min} \simeq 1.43 \times 10^{-3}\xi\left(\frac{\mathrm{F_{rms}}}{10\mu\mathrm{Jy}}\right)\left(\frac{10''}{\theta_b}\right)\left(\frac{\theta_H(z)}{\mathrm{arcsec}}\right). \quad (2)$$

The minimum power of radio halo detectable as a function of redshift for the case of $\xi = 7.0$ is shown in Fig. 4. The redshifts beyond 0.4 are essentially unexplored and SKA will provide the first glimpse of the properties of radio halos at those redshifts. The "off-state" of clusters which are below the current GMRT upper limits will be detected using the SKA1-low . This is critical to understand the cosmic ray contents of galaxy clusters.

5 Superclusters and filaments

Binary clusters and systems of multiple interacting clusters can be found in superclusters or as independent systems. Typically such systems may be either in a stage before they fall into each other or could have undergone the merger and are oscillating. In both these cases it is interesting to study the ICM in and around these clusters to probe the dynamics of diffuse matter and cosmic rays.

Superclusters such as the Shapley supercluster (SSC) are among the nearest systems available for study. About 28 clusters were identified within a volume of 2.5×10^5 $h^{-3}\mathrm{Mpc}^3$ – that is an over density of more than a factor of ten with respect to the mean density of Abell clusters at similar galactic latitudes (Scaramella et al., 1989). SSC is also the richest SC in terms of the presence of X-ray emitting clusters (Raychaudhury et al., 1991). Dedicated studies of this region in optical, radio and X-rays have revealed several sub-structures within this SSC (e.g. Venturi et al., 2000, and references therein). Recently observations of SSC were carried out with the SKA precursor, Murchison Widefield

Array (MWA) with the aim of probing diffuse radio emission at cluster and inter-cluster scales (Kale et al. 2016, in prep.).

The SKA1-low opens up the possibility of probing inter-cluster scale radio sources at even better sensitivity than possible with the current MWA. Apart from SSC other binary clusters and superclusters will be of interest to probe the acceleration of cosmic rays and magnetic fields in these regions. Targets of interest can be filaments between interacting clusters detected by Planck (Planck Collaboration et al., 2013).

Apart from the denser structures like the clusters of galaxies and galaxy groups, there are filaments in which a large fraction of the galaxies in the Universe reside. Filaments also contain a large reservoir of inter-galactic medium called the warm hot inter-galactic medium (WHIM) with temperatures in the range $10^5 - 10^7$ K that has been processed by accretion shocks and is extremely difficult to detect in most wavelength bands. Radio bands stand a chance of detecting it if the shocks accelerate electrons. A detection will be able to probe the cosmic rays and magnetic fields in the filaments. Flux densities of $\sim 0.12\mu$Jy at a redshift of 0.15 at 150 MHz have been predicted assuming that primary electrons are accelerated at cosmological shock waves (Araya-Melo et al., 2012). A radio detection of filaments has been predicted in regions where magnetic field is about ∼10 -100 nG (Vazza et al., 2015a). Recent MHD simulations using *ENZO* have predicted that a non-detection with the SKA can place constraints on the magnetic energy in the WHIM to be less than $\sim 1\%$ of the thermal energy (Vazza et al., 2015b).

Thus although it seems difficult to detect, a strong case exists for detections of filaments surrounding massive clusters. Recently filaments of temperatures $\sim 10^7$ K were detected in X-rays around the massive and merging cluster Abell 2744 (Eckert et al., 2015). If detected in radio, these can potentially constrain the magnetic field in them.

6 Tailed radio galaxies as tracers of inter-galactic weather

6.1 Previous studies

'Tailed' radio sources (Ryle and Windram, 1968) are characterised by a head identified with the optical galaxy and two trails of FR I radio source sweeping back from the head (Miley et al., 1972; Jaffe and Perola, 1973). These sources are usually found in rich cluster environments, where jets are understood to have been swept back by the deflecting pressure of the dense ICM. Furthermore, the long tails of these galaxies carry the imprint of relative motion between the non-thermal plasma and the ambient hot gas. Hence, in the parlance of the field, they reflect the weather conditions of ICM and the jet dynamics, which allows us to make quantitative statements about their dynamics and energetics. Two specific examples of the interaction between radio sources and the ICM are wide-angle tailed (WAT) and narrow-angle tailed (NAT) radio sources, where the latter are also addressed as the 'head-tail' radio sources.

Recently, a radio study was conducted, using GMRT for a sample of head-tail radio sources, concentrating on 3C129, NGC 1265 and IC 310 (Lal, 2009; Lal and Rao, 2004), which have archive X-ray data, and new X-ray observations were proposed for objects which are in poor environments where temperature and abundance variations are likely to be more visible in the X-rays (Rhee et al., 1994). When combined with radio data, these multi-waveband data probe a variety of studies, namely (i) collimation and surface brightness of the jets (Laing and Bridle, 2014, 2002), (ii) radio jet–ICM interaction (Perucho et al., 2012; Perucho, 2012), (iii) infall of tailed radio sources into the cluster, (iv) details of cluster merger (Douglass et al., 2011), (v) gas pressure to compare with equipartition pressure, (vi) energy losses, particle acceleration, and (vii) cluster centre ambiguities. The potential of such observations is also to reveal details of cluster mergers such as subsonic / transonic bulk flows, shocks and turbulence. Fortunately, the jets survive the encounter with the ICM, with possible shocks leading to the formation of the long tails, and specifically they seem to be devoid of the growth of Kelvin-Helmholtz instabilities (Loken et al., 1995).

6.2 Prospects for the SKA

To illustrate in detail, let us consider two specific science cases, (i) if the deceleration of jets in these objects is caused by internal entrainment or if the mass-load of the jet is external (Perucho, 2012; Perucho et al., 2011) and (ii) the manner in which the local ICM plays a role in shaping NAT and WAT

galaxies (Roettiger et al., 1996). To answer (i), observationally the transverse velocity profile of the radio jets can give clues to understand which of these two processes is more relevant; if former, no velocity profile across the jet is expected, whereas if it is latter there would be a velocity profile with slower layers at the jet boundaries (Laing and Bridle, 2002). Next to answer (ii), comparisons between the radio morphologies of tailed sources in cluster environments and the distribution of the thermal gas as seen in *Chandra* and *XMM-Newton* images, indicate that the thermal gas is almost always asymmetric and aligned towards the direction of the bending (Venkatesan et al., 1994), and many a times these clusters are undergoing mergers, resulting in large-scale flows of hot gas owing to the changing gravitational potential (Klamer et al., 2004). Therefore tailed radio sources in merging clusters are diagnostics of the ICM weather and of the evolving gravitational potential resulting from the merger as compared to (tailed) radio sources in relaxed clusters. This argument clearly answers the role played by relaxed and merging clusters in shaping WATs and NATs.

A series of tiered surveys with increasing sensitivity, but decreasing in areas are planned to be undertaken with SKA phase-1 (SKA-1). Briefly, the 1–2 GHz band of SKA 1, with 2 arcsec resolution and 2 μJy beam^{-1} will detect several orders of more number of WAT and NAT radio sources and hence their parent clusters with whom they are associated. Clearly, at this resolution and depth we will not only resolve the radio jet in longitudinal direction, but also in transverse direction and boost our statistical understanding of at least two specific science cases discussed above.

6.3 Building Statistics using SKA

VLA Fiant Images of the Radio Sky at Twenty-cm (FIRST) survey listed ∼384 WAT and NAT radio sources selected from 3000 deg^2 of sky. Of these (Blanton et al., 2001) have confirmed the existence of 40 clusters with redshifts up to $z \simeq 0.9$. To compare these, we next try to understand number of WATs and NATs likely to be detected with SKA surveys. The current deep surveys of smaller parts of the sky such as the ∼4 deg^2 of the ATLAS-CDFS (Australia Large Area Survey of the *Chandra* Deep Field–South) field was performed using ATCA at 1.4 GHz (Norris et al., 2011) with ∼11 arcsec resolution and a depth of 15 μJy beam^{-1}. Additionally, VLA image of the Extended-CDFS, again at 1.4 GHz with ∼2 arcsec resolution has a depth of 10 μJy beam^{-1} Miller et al. (2013). Although SKA 1 survey will be similar to this resolution, marginally more sensitive to the VLA–Extended-CDFS (Figure 5, Dehghan et al., 2014), (Figure 1, Johnston-Hollitt et al., 2015a) and (Johnston-Hollitt et al., 2015b). Out of ∼3000 radio sources, 45 are WAT or NAT radio sources and rest are extended or (complex) diffuse or ambiguous (Dehghan et al., 2011). Extrapolating from these detections, again using (Figure 1, Johnston-Hollitt et al., 2015a), the SKA level surveys will detect ∼10^6 WAT and NAT radio sources. The all-sky radio continuum survey using SKA 1 will provide more sensitive data to explore a variety of science goals, including a huge sample, ∼10^6 clusters of galaxies containing WAT and NAT radio sources. Statistical studies of such large samples of tailed radio sources will provide insights into both the internal characteristics of astrophysical jets and the surrounding ICM.

7 Summary

This chapter highlights the scientific problems in the area of galaxy clusters and the cosmic web that can be effectively addressed using the Square Kilometer Array. The outstanding problems that need to be addressed are:

a. the production and sustenance of relativistic particles and magnetic fields that are responsible for the observed diffuse radio emission on cluster-wide scales,

b. the relative importance of shocks, turbulent acceleration and hadronic models to the production of cluster-wide radio emission,

c. the detailed properties of the intra-cluster medium using cluster radio galaxies as tracers, and

d. the faint radio emission arising in structure formation shocks (the cosmic web).

An underlying theme in the observational study of clusters and the cosmic web is the detection of low surface brightness and extended radio emission over a wide range of frequencies like 0.1 - 10 GHz.

SKA, with its long baselines and good short spacing coverage, will be an ideal instrument to detect these features. It is expected that SKA will reach detection limits that are a factor of 10 to 50 lower compared to those of the existing telescopes. This improved sensitivity is expected to discover an order of magnitude larger number of clusters with faint diffuse radio emission hitherto undetected. These observations from SKA are expected to revolutionise the field of clusters and the cosmic web.

References

Ackermann, M., Ajello, M., Albert, A., Allafort, A., Atwood, W. B., Baldini, L., Ballet, J., Barbiellini, G., Bastieri, D., Bechtol, K., Bellazzini, R., Bloom, E. D., Bonamente, E., Bottacini, E., Brandt, T. J., Bregeon, J., Brigida, M., Bruel, P., Buehler, R., Buson, S., Caliandro, G. A., Cameron, R. A., Caraveo, P. A., Cavazzuti, E., Chaves, R. C. G., Chiang, J., Chiaro, G., Ciprini, S., Claus, R., Cohen-Tanugi, J., Conrad, J., D'Ammando, F., de Angelis, A., de Palma, F., Dermer, C. D., Digel, S. W., Drell, P. S., Drlica-Wagner, A., Favuzzi, C., Franckowiak, A., Funk, S., Fusco, P., Gargano, F., Gasparrini, D., Germani, S., Giglietto, N., Giordano, F., Giroletti, M., Godfrey, G., Gomez-Vargas, G. A., Grenier, I. A., Guiriec, S., Gustafsson, M., Hadasch, D., Hayashida, M., Hewitt, J., Hughes, R. E., Jeltema, T. E., Jóhannesson, G., Johnson, A. S., Kamae, T., Kataoka, J., Knödlseder, J., Kuss, M., Lande, J., Larsson, S., Latronico, L., Llena Garde, M., Longo, F., Loparco, F., Lovellette, M. N., Lubrano, P., Mayer, M., Mazziotta, M. N., McEnery, J. E., Michelson, P. F., Mitthumsiri, W., Mizuno, T., Monzani, M. E., Morselli, A., Moskalenko, I. V., Murgia, S., Nemmen, R., Nuss, E., Ohsugi, T., Orienti, M., Orlando, E., Ormes, J. F., Perkins, J. S., Pesce-Rollins, M., Piron, F., Pivato, G., Rainò, S., Rando, R., Razzano, M., Razzaque, S., Reimer, A., Reimer, O., Ruan, J., Sánchez-Conde, M., Schulz, A., Sgrò, C., Siskind, E. J., Spandre, G., Spinelli, P., Storm, E., Strong, A. W., Suson, D. J., Takahashi, H., Thayer, J. G., Thayer, J. B., Thompson, D. J., Tibaldo, L., Tinivella, M., Torres, D. F., Troja, E., Uchiyama, Y., Usher, T. L., Vandenbroucke, J., Vianello, G., Vitale, V., Winer, B. L., Wood, K. S., Zimmer, S., Fermi-LAT Collaboration, Pinzke, A., and Pfrommer, C.: 2014, ApJ **787**, 18

Ackermann, M., Ajello, M., Allafort, A., Baldini, L., Ballet, J., Barbiellini, G., Bastieri, D., Bechtol, K., Bellazzini, R., Blandford, R. D., Blasi, P., Bloom, E. D., Bonamente, E., Borgland, A. W., Bouvier, A., Brandt, T. J., Bregeon, J., Brigida, M., Bruel, P., Buehler, R., Buson, S., Caliandro, G. A., Cameron, R. A., Caraveo, P. A., Carrigan, S., Casandjian, J. M., Cavazzuti, E., Cecchi, C., Çelik, Ö., Charles, E., Chekhtman, A., Cheung, C. C., Chiang, J., Ciprini, S., Claus, R., Cohen-Tanugi, J., Colafrancesco, S., Cominsky, L. R., Conrad, J., Dermer, C. D., de Palma, F., Silva, E. d. C. e., Drell, P. S., Dubois, R., Dumora, D., Edmonds, Y., Farnier, C., Favuzzi, C., Frailis, M., Fukazawa, Y., Funk, S., Fusco, P., Gargano, F., Gasparrini, D., Gehrels, N., Germani, S., Giglietto, N., Giordano, F., Giroletti, M., Glanzman, T., Godfrey, G., Grenier, I. A., Grondin, M.-H., Guiriec, S., Hadasch, D., Harding, A. K., Hayashida, M., Hays, E., Horan, D., Hughes, R. E., Jeltema, T. E., Jóhannesson, G., Johnson, A. S., Johnson, T. J., Johnson, W. N., Kamae, T., Katagiri, H., Kataoka, J., Kerr, M., Knödlseder, J., Kuss, M., Lande, J., Latronico, L., Lee, S.-H., Lemoine-Goumard, M., Longo, F., Loparco, F., Lott, B., Lovellette, M. N., Lubrano, P., Madejski, G. M., Makeev, A., Mazziotta, M. N., Michelson, P. F., Mitthumsiri, W., Mizuno, T., Moiseev, A. A., Monte, C., Monzani, M. E., Morselli, A., Moskalenko, I. V., Murgia, S., Naumann-Godo, M., Nolan, P. L., Norris, J. P., Nuss, E., Ohsugi, T., Omodei, N., Orlando, E., Ormes, J. F., Ozaki, M., Paneque, D., Panetta, J. H., Pepe, M., Pesce-Rollins, M., Petrosian, V., Pfrommer, C., Piron, F., Porter, T. A., Profumo, S., Rainò, S., Rando, R., Razzano, M., Reimer, A., Reimer, O., Reposeur, T., Ripken, J., Ritz, S., Rodriguez, A. Y., Romani, R. W., Roth, M., Sadrozinski, H. F.-W., Sander, A., Saz Parkinson, P. M., Scargle, J. D., Sgrò, C., Siskind, E. J., Smith, P. D., Spandre, G., Spinelli, P., Starck, J.-L., Stawarz, Ł., Strickman, M. S., Strong, A. W., Suson, D. J., Tajima, H., Takahashi, H., Takahashi, T., Tanaka, T., Thayer, J. B., Thayer, J. G., Tibaldo, L., Tibolla, O., Torres, D. F., Tosti, G., Tramacere, A., Uchiyama, Y., Usher, T. L., Vandenbroucke, J., Vasileiou, V., Vilchez, N., Vitale, V., Waite, A. P., Wang, P., Winer, B. L., Wood, K. S., Yang, Z., Ylinen, T., and Ziegler, M.: 2010, ApJ **717**, L71

Araya-Melo, P. A., Aragón-Calvo, M. A., Brüggen, M., and Hoeft, M.: 2012, MNRAS **423**, 2325

Bagchi, J., Durret, F., Neto, G. B. L., and Paul, S.: 2006, *Science* **314**, 791

Bagchi, J., Enßlin, T. A., Miniati, F., Stalin, C. S., Singh, M., Raychaudhury, S., and Humeshkar, N. B.: 2002, *ArXiv e-prints* **7**, 249

Bagchi, J., Jacob, J., Gopal-Krishna, Werner, N., Wadnerkar, N., Belapure, J., and Kumbharkhane, A. C.: 2009, MNRAS **399**, 601

Bagchi, J., Sirothia, S. K., Werner, N., Pandge, M. B., Kantharia, N. G., Ishwara-Chandra, C. H., Gopal-Krishna, Paul, S., and Joshi, S.: 2011, *ApJ* **736**, L8

Basu, K.: 2012, *MNRAS* **421**, L112

Blanton, E. L., Gregg, M. D., Helfand, D. J., Becker, R. H., and Leighly, K. M.: 2001, AJ **121**, 2915

Blasi, P. and Colafrancesco, S.: 1999, *Astroparticle Physics* **12**, 169

Bonafede, A., Feretti, L., Murgia, M., Govoni, F., Giovannini, G., Dallacasa, D., Dolag, K., and Taylor, G. B.: 2010, A&A **513**, A30

Bonafede, A., Intema, H., Brüggen, M., Vazza, F., Basu, K., Sommer, M., Ebeling, H., de Gasperin, F., Röttgering, H. J. A., van Weeren, R. J., and Cassano, R.: 2015, MNRAS **454**, 3391

Bond, J. R., Kofman, L., and Pogosyan, D.: 1996, Nature **380**, 603

Bravi, L., Gitti, M., and Brunetti, G.: 2016, MNRAS **455**, L41

Brown, S., Emerick, A., Rudnick, L., and Brunetti, G.: 2011, ApJ **740**, L28

Brunetti, G.: 2011, *MMSAI* **82**, 515

Brunetti, G., Blasi, P., Reimer, O., Rudnick, L., Bonafede, A., and Brown, S.: 2012, MNRAS **426**, 956

Brunetti, G., Giacintucci, S., Cassano, R., Lane, W., Dallacasa, D., Venturi, T., Kassim, N. E., Setti, G., Cotton, W. D., and Markevitch, M.: 2008, *Nature* **455**, 944

Brunetti, G. and Jones, T. W.: 2014, *International Journal of Modern Physics D* **23**, 30007

Brunetti, G. and Lazarian, A.: 2016, MNRAS

Brunetti, G., Setti, G., Feretti, L., and Giovannini, G.: 2001, *MNRAS* **320**, 365

Brunetti, G., Venturi, T., Dallacasa, D., Cassano, R., Dolag, K., Giacintucci, S., and Setti, G.: 2007, *ApJ* **670**, L5

Cassano, R., Bernardi, G., Brunetti, G., Brüggen, M., Clarke, T., Dallacasa, D., Dolag, K., Ettori, S., Giacintucci, S., Giocoli, C., Gitti, M., Johnston-Hollitt, M., Kale, R., Markevich, M., Norris, R., Pommier, M. P., Pratt, G., Rottgering, H. J. A., and Venturi, T.: 2015, *Advancing Astrophysics with the Square Kilometre Array (AASKA14)* p. 73

Cassano, R. and Brunetti, G.: 2005, MNRAS **357**, 1313

Cassano, R., Brunetti, G., and Setti, G.: 2006, *MNRAS* **369**, 1577

Condon, J. J.: 2002, in S. Stanimirovic, D. Altschuler, P. Goldsmith, and C. Salter (eds.), *Single-Dish Radio Astronomy: Techniques and Applications*, Vol. 278 of *Astronomical Society of the Pacific Conference Series*, pp 155–171

Condon, J. J., Cotton, W. D., Greisen, E. W., Yin, Q. F., Perley, R. A., Taylor, G. B., and Broderick, J. J.: 1998, *AJ* **115**, 1693

Cuciti, V., Cassano, R., Brunetti, G., Dallacasa, D., Kale, R., Ettori, S., and Venturi, T.: 2015, A&A **580**, A97

de Gasperin, F., Intema, H. T., van Weeren, R. J., Dawson, W. A., Golovich, N., Wittman, D., Bonafede, A., and Brüggen, M.: 2015, MNRAS **453**, 3483

Dehghan, S., Johnston-Hollitt, M., Franzen, T. M. O., Norris, R. P., and Miller, N. A.: 2014, AJ **148**, 75

Dehghan, S., Johnston-Hollitt, M., Mao, M., Norris, R. P., Miller, N. A., and Huynh, M.: 2011, *Journal of Astrophysics and Astronomy* **32**, 491

Dennison, B.: 1980, ApJ **239**, L93

Donnert, J., Dolag, K., Brunetti, G., and Cassano, R.: 2013, *MNRAS* **429**, 3564

Douglass, E. M., Blanton, E. L., Clarke, T. E., Randall, S. W., and Wing, J. D.: 2011, ApJ **743**, 199

Dwarakanath, K. S. and Kale, R.: 2009, ApJ **698**, L163

Dwarakanath, K. S., Malu, S., and Kale, R.: 2011, *Journal of Astrophysics and Astronomy* **32**, 529

Ebeling, H., Edge, A. C., Mantz, A., Barrett, E., Henry, J. P., Ma, C. J., and van Speybroeck, L.: 2010, MNRAS **407**, 83

Eckert, D., Jauzac, M., Shan, H., Kneib, J.-P., Erben, T., Israel, H., Jullo, E., Klein, M., Massey, R., Richard, J., and Tchernin, C.: 2015, Nature **528**, 105

Enßlin, T. A., Biermann, P. L., Klein, U., and Kohle, S.: 1998, *A&A* **332**, 395

Enßlin, T. A. and Gopal-Krishna: 2001, *A&A* **366**, 26

Felten, J. E., Gould, R. J., Stein, W. A., and Woolf, N. J.: 1966, ApJ **146**, 955

Feretti, L., Giovannini, G., Govoni, F., and Murgia, M.: 2012, *AApR* **20**, 54

Feretti, L., Orrù, E., Brunetti, G., Giovannini, G., Kassim, N., and Setti, G.: 2004, A&A **423**, 111

Fujita, Y., Kohri, K., Yamazaki, R., and Kino, M.: 2007, ApJ **663**, L61

Giacintucci, S., Kale, R., Wik, D. R., Venturi, T., and Markevitch, M.: 2013, ApJ **766**, 18

Giacintucci, S., Markevitch, M., Brunetti, G., ZuHone, J. A., Venturi, T., Mazzotta, P., and Bourdin, H.: 2014a, ApJ **795**, 73

Giacintucci, S., Markevitch, M., Venturi, T., Clarke, T. E., Cassano, R., and Mazzotta, P.: 2014b, *ApJ* **781**, 9

Giovannini, G., Feretti, L., Venturi, T., Kim, K.-T., and Kronberg, P. P.: 1993, ApJ **406**, 399

Giovannini, G., Tordi, M., and Feretti, L.: 1999, *New Astr. Rev.* **4**, 141

Girardi, M., Biviano, A., Giuricin, G., Mardirossian, F., and Mezzetti, M.: 1993, ApJ **404**, 38

Gitti, M., Brunetti, G., and Setti, G.: 2002, A&A **386**, 456

Govoni, F., Murgia, M., Feretti, L., Giovannini, G., Dallacasa, D., and Taylor, G. B.: 2005, A&A **430**, L5

Hlavacek-Larrondo, J., Allen, S. W., Taylor, G. B., Fabian, A. C., Canning, R. E. A., Werner, N., Sanders, J. S., Grimes, C. K., Ehlert, S., and von der Linden, A.: 2013, *ArXiv e-prints*

Hoeft, M. and Brüggen, M.: 2007, MNRAS **375**, 77

Iapichino, L. and Brüggen, M.: 2012, MNRAS **423**, 2781

Jaffe, W. J. and Perola, G. C.: 1973, A&A **26**, 423

Johnston-Hollitt, M., Dehghan, S., and Pratley, L.: 2015a, *Advancing Astrophysics with the Square Kilometre Array (AASKA14)* p. 101

Johnston-Hollitt, M., Dehghan, S., and Pratley, L.: 2015b, in F. Massaro, C. C. Cheung, E. Lopez, and A. Siemiginowska (eds.), *Extragalactic Jets from Every Angle*, Vol. 313 of *IAU Symposium*, pp 321–326

Kale, R. and Dwarakanath, K. S.: 2009, ApJ **699**, 1883

Kale, R. and Dwarakanath, K. S.: 2010, ApJ **718**, 939

Kale, R. and Dwarakanath, K. S.: 2012, *ApJ* **744**, 46

Kale, R., Dwarakanath, K. S., Bagchi, J., and Paul, S.: 2012, MNRAS **426**, 1204

Kale, R., Venturi, T., Giacintucci, S., Dallacasa, D., Cassano, R., Brunetti, G., Cuciti, V., Macario, G., and Athreya, R.: 2015, *ArXiv e-prints*

Kale, R., Venturi, T., Giacintucci, S., Dallacasa, D., Cassano, R., Brunetti, G., Macario, G., and Athreya, R.: 2013, A&A **557**, A99

Kang, H.: 2003, *Journal of Korean Astronomical Society* **36**, 111

Kang, H. and Ryu, D.: 2016, *ArXiv e-prints*

Keshet, U. and Loeb, A.: 2010, ApJ **722**, 737

Klamer, I., Subrahmanyan, R., and Hunstead, R. W.: 2004, MNRAS **351**, 101

Laing, R. A. and Bridle, A. H.: 2002, MNRAS **336**, 328

Laing, R. A. and Bridle, A. H.: 2014, MNRAS **437**, 3405

Lal, D. V.: 2009, in D. J. Saikia, D. A. Green, Y. Gupta, and T. Venturi (eds.), *The Low-Frequency Radio Universe*, Vol. 407 of *Astronomical Society of the Pacific Conference Series*, p. 157

Lal, D. V. and Rao, A. P.: 2004, A&A **420**, 491

Large, M. I., Mathewson, D. S., and Haslam, C. G. T.: 1959, Nature **183**, 1663

Lindner, R. R., Aguirre, P., Baker, A. J., Bond, J. R., Crichton, D., Devlin, M. J., Essinger-Hileman, T., Gallardo, P., Gralla, M. B., Hilton, M., Hincks, A. D., Huffenberger, K. M., Hughes, J. P., Infante, L., Lima, M., Marriage, T. A., Menanteau, F., Niemack, M. D., Page, L. A., Schmitt, B. L., Sehgal, N., Sievers, J. L., Sifón, C., Staggs, S. T., Swetz, D., Weiß, A., and Wollack, E. J.: 2015, ApJ **803**, 79

Loken, C., Roettiger, K., Burns, J. O., and Norman, M.: 1995, ApJ **445**, 80

Malu, S. S. and Subrahmanyan, R.: 2011, *Journal of Astrophysics and Astronomy* **32**, 541

Malu, S. S., Subrahmanyan, R., Wieringa, M., and Narasimha, D.: 2010, *ArXiv e-prints*

Mazzotta, P. and Giacintucci, S.: 2008, ApJ **675**, L9

Miley, G. K., Perola, G. C., van der Kruit, P. C., and van der Laan, H.: 1972, Nature **237**, 269

Miller, N. A., Bonzini, M., Fomalont, E. B., Kellermann, K. I., Mainieri, V., Padovani, P., Rosati, P., Tozzi, P., and Vattakunnel, S.: 2013, ApJS **205**, 13

Miniati, F., Ryu, D., Kang, H., Jones, T. W., Cen, R., and Ostriker, J. P.: 2000, *ApJ* **542**, 608

Mitchell, R. J. and Culhane, J. L.: 1977, MNRAS **178**, 75P

Norris, R. P., Hopkins, A. M., Afonso, J., Brown, S., Condon, J. J., Dunne, L., Feain, I., Hollow, R., Jarvis, M., Johnston-Hollitt, M., Lenc, E., Middelberg, E., Padovani, P., Prandoni, I., Rudnick, L., Seymour, N., Umana, G., Andernach, H., Alexander, D. M., Appleton, P. N., Bacon, D., Banfield, J., Becker, W., Brown, M. J. I., Ciliegi, P., Jackson, C., Eales, S., Edge, A. C., Gaensler, B. M., Giovannini, G., Hales, C. A., Hancock, P., Huynh, M. T., Ibar, E., Ivison, R. J., Kennicutt, R., Kimball, A. E., Koekemoer, A. M., Koribalski, B. S., López-Sánchez, Á. R., Mao, M. Y., Murphy, T., Messias, H., Pimbblet, K. A., Raccanelli, A., Randall, K. E., Reiprich, T. H., Roseboom, I. G., Röttgering, H., Saikia, D. J., Sharp, R. G., Slee, O. B., Smail, I., Thompson, M. A., Urquhart, J. S., Wall, J. V., and Zhao, G.-B.: 2011, PASA **28**, 215

Ogrean, G. A., Brüggen, M., van Weeren, R. J., Burgmeier, A., and Simionescu, A.: 2014, MNRAS **443**, 2463

Owen, F. N., Rudnick, L., Eilek, J., Rau, U., Bhatnagar, S., and Kogan, L.: 2014, ApJ **794**, 24

Padmanabhan, T.: 2000, *Theoretical Astrophysics - Volume 1, Astrophysical Processes*

Pandey-Pommier, M., Richard, J., Combes, F., Dwarakanath, K. S., Guiderdoni, B., Ferrari, C., Sirothia, S., and Narasimha, D.: 2013, A&A **557**, A117

Pandey-Pommier, M., van Weeren, R. J., Ogrean, G. A., Combes, F., Johnston-Hollitt, M., Richard, J., Bagchi, J., Guiderdoni, B., Jacob, J., Dwarakanath, K. S., Narasimha, D., Edge, A., Ebeling, H., Clarke, T. E., and Mroczkowski, T.: 2015, in F. Martins, S. Boissier, V. Buat, L. Cambrésy, and P. Petit (eds.), *SF2A-2015: Proceedings of the Annual meeting of the French Society of Astronomy and Astrophysics*, pp 247–252

Paul, S., Iapichino, L., Miniati, F., Bagchi, J., and Mannheim, K.: 2011, *ApJ* **726**, 17

Perucho, M.: 2012, *International Journal of Modern Physics Conference Series* **8**, 241

Perucho, M., Quilis, V., and Martí, J.-M.: 2011, ApJ **743**, 42

Perucho, M., Quilis, V., and Martí, J.-M.: 2012, in N. V. Pogorelov, J. A. Font, E. Audit, and G. P. Zank (eds.), *Numerical Modeling of Space Plasma Slows (ASTRONUM 2011)*, Vol. 459 of *Astronomical Society of the Pacific Conference Series*, p. 155

Petrosian, V.: 2001, ApJ **557**, 560

Petrosian, V. and East, W. E.: 2008, ApJ **682**, 175

Pfrommer, C. and Enßlin, T. A.: 2004, A&A **413**, 17

Pizzo, R. F., de Bruyn, A. G., Bernardi, G., and Brentjens, M. A.: 2011, A&A **525**, A104

Planck Collaboration, Ade, P. A. R., Aghanim, N., Armitage-Caplan, C., Arnaud, M., Ashdown, M., Atrio-Barandela, F., Aumont, J., Aussel, H., Baccigalupi, C., and et al.: 2014, A&A **571**, A29

Planck Collaboration, Ade, P. A. R., Aghanim, N., Arnaud, M., Ashdown, M., Atrio-Barandela, F., Aumont, J., Baccigalupi, C., Balbi, A., Banday, A. J., and et al.: 2013, A&A **550**, A134

Planck Collaboration, Ade, P. A. R., Aghanim, N., Arnaud, M., Ashdown, M., Aumont, J., Baccigalupi, C., Balbi, A., Banday, A. J., Barreiro, R. B., and et al.: 2011, A&A **536**, A8

Raychaudhury, S., Fabian, A. C., Edge, A. C., Jones, C., and Forman, W.: 1991, MNRAS **248**, 101

Reichardt, C. L., Stalder, B., Bleem, L. E., Montroy, T. E., Aird, K. A., Andersson, K., Armstrong, R., Ashby, M. L. N., Bautz, M., Bayliss, M., Bazin, G., Benson, B. A., Brodwin, M., Carlstrom, J. E., Chang, C. L., Cho, H. M., Clocchiatti, A., Crawford, T. M., Crites, A. T., de Haan, T., Desai, S., Dobbs, M. A., Dudley, J. P., Foley, R. J., Forman, W. R., George, E. M., Gladders, M. D., Gonzalez, A. H., Halverson, N. W., Harrington, N. L., High, F. W., Holder, G. P., Holzapfel, W. L., Hoover, S., Hrubes, J. D., Jones, C., Joy, M., Keisler, R., Knox, L., Lee, A. T., Leitch, E. M., Liu, J., Lueker, M., Luong-Van, D., Mantz, A., Marrone, D. P., McDonald, M., McMahon, J. J., Mehl, J., Meyer, S. S., Mocanu, L., Mohr, J. J., Murray, S. S., Natoli, T., Padin, S., Plagge, T., Pryke, C., Rest, A., Ruel, J., Ruhl, J. E., Saliwanchik, B. R., Saro, A., Sayre, J. T., Schaffer, K. K., Shaw, L., Shirokoff, E., Song, J., Spieler, H. G., Staniszewski, Z., Stark, A. A., Story, K., Stubbs, C. W., Šuhada, R., van Engelen, A., Vanderlinde, K., Vieira, J. D., Vikhlinin, A., Williamson, R., Zahn, O., and Zenteno, A.: 2013, ApJ **763**, 127

Rhee, G., Burns, J. O., and Kowalski, M. P.: 1994, AJ **108**, 1137

Roettiger, K., Burns, J. O., and Loken, C.: 1996, ApJ **473**, 651

Ryle, M. and Windram, M. D.: 1968, MNRAS **138**, 1

Scaramella, R., Baiesi-Pillastrini, G., Chincarini, G., Vettolani, G., and Zamorani, G.: 1989, Nature **338**, 562

Spergel, D. N., Verde, L., Peiris, H. V., Komatsu, E., Nolta, M. R., Bennett, C. L., Halpern, M., Hinshaw, G., Jarosik, N., Kogut, A., Limon, M., Meyer, S. S., Page, L., Tucker, G. S., Weiland, J. L., Wollack, E., and Wright, E. L.: 2003, ApJS **148**, 175

Springel, V., White, S. D. M., Jenkins, A., Frenk, C. S., Yoshida, N., Gao, L., Navarro, J., Thacker, R., Croton, D., Helly, J., Peacock, J. A., Cole, S., Thomas, P., Couchman, H., Evrard, A., Colberg, J., and Pearce, F.: 2005, Nature **435**, 629

Stroe, A., Shimwell, T., Rumsey, C., van Weeren, R., Kierdorf, M., Donnert, J., Jones, T. W., Röttgering, H. J. A., Hoeft, M., Rodríguez-Gonzálvez, C., Harwood, J. J., and Saunders, R. D. E.: 2016, MNRAS **455**, 2402

Subramanian, K., Shukurov, A., and Haugen, N. E. L.: 2006, MNRAS **366**, 1437

Sunyaev, R. A. and Zeldovich, Y. B.: 1972, *Comments on Astrophysics and Space Physics* **4**, 173

Trasatti, M., Akamatsu, H., Lovisari, L., Klein, U., Bonafede, A., Brüggen, M., Dallacasa, D., and Clarke, T.: 2015, A&A **575**, A45

van Weeren, R. J., Brüggen, M., Röttgering, H. J. A., Hoeft, M., Nuza, S. E., and Intema, H. T.: 2011, *A&A* **533**, A35

van Weeren, R. J., Intema, H. T., Lal, D. V., Andrade-Santos, F., Brüggen, M., de Gasperin, F., Forman, W. R., Hoeft, M., Jones, C., Nuza, S. E., Röttgering, H. J. A., and Stroe, A.: 2014a, ApJ **786**, L17

van Weeren, R. J., Intema, H. T., Lal, D. V., Bonafede, A., Jones, C., Forman, W. R., Röttgering, H. J. A., Brüggen, M., Stroe, A., Hoeft, M., Nuza, S. E., and de Gasperin, F.: 2014b, ApJ **781**, L32

van Weeren, R. J., Röttgering, H. J. A., Brüggen, M., and Hoeft, M.: 2010, *Science* **330**, 347

Vazza, F. and Brüggen, M.: 2014, MNRAS **437**, 2291

Vazza, F., Ferrari, C., Bonafede, A., Brüggen, M., Gheller, C., Braun, R., and Brown, S.: 2015a, *Advancing Astrophysics with the Square Kilometre Array (AASKA14)* p. 97

Vazza, F., Ferrari, C., Brüggen, M., Bonafede, A., Gheller, C., and Wang, P.: 2015b, A&A **580**, A119

Venkatesan, T. C. A., Batuski, D. J., Hanisch, R. J., and Burns, J. O.: 1994, ApJ **436**, 67

Venturi, T., Bardelli, S., Morganti, R., and Hunstead, R. W.: 2000, MNRAS **314**, 594

Venturi, T., Giacintucci, S., Brunetti, G., Cassano, R., Bardelli, S., Dallacasa, D., and Setti, G.: 2007, A&A **463**, 937

Venturi, T., Giacintucci, S., Dallacasa, D., Cassano, R., Brunetti, G., Bardelli, S., and Setti, G.: 2008, *A&A* **484**, 327

Willson, M. A. G.: 1970, MNRAS **151**, 1

Zel'dovich, Y. B.: 1970, A&A **5**, 84

ZuHone, J., Brunetti, G., Giacintucci, S., and Markevitch, M.: 2014, *ArXiv e-prints*

ZuHone, J. A., Markevitch, M., Brunetti, G., and Giacintucci, S.: 2013, ApJ **762**, 78

AGN feedback with SKA

Asif Iqbal*[1], Biman B. Nath[2], Subhabrata Majumdar[3], Prateek Sharma[4], Ruta Kale[5], Mahadev Pandge[6], Somak Raychaudhury[7], and Manzoor A. Malik[1]

[1] *Department of Physics, University of Kashmir, Hazratbal, Srinagar, J&K, 190011, India*
[2] *Raman Research Institute, Bangalore, 560080, India*
[3] *Tata Institute of Fundamental Research, Mumbai, 400005, India*
[4] *Indian Institute of Science, Bangalore, 560080, India*
[5] *National Centre for Radio Astrophysics, Pune, India*
[6] *Department of Physics, Dayanand Science College, Latur, 413512, India*
[7] *Inter-University Centre for Astronomy & Astrophysics, Pune, India*

Abstract

AGN feedback is regarded as an important non-gravitational process in galaxy clusters, providing useful constraints on large scale structure formation. In view of upcoming data, particularly from radio surveys with next-generation facilities like SKA, along with major breakthroughs in X-ray sensitivity, high spatial and spectral resolutions, we review AGN feedback from galaxy clusters and present overview of this probe in the cosmological context along with the recent results. We discuss current major issues regarding modeling of AGN feedback and its impact on the surrounding medium and the major breakthroughs we can expect from the future multi-frequency SKA instrument.

1 Introduction

Clusters of galaxies are the largest virialized objects in the universe and the youngest ones in the hierarchical scenario of structure formation. This makes them ideal probes of the large scale structure of the universe and, hence, of cosmological parameters. For example, the abundance of galaxy clusters provides sensitive constraints on the cosmological parameters that govern the growth of structures in the universe (Holder et al., 1991, Gladders et al., 2007, Vikhlinin et al., 2009, Jimenez & Verde, 2009, Andersson et al., 2011, Allen et al., 2011, Bocquet, 2015). In the scenario of hierarchical structure formation, galaxy clusters are formed from the merger of smaller units (galaxies, groups and small clusters) due to the gravitational collapse. About 90% of the total baryons in galaxy clusters is are in the form of a hot ($10^7 - 10^8$ K) diffuse plasma, called the intra-cluster medium (ICM) which radiates in soft X-ray bands via thermal bremsstrahlung. By observing this X-ray emission, one can study the thermodynamic properties of the ICM, which in turn can help us in determining the dark matter profile in galaxy clusters.

High quality X-ray data have provided a number of interesting details regarding the thermodynamic proper of the ICM. For example, it has been found that there is a break in the self-similar scaling relations predicted by pure gravitational collapse of dark matter halos (Kaiser, 1986, Edge & Stewart, 1991, Andreonet al., 2011, Bonamente et al., 2008, Battaglia et al., 2012). Similarly an entropy excess has been observed in cluster cores (Cavagnolo et al., 2009, Pratt et al., 2010, Eckert et al., 2013). Moreover, observations of the cool regions of galaxy clusters show very little evidence of gas cooling and negative temperature gradient outside cores, which is more pronounced in the cool core clusters (Vikhlinin et al., 2005, Leccardi & Molendi, 2008). Such issues can be addressed both through observations and simulations and these point towards cosmological scenarios where a number of non-gravitational astrophysical processes like star formation, feedback from supernova and AGN (Active Galactic Nuclei) take place. It has been found that radio emission from AGN feedback strongly correlate with the non-gravitational energy at cluster cores (Chaudhuri et al., 2012, 2013, Pike et al., 2014, Planelles et al., 2014). The presence of the cavities in bright galaxies (Pandge et al., 2012) and in the ICM near the cluster centers

*asif.iqbal31@gmail.com

(Hlavacek-Larrondo et al., 2012, 2015) is believed to be direct evidence of the conversion of the mechanical energy associated with the AGN jets into the thermal energy of the gas and possible small fraction of the non-thermal (relativistic) component.

Studies at radio wavelengths have also revealed diffuse radio sources (giant halos, relics, mini halos), which cannot be generally associated with any central radio galaxy (AGN). Diffuse radio halos (giant halos, relics) can be produced by the acceleration of particles in fossil radio plasma, or directly of thermal electrons of the ICM through shocks and/or MHD turbulence during cluster mergers (Brunetti et al., 2001, Gitti et al., 2002, Cassano & Brunetti, 2005). They can be also produced from "secondary electrons" as a result from inelastic collisions between CR protons and the thermal nuclei of the ICM during cluster merger while relics are most likely associated with shock waves which formed during mergers (Dennison, 1980, Blasi & Colafrancesco, 1999). The relativistic electrons in radio mini-halos would instead be ejected by their central AGN and subsequently re-accelerated by the ICM turbulence originating in the cluster cooling core (Gitti et al., 2002). Mini-halos are diffuse, faint radio sources and are found mostly at the cluster center and are normally of size $\sim 100-500$ kpc comparable to that of the cluster cool core, with steep radio spectra. Apart from being much smaller than giant radio halos and relics which are typically found in disturbed/non cool-core clusters powered by cluster mergers, radio mini-halos are qualitatively similar. The importance of GMRT radio survey stands out, which has provided us statistical basis on the occurrence of giant radio halos in the critical redshift range $0.2-0.4$ (Venturi et al., 2008, Cassano et al., 2008). These results from GMRT radio halo survey have provide observational support to the re-acceleration scenario for the formation of radio halos.

It has become clear that the studies from the large-area surveys like GMRT, VLA, LOFAR, SKA (Condon et al., 1998, Haarlem et al., 2013, Blake et al, 2004) will provide us useful insights of the large scale structure formation and in our understanding of cosmological model. Motivated by the fact that the future SKA telescope, in which India will also play a major part, it is expected to detect thousands of galaxy clusters up to redshift ~ 0.6 and several hundreds at redshift $z > 1.5$ using radio sources associated with the AGN as well as ICM (Gitti et al., 2014). In this article, we mainly focus on the radio emission from AGN and its effect on the surrounding ICM in galaxy clusters keeping in mind the physics that we can do with SKA. The cluster detections via radio sources using SKA, in combination with datasets such as X-ray and CMB will provide us useful insights of their overall properties of clusters like such as masses, luminosities or temperatures and their deviations from the self-similar scaling relations (Jarvis & Rawlings, 2004). The SKA will be able to follow-up galaxy clusters using the SZ signature from which one can in principle can study the effect of the AGN feedback on the S-Z power spectrum and thus the evolution of the large scale structures by correlating the radio luminosity with thermodynamic properties of the ICM (Chaudhuri et al., 2013, Grainge et al., 2014). Moreover, the study of AGN feedback using SKA could also help us understanding the regulation of cool cores (Gitti et al., 2014, Combes, 2015). Another major breakthrough with SKA will be in the investigation of radio-mode AGN feedback at high redshift which will help us in characterization of the radio lobes produced by the relativistic electrons which are responsible for carving the cavities in the ICM clearly observed in X-ray local clusters (Hlavacek-Larrondo et al., 2012, 2015). SKA will help to probe the nature of dark energy by mapping out large-scale structure, primarily using the 21cm emission line of neutral hydrogen (HI) to detect galaxies and measure their redshifts (Jarvis & Rawlings, 2004).

2 AGN feedback in galaxy clusters

In order to obtain robust estimates of cosmological parameters from galaxy cluster surveys, one requires precise knowledge about the evolution of galaxy clusters with redshift and the thermodynamical properties of ICM. In the simplest cases, where one considers pure gravitational collapse, cluster scaling relations are expected to follow simple self-similarity (Kaiser, 1986). X-ray scaling relations have been widely used to test the strength of correlations between cluster properties and to probe the extent of self-similarity of clusters (Edge & Stewart, 1991, Pike et al., 2014, Morandi et al., 2007, Comis et al., 2011, Ettori, 2013). For example, the luminosity-temperature ($L_x - T$) relation for self-similar models predict a shallower slope ($L_x \propto T^{\,2}$) than observed ($L_x \propto T^{\,3}$) (Edge & Stewart, 1991, Andreonet al., 2011). Observations show that there is break in the self-similarity in galaxy clusters, with a steeper slope for low mass clusters. Similarly, SZ effect scaling relations have been largely studied both analytically and by numerical simulations, and these studies also show discrepancies between observations and prediction

from a pure gravitational model (Bonamente et al., 2008, Battaglia et al., 2012, Holder & Carlstrom, 2001, Zhang & Wu, 2003).

One may argue that radiative cooling may have role for the steepness of the $L_x - T$ relation by eliminating gas more efficiently particularly in low-mass systems (Lewis, 2000, Yoshida et al., 2002, Wu & Xue, 2002) but this processes produces a drastic overprediction of the amount of cold gas which is clearly not consistent with the present observations. Another observational mystery is the "cooling-flow" problem in the galaxy cluster. Since it is found that the cooling time in the galaxy clusters cores is smaller than the age of the cluster, a central inflow of cool gas called cooling flow is expected to occur (Cowie & Binney, 1977, Fabian & Nulsen, 1977). Under these conditions, the gas slowly loses pressure support and falls towards the central galaxy. However, it has been found that rate of gas cooling and estimated rate of accretion onto the central galaxy is rather high in many cases (Fabian et al., 1984), implying that a significant amount of gas cooler than 1-2 keV should be present in the center which not consistent with the latest optical and X-ray observations suggesting that it is simply not the case (McNamara et al., 2000, Balogh et al., 2001, Peterson et al., 2003). Secondly, low star formation rates of central galaxies (Johnstone et al., 1987, O'Connell & McNamara, 1989, Allen et al., 1995) provide additional proof for the absence of significant amount of cooling in cluster cores. In addition, recent observations with radio and X-ray telescopes have also revealed complexity of the ICM physics, such as cold fronts, radio ghosts, cluster turbulence and nearly uniform high metallicity.

All these findings suggest that there must be a physical process that offsets the radiative cooling in the cluster cores, thus preventing the gas from falling out of the ICM in a cooling flow. Such studies has revealed the importance of complex non-gravitational processes, such as injection of energy feedback from AGN, radiative cooling, supernovae, and star formation, influencing the thermal structure of ICM, particularly in low mass (temperature) clusters (Pratt et al., 2010, Eckert et al., 2013, Chaudhuri et al., 2012, 2013, Voit et al., 2002, 2005). The first direct evidence for non-gravitational entropy in galaxy clusters and galaxy groups was given by (David et al., 1996) using *ROSAT PSPC* observations. (Ponman et al., 1999) found flatter entropy profile in galaxy cores and (Helsdon & Ponman, 2000) results indicated much steeper slope (~ 4.9) for luminosity-temperature relation than observed in galaxy clusters. Motivated by these findings several groups have reported similar conclusions using both numerical and semi analytical models with a entropy floor of the order of $200 - 400$ keV cm^2 (Eckert et al., 2013, Bialek et al., 2001, Borgani et al., 2005). By investigating the effect of excess energy on the density profiles of gas halo's by using semi-analytic model, the excess energy per particle has been estimated to be around $1 - 3$ keV (Wu et al., 2000). Similarly, (Chaudhuri et al., 2012, 2013) estimated the energy per particle up to r_{500} to be between $1.6 - 2.7$ keV using AMR and SPH simulations.

A recent promising development in understanding the state of the ICM is based on the concept of *local* thermal instability in core which is in rough *global* thermal balance. In isobaric conditions of the ICM, slightly denser blobs of the ICM are expected to cool faster than their surroundings. However, this local thermal instability results in cold gas only if the ratio of the ICM cooling time and the gravitational free-fall time is less than a critical value close to 10 (Sharma et al., 2012a, Meece et al., 2015, Choudhury & Sharma, 2016). This criterion quantitatively explains the observed entropy threshold ($\lesssim 30$ keV cm^2) for the presence of Hα luminosity and radio bubbles (Cavagnolo et al., 2008). Local thermal instability picture ties together with the cold mode feedback (as opposed to hot-mode Bondi accretion; (Pizzolato & Soker, 2005, 2010) which explains several observations (Voit et al., 2015). Thermal instability and condensation model also has important implications for the $L_x - T$ relation and the missing baryons problem (Sharma et al., 2012b).

Theoretical studies have often invoked some sort of non-gravitational heating to explain the cluster excess energy in ICM. However, the main unsolved issue in these models remains the origin and nature of the physical sources that cause the extra heating of the ICM. Although, Supernovae feedback is essential to explain the enrichment of the ICM to the observed metallicity level and heavy-element abundances but they provide insufficient estimates of energy per particle (< 1 keV) as compared to recent observations. Moreover, they are also inefficient to quench cooling in massive galaxies (Springel et al., 2005). An older idea to explain excess energy is that of preheating. This proposes that the cluster forms from an already preheated and enriched gas due to feedback processes (like galactic winds) heating up the surrounding gas at high redshifts. The preheating model was first proposed by (Kaiser, 1991) and has since been developed/improved by many (Evrard & Henry, 1991, Babul et al., 2002). The preheating scenarios require ~ 1 keV energy per particle to explain break in the self-similarity scaling relations (Borgani et al., 2001, Tozzi & Norman, 2001, Finoguenov et al., 2003). The simplest preheating model assumes

constant entropy level of ~ 250 keV cm^2 along with the radiative cooling. Although, early preheating models could describe the scaling relations in clusters but they suffered from a few drawbacks with regard to details. For example, such models predict isentropic cores particularly in the low mass clusters (Ponman et al., 2003) and the excess of entropy in the outskirts of the clusters (Voit et al., 2003) which is not consistent with observations. There is a growing evidence that AGN feedback mechanism provides a major source of heating for the ICM gas, thereby reducing the number of cooling flow clusters (Chaudhuri et al., 2012, 2013, Pike et al., 2014, Planelles et al., 2014, Guo & Oh, 2008, Gaspari et al., 2011). The AGN-jet simulations have reached a stage where they can suppress the cooling flow for a cosmological timescale and produce results matching with observations (Gaspari et al., 2012, Li et al., 2015, Prasad et al., 2015). Understanding the physics of the hot gas and its connection with the relativistic plasma ejected by the AGN is key for understanding the growth and evolution of galaxies and their central black holes, the history of star formation, and the formation of large-scale structures.

The effect of AGN feedback can occur at different scales ranging from galaxy formation to cool-core clusters. In case of galaxy formation, it reduces the galaxy luminosity function by suppressing the over-production of massive elliptical galaxies as predicted by dark matter only simulations, while in case of cool-core systems it solves the cooling flow problem. Additionally, it also gives helpful insights about the observed relation between the black hole mass and the bulge velocity dispersion (Gebhardt et al., 2000). However, many questions regarding the the physics of AGN feedback and how it interacts with the surrounding ICM, remain unanswered. Several different mechanisms have been put forward and have been investigated numerically and through observations. These include radiative heating by quasars called "radiative feedback" (Ciotti & Ostriker, 1997, William & Fabrizio, 2007) or bipolar mechanical outflows/jets called "kinetic feedback" (Gaspari et al., 2011, Zanni et al., 2005). While quasars might have been an important source of heating at high redshift, with the peak distribution at $z \sim 2$ (Nesvadba et al., 2008, Dunn et al., 2010), however, in low-redshift systems it seems likely that massive black holes mostly accrete mass and return energy in a radiatively inefficient way (Fabian & Rees, 1995). Recent observations suggest advection dominated accretion flow (ADAF) systems as the primary power source behind local AGN's (Narayan & McClintock, 2008). Recent and upcoming X-ray and radio observations could help us to narrow down search for physical feedback scenarios (Gitti et al., 2012). The detection of radio-filled X-ray cavities/bubbles, lobes, ellipsoidal weak shocks and iron enhancements along the radio jet trajectory strongly suggests that low redshift AGNs introduce energy directionally and in mechanical form through bipolar massive jets. Studies of X-ray deficient cavities allow us to derive the relationship between the mechanical energy injected and radio emission of AGN jets and lobes. Such a relationship is of great interest because it helps to understand the physics of AGN jets (O'Sullivan et al., 2011). Studies from high resolution Chandra X-ray telescope have found that AGN can inject up to about $10^{58}-10^{62}$ erg per outburst into the ICM which is not only sufficient to to quench the cooling of the ICM and increase its energy but also suppresses star formation and the growth of luminous galaxies (Birzan et al., 2004, McNamara & Nulsen, 2007). In order to gain more physical picture of the nature of interactions between the AGN feedback and ICM and the extent of balance between mechanical power fed by the AGN versus radiative loss of ICM, it is important to explore X-ray bright systems with apparent signatures of such interactions.

3 Probing AGN feedback in galaxy clusters with SKA

3.1 Estimates of feedback energy and correlation with radio luminosity

The thermodynamic history of the ICM, and hence any energetics, is fully encoded in the entropy of the ICM. The ICM entropy profile is defined as[1] $K(r) = k_B T n_e(r)^{-2/3}$, where k_B is the Boltzmann constant. Non-radiative simulations, which encodes only gravitational/shock heating, predict entropy profiles of the form $K(r) \propto r^{1.1}$ (Voit et al., 2005). By comparing the observed entropy profiles with theoretically expected entropy profiles based on non-radiative and non-feedback simulations can be used to determine the nature and degree of feedback. This idea was developed and used recently by Chaudhuri et al. (2012, 2013) who estimated the non-gravitational energy deposition profile up to r_{500} by comparing the observed entropy profiles with a benchmark entropy profile without feedback (Voit et al., 2005) for the *REXCESS* sample of 31 clusters (Pratt et al., 2010), observed with *XMM-Newton*. They found an excess mean

[1]Thermodynamic definition of specific entropy being $S = \ln K^{3/2} +$ constant

energy per particle to be ~ 1.6 keV and ~ 2.7 keV up to r_{500} using benchmark entropy for AMR and SPH simulations respectively with strongly correlation with AGN feedback. They also observed profiles of non-gravitational energy ΔE_{ICM} for CC and NCC clusters to be very different and it reached much lower values for CC clusters in the innermost regions as a result of a greater amount of energy lost due to radiative cooling in CC clusters. However, adding energy lost due to cooling to ΔE_{ICM}, the mean profiles for CC and NCC appear to become more or less similar. By calculating the radio luminosity L_R of the central radio sources within $0.3r_{500}$ from the NVSS catalog, Chaudhuri et al. (2013) found that this quantity is correlated with the bolometric luminosity L_X for both CC and NCC clusters. While the high temperature CC and NCC clusters show a positive relation between feedback energy and L_R, the three low temperature NCC clusters in the sample were found to have opposite trend. Moreover, their study also found that $L_R - \Delta E_{ICM}$ relation shows a strong trend for both the CC and NCC clusters with similar power law slopes for the CC and NCC clusters (although with different normalizations) even though L_R in the CC clusters was found to be much higher than NCC for same temperature.

All these results indicate that AGN feedback from the central radio galaxies much provide a significant component of feedback energy in both CC and NCC clusters. A combination of the SKA arrays and their receivers at a wide range of frequencies and angular resolutions will be ideal for this kind of study. According to the results of (Chaudhuri et al., 2013), radio-loud AGNs with luminosity 10^{23} J s^{-1} Hz^{-1} at 1.4 GHz are important for low mass clusters, with X-ray luminosity $\leq 10^{44}$ erg s^{-1}. These radio-loud AGNs are also the most abundant according to the radio galaxy luminosity function. The flux density of such a radio-loud AGN at $z = 0.2$ is ~ 1 mJy, and at $z = 0.5$, it is ~ 0.1 mJy. Therefore, SKA sensitivity will allow one to not only have a reliable estimate of the total radio power in low mass clusters at low redshift, but will also allow one to determine the redshift evolution of the role of radio-loud AGNs in clusters. In particular, this makes it an indispensable tool for searching for old, dying radio sources, and for the construction of complete, flux density in the AGN's. The high sensitivity of the SKA along with its wide field of view will help us in identification of objects of the same morphological type. High resolution imaging of jets and lobes from SKA will help us in detailed physics analyses.

3.2 Kinetic feedback of BCGs

The Brightest Cluster Galaxies (BCGs) or the first ranked galaxies in clusters are the most massive elliptical galaxies and show the highest probability to be radio loud. The BCGs impact the ICM through quasar mode and/or kinetic mode activity and are argued to be responsible for the offsetting the cooling of cluster cores. The impact of the ICM on the BCG to regulate its radio duty cycle is still not well understood. It is an open issue whether the large scale merging activity among clusters can affect the radio loudness of the BCG. A recent study of the radio luminosity function of a sample of 59 BCGs in the Extended GMRT Radio Halo Survey cluster sample ($0.2 < z < 0.4$, $L_{X[0.1-2.4\mathrm{keV}]} > 5 \times 10^{44}$ erg s^{-1}) (Venturi et al., 2008, Kale et al., 2015a, 2013, Venturi et al., 2007), has shown that the fraction of radio loudness reaches about 90% in BCGs in relaxed clusters as compared to 30% in BCGs in merging or non-relaxed clusters (Kale et al., 2015b). The sample is not large enough to conclude if the shape of the radio luminosity function of BCGs in relaxed and merging cluster is different. The all sky surveys and pointed surveys of galaxy clusters with the SKA-low and SKA-mid will be able to provide large samples of radio BCGs in clusters to redshifts of 1 or even further. These complete samples of radio BCGs, in combination with X-ray properties can be used to understand if and how the large-scale properties of the ICM affect the radio loudness of BCGs.

3.3 Cool core clusters and radio mini-halos

Evidence gathered from the observations over several decades suggest the presence of central FR-I type radio galaxies in about 70% of the cooling core clusters (Worrall & Birkinshaw, 1994, Komossa & Böhringer, 1999, Worrall, 2000). With the advent of the high-resolution X-ray observations using the present generation X-ray telescopes, it is well established that the central radio source produces a profound effect on the ICM. In particular, the X-ray images obtained at the superb spatial resolution using the Chandra telescope revealed that the hot gas in many cool core systems is not smoothly distributed, but instead exhibits highly disturbed structures including cavities or bubbles, shocks, ripples and sharp density discontinuities. Comparison of these features with the radio images at similar angular resolutions have revealed that these disturbances are originated due to the AGN jets (Blanton et al., 2001, Croston et al.,

2003, Fabian et al., 2003). In-depth analysis of individual systems along with the systematic studies of cavity samples (Wise et al., 2007, Gitti et al., 2009, Raffertyet al., 2008, David et al., 2011) have enabled us to investigate global properties of the X-ray cavities as well as shed light of the feedback mechanism in the cool core clusters. In galaxy clusters at low redshift, observations suggest that the central AGN activity due to advection dominated accretion flow (ADAF) systems as the primary power source behind local AGN's (Narayan & McClintock, 2008). Theoretically, it has been shown that these bubbles may rise buoyantly and raise some of the central cool gas (Churazov et al., 2001).

Diffuse non-thermal emission has also been observed in a number of cool-core clusters, where the radio-loud brightest cluster galaxy (BCG) is surrounded by a "radio mini-halo". Mini-halos are believed to be generated from the ICM (instead of being connected with the radio bubbles) where the thermal plasma and the relativistic electron population are mixed (Gitti et al., 2002, ZuHone et al., 2013). Only handful of radio mini halos have been detected so far due to the limitations of current radio interferometers and difficulty in separating their diffuse, low surface brightness emission from the bright emission of the central radio source. However, due to very good sensitivity to diffuse emission, high dynamic range and good spatial resolution SKA is expected to detect large number of such objects. This will allow us to reach a better understanding of their origin and physical properties of these astrophysical sources.

3.4 Feedback in group scale environment

Even though AGN feedback is well understood in the cooling flow clusters, however, due to the characteristic differences between groups and clusters, knowledge of cavity physics in clusters may not be directly applicable for that in groups (O'Sullivan et al., 2011). Systematic study of galaxy groups with AGN-IGM interactions in the nearby region is important to understand the AGN feedback in relatively shallower systems. Due to their shallower gravitational potentials, the AGN outbursts in such systems are believed to produce a larger impact on the intra-groups medium. This study is also important because the relationship between AGNs and hot gas can significantly influence galaxy evolution in the group environment. The groups selected from nearby region are also useful to probe regions closer to the central black hole with greater details. Therefore, combination of X-ray data and observations with SKA will give a complete picture of AGN feedback in group scale environment.

3.5 ICM morphology and cluster cosmology

Is has been pointed out that X-ray observables are sensitive to non-gravitational processes such as radiative cooling, AGN feedback and and that the X-ray scaling relation has relatively large intrinsic scatter (Edge & Stewart, 1991, Pike et al., 2014, Morandi et al., 2007, Comis et al., 2011, Ettori, 2013). Therefore, in order to obtain any robust estimates cosmological one requires precise knowledge about the evolution of galaxy clusters with redshift and the thermodynamical properties of ICM. The utility of large SZ surveys for determining cosmological parameters from cluster abundances and SZ power spectrum is limited by proper incorporation energetic feedback from AGN's in simulations. Therefore, it is utmost important to understand the nature and the extent of the non-gravitational feedback in galaxy clusters out to the virial radius so as to properly calibrate the scaling relations and theoretical models. With major advance in X-ray sensitivity, spectral resolution and high spatial resolution, in combination with future radio observations especially from SKA one may be able to make breakthroughs in these aspects of cluster physics.

3.6 Evolution of radio lobes

The synchrotron radiation emitted by the relativistic electrons in radio bubbles fades and becomes difficult to detect after about 10^8 years. Moreover, the X-ray surface brightness depressions are only visible near the center of the cluster where the contrast is large. Thus, it is unclear how far AGN driven cavities rise in the cluster, their interaction with the ICM, and how they evolve at late stages. Owing to high sensitivity and frequency range, SKA will be able to trace evolution inflated bubbles to much larger distances in the cluster. This will also offer us unique opportunity to study the the physical properties relativistic gas inside the bubbles, such as the buoyancy, equation of state, magnetic field and hydrodynamical instabilities in bubble and their interaction with the ICM (Scannapieco & Bruggen, 2008, 2015). One can, therefore, in principal do the detailed study of the spectral evolution of the fading

radio lobes both in synchrotron and Compton regime in the varying magnetic field which drives the expansion (Goldshmidt & Rephaeli, 1994).

4 Summary

Galaxy clusters being largest virialised systems known, therefore, are an important source of information regarding the universe and its large scale structure. In this review, we have made in depth analysis of AGN feedback from galaxy clusters and demonstrated the potential use of this effect in probing cosmology along with the recent developments. We discussed recent developments regarding the AGN outbursts and its possible contribution to excess entropy (preheating) in the hot atmospheres of groups and clusters, its correlation with the feedback energy in ICM and quenching of cooling flows. A robust explanation for the mechanism behind AGN feedback in galaxies, groups and clusters is essential in understanding the formation of large scale structure of the universe. Moreover, any attempt of obtaining robust cosmological information will require more detailed cluster modeling, the accurately calibrated selection function as well as extensive modeling of interaction of ICM with the expanding radio lobes from AGN. The much improved multi frequency measurements and high spatial resolution in near future due SKA as well as up coming data from cluster surveys from Planck S-Z, Euclid, eROSITA, ASTRO-H along with breakthrough in X-ray sensitivity and spectral resolution at high spatial resolution will have unique ability to answer the most important outstanding questions as to how this mode of feedback operates and its impact on the surrounding medium, and therefore should provide major breakthroughs in understanding the co-evolution of AGN, galaxies and large-scale structure of the universe structure.

References

Holder G., Haiman Z. & Mohr J. J., 2001, ApJL, 560, L111

Gladders M. D., Yee H. K. C., Majumdar S., Barrientos L. F., Hoekstra H., Hall P. B. & Infante L., 2007, ApJ, 655, 128

Vikhlinin A. et al., 2009, ApJ, 692, 1060

Jimenez R. & Verde L., 2009, Phys. Rev. D, 80, 127302

Andersson et al., 2011, ApJ, 738, 25

Allen S. W., Evrard A. E. & Mantz A. B., 2011, ARA&A, 49, 409

Bocquet S., 2015, ApJ, 799, 214

Kaiser N., 1986, MNRAS, 222, 323

Edge A.C & Stewart G. C., 1991, MNRAS, 252, 414

Andreon S., Trinchieri G. & Pizzolato F., 2011, MNRAS, 412, 2391

Bonamente M., Joy M. LaRoque S. J.; Carlstrom J. E., Nagai D. & Marrone D. P., 2008, ApJ, 675, 106

Battaglia N., Bond J. R., Pfrommer C. & Sievers J. L., 2012, ApJ, 758, 74

Cavagnolo K. W., Donahue M., Voit, G. M. & Sun, M., 2009, ApJS, 182,12

Pratt G. W., Arnaud M., Piffaretti R., Böhringer H., Ponman T. J., Croston J. H., Voit G. M., Borgani S. & Bower R. G., 2010, A&A, 511, 14

Eckert D., Molendi S., Vazza F., Ettori S. & Paltani S., 2013a, A&A, 551, A22

Vikhlinin A., Markevitch M., Murray S. S., Jones C., Forman W. & Van Speybroeck L., 2005, ApJ, 628, 655

Leccardi A. & Molendi, S., 2008, A&A, 486, 359

Chaudhuri A., Nath B. B. & Majumdar S., 2012, ApJ, 759, 5

Chaudhuri A., Majumdar S. & Nath B. B., 2013, ApJ, 776, 84

Pike S. R., Kay S. T., Newton R. D. A., Thomas P. A. & Jenkins A., 2014, MNRAS, 445, 1774

Planelles S. et al. 2014, MNRAS, 438, 195

Pandge M. B., Vagshette N. D., David L. P., Patil M. K. 2012, MNRAS, 421, 808

Hlavacek-Larrondo J.et al., 2012, MNRAS, 421, 1360

Hlavacek-Larrondo J.et al., 2015, ApJ, 805, 35

Brunetti G., Cappi M., Setti G., Feretti L. & Harris D. E., 2001, A&A, 372, 755

Gitti M., Brunetti G. & Setti G., 2002, A&A, 386, 456

Venturi T. et al., 2008, A&A, 484, 327

Cassano R. et al., 2008, A&A, 480, 687

Cassano R. & Brunetti, G., 2005, MNRAS, 357, 1313

Dennison B., 1980, A&A, 239, L93

Blasi P. & Colafrancesco S., 1999, Astroparticle Physics, 12, 169

Condon J. J. et al., 1998, ApJ, 115, 1693

van Haarlem M. P. et. al., 2013, A&A, 53, A2

Blake C. A., Abdalla F. B., Bridle S. L. & Rawlings S., 2004, New Astron. Rev., 48, 1063

Gitti, M. et. al., 2014, proceedings of Advancing Astrophysics with the Square Kilometre Array

Combes F., 2015, Journal of Instrumentation, 10, C09001

Jarvis M. J. & Rawlings S., 2004, New Astron. Rev., 48, 1174

Grainge, K. et. al., 2014, proceedings of Advancing Astrophysics with the Square Kilometre Array

Morandi A., Ettori S. & Moscardini L., 2007, MNRAS, 379, 518

Comis B., de Petris M., Conte A., Lamagna L. & de Gregori S. 2011, MNRAS, 418, 1089

Ettori S., 2013, MNRAS, 435, 1265

Holder G. P. & Carlstrom J. E., 2001, ApJ, 558, 515

Zhang Y.-Y. & Wu X.-P., 2003, ApJ, 583, 529

Lewis G. F, 2000, ApJ, 536, 623

Yoshida N. Stoehr F., Springel V. & White S. D. M., 2002, ApJ, 335, 762

Wu X.-P. & Xue Y.-J., 2002, ApJ, 572, 19

Cowie L. L. & Binney J., 1977, ApJ, 215, 723

Fabian A. C. & Nulsen P. E. J., 1977, MNRAS, 180, 497

Fabian A. C. & Nulsen P. E. J., Canizares C. R., 1984, Nature, 310, 733

McNamara B. R. et al., 2000, ApJ, 534, L135

Balogh M. L., Pearce F. R., Bower R. G. & Kay S. T., 2001, MNRAS, 326, 1228

Peterson J. R. et al., 2003, ApJ, 590, 207

Johnstone R. M., Fabian A. C. & Nulsen P. E. J., 1987, MNRAS, 224, 75

O'Connell R. W. & McNamara B. R., 1989, AJ, 90, 180

Allen S. W., Fabian A. C., Edge A. C., Bohringer H. & White D. A., 1995, MNRAS, 275, 741

Voit G. M., Bryan G. L., Balogh M. L. & Bower R. G., 2002, ApJ, 576, 601

Voit G. M., Kay S. T. & Bryan G. L., 2005, ApJ, 364, 909

David L. P., Jones C. & Forman W., ApJ, 473, 692

Ponman T. J., Cannon D. B. & Navarro J. F., 1999, Nature, 6715, 135

Helsdon S. F. & Ponman T. J., MNRAS, 315, 356

Wu K. K. S., Fabian A. C. & Nulsen P. E. J. 2000, MNRAS, 318, 889

Bialek J. J., Evrard A. E. & Mohr J. J., 2001, ApJ, 555, 597

Borgani S. et al., 2005, MNRAS, 361, 233

Sharma P., McCourt M., Quataert E. & Parrish I., 2012a, MNRAS, 420, 3174

Meece G. R., O'Shea B. & Voit G. M., 2015, ApJ, 808, 43

Choudhury P. P. & Sharma P., 2016, MNRAS, 457, 2254

Cavagnolo K. W., Donahue M., Voit G. M. & Sun M., 2008, ApJ, 683, L107

Pizzolato F. & Soker N., 2005, ApJ, 632, 821

Pizzolato F. & Soker N., 2010, MNRAS, 408, 921

Voit G. M., Donahue M., Bryan G. L. & McDonald M., 2015, Nature, 519, 203

Sharma P., McCourt M., Parrish I. & Quataert E., 2012b, MNRAS, 427, 1219

Gaspari M., Ruszkowski M. & Sharma P., 2012, ApJ, 746, 94

Li Y., Bryan G. L., Ruszkowski M. & Voit G. M., O'Shea B. W., Donahue M. 2015, 811, 73

Prasad D., Sharma P. & Babul A., 2015, ApJ, 811, 108

Springel V., Di Matteo T. & Hernquist L., 2005, ApJ, 620, L79

Kaiser N., 1991, ApJ, 383, 104

Evrard A. E. & Henry J. P., 1991, ApJ, 383, 95

Babul A., Balogh M. L., Lewis G. F. & Poole G. B., 2002, MNRAS, 330, 329

Borgani S. et al., 2001, ApJ, 559, 106, 71

Tozzi P. & Norman C., 2001, ApJ, 546, 63

Finoguenov A., Borgani S., Tornatore L. & Böhringer H., 2003, A&A, 398, 35

Ponman T. J., Sanderson A. J. R. & Finoguenov A., 2003, MNRAS, 343, 331

Voit G. M et al., 2003, Apj, 593, 272

Guo F. & Oh S. P., 2008, MNRAS, 384, 251

Gaspari M., Brighenti F., D'Ercole A. & Melioli C, 2011, MNRAS, 415, 1549

Gebhardt K. et al., 2000, ApJ, 539, L13

Ciotti L. & Ostriker J. P., 1997, ApJ, 487, L105

William G. M. & Fabrizio B., 2007, ApJ, 676, 880

Zanni C., Murante G., Bodo G., Massaglia S., Rossi P. & Ferrari A., 2004, A&A, 429, 399

Nesvadba N. P. H., Lehnert M. D., De Breuck C., Gilbert A. M. & van Breugel W., 2008, A&A, 491, 407-

Dunn J. P. et al. 2010, ApJ, 709, 611

Fabian A. C. & Rees M. J. 1995, MNRAS, 227, L55

Narayan R. & McClintock J. E. 2008, New Astron. Rev., 51, 733

Gitti M., Brighenti F. & McNamara B. R. 2012, Advances in Astronomy, 950641

O'Sullivan E. et al., 2011, ApJ, 735, 11

Birzan L., Rafferty D. A., McNamara B. R., Wise M. W. & Nulsen P. E. J., 2004, ApJ, 607, 800

McNamara B. R. & Nulsen P. E. J., 2007, ARAA., 54, 117

Kale R. et al., 2015a, A&A, 581, 23

Kale R. et al., 2013, A&A, 557, 99

Venturi T. et al., 2007, A&A, 463, 937

Kale R. et al., 2015b, A&A, 579, 92

Worrall, D. M. & Birkinshaw, M., 1994, ApJ, 427, 134.

Komossa, S. & Böhringer, H., 1999, A&A, 344, 755.

Worrall, D.M. 2000, ApJ, 530, 719.

Blanton, E. L., Sarazin, C. L., McNamara, B. R., & Wise, M. W., 2001, ApJ, 558, L15.

Croston, J. H., Hardcastle, M. J., Birkinshaw, M., & Worrall, D. M., 2003, MNRAS, 346, 1041.

Fabian, A. C. et al., 2003, MNRAS, 344, L43

Wise, M. W., McNamara, B. R., Nulsen, P. E. J., Houck, J. C., & David, L. P., 2007, ApJ, 659, 1153

Gitti, M. et al., 2009, in American Institute of Physics Conference Series, Vol. 1201, S. Heinz & E.Wilcots, ed., pp. 233

Rafferty, D. A., McNamara, B. R., & Nulsen, P. E. J., 2008, ApJ, 687, 899

David, L. P. et al., 2011, ApJ, 728, 162

Churazov E., Bruggen M., Kaiser C. R., Böhringer H. & Forman W., 2001, ApJ, 554, 261

ZuHone J. A., Markevitch M., Brunetti G. & Giacintucci S., 2013, ApJ, 762, 78

Scannapieco E. & Bruggen M., 2008, ApJ, 686, 927

Scannapieco E. & Bruggen M., 2015, ApJ, 805, 158

Goldshmidt O. & Rephaeli Y., 1994, ApJ, 431, 586

From Nearby Low Luminosity AGN to High Redshift Radio Galaxies: Science Interests with SKA

P. Kharb*[1], D. V. Lal[2], V. Singh[3], J. Bagchi[4], C. H. Ishwara Chandra[2], A. Hota[5], C. Konar[6], Y. Wadadekar[2], P. Shastri[1], M. Das[1], K. Baliyan[3], and B. Nath[7]

[1]*Indian Institute of Astrophysics, II Block, Koramangala, Bangalore 560034, India*
[2]*National Centre for Radio Astrophysics - TIFR, Post Bag 3, Ganeshkhind, Pune 411007, India*
[3]*Astronomy & Astrophysics Division, Physical Research Laboratory, Ahmedabad 380009, India*
[4]*Inter-University Centre for Astronomy and Astrophysics, Pune, India*
[5]*UM-DAE Centre for Excellence in Basic Sciences, Vidyanagari, Mumbai 400098, India*
[6]*Amity University, Sector 125, Noida 201301, India*
[7]*Raman Research Institute, C. V. Raman Avenue, Sadashivanagar, Bangalore 560080, India*

Abstract

We present detailed science cases that the Indian AGN community is interested in pursuing with the upcoming Square Kilometre Array (SKA). These range from understanding low luminosity active galactic nuclei in the nearby Universe to powerful radio galaxies at high redshifts. Important unresolved science questions in AGN physics are discussed. Ongoing low-frequency surveys with the SKA pathfinder telescope GMRT, are highlighted.

1 Introduction

Active galactic nuclei (AGN) are the centres of galaxies that emit copious amounts of radiation spanning the entire electromagnetic spectrum. It is now widely agreed that AGN are accreting supermassive black holes (SMBH; masses $10^6 - 10^9$ $M_\odot$), where the enormous energy is the outcome of the release of gravitational potential energy (Lynden-Bell, 1969). Somewhere in the interface between the SMBH and the accretion disk, bipolar jets or outflows are launched (e.g., Rees et al., 1982). The details of the launch mechanism are still unclear, although magnetic fields are widely believed to be instrumental in the production and collimation of these outflows (Blandford and Znajek, 1977; McKinney, 2006; Tchekhovskoy et al., 2011). Strong and prominent emission lines in the optical-infrared spectrum, which are considered to be the hallmark signature of an AGN, are produced in fast-moving gas clouds around the black hole-accretion disk system (the "central engine"): different cloud speeds and electron densities have led to the demarcation into broad and narrow line regions (BLR, NLR). The BLR in some AGN are obscured from certain lines of sight by a dusty torus or a warped disk, giving rise to the classification of type 1 (BLR and NLR visible) and type 2 (BLR obscured but NLR visible), and a unified scheme that attempts to link the two types on the basis of orientation (Antonucci, 1993; Netzer, 2015). Seyfert type 1s (with broad and narrow permitted emission lines in their spectra) and type 2s (with only narrow permitted and forbidden lines in their spectra) are expected to be the same phenomenon, only differing by orientation.

The development of radio interferometry in the 1960s led to the discovery of kiloparsec-scale jets in AGN. Large-scale jets that are observed in only about 15−20% of AGN, emit at radio frequencies via the synchrotron process. Highly energetic electrons in these jets can sometimes emit optical and X-ray synchrotron photons as well (Sparks et al., 2000; Worrall et al., 2001). It was first pointed out by Fanaroff and Riley (1974) that kiloparsec-scale jets in radio galaxies exhibited primarily two radio morphologies: the Fanaroff-Riley (FR) type I galaxies had broad jets that flared into diffuse radio plumes / lobes, while the FR type II galaxies had collimated jets that terminated in regions of high surface brightness called

*kharb@iiap.res.in

"hot spots" with the back-flowing plasma or the plasma left behind by the advancing jet, forming the radio lobes. The total radio power of the FRI and FRII sources also differed: the dividing line at 178 MHz was at $L_{178} \simeq 2 \times 10^{25}$ W Hz^{-1}, with the FRII sources being more powerful. The FR dichotomy is one of the major unresolved problems in jet astrophysics: it is not clear why the jets in FRIIs are powerful enough to produce hot spots, while they apparently lack power in FRIs. Differences in the mass or spin of the SMBH, accretion rate and/or mode, jet-medium interaction, host galaxy type and the galactic environments, are some of the explanations put forth to explain the FR dichotomy (Meier, 1999; Baum et al., 1995; Prestage and Peacock, 1988).

The radio-loud unified scheme proposes that BL Lac objects are the pole-on counterparts of FRI radio galaxies while the radio-loud quasars are the pole-on counterparts of FRII radio galaxies (Urry and Padovani, 1995). BL Lacs and quasars are collectively referred to as "blazars". Rapid variability at all wavelengths, high degrees of polarisation and superluminal jet motion, which are all the defining characteristics of blazars, are fully consistent with the suggestion of relativistic jets pointing close to our line of sight. Spectral energy distributions (SEDs) generated from multiwavelength studies of these blazars have revealed interesting trends: the synchrotron emission peaks at submm to IR (frequency range $10^{13} - 10^{14}$ Hz) for the low frequency-peaked BL Lacs (LBLs) and flat-spectrum radio quasars (FSRQs), while they peak at UV to X-rays (frequency range of $10^{17} - 10^{18}$ Hz) for the high frequency-peaked BL Lacs (HBLs) (Padovani and Giommi, 1995). Sambruna et al. (1996) and others have suggested that there are intrinsic differences in the physical parameters of these blazar sub-classes, with HBLs having higher magnetic fields/electron energies and smaller sizes than the low frequency peaked blazars.

The vast majority of AGN however, do not exhibit powerful radio jets or outflows. Seyfert galaxies and LINERs[1] fall under this category. Kellermann et al. (1989) classified AGN into the "radio-loud" and "radio-quiet" categories on the basis of their ratio (R) of radio flux density at 5 GHz to optical flux density in the $B-$band: R was $\ll 10$ for radio-quiet AGN. Difference in black hole masses, spins, accretion rates/modes, have been proposed to explain the radio-loud/radio-quiet divide (Laor, 2000; Tchekhovskoy et al., 2010; Sikora et al., 2007; Garofalo, 2013). According to the "spin paradigm", powerful radio jets originate near rapidly spinning accreting SMBHs found in bulge-dominated systems and are launched at relativistic speeds via the magnetohydrodynamic (MHD) Blandford-Znajek (BZ) mechanism (Blandford and Znajek, 1977). Alternatively, in the Blandford-Payne (BP) mechanism (Blandford and Payne, 1982), jet power is extracted from the rotation of the accretion disk itself, via the magnetic field threading it, without invoking a rapidly spinning black hole. However, in both the processes the intensity and geometry of the magnetic field near the black hole horizon strongly influence the Poynting flux of the emergent jet (Beckwith et al., 2008). This has given rise to the "magnetic flux paradigm", which proposes that jet launching and collimation require strong magnetic flux anchored to an ion-supported torus of optically thin, geometrically thick, extremely hot gas with poor radiative efficiency (Sikora and Begelman, 2013). In general, a radiatively efficient fast accretion mode (or "quasar" mode) has typically been associated with "radio-quiet" AGN, while a radiatively inefficient slow accretion mode (or "radio" mode) has typically been associated with "radio-loud" AGN (Croton et al., 2006).

There is also evidence to suggest that galaxy mergers influence the radio-loudness of sources (Heckman et al., 1986; Deane et al., 2014). We know that galaxy-galaxy mergers are an important phase of galaxy evolution (Schweizer, 1982; Mihos and Hernquist, 1996; Cox et al., 2006). Galaxy mergers are especially important at high redshifts, where the galaxy density was higher compared to the present Universe. As all massive galaxies are expected to harbour supermassive black holes in their centres (Kormendy and Ho, 2013), galaxy mergers are expected to lead to a large fraction of binary black hole systems. Such systems have so far been identified in only a handful of sources (e.g., Deane et al., 2014; Müller-Sánchez et al., 2015). Radio sources that exhibit double peaks in their emission line spectra are good candidates for binary AGN (Liu et al., 2010; Rosario et al., 2011; Comerford et al., 2013). As are sources exhibiting highly distorted jets and lobes, called X-shaped sources (Cheung, 2007; Lal and Rao, 2007). The search for dual AGN and a multi-wavelength study of dual AGN candidates can provide a different but unique perspective on the close interplay between the central SMBH and its host galaxy. Galaxy mergers are likely to be driving gas into the centres of merging galaxies, thereby providing fuel to be accreted on to the black holes. Yet not all dual AGN candidates exhibit one or two sets of bipolar kiloparsec-scale jets. The reasons for this absence are important and unclear.

One way to detect dual AGN is through the technique of very long baseline interferometry (VLBI).

[1]Low-Ionization Nuclear Emission-line Region

Table 1: SKA bands, including proposed changes in the low-frequency band definitions for SKA1-MID (Ref. ECP150027).

		MeerKAT ν (MHz)	SKA-Now ν (MHz)	SKA-Final ν (MHz)
SKA1-LOW		···	50-350	···
SKA1-MID	Band 1	580-1015	350-1050	475-875
	Band 2	900-1670	950-1760	795-1470
	Band 3	···	1650-3050	1650-3050

For VLBI, unconnected radio telescopes located in separate parts of the world, work together to produce a single large radio telescope with milliarsecond resolution. This translates to parsec-scales at the distance of the AGN we aim to study. One of the most robust detections of a binary black hole system have been made by Rodriguez et al. (2006) using multi-frequency VLBI. Moreover, multi-epoch VLBI observations are now determining jets speeds in blazars, radio galaxies, Seyferts and LINERs (e.g., Ulvestad et al., 1999; Lister et al., 2009). These studies have found that the jets in radio-loud AGN are typically faster than those in radio-quiet AGN. However the reasons for the differences are not clear. Are jets being launched with different speeds by different mechanisms or they getting slowed down by interacting with the surrounding medium ? (e.g., Bicknell, 1986; Laing and Bridle, 2002). The role played by jet-medium interaction in jet propagation is another important unsettled question in jet astrophysics. Bent radio jets in radio galaxies residing in galaxy clusters demonstrate the significance of jet-medium interaction (e.g., O'Dea and Owen, 1985), while VLBI observations suggest that jet differences occur close to the jet launching sites (e.g., Lister et al., 2009; Kharb et al., 2010).

In the sections ahead, we discuss the work that has been carried out on these science areas by the AGN community in India. Sections are divided around the key unresolved science questions in AGN physics. We describe how SKA will help in resolving these science questions.

2 SKA Surveys

Here we discuss the expected sensitivity levels and angular resolutions for the upcoming SKA configurations, and the all-sky surveys that will be undertaken with SKA.

SKA1-LOW (50−350 MHz)

One can make an all-sky continuum survey reaching a confusion noise of $\sim$ 20 μJy beam^{-1} at 120 − 150 MHz, with an angular resolution of $\sim 10''$, in a time scale of two years. To get rid of confusion noise, one can use frequencies $\geq$200 MHz and reach an *rms* noise of $\sim$10 μJy beam^{-1} with $5''$ resolution, again in a time scale of two years. Table 6 of Prandoni and Seymour (2015) shows that in one hour of integration, one would achieve an *rms* noise of $\sim$15.7 μJy beam^{-1} at 50 MHz, for a field of view of 39 square degrees, assuming a bandwidth of 250 MHz (full bandwidth). We note that deeper imaging with integration times of $100 - 1000$ per field is ruled out below $200 - 250$ MHz.

SKA1-MID Band-1 (350−1050 MHz)

(Eventually this band may cover only the frequency range 475−875 MHz.) One hour of integration would result in an *rms* noise of $\sim$1.7 μJy beam^{-1} at 700 MHz for a field of view of 1.4 square degrees, assuming a bandwidth of 700 MHz (full bandwidth).

SKA1-MID Band-2 (950−1760 MHz)

One hour of integration would result in an *rms* noise of $\sim$0.8 μJy beam^{-1} at 1.4 GHz, for a field of view of 0.35 square degrees, assuming a bandwidth of 810 MHz.

SKA1-MID Band-3 (1650−3050 MHz)

One hour of integration would result in an *rms* noise of $\sim$0.7 μJy beam^{-1} at 2.35 GHz, for a field of view of 0.12 square degrees, assuming a bandwidth of 1400 MHz. Smaller chunks of 100 MHz bandwidth would result in $\sim$2.8 μJy beam^{-1} in one hour of integration time.

We will make use of these sensitivity estimates in the proposed science goals ahead.

3 Jet Formation in AGN

Only around 15% or so of AGN possess powerful kiloparsec-scale jets or outflows. Nearly 85% of the sources fall under the "radio-quiet" AGN category. Comparing and contrasting sources that possess jets with those that do not, is crucial for learning about jet formation. We discuss below how the "radio-loud/radio-quiet" divide can be, and is being tested on different fronts. First, sensitive radio observations are detecting kiloparsec-scale radio structures (KSRs) in Seyfert and LINER galaxies. These jets and lobes can extend from a kiloparsec to 10 kpc, or larger. The host galaxies of these are typically lenticular or S0-type. Second, sensitive radio observations are detecting giant radio jets in spiral galaxies. Both these findings are challenging the previous well-accepted suggestions in the literature that large radio jets are only produced in elliptical galaxies, and not in spiral galaxies (McLure et al., 1999). In the next two sections, we discuss these points individually.

3.1 KSRs in "Radio-quiet" Seyferts & LINERs

Gallimore et al. (2006) have detected KSRs in $>$ 44% of Seyfert galaxies belonging to the volume-limited CfA+12μm sample when observed with the sensitive D-array configuration of the VLA at 5 GHz. Singh et al. (2015b) found that $>$ 43% of Seyferts belonging to a sample derived from the VLA FIRST[2] and NVSS[3] surveys, possessed KSRs. Low frequency observations with the GMRT at 610 MHz are finding an even larger fraction of KSRs in Seyfert and LINER galaxies ($>$ 50%, Pavana M. et al., in preparation).

While Seyfert galaxies have traditionally been categorised as "radio-quiet" AGN, Ho and Peng (2001) have demonstrated that when the optical nuclear luminosities are extracted through high resolution observations (e.g., from the *Hubble Space Telescope*) and the galactic bulge emission is properly accounted for by using specialized software like `GALFIT`, then the majority of Seyfert galaxies shift into the "radio-loud" class. Kharb et al. (2014) have confirmed this trend in the Extended 12μm Seyfert sample. From their FIRST+NVSS VLA study, Singh et al. (2015b) have found that $\sim$15% of their Seyfert/LINER sample fall under the "radio-loud" category, following the definition of Kellermann et al. (1989).

Moreover, Kharb et al. (2014) found a continuous distribution in the radio-loudness parameters of Seyfert galaxies and low-luminosity FRI radio galaxies. We need to look closely at Seyferts with KSRs and low luminosity FRI radio galaxies with weak radio jets, which together constitute the low-luminosity "intermediate" AGN population. If accurate black hole masses can be estimated for all low-luminosity "intermediate" AGN, along with their core X-ray and radio luminosties, then they could be placed on the fundamental plane (e.g., Merloni et al., 2003), to see where they lie. If their fundamental plane is offset from the rest of the classical objects, it may suggest a new mode of disk-jet coupling in these sources.

The SKA1-MID array has the potential to study weak KSRs in Seyfert, LINERs and low-luminosity FRI radio galaxies. The angular resolution 2 that will be achieved ranges between 0.4″ at 1.4 GHz (band 2) and 0.07″ at 8.3 GHz (band 5). The three-tier survey at bands 1 and 2 (1 and 1.4 GHz) will also be ideal for carrying out this project (see Table 1 in Prandoni and Seymour, 2015). It is expected that SKA will detect a much larger number of radio-"intermediate" sources, that will fill the radio-loud/radio-quiet divide.

3.2 Giant Radio Jets in Spiral Galaxies

With the advent of sensitive low radio frequency telescopes like the GMRT and LOFAR, several giant radio jets (extents $\gg$ 100 kpc) that are hosted in massive spiral galaxies, have been discovered (e.g., Ledlow et al., 1998; Hota et al., 2011; Bagchi et al., 2014; Mao et al., 2015; Singh et al., 2015a). The

[2]Faint Images of the Radio Sky at Twenty cm
[3]NRAO VLA Sky Survey

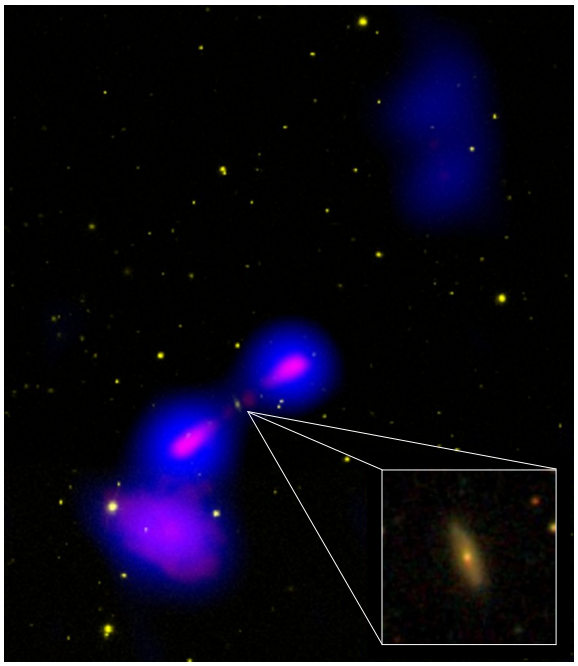

Figure 1: The composite image of Speca (Hota et al., 2011). The NVSS image is shown in blue, while the GMRT 325 MHz image is shown in red. The optical background from the SDSS is shown in yellow. Inset shows the SDSS colour image of the host galaxy.

standard paradigm to explain the elliptical hosts of large radio galaxies, invokes the process of two large spiral galaxies merging into an elliptical. In this process, the central supermassive black holes of each spiral galaxy also merge and grow in mass. Therefore, the discovery of a few spiral galaxies hosting large or giant radio galaxies suggest alternate ways, other than mergers, of creating conducive physical conditions for the formation of radio galaxies. If the central black hole can grow big and spin fast, under whatever circumstance, it may be possible to create large radio jets.

Twelve years after the finding of the first large radio galaxy hosted in a disk galaxy (J0315−1906) by Ledlow et al. (1998), Hota et al. (2011) reported the finding of the second such galaxy 'Speca' (SDSS J140948.85−030232.5; see Figure 1), primarily using SDSS, NVSS and GMRT (325 MHz) observations. Subsequently, Bagchi et al. (2014) reported the clearest case so far, of a spiral host in the source J2345−0449 (see Figure 2). With the help of web-based citizen-scientists project (Radio Galaxy Zoo), Mao et al. (2015) detected another such case in J1649+2635 from a sample of 65,492 galaxies. By similar automated archive cross-matching of SDSS, NVSS and FIRST data, Singh et al. (2015a) have reported three new cases of spiral-host radio galaxies (viz., J0836+0532, J1159+5820, J1352+3126). Although J1649+2635 shows an optically-blue grand-design spiral pattern, it is buried inside a huge old-stellar halo, unlike any spiral galaxy we know. Both J1352+3126 and J1159+5820 show clear signs of tidal interaction or past merger. Therefore, J0315−1906, Speca, J2345−0449 and J0836+0532 are the only four cases of clear spiral-host large radio galaxies.

Out of these four galaxies, two of them are giant and show episodic activity: J2345−0449 is a DDRG of extent 1.6 Mpc, and Speca is likely a triple-double radio galaxy of extent 1.3 Mpc. Both these systems are hosted by extremely large and massive spirals. J2345−0449 is massive ($M_{dyn} \sim 1.0 \times 10^{12}$ $M_{\odot}$), has a diameter of nearly 50 kpc, a fast rotation speed (∼430 km s^{-1}) and a high central velocity dispersion ($\sigma \sim 100$ km s^{-1}; Bagchi et al., 2014). Similarly, observations with the Subaru telescope show Speca to be large (∼60 kpc) with a rotation speed of nearly 370 km s^{-1} (Hota et al., 2014).

As suggested in these works, such galaxies have likely grown in isolation without mergers but co-planar accretion directly from cosmic-filaments or surrounding medium, and are expected to be more numerous at higher redshifts. None of these sources so far shown an FRI-type radio morphology. This

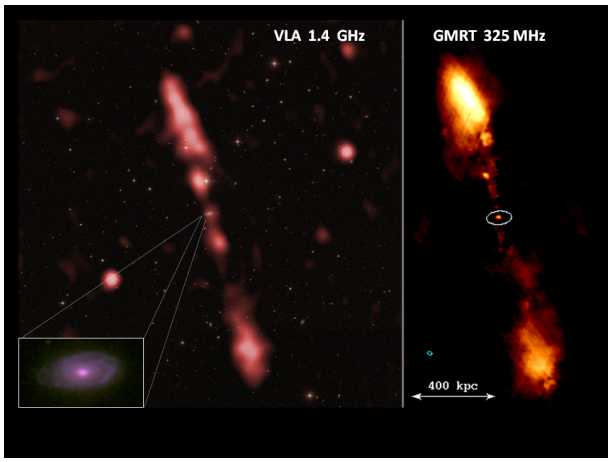

Figure 2: The composite image of J2345−0449 (Bagchi et al., 2014). The radio image from the NVSS at 1.4 GHz and the GMRT at 325 MHz are shown in red and orange. The inset shows the RGB-colour image of the host galaxy from the CFHT.

is likely to be due to the lack of sensitivity, especially for the high redshift sources. Once we have a larger number of such sources, the following questions can be asked: is there a difference in the bar fraction or metallicity in these host galaxies, or the presence of double nuclei ? Are there differences in the molecular gas fraction compared to other spiral galaxies, etc. ? Observing samples of massive spirals with the SKA (see Section 6.1 for more details), specially at low frequencies, will increase the probability of finding several more spiral-host large radio galaxies, which have been missed in current surveys. Even before the operation of SKA1, the sample of such spiral galaxies will increase by two orders of magnitude via optical spectroscopic surveys like DESI[4]. High-resolution VLBI imaging and polarisation mapping of the inner radio jets near the core, in the disk/corona collimation region, would be very informative for understanding the jet launching process in these highly unusual AGN.

Using the VLA FIRST survey, Proctor (2011) and Machalski et al. (2001) had listed three dozen FRII or FRI/II sources with angular sizes between brightest regions $\gtrsim 3'$ and a flux density limit from 3000 deg^2. We try to estimate the number of GRGs likely to be detected with SKA surveys. Extrapolating from these earlier detections, and using Figure 1 from Johnston-Hollitt et al. (2015), the SKA surveys will detect about a few times 10^4 GRG sources (see also Ruta et al. 2016). If we make a conservative estimate that $\sim$10% are of these are in spiral galaxies, we will have a thousand new GRGs which are hosted by spirals. In other words, an all-sky radio continuum survey using SKA1 will provide statistically large samples for us to study morphology of giant radio jets and their launching processes.

4 Jet Morphology: Clues to Formation and Propagation

Jets in AGN span parsec to mega-parsec scales, and have speeds ranging from a few thousand km s^{-1} to a fraction of the speed of light. Their morphologies are diverse: they can be bent, S- or Z-shaped, flaring or highly collimated. They can possess terminal hotspots or be plume-like with no clear jet termination. These morphologies can indicate differences in the jet launch speeds and/or jet-medium interaction. Attempts to unify this large variety of jet structures have been made. We discuss ahead the successes and failures of these attempts.

[4]Dark Energy Spectroscopic Instrument

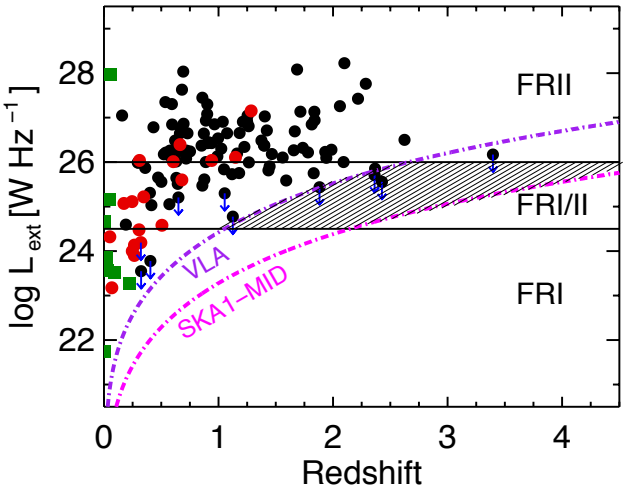

Figure 3: 1.4 GHz extended luminosity versus redshift for the MOJAVE sample (Kharb et al., 2010). Black and red circles denote quasars and BL Lac objects, respectively, while green squares denote radio galaxies. Core-only sources are represented as upper limits with downward arrows. The solid lines indicate the FRI−FRII divide (extrapolated from 178 MHz to 1.4 GHz assuming a spectral index, α=0.8), following Ledlow and Owen (1996) and Landt et al. (2006). The purple line denotes the sensitivity limit for the historical VLA which was used to carry out the MOJAVE study, while the magenta line denotes the sensitivity limit for the upcoming SKA1-MID array (see Table 1; Dewdney et al., 2013). SKA will be able to detect nearly twice as many "intermediate" or "hybrid FRI/II" sources, compared to previous studies.

4.1 The FR Divide & Radio-loud Unification

The simple radio-loud unified scheme linking BL Lac objects to FRI and quasars to FRII sources, has been challenged by Kharb et al. (2010) on the basis of their kiloparsec-scale radio study of the MOJAVE[5] blazar sample. Kharb et al. examined the MOJAVE sample of 135 blazars (Lister et al., 2009), using high-resolution 1.4 GHz data from the VLA. They found that a substantial fraction ($\approx$ 20%) of MOJAVE quasars and BL Lacs had total radio powers that were "intermediate" between FRIs and FRIIs (see Figure 3). Many BL Lac objects had lobe luminosities ($\approx$ 30%) and hot spots ($\approx$ 60%) like quasars. In addition, they found a strong correlation between the kiloparsec-scale lobe luminosities and parsec-scale jet speeds: the large-scale jet and lobe emission knew about the small-scale jet as it was launched. It therefore appeared that the fate of the AGN was decided at its birth!

These results have important implications for the inner workings of AGN. Therefore, they need to be re-examined with higher sensitivity radio data, as will become available with SKA. As is clear from Figure 3, the much lower sensitivity limits of SKA1-MID at GHz frequencies, is likely to detect nearly twice as many "intermediate" or "hybrid FRI/II" sources, than previous studies carried out with the VLA. The SKA1-LOW and SKA1-survey are ideal for detecting the full extent of the diffuse lobe emission in radio galaxies and blazars. SKA1-LOW is expected to operate between $0.05 - 0.35$ GHz, while SKA1-survey will operate between $0.65 - 1.67$ GHz (Table 1; Dewdney et al., 2013). The resolution of SKA1-LOW would typically be around 11 arcsec, while the SKA1-survey will be around 0.9 arcsec. The three-tier survey at bands 1 and 2 (1.0 and 1.4 GHz) will be ideal for carrying out this project (see Prandoni and Seymour, 2015). In addition these sensitive data will become available for a much larger population of radio sources including the so-called "core-only" sources ($\approx$ 7% in the MOJAVE complete sample; Kharb et al., 2010, see upper limits in Figure 3). There are suggestions that these "core-only" blazars are another beast altogether (e.g., Punsly et al., 2015). SKA will help to find out whether this is a new class of sources or sources with very faint extended emission, beyond the reach of present day radio telescopes. Perhaps they exhibit episodic activity and are currently switched off: the faint emission from the previous episodes is not detectable. SKA1-LOW and SKA-MID are required to settle these

[5]Monitoring of Jets in AGN with VLBA Experiments. http://www.physics.purdue.edu/MOJAVE

questions. Our (historical) VLA observations at 1.4 GHz could not detect extended radio emission below 10−50 μJy beam^{-1}, but SKA1-MID will be able to detect emission that is as low at 0.7 μJy beam^{-1} (Table 1; Dewdney et al., 2013), thereby increasing the overall sensitivity by a factor of 10 to 70.

4.2 Probing Blazar Nuclei with SED Modelling

A large number of blazars (radio-loud quasars and BL Lac objects) are being detected in the *Fermi* gamma-ray survey of the sky. For many sources, it is a difficult proposition to find their association in various energy regimes and their identification (e.g., LBL, HBL) owing mostly to lack of data. Multi-frequency observations at all frequencies and optical and radio polarization measurements are required. While one can use polarization information to identify and broadly classify blazar classes, continuum fluxes at all possible energy regimes are required to generate the SEDs. Blazar candidate CGRaBS J0211+1051 was detected by *Fermi* in a flaring mode. Chandra et al. (2012) carried out optical polarization observations on this source with the Mount Abu Infrared Observatory, India, in 2011. High and variable degree of polarization (9−20%) was detected. Based on that, they proposed the source to belong to the LBL class. To confirm this, a multi-frequency study was carried out for this source using data from the MOJAVE, *Planck*, *WISE*, *Swift*, our own data from the Mount Abu, *Fermi* and *VERITAS*. The SED showed that low energy (synchrotron) peak falls at 10^{14} Hz, confirming it to be a low-energy peaked blazar. The light-curves show variations in the high energy gamma-rays to be correlated with X-ray, UV and optical variations, perhaps indicating to their co-spatial origin and associating counter-parts in various energy regimes (Chandra et al., 2014).

Multi-band continuum data from SKA will greatly benefit generation of SEDs for blazars while polarization-sensitive VLBI data will be useful for localizing the emission regions in the jet.

4.3 Estimating Radio Lobe Energetics

X-ray observations of radio galaxy lobes have shown that the electrons responsible for the synchrotron radiation in radio wavelengths can also scatter the cosmic microwave background radiation photons to X-ray wavelengths. This up-scattering requires that the Lorentz factors of the electrons be of order $\sim 10^4$, which implies that the regions in the lobe which would be X-ray bright would also be bright in low frequency (few hundred MHz) radio wavelengths, for typical values of magnetic fields (Nath, 2010). However, the surface brightness of these regions is likely to be low. Observations with SKA would be useful in determining the physical processes at work in the radio lobes (back flow, cooling of electrons due to adiabatic expansion of lobe, through radiation etc.).

5 Jet Kinematics and Magnetic Field Structure

Differences in jet launching speeds and magnetic field structures are widely believed to be important in explaining the wide variety of jets observed. Multi-epoch VLBI observations are essential to measure jets speeds on parsec and sub-parsec scales. The feasibility of carrying out VLBI and polarization-sensitive VLBI with SKA (or SKA-VLBI) has been discussed by Paragi et al. (2015). Polarization-sensitive VLBI observations estimate the projected magnetic field structures in parsec-scale jets (Gabuzda et al., 1994). Polarisation measurements in kiloparsec-scale jets and lobes reveal the effects of jet-medium interaction on inter-galactic scales (Liu and Pooley, 1991; Laing, 1996; Kharb et al., 2012).

5.1 Jet Speeds from Multi-epoch VLBI

Using VLBI images of a rigorously selected sample of Seyfert galaxies, Lal et al. (2004) have shown that the radio properties of the compact parsec-scale features are consistent at large with the unified scheme for Seyfert galaxies (see Section 1), with no significant evidence for relativistic beaming in their jets. Some detected parsec-scale features in these sources could be termination points of the radio jets. The high-resolution, parsec-scale study of low-luminosity AGN is challenging because these sources have very low radio flux densities, typically less than a few milli-Jansky. Therefore the correlated flux densities of only a handful of sources meet the sensitivity thresholds currently offered by global VLBI. VLBI can only study AGN radio emission which is of the order of at least a few milli-Jansky. SKA-VLBI will be

able to decrease this flux density limit by several orders of magnitude. This will allow us to study jets in low luminosity AGN.

5.2 Magnetic Fields via Polarimetry

Magnetic fields are widely believed to be instrumental in jet creation, jet launching, jet collimation and jet propagation in AGN. Since radio jets emit via the synchrotron mechanism, magnetic field structures can be traced via radio polarimetric observations.

5.2.1 Polarimetry on Parsec-scales

Polarization-sensitive VLBI (VLBP) observations of 4 FRI galaxies at 8 GHz with a global VLBI array by Kharb et al. (2005) were among the first observations carried out on this relatively weak class of sources. Almost all previous such observations had been carried out on the more radio powerful FRII radio galaxies and blazars. Kharb et al. (2005) found a 100% detection rate of jet polarization in the four FRI radio galaxies they observed and a suggestion of a "spine-sheath" magnetic field structure. Furthermore, the detection of significant core polarization was consistent with FRI radio galaxies lacking the putative dusty torus (Chiaberge et al., 1999; Kharb and Shastri, 2004), the inner ionized region of which should have depolarized the core emission. The global VLBI array used in this study included the 100 m Effelsberg antenna: without the inclusion of this large single dish telescope, the VLBI array would not have been as sensitive and the success rate of detection would not have been 100%. A multi-frequency (5, 8, 15 GHz) VLBP study of these sources revealed a gradient in rotation measure (RM) across the jet of one radio galaxy, 3C 78. Such a gradient suggests the presence of a helical magnetic field (Blandford, 1993; Kharb et al., 2009). Similar multi-frequency VLBP observations of a complete sample of UGC FRI radio galaxies, revealed sheath-like magnetic field structures in several sources (Kharb et al., 2012).

SKA-VLBI with SKA1-MID and/or SKA1-SUR, observing together in the $1 - 15$ GHz frequency range with the current VLBI arrays and future large aperture telescope like FAST (Nan et al., 2011), is expected to outperform current global VLBI arrays including the most sensitive current telescopes (Paragi et al., 2015). Faraday rotation measurements and the search for RM gradients in both the approaching and receding jets of relatively-plane-of-sky radio galaxies of the FRI and FRII types, need to be carried out, in order to probe the complex magnetic field structures, without relativistic effects that can dominate in the low inclination blazars. Since radio galaxies are much weaker than blazars in total radio emission, this study can only be carried out for a large enough number of sources with the future SKA-VLBI.

5.2.2 Polarimetry on Kiloparsec-scales

Multi-frequency polarization-sensitive observations with the VLA of a sample of 13 FRII radio galaxies, revealed interesting correlations on kiloparsec-scales (Kharb et al., 2008). A strong correlation between lobe depolarization and lobe spectral index ("Liu-Pooley effect") was observed: radio lobes with a flatter spectrum exhibited lower depolarization. The lobe depolarization difference was correlated with the arm-length ratio: the shorter lobe in the source was more depolarized. This strongly suggested that lobe depolarization depends significantly on environmental asymmetries in radio galaxies. Most interestingly, Gabuzda et al. (2015) have recently found suggestions for an ordered toroidal magnetic field component in the AGN 5C 4.114 on kiloparsec scales, through RM observations.

6 AGN Lifetimes and Duty-Cycle

The lifetimes of radio sources have been inferred from several arguments. Spectral ageing analysis has been a powerful tool to infer radio source ages. Giant radio galaxies (GRGs) push the limits of the lifetimes for radio sources. It is also clear that AGN activity is episodic in nature (e.g., Davies, 1990; Saikia and Jamrozy, 2009). Attempts have been made to infer the AGN duty-cycle (e.g., Greene and Ho, 2007). These are essential to understand why only a fraction of all galaxies in the Universe have nuclei that are "active", even though all massive galaxies host supermassive black holes.

6.1 Giant Radio Galaxies

Giant radio galaxies can be used as pointers of black hole physics and 'barometers' of the intergalactic medium in the cosmic-web (e.g., Nath, 1995). GRGs, whose lobes span ∼1 Mpc or more are among the largest, most luminous objects in the Universe (Ishwara-Chandra and Saikia, 1999). Majority of GRGs show FRII morphologies. Due to sensitivity limitations of the present radio telescopes like the EVLA or GMRT, most of the GRGs found so far are in the nearby universe ($z \lesssim 0.7$). Recently, Sebastian et al. (2015, in preparation) have discovered a 2.2 Mpc giant radio source at a redshift of 0.56 in the field of LBDS-Lynx[6]. This appeared as a faint elongated source in the deep 150 MHz images with the GMRT, implying that the deeper radio surveys at low frequencies such as using SKA-LOW have the potential to discover many giant radio sources at redshift > 0.5.

It is unclear if the large sizes of GRGs reflect the high efficiency of radio jets produced from the central engine, or they grow to enormous sizes due to their favourable location within a low density ambient medium. Approximately half of the baryons in the present day Universe are still unaccounted for ('missing'), in the sense that these baryons are believed to reside in the large galaxy filaments, in the form of warm-hot intergalactic medium (WHIM), as part of the cosmic-web structure of the universe. The large extents of GRGs provide an excellent opportunity to use them as 'barometers' for probing the physical properties of this WHIM gas (its temperature, pressure and magnetic field). For this purpose a sensitive search using SKA and LOFAR for Mpc scale radio sources in the vicinity of galaxy filaments and perhaps inside the voids, surrounded by sheets of galaxies would be extremely valuable. The discovery of large numbers of giant radio galaxies in the distant universe will be greatly facilitated by the concurrent operation of SKA1 and LSST[7]. Accurate photometric redshifts for millions of galaxies provided by LSST will be critical in this effort.

In Section 3.2, we had estimated the number of GRGs likely to be detected with SKA surveys by extrapolating from the detections seen in VLA FIRST survey images (Proctor, 2011; Machalski et al., 2001) and Figure 1 from Johnston-Hollitt et al. (2015). Briefly, an all-sky radio continuum survey using SKA1 will provide statistically large samples, a few times 10^4 GRGs and their environments for us to study morphology of giant radio jets.

6.2 Double-double Radio Galaxies

After cessation of a given jet launching episode of a given radio galaxy, when a new episode starts and forms a new pair of jets, which plough through the cocoon material dumped by the previous jet activity, the radio galaxy is known as a double-double radio galaxy (DDRG). The duration of the active phase is a few to a few 100 Myr, and the duration of the quiescent phase is a few 10^5 to a few 10^8 yr (Konar et al., 2013). As the outer relic lobes are expected to be steep spectral plasma, a few new DDRGs have been discovered using the low radio frequency observations with the GMRT: detailed spectral ageing analyses have been performed after incorporating complementary high-frequency data from the VLA (e.g., Saikia et al., 2006; Konar et al., 2006; Nandi et al., 2014). Tamhane et al. (2015) have discovered a new Mpc-sized radio galaxy at z=1.32 in the XMM-LSS field. This object also shows evidence of episodic activity as well as inverse Compton scattered X-ray photons. At present, such high redshift objects are rare.

The most important question for the DDRGs is whether the jet power remains same/similar in two consecutive episodes. Konar and Hardcastle (2013) investigated this issue and found a reasonably strong evidence that the jet power, at least in a section of DDRGs, remain same/similar in two consecutive episodes. They found that the injection spectral indices of inner and outer lobes are similar and found an $\alpha_{inj}^{in} - \alpha_{inj}^{out}$ correlation between the injection spectral indices of inner and outer double. This they interpreted as due to the similar jet power in different episodes. Konar and Hardcastle (2013) however, were studying only a few sources. In the SKA era, we expect hundreds of DDRGs to be discovered and one can verify this $\alpha_{inj}^{in} - \alpha_{inj}^{out}$ correlation. Also we can check the universality of this relation (i.e. whether this correlation is true for all DDRGs or for a specific kinds of DDRGs).

Konar and Hardcastle (2013) also found the smallest duration so far of quiescent phase between two episodes, which is $\sim 10^5$ yr. A statistical study to find the distribution of quiescent phase of DDRGs

[6]Leiden-Berkeley Deep Survey - Lynx
[7]The Large Synoptic Survey Telescope

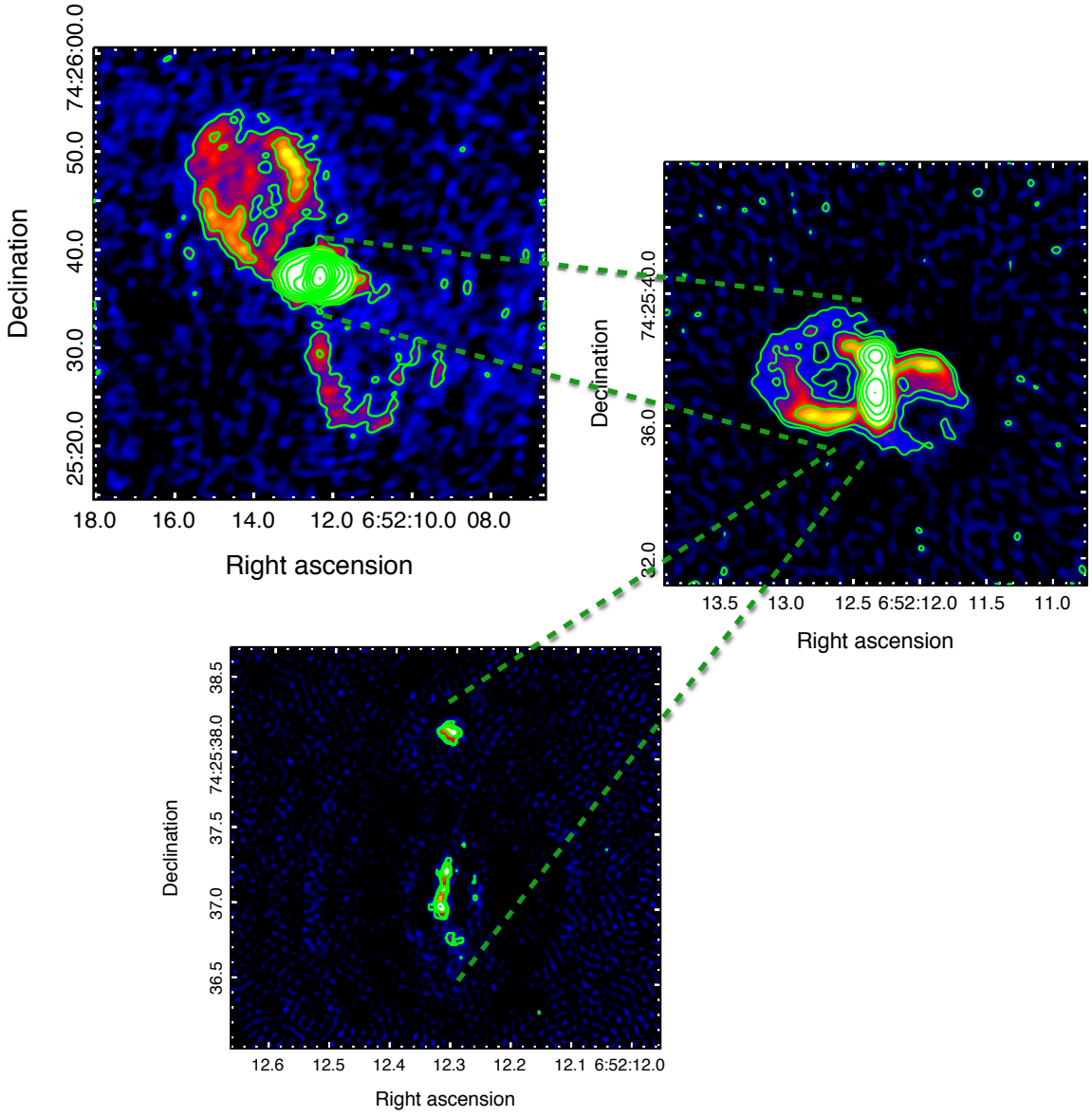

Figure 4: The Seyfert galaxy Markarian 6 exhibits three sets of radio lobes/jets which are nearly perpendicular to each other (Kharb et al., 2006). The detection of these structures required sensitive observations with multiple arrays and frequencies with the VLA. Steep-spectrum radio lobes from previous episodes of the AGN activity require sensitive low frequency observations, as will become available with SKA. Many such complex radio morphology sources are likely to be detected then.

is very important to constrain the accretion physics at the central engine. In the SKA era, with the expected discovery of many new DDRGs, we can hope to study such a distribution.

Another important goal is to find the oldest plasma around the outer double of the known DDRGs from SKA-generated images. So far, the oldest known plasma of outer double of DDRGs is 200 Myr for the source 4C 29.30 (Jamrozy et al., 2007). While pushing the limit of detecting old/relic radio plasma in DDRGs with SKA it is likely that we will discover more triple-double radio galaxies (TDRGs). So far, there has been only two reports on such sources: B0925+420 (Brocksopp et al., 2007) and Speca (Hota et al., 2011). Three episodes of AGN jet/lobe activities have been seen in two other cases though can not be called radio galaxy. In the Seyfert galaxy Mrk 6, three clear episodes are seen in three different orientations (Kharb et al., 2006, see Figure 4). Furthermore in NGC 5813, three pairs of cavities in X-ray emission have been found and later detected to contain old relativistic plasma by GMRT observations (Randall et al., 2011). However, it is clear that we can expect to detect many new DDRGs and TDRGs with SKA because of the higher sensitivity. From the top left panel of Figure 1 of Prandoni and Seymour (2015), we see that the 5σ SKA *rms* noise at around 100 MHz is $\sim$0.2 mJy beam^{-1}. This is much below most of the existing surveys (as is evident from the figure), and also much below the *rms* noise of GMRT images (1 sigma $\sim$a few mJy beam^{-1} by no automated algorithm) at $\sim$150 MHz after 8 hours of integration. The higher resolution of SKA will help us probe the jet-lobe structure well. These will be useful to find some new aspects of jet physics, as well as to verify the already done work mentioned above.

6.3 Episodic Activity in Low-luminosity AGN

Observations of the Seyfert galaxies NGC 4235 and NGC 4594 (the Sombrero galaxy), with the GMRT at 325 and 610 MHz, have revealed signatures of episodic AGN activity in them (Kharb et al., 2016). Both the 610 MHz total intensity and the $325-610$ MHz spectral index images suggest the presence of a "relic" radio lobe in NGC 4235, suggestive of episodic activity in this galaxy. This makes NGC 4235 only the second known Seyfert galaxy after Mrk 6 (see Figure 4) to show clear signatures of episodic activity. Based on a simple spectral ageing analysis, the relic outer lobe appears to be at least two times older than the present lobe. This implies that the AGN in NGC 4235 was switched "off" for the same time that it has been "on" for the current episode. A $\sim$ 3 kpc linear, steep-spectrum "spur-like" feature is observed nearly perpendicular to the double-lobed structure in NGC 4594. Since the VLBI jet in NGC 4594 is perpendicular to this linear feature, the AGN does not seem to be currently fuelling it.

As mentioned in the previous section, the detection of diffuse low surface brightness emission from old and relic lobes, requires sensitive low frequency observations, as will become available with the SKA1-LOW survey at 120 MHz. To illustrate this further, we use the well studied sources in the VLA FIRST survey Proctor (2011) and Machalski et al. (2001), which listed 242 systems including triple-double systems and over $\sim$600 more candidates. Additionally, Sirothia et al. (2009a) listed 374 sources from an $18'$ square ELAIS-N1 field using the GMRT at 325 MHz up to a median *rms* noise of $\sim$40 μJy with an angular resolution of $\sim 8''$. Although SKA 1 surveys will have similar resolution, they will be more sensitive than the GMRT ELAIS-N1. Extrapolating from these detections, using (Figure 1, Johnston-Hollitt et al., 2015), the SKA surveys will detect $\sim 10^7$ DDRG sources. An all-sky radio continuum survey using SKA1 will provide statistically large samples for us to study morphology of radio jets in DDRGs and the nature of episodic activity in them.

7 Population of High-Redshift Radio Galaxies

It is important to discover high redshifts radio galaxies (HzRGs) for several reasons. First, the host galaxies of HzRGs are among the most massive intensely star-forming galaxies and are believed to be progenitors of massive elliptical galaxies in the local universe (McLure et al., 2004; Seymour et al., 2007). Second, HzRGs are known to reside in dense environments, and therefore, they can be used as the tracers of (proto)clusters (Venemans et al., 2007; Galametz et al., 2012). Third, the radio luminosity function of HzRGs beyond redshift of 3 is poorly constrained. In fact, it is unclear whether there is a genuine dearth of HzRGs at $z > 3$ or the observed deficiency is merely due to selection effect. Fourth, since supermassive blackholes are essential ingredients of radio powerful AGN, the formation of SMBHs at such early epochs can also be probed using HzRGs. Also, HzRGs are complementary to the emerging

population of Lyman break galaxy population at high-redshifts, which are less massive by one to two orders of magnitude than host galaxies of HzRGs. Therefore, the identification and study of HzRGs are important to understand the formation and evolution of galaxies at higher redshifts and in dense environments.

Given the observed correlation between the steepness of the radio spectrum and cosmological redshift (i.e., the $z - \alpha$ correlation), ultra steep spectrum (USS) radio sources are one of the efficient tracers of powerful HzRGs (Ishwara-Chandra et al., 2010a; Ker et al., 2012). Using deep 150 MHz ($1\sigma \sim$0.7 mJy beam^{-1}) observations of LBDS-Lynx field, Ishwara-Chandra et al. (2010a) reported that among the 150 radio sources with spectra steeper than -1, about two-third of these are not detected in SDSS, and therefore suggested them to be strong HzRGs candidates. In contrast to searches for powerful HzRGs from radio surveys of moderate depths, fainter USS samples derived from deeper radio surveys can be useful in finding HzRGs at even higher redshifts and in unveiling a population of obscured weaker radio-loud AGN at moderate redshifts. Using 325 MHz GMRT observations and 1.4 GHz VLA observations available in two subfields (VLA-VIMOS VLT Deep Survey, VLA-VVDS, and Subaru X-ray Deep Field, SXDF) of the XMM-LSS field, Singh et al. (2014) have derived a large sample of 160 faint USS radio sources and characterised their nature. Their study shows that the criterion of ultra steep spectral index remains a reasonably efficient method to select high-z sources even at sub-mJy flux densities. In addition to powerful HzRG candidates, their faint USS sample also contains populations of weaker radio-loud AGNs potentially hosted in obscured environments.

Ishwara-Chandra et al. (2011, 2010b) using the redshift spectral index correlation have found radio galaxies with $z > 3$ using GMRT in the deep 150 MHz LBDS-Lynx field having an rms noise of $\sim$0.7 mJy and an angular resolution of $\sim 17''$. Spectral index was estimated by cross-correlating these sources detected at 150 MHz using GMRT and combining it with the available observations at 327, 610, 1400 and 4860 MHz and also using available radio surveys, e.g., the Westerbork Northern Sky Survey at 327 MHz and the NVSS and FIRST at 1400 MHz. They detected about 765 sources in about 15 deg^2 and of which about 150 radio sources with spectra steeper than 1.0; furthermore, about 100 sources are not detected in the Sloan Digital Sky Survey, hence are strong candidate high-redshift radio galaxies. Although SKA 1 survey will be both, higher in angular resolution, more sensitive to the GMRT 150 MHz image of LBDS-Lynx field, we will detect a few a few million candidates for the high-redshift radio galaxies using (Figure 1, Johnston-Hollitt et al., 2015) at the SKA level surveys. Needless to state, all-sky radio continuum survey using SKA 1 will provide more sensitive data to explore a variety of science goals, including a huge sample of candidate high-redshift radio galaxies and their environments.

7.1 Infrared-Faint Radio Sources

Recent deep radio surveys combined with auxiliary InfraRed (IR) surveys have discovered the population called Infrared-Faint Radio Sources (IFRSs), that are relatively bright radio sources with very faint or no counterpart in infrared and optical wavelengths (see Middelberg et al., 2008; Norris et al., 2011). IFRSs generally exhibit steep radio spectra ($\alpha < -1$), high brightness temperature, $T_B \sim 10^6$ K and polarisation in radio, and thus indicating them to be AGN rather than star forming galaxies (Norris et al., 2007; Banfield et al., 2011).

A search for 3.6 μm counterparts of 1.4 GHz radio sources in 0.8 deg^{-2} in the SXDF yields seven IFRSs distributed over the redshift of 1.7 to 4.2 with their radio luminosities spanning over 10^{25} W Hz^{-1} to 10^{27} W Hz^{-1} (Singh et al. in preparation). This indicates that most, if not all, IFRSs are potentially high-redshift ($z > 2$) radio-loud AGN suffering from heavy dust extinction. Zinn et al. (2011) compiled a catalogue of 55 IFRSs in four deep fields (e.g., CDFS ($S_{1.4\,GHz} \sim 186$ μJy at 5σ), ELAIS-S1 ($S_{1.4\,GHz} \sim 160$ μJy at 5σ), FLS ($S_{1.4\,GHz} \sim 105$ μJy at 5σ), and COSMOS ($S_{1.4\,GHz} \sim 65$ μJy at 5σ)), although without redshift estimates.

Using IFRSs samples Zinn et al. (2011) showed that the surface number density of IFRSs increases with the depth of radio survey and can be best represented as $N_s = (30.8 \pm 15.0)\ \exp(-0.014 \pm 0.006)\ 5\sigma_{radio}$, where N_s is the number of IFRSs per square degree and σ_{radio} is the *rms* noise in mJy. Assuming the SKA1-survey 5σ flux density limit of 20 μJy, the best fit equation gives IFRS surface density to be $\sim 30.8 \pm 15$. Therefore, we can expect to detect large number of IFRS using proposed SKA surveys. However, deep optical and IR observations will also be required to estimate their redshifts and to study their dusty host galaxies.

8 Dual AGN in Galaxy Nuclei

In the merger driven picture of galaxy evolution, as galaxies merge their supermassive black holes spiral into the centre of the merger remnant forming SMBH pairs (e.g., Begelman et al., 1980). If the black holes are accreting mass, they will form a binary or dual active galactic nuclei that may also produce radio jets normal to their accretion disks and along the direction of black hole spin. At separations of 1 to 10 kpc the SMBHs pairs are generally called dual SMBHs or dual AGN (DAGN). At closer separations, of a few times 10 parsec or less, the SMBHs become gravitationally bound and form SMBH binaries or binary AGNs. In this stage, stars are ejected from the surrounding region until finally the SMBH orbit shrinks through the emission of gravitational radiation and the SMBHs coalesce (Berczik et al., 2006). According to merger models, dual SMBHs/AGNs in galaxies should be common. However, the number of confirmed sub-kpc dual AGN is only around 20 (Deane et al., 2014; Müller-Sánchez et al., 2015). The low detection rate is partly because optical or X-ray observations cannot reach the required sub-arsecond resolution, and partly due to dust obscuration. Radio observations are unaffected by dust obscuration and can yield sub-arcsecond images of DAGN, making them the most efficient frequency for the detection of dual AGN.

Most of the early dual AGN were detected serendipitously due to radio variability (OJ 287; Valtonen et al., 2008), misaligned radio jets/lobes (e.g., RBS 797; Gitti et al., 2013) or double X-ray sources in galaxy nuclei (Fabbiano et al., 2011). However, binary/dual AGN can be detected indirectly at optical wavelength using double peaked emission lines in the nuclear spectra of galaxies (e.g., Liu et al., 2010). The double peaks can arise from the Doppler shifts between the emission lines from the two AGN. Large samples of potential dual AGN have been drawn from SDSS nuclear spectra of galaxies (Ge et al., 2012) using the [O III] emission line as the principal tracer since it arises from the outer NLR in AGN. However, double peaked emission lines can also arise from powerful bipolar outflows associated with AGN activity (Rosario et al., 2010), super-winds from nuclear star formation or emission from gas rotating in nuclear disks close to the accreting SMBH (Kharb et al., 2015).

The SKA1-MID array using band 5 (frequency range $5-14$ GHz) or SKA-VLBI, are needed to detect closely separated binary black holes. These configurations will result in angular resolutions ranging from 0.2 arscec to milli-arcseconds. Through high frequency 8 GHz observations with the EVLA, Khatun et al. (2016, MNRAS, submitted) have detected the signatures of a precessing jet, likely arising from a binary black hole system, in a nearby double-peaked emission-line AGN. Dual or binary AGN at close separations are ideal candidates for gravitational wave studies of merging supermassive black holes. SKA will enable us to detect at radio frequencies large samples of such candidates for targeted gravitational wave observations (Abbott et al., 2016).

9 The Radio Sky at μJy Levels: Serendipitous Discoveries

SKA would probe sub-mJy and micro-Jy radio source population, which is believed to be largely associated with massive star formation in distant star forming galaxies. However, a significant fraction of all the sub-mJy sources are also identified with low-luminosity AGN. The remaining, smaller fraction of the faint radio source population are associated with either extremely faint optical identifications, or remain unidentified altogether. We also know that AGN fraction increases rapidly at higher (sub-mJy) flux density limits (Garrett, 2002). Therefore, labelling sources as pure "starbursts" or pure "AGN" is misleading; it is possible, even likely, that both phenomena co-exist in some of these faint systems.

Presently, we are just beginning to appreciate the fact that deep radio observations of a few fields has led us to a sensitivity level where we can expect to detect many discrete radio sources in a single field of view (Garrett, 2002). This is quite far from the traditional high-resolution high-frequency, small field of view observations of fields, where very compact, and often very bright radio sources are detected. Several state of the art modes of SKA correlator, making full use of the raw data, i.e., to map out the primary beam response of individual resolution elements in their entirety, or simultaneous multiple-field correlation, coupled with incredibly fast data output rates would be key to achieve goals of very high angular resolution imaging of large areas of sky in a single pointing. These radio images would then match the large areas of the sky, which are being routinely surveyed in great detail by optical and near-IR instruments.

10 Radio Continuum Surveys with the GMRT

The GMRT has been recognised as a pathfinder radio telescope for SKA. Here we briefly describe some of the deep and wide radio continuum surveys carried out with GMRT.

10.1 GMRT 325 MHz Survey of Herschel Fields

The XMM-LSS field has been surveyed with the GMRT at 325 MHz (Wadadekar et al. in preparation). This survey covers an area of $\sim$12 deg^{-2} and overlaps fully with the SWIRE and HerMES survey areas in the XMM-LSS field. The 325 MHz GMRT mosaice image has an average rms noise of $\sim$ 160 μJy, while in the central region the rms noise reaches down to $\sim$ 120 μJy, with a synthesized beam-size of $\sim 10''.2 \times 7''.9$. The 325 MHz survey of XMM-LSS is one of the deepest low-frequency surveys over such a wide sky area and it detects $\sim$2553/3304 radio sources at $\geq 5\sigma$ with an rms noise cut-off $\leq$ 200/300 μJy, where an rms-noise image is used for source extraction to account for non-uniformity. It is worth noting that these 325 MHz observations are about five times deeper than the previous 325 MHz observations of the XMM-LSS field (e.g., Cohen et al., 2003; Tasse et al., 2007), and result in a manifold increase in the source density. Nearly 3.8 deg^{-2} area of the European Large-Area ISO Survey-North 1 (ELAIS-N1) field has been imaged at 325 MHz with the GMRT (Sirothia et al., 2009b). At present, it is the most sensitive 325 MHz radio survey with a median rms noise of $\sim$ 40 μJy beam^{-1}: 1286 sources with a total flux density above $\sim$ 270 μJy have been detected.

10.2 GMRT 610 MHz Survey of the Spitzer xFLS Field

Garn et al. (2007) have carried out a 610 MHz survey of the Spitzer extragalactic First Look Survey field (xFLS). This survey covers a total area of $\sim$4 deg^{-2} in seven individual pointings with an *rms* noise of $\sim$ 30 μJy and resolution of $5''.8 \times 4''.7$. This survey has detected a total of 3944 sources above the 5σ level.

10.3 TIFR 150 MHz GMRT Sky Survey

The TIFR GMRT Sky Survey (TGSS) is a radio continuum survey at 150 MHz carried out with GMRT. This survey covers $\sim$37,000 deg^{-2} of the sky north of declination of -53 degrees and reaches an rms noise level of 5$-$7 mJy beam^{-1}, with an angular resolution of $\sim$25 arcsec (Intema et al., 2016). The first release TGSS has produced a catalog of 0.64 million radio sources at the 7 sigma level. More details about the TGSS can be found at http://tgss.ncra.tifr.res.in/. This survey and products from it will provide a reference for various new low-frequency telescopes, in particular SKA-LOW.

11 Concluding Remarks

We have summarised various science interests of a good fraction of the AGN community in India. Whether it comes to detecting "intermediate" sources between the radio-loud and radio-quiet classes, or "intermediate" sources between FRIs and FRIIs, relic emission from previous activities of the AGN, giant FRI jets in spiral galaxies, double-double or triple-double radio galaxies, or faint ultra-steep spectrum sources at high redshifts, higher sensitivity data that are at present unavailable, are required. The various SKA configurations and the upcoming SKA surveys will meet these needs. VLBI is required to probe the regions close to the central black holes. Again, an increase in sensitivity is crucial. SKA-VLBI which could include large single antennas like the upcoming FAST radio telescope, will be able to study parsec and sub-parsec-scale radio jets and their magnetic field structures in low luminosity AGN, which have so far remained below the sensitivity limits of the current VLBI arrays.

References

Abbott, B. P., Abbott, R., Abbott, T. D., Abernathy, M. R., Acernese, F., Ackley, K., Adams, C., Adams, T., Addesso, P., Adhikari, R. X., and et al.: 2016, *Physical Review Letters* **116(6)**, 061102

Antonucci, R.: 1993, ARA&A **31**, 473

Bagchi, J., Vivek, M., Vikram, V., Hota, A., Biju, K. G., Sirothia, S. K., Srianand, R., Gopal-Krishna, and Jacob, J.: 2014, ApJ **788**, 174

Banfield, J. K., George, S. J., Taylor, A. R., Stil, J. M., Kothes, R., and Scott, D.: 2011, ApJ **733**, 69

Baum, S. A., Zirbel, E. L., and O'Dea, C. P.: 1995, ApJ **451**, 88

Beckwith, K., Hawley, J. F., and Krolik, J. H.: 2008, ApJ **678**, 1180

Begelman, M. C., Blandford, R. D., and Rees, M. J.: 1980, Nature **287**, 307

Berczik, P., Merritt, D., Spurzem, R., and Bischof, H.-P.: 2006, ApJ **642**, L21

Bicknell, G. V.: 1986, ApJ **300**, 591

Blandford, R. D.: 1993, *Astrophysical Jets*, Space Telescope Science Inst. Symp. Ser.6, eds. D. Burgarella, M. Livio, & C. P. O'Dea (Cambridge Univ. Press), p.15

Blandford, R. D. and Payne, D. G.: 1982, MNRAS **199**, 883

Blandford, R. D. and Znajek, R. L.: 1977, MNRAS **179**, 433

Brocksopp, C., Kaiser, C. R., Schoenmakers, A. P., and de Bruyn, A. G.: 2007, MNRAS **382**, 1019

Chandra, S., Baliyan, K. S., Ganesh, S., and Foschini, L.: 2014, ApJ **791**, 85

Chandra, S., Baliyan, K. S., Ganesh, S., and Joshi, U. C.: 2012, ApJ **746**, 92

Cheung, C. C.: 2007, AJ **133**, 2097

Chiaberge, M., Capetti, A., and Celotti, A.: 1999, A&A **349**, 77

Cohen, A. S., Röttgering, H. J. A., Kassim, N. E., Cotton, W. D., Perley, R. A., Wilman, R., Best, P., Pierre, M., Birkinshaw, M., Bremer, M., and Zanichelli, A.: 2003, ApJ **591**, 640

Comerford, J. M., Schluns, K., Greene, J. E., and Cool, R. J.: 2013, ApJ **777**, 64

Cox, T. J., Jonsson, P., Primack, J. R., and Somerville, R. S.: 2006, MNRAS **373**, 1013

Croton, D. J., Springel, V., White, S. D. M., De Lucia, G., Frenk, C. S., Gao, L., Jenkins, A., Kauffmann, G., Navarro, J. F., and Yoshida, N.: 2006, MNRAS **365**, 11

Davies, R. D.: 1990, in F. Sanchez and M. Vazquez (eds.), *New Windows to the Universe*, Vol. 2, pp 81–99

Deane, R. P., Paragi, Z., Jarvis, M. J., Coriat, M., Bernardi, G., Fender, R. P., Frey, S., Heywood, I., Klöckner, H.-R., Grainge, K., and Rumsey, C.: 2014, Nature **511**, 57

Dewdney, P., Turner, W., Millenaar, R., McCool, R., Lazio, J., and Cornwell, T.: 2013, *"SKA1 System Baseline Design", Document number SKA-TEL-SKO-DD-001 Revision 1*

Fabbiano, G., Wang, J., Elvis, M., and Risaliti, G.: 2011, Nature **477**, 431

Fanaroff, B. L. and Riley, J. M.: 1974, MNRAS **167**, 31P

Gabuzda, D. C., Knuettel, S., and Bonafede, A.: 2015, A&A **583**, A96

Gabuzda, D. C., Mullan, C. M., Cawthorne, T. V., Wardle, J. F. C., and Roberts, D. H.: 1994, ApJ **435**, 140

Galametz, A., Stern, D., De Breuck, C., Hatch, N., Mayo, J., Miley, G., Rettura, A., Seymour, N., Stanford, S. A., and Vernet, J.: 2012, ApJ **749**, 169

Gallimore, J. F., Axon, D. J., O'Dea, C. P., Baum, S. A., and Pedlar, A.: 2006, AJ **132**, 546

Garn, T., Green, D. A., Hales, S. E. G., Riley, J. M., and Alexander, P.: 2007, MNRAS **376**, 1251

Garofalo, D.: 2013, MNRAS **434**, 3196

Garrett, M. A.: 2002, A&A **384**, L19

Ge, J.-Q., Hu, C., Wang, J.-M., Bai, J.-M., and Zhang, S.: 2012, ApJS **201**, 31

Gitti, M., Giroletti, M., Giovannini, G., Feretti, L., and Liuzzo, E.: 2013, A&A **557**, L14

Greene, J. E. and Ho, L. C.: 2007, ApJ **667**, 131

Heckman, T. M., Smith, E. P., Baum, S. A., van Breugel, W. J. M., Miley, G. K., Illingworth, G. D., Bothun, G. D., and Balick, B.: 1986, ApJ **311**, 526

Ho, L. C. and Peng, C. Y.: 2001, ApJ **555**, 650

Hota, A., Croston, J. H., Ohyama, Y., Stalin, C. S., Hardcastle, M. J., Konar, C., Aravind, R. P., Agarwal, S. M., Dharmik Bhoga, S. A., Dabhade, P. A., Kamble, A. A., Mohanty, P. K., Mukherjee, A., Pandey, A. V., Patra, A., Pechetti, R., Raut, S. S., Sushma, V., Vaddi, S., and Verma, N.: 2014, *ArXiv e-prints*

Hota, A., Sirothia, S. K., Ohyama, Y., Konar, C., Kim, S., Rey, S.-C., Saikia, D. J., Croston, J. H., and Matsushita, S.: 2011, MNRAS **417**, L36

Intema, H. T., Jagannathan, P., Mooley, K. P., and Frail, D. A.: 2016, *ArXiv e-prints*

Ishwara-Chandra, C. H. and Saikia, D. J.: 1999, MNRAS **309**, 100

Ishwara-Chandra, C. H., Sirothia, S. K., Wadadekar, Y., and Pal, S.: 2011, *Journal of Astrophysics and Astronomy* **32**, 609

Ishwara-Chandra, C. H., Sirothia, S. K., Wadadekar, Y., Pal, S., and Windhorst, R.: 2010a, MNRAS **405**, 436

Ishwara-Chandra, C. H., Sirothia, S. K., Wadadekar, Y., Pal, S., and Windhorst, R.: 2010b, MNRAS **405**, 436

Jamrozy, M., Konar, C., Saikia, D. J., Stawarz, Ł., Mack, K.-H., and Siemiginowska, A.: 2007, MNRAS **378**, 581

Johnston-Hollitt, M., Dehghan, S., and Pratley, L.: 2015, *Advancing Astrophysics with the Square Kilometre Array (AASKA14)* p. 101

Kellermann, K. I., Sramek, R., Schmidt, M., Shaffer, D. B., and Green, R.: 1989, AJ **98**, 1195

Ker, L. M., Best, P. N., Rigby, E. E., Röttgering, H. J. A., and Gendre, M. A.: 2012, MNRAS **420**, 2644

Kharb, P., Capetti, A., Axon, D. J., Chiaberge, M., Grandi, P., Robinson, A., Giovannini, G., Balmaverde, B., Macchetto, D., and Montez, R.: 2012, AJ **143**, 78

Kharb, P., Das, M., Paragi, Z., Subramanian, S., and Chitta, L. P.: 2015, ApJ **799**, 161

Kharb, P., Gabuzda, D. C., O'Dea, C. P., Shastri, P., and Baum, S. A.: 2009, ApJ **694**, 1485

Kharb, P., Lister, M. L., and Cooper, N. J.: 2010, ApJ **710**, 764

Kharb, P., O'Dea, C. P., Baum, S. A., Colbert, E. J. M., and Xu, C.: 2006, ApJ **652**, 177

Kharb, P., O'Dea, C. P., Baum, S. A., Daly, R. A., Mory, M. P., Donahue, M., and Guerra, E. J.: 2008, ApJS **174**, 74

Kharb, P., O'Dea, C. P., Baum, S. A., Hardcastle, M. J., Dicken, D., Croston, J. H., Mingo, B., and Noel-Storr, J.: 2014, MNRAS **440**, 2976

Kharb, P. and Shastri, P.: 2004, A&A **425**, 825

Kharb, P., Shastri, P., and Gabuzda, D. C.: 2005, ApJ **632**, L69

Kharb, P., Srivastava, S., Singh, V., Gallimore, J., Ishwara-Chandra, C. H., and Hota, A.: 2016, MNRAS, *submitted*

Konar, C. and Hardcastle, M. J.: 2013, MNRAS **436**, 1595

Konar, C., Hardcastle, M. J., Jamrozy, M., and Croston, J. H.: 2013, MNRAS **430**, 2137

Konar, C., Saikia, D. J., Jamrozy, M., and Machalski, J.: 2006, MNRAS **372**, 693

Kormendy, J. and Ho, L. C.: 2013, ARA&A **51**, 511

Laing, R. A.: 1996, in R. D. Ekers, C. Fanti, and L. Padrielli (eds.), *Extragalactic Radio Sources*, Vol. 175 of *IAU Symposium*, p. 147

Laing, R. A. and Bridle, A. H.: 2002, MNRAS **336**, 1161

Lal, D. V. and Rao, A. P.: 2007, MNRAS **374**, 1085

Lal, D. V., Shastri, P., and Gabuzda, D. C.: 2004, A&A **425**, 99

Landt, H., Perlman, E. S., and Padovani, P.: 2006, ApJ **637**, 183

Laor, A.: 2000, ApJ **543**, L111

Ledlow, M. J. and Owen, F. N.: 1996, AJ **112**, 9

Ledlow, M. J., Owen, F. N., and Keel, W. C.: 1998, ApJ **495**, 227

Lister, M. L., Cohen, M. H., Homan, D. C., Kadler, M., Kellermann, K. I., Kovalev, Y. Y., Ros, E., Savolainen, T., and Zensus, J. A.: 2009, AJ **138**, 1874

Liu, R. and Pooley, G.: 1991, MNRAS **253**, 669

Liu, X., Greene, J. E., Shen, Y., and Strauss, M. A.: 2010, ApJ **715**, L30

Lynden-Bell, D.: 1969, Nature **223**, 690

Machalski, J., Jamrozy, M., and Zola, S.: 2001, A&A **371**, 445

Mao, M. Y., Owen, F., Duffin, R., Keel, B., Lacy, M., Momjian, E., Morrison, G., Mroczkowski, T., Neff, S., Norris, R. P., Schmitt, H., Toy, V., and Veilleux, S.: 2015, MNRAS **446**, 4176

McKinney, J. C.: 2006, MNRAS **368**, 1561

McLure, R. J., Kukula, M. J., Dunlop, J. S., Baum, S. A., O'Dea, C. P., and Hughes, D. H.: 1999, MNRAS **308**, 377

McLure, R. J., Willott, C. J., Jarvis, M. J., Rawlings, S., Hill, G. J., Mitchell, E., Dunlop, J. S., and Wold, M.: 2004, MNRAS **351**, 347

Meier, D. L.: 1999, ApJ **522**, 753

Merloni, A., Heinz, S., and di Matteo, T.: 2003, MNRAS **345**, 1057

Middelberg, E., Norris, R. P., Tingay, S., Mao, M. Y., Phillips, C. J., and Hotan, A. W.: 2008, A&A **491**, 435

Mihos, J. C. and Hernquist, L.: 1996, ApJ **464**, 641

Müller-Sánchez, F., Comerford, J. M., Nevin, R., Barrows, R. S., Cooper, M. C., and Greene, J. E.: 2015, ApJ **813**, 103

Nan, R., Li, D., Jin, C., Wang, Q., Zhu, L., Zhu, W., Zhang, H., Yue, Y., and Qian, L.: 2011, *International Journal of Modern Physics D* **20**, 989

Nandi, S., Roy, R., Saikia, D. J., Singh, M., Chandola, H. C., Baes, M., Joshi, R., Gentile, G., and Patgiri, M.: 2014, ApJ **789**, 16

Nath, B. B.: 1995, MNRAS **274**, 208

Nath, B. B.: 2010, MNRAS **407**, 1998

Netzer, H.: 2015, ARA&A **53**, 365

Norris, R. P., Afonso, J., Cava, A., Farrah, D., Huynh, M. T., Ivison, R. J., Jarvis, M., Lacy, M., Mao, M., Maraston, C., Mauduit, J.-C., Middelberg, E., Oliver, S., Seymour, N., and Surace, J.: 2011, ApJ **736**, 55

Norris, R. P., Tingay, S., Phillips, C., Middelberg, E., Deller, A., and Appleton, P. N.: 2007, MNRAS **378**, 1434

O'Dea, C. P. and Owen, F. N.: 1985, AJ **90**, 927

Padovani, P. and Giommi, P.: 1995, MNRAS **277**, 1477

Paragi, Z., Godfrey, L., Reynolds, C., and 79 coauthors: 2015, *Advancing Astrophysics with the Square Kilometre Array (AASKA14)* p. 143

Prandoni, I. and Seymour, N.: 2015, *Advancing Astrophysics with the Square Kilometre Array (AASKA14)* p. 67

Prestage, R. M. and Peacock, J. A.: 1988, MNRAS **230**, 131

Proctor, D. D.: 2011, ApJS **194**, 31

Punsly, B., Marziani, P., Kharb, P., O'Dea, C. P., and Vestergaard, M.: 2015, ApJ **812**, 79

Randall, S. W., Forman, W. R., Giacintucci, S., Nulsen, P. E. J., Sun, M., Jones, C., Churazov, E., David, L. P., Kraft, R., Donahue, M., Blanton, E. L., Simionescu, A., and Werner, N.: 2011, ApJ **726**, 86

Rees, M. J., Begelman, M. C., Blandford, R. D., and Phinney, E. S.: 1982, Nature **295**, 17

Rodriguez, C., Taylor, G. B., Zavala, R. T., Peck, A. B., Pollack, L. K., and Romani, R. W.: 2006, ApJ **646**, 49

Rosario, D. J., McGurk, R. C., Max, C. E., Shields, G. A., Smith, K. L., and Ammons, S. M.: 2011, ApJ **739**, 44

Rosario, D. J., Shields, G. A., Taylor, G. B., Salviander, S., and Smith, K. L.: 2010, ApJ **716**, 131

Saikia, D. J. and Jamrozy, M.: 2009, *Bulletin of the Astronomical Society of India* 37

Saikia, D. J., Konar, C., and Kulkarni, V. K.: 2006, MNRAS **366**, 1391

Sambruna, R. M., Maraschi, L., and Urry, C. M.: 1996, ApJ **463**, 444

Schweizer, F.: 1982, ApJ **252**, 455

Seymour, N., Stern, D., De Breuck, C., Vernet, J., Rettura, A., Dickinson, M., Dey, A., Eisenhardt, P., Fosbury, R., Lacy, M., McCarthy, P., Miley, G., Rocca-Volmerange, B., Röttgering, H., Stanford, S. A., Teplitz, H., van Breugel, W., and Zirm, A.: 2007, ApJS **171**, 353

Sikora, M. and Begelman, M. C.: 2013, ApJ **764**, L24

Sikora, M., Stawarz, Ł., and Lasota, J.-P.: 2007, ApJ **658**, 815

Singh, V., Beelen, A., Wadadekar, Y., Sirothia, S., Ishwara-Chandra, C. H., Basu, A., Omont, A., McAlpine, K., Ivison, R. J., Oliver, S., Farrah, D., and Lacy, M.: 2014, A&A **569**, A52

Singh, V., Ishwara-Chandra, C. H., Sievers, J., Wadadekar, Y., Hilton, M., and Beelen, A.: 2015a, MNRAS **454**, 1556

Singh, V., Ishwara-Chandra, C. H., Wadadekar, Y., Beelen, A., and Kharb, P.: 2015b, MNRAS **446**, 599

Sirothia, S. K., Dennefeld, M., Saikia, D. J., Dole, H., Ricquebourg, F., and Roland, J.: 2009a, MNRAS **395**, 269

Sirothia, S. K., Dennefeld, M., Saikia, D. J., Dole, H., Ricquebourg, F., and Roland, J.: 2009b, MNRAS **395**, 269

Sparks, W. B., Baum, S. A., Biretta, J., Macchetto, F. D., and Martel, A. R.: 2000, ApJ **542**, 667

Tamhane, P., Wadadekar, Y., Basu, A., Singh, V., Ishwara-Chandra, C. H., Beelen, A., and Sirothia, S.: 2015, MNRAS **453**, 2438

Tasse, C., Röttgering, H. J. A., Best, P. N., Cohen, A. S., Pierre, M., and Wilman, R.: 2007, A&A **471**, 1105

Tchekhovskoy, A., Narayan, R., and McKinney, J. C.: 2010, ApJ **711**, 50

Tchekhovskoy, A., Narayan, R., and McKinney, J. C.: 2011, MNRAS **418**, L79

Ulvestad, J. S., Wrobel, J. M., Roy, A. L., Wilson, A. S., Falcke, H., and Krichbaum, T. P.: 1999, ApJ **517**, L81

Urry, C. M. and Padovani, P.: 1995, PASP **107**, 803

Valtonen, M. J., Lehto, H. J., Nilsson, K., Heidt, J., Takalo, L. O., Sillanpää, A., Villforth, C., Kidger, M., Poyner, G., Pursimo, T., Zola, S., Wu, J.-H., Zhou, X., Sadakane, K., Drozdz, M., Koziel, D., Marchev, D., Ogloza, W., Porowski, C., Siwak, M., Stachowski, G., Winiarski, M., Hentunen, V.-P., Nissinen, M., Liakos, A., and Dogru, S.: 2008, Nature **452**, 851

Venemans, B. P., Röttgering, H. J. A., Miley, G. K., van Breugel, W. J. M., de Breuck, C., Kurk, J. D., Pentericci, L., Stanford, S. A., Overzier, R. A., Croft, S., and Ford, H.: 2007, A&A **461**, 823

Worrall, D. M., Birkinshaw, M., and Hardcastle, M. J.: 2001, MNRAS **326**, L7

Zinn, P.-C., Middelberg, E., and Ibar, E.: 2011, A&A **531**, A14

Probing statistical isotropy with radio sources

Shamik Ghosh[1], Pankaj Jain*[1], Rahul Kothari[1], Sharvari Nadkarni-Ghosh[1], and Prabhakar Tiwari[2]

[1] *Physics Department, I.I.T. Kanpur, Kanpur 208016, India*
[2] *Technion- Israel Institute of Technology, 32000 Haifa, Israel*

Abstract

There currently exist many observations which are not consistent with the cosmological principle. In particular, several different data sets indicate a preferred direction pointing approximately towards the Virgo cluster. We also observe a hemispherical anisotropy in the Cosmic Microwave Background Radiation (CMBR) temperature fluctuations. Although these inconsistencies may be attributed to systematic effects, there remains the possibility that they indicate new physics and various theories have been proposed to explain them. One possibility is the generation of perturbation modes during the early pre-inflationary epoch, when the Universe need not have been homogenous and isotropic. Better measurements will provide better constrains on these theories. We review these observations with particular emphasis on those relevant for Square Kilometre Array (SKA). In particular, we propose measurement of the dipole in number counts, sky brightness, polarized flux and polarization orientations of radio sources. We also suggest test of alignment of linear polarizations of sources as a function of their relative separation. Finally we propose measurement of hemispherical anisotropy or equivalently dipole modulation in radio sources.

1 Introduction

The Big Bang model is based on the cosmological principle which states that the Universe is isotropic and homogeneous, i.e. there is no preferred direction or position. It is essentially an assumption and cannot be proven on the basis of fundamental symmetry principles, such as, rotational and translational invariance. In particular, it applies only in a statistical sense, after averaging over distances of order 100 Mpc. Furthermore there is a preferred frame of reference, the so called cosmic frame of rest. The Universe appears isotropic and homogeneous only in this frame. Within the Big Bang paradigm, the Universe may not be isotropic and homogeneous at very early times. It acquires this property during inflation. It has been explicitly shown that starting from a wide range of anisotropic but homogeneous Bianchi models, the Universe quickly becomes isotropic during inflation (Wald, 1983). However other models also exist which do not obey this principle.

Observationally it is easier to test isotropy in contrast to homogeneity because it requires only angular positions of the sources. A test of homogeneity requires three dimensional mapping of the Universe. Here we shall primarily be interested in observations which test isotropy. However we point out that an observed violation of isotropy may arise in a fundamental model which may be anisotropic or inhomogeneous or both.

Even within the Big Bang model, the Universe is not strictly isotropic and homogeneous. It obeys this property only in a statistical sense in the cosmic frame of rest. For example, let us consider the matter density $\rho(t, \vec{x})$ where t is the cosmic time and $\vec{x}$ the comoving coordinate. Its spatial distribution can be expressed as,

$$\rho(t, \vec{x}) = \rho_0(t) + \delta\rho(t, \vec{x})\,. \tag{1}$$

Here $\rho_0(t)$ is the mean density and $\delta\rho$ the fluctuations, such that

$$\langle \delta\rho(t, \vec{x}) \rangle = 0\,. \tag{2}$$

*pkjain@iitk.ac.in

Here the angular brackets represent ensemble average. An estimate of this mean is obtained by averaging $\delta\rho$ over a sufficiently large patch of the Universe. We expect this distance scale to be of order 100 Mpc. At smaller scales the matter density shows considerable clustering and the cosmological principle does not apply. Statistical isotropy (SI) and homogeneity implies that

$$\langle \delta\rho(t,\vec{x})\delta\rho(t,\vec{x}')\rangle = f(|\vec{x}-\vec{x}'|)\,, \tag{3}$$

i.e., the two point correlations depend only on the distance between the two points and not on the direction or the position. If we relax the assumption of isotropy then these correlations can also depend on the direction of the vector $\vec{x}-\vec{x}'$. If we also allow inhomogeneity, then we can also get dependence on the mean position $(\vec{x}+\vec{x}')/2$. As we have mentioned above statistical isotropy applies only in the cosmic frame of rest. If we are in motion with respect to this frame with velocity $\vec{v}$, then at leading order in $|\vec{v}|$, the matter distribution is expected to show a dipole distribution peaked in the direction of $\vec{v}$.

Within the Big Bang model the CMBR temperature can be decomposed as

$$T(\hat{n}) = T_0 + T_1\hat{\lambda}\cdot\hat{n} + \Delta T(\hat{n}) \tag{4}$$

where $\hat{n}$ is a unit vector in the direction of observation, T_0 the mean temperature, T_1 the amplitude of the CMBR dipole, $\hat{\lambda}$ the dipole axis and ΔT the primordial fluctuations in temperature. Here the dipole contains both the kinematic contribution, arising due to local motion, as well as the contribution due to primordial fluctuations. Hence ΔT contains only multipoles corresponding to $l \geq 2$, i.e., quadrupole and higher. We use the spherical polar coordinates (θ,ϕ) to label the direction of observation. As in the case of density fluctuations, we have

$$\langle \Delta T(\hat{n})\rangle = 0\,. \tag{5}$$

Observationally, $T_0 \approx 2.73$K, $T_1/T_0 \sim 10^{-3}$ and $\Delta T/T_0 \sim 10^{-5}$. Statistical isotropy implies that the two point correlation function

$$\langle \Delta T(\hat{n}_i)\Delta T(\hat{n}_j)\rangle = C(\hat{n}_i\cdot\hat{n}_j)\,, \tag{6}$$

i.e., it is a function only of the angle between the two observation points $\hat{n}_i$ and $\hat{n}_j$. It is useful to expand the temperature fluctuations in terms of the spherical harmonics. We obtain

$$\frac{\Delta T(\hat{n})}{T_0} = \sum_{lm} a_{lm}Y_{lm}(\hat{n}) \tag{7}$$

where a_{lm} are the coefficients of this expansion. These also satisfy $\langle a_{lm}\rangle = 0$. Furthermore statistical isotropy implies that

$$\langle a_{lm}a^*_{l'm'}\rangle_{\rm iso} = C_l\delta_{ll'}\delta_{m,m'}\,, \tag{8}$$

where C_l is the standard CMBR power.

The cosmological principle is supported by the Cosmic Microwave Background Radiation (CMBR) and galaxy surveys. The observed CMBR temperature $T(\theta,\phi)$ is found to be isotropic to a very good approximation. As mentioned above, the largest deviation from isotropy arises due to dipole which is of order 10^{-3}. The dominant contribution to dipole arises due to the velocity of the solar system ($\vec{v}_{\rm CMB}$) relative to the cosmic frame of rest. Its magnitude is found to be $v_{\rm CMB} = 369 \pm 0.9$ Km/s and direction, $l = 263.99^\circ \pm 0.14^\circ$, $b = 48.26^\circ \pm 0.03^\circ$ in galactic coordinates (Kogut et al., 1993; Hinshaw et al., 2009). The number density and brightness of distant radio galaxies is also observed to be isotropic to a good approximation. However there are many observations which suggest a potential violation of the cosmological principle. In particular the local velocity $\vec{v}_{\rm radio}$ extracted from the observed dipole in the number density and brightness of radio sources is not found to be in agreement with $\vec{v}_{\rm CMB}$. The direction agrees but the magnitude is found to be approximately three times larger. We review such observed violations of the cosmological principle in the next section. In section 3 we shall present a theoretical model which may potentially explain these observations. In section 4 we shall discuss tests of statistical isotropy at Square Km Array (SKA) and will conclude in section 5.

2 Observed violations of statistical isotropy

The assumption of statistical isotropy is built into the Inflationary Big Bang model, which is the Standard Model of Cosmology. The predictions of the standard model agree remarkably well with observations

which is a real success for the modern era of precision cosmology. Despite the success of the theory there are tantalising evidences which highlight small but persistent departures from the predictions of the isotropic theory. Such observations are mostly in the large distance scale observations. In this section we will discuss some of the observed violations in statistical isotropy from different observations with a particular emphasis on those relevant for SKA.

2.1 Kinematic Dipole

Before we discuss the major observations of SI violation, it is important to understand that the Cosmological Principle is valid only in the cosmic frame of rest. The Earth is not at rest with respect to this frame. It is rotating about the Sun, which in turn is rotating about the centre of the Milky Way; the Milky Way moves with respect to the Local Group barycenter, which in turn moves about the large scale structures around it. The combined motion due to these peculiar velocities ensures that our frame of observation has a relative velocity with respect to the cosmic frame of rest. Observation of even an isotropic field from such a frame precludes a dipole. This dipole due to Doppler shift of the CMB photons is called the kinematic dipole.

We denote the peculiar velocity of our observation frame by $\vec{v}$ and define $\vec{\beta} = \vec{v}/c$. If the temperature field and direction in the cosmic rest frame are identified as T' and $\hat{n}'$ and the unprimed symbols denote the observations in our frame, then

$$T(\hat{n}) = \frac{T'(n')}{\gamma(1 - \hat{n} \cdot \vec{\beta})}, \tag{9}$$

and

$$\hat{n} = \frac{\hat{n}' + [(\gamma - 1)\hat{n}' \cdot \hat{v} + \gamma\beta]\hat{v}}{\gamma(1 + \hat{n}' \cdot \vec{\beta})} \tag{10}$$

where $\gamma = \sqrt{1 - \beta^2}$. Due to Doppler shifting the intensity distribution of the CMB photons gets modified. We measure $T(\hat{n})$ and use these relations to obtain the temperature field in the cosmic rest frame along with the peculiar velocity of the observation frame.

The large scale structures also acquire a dipole due to Doppler and aberration effects caused by our local motion. The flux density of radio sources typically shows a power law dependence on frequency. Furthermore the number density of sources depends on the flux density. Most large scale structure surveys operate in limited frequency ranges and have a lower limit on the flux density. Due to Dopplet effect, the frequencies in the direction of motion of the frame are blueshifted and are redshifted in the opposite direction. Due to this effect and the intensity cuts on the survey, sources will shift in and out of the range of observations. Hence in the direction of motion more objects are blueshifted into the observation frequencies while in the other hemispheres more sources are redshifted out of the range. Combining the two effects — the Doppler shift leads to a small dipole in a limited frequency and intensity range large scale structure survey (Ellis and Baldwin, 1984; Tiwari et al., 2015).

The motion of the reference frame also leads to the aberration effect. This produces a shift in the angular position of the source. Thus the apparent positions of an isotropic distribution of sources get shifted towards the direction of motion of the frame, creating a dipole. This effect is of the same order as $\beta \sim 10^{-3}$ and is relevant for large scale structure dipole studies. Combined effect of the Doppler shift and aberration produces the *kinematic dipole*.

2.2 Observed Dipole in Large Scale Structures

Large scale structures are essentially objects formed by non-linear physics. When observed on small survey volumes the non-linear physics produces structures that would deviate from isotropy and homogeneity. Thus the local non-linear components of a survey would produce a *local structure dipole*. This is not a violation of SI, because the Cosmological Principle is not valid on this scale. It is only when a very large survey volume, of length scales greater than a few hundred Mpc is considered that the Cosmological Principle is valid and can be tested for SI violations. If a dipole component is present over and above the local stucture and the kinematic dipole, then it is of cosmological origin and is called the *intrinsic dipole*. We are essentially interested in the intrinsic component in SI violation study.

The most significant study of dipoles in the large scale structure has been done with the NRAO VLA Sky Survey (NVSS) radio catalogue containing 1773484 radio sources (Condon et al., 1998). The

survey's operating frequency is 1.4 GHz and covers the entire northern hemisphere above a declination of -40° and has a mean redshift ~ 1. For radio sources, in the cosmic rest frame, the flux density S follows a power law relation with frequency ν, $S \propto \nu^{-\alpha}$, with $\alpha \approx 0.75$. The differential number count of radio sources per unit solid angle per unit flux density follows the power law: $n(\theta, \varphi, S) \propto S^{-1-x}$, where the spectral index x is close to unity. Due to the kinematic effects discussed above, it is clear that both the number counts and sky brightness would show a dipole. We denote these by $\vec{D}_N^{\rm kin}$ and $\vec{D}_S^{\rm kin}$ respectively. These kinematic dipoles are given by (Ellis and Baldwin, 1984; Tiwari et al., 2015)

$$\vec{D}_S^{\rm kin} = [2 + x(1+\alpha)]\vec{\beta} \qquad \vec{D}_N^{\rm kin} = [2 + x(1+\alpha)]\vec{\beta}\,. \tag{11}$$

Since the velocity of our observation frame with respect to the cosmic rest frame is already known from CMB experiments we can make a prediction for the kinematic dipole.

The earliest attempt to extract the NVSS dipole was made by the Blake and Wall (Blake and Wall, 2002), where they claimed to find the dipole amplitude approximately two sigmas larger than the expected kinematic dipole. The extracted direction, however, showed good agreement with expectations. This was revisited later by several authors, who found an even larger deviation from the amplitude of the kinematic dipole. These results are summarised in Table 1.

Authors	$D_o \quad (\times 10^{-2})$	v ($\times 10^3$ in km/s)	(l, b)
Blake & Wall (2002)	1.05 ± 0.42	0.9 ± 0.3	$(245^\circ, 41^\circ)$
Singal (2012)	1.8 ± 0.3	1.32 ± 0.54	$(239^\circ, 44^\circ)$
Gibelyou and Huterer (2012)	2.7 ± 0.5	1.4 ± 0.3	$(214^\circ, 15^\circ)$
Tiwari et. al. (2015) D_N	1.25 ± 0.40	1.00 ± 0.32	$(261^\circ, 37^\circ)$
Tiwari et. al. (2015) D_S	1.51 ± 0.57	1.21 ± 0.46	$(269^\circ, 43^\circ)$
Rubart and Schwarz. (2013)	1.8 ± 0.6	1.5 ± 0.5	$(239^\circ, 44^\circ)$

Table 1: *NVSS observed dipole amplitude, observation frame peculiar velocity and direction.* Collected results (Blake and Wall, 2002; Singal, 2011; Gibelyou and Huterer, 2012; Tiwari et al., 2015; Rubart and Schwarz, 2013) for the NVSS dipole amplitude and direction with flux densities > 20 mJy (> 15 mJy for Gibelyou and Huterer). Here D_o is the total observed dipole and v is the peculiar velocity of the observation frame, calculated from D_o.

We note that the result obtained by Gibelyou and Huterer (Gibelyou and Huterer, 2012) shows a much larger deviation from others. Rubart and Schwarz have shown (Rubart and Schwarz, 2013) that the dipole amplitude estimator used by Gibelyou and Huterer is biased. It has a direction bias and as a consequence their dipole direction estimates are not in agreement with the other results. The Blake and Wall amplitude is smaller than that obtained by any of the other authors. Our study of the NVSS dipole (Tiwari et al., 2015) involved studying not just the number count but also the sky brightness dipole. Both observables show similar results with amplitudes exceeding the kinematic dipole predictions by approximately two sigmas. Such excess dipole on such large distance scales suggests a mild signal of potential violation of SI.

The results discussed above while being intriguing needs to be reassessed with other data sets due to the limitations of the NVSS catalogue. The NVSS is compiled by use of two different array configurations, one above declination of -10° and one below. This results in systematics in a catalogue. The mean number count becomes a function of declination. Plots of number count density show a large and significant dip below a declination of -15° and a small but linear systematic decrease with increasing right ascension. With a flux cut > 15 mJy, the effect of these systematics can be suppressed to the level where they are no longer visible to the naked eye on plotting. While the work done with the NVSS data try to limit the effect of such systematics, having another deep survey with large sky coverage to test out these results would be very important before we can be sure of SI violation.

The NVSS also contains information about the polarisation of the sources. It provides Stokes parameters Q and U for these sources. Using them we define the polarised flux as $P = \sqrt{Q^2 + U^2}$ and the degree of polarisation as $\mathfrak{p} = P/S$. The polarised flux density, for radio sources, follows a power law, $P \propto \nu^{-\alpha_P}$, with $\alpha_P \approx 0.75$. The differential number count per unit solid angle, per total flux density S and polarised flux density P is given as $n(\theta, \varphi, P, S) \propto S^{-1-x} P^{-1-x_P}$. These are relations in the cosmic rest frame, so for reasons similar to those discussed previously, the integrated linear flux would also show

effects of the motion of the observation frame. The kinematic dipole in the number count of significantly polarised sources and the integrated polarised flux density is given by:

$$\vec{D}^{\rm kin}_{N_P} = [2 + x(1+\alpha) + x_P(1+\alpha_P)]\vec{\beta} \tag{12}$$

$$\vec{D}^{\rm kin}_{P} = [2 + x(1+\alpha) + x_P(1+\alpha_P)]\vec{\beta} \tag{13}$$

The extracted velocities are shown in Table 2. It clearly shows deviation from expectations of a kinematic dipole.

Dipole type	D_o $(\times 10^{-2})$	v $(\times 10^3$ in km/s)	(l, b)
D_{N_P}	3.3 ± 0.8	2.38 ± 0.61	$(207°, 37°)$
D_P	4.9 ± 1.2	2.87 ± 0.68	$(244°, 20°)$

Table 2: *NVSS integrated polarised flux dipole amplitude, observation frame peculiar velocity and direction.* Results from Tiwari and Jain (Tiwari and Jain, 2015a) with a lower limit on total flux density of 30 mJy and polarised flux density range of $0.1 < P < 100$ mJy.

The 2010 study (Itoh et al., 2010) by Itoh et. al. of the Sloan Digital Sky Survey (SDSS) also has some fascinating hints of SI violations. The SDSS 6th Data Release photometric catalogue contains over 200 million sources and covers an area of around 8000 deg^2, with photometric data in five band passes. While the SDSS has very high fidelity data with well low and understood systematics, its sky coverage is small at about 20% with a mean redshift ~ 0.3. This makes the catalogue difficult to use for cosmological purpose. There are also some issues which need to be taken care of in constructing the sample for analysis. The first is to ensure that stars are carefully and reliably removed from analysis. Putting appropriate magnitude range helps with isolating the galaxies. Another well known feature of the SDSS catalogue is the presence of local clustering at large scales. The most well known feature of the SDSS is the *Sloan Great Wall*, at a redshift of ~ 0.08. Such local clustering has to be removed reliably before the intrinsic dipole is studied.

The expected kinematic dipole amplitude in the SDSS is found to be 1.231×10^{-3} (Itoh et al., 2010). The authors worked with four galaxy samples with different ranges in brightness and photometric redshift. Of them we only discuss two here. These are those samples which are deepest, more relevant from a cosmological point of view. The results we discuss are for the bright deep (BD) and the faint deep (FD) samples. For both, the maximum photometric redshift is ~ 0.9. The authors performed a χ^2 minimisation with the full covariance matrix. For the BD sample the authors obtained a dipole amplitude of $0.87^{+0.59}_{-0.57} \times 10^{-2}$ along $(l = 290°, b = -10°) \pm 100°$. The FD sample gave a dipole amplitude of $(1.21 \pm 0.23) \times 10^{-2}$ along $(l = 280°, b = 75°) \pm 33°$.

The authors found a dipole excess in all but the BD sample. They suggested that possible contamination in the FD samples from incomplete star-galaxy separation and with incorrectly removed clustering in the data might've caused this large measured dipole. Another reason for difference might be the due to the issue of the small sky coverage of the survey. They hoped that a sky survey with wider coverage would be able to settle the issue.

Yoon et. al. in their 2014 work (Yoon et al., 2014) found a dipole in the Wide-field Infrared Survey Explorer-Two Micron All Sky Survey (WISE-2MASS) catalogues. The WISE catalogue has 757 million sources which are however uncategorised. The authors use the 2MASS catalogue with joint intensity limits to select data for analysis. The GAMA D2 data was used to model the redshift distribution for the WISE catalogue. The selected object field is shallow with mean redshift of 0.139 and goes up to a maximum of 0.4. They follow a method similar to that of Gibelyou and Huterer (Gibelyou and Huterer, 2012) to estimate the dipole. With a 20° galactic plane cut, the result they obtained was $(5.2 \pm 0.2) \times 10^{-2}$ along $(l = 308° \pm 4°, b = -14° \pm 2°)$, which exceeded the theoretical expectations from local structure dipole. The theoretical dipole amplitude expected being 2.3 ± 1.2. They did not consider the effect of the kinematic dipole which has an order of magnitude lesser contribution and could not be sufficiently tested with the shallow data.

In the last few years the tests of SI violations with large scale structures have gathered steam. With deeper data and with greater sky coverage, better constraints can be put on SI violations and thereby constraining SI violating model parameters and mechanisms. With improvement in data fidelity and understanding of systematics, we may be able to reduce these errors and find out if truly these SI violations are consistent.

2.3 Virgo Alignment

A very curious feature of SI violations is the alignment of various preferred directions in different data sets. Several observations at wide range of frequencies suggest a preferred direction pointing roughly towards the Virgo supercluster, which is close to the direction of the observed CMBR dipole. We have already discussed the difference in the the magnitudes of $\vec{v}_{\rm CMB}$ and $\vec{v}_{\rm radio}$, extracted from number counts, sky brightness as well as polarized radio flux. Furthermore, the CMB quadrupole, CMB octopole, radio and optical polarizations from distant sources also indicate a preferred direction pointing roughly towards Virgo. Next we briefly describe each of these effects.

The distribution of polarization angles of distant radio galaxies indicates a dipole pattern. Here the observable is $\beta = \chi - \phi$, where χ is the linear polarization angle and ϕ is the orientation angle of the galaxy. This parameter shows a dipole distribution across the sky. The significance of the effect is found to be 3.5σ after making a cut which eliminates the central peak in the distribution of the rotation measures (RM) (Jain and Ralston, 1999; Jain and Sarala, 2006). The preferred direction of the dipole is found to be $l = 259^{\rm o}$, $b = 62^{\rm o}$ in galactic coordinates.

The CMBR quadrupole and the octopole, i.e. multipoles corresponding to $l = 2, 3$, also indicate a preferred direction ($(l, b) \sim (250^\circ, 60^\circ)$), pointing roughly towards Virgo. Statistical isotropy would imply that these are independent of one another as well of other multipoles, such as the dipole. However the preferred axis of both these multipoles points approximately in the direction of the CMB dipole (de Oliveira-Costa et al., 2004; Ralston and Jain, 2004). This is rather surprising! Furthermore, it is difficult to explain this alignment in terms of bias or foreground effects (Aluri et al., 2011). The procedure for extraction of the preferred direction has been developed in (de Oliveira-Costa et al., 2004; Ralston and Jain, 2004; Samal et al., 2008). One may either maximize the angular momentum dispersion $\langle \frac{\delta T}{T} | (\hat{n} \cdot \hat{L})^2 | \frac{\delta T}{T} \rangle$ (de Oliveira-Costa et al., 2004; Bennett et al., 2011). Alternatively one may calculate the principle eigenvector of the power tensor for the two modes (Ralston and Jain, 2004; Samal et al., 2008, 2009). For $l = 2, 3$ it has a simple interpretation. Both these multipoles appear to be planar, i.e., all the hot and cold spots lie roughly in the plane. The direction perpendicular to this is the preferred axis. In more detail, one finds that most of the contribution to the octopole power comes from the $|m| = 3$ coefficients. When maximized over direction the $|a_{3,3}|^2$ and $|a_{3,-3}|^2$ contribute approximately 94% of the total power in the octopole (Bennett et al., 2011). This unusual planar power distribution in octopole is another CMB anomaly at large length scales.

The optical polarizations from distant quasars show an alignment over very large distance scales (Hutsemekers, 1998; Jain et al., 2004), i.e. the linear polarizations of different sources are observed to point in the same direction. A very strong alignment effect is seen in the direction of Virgo as well as in the diametrically opposite direction. The angular dependence of the two point correlations of these polarizations were studied in (Ralston and Jain, 2004). This dependence was not found to be statistically significant. However it is interesting that the correlations were found to maximize along an axis pointing towards Virgo (Ralston and Jain, 2004). Hence we see that a wide range of phenomenon, ranging from radio number densities, sky brightness, polarized flux, polarization angles, CMBR dipole, quadrupole and octupole as well as the optical polarizations from quasars indicate a preferred direction pointing approximately towards Virgo. Below we mention one more effect related to CMBR which also indicates this direction.

2.4 Dipole Modulation in CMBR

The present era of precision cosmology was ushered in by the precision measurements of the cosmic microwave background (CMB), so our most important indicators of SI violations have come from the CMB observations. Of the various departures from SI predictions, the dipole modulation of the CMB temperature fluctuation field is the most important. The original claims were made by Hansen et. al. (Hansen et al., 2004) in their 2004 papers reporting a hemispherical power asymmetry in the CMB temperature observations made by the Wilkinson Microwave Anisotropy Probe (WMAP). The authors masked the galactic plane in the CMB temperature maps and analysed the binned angular power spectrum on circular patches of varying sizes, oriented about different directions in the sky. They reported significantly different C_ℓ's in the northern and southern galactic hemispheres for the multipole range $2 - 40$. The $2-4$ range was reported to have contribution from the galactic foreground residuals and the signal being directional along the galactic poles. The power spectrum estimates in $5 - 40$ range however showed

asymmetry levels which could not be justified by systematics and noise. The asymmetry in $5-40$ range was found to maximise along $(57^\circ, 10^\circ)$ in Galactic coordinates, which is close to the ecliptic axis. In the frame of maximum asymmetry they found that all the $5-40$ multipoles in the northern hemisphere have less power than than the average amplitudes, while in the southern hemisphere most of the multipoles in the range have more power than the average amplitude. The authors also claimed a similar signal of lower significance in the COsmic Background Explorer (COBE) data thereby ruling out systematics as a possible source of the signal.

In 2006 Gordon proposed (Gordon, 2007) a model of linear modulation of the isotropic temperature fluctuation field to phenomenologically represent hemispherical anisotropy. In this model, the temperature fluctuation (δT) observed along a direction $\hat{n}$, is given by

$$\delta T(\hat{n}) = \delta T_{\rm iso}(\hat{n})\left[1 + f(\hat{n})\right], \tag{14}$$

where $f(\hat{n})$ is a direction dependent function that modulates $\delta T_{\rm iso}$, the isotropic temperature fluctuation field [1]. The modulating function $f(\hat{n})$ is assumed as $A\hat{\lambda}\cdot\hat{n}$. This linear modulation along a preferred direction $\hat{\lambda}$ and with amplitude A, would result in a dipole modulation at the surface of last scattering. However, it is important to understand that hemispherical power asymmetry is not the same as dipole modulation. A dipole modulation model will naturally give rise to hemispherical asymmetry but hemispherical power asymmetry does not necessitate a dipole modulation, which is a more complex.

In 2009, following the release of WMAP five-year data, Hoftuft et. al. (Hoftuft et al., 2009) estimated the three parameters A, and two components of $\hat{\lambda}$ from the data maximizing the log-likelihood for the dipole modulation model. The observed data along a direction $(\hat{n})$ is written as in (14) but with an additive noise term to read $d(\hat{n}) = \delta T(\hat{n}) + N(\hat{n})$. The signal covariance matrix for such a model is given by (Hoftuft et al., 2009)

$$\mathbf{S}_{\rm mod}(\hat{n},\hat{m}) = \left[1 + A\hat{\lambda}\cdot\hat{n}\right]\mathbf{S}_{\rm iso}(\hat{n},\hat{m})\left[1 + A\hat{\lambda}\cdot\hat{m}\right]. \tag{15}$$

The isotropic signal covariance matrix $\mathbf{S}_{\rm iso}$ is written as

$$\mathbf{S}_{\rm iso}(\hat{n},\hat{m}) = \frac{1}{4\pi}\sum_i (2\ell+1)C_\ell P_\ell(\hat{n}\cdot\hat{m}). \tag{16}$$

Here the P_ℓs are the Legendre polynomials. The full covariance matrix then reads (Hoftuft et al., 2009)

$$\mathbf{C} = \mathbf{S}_{\rm mod}(A,\hat{\lambda}) + \mathbf{S}_{\rm iso} + \mathbf{N} + \mathbf{F}, \tag{17}$$

with $\mathbf{N}$ and $\mathbf{F}$ as noise covariance and foregrounds respectively. Assuming the signal and noise both to be Gaussian the log-likelihood takes the form (Hoftuft et al., 2009):

$$-2\ln\mathcal{L}(A,\hat{\lambda}) = \mathbf{d}^T\mathbf{C}^{-1}\mathbf{d} + \ln|\mathbf{C}|. \tag{18}$$

The best-fit results in the $\ell \leq 64$ range by maximizing the log-likelihood is contained in Table 3. The dipole modulation signal was claimed with a 3.3σ significance for $\ell \leq 64$.

We have shown (Rath and Jain, 2013) that for a dipole modulated temperature fluctuation field given by Eq. 14, with the preferred direction $\hat{\lambda}$ chosen along $\hat{z}$, the two point correlation function of the spherical harmonic coefficients $a_{\ell m}$ is given by

$$\begin{aligned}\langle a_{\ell m}a^*_{\ell' m'}\rangle &= \langle a_{\ell m}a^*_{\ell' m'}\rangle_{\rm iso} + \langle a_{\ell m}a^*_{\ell' m'}\rangle_{\rm dm}\\ &= C_\ell\delta_{\ell\ell'}\delta_{mm'} + A\left(C_{\ell'} + C_\ell\right)\times\\ &\left[\sqrt{\frac{(\ell-m+1)(\ell+m+1)}{(2\ell+1)(2\ell+3)}}\delta_{\ell',\ell+1} + \sqrt{\frac{(\ell-m)(\ell+m)}{(2\ell+1)(2\ell-1)}}\delta_{\ell',\ell-1}\right]\delta_{m'm}.\end{aligned} \tag{19}$$

This implies that for a dipole modulated temperature field, the covariance matrix, in spherical harmonic space is not diagonal. The added modulation gives rise to non-zero correlations between ℓ and $\ell+1$ and

[1] Note that we have changed the sign in front of $f(\hat{n})$ from '$-$' to '$+$' to keep consistency with later work.

Result from	A	(l,b)
Hoftuft et. al. (W5)	0.072 ± 0.022	$(224^\circ, -27^\circ) \pm 24^\circ$
Ade et. al. (P13)	0.065 ± 0.021	$(226^\circ, -17^\circ) \pm 24^\circ$
Ade et. al. (P15)	0.066 ± 0.021	$(225^\circ, -18^\circ) \pm 24^\circ$
Rath et. al. (W9)	0.090 ± 0.029	$(227^\circ, -14^\circ)$
Rath et. al. (P13)	0.074 ± 0.019	$(229^\circ, -16^\circ)$
Ghosh et. al. (P15)	0.078 ± 0.019	$(242^\circ \pm 16^\circ, -17^\circ \pm 20^\circ)$

Table 3: *Best-fit values for the dipole modulation parameters.* Results from (Hoftuft et al., 2009; Ade et al., 2014, 2015; Rath et al., 2015; Ghosh et al., 2016) are contained here for both the likelihood and statistic method. W5 and W9 stand for WMAP five-year and nine-year datasets respectively, P13 and P15 stand for Planck 2013 and 2015 SMICA maps.

ℓ and $\ell - 1$. So we have studied the dipole modulation feature using this property of non-zero ℓ, $\ell + 1$ correlations by defining a statistic S_H as

$$S_H = \sum_{\ell=\ell_{\min}}^{\ell_{\max}} \frac{\ell(\ell+1)}{(2\ell+1)} \sum_{m=-\ell}^{\ell} a_{\ell m} a^*_{\ell' m'} \tag{20}$$

which is a summed estimate of the ℓ, $\ell + 1$ correlations in the range $\ell_{\min} \leq \ell \leq \ell_{\max}$. The analysis was performed by setting $\ell_{\min} = 2$ and $\ell_{\max} = 64, 128$ for extraction of different parameters. Some of the results of this analysis are shown in Table 3 and show good agreement with other estimates.

The hemispherical power asymmetry and dipole modulation have persisted in the data for three generations of satellite based CMB experiments. The Planck experiment team has tested for both the hemispherical power asymmetry and dipole modulation in their CMB data, finding evidence for both (Ade et al., 2014, 2015). The dipole modulation signal has persisted at $\sim 3\sigma$ level in the 2013 and 2015 data release. The results of the Planck team and the corresponding results with the maximum statistic method are shown in Table 3 for comparison.

A test of dipole modulation or equivalently hemispherical anisotropy for the polarization E modes has also been carried out in (Ghosh et al., 2016). The low l multipoles of the polarization field are unreliable. Hence the authors only considered multipoles $l \geq 40$. Furthermore they did not test the significance of the effect since it required extensive numerical work in modelling detector noise. Interestingly it was found that the preferred direction in the range $40 \leq l \leq 100$ again points in the direction of Virgo. The direction starts to shift as we extend the upper limit on l. Although the statistical significance of the effect is unknown, it is interesting that the low l multipoles again prefer a direction towards Virgo.

2.5 Dipole Modulation in large Scale Structures

A signal of the dipole modulation has also been investigated in the large scale structures. The first attempt in this direction was done by Hirata in 2009 using SDSS quasars (Hirata, 2009). His approach to the problem of searching the large scale structures for dipole modulation was based on the variation of the amplitude of the linear power spectrum σ_8. If the CMB hemispherical asymmetry and dipole modulation are of cosmological origins then they should be linked to the primordial curvature perturbations. Such a situation would lead to a gradient in the amplitude of the power spectrum along the preferred direction of the dipole. Since the growth and abundance of large scale structures is very sensitive to the value of σ_8, the gradient of this parameter can be constrained from the number variations of the large scale structures.

The SDSS quasars were chosen by Hirata to test out the variation of σ_8. This set had deep distance spread with wide angular coverage. Since the quasars are highly biased structures, any small variation in σ_8 would have larger effects. Since these are SDSS objects the systematics are fairly well understood. One of the drawbacks of the dataset chosen is that the number density of such quasars is small, roughly 1 deg^{-2}. When the preferred direction is fixed along that obtained by Eriksen et. al. ($l = 225^\circ, b = -27^\circ$), the amplitude of dipole modulation was found as $A = -0.0018 \pm 0.0044$. A search for the best fit direction did not reveal a statistically significant signal. Overall, Hirata's work is strongly indicative of no dipole modulation in the large scale structures.

The 2013 work (Fernández-Cobos et al., 2014) by Fernández-Cobos et. al. searched for the dipole modulation signal in the NVSS. Their approach is a logical extension of the Hoftuft et. al. method, described at the beginning of this section, to the large scale structures, working with the galaxy angular power spectra C_ℓ^{GG}. They worked with three lower flux cuts of 2.5, 5.0 and 10.0 mJy. They corrected for the declination dependent systematics, only for the case of the 2.5 mJy cut, by dividing the entire data map into 70 strips of equal area and rescaling the number density. From their simulation they forecasted a non-negligible dipole modulation with $A = 0.065 \pm 0.013$ along the direction $(l = 224^\circ, -14^\circ) \pm 17^\circ$. However they do not find any evidence of dipole modulation. The modulation amplitude A was found to be 0.003 ± 0.015 for 2.5 mJy cut, 0.011 ± 0.016 for 5.0 mJy cut and 0.007 ± 0.014 for 10.0 mJy cut, all of the amplitudes being compatible within 1σ of zero modulation amplitude.

2.6 Alignment of linear polarizations of radio sources

The linear polarizations of radio sources show alignment with one another, analogous to the alignment of optical polarizations from quasars. An alignment on the distance scale of 100 Mpc was reported in (Tiwari and Jain, 2013) in the JVAS/CLASS sources with polarized flux greater than 1 mJy. This has subsequently been confirmed in (Shurtleff, 2014; Pelgrims and Hutsemékers, 2015). An alignment on larger distance scales for the subsample of QSOs in this data set has also been reported in (Pelgrims and Hutsemékers, 2015). An alignment on the scale of 100 Mpc may be expected within the framework of Big Bang cosmology since sources show correlation with one another on such distance scales. In (Tiwari and Jain, 2015b) the authors argued that this alignment is induced by the correlations in the cluster magnetic field. Within the framework of this model the authors extracted the spectral index of the cluster magnetic field. The extracted value of 2.74 ± 0.04 shows good agreement with the value expected on the basis of cosmological magneto-hydrodynamic simulations (Dolag et al., 2002). Despite this agreement the alignment effect needs to be tested carefully by future surveys. The alignment might arise due to bias and furthermore it is found that the significance of the effect reduces considerably if the jackknife errors are taken into account (Tiwari and Jain, 2015b). The authors argued that we require at least four times larger data set in order to have a reliable confirmation of this effect.

2.7 Other Anomalies

Other CMB anomalies worth mentioning are the Cold Spot and the parity asymmetry. Cruz et. al. (Cruz et al., 2005) reported in 2004, an anomalous cold spot at $(l = 209^\circ, b = -57^\circ)$ with a size of 10°. To understand the parity asymmetry we have to think of the temperature field being sum of even and odd parity fields. The even and odd parity can be characterised by

$$P^+ = \sum_{\ell=2}^{\ell_{\max}} 2^{-1}(1 + (-1)^\ell)\ell(\ell+1)/2\pi C_\ell \tag{21}$$

$$P^- = \sum_{\ell=2}^{\ell_{\max}} 2^{-1}(1 - (-1)^\ell)\ell(\ell+1)/2\pi C_\ell \tag{22}$$

The ratio P^+/P^- denotes the ratio of the even parity contribution to the odd parity contribution. It was reported around 2010 (Kim and Naselsky, 2010; Aluri and Jain, 2012), that the ratio is anomalously large when summing over the largest angular scales. Summing the multipoles $2 \leq \ell \leq 22$ the results for the ratio for WMAP 7 year data was 0.71, indicating a larger contribution from the even parity. Both these anomalies continue to exist in the Planck CMB data.

3 Theoretical Expectations

It is generally believed that the effects reviewed in the previous section are inconsistent with the Big Bang cosmological model. Although these observations appear to be in conflict with the cosmological principle, it has been shown in (Aluri and Jain, 2012; Rath et al., 2013) that they can be accommodated within the Big Bang paradigm. The basic idea is that the early pre-inflationary phase of the Universe may not be isotropic and homogeneous. It acquires this property during the early phase of inflation.

This has been explicitly demonstrated for the case of Bianchi models (Wald, 1983) which are anisotropic but homogeneous. It has also been shown that, for a wide range of parameters, modes generated during this early period can re-enter the horizon before the current era and hence affect observations (Aluri and Jain, 2012; Rath et al., 2013). This implies that although the background evolution is isotropic and homogeneous, the perturbations need not respect the cosmological principle. Interestingly the dominant effect is expected for low k modes, which observationally appear to show the largest deviation from isotropy. This phenomenon has been explicitly demonstrated in (Rath et al., 2013) where the quadrupole and octopole alignment is explained in terms of an early anisotropic phase of inflation. Similar ideas have been explored in order to explain the hemispherical anisotropy (Rath et al., 2015; Jain and Rath, 2015; Kothari et al., 2015a; Ghosh et al., 2016). However in this case an explicit model requires either an inhomogeneous Universe (Carroll et al., 2010; Rath et al., 2015) or space-time noncommutativity (Jain and Rath, 2015; Kothari et al., 2015b). A detailed analysis of such models is so far not available in the literature. Here we briefly review some basic results which have been obtained by assuming a model primordial power spectrum.

Let us first consider the primordial power spectrum in real space, defined as,

$$F(\vec{R},\vec{X}) = \langle \delta(\vec{x})\delta(\vec{x}^{\,'})\rangle \tag{23}$$

where $\delta(\vec{x})$ is the primordial density fluctuation at comoving coordinate $\vec{x}$, $\vec{R} = \vec{x} - \vec{x}^{\,'}$ and $\vec{X} = (\vec{x}+\vec{x}^{\,'})/2$. In (Kothari et al., 2015a) the authors consider the following inhomogenous model:

$$F\left(\vec{R},\vec{X}\right) = f_1(R) + \sin\left(\vec{\lambda}\cdot\frac{\vec{X}}{\tau_0} + \delta\right) f_2(R), \tag{24}$$

where $\hat{\lambda}$ and δ are parameters and τ_0 is the current conformal time. Here the second term represents the contribution due to inhomogeneity. In Fourier space, the corresponding power spectrum is given by,

$$\left\langle \delta(\vec{k})\delta^*(\vec{k}')\right\rangle = P_{\rm iso}(k)\delta^3\left(\vec{k}-\vec{k}'\right) - \frac{i}{2}g(k_+)\left[\delta^3\left(\vec{k}-\vec{k}'+\frac{\vec{\lambda}}{\tau_0}\right) - \delta^3\left(\vec{k}-\vec{k}'-\frac{\vec{\lambda}}{\tau_0}\right)\right] \tag{25}$$

where

$$g\left(k_+\right) = \int \frac{d^3R}{(2\pi)^3}\exp\left[i\left(\vec{k}+\vec{k}'\right)\cdot\frac{\vec{R}}{2}\right] f_2(R),$$

and $\vec{k}_+ = (\vec{k}+\vec{k}')/2$. This model leads to correlations between multipoles l and $l\pm 1$ of CMB, as expected in the case of dipole modulated temperature field (see Eq. 19). The authors (Kothari et al., 2015a) parameterize the function $g(k)$ as a power law, i.e.,

$$g(k) = g_0 P_{\rm iso}(k)(k\tau_0)^{-\alpha} \tag{26}$$

where g_0 and α are parameters. A fit to the CMB dipole modulation data suggests that $\alpha \approx 1$. A similar analysis has also been carried out for an anisotropic but homogeneous model (Kothari et al., 2015a). As explained earlier, such a model is possible only within the framework of non-commutative space-times.

A study of the implications of such a primordial model on large scale structures is so far not available in the literature. We expect that predictions based on such models will become available by the time SKA becomes operational.

3.1 The galaxy power spectrum and ΛCDM power spectrum

For tests at SKA our primary aim is to study the distribution of galaxies at large distances or equivalently their angular power spectrum C_l. We next briefly discuss the relation between ΛCDM power spectrum $P(k)$ to C_l. Let $\mathcal{N}(\hat{r})$ be the projected number density (per steradian) in the direction $\hat{r}$, and $\bar{\mathcal{N}}$ be the mean number density averaged over the sky. We write the number density $\mathcal{N}(\hat{r}) = \bar{\mathcal{N}}(1+\Delta(\hat{r}))$, where $\Delta(\hat{r})$ represents the projected number surface density contrast. Let the three-dimensional dark matter density contrast be represented as $\delta_m(\vec{r}, z(r))$, where $(\vec{r}, z(r))$ represent a unique location in space and time. The vector $\vec{r}$ stands for comoving distance r in direction $\hat{r}$ and $z(r)$ is the redshift corresponding

to comoving distance r. Assuming linear galaxy biasing $b(z)$ and linear growth factor $D(z)$ to density contrast we write the corresponding galaxy contrast $\delta_g(\vec{r}, z(r)) = \delta_m(\vec{r}, z=0)D(z)b(z)$. Now we can write the theoretical expression for $\Delta(\hat{r})$ as,

$$\begin{aligned}\Delta(\hat{r}) &= \int_0^\infty \delta_g(\vec{r}, z(r))p(r)dr \\ &= \int_0^\infty \delta_m(\vec{r}, z=0)D(z)b(z)p(r)dr, \end{aligned} \tag{27}$$

where $p(r)\mathrm{d}r$ is the probability of observing a galaxy between r and $(r+dr)$. The expansion of $\Delta(\hat{r})$ in spherical harmonics and subsequent harmonic coefficients, $\tilde{a}_{lm}$, similar to equation (7), is given as,

$$\begin{aligned}\tilde{a}_{lm} &= \int d\Omega \Delta(\hat{r}) Y_{lm}(\hat{r}) \\ &= \int d\Omega Y_{lm}(\hat{r}) \int_0^\infty \delta_m(\vec{r}, z=0)D(z)b(z)p(r)dr\ . \end{aligned} \tag{28}$$

To write the harmonic coefficients, $\tilde{a}_{lm}$, in terms of the k-space density field $\delta_{\vec{k}}$, we expand $\delta_m(\vec{r}, z=0)$ in Fourier domain,

$$\delta_m(\vec{r}, z=0) = \frac{1}{(2\pi)^3}\int d^3k \delta_{\vec{k}} \mathrm{e}^{i\vec{k}\cdot\vec{r}}\ , \tag{29}$$

and substitute

$$\mathrm{e}^{i\vec{k}\cdot\vec{r}} = 4\pi \sum_{l,m} i^l j_l(kr) Y^*_{lm}(\hat{r}) Y_{lm}(\hat{k})\ ,$$

where j_l is the spherical Bessel function of first kind for integer l. Subsequently we write

$$\tilde{a}_{lm} = \frac{i^l}{2\pi^2}\int D(z)b(z)p(r)dr \int d^3k \delta_{\vec{k}} j_l(kr) Y^*_{lm}(\hat{k})\ . \tag{30}$$

Following equation (30) we write the theoretical angular power spectrum $\tilde{C}_l$ as,

$$\begin{aligned}\tilde{C}_l &= <|\tilde{a}_{lm}|^2> \\ &= \frac{2}{\pi}\int dk k^2 P(k) \left| \int_0^\infty D(z)b(z)p(r)dr j_l(kr) \right|^2 \\ &= \frac{2}{\pi}\int dk k^2 P(k) W^2(k)\ . \end{aligned} \tag{31}$$

where $W(k) = \int_0^\infty D(z)b(z)p(r)dr j_l(kr)$ is the window function in k-space. We have also used $< \delta_{\vec{k}}\delta_{\vec{k}'} >= (2\pi)^3\delta(\vec{k}-\vec{k}')P(k)$ where $P(k)$ is ΛCDM power spectrum.

3.2 Observational C_l

The observational estimate of C_l anologous to theoretical $\tilde{C}_l$ given in equation (31) is,

$$C_l^{\mathrm{obs}} = \frac{\langle |a'_{lm}|^2 \rangle}{J_{lm}} - \frac{1}{\bar{\mathcal{N}}} \tag{32}$$

where $a'_{lm} = \int_{\mathrm{survey}} d\Omega \Delta(\hat{r}) Y_{lm}(\hat{r})$ and $J_{lm} = \int_{\mathrm{survey}} |Y_{lm}|^2 \mathrm{d}\Omega$, the J_{lm} is an approximate correction factor for the partial survey region (Peebles, 1980). The term $\frac{1}{\bar{\mathcal{N}}}$ removes the contribution from the Poissonian shot-noise.

The error in above estimate of power spectrum due to cosmic variance, sky coverage and shot-noise is as follows:

$$\Delta C_l = \sqrt{\frac{2}{(2l+1)f_{\mathrm{sky}}}} \left(C_l^{\mathrm{obs}} + \frac{1}{\bar{\mathcal{N}}} \right) \tag{33}$$

where $f_{\rm sky}$ is the fraction of sky observed in the survey. Notice that the above error estimate is applicable in case of the 2-point galaxy-galaxy angular power spectrum (C_l^{gg}). The lensing shear power spectrum is deduced considering shape measurements of the galaxies. The shear angular power spectrum error estimate is given by,

$$\Delta C_l = \sqrt{\frac{2}{(2l+1)f_{\rm sky}}}\left(C_l^{\rm obs} + \frac{\sigma_\epsilon^2}{\bar{\mathcal{N}}}\right) \tag{34}$$

where σ_ϵ is the RMS variance of the ellipticity distribution. Furthermore, for the case of polarized sources, assuming that the polarization position angle is an unbiased tracer of the intrinsic morphological orientation of the galaxy with a scatter of $\alpha_{\rm rms}$, the corresponding error estimate is as follows (Brown and Battye, 2011b,a):

$$\Delta C_l = \sqrt{\frac{2}{(2l+1)f_{\rm sky}}}\left(C_l^{\rm obs} + \frac{16\alpha_{\rm rms}^2\sigma_\epsilon^2}{\bar{\mathcal{N}}}\right) . \tag{35}$$

4 Tests of statistical isotropy at SKA

We propose the following tests of statistical isotropy in large scale structures:

1. Determination of the dipole in number counts and sky brightness of radio sources in order to test its consistency with the kinematic dipole.
2. Determination of the dipole in number counts of radio sources with non-zero polarization as well as in the polarized flux.
3. Testing the alignment of linear polarizations of radio sources as a function of their relative separation.
4. Testing the presence of dipole modulation in radio sources.
5. Determination of the dipole anisotropy in the offsets between linear polarization angles and the galaxy orientation angles.

4.1 SKA technical details and capabilities

The SKA will be a highly flexible instrument with unprecedented observational capabilities. It will consist of an inner core and outer stations arranged in a log-spiral pattern. The full array will be extended to at least 3000 km from the central core. This will be the largest radio telescope in the world and will revolutionize our understanding of the Universe. The SKA will operate in frequency range from 70 MHz to 10 GHz (see (Dewdney et al., 2013) for more details).

The SKA will perform both redshift (HI) surveys and radio continuum surveys in frequency range from 70 MHz to 10 GHz. There will be two phases of SKA observations. The final phase of SKA is expected to map out 1 billion galaxies over a sky area of $f_{\rm sky} \sim 3/4$, out to a redshift of $z \sim 2$. This will reduce the shot-noise in galaxy angular power spectrum (see equation (32)) by a factor of 3000. The resulting shot-noise will be 3 orders of magnitude lower than ΛCDM $\tilde{C}_l$ and will be negligible in comparison to cosmic variance (equation (33)).

The SKA will yield the measurements of various cosmological parameters with unprecedented precision. The anisotropy tests at various scales will improve immensely. The dipole anisotropy observed in NVSS brightness and polarization will be clearly settled. At present the signal is observed at $\sim 3\sigma$ (Tiwari et al., 2015). The radio galaxy biasing consideration gives similar significance for reasonable radial number density and galaxy bias values (Tiwari and Nusser, 2015). The galaxy-bias is a nuisance in relating the galaxy clustering to underlying dark matter distribution. The biasing is almost stochastic, scale-dependent, redshift dependent and non-linear (Dekel and Lahav, 1999). The bias determination is almost always indirect as we always need the underlying dark matter density power spectrum to extract bias from galaxy clustering. As discussed earlier, the NVSS total source count is $\sim 1.8 \times 10^6$. The SKA source count is expected to be roughly two orders of magnitude larger (Wilman et al., 2008). This also applies to the polarized source density. The wide and deep polarization surveys with SKA will reach to μJy flux limit. The deep polarization survey (2 μJy) will probe the source population as a function

of flux, luminosity and redshift, whereas the wide (33,000 deg^2, sensitive up to 10 μJy) survey will reveal the large scale clustering of polarized galaxies. Hence the statistical error in source counts, sky brightness, polarized number count as well as polarized flux will be sufficiently small in order to reliably extract the signal of dipole anisotropy. However one has to carefully remove systematic effects from data.

Besides the galaxy biasing described above, the most important systematic effect is the contribution due to local clustering dipole (Blake and Wall, 2002; Singal, 2011; Gibelyou and Huterer, 2012; Rubart and Schwarz, 2013; Tiwari et al., 2015; Schwarz et al., 2015). So far this has been removed by cross correlating with catalogues of known nearby galaxies (Blake and Wall, 2002). With SKA redshift survey the exact radial number density will be known. The large area survey coverage and depth in redshift with SKA observation will allow us to measure the galaxy clustering at largest scale ever. The SKA galaxy power spectrum will cover the turnover ($k < 0.02$ h Mpc^{-1}) of ΛCDM power spectrum. This will also allow a better constrain on galaxy bias. The NVSS survey also suffers from significant declination bias due to two different array configurations used for different declinations. While this may not be an issue for SKA, a declination bias centered at the array location may arise (Tiwari and Jain, 2015a). Such a bias has been identified in the NVSS survey, particularly for the sample with low flux cutoff, and can be effectively removed by the procedure described in (Tiwari and Jain, 2015a). Yet another systematic effect arises in relating the extracted dipole from data to the local speed. The main issue here is the deviation of the distribution of number density $n(S)$ as a function of the flux S from a pure power law. However it has been shown that a generalized distribution fits the data very well and one can extract the local speed very accurately using this fit (Tiwari et al., 2015; Tiwari and Jain, 2015a).

Further the resolved shape of billion galaxies from SKA will give the best shear measurements. The light from distant galaxy follow the geodesics, which bends according to the presence of matter in intervening space. This results as a shape distortion following the matter distribution fluctuations along the line of sight. This enables the direct mapping of mass distribution (luminous + non-luminous) and dark energy measurements. The statistical error in auto-shear power spectrum with SKA will decrease by a factor of $\sim$ 3000 due to high number surface density ($\sim 10^5$ deg^2) and reliable shape measurements (Demetroullas and Brown, 2016). With such huge improvement in statistics, it will be challenging to control the corresponding systematics. Cross-correlations between shear maps from SKA and LSST/*Euclid* can remove observational systematics.

The enhanced polarization survey at SKA will also allow us to reliably test the alignment of linear polarizations as a function of the angular separation among galaxies (Tiwari and Jain, 2013, 2015b). With two orders of magnitude increase in the number of sources, the effect will be seen clearly if present in data. Furthermore the SKA redshift survey would allow a 3 dimensional analysis which will provide an unambiguous test of this phenomenon, both at the supercluster scale (Tiwari and Jain, 2013, 2015b) and on larger cosmological distance scales (Pelgrims and Hutsemékers, 2015). Within the framework of the theoretical model of (Tiwari and Jain, 2015b), it will allow a clean extraction of the spectral index of the cluster magnetic field.

SKA will also make measurements of linear polarizations at different frequencies for a very large sample of sources (Beck and Gaensler, 2004; Haverkorn et al., 2015). The main purpose of these measurements is the Faraday rotation measures which will provide information about the milky way magnetic field. However these will also allow measurements of the host polarization position angles. For the case of active galaxies, if we are also able to determine the orientation of the jets, it is possible to test the dipole anisotropy claimed in (Jain and Ralston, 1999). We point out that the extraction of rotation measures and polarization position angles may be facilitated by the refined technique developed in (Sarala and Jain, 2002).

5 Discussion and Conclusions

The tantalizing possibility that the Cosmological principle may be violated is indicated by many observations. The most prominent of these effects is the so called Virgo Alignment, which refers to a wide range of phenomena indicating a preferred direction pointing towards Virgo. The SKA has the capability to convincingly test several of these effects. These include the dipole anisotropy in radio polarization angles (Jain and Ralston, 1999), the dipole in the number counts and sky brightness (Blake and Wall, 2002; Singal, 2011; Gibelyou and Huterer, 2012; Tiwari et al., 2015; Rubart and Schwarz, 2013) and in the polarized number counts and polarized flux (Tiwari and Jain, 2015a). These observations may indicate

that we need to go beyond the standard Big Bang cosmology. Alternatively they may be explained by pre-inflationary anisotropic and/or inhomogeneous modes (Aluri and Jain, 2012; Rath et al., 2013). In either case, confirmation of this alignment effect is likely to revolutionize cosmology. SKA will also test the signal of dipole modulation in large scale structure. Finally it will test the alignment of radio polarizations. It has been suggested that the alignment is induced by the correlations in the cluster magnetic field (Tiwari and Jain, 2015b). Hence if confirmed this phenomenon might provide a tool to study the statistical properties of the large scale magnetic field.

References

Ade, P. A. R. et al.: 2014, *Astron. Astrophys.* **571**, A23

Ade, P. A. R. et al.: 2015

Aluri, P. K. and Jain, P.: 2012, *Modern Physics Letters A* **27**, 1250014

Aluri, P. K. and Jain, P.: 2012, *Mon. Not. Roy. Astron. Soc.* **419**, 3378

Aluri, P. K., Samal, P. K., Jain, P., and Ralston, J. P.: 2011, MNRAS **414**, 1032

Beck, R. and Gaensler, B. M.: 2004, *New Astronomy Reviews* **48**, 1289

Bennett, C. L. et al.: 2011, *Astrophys. J. Suppl.* **192**, 17

Blake, C. and Wall, J.: 2002, *Nature* **416**, 150

Brown, M. L. and Battye, R. A.: 2011a, ApJ **735**, L23

Brown, M. L. and Battye, R. A.: 2011b, MNRAS **410**, 2057

Carroll, S. M., Tseng, C.-Y., and Wise, M. B.: 2010, *Phys. Rev. D* **81**, 083501

Condon, J. J., Cotton, W. D., Greisen, E. W., Yin, Q. F., Perley, R. A., Taylor, G. B., and Broderick, J. J.: 1998, *AJ* **115(5)**, 1693

Cruz, M., Martinez-Gonzalez, E., Vielva, P., and Cayon, L.: 2005, *Mon. Not. Roy. Astron. Soc.* **356**, 29

de Oliveira-Costa, A., Tegmark, M., Zaldarriaga, M., and Hamilton, A.: 2004, *Phys. Rev.* **D69**, 063516

Dekel, A. and Lahav, O.: 1999, ApJ **520**, 24

Demetroullas, C. and Brown, M. L.: 2016, MNRAS **456**, 3100

Dewdney, P. E., Turner, W., Millenaar, R., McCool, R., Lazio, J., and J., C. T.: 2013, *SKA Organisation*

Dolag, K., Bartelmann, M., and Lesch, H.: 2002, A&A **387**, 383

Ellis, G. F. R. and Baldwin, J. E.: 1984, *MNRAS* **206**, 377

Fernández-Cobos, R., Vielva, P., Pietrobon, D., Balbi, A., Martínez-González, E., and Barreiro, R. B.: 2014, *Mon. Not. Roy. Astron. Soc.* **441(3)**, 2392

Ghosh, S., Kothari, R., Jain, P., and Rath, P. K.: 2016, *JCAP* **1601(01)**, 046

Gibelyou, C. and Huterer, D.: 2012, *Mon. Not. Roy. Astron. Soc.* **427**, 1994

Gordon, C.: 2007, *Astrophys. J.* **656**, 636

Hansen, F. K., Banday, A. J., and Gorski, K. M.: 2004, *Mon. Not. Roy. Astron. Soc.* **354**, 641

Haverkorn, M., Akahori, T., Carretti, E., Ferrière, K., Frick, P., Gaensler, B., Heald, G., Johnston-Hollitt, M., Jones, D., Landecker, T., Mao, S. A., Noutsos, A., Oppermann, N., Reich, W., Robishaw, T., Scaife, A., Schnitzeler, D., Stepanov, R., Sun, X., and Taylor, R.: 2015, *Advancing Astrophysics with the Square Kilometre Array (AASKA14)* p. 96

Hinshaw, G. et al.: 2009, *Astrophys. J. Suppl.* **180**, 225

Hirata, C. M.: 2009, *JCAP* **0909**, 011

Hoftuft, J., Eriksen, H. K., Banday, A. J., Gorski, K. M., Hansen, F. K., and Lilje, P. B.: 2009, *Astrophys. J.* **699**, 985

Hutsemekers, D.: 1998, A&A **332**, 410

Itoh, Y., Yahata, K., and Takada, M.: 2010, *Phys. Rev.* **D82**, 043530

Jain, P., Narain, G., and Sarala, S.: 2004, *Mon. Not. Roy. Astron. Soc.* **347**, 394

Jain, P. and Ralston, J. P.: 1999, *Modern Physics Letters A* **14**, 417

Jain, P. and Rath, P. K.: 2015, *Eur. Phys. J.* **C75**, 113

Jain, P. and Sarala, S.: 2006, *J. Astrophys. Astron.* **27**, 443

Kim, J. and Naselsky, P.: 2010, *Astrophys. J.* **714**, L265

Kogut, A. et al.: 1993, *Astrophys. J.* **419**, 1

Kothari, R., Ghosh, S., Rath, P. K., Kashyap, G., and Jain, P.: 2015a

Kothari, R., Rath, P. K., and Jain, P.: 2015b

Peebles, P. J. E.: 1980, *The large-scale structure of the universe*

Pelgrims, V. and Hutsemékers, D.: 2015, MNRAS **450**, 4161

Ralston, J. P. and Jain, P.: 2004, *Int. J. Mod. Phys.* **D13**, 1857

Rath, P. K., Aluri, P. K., and Jain, P.: 2015, *Phys. Rev.* **D91**, 023515

Rath, P. K. and Jain, P.: 2013, *JCAP* **1312**, 014

Rath, P. K., Mudholkar, T., Jain, P., Aluri, P. K., and Panda, S.: 2013, *JCAP* **1304**, 007

Rubart, M. and Schwarz, D. J.: 2013, *Astron. Astrophys.* **555**, A117

Samal, P. K., Saha, R., Jain, P., and Ralston, J. P.: 2008, *Mon. Not. Roy. Astron. Soc.* **385**, 1718

Samal, P. K., Saha, R., Jain, P., and Ralston, J. P.: 2009, *Mon. Not. Roy. Astron. Soc.* **396**, 511

Sarala, S. and Jain, P.: 2002, *Journal of Astrophysics and Astronomy* **23**, 137

Schwarz, D. J., Bacon, D., Chen, S., Clarkson, C., Huterer, D., Kunz, M., Maartens, R., Raccanelli, A., Rubart, M., and Starck, J.-L.: 2015, *PoS* **AASKA14**, 032

Shurtleff, R.: 2014, *arXiv:1408.2514*

Singal, A. K.: 2011, *Astrophys. J.* **742**, L23

Tiwari, P. and Jain, P.: 2013, *Int. J. Mod. Phys.* **D22(14)**, 1350089

Tiwari, P. and Jain, P.: 2015a, *MNRAS* **447**, 2658

Tiwari, P. and Jain, P.: 2015b, *ArXiv e-prints*

Tiwari, P., Kothari, R., Naskar, A., Nadkarni-Ghosh, S., and Jain, P.: 2015, *Astropart. Phys.* **61**, 1

Tiwari, P. and Nusser, A.: 2015, *arXiv:1509.02532*

Wald, R. M.: 1983, Phys. Rev. D **28**, 2118

Wilman, R. J., Miller, L., Jarvis, M. J., Mauch, T., Levrier, F., Abdalla, F. B., Rawlings, S., Klöckner, H.-R., Obreschkow, D., Olteanu, D., and Young, S.: 2008, *Monthly Notices of the Royal Astronomical Society* **388(3)**, 1335

Yoon, M., Huterer, D., Gibelyou, C., Kovács, A., and Szapudi, I.: 2014, *Mon. Not. Roy. Astron. Soc.* **445**, L60

Evolution of galaxies through absorption lines: perspective of SKA-India H I Working Group

N. Gupta*[1] and R. Dutta[1]

[1] *IUCAA, Post Bag 4, Ganeshkhind, Pune 411007, India*

Abstract

Deep galaxy surveys have revealed that the global star formation rate density in the universe peaks at $1 \leq z \leq 2$ and sharply declines towards $z = 0$. The star formation rate (SFR) is directly related to the amount and physical properties of the cold gas present in galaxies. Since very little is known about this component of ISM beyond the local Universe, a deep blind spectroscopic survey that will reveal it in an unbiased way is essential to unravel the physical processes that drive the evolution of SFR. H I 21-cm absorption line provides an excellent tool to trace the evolution of cold atomic gas in galaxies. In this article, we summarize the current status of intervening H I 21-cm absorption line studies and future prospects with upcoming SKA pathfinders and SKA1.

1 Introduction

A key question in the modern astrophysics is to understand how the star formation in galaxies proceeds and leads to the present-day Universe. In recent years, radio and optical/IR observations of local Universe have established a strong relationship between the star formation rate and the properties of the cold atomic and molecular gas in galaxies (e.g. Leroy et al. 2008). The cosmic evolution of the global comoving star-formation rate density (SFRD) is also now reasonably well constrained up to z$\sim$8 (Fig. 1). In particular, the observations have established that there is a peak in the comoving SFRD at $1 \leq z \leq 2$ followed by a sharp decrease towards $z \sim 0$ (Madau & Dickinson 2014). One expects the redshift evolution of the SFRD to be intimately related to the redshift evolution of the cosmological mass density of neutral ($\Omega_{\rm HI}$) and molecular gas.

But despite intensive efforts, the best available telescopes till date have been successful in detecting distant cold gas reservoirs in emission in only in the most massive galaxies. Consequently, very little is known about the evolution of cold atomic and molecular gas in galaxies beyond the local Universe. The advent of various SKA pathfinders and eventually SKA is an unique opportunity to make breakthrough observations in this field. In particular, it will be possible to carry out large *unbiased* surveys of H I 21-cm absorption, which is an excellent tracer of cold atomic gas, to carry out an unbiased census of the cold gas in normal galaxies, irrespective of their physical properties such as morphology and mass, and understand the physical processes that control the evolution of the star formation history of the Universe.

This article is organized as follows: first we summarize the current status of the H I 21-cm absorption line studies. We focus primarily on *intervening* absorbers i.e. absorbers concerned with the normal galaxies rather than the *associated* absorbers which are concerned with the gas associated with Active Galactic Nuclei (AGNs). Next we introduce the activities and plans for various SKA pathfinders, and conclude with the prospects with SKA-1.

2 Current status of H I 21-cm absorption line studies

While the H I content of galaxies can be best probed by surveys of 21-cm emission, limited sensitivity of current radio telescopes does not allow them to reach beyond the local Universe (see e.g. Zwaan et

*ngupta@iucaa.in

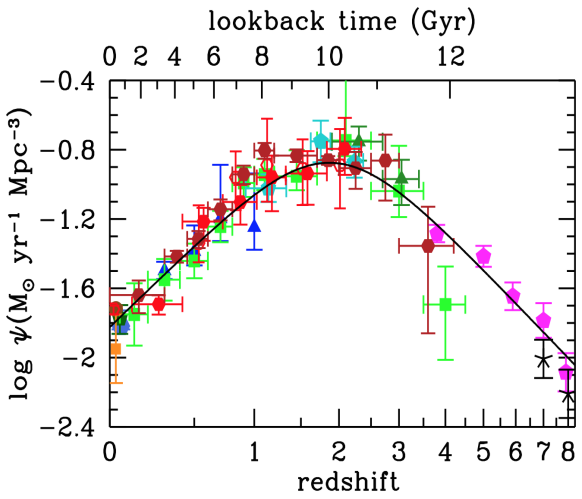

Figure 1: Star formation rate density as a function of redshift (Madau et al. 2014).

al. 2005 for $z \sim 0$; Verheijen et al. 2007 and Catinella et al. 2015 for direct detections at $z \sim 0.3$; Lah et al. 2007 for statistical detection of H I at $z \sim 0.24$). On the contrary, detection of H I in the spectra of distant QSOs in the form of damped Lyman-α absorption (DLA) provides a luminosity unbiased way of probing the evolution of the H I content in the universe (Noterdaeme et al. 2012). Similarly, the detectability of 21-cm absorption lines is not limited by distance and depends only on the brightness of background quasar and 21-cm absorption gas cross-section. Specifically, the H I column density for an optically thin cloud that covers a fraction f_c of the background radio source is related to the 21-cm optical depth $\tau(v)$ in a velocity interval v–v+dv and to the spin temperature (T_s) by

$$N(\mathrm{H\ I}) = 1.835 \times 10^{18}\ \frac{T_s}{f_c} \int \tau(v)\ \mathrm{d}v\ \mathrm{cm}^{-2}. \quad (1)$$

It is widely believed that the spin temperature (T_s) of the H I gas is a reliable tracer of the kinetic temperature. In addition, the width of the 21-cm line detected in a high resolution spectrum yields a direct measurement of (or stringent upper limit on) the kinetic temperature. Thus, H I 21-cm absorption line can be used to trace the thermal state of the atomic gas and the evolution of the filling factor of cold atomic gas in galaxies.

In fact, most of our understanding of the physical state of H I gas in the Galactic interstellar medium (ISM) is based on the 21-cm emission and absorption line studies. In the Milky Way, there have been many surveys for H I 21-cm emission and absorption line. Consequently, it is known that the atomic gas is present in two dominant phases: the cold (∼100 K) and warm (∼8000 K) neutral medium (i.e. CNM and WNM). Further, it has been observed that about 50% of the atomic gas is in WNM and at least ∼50% of the WNM lies in the thermally unstable range of 500 - 5000 K (e.g. Heiles & Troland 2003). The multiphase pressure equilibrium models and supernova driven hydrodynamical simulations of the Galactic interstellar medium (ISM) have shown that the volume filling factors of CNM and WNM, and the interstellar pressures over which these two phases can be sustained depend crucially on various heating and cooling processes − whose rates are tightly coupled with the *in situ* star formation (e.g. Wolfire et al. 2003).

Despite obvious advantages of combining 21-cm emission and absorption line measurements in revealing the physical state of atomic gas, the technique is scarcely applied beyond the Milky Way. The main reasons are (1) the difficulty in detecting 21-cm emission line beyond the local Universe, (2) the scarcity of sight lines towards bright sources at small impact parameters that can be used to detect 21-cm absorption from gas in galaxies, and (3) narrow bandwidths and unfriendly RFI environments prevailing in most observatories. Consequently, most of the H I 21-cm surveys were designed to detect

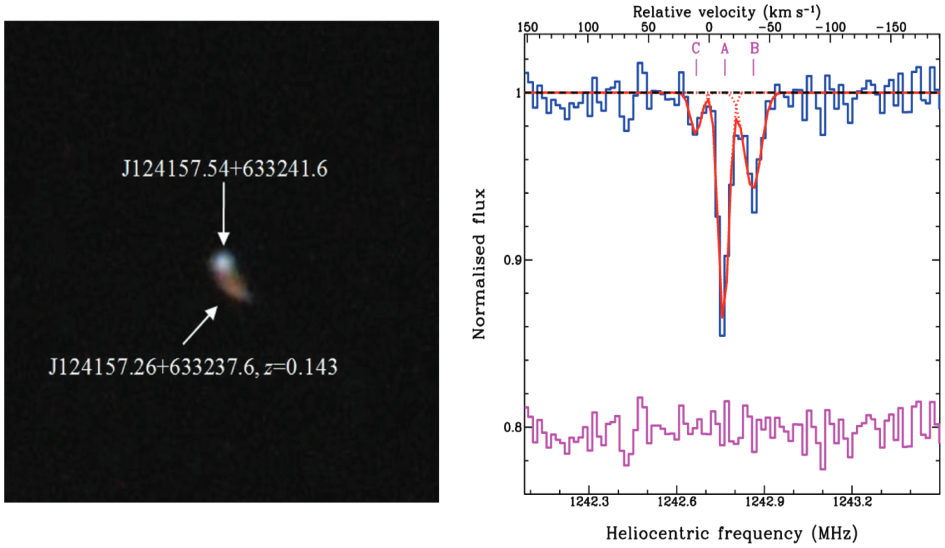

Figure 2: Colour representation of the quasar (z_q = 2.625 SDSS J124157.54+633241.6) galaxy (z_g=0.143 SDSS J124157.26+633237.6) pair. The image is 77 arcsec on a side, with north-east towards the top left corner, and centred on the QSO. Also shown is the 21-cm absorption detected from the foreground galaxy (Gupta et al. 2010).

21-cm absorption from gas pre-selected by the presence of a DLA or strong Mg II absorption (e.g. Briggs & Wolfe, 1983; Kanekar et al. 2003, 2009, 2014; Gupta et al. 2009, 2012; Srianand et al. 2010, 2012). Recently, there have also been searches towards sight lines selected on the basis of presence of low-z (z<0.3) galaxies at low impact parameters (<20 kpc ; Fig. 2; e.g. Gupta et al. 2010, 2013; Borthakur at el. 2010; Dutta et al. 2016). Overall, about 50 intervening 21-cm absorbers at z <3.5 are known. The detection rates are generally small (10-20%), and the results imply that atomic gas in high-z ($z > 2$) DLAs is predominantly constituted by the warm neutral medium. Fig. 3 shows the number per unit redshift range of 21-cm absorbers over 0< z <3.5 measured using 21-cm absorption searches based on DLAs and Mg II systems (Gupta et al. 2012).

While these observations have advanced our understanding of the physical state of atomic gas in distant galaxies, the sample sizes and number of detections have been very small. In addition, the searches in different ranges have been based on samples of different atomic or ionic species which complicates the overall interpretation. For example, the samples at $z > 2$ are based on the DLAs whereas at $0.3 < z < 2$ on the Mg II systems which selects both the DLAs and sub-DLAs, and at $z < 0.3$ on the basis of galaxy impact parameter. It is also well known that the optical spectroscopic surveys such as SDSS are performed after the color selection of QSO candidates and are biased against the dusty sight lines that are relevant for the cold atomic and molecular absorption lines that can be searched at radio wavelengths (e.g., Carilli et al. 1998). Therefore, radio absorption line surveys based on the samples of optical absorption lines provide a very incomplete view of the evolution of the cold atomic and molecular gas in the galaxies. The blind searches of radio absorption lines are required to overcome this barrier and eliminate the biases due to the pre-selection based on different atomic/ionic species. Such large spectroscopic surveys will be possible with the upcoming Square Kilometre Array (SKA) Pathfinders such as APERTIF, ASKAP, JVLA, MeerKAT and uGMRT.

3 Upcoming surveys and future prospects

Taking advantage of large instantaneous bandwidths, large field-of-view and RFI-free environment, several blind 21-cm absorption line searches are planned at various SKA pathfinders. For example, the

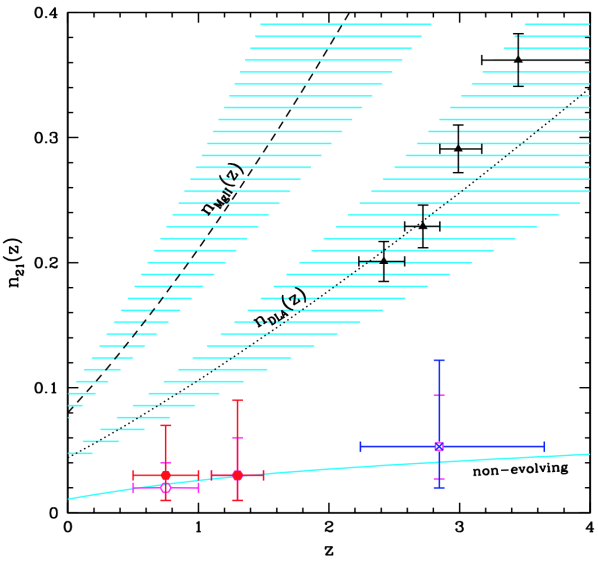

Figure 3: Number of 21-cm absorbers per unit redshift range, n_{21}(z). Open circles are for no correction for partial coverage implied by VLBI maps. Filled circles correspond to n_{21} after the optical depths have been corrected for partial coverage. The n_{21} based on DLAs at $z > 2$ are plotted as squares and crosses with the latter corresponding to values after correcting for partial coverage. The curve for non-evolving population of 21-cm absorbers normalized at n_{21} (z = 1.3) is also plotted. Lines and dashed areas show the number of absorbers per unit redshift for DLAs (Rao et al. 2006, dotted line) and strong Mg II absorbers (Prochter et al. 2006, dashed line). Triangles are the number per unit redshift of DLAs measured from the sample of Noterdaeme et al. (2009).

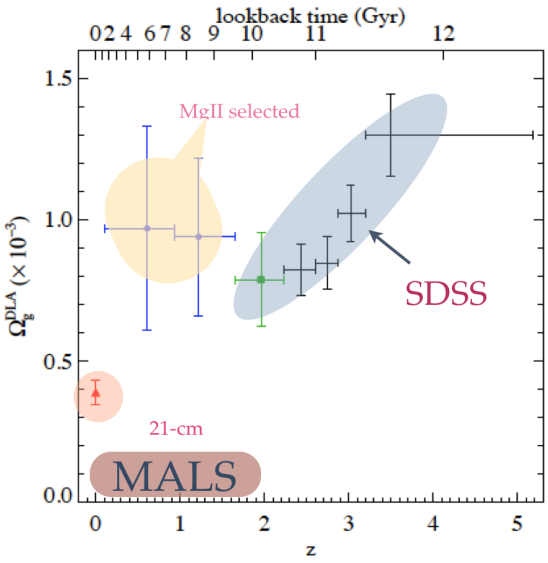

Figure 4: Plot showing redshift coverage of the MeerKAT Absorption Line Survey (MALS). Also shown are the constraints on H I mass density based on 21-cm emission ($z \sim 0$), Mg II based DLA searches ($0.3 < z < 1.5$), and DLAs ($z > 2$). MALS will trace the evolution of cold gas in galaxies over $0 < z < 1.5$

MeerKAT Absorption Absorption Line Survey (MALS[1]; PIs: N. Gupta and R. Srianand) will carry out the most sensitive search of 21-cm and OH absorption line over $0< z <1.8$, the redshift range over which most of the evolution in the SFRD takes place (Fig. 4). Along with the detection of several hundred 21-cm absorbers, the following breakthroughs are expected:

- Reliable measurement of the number density of 21-cm absorbers per unit redshift i.e. CNM filling factor and its evolution at $0 \leq z \leq 1.5$.
- Measurement of the number density per unit redshift of OH absorbers over the redshift range $0 \leq z \leq 1.8$.
- Constraints on the redshift clustering of H I 21-cm and OH absorbers.
- Tightest constraints on the variation of fundamental constants of physics using radio absorption lines.
- Estimate the dust bias involved in the 21-cm searches towards optically selected radio sources.

The survey will also enable us (i) to probe the magnetic field in galaxies through Faraday rotation and Zeeman splitting, (ii) to study the properties of 21-cm and OH absorbers associated AGNs and (iii) to understand the systematics involved in 21-cm absorption surveys based on Mg II/DLA selection.

Similarly, ASKAP and APERTIF will take advantage of large field-of-views to cover much larger (but with less sensitivity) areas of the sky at $z < 0.3$ and $0.5< z <1$, respectively. While the principle targets of all these surveys is 21-cm absorption line, the surveys will also simultaneously carry out OH absorption line search, and thus provide constraint on both atomic and molecular gas properties of galaxies. The uGMRT with low-frequency coverage and much longer baselines will be able to extend these studies to high-redshifts ($z \sim 4$) and/or higher spatial resolution. Several hundred 21-cm absorbers are expected to be detected from these surveys.

Morganti et al. (2015) provide a list of potential surveys that can be carried out with SKA-mid and SKA-low (see also Kanekar & Briggs 2003). These surveys will enable 21-cm and OH absorption line searches upto $z < 8$, redshift measurements and hence discovery of high-z quasars which are otherwise

[1]http://public.ska.ac.za/meerkat/meerkat-large-survey-projects

unobservable at optical wavelengths, sub-arcsecond scale resolution spectroscopy of 21-cm and OH absorbers revealing the structure and gas physics at parsec scales. The SKA-India H I SWG is pursuing a wide range of astrophysical problems in this domain, and working actively to create an astronomical database for the community to study the ISM in galaxies using SKA-pathfinders, SKA1 and, also, supplement these with multi-wavelength datasets from various existing (e.g. SALT, NOT, VLT, etc) and eventually TMT, which Indian community will have direct access to.

References

Borthakur at el. 2010, ApJ, 713, 131

Briggs & Wolfe, 1983, ApJ, 268, 76

Carilli et al. 1998, ApJ, 494, 175

Catinella et al. 2015, MNRAS, 446, 3526

Dutta et al. 2016, MNRAS, 456, 4209

Gupta et al. 2009, MNRAS, 398, 201

Gupta et al. 2010, MNRAS, 408, 849

Gupta et al. 2012, A&A, 544, 21

Gupta et al. 2013, A&A, 558, 84

Heiles & Troland 2003, ApJ, 586, 1067

Kanekar et al. 2003, A&A, 399, 857

Kanekar et al. 2009, MNRAS, 396, 385

Kanekar et al. 2014, MNRAS, 438, 2131

Lah et al. 2007, MNRAS, 376, 1357

Leroy et al. 2008, AJ, 136, 2782

Madau & Dickinson 2014, ARA&A, 52, 415

Morganti et al. 2015, ASKA, ConfE, 134

Noterdaeme et al. 2009, A&A, 503, 765

Noterdaeme et al. 2012, A&A, 547, L1

Prochter et al. 2006, ApJ, 639, 766

Rao et al. 2006, ApJ, 636, 610

Srianand et al. 2010, MNRAS, 405, 1888

Srianand et al. 2010, MNRAS, 412, 651

Verheijen et al. 2007, ApJ, 668, L9

Wolfire et al. 2003, ApJ, 443, 152

Zwaan et al. 2005, MNRAS, 359, L30

Cosmology and Astrophysics Using the Post-reionization HI

Anjan Ananda Sen*[1], Tapomoy Guha Sarkar[2], Azam Hussain[1], Shruti Thakur[1], Aseem Paranjape[3], and Tirthankar Roy Choudhury[4]

[1] *Centre for Theoretical Physics, Jamia Millia Islamia, New Delhi-110025, India*
[2] *Department of Physics, Birla Institute of Technology and Science, Pilani, Rajasthan, 333031. India*
[3] *Inter-University Center for Astronomy & Astrophysics, Post Bag 4, Ganeshkhind, Pune 411007, India*
[4] *National Centre for Radio Astrophysics, TIFR, Post Bag 3, Ganeshkhind, Pune 411007, India*

Abstract

We discuss the prospects of using the redshifted 21 cm emission from neutral hydrogen in the post-reionization epoch to study cosmology and galaxy formation. The main aim of the article is to highlight the efforts of Indian scientists in this area with the SKA in mind. It turns out that the intensity mapping surveys from SKA can be instrumental in obtaining tighter constraints on the dark energy models. Cross-correlation of the HI intensity maps with the Lyα forest data can be useful in measuring the BAO scale. Finally, we also discuss the possibilities of studying HI within galaxies using HI galaxy surveys and cross correlating with optical data.

1 Introduction

The post-reionization ($z \lesssim 6$) evolution of neutral hydrogen (HI) is of great interest from the point of view of both galaxy formation as well as cosmology. After reionization, the bulk of HI is expected to reside in galaxies in the form of clumpy, self-shielded clouds (Wolfe et al., 1986; Lanzetta et al., 1991; Storrie-Lombardi and Wolfe, 2000; Gardner et al., 1997; Prochaska et al., 2005). The radio observations of the redshifted 21 cm line promise to be a powerful probe of HI, and it is expected that present and upcoming facilities like the GMRT[1], MeerKAT[2], CHIME[3] and SKA[4] would play important roles in this area.

The 21 cm line can used in various ways to study the HI. It is already being used extensively in detecting and studying absorption systems (e.g., DLAs) along lines of sight towards distant radio sources (e.g., see the article by Gupta and Dutta in this science book). These studies are complementary to those done using UV / optical telescopes (Noterdaeme et al., 2012; Prochaska and Wolfe, 2009; Prochaska et al., 2005; Zafar et al., 2013). An alternate way is to detect the HI in emission. The most standard method is to detect individual galaxies in HI through the so called HI galaxy redshift surveys (Barnes et al., 2001; Meyer et al., 2004; Zwaan et al., 2005; Jaffé et al., 2012; Rhee et al., 2013; Giovanelli et al., 2005; Martin et al., 2010; Catinella et al., 2010; Lah et al., 2007, 2009). An alternate way is to detect only the integrated HI emission of galaxies at each sky location without attempting to resolve the individual objects, a technique known as HI intensity mapping (Bharadwaj and Sethi, 2001; Chang et al., 2010; Masui et al., 2013; Switzer et al., 2013).

This article focuses mainly on Indian interests related to studying cosmology and galaxy formation using HI emission in the post-reionization universe. The main science cases which have been considered here are (i) the constraints on dark energy using HI intensity mapping experiments, (ii) measuring the BAO using the cross correlation of intensity mapping and Lyα forest and (iii) probing galaxy formation through cross correlating HI galaxy surveys with the optical surveys.

*anjsen@gmail.com
[1] http://gmrt.ncra.tifr.res.in/
[2] http://www.ska.ac.za/meerkat/
[3] http://chime.phas.ubc.ca
[4] https://www.skatelescope.org

2 Dark energy constraints from intensity mapping experiments

The large-scale clustering of the HI in the post-reionization epoch is expected to directly probe the nature of dark energy through the imprints of a given model on the background evolution and growth of structures. As a direct probe of cosmological structure formation, 21-cm intensity mapping may allow us to distinguish between dark energy models which areotherwise degenerate at the level of their prediction of background evolution.

2.1 Constraints from angular power spectra

We start with a general interacting picture where the DE scalar field is coupled to the DM sector of the Universe. The visible matter sector (baryons) is not coupled with the DE scalar field. There has been numerous studies in the literature on such "*Coupled Quintessence*" (Amendola, 2000, 2004) models. Here we also follow the same formalism. The relevant equations are given below (Hussain et al., 2016):

$$\begin{aligned} \ddot{\phi} + \frac{dV}{d\phi} + 3H\dot{\phi} &= C(\phi)\rho_d \\ \dot{\rho_d} + 3H(\rho_d) &= -C(\phi)\rho_d\dot{\phi} \\ \dot{\rho_b} + 3H(\rho_b) &= 0 \end{aligned} \tag{1}$$

$$H^2 = \frac{\kappa^2}{3}(\rho_b + \rho_d + \rho_\phi). \tag{2}$$

This is complemented by the flatness condition

$$1 = \frac{\kappa^2\rho_b}{3H^2} + \frac{\kappa^2\rho_d}{3H^2} + \frac{\kappa^2\dot{\phi}^2}{6H^2} + \frac{\kappa^2 V(\phi)}{3H^2} \tag{3}$$

Here $C(\phi)$ represents coupling parameter between the scalar field and dark matter. Subscript "d" represents the DM sector and subscript "b" represents the baryonic sector. The details of the physics for the interaction between the dark energy and the dark matter is largely unknown. In view of this, we assume phenomenologically $C(\phi)$ to be a constant in our subsequent calculations. This is similar to the earlier work by Amendola (Amendola, 2000, 2004) and collaborators on coupled quintessence. For $C = 0$ we recover the uncoupled case,hence the system allows us to study both coupled and uncoupled cases. Hence the set up allows to study both the coupled and uncoupled case.

To study the growth of matter fluctuations in the linear regime, we work in the longitudinal gauge (Hussain et al., 2016):

$$ds^2 = a^2\left[-(1+2\Phi)d\tau^2 + (1-2\Psi)dx^i dx_i\right], \tag{4}$$

where τ is the conformal time and Φ and Ψ are the two gravitational potentials. In the absence of any anisotropic stress $\Phi = \Psi$.

We write the equations for the perturbations in dark matter density in the Newtonian limit. This is valid assumption for sub horizon scales. In these scales, one can safely ignore the clustering in the scalar field. Under these assumptions, the linearized equations governing the growth of fluctuations in dark matter is given by:

$$\delta_d'' + \left(1 + \frac{\mathcal{H}'}{\mathcal{H}} - 2\beta_d x\right)\delta_d' - \frac{3}{2}(\gamma_{dd}\delta_d\Omega_d) = 0. \tag{5}$$

The prime denotes differentiation w.r.t to $\log a$. x is given by equation (4). Here $\beta_d = W$, $\gamma_{dd} = 1 + 2\beta_d^2$, $\mathcal{H}$ is the conformal Hubble parameter $\mathcal{H} = aH$ and δ_d is the linear density contrast for the DM. We solve the equation with the initial conditions $\delta_d \sim a$ and $\frac{d\delta_d}{da} = 1$ at decoupling $a \sim 10^{-3}$. This is valid since the universe is matter-dominated at the epoch of decoupling. We take the Fourier transform of the above equation and define the linear growth function D_d and the linear growth rate f_d as

$$\delta_{dk}(a) \equiv D_d(a)\delta_{dk}^{ini} \tag{6}$$

$$f_d = \frac{d\ln D_d}{d\ln a}. \tag{7}$$

The linear dark matter power spectrum defined as

$$P(k,z) = A_0 k^{n_s} T^2(k) D_{dn}^2(z). \tag{8}$$

Here A_0 is the normalization constant fixed by σ_8 normalization, n_s is spectral index for the primordial density fluctuations generated through inflation, $D_{dn}(z)$ is growth function normalized such as it is equal to unity at $z = 0$ i.e. $D_{dn}(z) = \frac{D_d(z)}{D_d(0)}$ and $T(k)$ is the transfer function as prescribed by Eisenstein and Hu (Eisenstein and Hu, 1999).

The neutral hydrogen (HI) distribution in post-reionization epoch is modeled by a mean neutral fraction $\bar{x}_{\rm HI}$ which remains constant over a wide redshift range $z \leq 6$ (Storrie-Lombardi et al., 1996; P'eroux et al., 2003) and a linear bias parameter b_T which relates the HI fluctuations to the fluctuations in the underlying dark matter distributions (Bagla et al., 2010; Guha Sarkar et al., 2012). The quantity of interest is the fluctuation of the excess HI 21 cm brightness temperature δT_b. If the peculiar velocities of the gas are sourced by dark matter over densities then the angular power spectrum of the brightness temperature in the flat sky limit is given by (Datta et al., 2007)

$$C_l = \frac{\bar{T}^2 \bar{x}_{HI}^2 b_T^2}{\pi r^2} \int_0^\infty dk_\parallel \; (1 + \beta\mu^2)^2 \; P(k,z) \tag{9}$$

where $P(k,z)$ is the dark matter power spectrum defined in equation (12), $k = \sqrt{k_\parallel^2 + \frac{l^2}{r^2}}$, $\mu = \frac{k_\parallel}{k}$ and $\beta = \frac{f_d(z)}{b_T}$ with $f_d(z)$ is the growth factor for dark matter defined in equation (11). Here r is the comoving distance upto redshift z and the average brightness temperature $\bar{T}$ is given by

$$\bar{T}(z) = 4.0{\rm mK}(1+z)^2 \left(\frac{\Omega_{b0}h^2}{0.02}\right)\left(\frac{0.7}{h}\right)\left(\frac{H_0}{H(z)}\right). \tag{10}$$

We adopt the value of $\Omega_{HI} = 10^{-3}$ at $z < 3.5$. This yields $\bar{x}_{HI} = 2.45 \times 10^{-2}$ which is assumed to be constant across the redshift range of our interest.

2.2 Results

We consider a radio interferometric measurement of the power spectrum of the 21 cm brightness temperature. The directly measured 'Visibility' is a function of frequency ν and baseline $\mathbf{U} = \mathbf{k}_\perp r/2\pi$ and allows us to compute the angular power spectrum C_l directly using Visibility-Visibility correlation (Bharadwaj and Ali, 2005) with the association $l = 2\pi U$.

The noise in the measurement of angular power spectrum comes from cosmic variance on small scales and instrument noise on smalls scales. We have

$$\Delta C_l = \sqrt{\frac{2}{(2l+1)\Delta l f_{sky} N_p}} \, (C_l + N_l) \tag{11}$$

where N_p denotes the number of pointings of the radio interferometer, f_{sky} is the fraction of sky observed in a single pointing, and Δl is the width of the l bin.

We consider a radio interferometer with parameters roughly following the specifications of SKA1-mid [5]. The fiducial redshift $z = 1.5$ corresponds to an observing frequency of 568MHz which falls in the band of frequencies to be probed by SKA1-mid. We consider a frequency bandwidth of 32MHz around the central frequency. The array is assumed to be composed of 200 dishes each of diameter 15m. The antennae are distributed in a manner such that 75% of the dishes are within 2.5Km radius and the density of antennae are assumed to fall off radially as r^{-2}. We also use $T_{syst} = 180\left(\frac{\nu}{180{\rm MHz}}\right)^{-2.6}$ K. in our error estimates. With this we calculate the error bar ΔC_l for SKA1-mid assuming a fiducial ΛCDM model with $\Omega_\Lambda = 0.7$, $\Omega_{b0} = 0.05$, $n_s = 1$, $h = 0.7$ and $\sigma_8 = 0.8$. We also fix the constant linear bias to be 1.0 at the fiducial redshift from numerical simulations of the 21cm signal. For detail derivation of the noise, we refer readers to (Hussain et al., 2016).

[5] http://www.skatelescope.org/wp-content/uploads/2012/07/SKA-TEL-SKO-DD-001-1_BaselineDesign1.pdf

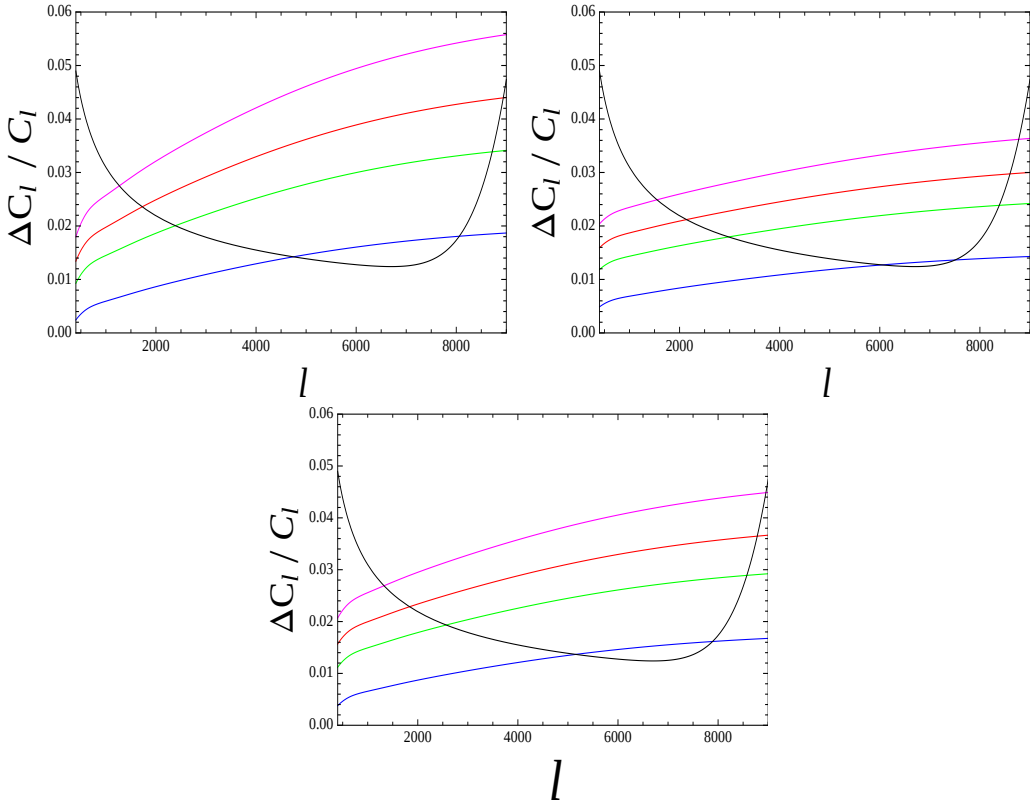

Figure 1: (*left*) The relative difference of the 21-cm angular power spectrum from the fiducial ΛCDM at a redshift $z = 1.5$. $(W = 0.04, \lambda_i = 0.5)$, $(W = 0.05, \lambda_i = 0.5)$, $(W = 0.06, \lambda_i = 0.5)$, $(W = 0.07, \lambda_i = 0.5)$, $(W = 0.08, \lambda_i = 0.5)$ from bottom to top for linear potential $V \sim \phi$. $\Omega_{m0} = 0.3$ for all the plots. The black line corresponds to the noise level with SKA1-mid like telescope assuming the fiducial ΛCDM value model. (*right and bottom*) Same as left but for inverse-squared and square potentials respectively. Figure taken from (Hussain et al., 2016).

In figure 1, we show the deviation of the dark energy models models from ΛCDM universe in terms of the angular power spectra for HI intensity mapping for three different potentials. It is clearly visible that most of these models can be ruled out in comparison with ΛCDM model with future SKA1-mid data in an intermediate multipole region around $l \sim 7000$ at a 2σ to 5σ confidence level (Hussain et al., 2016). We should stress that all these models are statistically indistinguishable at the level of their predictions about background evolution. Yet the future SKA measurements can potentially distinguish these models from ΛCDM with significant confidence level.

Also if we put $W = 0$ in all these cases, the fractional difference with ΛCDM will be much less than the error bar and can not be distinguished at all from ΛCDM with future survey like SKA1-mid.

3 Constraints from BAO measurements using different diagnostics

Primordial cosmological density fluctuations drive acoustic waves in the cosmological baryon-photon plasma which gets frozen once recombination takes place at about $z \sim 1000$. This leaves a distinct oscillatory signature on the CMBR temperature anisotropy power spectrum (Peebles and Yu, 1970). The sound horizon at the epoch of recombination sets a standard ruler that maybe used to calibrate cosmological distances. Baryons contribute to 15% of the total matter budget, and the baryon acoustic

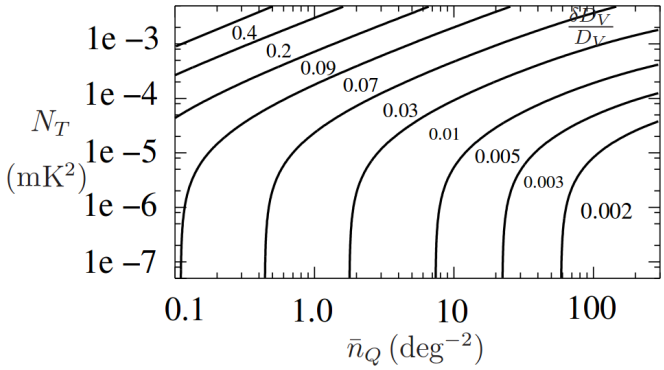

Figure 2: The error contours for the distance measure.

oscillations (BAO) are hence also imprinted in the late time clustering of non-relativistic matter. The baryon acoustic oscillation (BAO) is a powerful probe of cosmological parameters (Seo and Eisenstein, 2003). Measuring BAO signal allows us to measure the angular diameter distance D_A and the Hubble parameter $H(z)$ as functions of redshift using the the transverse and the longitudinal oscillations respectively. These provide means for placing strong constraints on dark energy models. The cross-correlation of the Ly-α forest and redshifted 21-cm emission from the post-reionization epoch is believed to be a tool for mapping out the large-scale structures for redshifts $z \leq 6$. This mitigates several observational issues like foreground subtraction which poses serious challenge towards detecting the 21-cm signal. The possibility of detecting the BAO signal with the cross-correlation signal is investigated (Sarkar and Bharadwaj, 2013).

For the Ly-α forest survey, we have considered typical surveys like BOSS and BIGBOSS which are expected have a high number density of quasars of 16 deg^{-2} and 64 deg^{-2} respectively. We find that it is necessary to achieve a noise level of 1.1×10^{-5} mK^2 and 6.25×10^{-6} mK^2 per field of view in the redshifted 21-cm observations to detect the angular and radial BAO respectively with BOSS at a redshift $z = 2.5$. The corresponding noise levels are 3.3×10^{-5} mK^2 and 1.7×10^{-5} mK^2 for BIGBOSS. These noise levels should be attainable by 100 hrs observations in 100 pointings with SKA1-mid roughly covering the full sky coverage of BOSS. It is possible to measure the distance measure D_V with $D_V^3 = (1+z)^2 D_A(z) cz/H(z)$ at $\delta D_V/D_V = 2\%$ from the cross-correlation signal with $N_T = 3 \times 10^{-4}$ mK^2. We have $(\delta D_V/D_V, \delta D_A/D_A, \delta H/H) = (1.3, 1.5, 1.3)\%$ and $(0.67, 0.78, 0.74)\%$ at $N_T = 10^{-4}$mK^2 and $N_T = 10^{-5}$mK^2 at the fiducial redshift $z = 2.5$.

4 Studying HI in galaxies using the SKA and optical observations

As we have seen in the previous two sections, the large-scale distribution of HI can be a useful tool for studying cosmology. On the other hand, understanding the mechanisms that decide how HI is distributed in galaxies would help understand the galaxy formation process. For example, such studies would yield clues into the processes that determine star formation across galaxy groups, a question that has gained particular interest recently in the context of the so-called 'galactic conformity' observed in SDSS groups (Weinmann et al., 2006; Knobel et al., 2015; Kauffmann et al., 2013), which also shows hints of extending to the HI distribution in galaxies (Wang et al., 2015). Interestingly, modelling the cross talk between galaxy properties and HI can help in forecasting the ability of experiments such as the SKA to extract cosmological information through probes such as intensity mapping (Padmanabhan et al., 2015; Seehars et al., 2016; Padmanabhan et al., 2016). In particular, such modelling will help us understand the constraining power of cross-correlation studies using the SKA and optical instruments such as the HSC

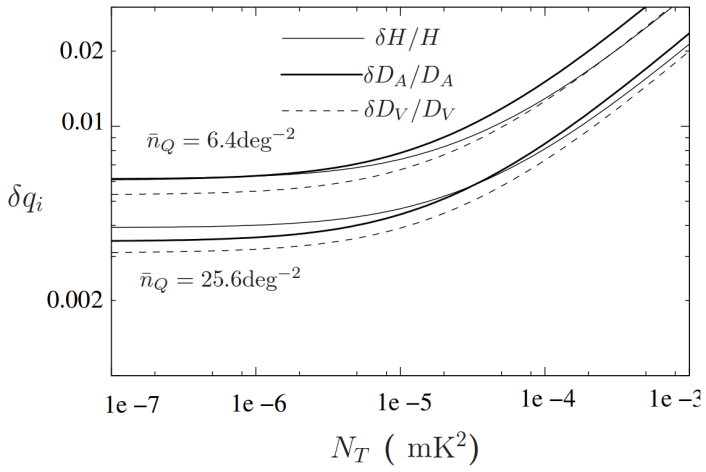

Figure 3: Error prediction for BOSS and BIGBOSS

(Subaru)[6], LSST[7], Euclid[8], TMT[9] in addressing cosmological questions such as the nature of dark energy and dark matter, neutrino masses, etc.

There has already been significant developments in modelling the HI distribution, e.g., semi-analytical models (SAMs) with multiple prescriptions for winds (Davé et al., 2013), SAMs with photoionisation feedback (Kim et al., 2015, 2016), simulations with AGN feedback (Villaescusa-Navarro et al., 2016), etc. A complementary approach, which we propose to attempt, would be to first model the low-z HOD by cross correlating existing observations of HI and optical. This would involve using the scaling relations from surveys like the GASS (Catinella et al., 2010). The model should then be able to predict the HI clustering, particularly at small scales, and also be useful for studying HI conformity if it exists. In addition, it can be used for predicting the HOD at higher redshifts which would be probed in the near future, e.g., by cross correlating the HI galaxy survey from SKA with other telescopes like Euclid.

5 Summary

The 21 cm line from HI in the post-reionization universe can be a strong probe of cosmology and galaxy formation. In this article, we have discussed predictions and forecasts for probing a large class of scalar field dark energy models using angular power spectra for the intensity mapping from SKA. The intensity mapping experiments can be useful in probing the BAO too, in particular, when the data is cross correlated with Lyα forest experiments like the BIGBOSS. Finally, we have discussed the possibility of understanding the distribution of HI within galaxies using the cross correlation of HI galaxy surveys with the optical and thus look for insights in galaxy formation.

The main difficulty in detecting the cosmological redshifted 21-cm signal is the presence of astrophysical foregrounds from galactic and extra galactic sources that are several orders of magnitude larger than the signal. One thus requires a very careful subtraction of these foregrounds before a statistical detection of the cosmological signal can be confirmed. In this sense, the cross-correlation studies discussed here are expected to be more efficient in dealing with the experimental systematics. The future thus looks promising with a number of facilities (SKA, Euclid, LSST) expected to be active in different wave bands.

[6]http://www.naoj.org/Projects/HSC/
[7]http://www.lsst.org/
[8]http://sci.esa.int/euclid/
[9]http://www.tmt.org/

References

Amendola, L.: 2000, *Phys. Rev. D* **62(4)**, 043511

Amendola, L.: 2004, *Phys. Rev. D* **69(10)**, 103524

Bagla, J. S., Khandai, N., and Datta, K. K.: 2010, *Mon. Not. Roy. Ast. Soc.* **407**, 567

Barnes, D. G., Staveley-Smith, L., de Blok, W. J. G., Oosterloo, T., Stewart, I. M., Wright, A. E., Banks, G. D., Bhathal, R., Boyce, P. J., Calabretta, M. R., Disney, M. J., Drinkwater, M. J., Ekers, R. D., Freeman, K. C., Gibson, B. K., Green, A. J., Haynes, R. F., te Lintel Hekkert, P., Henning, P. A., Jerjen, H., Juraszek, S., Kesteven, M. J., Kilborn, V. A., Knezek, P. M., Koribalski, B., Kraan-Korteweg, R. C., Malin, D. F., Marquarding, M., Minchin, R. F., Mould, J. R., Price, R. M., Putman, M. E., Ryder, S. D., Sadler, E. M., Schröder, A., Stootman, F., Webster, R. L., Wilson, W. E., and Ye, T.: 2001, *Mon. Not. Roy. Ast. Soc.* **322**, 486

Bharadwaj, S. and Ali, S. S.: 2005, *Mon. Not. Roy. Ast. Soc.* **356**, 1519

Bharadwaj, S. and Sethi, S. K.: 2001, *Journal of Astrophysics and Astronomy* **22**, 293

Catinella, B., Schiminovich, D., Kauffmann, G., Fabello, S., Wang, J., Hummels, C., Lemonias, J., Moran, S. M., Wu, R., Giovanelli, R., Haynes, M. P., Heckman, T. M., Basu-Zych, A. R., Blanton, M. R., Brinchmann, J., Budavári, T., Gonçalves, T., Johnson, B. D., Kennicutt, R. C., Madore, B. F., Martin, C. D., Rich, M. R., Tacconi, L. J., Thilker, D. A., Wild, V., and Wyder, T. K.: 2010, *Mon. Not. Roy. Ast. Soc.* **403**, 683

Chang, T.-C., Pen, U.-L., Bandura, K., and Peterson, J. B.: 2010, *Nature* **466**, 463

Datta, K. K., Choudhury, T. R., and Bharadwaj, S.: 2007, *Mon. Not. Roy. Ast. Soc.* **378**, 119

Davé, R., Katz, N., Oppenheimer, B. D., Kollmeier, J. A., and Weinberg, D. H.: 2013, *Mon. Not. Roy. Ast. Soc.* **434**, 2645

Eisenstein, D. J. and Hu, W.: 1999, *Astroph. J.* **511**, 5

Gardner, J. P., Katz, N., Hernquist, L., and Weinberg, D. H.: 1997, *Astroph. J.* **484**, 31

Giovanelli, R., Haynes, M. P., Kent, B. R., Perillat, P., Saintonge, A., Brosch, N., Catinella, B., Hoffman, G. L., Stierwalt, S., Spekkens, K., Lerner, M. S., Masters, K. L., Momjian, E., Rosenberg, J. L., Springob, C. M., Boselli, A., Charmandaris, V., Darling, J. K., Davies, J., Garcia Lambas, D., Gavazzi, G., Giovanardi, C., Hardy, E., Hunt, L. K., Iovino, A., Karachentsev, I. D., Karachentseva, V. E., Koopmann, R. A., Marinoni, C., Minchin, R., Muller, E., Putman, M., Pantoja, C., Salzer, J. J., Scodeggio, M., Skillman, E., Solanes, J. M., Valotto, C., van Driel, W., and van Zee, L.: 2005, *Astron. J.* **130**, 2598

Guha Sarkar, T., Mitra, S., Majumdar, S., and Choudhury, T. R.: 2012, *Mon. Not. Roy. Ast. Soc.* **421**, 3570

Hussain, A., Thakur, S., Sarkar, T. G., and Sen, A. A.: 2016

Jaffé, Y. L., Poggianti, B. M., Verheijen, M. A. W., Deshev, B. Z., and van Gorkom, J. H.: 2012, ApJ **756**, L28

Kauffmann, G., Li, C., Zhang, W., and Weinmann, S.: 2013, *Mon. Not. Roy. Ast. Soc.* **430**, 1447

Kim, H.-S., Wyithe, J. S. B., Baugh, C. M., Lagos, C. d. P., Power, C., and Park, J.: 2016, *ArXiv e-prints*

Kim, H.-S., Wyithe, J. S. B., Power, C., Park, J., Lagos, C. d. P., and Baugh, C. M.: 2015, *Mon. Not. Roy. Ast. Soc.* **453**, 2315

Knobel, C., Lilly, S. J., Woo, J., and Kovač, K.: 2015, *Astroph. J.* **800**, 24

Lah, P., Chengalur, J. N., Briggs, F. H., Colless, M., de Propris, R., Pracy, M. B., de Blok, W. J. G., Fujita, S. S., Ajiki, M., Shioya, Y., Nagao, T., Murayama, T., Taniguchi, Y., Yagi, M., and Okamura, S.: 2007, *Mon. Not. Roy. Ast. Soc.* **376**, 1357

Lah, P., Pracy, M. B., Chengalur, J. N., Briggs, F. H., Colless, M., de Propris, R., Ferris, S., Schmidt, B. P., and Tucker, B. E.: 2009, *Mon. Not. Roy. Ast. Soc.* **399**, 1447

Lanzetta, K. M., Wolfe, A. M., Turnshek, D. A., Lu, L., McMahon, R. G., and Hazard, C.: 1991, ApJS **77**, 1

Martin, A. M., Papastergis, E., Giovanelli, R., Haynes, M. P., Springob, C. M., and Stierwalt, S.: 2010, *Astroph. J.* **723**, 1359

Masui, K. W., Switzer, E. R., Banavar, N., Bandura, K., Blake, C., Calin, L.-M., Chang, T.-C., Chen, X., Li, Y.-C., Liao, Y.-W., Natarajan, A., Pen, U.-L., Peterson, J. B., Shaw, J. R., and Voytek, T. C.: 2013, ApJ **763**, L20

Meyer, M. J., Zwaan, M. A., Webster, R. L., Staveley-Smith, L., Ryan-Weber, E., Drinkwater, M. J., Barnes, D. G., Howlett, M., Kilborn, V. A., Stevens, J., Waugh, M., Pierce, M. J., Bhathal, R., de Blok, W. J. G., Disney, M. J., Ekers, R. D., Freeman, K. C., Garcia, D. A., Gibson, B. K., Harnett, J., Henning, P. A., Jerjen, H., Kesteven, M. J., Knezek, P. M., Koribalski, B. S., Mader, S., Marquarding, M., Minchin, R. F., O'Brien, J., Oosterloo, T., Price, R. M., Putman, M. E., Ryder, S. D., Sadler, E. M., Stewart, I. M., Stootman, F., and Wright, A. E.: 2004, *Mon. Not. Roy. Ast. Soc.* **350**, 1195

Noterdaeme, P., Petitjean, P., Carithers, W. C., Pâris, I., Font-Ribera, A., Bailey, S., Aubourg, E., Bizyaev, D., Ebelke, G., Finley, H., Ge, J., Malanushenko, E., Malanushenko, V., Miralda-Escudé, J., Myers, A. D., Oravetz, D., Pan, K., Pieri, M. M., Ross, N. P., Schneider, D. P., Simmons, A., and York, D. G.: 2012, A&A **547**, L1

Padmanabhan, H., Choudhury, T. R., and Refregier, A.: 2015, *Mon. Not. Roy. Ast. Soc.* **447**, 3745

Padmanabhan, H., Choudhury, T. R., and Refregier, A.: 2016, *Mon. Not. Roy. Ast. Soc.* **458**, 781

Peebles, P. J. E. and Yu, J. T.: 1970, *Astrophys. J.* **162**, 815

P'eroux, C., McMahon, R. G., Storrie-Lombardi, L. J., and Irwin, M. J.: 2003, *Mon. Not. Roy. Ast. Soc.* **346**, 1103

Prochaska, J. X., Herbert-Fort, S., and Wolfe, A. M.: 2005, *Astroph. J.* **635**, 123

Prochaska, J. X. and Wolfe, A. M.: 2009, *Astroph. J.* **696**, 1543

Rhee, J., Zwaan, M. A., Briggs, F. H., Chengalur, J. N., Lah, P., Oosterloo, T., and van der Hulst, T.: 2013, *Mon. Not. Roy. Ast. Soc.* **435**, 2693

Sarkar, T. G. and Bharadwaj, S.: 2013, *JCAP* **1308**, 023

Seehars, S., Paranjape, A., Witzemann, A., Refregier, A., Amara, A., and Akeret, J.: 2016, J. Cosmology Astropart. Phys. **3**, 001

Seo, H.-J. and Eisenstein, D. J.: 2003, *Astrophys. J.* **598**, 720

Storrie-Lombardi, L. J., McMahon, R. G., and Irwin, M. J.: 1996, *Mon. Not. Roy. Ast. Soc.* **283**, L79

Storrie-Lombardi, L. J. and Wolfe, A. M.: 2000, *Astroph. J.* **543**, 552

Switzer, E. R., Masui, K. W., Bandura, K., Calin, L.-M., Chang, T.-C., Chen, X.-L., Li, Y.-C., Liao, Y.-W., Natarajan, A., Pen, U.-L., Peterson, J. B., Shaw, J. R., and Voytek, T. C.: 2013, *Mon. Not. Roy. Ast. Soc.* **434**, L46

Villaescusa-Navarro, F., Planelles, S., Borgani, S., Viel, M., Rasia, E., Murante, G., Dolag, K., Steinborn, L. K., Biffi, V., Beck, A. M., and Ragone-Figueroa, C.: 2016, *Mon. Not. Roy. Ast. Soc.* **456**, 3553

Wang, E., Wang, J., Kauffmann, G., Józsa, G. I. G., and Li, C.: 2015, *Mon. Not. Roy. Ast. Soc.* **449**, 2010

Weinmann, S. M., van den Bosch, F. C., Yang, X., and Mo, H. J.: 2006, *Mon. Not. Roy. Ast. Soc.* **366**, 2

Wolfe, A. M., Turnshek, D. A., Smith, H. E., and Cohen, R. D.: 1986, ApJS **61**, 249

Zafar, T., Péroux, C., Popping, A., Milliard, B., Deharveng, J.-M., and Frank, S.: 2013, A&A **556**, A141

Zwaan, M. A., Meyer, M. J., Staveley-Smith, L., and Webster, R. L.: 2005, *Mon. Not. Roy. Ast. Soc.* **359**, L30

The redshifted HI 21 cm signal from the post-reionization epoch: Cross-correlations with other cosmological probes

T. Guha Sarkar*[1], K. K. Datta[2], A. K. Pal[1], T. Roy Choudhury[3], and S. Bharadwaj[4]

[1] *Department of Physics, Birla Institute of Technology and Science, Pilani 333031, India.*
[2] *Department of Physics,Presidency University, Kolkata, India.*
[3] *National Centre for Radio Astrophysics, Pune, India.*
[4] *Department of Physics, Indian Institute of Technology Kharagpur, India.*

Abstract

Intensity mapping of the H I distribution using the redshifted 21 cm observations opens up a new window towards our understanding of cosmological background evolution and structure formation. This is a key science goal of several upcoming radio telescopes including the Square Kilometer Array (SKA). In this article we focus on the post-reionization signal and investigate the of cross correlating the 21 cm signal with other tracers of the large scale structure. We consider the cross-correlation of the post-reionization 21 cm signal with the Lyman-α forest, Lyman-break galaxies and late time anisotropies in the CMBR maps like weak lensing and the Integrated Sachs Wolfe effect. We study the feasibility of detecting the signal and explore the possibility of obtaining constraints on cosmological models using it. In this review we summarise the work done by our group on the cross-correlation signals and the prospects for detection with the SKA1-mid.

1 Introduction

Intensity mapping of the neutral hydrogen (H I) distribution through observations of the redshifted 21-cm radiation is an important probe of cosmological evolution and structure formation in the post reionization epoch Bharadwaj & Sethi (2001); Wyithe & Loeb (2009); Loeb & Wyithe (2008); Chang et al. (2008). The epoch of reionization is believed to have completed by redshift $z \sim 6$ Fan et al. (2006). In the post-reionization era bulk of the HI gas are housed in the self shielded Damped Ly-α (DLA) systems. These DLA clouds are the predominant source of the HI 21-cm signal. Intensity mapping involves a low resolution imaging of collective HI 21-cm radiation background without resolving the individual DLAs. Such a tomographic imaging shall naturally yield enormous astrophysical and cosmological information regarding the large scale matter distribution, structure formation and expansion history of the background Universe in the post-reionization epoch Chang et al. (2008); Wyithe (2008); Bharadwaj et al. (2009); Camera et al. (2013); Bull et al. (2015). Several radio interferometric arrays like the Giant Metrewave Radio Telescope (GMRT) [1], the Ooty Wide Field Array (OWFA) Ali & Bharadwaj (2014), the Canadian Hydrogen Intensity Mapping Experiment (CHIME) [2], the Meer-Karoo Array Telescope (MeerKAT) [3], the Square Kilometer Array (SKA) [4] are aimed towards observing the cosmological background 21-cm radiation. Detecting the 21 cm signal, is however extremely challenging. This is primarily because of the large astrophysical foregrounds Santos et al. (2005); Di Matteo et al. (2002); Ghosh et al. (2010) from galactic and extra-galactic sources which are several order of magnitude greater than the signal .

Cross-correlating the 21 cm signal with other probes may mitigate the severe effect of foreground contaminants and other systematics which plagues the signal. The main advantage of cross-correlation

*tapomoy1@gmail.com
[1] http://gmrt.ncra.tifr.res.in/
[2] http://chime.phas.ubc.ca/
[3] http://www.ska.ac.za/meerkat/
[4] https://www.skatelescope.org/

is that the cosmological origin of the signal can be ascertained only if it is detected with statistical significance in cross- correlation. Cosmological parameter estimation often involves a joint analysis of two data sets and this would involve not only the auto-correlation but also the cross-correlation information. Further, the two independent probes may focus on specific Fourier modes with high signal to noise ratio and in such cases the cross-correlation signal takes advantage of both the probes simultaneously. This has been studied in the context of BAO (Guha Sarkar & Bharadwaj, 2013). It is to be noted that if the observations of the independent probes are perfect, there shall be no advantage of using the cross correlation. However, we expect the first generation measurements of the redshifted HI 21 cm signal to have large systematic errors and foreground residuals. For a detection of the 21 cm signal and subsequent cosmological investigations these measurements can be cross-correlated with other tracers of large scale structure to yield information from the 21 cm signal which may not be possible with the low SNR auto correlation signal. In this article we consider the cross-correlation of the 21 cm signal with the Ly-α flux distribution. On large scales both the Ly-α forest absorbed flux and the redshifted 21-cm signal are, believed to be biased tracers of the underlying dark matter (DM) distribution McDonald (2003); Bagla et al. (2010); Guha Sarkar et al. (2012); Villaescusa-Navarro et al. (2014). The clustering property of these signals, is then, directly related to the dark matter power spectrum. We investigate the possibility of using the cross-correlation of the 21-cm signal and the Ly-α forest for cosmological parameter estimation, neutrino mass measurement, studying BAO features and primordial bispectrum. We also investigate the possibility of correlating the post-reionization 21-cm signal with CMBR maps like the weak lensing and ISW anisotropies.

2 Cross-correlation between cosmological signals (General Formalism)

Consider two cosmological fields $A(\mathbf{k})$ and $B(\mathbf{k})$. These could, for example represent two tracers of large scale structure. We define the cross correlation estimator $\hat{E}$ as

$$\hat{E} = \frac{1}{2} \left[AB^* \ + \ BA^* \right] \tag{1}$$

We note that A and B can be complex fields. We are interested in the variance

$$\sigma^2_{\hat{E}} = \langle \hat{E}^2 \rangle - \langle \hat{E} \rangle^2 \tag{2}$$

Noting that $\langle A(\mathbf{k}) \ A(\mathbf{k}) \rangle = \langle A(\mathbf{k}) \ A^*(-\mathbf{k}) \rangle = 0$, we have

$$\langle \hat{E}^2 \rangle = \frac{1}{2} \left[\langle AA^* \rangle \langle BB^* \rangle \ + \ |\langle AB \rangle|^2 \ + \ 3 \, |\langle AB^* \rangle|^2 \right] \tag{3}$$

Further, the term $\langle AB \rangle$ can be dropped since

$$\langle A(\mathbf{k}) \ B(\mathbf{k}) \rangle = \langle A(\mathbf{k}) \ B^*(-\mathbf{k}) \rangle = C\delta_{\mathbf{k},-\mathbf{k}} = 0 \tag{4}$$

This gives

$$\sigma^2_{\hat{E}} = \langle \hat{E}^2 \rangle - \langle \hat{E} \rangle^2 = \frac{1}{2} [\langle AA^* \rangle \langle BB^* \rangle \ + \ |\langle AB \rangle|^2] \tag{5}$$

The variance is suppressed by a factor of N_c for that many number of independent estimates. Thus, finally we have

$$\sigma^2_{\hat{E}} = = \frac{1}{2N_c} [\langle AA^* \rangle \langle BB^* \rangle \ + \ |\langle AB \rangle|^2] \tag{6}$$

3 Cross-correlation of Post-reionization 21 cm signal with Lyman-α forest

Neutral gas in the post reionization epoch produces distinct absorption features, in the spectra of background quasars Rauch (1998). The Ly-α forest, traces the HI density fluctuations along one dimensional quasar lines of sight. The Ly-α forest observations finds several cosmological applications Croft et al.

(1999b); Mandelbaum et al. (2003); Lesgourgues et al. (2007); Croft et al. (1999a); McDonald & Eisenstein (2007); Gallerani et al. (2006). On large cosmological scales the Ly-α forest and the redshifted 21-cm signal are, both expected to be biased tracers of the underlying dark matter (DM) distribution McDonald (2003); Bagla et al. (2010); Guha Sarkar et al. (2012); Villaescusa-Navarro et al. (2014). This allows to study their cross clustering properties in n-point functions. Also the Baryon Oscillation Spectroscopic Survey (BOSS) [5] is aimed towards probing the dark energy through measurements of the BAO signature in Ly-α forest Delubac et al. (2014). The availability of Ly-α forest spectra with high signal to noise ratio for a large number of quasars from the BOSS survey allows 3D statistics to be done with Ly-α forest data Pâris et al. (2014); Slosar et al. (2011a).

Detection these signals are observationally challenging. For the HI 21-cm a detection of the signal requires careful modeling and subtraction of the foregrounds Ghosh et al. (2011); Alonso et al. (2015). Some of the difficulties faced by Ly-α observations include proper modelling and subtraction of the continuum, fluctuations of the ionizing sources, poor modeling of the temperature-density relation McDonald et al. (2001) and metal lines contamination Kim et al. (2007). The two signals are tracers of the underlying dark matter distribution. Thus they are correlated on large scales. However foregrounds and other systematics are uncorrelated between the two independent observations. Hence, the cosmological nature of a detected signal can be only ascertained in a cross-correlation. The 2D and 3D cross correlation of the redshifted HI 21-cm signal with other tracers such as the Ly-α forest, and the Lyman break galaxies have been proposed as a way to avoid some of the observational issues Guha Sarkar et al. (2011); Villaescusa-Navarro et al. (2015a). The foregrounds in HI 21-cm observations appear as noise in the cross correlation and hence, a significant degree foreground cleaning is still required for a detection.

We use δ_T to denote the redshifted 21-cm brightness temperature fluctuations and $\delta_{\mathcal{F}}$ as the fluctuation in the transmitted flux through the Ly-α forest. We write $\delta_{\mathcal{F}}$ and δ_T in Fourier space as

$$\delta_a(\mathbf{r}) = \int \frac{d^3\mathbf{k}}{(2\pi)^3}\, e^{i\mathbf{k}.\mathbf{r}} \Delta_a(\mathbf{k})\,. \tag{7}$$

where $a = \mathcal{F}$ and T refer to the Ly-α forest transmitted flux and 21-cm brightness temperature respectively. On large scales we may write

$$\Delta_a(\mathbf{k}) = C_a[1 + \beta_a \mu^2]\Delta(\mathbf{k}) \tag{8}$$

where $\Delta(\mathbf{k})$ is the dark matter density contrast in Fourier space and μ denotes the cosine of the angle between the line of sight direction $\hat{\mathbf{n}}$ and the wave vector ($\mu = \hat{\mathbf{k}} \cdot \hat{\mathbf{n}}$). β_a is similar to the linear redshift distortion parameter. The corresponding power spectra are

$$P_a(k, \mu) = C_a^2[1 + \beta_a \mu^2]^2 P(k) \tag{9}$$

where $P(k)$ is the dark matter power spectrum.

For the 21-cm brightness temperature fluctuations we have

$$C_T = 4.0\,\mathrm{mK}\, b_T\, \bar{x}_{\mathrm{HI}} (1+z)^2 \left(\frac{\Omega_{b0} h^2}{0.02}\right) \left(\frac{0.7}{h}\right) \left(\frac{H_0}{H(z)}\right) \tag{10}$$

The neutral hydrogen fraction $\bar{x}_{\mathrm{HI}}$ is assumed to be a constant with a value $\bar{x}_{\mathrm{HI}} = 2.45 \times 10^{-2}$ Lanzetta et al. (1995); P'eroux et al. (2003); Noterdaeme et al. (2009). For the HI 21-cm signal the parameter β_T, is the ratio of the growth rate of linear perturbations $f(z)$ and the HI bias b_T. The 21 cm bias is assumed to be a consnt. This assumption of linear bias is supported by numerical simulations Bagla et al. (2010); Guha Sarkar et al. (2012) which shows that over a wide range of scales, a constant bias model is adequate to describe the 21 cm signal in the postreionization epoch ($z < 3$). We adopt a constant bias $b_T = 2$ from simulations Bagla et al. (2010); Guha Sarkar et al. (2012); Villaescusa-Navarro et al. (2014). For the Ly-α forest, $\beta_{\mathcal{F}}$, can not be interpreted in the same manner as β_T. This is because of the non-linear relationship between Ly-α transmitted flux and the underlying dark matter distribution Slosar et al. (2011a). The parameters $(C_{\mathcal{F}}, \beta_{\mathcal{F}})$ are independent of each other the IGM.

We adopt an approximate values $(C_{\mathcal{F}}, \beta_{\mathcal{F}}) \approx (-0.15, 1.11)$ from the numerical simulations of Ly-α forest McDonald (2003). We note that for cross-correlation studies the Ly-α forest has to be smoothed to the resolution of the HI 21 cm frequency channels.

[5] https://www.sdss3.org/surveys/boss.php

We now consider the 3D cross-correlation power spectrum of the HI 21-cm signal and Ly-α forest flux. Consider an observational survey volume V which consists of a patch $L \times L$ on the sky and of thickness l along the radial line of sight direction. We still consider the flat sky approximation. The Ly-α flux fluctuations are now written as a field in the 3-D space as

$$\delta_{\mathcal{F}}(\vec{r}) = \left[\frac{\mathcal{F}(\vec{r}) - \bar{\mathcal{F}}}{\bar{\mathcal{F}}} \right] \tag{11}$$

The observed quantity is $\delta_{\mathcal{F}o}(\vec{r}) = \delta_{\mathcal{F}o}(\vec{r}) \times \rho(\vec{r})$, where the sampling function $\rho(\vec{r})$ is defined as

$$\rho(\vec{r}) = \frac{\sum_a w_a \, \delta_D^2(\vec{r}_\perp - \vec{r}_{\perp a})}{l \sum_a w_a} \tag{12}$$

and is normalized to unity ($\int dV \rho(\vec{r}) = 1$). The summation as before extends up to N. The weights w_a shall in general be related to the pixel noise variance. However, for measurements of transmitted flux with high SNR, the effect of the weight functions can be ignored. With this simplifying assumption we have chosen $w_a = 1$, whereby $\sum_a w_a = N$. In Fourier space we have

$$\Delta_{\mathcal{F}}(\vec{k}) = \int_{-L/2}^{L/2} \int_{-L/2}^{L/2} \int_{-l/2}^{l/2} d^2\vec{r_\perp} dr_\parallel \; e^{i\vec{k}\cdot\vec{r}} \; \delta_{\mathcal{F}}(\vec{r}) \tag{13}$$

One may relate $\vec{k}_\perp$ to $\vec{U}$ as $\vec{k}_\perp = \frac{2\pi\vec{U}}{r}$. We have, in Fourier space

$$\Delta_{\mathcal{F}o}(\vec{k}) = \tilde{\rho}(\vec{k}) \otimes \Delta_{\mathcal{F}}(\vec{k}) + \Delta_{N\mathcal{F}}(\vec{k}) \tag{14}$$

where $\tilde{\rho}$ is the Fourier transform of ρ and $\otimes$ denotes a convolution defined as

$$\tilde{\rho}(\vec{k}) \otimes \Delta_{\mathcal{F}}(\vec{k}) = \frac{1}{V} \sum_{\vec{k}'} \; \tilde{\rho}(\vec{k} - \vec{k}') \Delta_{\mathcal{F}}(\vec{k}') \tag{15}$$

$\Delta_{N\mathcal{F}}(\vec{k})$ denotes a possible noise term. Similarly the 21-cm signal in Fourier space is written as

$$\Delta_{To}(\vec{k}) = \Delta_T(\vec{k}) + \Delta_{NT}(\vec{k}) \tag{16}$$

where Δ_{NT} is the corresponding noise.

The cross-correlation 3-D power spectrum $P_c(\vec{k})$ for the two fields is defined as

$$\langle \; \Delta_{\mathcal{F}}(\vec{k}) \Delta_T^*(\vec{k}') \; \rangle = V P_c(\vec{k}) \delta_{\vec{k},\vec{k}'} \tag{17}$$

Similarly, we define the two auto-correlation multi frequency angular power spectra, $P_T(\vec{k})$ for 21-cm radiation and $P_{\mathcal{F}}(\vec{k})$ for Lyman-α forest flux fluctuations as

$$\langle \; \Delta_T(\vec{k}) \Delta_T^*(\vec{k}') \; \rangle = V P_T(\vec{k}) \delta_{\vec{k},\vec{k}'} \tag{18}$$

$$\langle \; \Delta_{\mathcal{F}}(\vec{k}) \Delta_{\mathcal{F}}^*(\vec{k}') \; \rangle = V P_{\mathcal{F}}(\vec{k}) \delta_{\vec{k},\vec{k}'} \tag{19}$$

We define the cross-correlation estimator $\hat{\mathcal{E}}$ as

$$\hat{\mathcal{E}}(\vec{k},\vec{k}') = \frac{1}{2} \left[\Delta_{\mathcal{F}o}(\vec{k}) \Delta_{To}^*(\vec{k}') + \Delta_{\mathcal{F}o}^*(\vec{k}) \Delta_{To}(\vec{k}') \right] \tag{20}$$

We are interested in the statistical properties of this estimator. Using the definitions of $\Delta_{\mathcal{F}o}(\vec{k})$ and $\Delta_{To}(\vec{k})$ we have the expectation value of $\hat{\mathcal{E}}$ as

$$\begin{aligned} \langle \; \hat{\mathcal{E}}(\vec{k},\vec{k}') \; \rangle = & \frac{1}{2} \langle \; [\tilde{\rho}(\vec{k}) \otimes \Delta_{\mathcal{F}}(\vec{k}) + \Delta_{N\mathcal{F}}(\vec{k})] \times [\Delta_T^*(\vec{k}') + \Delta_{NT}^*(\vec{k}')] \; \rangle \\ & + \frac{1}{2} \langle \; [\tilde{\rho}^*(\vec{k}) \otimes \Delta_{\mathcal{F}}{}^*(\vec{k}) + \Delta_{N\mathcal{F}}^*(\vec{k})] \times [\Delta_T(\vec{k}') + \Delta_{NT}(\vec{k}')] \; \rangle \end{aligned} \tag{21}$$

We shall now assume that the quasars are randomly distributed and are not clustered and the different noises are uncorrelated. Further, we note that the quasars are assumed to be at a redshift different from rest of the quantities and hence ρ can be assumed to be uncorrelated with both Δ_T and $\Delta_{\mathcal{F}}$. Therefore we have

$$\langle\ \hat{\mathcal{E}}(\vec{k},\vec{k}')\ \rangle = \frac{1}{V}\sum_{\vec{k''}}\langle\tilde{\rho}(\vec{k}-\vec{k}'')\rangle \times VP_{\mathcal{F}T}(\vec{k}'')\delta_{\vec{k}'',\vec{k}'} \tag{22}$$

Noting that

$$\langle\tilde{\rho}(\vec{k})\rangle = \delta_{\vec{k}_\perp,0}\delta_{\vec{k}_\parallel,0} \tag{23}$$

we have

$$\langle\ \hat{\mathcal{E}}(\vec{k},\vec{k}')\ \rangle = P_{\mathcal{F}T}(\vec{k})\delta_{\vec{k},\vec{k}'} \tag{24}$$

Thus, the expectation value of the estimator faithfully returns the quantity we are probing, namely the 3-D cross-correlation power spectrum $P_{\mathcal{F}T}(\vec{k})$.

We next consider the variance of the estimator $\hat{\mathcal{E}}$ defined as

$$\sigma^2_{\hat{\mathcal{E}}} = \langle\hat{\mathcal{E}}^2\rangle - \langle\hat{\mathcal{E}}\rangle^2 \tag{25}$$

$$\sigma^2_{\hat{\mathcal{E}}} = \frac{1}{2}\langle\Delta_{\mathcal{F}o}(\vec{k})\Delta^*_{\mathcal{F}o}(\vec{k})\rangle\langle\Delta_{To}(\vec{k}')\Delta^*_{To}(\vec{k}')\rangle + \frac{1}{2}|\langle\Delta_{\mathcal{F}o}(\vec{k})\Delta^*_{To}(\vec{k}')\rangle|^2 \tag{26}$$

We saw that

$$\langle\Delta_{\mathcal{F}o}(\vec{k})\Delta^*_{To}(\vec{k}')\rangle = P_{\mathcal{F}T}(\vec{k})\delta_{\vec{k},\vec{k}'} \tag{27}$$

and we note that

$$\langle\Delta_{To}(\vec{k})\Delta^*_{To}(\vec{k})\rangle = V[P_T(\vec{k}) + N_T(\vec{k})] \tag{28}$$

where N_T is the 21-cm noise power spectrum. We also have for the Ly-α forest

$$\langle\Delta_{\mathcal{F}o}(\vec{k})\Delta^*_{\mathcal{F}o}(\vec{k})\rangle = \langle\ \tilde{\rho}(\vec{k})\otimes\Delta_{\mathcal{F}}(\vec{k})\ \tilde{\rho}^*(\vec{k})\otimes\Delta_{\mathcal{F}}{}^*(\vec{k})\ \rangle + N_{\mathcal{F}}L^2 \tag{29}$$

where $N_{\mathcal{F}}$ is the Noise power spectrum corresponding to the Ly-α flux fluctuations. Using the relation

$$\langle\ \tilde{\rho}(\vec{k})\tilde{\rho}^*(\vec{k'})\ \rangle = \frac{1}{N}\delta_{\vec{k_\perp},\ \vec{k'_\perp}}\delta_{k_\parallel,0}\delta_{k'_\parallel,0} + (1-\frac{1}{N})\delta_{\vec{k},0}\delta_{\vec{k'},0} \tag{30}$$

we have

$$\langle\Delta_{\mathcal{F}o}(\vec{k})\Delta^*_{\mathcal{F}o}(\vec{k})\rangle = \frac{1}{V^2}\sum_{\vec{k_1},\vec{k_2}}\langle\tilde{\rho}(\vec{k}-\vec{k}_1)\tilde{\rho}^*(\vec{k}-\vec{k}_2)\rangle\langle\Delta_{\mathcal{F}}(\vec{k}_{1\perp},k_{1\parallel})\Delta^*_{\mathcal{F}}(\vec{k}_{2\perp},k_{2\parallel})\rangle \tag{31}$$

or

$$\langle\Delta_{\mathcal{F}o}(\vec{k})\Delta^*_{\mathcal{F}o}(\vec{k})\rangle = \frac{1}{V^2}\sum_{\vec{k_1},\vec{k_2}}\delta_{(\vec{k}-\vec{k_1}),0}\delta_{(\vec{k}-\vec{k_2}),0} + \frac{1}{N}\left(\delta_{(\vec{k_\perp}-\vec{k_{1\perp}}),(\vec{k_\perp}-\vec{k_{2\perp}})}\delta_{(k_\parallel-k_{1\parallel}),(k_\parallel-k_{2\parallel})}\right)$$
$$\times\langle\Delta_{\mathcal{F}}(\vec{k}_{1\perp},k_{1\parallel})\Delta^*_{\mathcal{F}}(\vec{k}_{2\perp},k_{2\parallel})\rangle \tag{32}$$

This gives

$$\sigma^2_{\hat{\mathcal{E}}} = \frac{1}{2}\left[\frac{1}{N}\sum_{\vec{k_\perp}}P_{\mathcal{F}}(\vec{k}) + P_{\mathcal{F}}(\vec{k}) + N_{\mathcal{F}}\right]\times\left[P_T(\vec{k}) + N_T\right] + \frac{1}{2}P^2_{\mathcal{F}T} \tag{33}$$

Writing the summation as an integral we get

$$\sigma^2_{\hat{\mathcal{E}}} = \frac{1}{2}\left[\frac{1}{\bar{n}}\left(\int d^2\vec{k_\perp}\ P_{\mathcal{F}}(\vec{k})\right) + P_{\mathcal{F}}(\vec{k}) + N_{\mathcal{F}}\right]\times\left[P_T(\vec{k}) + N_T\right] + \frac{1}{2}P^2_{\mathcal{F}T}$$

where $\bar{n}$ is the angular density of quasars and $\bar{n} = N/L^2$. We assume that the variance $\sigma^2_{\mathcal{F}N}$ of the pixel noise contribution to $\delta_{\mathcal{F}}$ is the same across all the quasar spectra whereby we have $N_{\mathcal{F}} = \sigma^2_{\mathcal{F}N}/\bar{n}$ for

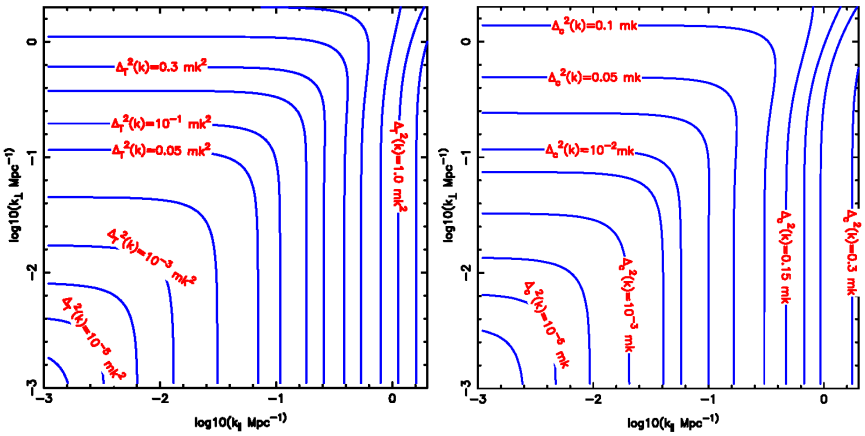

Figure 1: Figure showing the 3D power spectrum in redshift space at a fiducial redshift $z = 2.5$. The left panel shows the 21-cm power spectrum $\Delta_T^2 = k^3 P_{TT}(\mathbf{k})/2\pi^2$ and the right panel shows the cross-correlation power spectrum $\Delta_C^2 = k^3 P_{T\mathcal{F}}(\mathbf{k})/2\pi^2$. Figure reference Guha Sarkar & Datta (2015)

its noise power spectrum. An uniform weighing scheme for all quasars is a good approximation when most of the spectra are measured with a sufficiently high SNR McQuinn & White (2011). We have not incorporated quasar clustering which is supposed to be sub-dominant as compared to Poisson noise. In reality, the clustering would enhance the term $\left(P_{\mathcal{F}\mathcal{F}}^{\rm 1D}(k_\parallel)P_w^{\rm 2D} + N_{\mathcal{F}}\right)$ by a factor $(1 + \bar{n}C_Q(\mathbf{k}_\perp))$, where $C_Q(\mathbf{k}_\perp)$ is the angular power spectrum of the quasarsMyers et al. (2007).

For a radio-interferometric measurement of the 21-cm signal we have (McQuinn et al., 2006; Wyithe et al., 2008)

$$N_T(k,\nu) = \frac{T_{sys}^2}{Bt_0}\left(\frac{\lambda^2}{A_e}\right)^2 \frac{r_\nu^2 L}{n_b(U,\nu)} \tag{34}$$

Here T_{sys} denotes the system temperature. $B$is the observation bandwidth, t_0 is the total observation time, r_ν is the comoving distance to the redshift z , $n_b(U,\nu)$ is the density of baseline U, and A_e is the effective collecting area of each antenna.

3.1 The cross correlation signal and constraints with SKA

We investigate the possibility of detecting the signal using the upcoming SKA-mid phase1 telescope and future Ly-α forest surveys with very high quasar number densities. Two separate telescopes named SKA-low and SKA-mid operating at two different frequency bands and will be constructed in Australia and South Africa respectively in two phases. For this work we consider the instruments SKA1-mid which will be built in phase 1. The instrument specifications such as the total number of antennae, antenna distribution, frequency coverage, total collecting area etc., have not been fixed yet and might change in future. We use the specifications considered in some recent documents, i.e., the 'Baseline Design Document' and 'SKA Level 1 Requirements (revision 6)' which are available on the SKA website[6]. We assume that the SKA1-mid will operate in the frequency range from 350 MHz to 14 GHz. It will have a total of 250 antennae of 7.5 meters radius each [7]. We use the baseline distribution given in (Villaescusa-Navarro et al., 2015b) (figure 6-blue line) for the calculation presented here. We note that, the baseline distribution used here is consistent with the projected antenna layout distribution with 40%, 54%, 70%, 81% and 100% of the total antennae are enclosed within 0.4 km, 1 km, 2.5 km, 4 km and 100 km radius respectively (for details see table 6 in the document 'Baseline Design Document').

[6]https://www.skatelescope.org/key-documents/

[7]In one of the recent documents "SKA Level 1 Requirements (revision 6)" ,(https://www.skatelescope.org/key-documents/) it is pointed out that only $\sim 50\%$ of these antennae may be built initially. One has to consider ~ 4 times the total observation time proposed in this paper to achieve the same label of constraints presented here with this downgraded design. However, this is a rough scaling and revised baseline distribution may change the analysis considerably.

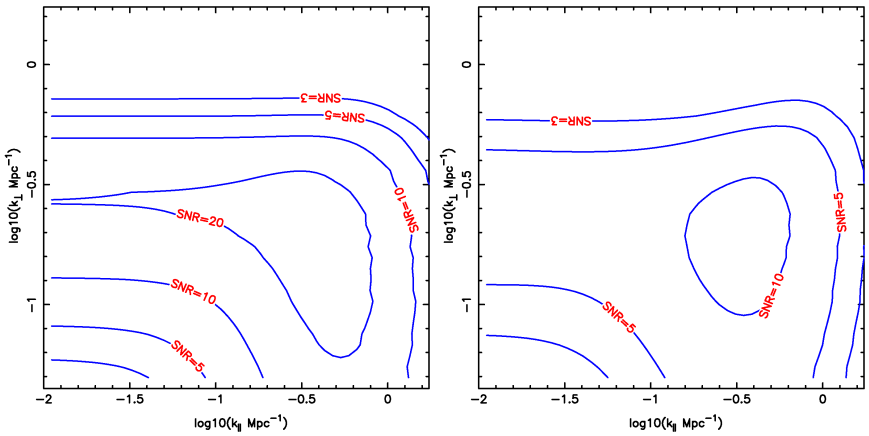

Figure 2: SNR contours for the 21-cm auto-correlation power spectrum in redshift space at $z = 2.5$. We have considered a 400hrs observation at 405MHz and assumed that complete foreground removal is done. Figure reference Guha Sarkar & Datta (2015)

The fiducial redshift of $z = 2.5$ is justified since the quasar distribution peaks in the range $2 < z < 3$. Only a smaller part of the quasar spectra corresponding to an approximate band $\Delta z \sim 0.4$ is used to avoid contamination from metal lines and quasar proximity effect. The cross-correlation can however only be computed in the region of overlap between the 21-cm signal and the Ly-α forest field.

The left panel of the figure (1) shows the dimensionless redshift space 21-cm power spectrum ($\Delta^2_T(k_\perp, k_{||}) = k^3 P_T(k_\perp, k_{||})/2\pi^2$) at $z = 2.5$. We can see that the power spectrum is not circularly symmetric in the ($k_{||}$, $k_\perp$) plane. The asymmetry is related to the redshift space distortion parameter. The right panel of figure (1) shows the 21-cm and Ly-α cross-power spectrum.

We first consider that a perfect foreground subtraction is achieved. The left panel of the figure (2) shows the SNR contours for the 21-cm auto correlation power spectrum for a 400hrs observation and total 32MHz bandwidth at a frequency 405.7MHz. We have taken a bin $(\Delta k, \Delta\theta) = (k/5, \pi/10)$. The SNR reaches at the peak (> 20)at intermediate value of $(k_\perp, k_{||}) = (0.4, 0.4)\,\mathrm{Mpc}^{-1}$. We find that 5σ detection is possible in the range $0.08 \lesssim k_\perp \lesssim 0.6\,\mathrm{Mpc}^{-1}$ and $0.1 \lesssim k_{||} \lesssim 1.5\,\mathrm{Mpc}^{-1}$. The range for the 10σ detection is $0.12 \lesssim k_\perp \lesssim 0.5\,\mathrm{Mpc}^{-1}$ and $0.2 \lesssim k_{||} \lesssim 1.2\,\mathrm{Mpc}^{-1}$. At lower values of k the noise is dominated by cosmic variance whereas, the noise is predominantly instrumental at large k.

The right panel of the figure (2) shows the SNR contours for the Ly-α 21-cm cross-correlation power spectrum. For the 21 cm signal, a 400hrs observation is considered. We have taken $\bar{n} = 30\mathrm{deg}^{-2}$, and the Ly-$\alpha$ spectra are assumed to be measured at a 2σ sensitivity level. We use β_F to be 1.11 and overall normalization factor $C_F = -0.15$ consistent with recent measurements Slosar et al. (2011b). Although the overall SNR for the cross power spectrum is lower compared to the 21-cm auto power spectrum, 5σ detection is ideally possible for the $0.1 \lesssim k_\perp \lesssim 0.4\,\mathrm{Mpc}^{-1}$ and $0.1 \lesssim k_{||} \lesssim 1\,\mathrm{Mpc}^{-1}$. The SNR peaks ($> 10$)at $(k_\perp, k_{||}) \sim (0.2, 0.3)\,\mathrm{Mpc}^{-1}$. The error in the cross-correlation can be reduced either by increasing the QSO number density or by increasing the observing time for HI 21-cm survey. The QSO number density is already in the higher side for the BOSS survey that we consider. The only way to reduce the variance is to consider more observation time for HI 21-cm survey and enhance the survey volume.

3.2 Parameter estimation using the cross-correlation

We now consider the precision at which we can constrain various model parameters using the Fisher matrix analysis. Figure (4) shows the 68.3%, 95.4% and 99.8% confidence contours obtained using the Fisher matrix analysis for the parameters $(A, \beta_T, \beta_\mathcal{F}, \Omega_\Lambda)$. The table 1 summarises the $1-\sigma$ error these parameters. The parameters (Ω_Λ, A) are constrained much better that $\beta_\mathcal{F}$ and β_T at (3.5%, 8%). The error projections presented here are for a single field of view radio observation. The noise scales as $\sigma/\sqrt{N}$ where N is the number of pointings.

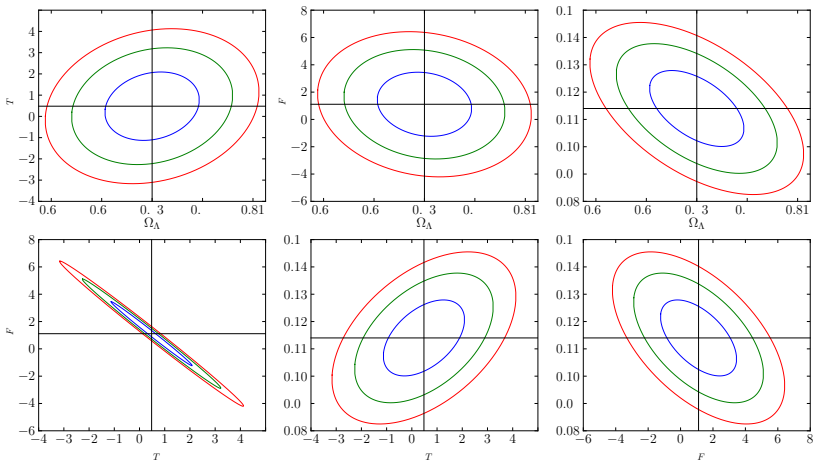

Figure 3: The $68.3\%, 95.4\%$ and 99.8% confidence ellipses for the parameters $(A, \beta_T, \beta_{\mathcal{F}}, \Omega_\Lambda)$. Figure reference Guha Sarkar & Datta (2015).

Table 1: This shows $1-\sigma$ error on various parameters for a single field observation.

Parameters	Fiducial Value	1σ Error (marginalized)	1σ Error (conditional)
β_T	0.48	1.06	0.04
$\beta_{\mathcal{F}}$	1.11	1.55	0.05
Ω_Λ	0.73	0.025	0.013
A	0.114	0.01	0.002

We also consider conditional error on each of the parameters assuming that the other three are known. $1-\sigma$ error in β_T and $\beta_{\mathcal{F}}$ are 8.5% and 4.5% respectively for single pointing. For 10 independent radio observations the conditional errors improve to 2.7%, 1.4%, 0.4% and 0.6% for β_T, $\beta_{\mathcal{F}}$, Ω_Λ and A respectively. These constraints on the redshift space distortion parameters β from our cross-correlation analysis are competitive with other cosmological probes Font-Ribera et al. (2012); Slosar et al. (2011a). Further, we note that higher density of QSOs and improved SNR for the individual QSO spectra shall also provide stronger constraints.

3.3 BAO imprint on the cross-correlation signal

The characteristic scale of the BAO is set by the sound horizon s at the epoch of recombination The comoving length-scale s defines a transverse angular scale $\theta_s = s[(1+z)D_A(z)]^{-1}$ and a radial redshift interval $\Delta z_s = sH(z)/c$, where $D_A(z)$ and $H(z)$ are the angular diameter distance and Hubble parameter respectively. The comoving length-scale $s = 143\,\mathrm{Mpc}$ corresponds to $\theta_s = 1.38^\circ$ and $\Delta z_s = 0.07$ at $z = 2.5$. Measurement of θ_s and Δz_s separately, allows the independent determination of $D_A(z)$ and $H(z)$ and thereby constrain background cosmological evolution. Here we consider the possibility of measurement of these two parameters from the imprint of BAO features on the cross-correlation power spectrum.

The Fisher matrix is given by (Guha Sarkar & Bharadwaj, 2013)

$$F_{ij} = \frac{V}{(2\pi)^3}\int \frac{d^3\mathbf{k}}{[P^2_{\mathcal{F}T}(\mathbf{k}) + P_{\mathcal{F}\mathcal{F}o}(\mathbf{k})P_{TTo}(\mathbf{k})]}\frac{\partial P_{\mathcal{F}T}(\mathbf{k})}{\partial q_i}\frac{\partial P_{\mathcal{F}T}(\mathbf{k})}{\partial q_j} \tag{35}$$

where q_i refer to the cosmological parameters to be constrained. This BAO information is mainly present at small $\mathbf{k}$ (large scales) with the first peak at roughly $k \sim 0.045\mathrm{Mpc}^{-1}$. The subsequent oscillations are greatly suppressed by $k \sim 0.3\mathrm{Mpc}^{-1}$ which is within the limits of the $\mathbf{k}_\perp$ and $k_\parallel$ integrals. We use $P_b = P - P_c$ to isolate the purely baryonic features in the power spectrum, and we use this in the derivative $\partial P(k)/\partial q_i$. Here P_c refers to the CDM power spectrum without any baryonic features. This gives

$$P_b(\mathbf{k}) = \sqrt{8\pi^2}A\,\frac{\sin x}{x}\,\exp\left[-\left(\frac{k}{k_{silk}}\right)^{1.4}\right]\exp\left[-\left(\frac{k^2}{2k^2_{nl}}\right)\right] \tag{36}$$

where k_{silk} and k_{nl} denotes the scale of 'Silk-damping' and 'non-linearity' respectively. We have used $k_{nl} = (3.07\,h^{-1}\mathrm{Mpc})^{-1}$ and $k_{silk} = (7.76\,h^{-1}\mathrm{Mpc})^{-1}$ from Seo & Eisenstein (2007). The quantity $x = \sqrt{k_\perp^2 s_\perp^2 + k_\parallel^2 s_\parallel^2}$ where $s_\perp$ and $s_\parallel$ corresponds to θ_s and Δz_s in units of distance. A is an overall normalization constant. The value of s is precisely from CMBR anisotropy observations, and the values of $s_\perp$ and $s_\parallel$ are equal to s for the reference values of D_A and $H(z)$. Changes in D_A and $H(z)$ manifest as changes in the values of $s_\perp$ and $s_\parallel$ respectively, and thus the fractional errors in $s_\perp$ and $s_\parallel$ correspond to fractional errors in D_A and $H(z)$ respectively. We choose $q_1 = \ln(s_\perp^{-1})$ and $q_2 = \ln(s_\parallel)$ as the cosmological parameters to be constrained, and determine the precision at which it will be possible to measure these using the BAO features in the cross-correlation signal. We use the formalism outlined in Seo & Eisenstein (2007), whereby we construct the $2-D$ Fisher matrix

$$F_{ij} = VA^2\int dk\int_{-1}^{1} d\mu \frac{k^2\exp[-2(k/k_{silk})^{1.4} - (k/k_{nl})^2]}{[P^2_{\mathcal{F}T}(k) + P_{\mathcal{F}\mathcal{F}o}(\mathbf{k})P_{TTo}(\mathbf{k})/F^2_{\mathcal{F}T}(\mu)]} f_i(\mu)f_j(\mu) \tag{37}$$

$$F_{\mathcal{F}T}(\mu) = \frac{H(z)}{r^2 c}C_{\mathcal{F}}C_T\,(1+\beta_{\mathcal{F}}\mu^2)(1+\beta_T\mu^2) \tag{38}$$

where $f_1 = \mu^2 - 1$ and $f_2 = \mu^2$. The Cramer-Rao bound $\delta q_i = \sqrt{F_{ii}^{-1}}$ is used to calculate the maximum theoretical error in the parameter q_i. A combined distance measure D_V, also referred to as the "dilation factor" Eisenstein et al. (2005)

$$D_V(z)^3 = (1+z)^2 D_A(z)\frac{cz}{H(z)} \tag{39}$$

is often used as a single parameter to quantify BAO observations . We use $\delta D_V/D_V = \frac{1}{3}(4F_{11}^{-1} + 4F_{12}^{-1} + F_{22}^{-1})^{0.5}$ to obtain the relative error in D_V. The dilation factor is known to be particularly useful when the individual measurements of D_A and $H(z)$ have low signal to noise ratio.

The Fisher matrix formalism is used to determine the accuracy with which it will be possible to measure cosmological distances using this cross-correlation signal.

The limits $\bar{n}_Q \to \infty$ and $N_T \to 0$, which correspond to $P_{\mathcal{F}\mathcal{F}o} \to P_{\mathcal{F}\mathcal{F}}$ and $P_{TTo} \to P_{TT}$, set the SNR only limited by cosmic variance. In this limit, where the SNR depends only on the survey volume corresponding to the total field of view we have $\delta D_V/D_V = 0.15\%$, $\delta H/H = 0.25\%$ and $D_A/D_A = 0.15\%$ which are independent of any of the other observational details. The fractional errors decrease slowly beyond $\bar{n}_Q > 50\mathrm{deg}^{-2}$ or $N_T < 10^{-6}\mathrm{mK}^2$. We find that parameter values $\bar{n}_Q \sim 6\,\mathrm{deg}^{-2}$ and $N_T \sim 4.7 \times 10^{-5}$ mK^2, attainable with BOSS and SKA1 mid are adequate for a 1% accuracy, whereas $\bar{n}_Q \sim 2\,\mathrm{deg}^{-2}$ and $N_T \sim 3 \times 10^{-3}$ mK^2 are adequate for a $\sim 10\%$ accuracy in measurement of D_V. With a BOSS like survey is possible to achieve the fiducial value $\delta D_V/D_V = 2.0\%$ from the cross-correlation at $N_T = 2.9 \times 10^{-4}\mathrm{mK}^2$. The error varies slower than $\sqrt{N_T}$ in the range $N_T = 10^{-4}\mathrm{mK}^2$ to $N_T = 10^{-5}\mathrm{mK}^2$. We have $(\delta D_V/D_V, \delta D_A/D_A, \delta H/H) = (1.3, 1.5, 1.3)\,\%$ and $(0.67, 0.78, 0.74)\,\%$ at $N_T = 10^{-4}\mathrm{mK}^2$ and at $N_T = 10^{-5}\mathrm{mK}^2$ respectively. The errors do not significantly go down much further for $N_T < 10^{-5}\mathrm{mK}^2$, and we have $(0.55, 0.63, 0.63)\,\%$ at $N_T = 10^{-6}\mathrm{mK}^2$.

3.4 Constraints on Neutrino mass

Free streaming of neutrinos causes a power suppression on large scales. This suppression of dark matter power spectrum shall imprint itself on the cross-correlation of Ly-α forest and 21 cm signal (Pal & Guha Sarkar, 2016). We have suggested this as a possible way to constrain neutrino mass. We have considered a BOSS like Ly-α survey with a quasar density of 30 deg^{-2} with an average 3σ sensitivity for the measured spectra. We have also assumed a 21 cm intensity mapping experiment at a fiducial redshift $z = 2.5$ corresponding to a frequency 406MHz using a SKA1-mid like instrument with 250 dishes each of diameter 15m. We have assumed a $(\Omega_\Lambda, \Omega_m, \Omega_r, h, \sum_i m_i)$=$(0.6825, 0.3175, 0.00005, 0.6711, 0.1\mathrm{ev})$ (Planck Collaboration et al., 2014) for this analysis. The Fisher matrix analysis using a two parameter $(\Omega_m.\Omega_\nu)$ shows that For a 10.000 hrs radio observation distributed over 25 pointings of 400 hrs each the parameters Ω_m and Ω_ν are measurable at 0.321% and 3.671%. respectively [see figure (4)]. We find it significant that instead of a deep long duration observation in one small field of view, it is much better if one divides the total observation time over several pointings and thereby increasing survey volume. For 100 pointings each of $100hrs$ one can get a 2.36% measurement of Ω_ν. This is close to the cosmic variance limit at the fiducial redshift and the given observations. In the ideal limit one may measure Ω_ν at a 2.45% level which corresponds to a measurement of $\sum m_\nu$ at the precision of (0.1 ± 0.012) eV.

4 Cross-correlation with Lyman break galaxies

The cross-correlation between the HI 21-cm signal and the Lyman break galaxies is another important tool to probe the large scale structure of the Universe at post reionization epoch. This has been studied recently (Villaescusa-Navarro et al., 2015b) using a high resolution N-body simulation. Prospects for detecting such a signal using the SKA1-mid and SKA1-low telescopes together with a Lyman break galaxy spectroscopic survey with the same volume have also been investigated. It is found that the cross power spectrum can be detected with a SNR up to ~ 10 times higher than the HI 21-cm auto power spectrum. Like in all other cross power spectrum the Lyman break galaxy and HI 21-cm cross power spectrum is expected to be extracted more reliably from the much stronger by spectrally smoothed foreground contamination compared to the HI 21-cm auto power spectrum.

5 Cross-correlation of HI 21 cm signal with CMBR

5.1 Weak Lensing

Gravitational lensing deflects the CMBR photons which are free streaming from the epoch of recombination $z \sim 1000$. This forms a secondary anisotropy in the CMBR temperature anisotropy maps (Lewis & Challinor (2006)). The weak lensing of CMBR can, in principle be used to probe the universe at distances ($z \sim 1100$) much larger than any galaxy- redshift surveys. Measurement of secondary anisotropies in CMBR, uses the cross correlation of some relevant observable (related to the CMB fluctuations) with some tracer of the large scale structure (Hirata et al. (2004a); Smith et al. (2007); Hirata et al. (2004b)).

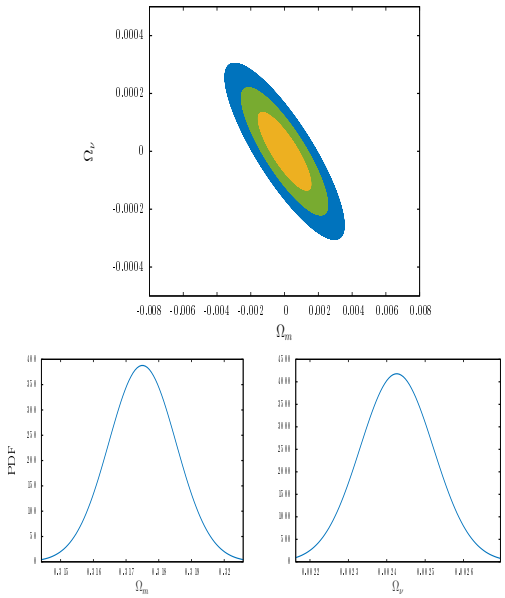

Figure 4: 68.3%,95.4% and 99.8% ellipse for 10000 hrs. observations for 25 pointings with each pointing of 400 hrs. The marginalized one dimensional probability distribution function (PDF) for Ω_m and Ω_ν are also shown. Figure reference Pal & Guha Sarkar (2016)

For weak lensing statistics one uses 'convergence' and the 'shear' which quantify the distortion of the maps due to lensing. Convergence (κ) measures the lensing effect through its direct dependence on the gravitational potential along the line of sight and is thereby a direct probe of cosmology. The difficulty in precise measurement of lensing is the need for very high resolutions in the CMBR maps, since typical deflections over cosmological scales is only a few arcminutes. The non-Gaussianity imprinted by lensing on smaller scales allows a statistical detection for surveys with low angular resolution. Cross-correlation with traces, limits the effect of systematics and thereby increases the signal to noise. The weak lensing observables like convergence are constructed using various estimators through quadratic combination of the CMBR maps(T, E, B) (Seljak & Zaldarriaga (1999); Hu (2001); Hu & Okamoto (2002)). The reconstructed convergence field can then be used for cross correlation.

We have investigated the possibility of using the post-reionization HI as a tracer of the underlying large scale structure to probe weak lensing (Guha Sarkar, 2010). Cosmic shear fields imprint the underlying distribution of matter over large scales. We have studied the cross correlation between the fluctuations in the 21-cm brightness temperature maps and the weak lensing convergence field. We can probe the line of sight integral effect of weak lensing at any intermediate redshift by suitably tuning the frequency band for 21-cm observation. The cross-correlation power spectrum can independently quantify the cosmic evolution and structure formation at redshifts $z \leq 6$. The cross-correlation power spectrum may also independently compare the various de-lensing estimators that separate the lensing contribution from the CMBR maps.

The distortions caused by the deflection is the quantity of study in weak lensing. At the lowest order, magnification of the signal is contained in the convergence. The convergence field is a line of sight integral of the matter over density δ given by (Van Waerbeke & Mellier (2003))

$$\kappa(\hat{\mathbf{n}}) = \frac{3}{2}\Omega_{m0}\left(\frac{H_0}{c}\right)^2 \int_{\eta_0}^{\eta_{LSS}} d\eta F(\eta)\delta(\mathcal{D}(\eta)\hat{\mathbf{n}}, \eta) \tag{40}$$

and $F(\eta)$ is given by

$$F(\eta) = \frac{\mathcal{D}(\eta_{LSS} - \eta)\mathcal{D}(\eta)D_+(\eta)}{\mathcal{D}(\eta_{LSS})a(\eta)} \tag{41}$$

Here, D_+ denotes the usual growing mode for the density contrast δ, and η_{LSS} denotes the conformal time corresponding to the last scattering surface. The comoving angular diameter distance $\mathcal{D}(\chi) = \chi$ for flat universe, $\mathcal{D}(\chi) = \sin(K\chi)/K$ for $K = |1-\Omega_m-\Omega_\Lambda|^{1/2}H_0/c < 0$ and $\mathcal{D}(\chi) = \sinh(K\chi)/K$ for $K > 0$ Universe. The convergence power spectrum is defined as $\langle\ a^\kappa_{\ell m}a^{\kappa *}_{\ell' m'}\ \rangle = C^\kappa_\ell \delta_{\ell\ell'}\delta_{mm'}$. where $a^\kappa_{\ell m}$ are the expansion coefficients in spherical harmonic basis. The Convergence auto-correlation power spectrum for large ℓ can be approximately written as

$$\mathcal{C}^\kappa_\ell \approx \frac{9}{4}\Omega^2_{m0}\left(\frac{H_0}{c}\right)^4 \int d\eta \frac{F^2(\eta)}{\mathcal{D}^2(\eta)} P\left(\frac{\ell}{\mathcal{D}(\eta)}\right) \tag{42}$$

The cross correlation angular power spectrum between the post-reionization H I 21-cm brightness temperature signal and the convergence field, is given by

$$\mathcal{C}^{HI-\kappa}_\ell = A(z_{\rm HI}) \int dk \left[k^2 P(k) \mathcal{I}_\ell(kr_{\rm HI}) \int d\eta F(\eta) j_\ell(kr)\right] \tag{43}$$

where $P(k)$ is the present day dark matter power spectrum, and

$$A(z) = \frac{3}{\pi}\Omega_{m0}\left(\frac{H_0}{c}\right)^2 \bar{T}(z)\bar{x}_{\rm HI} D_+(z) \tag{44}$$

We note that the convergence field $\kappa(\hat{\mathbf{n}})$, is not directly measurable in CMBR experiments. It is reconstructed from the CMBR maps through the use of various statistical estimators (Hanson et al. (2009); Kesden et al. (2003); Cooray & Kesden (2003)). The cross-correlation angular power spectrum, $\mathcal{C}^{HI-\kappa}_\ell$, does not directly de-lens the CMB maps. It however uses the reconstructed weak lensing field, and is hence sensitive to the underlying de-lensing tools, and the cosmological model. The cross-correlation angular power spectrum may provide a way to independently compare various de-lensing estimators.

The cross-correlation power spectrum follows the same shape as the matter power spectrum. The signal peaks at a particular ℓ which scales as $\ell \propto r_{\rm HI}$ when the redshift is changed. The angular distribution of power clearly follows the underlying clustering properties of matter. The amplitude depends on several factors which are related to cosmological model and the H I distribution at $z_{\rm HI}$. The angular diameter distances directly also depends directly on the cosmological parameters. The cross-correlation signal may hence be used independently for joint estimation of cosmological parameters.

We shall now discuss the prospect of detecting the cross-correlation signal. Detecting the cross-correlation is less likely to be affected by foregrounds or other systematics. We shall subsequently assume that foregrounds have been largely removed from the H I signal. The error in the cross-correlation signal has the contribution due to instrumental noise and sample variance. Sample variance however puts a fundamental bound on the detectability of the signal. The sample variance for the cross-correlation angular power spectrum $\mathcal{C}^{HI-\kappa}_\ell$ is given by

$$\sigma^2_{SV} = \frac{\mathcal{C}^\kappa_\ell \mathcal{C}^{HI}_\ell}{(2\ell+1)N_c f_s \Delta\ell} \tag{45}$$

The numerator contains the auto-correlation angular power spectra. $\Delta\ell$ represents a band in ℓ and f_s is fraction of sky common to the convergence field κ and field of view of the 21 cm observation. N_c denotes the number of independent estimates of the signal.

We have used the ideal hypothetical possibility of a full sky 21 cm survey that is $f_s = 1$, and used $\Delta\ell = 1$. The predicted S/N is found to be ~ 2 and is not high enough for a statistically significant detection which requires $S/N \geq 3$. Choosing a $\Delta\ell = 10$ for $\ell \leq 100$ and $\Delta\ell = 100$ for $\ell > 100$ will however produce a $S/N > 3$. This establishes that, with full sky coverage and negligible instrumental noise, the binned cross-correlation power spectrum is detectable. The S/N estimate is based on H I observation at only one frequency. The 21- cm observations allow us to probe a continuous range of redshifts. This allows us to further increase the S/N by collapsing the signal from various redshifts. In principle, a broad band 21-cm experiment may further increase the S/N.

It is possible to increase the S/N by collapsing the signal from different scales ℓ and thereby test the feasibility of a statistically significant detection. The Signal to Noise cumulated upto a multipole ℓ is defined as

$$\left(\frac{S}{N}\right)^2 = \sum_0^\ell \frac{(2\ell'+1)N_c f_s (\mathcal{C}^{HI-\kappa}_{\ell'})^2}{(\mathcal{C}^{HI}_{\ell'} + N^{HI}_{\ell'})(\mathcal{C}^\kappa_{\ell'} + N^\kappa_{\ell'})} \tag{46}$$

N_ℓ^κ and N_ℓ^{HI} denotes the noise power spectrum for κ and H I observations respectively. Ignoring the instrument noises we note that there is a significant increase in the S/N by cumulating over multipoles ℓ. This implies that a statistically significant detection of $\mathcal{C}_\ell^{HI-\kappa}$ is possible and the signal is not limited cosmic variance. It is important to push instrumental noise to the limit set by cosmic variance for a detection of the signal. At the relevant redshifts of interest, it is possible to reach such low noise levels with SKA. It is however important to scan large parts of the sky and thereby increase the survey volume.

Instrumental noise plays an important role at large multipoles (small scale). For a typical CMB experiment, the noise power spectrum (Marian & Bernstein (2007); Smith et al. (2006)) is given by $N_\ell = \sigma_{\rm pix}^2 \Omega_{\rm pix} W_\ell^{-2}$, where different pixels are assumed to have uncorrelated noise with uniform variance $\sigma_{\rm pix}^2 = s^2/t_{\rm pix}$, where s^2 and $t_{\rm pix}$ denotes pixel sensitivity and 'time spent on the pixel' respectively. $\Omega_{\rm pix}$ is the solid angle subtended per pixel and we choose a Gaussian beam $W_\ell = \exp[-\ell^2\theta_{\rm FWHM}^2/16\ln 2]$.

For H I observations, the quantity of interest is the complex Visibility which is used to estimate the power spectrum (Ali et al. (2008)). For a radio telescope with N antennae, system temperature T_{sys}, operating at a frequency ν, and band width B the noise correlation is given by $N_\ell^{HI} \propto \frac{1}{N(N-1)}\left[\frac{T_{sys}}{K}\right]^2 \frac{1}{T\sqrt{\Delta\nu B}}$.

Where T denotes total observation time, and K is related to the effective collecting area of the antenna dish. Binning in ℓ also reduces the noise. The bin $\Delta\ell = 1/2\pi^2\theta_0$ is chosen assuming a Gaussian beam of width θ_0. With a SKA like instrument (Ali et al. (2008)), one can in principle achieve a noise level much lesser than the signal by increasing the time of observation (a 5000 hour observation is sufficient even with the present SKA configuration) and also by increasing the band width of the instrument. Being inversely related to the number of antennae in the array, future designs can allow further suppression of the the system noise and achieve $N_\ell^{HI} << \mathcal{C}_\ell^{HI}$. This establishes the detectability of the cross-correlation signal. We would like to conclude by noting that correlation between weak lensing fields and 21 cm maps, quantified through $\mathcal{C}_\ell^{HI-\kappa}$ may allow an independent means to estimate cosmological parameters and also test various estimators for CMBR delensing.

5.2 ISW effect

In an Universe, dominated by the cosmological constant, Λ , the expansion factor of the universe, a, grows at a faster rate than the linear growth of density perturbations. This consequently implies that, the gravitational potential $\Phi \propto -\delta/a$ will decay. The ISW effect is caused by the change in energy of CMB photons as they traverse these linearly time dependent potentials. The presence of non-linear effects in the growth of the density perturbations modifies this simple linear picture, and would produce additional temperature fluctuations.

If the horizon size at the epoch of dark energy dominance (decay of the potential) by η_Λ, then the ISW effect is suppressed on scales $k \geq 2\pi/\eta_\Lambda$. This corresponds to an angular scale $\ell_\Lambda = 2\pi d/\eta_\Lambda$, where d is the angular diameter distance to the epoch of decay.

The ISW term is anisotropy is given by

$$\Delta T(\hat{\mathbf{n}})^{\rm ISW} = 2T \int_{\eta_{\rm LSS}}^{\eta_0} d\eta\eta\, \dot{\Phi}(r\hat{\mathbf{n}}, \eta). \tag{47}$$

The cross correlation angular power spectrum between HI 21 cm signal and ISW is given by (Guha Sarkar et al., 2009)

$$\mathcal{C}_\ell^{HI-ISW} = \mathcal{K}(z_{\rm HI}) \int dk\ P(k) \mathcal{I}_\ell(kr_{\rm HI}) \int_{\eta_{\rm LSS}}^{\eta_0} d\eta F(\eta) j_\ell(kr) \tag{48}$$

where $P(k)$ is the present day dark matter power spectrum,

$$\mathcal{K}(z) = -\bar{T}(z)\bar{x}_{\rm HI} D_+(z) \frac{6H_0^3\Omega_{m0}}{\pi c^3} \tag{49}$$

$$\mathcal{I}_\ell(x) = b j_\ell(x) - f\frac{d^2 j_\ell}{dx^2} \tag{50}$$

and

$$F(\eta) = \frac{D_+(f-1)H(z)}{H_0} \tag{51}$$

For large ℓ we can use the Limber approximation (Limber (1954); Afshordi et al. (2004)) which allows us to replace the spherical Bessel functions by a Dirac deltas as

$$j_\ell(kr) \approx \sqrt{\frac{\pi}{2\ell+1}}\delta_D(\ell+\frac{1}{2}-kr)$$

whereby the angular cross-correlation power spectrum takes the simple scaling of the form

$$\mathcal{C}_\ell^{HI-ISW} \sim \frac{\pi\mathcal{K}F}{2\ell^2}P(\frac{\ell}{r}) \tag{52}$$

where $P(k)$ is the present day dark matter power spectrum and all the other terms on the *rhs.* are evaluated at $z_{\rm HI}$. The dimensionless quantity f quantifies the growth of the dark matter perturbations, and the ISW effect is proportional to $f-1$. The term $f-1$ is a sensitive probe of dark energy. Here we estimate the viability of detecting the H I -ISW cross-correlation signal. Cosmic variance sets a fundamental limit in deciding whether the signal can at all be detected or not. Even in the cosmic variance limit at $z \sim 1.0$ with a 32 MHz observation we find that S/N < 0.45 for all $z_{\rm HI}$ and ℓ and a statistically significant detection is not possible in such cases. It is possible to increase S/N collapsing the signal at different multipoles ℓ. To test if a statistically significant detection is thus feasible we have collapsed all multipoles less than ℓ to evaluate the cumulative S/N defined as (Cooray (2002); Adshead & Furlanetto (2008)) We find that the contribution in the cumulated S/N comes from $\ell < 50$ at all redshifts $0.4 < z < 2$. The cross-correlation signal is largest at ($z \sim 0.4$) and is negligible for ($z > 3$). We further find that although there is an increase in S/N on collapsing the multipoles it is still less than unity. This implies that a statistically significant detection is still not possible. Thus, probing a thin shell of H I doesn't allow us to detect a cross correlation, the signal being limited by the cosmic variance. A cumulated S/N of ~ 1.6 is attained for redshift upto $z = 2$ and there is hardly any increase in S/N on cumulating beyond this redshift. This is reasonable because the contribution from the ISW effect becomes smaller beyond the redshift $z > 2$. This S/N is the theoretically calculated value for an ideal situation and is unattainable for most practical purposes. Incomplete sky coverage, and foreground removal issues would actually reduce the S/N and attaining a statistically significant level is not feasible.

References

Adshead P. J., Furlanetto S., 2008, Monthly Notices of Royal Astronomical Society, 384

Afshordi N., Loh Y., Strauss M. A., 2004, Physical Review D, 69, 083524

Ali S. S., Bharadwaj S., 2014, Journal of Astrophysics and Astronomy, 35, 157

Ali S. S., Bharadwaj S., Chengalur J. N., 2008, Monthly Notices of Royal Astronomical Society, 385, 2166

Alonso D., Bull P., Ferreira P. G., Santos M. G., 2015, Monthly Notices of Royal Astronomical Society, 447, 400

Bagla J. S., Khandai N., Datta K. K., 2010, Monthly Notices of Royal Astronomical Society, 407, 567

Bharadwaj S., Sethi S. K., 2001, Journal of Astrophysics and Astronomy, 22, 293

Bharadwaj S., Sethi S. K., Saini T. D., 2009, Physical Review D, 79, 083538

Bull P., Ferreira P. G., Patel P., Santos M. G., 2015, Astrophysical Journal, 803, 21

Camera S., Santos M. G., Ferreira P. G., Ferramacho L., 2013, Physical Review Letters, 111, 171302

Chang T., Pen U., Peterson J. B., McDonald P., 2008, Physical Review Letters, 100, 091303

Cooray A., 2002, Physical Review D, 65, 103510

Cooray A., Kesden M., 2003, New Astronomy, 8, 231

Croft R. A. C., Hu W., Davé R., 1999a, Physical Review Letters, 83, 1092

Croft R. A. C., Weinberg D. H., Pettini M., Hernquist L., Katz N., 1999b, Astrophysical Journal, 520, 1

Delubac T., et al., 2014, preprint, (arXiv:1404.1801)

Di Matteo T., Perna R., Abel T., Rees M. J., 2002, Astrophysical Journal, 564, 576

Eisenstein D. J., Zehavi I., Hogg D. W., Scoccimarro R., 2005, Astrophysical Journal, 633, 560

Fan X., et al., 2006, Astronomical Journal, 132, 117

Font-Ribera A., et al., 2012, Journal of Cosmology and Astroparticle Physics, 11, 59

Gallerani S., Choudhury T. R., Ferrara A., 2006, Monthly Notices of Royal Astronomical Society, 370, 1401

Ghosh A., Bharadwaj S., Ali S. S., Chengalur J., 2010, Submitted to MNRAS

Ghosh A., Bharadwaj S., Ali S. S., Chengalur J. N., 2011, Monthly Notices of Royal Astronomical Society, 418, 2584

Guha Sarkar T., 2010, Journal of Cosmology and Astro-Particle Physics, 2, 2

Guha Sarkar T., Bharadwaj S., 2013, Journal of Cosmology and Astroparticle Physics, 8, 023

Guha Sarkar T., Datta K. K., 2015, Journal of Cosmology and Astroparticle Physics, 8, 001

Guha Sarkar T., Datta K. K., Bharadwaj S., 2009, Journal of Cosmology and Astro-Particle Physics, 8, 19

Guha Sarkar T., Bharadwaj S., Choudhury T. R., Datta K. K., 2011, Monthly Notices of Royal Astronomical Society, 410, 1130

Guha Sarkar T., Mitra S., Majumdar S., Choudhury T. R., 2012, Monthly Notices of Royal Astronomical Society, 421, 3570

Hanson D., Challinor A., Lewis A., 2009, preprint, (arXiv:0911.0612)

Hirata C. M., Padmanabhan N., Seljak U., Schlegel D., Brinkmann J., 2004a, Physical Review D, 70, 103501

Hirata C. M., Padmanabhan N., Seljak U., Schlegel D., Brinkmann J., 2004b, Physical Review D, 70, 103501

Hu W., 2001, Astrophysical Journal Letters, 557, L79

Hu W., Okamoto T., 2002, Astrophysical Journal, 574, 566

Kesden M., Cooray A., Kamionkowski M., 2003, Physical Review D, 67, 123507

Kim T., Bolton J. S., Viel M., Haehnelt M. G., Carswell R. F., 2007, Monthly Notices of Royal Astronomical Society, 382, 1657

Lanzetta K. M., Wolfe A. M., Turnshek D. A., 1995, Astrophysical Journal, 440, 435

Lesgourgues J., Viel M., Haehnelt M. G., Massey R., 2007, Journal of Cosmology and Astro-Particle Physics, 11, 8

Lewis A., Challinor A., 2006, Phys. Rep., 429, 1

Limber D. N., 1954, Astrophysical Journal, 119, 655

Loeb A., Wyithe J. S. B., 2008, Physical Review Letters, 100, 161301

Mandelbaum R., McDonald P., Seljak U., Cen R., 2003, Monthly Notices of Royal Astronomical Society, 344, 776

Marian L., Bernstein G. M., 2007, Physical Review D, 76, 123009

McDonald P., 2003, Astrophysical Journal, 585, 34

McDonald P., Eisenstein D. J., 2007, Physical Review D, 76, 063009

McDonald P., Miralda-Escudé J., Rauch M., Sargent W. L. W., Barlow T. A., Cen R., 2001, Astrophysical Journal, 562, 52

McQuinn M., White M., 2011, Monthly Notices of Royal Astronomical Society, 415, 2257

McQuinn M., Zahn O., Zaldarriaga M., Hernquist L., Furlanetto S. R., 2006, Astrophysical Journal, 653, 815

Myers A. D., Brunner R. J., Nichol R. C., Richards G. T., Schneider D. P., Bahcall N. A., 2007, Astrophysical Journal, 658, 85

Noterdaeme P., Petitjean P., Ledoux C., Srianand R., 2009, A&A, 505, 1087

Pal A. K., Guha Sarkar T., 2016, preprint, (arXiv:1602.07893)

Pâris I., et al., 2014, A&A, 563, A54

P'eroux C., McMahon R. G., Storrie-Lombardi L. J., Irwin M. J., 2003, Monthly Notices of Royal Astronomical Society, 346, 1103

Planck Collaboration et al., 2014, A&A, 571, A16

Rauch M., 1998, Annual Review of Astronomy & Astrophysics, 36, 267

Santos M. G., Cooray A., Knox L., 2005, Astrophysical Journal, 625, 575

Seljak U., Zaldarriaga M., 1999, Physical Review Letters, 82, 2636

Seo H.-J., Eisenstein D. J., 2007, Astrophysical Journal, 665, 14

Slosar A., et al., 2011a, Journal of Cosmology and Astroparticle Physics, 9, 1

Slosar A., Font-Ribera A., Pieri M. M. e. a., 2011b, Journal of Cosmology and Astroparticle Physics, 9, 1

Smith K. M., Hu W., Kaplinghat M., 2006, Physical Review D, 74, 123002

Smith K. M., Zahn O., Doré O., 2007, Physical Review D, 76, 043510

Van Waerbeke L., Mellier Y., 2003, ArXiv Astrophysics e-prints,

Villaescusa-Navarro F., Viel M., Datta K. K., Choudhury T. R., 2014, Journal of Cosmology and Astroparticle Physics, 9, 50

Villaescusa-Navarro F., Viel M., Alonso D., Datta K. K., Bull P., Santos M. G., 2015a, Journal of Cosmology and Astroparticle Physics, 3, 034

Villaescusa-Navarro F., Viel M., Alonso D., Datta K. K., Bull P., Santos M. G., 2015b, Journal of Cosmology and Astroparticle Physics, 3, 034

Wyithe J. S. B., 2008, Monthly Notices of Royal Astronomical Society, 388, 1889

Wyithe J. S. B., Loeb A., 2009, Monthly Notices of Royal Astronomical Society, 397, 1926

Wyithe J. S. B., Loeb A., Geil P. M., 2008, Monthly Notices of Royal Astronomical Society, 383, 1195

Modelling the 21 cm Signal From the Epoch of Reionization and Cosmic Dawn

T. Roy Choudhury*[1], Kanan Datta[2], Suman Majumdar[3], Raghunath Ghara[1], Aseem Paranjape[4], Rajesh Mondal[5], Somnath Bharadwaj[5], and Saumyadip Samui[2]

[1] *National Centre for Radio Astrophysics, TIFR, Post Bag 3, Ganeshkhind, Pune 411007, India*
[2] *Department of Physics, Presidency University, 86/1 College Street, Kolkata - 700073, India*
[3] *Department of Physics, Blackett Laboratory, Imperial College, London SW7 2AZ, UK*
[4] *Inter-University Center for Astronomy & Astrophysics, Post Bag 4, Ganeshkhind, Pune 411007, India*
[5] *Department of Physics & Centre for Theoretical Studies, Indian Institute of Technology Kharagpur, Kharagpur - 721302, India*

Abstract

Studying the cosmic dawn and the epoch of reionization through the redshifted 21 cm line are among the major science goals of the SKA1. Their significance lies in the fact that they are closely related to the very first stars in the universe. Interpreting the upcoming data would require detailed modelling of the relevant physical processes. In this article, we focus on the theoretical models of reionization that have been worked out by various groups working in India with the upcoming SKA in mind. These models include purely analytical and semi-numerical calculations as well as fully numerical radiative transfer simulations. The predictions of the 21 cm signal from these models would be useful in constraining the properties of the early galaxies using the SKA data.

1 Introduction

One of the major science goals of the SKA is to study the redshifted 21 cm signal of neutral hydrogen from the cosmic dawn and the epoch of reionization (Mellema et al., 2013; Koopmans et al., 2015; Carilli, 2015). The cosmic dawn refers to a period when the first stars formed in the universe, while the epoch of reionization is when the HI in the intergalactic medium was being ionized by the UV radiation from the first stars (see, e.g., Barkana and Loeb, 2001). It is believed that this is process which extended over redshift ranges $15 \gtrsim z \gtrsim 6$ (Mitra et al., 2015). The redshifted 21 cm radiation is possibly the most promising method of detecting the distribution of the HI at these redshifts (Furlanetto et al., 2006; Pritchard and Loeb, 2012). The signal will contain information about how this process occurred, and will indirectly help in studying the properties of the first stars and the surrounding medium at those early epochs.

Detailed models of reionization are a crucial ingredient for interpreting the data and constraining the EoR. The difficulty in constructing models at such high redshifts is that there are practically no observational constraints on the physics of galaxy formation. As a result it is often not possible to have a good idea about the number of ionizing photons available. The models thus assume simple prescriptions to assign ionizing luminosities to dark matter haloes, and try to constrain the free parameters using existing observations.

This article is meant to highlight the advances made in modelling the EoR and cosmic dawn by members of the Indian community keeping the upcoming SKA in mind. It turns out that groups working in related areas have contributed to different types of modelling, starting from purely analytical ones to complex radiative transfer simulations. The main features of these models and their main results are summarised in the following sections.

*tirth@ncra.tifr.res.in

2 Present constraints on reionization history

The main components of building a reionization model are as follows:

- The abundance (and locations) of dark matter haloes form the first step as the sources of ionizing photons (galaxies) form within these haloes. In analytical models, one can use the standard forms of the halo mass function $dn(M,z)/dM$ given by, e.g., Press and Schechter (1974); Bond et al. (1991); Sheth and Tormen (1999), while in the N-body simulations, the masses and locations of these haloes are usually obtained by group finder algorithms, e.g., the Friends-of-friend (Davis et al., 1985).

- Given the dark matter haloes, one needs to work out the physical processes related to galaxy formation, stellar radiation and escape of ionizing photons. All these are highly uncertain at $z \gtrsim 6$, hence most reionization models tend to assume some prescription which relates the number of ionizing photons to the halo mass. The simplest of these assume the number of ionizing photons in the IGM produced by a halo of mass M to be given by

$$N_\gamma = \zeta \left(\frac{\Omega_H}{\Omega_m}\right) \frac{M}{m_H}, \tag{1}$$

  where ζ is an unknown parameter and all other symbols have their usual meanings. Physically ζ is a combination of star-forming efficiency, the number of ionizing photons produced by stars and the fraction of ionizing photons that escape from the host galaxy into the IGM. The above relation can also be written in terms of the number of photons in the IGM per unit time per unit comoving volume

$$\dot{n}_\gamma = \zeta n_H \frac{df_{\rm coll}}{dt}, \tag{2}$$

  where n_H is the comoving number density of hydrogen and $f_{\rm coll}$ is the mass fraction in collapsed haloes (called the collapsed fraction) that are forming stars. The collapsed fraction is related to the mass function by

$$f_{\rm coll} = \frac{1}{\bar{\rho}_m} \int_{M_{\rm min}}^{\infty} dM\ M\ \frac{dn(M,z)}{dM}, \tag{3}$$

  where $M_{\rm min}$ is the minimum mass of haloes that can form stars. The value of $M_{\rm min}$ is decided by the cooling efficiency of the gas in collapsed haloes, e.g., if the gas contains only atomic hydrogen, it is unable to cool at virial temperatures lower than 10^4 K while the presence of molecules can push the limit to ~ 300 K.

- The third component is a description of the inhomogeneous baryonic density field. In analytical models, this could be described by the PDF $P(\Delta_B)$ of the baryonic overdensity Δ_B (smoothed over the Jeans scale). Some standard forms that are used are the lognormal distribution (Bi and Davidsen, 1997; Choudhury et al., 2001a,b; Choudhury and Ferrara, 2005), or a fitting form motivated by the hydrodynamical simulations (Miralda-Escudé et al., 2000; Bolton and Becker, 2009). While simulating the baryonic densities, it is important to be able to resolve reasonably small scales so as to identify the dense optically thick systems. These regions, because of their high recombination rate, act as "sinks" of ionizing photons and can alter the distribution of ionized regions.

- Finally, given the ionization sources and the clumpy baryonic field, one has to solve the transfer of radiation through the IGM accounting for all relevant physical processes. The cosmological radiative transfer equation

$$\frac{\partial I_\nu}{\partial t} + \frac{c}{a(t)} \hat{\mathbf{n}} \cdot \nabla_{\mathbf{x}} I_\nu - H(t)\nu \frac{\partial I_\nu}{\partial \nu} + 3H(t) I_\nu = -c\kappa_\nu I_\nu + \frac{c}{4\pi}\epsilon_\nu, \tag{4}$$

  where $I_\nu \equiv I(t, \mathbf{x}, \mathbf{n}, \nu)$ is the monochromatic specific intensity of the radiation field, $\mathbf{n}$ is a unit vector along the direction of propagation of the radaiation, κ_ν is the absorption coefficient and ϵ_ν is the emissivity, has to be solved at every point in the seven-dimensional $(t, \mathbf{x}, \mathbf{n}, \nu)$ space. However, the high dimensionality of the problem makes the solution of the complete radiative transfer

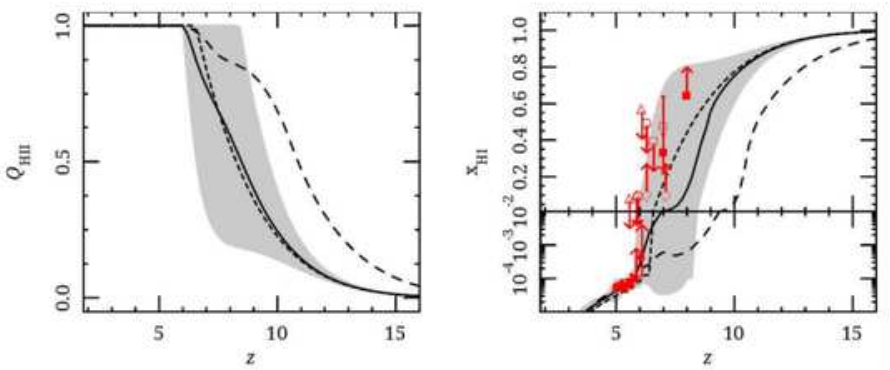

Figure 1: The mean value (solid lines) and its 2σ limits (shaded regions) for the ionized volume fraction (left panel) and the neutral hydrogen fraction (right panel) obtained using a PCA + MCMC analysis with Planck data . The fiducial model (short-dashed lines) and the model constrained using WMAP9 data (long-dashed lines) are also shown for comparison. We also show the observational limits on neutral hydrogen fraction $x_{\rm HI}(z)$ (right panel) from various measurements, for details see Mitra et al. (2015).

equation well beyond our capabilities, particularly since we do not have any obvious symmetries in the problem and often need high spatial and angular resolution in cosmological simulations. Hence, the approach to the problem has been to use different numerical schemes and approximations (Iliev et al., 2006a).

In analytical models, one can simplify the problem by taking the global average of equation (4) under the assumption that the mean free path of photons is significantly smaller than the horizon size (Choudhury, 2009). The equation can be written in terms of the volume filling factor $Q_{\rm HII}$ of ionized regions as

$$\frac{dQ_{\rm HII}}{dt} = \frac{\dot{n}_\gamma}{n_H} - Q_{\rm HII}\ \mathcal{C}\ \alpha(T)\ n_H, \tag{5}$$

where $\mathcal{C}$ is the clumping factor and $\alpha(T)$ is the recombination coefficient at a temperature T.

The uncertainties in the reionization models can, in principle, be constrained by comparing with existing data, in particular, the quasar absorption spectra blueward of the Lyα emission line and the measurements of the Thomson scattering optical depth from the CMB observations. One such physically motivated semi-analytical model (Mitra et al., 2011, 2012, 2015) which treats the ζ as an unknown function of z and constraints it using a Principal Component Analysis, predicts the evolution of $Q_{\rm HII}$ and the average neutral fraction $x_{\rm HI}$ as shown in Figure 1. One can see that the present data sets imply that reionization begins at $z \sim 15$ and is completed close to $z \sim 6$. There is still considerable uncertainty around the final stages of reionization as is shown by the width of the shaded regions around $z \sim 7-8$, and one expects the 21 cm experiments to play an important role in reducing the uncertainties.

3 Modelling the 21 cm signal from EoR

The basic principle which is central to the 21 cm experiments is the neutral hydrogen hyperfine transition line at a rest wavelength of 21 cm. This line, when redshifted, is observable at low frequencies ($\sim 90-200$ MHz for $z \sim 15-6$) against the CMB. The strength of the signal is quantified by the differential brightness temperature given by

$$\delta T_b = \bar{T}\ x_{\rm HI}\ \Delta_B\ \left(\frac{T_S - T_{\rm CMB}}{T_S}\right), \tag{6}$$

where T_S is the spin temperature of the gas and

$$\bar{T} = 27\ {\rm mK} \left(\frac{\Omega_B h^2}{0.023}\right) \left(\frac{0.15}{\Omega_m}\frac{1+z}{10}\right)^{1/2}. \tag{7}$$

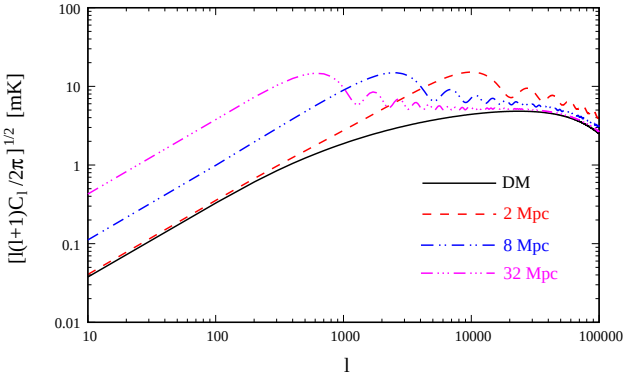

Figure 2: The angular power spectrum of HI brightness temperature fluctuations for a model with non-overlapping spherical bubbles of a fixed radius. The results are shown for three different values of the radius. Also shown is the power spectrum for dark matter linear fluctuations. See Datta et al. (2007) for details.

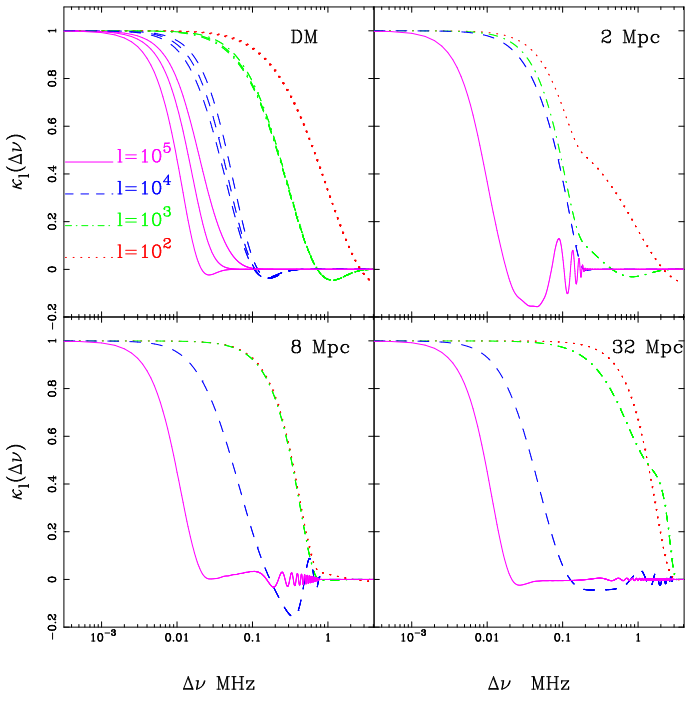

Figure 3: The frequency decorrelation function for four values of l. Results are shown for the dark matter fluctuations (upper left panel) and the reionization model with non-overlapping spherical bubbles of a fixed radius (the other three panels). See Datta et al. (2007) for details.

The quantities $x_{\rm HI}$ and Δ_B are the neutral hydrogen fraction and the baryonic overdensity respectively. The radio-interferometric observations would measure only the fluctuations in δT_b, e.g., the power spectrum $P(\mathbf{k})$ defined as

$$\langle \delta\hat{T}_b(\mathbf{k})\ \delta\hat{T}_b^*(\mathbf{k}')\rangle = (2\pi)^3\delta_D(\mathbf{k}-\mathbf{k}')P(\mathbf{k}), \tag{8}$$

where $\delta\hat{T}_b(\mathbf{k})$ is Fourier transform of δT_b. As can be seen from equation (6), the fluctuations in the signal are sourced by either fluctuations in the neutral hydrogen density field $x_{\rm HI}\ \Delta_B$ or in the spin temperature T_S. Unless one is interested in the very early stages of reionization (cosmic dawn), the IGM can be taken to be sufficiently heated by X-rays and the T_S coupled to the gas temperature through the Lyα coupling (Wouthuysen, 1952; Field, 1959). In that case $T_S \gg T_{\rm CMB}$ and hence the signal is simply $\delta T_b \propto x_{\rm HI}\ \Delta_B$, i.e., the signal will simply follow the neutral hydrogen distribution.

The above expressions do not account for the line of sight peculiar velocities of the gas which can make the power spectrum anisotropic. Other sources of anisotropies are the light cone effect and the AlcockPaczynski effect. In that case, the power spectrum can be denoted as $P(k,\mu)$, where μ is the direction cosine between the line of sight and $\mathbf{k}$. It is expected that the first generation of 21 cm experiments would measure the spherically averaged power spectrum $P_0(k) = \int_{-1}^{1}(d\mu/2)\ P(k,\mu)$.

A related quantity of interest which can be measured from the observation is the multi-frequency angular power spectrum (MAPS) defined as (Datta et al., 2007)

$$C_l(\Delta\nu) = \frac{1}{\pi r_\nu^2}\int_0^\infty dk_\parallel\ \cos(k_\parallel r'_\nu\Delta\nu)\ P(\mathbf{k}), \tag{9}$$

where r_ν is the comoving distance to the redshift $z = 1420\ {\rm MHz}/\nu - 1$ and $\mathbf{k}$ has a magnitude $k = \sqrt{k_\parallel^2 + l^2/r_\nu^2}$. The quantity $C_l(0)$ is essentially the two-dimensional power spectrum on a plane at the distance r_ν from the observer.

3.1 Analytical models

Analytical models of reionization are based on modelling the size distribution of ionized bubbles around galaxies, which then can be extended to obtain the power spectrum. The simplest model would be to approximate the ionization field as a collection of non-overlapping sphere of fixed radius R (Bharadwaj and Ali, 2005; Datta et al., 2007). The values of R and the number density of such bubbles $n_{\rm bub}$ can be chosen to obtain a particular ionized fraction $Q_{\rm HII}(z) = n_{\rm bub}\ 4\pi R^3/3$ at a given epoch. The quantity $C_l(0)$ for different values of R for such a model is shown in Fig 2. One can see that the signal is enhanced compared to the underlying dark matter fluctuations at angular scales larger than the bubble size. It peaks around a value of l which is inversely proportional to the angular size of the bubbles. The frequency decorrelation function $\kappa_l(\Delta\nu) = C_l(\Delta\nu)/C_l(0)$ as function of $\Delta\nu$ is plotted in Fig 3 which shows that the fluctuations decorrelate quite rapidly particularly for large l. This decorrelation can be useful in separating the cosmological signal from other astrophysical foregrounds which have relatively smooth frequency spectra.

These simple models of ionized bubbles do not account for the overlap and thus are valid only when the ionized fraction is very small. It is possible to account for such overlaps using the excursion set approach as was proposed by Furlanetto et al. (2004), which we refer to as FZH04. In this approach the condition for a spherical region of radius R having a density contrast δ (linearly extrapolated to present epoch) to be fully ionized $\langle Q_{\rm HII}\rangle_{\delta,R} \geq 1$ is given by a condition on the collapsed faction in the region

$$\langle f_{\rm coll}\rangle_{\delta,R} \geq \zeta^{-1}. \tag{10}$$

The condition for a region to be "self-ionized" can be converted into a condition in terms of the density contrast δ, and then problem reduces to the one for a barrier crossing. An improvement to the above model was proposed by Paranjape and Choudhury (2014) by accounting for the fact that haloes would preferentially form near the density peaks (Musso and Sheth, 2012; Paranjape and Sheth, 2012), known as the excursion sets peak (ESP) model. Fig 4 shows the bubble size distribution for the two models FZH04 and ESP for fixed values of the ionized fraction $Q_{\rm HII}$. The main effect of the ESP model is to predict bubbles of relatively larger sizes, a fact which was confirmed while calculating the bubble distribution from semi-numerical calculations. This implies that the power spectrum predicted from the ESP model would be very different from the earlier calculations, a fact which can play an important role in interpreting the 21 cm data.

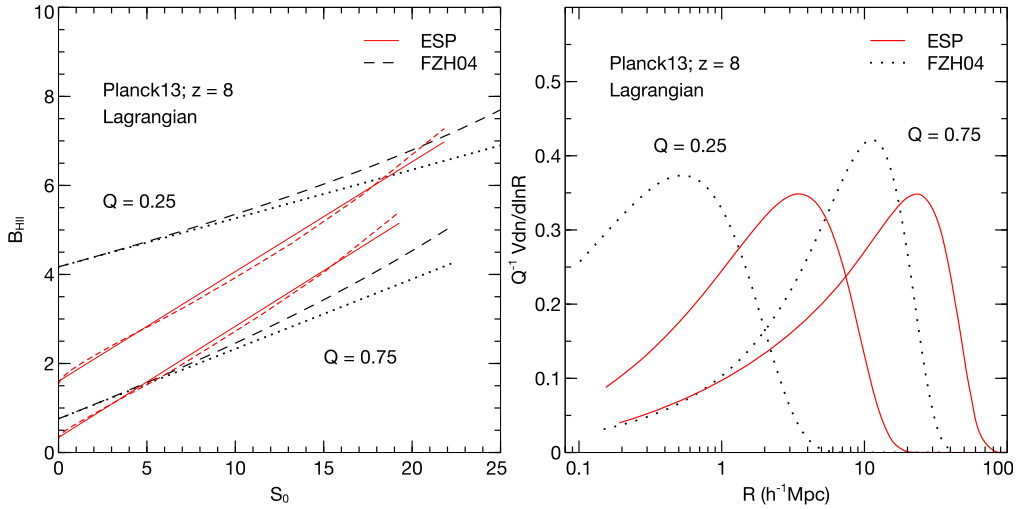

Figure 4: Comparison of the FZH04 (Furlanetto et al., 2004) and ESP (Paranjape and Choudhury, 2014) calculations at redshift $z = 8$ for the Planck13 cosmology at the same value of global ionized Lagrangian volume fraction. Left-hand panel: ionization barriers. Right-hand panel: normalized Lagrangian bubble size distributions corresponding to the linear barriers of the left-hand panel. See Paranjape and Choudhury (2014) for details.

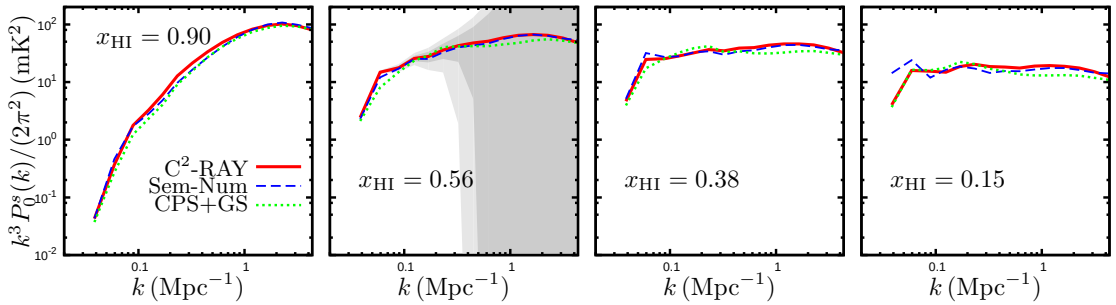

Figure 5: The spherically averaged power spectrum of the redshift space 21-cm signal for the radiative transfer simulation C^2-RAY and two different semi-numerical models. The shaded regions in light and dark gray represent the uncertainty due LOFAR-like system noise at 150 MHz for 1000 and 2000 hr of observation respectively. See Majumdar et al. (2014) for more details.

3.2 Semi-numerical models

Although the excursion-set based analytical calculations provide a reasonable description of the growth of HII regions during reionization, it is difficult to incorporate various complexities into the analytical framework e.g., the non-sphericity of bubble during overlap, the effects of line of sight peculiar velocities, quantifying the cosmic variance. It is often useful to have realisations of the ionization field so that one can construct realistic radio maps and other quantities relevant to the observations. One can use the radiative transfer simulations to generate such maps, however, they are often not suited for exploring the parameter space.

A compromise has been proposed where it is possible to generate HI maps without running the full simulation. These semi-numerical methods are based on the excursion set formalism discussed in the previous section and can be used for generating reasonably large volumes in a small amount of time (Mesinger and Furlanetto, 2007; Geil and Wyithe, 2008). One of these methods is based on generating the DM density field using the perturbation theory, calculating the collapsed fraction within each grid cell (of size R and density contrast δ) using the analytical expression for the conditional mass function and then generating the ionization field using the excursion set formalism (Mesinger et al., 2011). A slightly different approach is to run a full dark matter only N-body simulation and identify the haloes using a suitable group-finder algorithm (Zahn et al., 2007; Choudhury et al., 2009). The method for generating the ionization field remains the same, i.e., using the excursion set formalism.

To understand how these semi-numerical models work, let us assume that we have a realisation of the density field along with the collapsed fraction at each grid point of the simulation box. The basic idea is to compute the spherically averaged collapsed fraction $\langle f_{\rm coll}\rangle_R$ for each grid point in the box for a wide range of R values. If the self-ionization condition (10) is satisfied for any R, then the grid point is flagged as ionized. Points which fail to satisfy the condition are assigned a neutral fraction $\zeta\langle f_{\rm coll}\rangle_{R_{\rm cell}}$, where $R_{\rm cell}$ is the size of the grid cell typically set by the resolution of the map. The procedure is repeated for all points in the simulation volume. The method thus provides a realisation of the ionization field for a given value of ζ.

One important physical process which is not taken into account in the above discussion is the recombination. A significant fraction of the ionizing photons may be lost in ionizing the recombined hydrogen atoms, which may lead to very different HI topology. In the simplest case where recombinations are taken to be spatially homogeneous, the effect can be absorbed in the definition of ζ. In other words, one can rewrite the ionization condition as

$$\langle f_{\rm coll}\rangle_R \geq \zeta^{-1}(1+\bar{N}_{\rm rec}) \equiv \zeta_{\rm eff}^{-1}, \tag{11}$$

where $\bar{N}_{\rm rec}$ is the average number of recombinations per hydrogen atom. Since $\bar{N}_{\rm rec}$ is assumed to be independent of the spatial point under consideration, the above equation is simply the earlier ionization condition (10) with the redefinition $\zeta \rightarrow \zeta_{\rm eff}$.

In reality, however, the recombinations are not homogeneous. In fact, the high density regions will tend to recombine faster and will be able to "shield" themselves from the ionizing radiation. These regions would act as "sinks" of ionizing photons. One way of implementing the effect of such sinks into the semi-numerical models is by including an additional condition for ionization (Choudhury et al., 2009)

$$\langle n_\gamma\rangle_R \geq n_H \, \frac{\epsilon t_H}{t_{\rm rec}} \, \frac{L}{R}, \tag{12}$$

where $\langle n_\gamma\rangle_R$ is the number density of ionizing photons averaged over the region of radius R, $t_{\rm rec}$ is the recombination time-scale, ϵt_H is the time-scale over which the recombination term has significant contribution with t_H being the Hubble time and L is the comoving size of the absorbing region, usually taken to be the local Jeans scale. The effect of these recombinations is that the reionization becomes outside-in once a substantial fraction of the IGM is ionized (in contrast to models without sinks where the process is always inside-out). The presence of sinks predict smaller amplitude of fluctuations at scales $k \sim 0.1$ Mpc^{-1} accessible to first generation of 21 cm experiments.

This model of Choudhury et al. (2009) was used by Majumdar et al. (2013) to study the effect of peculiar velocities on the signal. It was proposed that the magnitude and nature of the ratio between the quadrupole and monopole moments of the power spectrum (P_2^s/P_0^s) can be a possible probe for the epoch of reionization. The same semi-numerical models have also been used for showing that the 21 cm

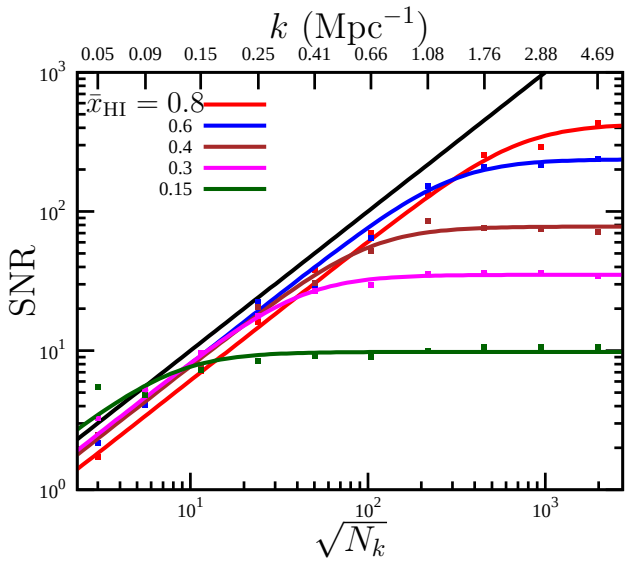

Figure 6: The SNR as a function of $\sqrt{N_k}$. The 45° black line shows the SNR expected for a Gaussian random field. For the $\bar{x}_{\rm HI}$ values mentioned in the figure, the data points (squares) show the simulated SNR and the solid lines show the fit given by Equation 1 of (Ref. Mondal et. al 2015). The k value corresponding to each k bin is shown in the top x axis.

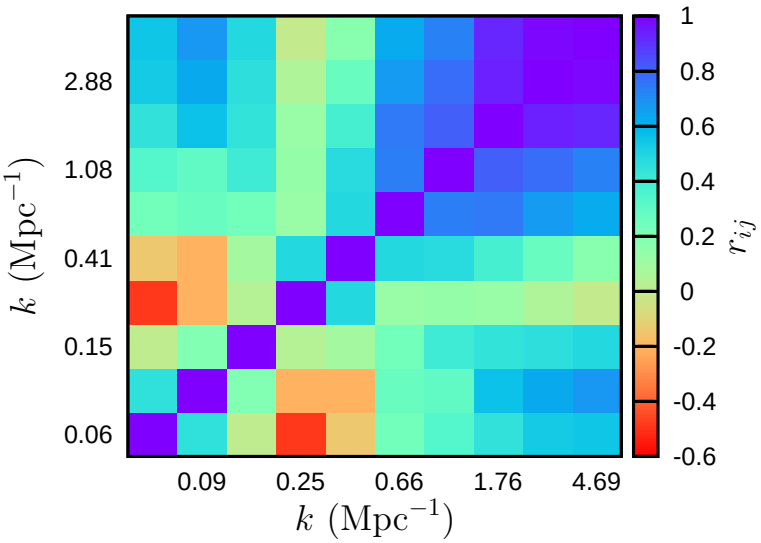

Figure 7: The correlation coefficient $r_{ij} = C_{ij}/\sqrt{C_{ii}C_{jj}}$, where C_{ij} is the EoR 21-cm power spectrum error covariance.

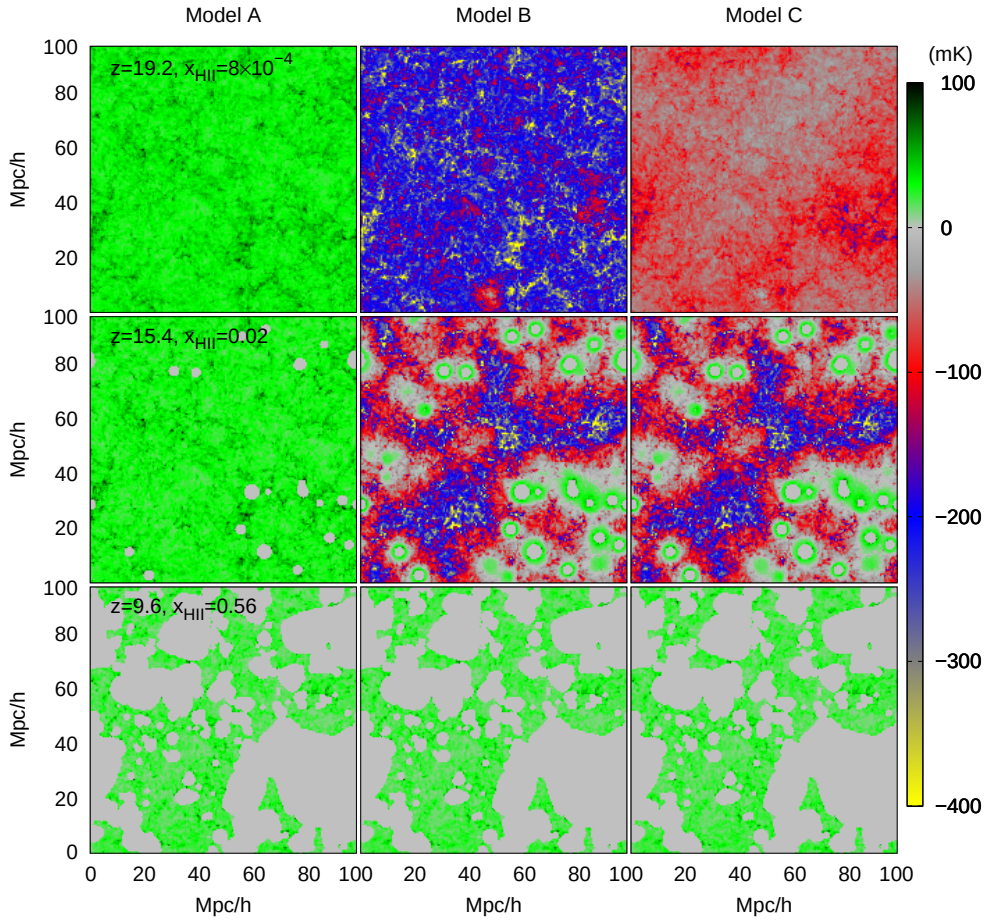

Figure 8: The brightness temperature maps for three different redshifts for three different models A, B and C. Model A assumes the IGM to be Lyα coupled and highly heated ($T_S \gg T_{\rm CMB}$). Model B assumes the IGM to be strongly Lyα coupled but self-consistently heated by X-rays, while model C considers Lyα coupling and X-ray heating self-consistently. See Ghara et al. (2015a) for details.

anisotropy is best measured by the quadrupole moment of the power spectrum, i.e., it evolves predictably as a function of $Q_{\rm HII}$ (Majumdar et al., 2016).

Since the semi-numerical simulations are quite fast in terms of their computing time, they are suitable for studying various statistical properties of the signal which may require large number of realisations. One such application is to study the effects of non-Gaussianity of the ionization field on error predictions for the power spectrum (Mondal et al., 2015, 2016). Unlike the Gaussian case where SNR $\propto N_k^{1/2}$, N_k being the number Fourier modes in a given k-bin, the SNR has upper limit which cannot be exceeded by increasing N_k (Mondal et al., 2015) which can be seen in Fig 6. This could have severe implications for estimating the sensitivities for the future 21 cm experiments. In fact, one can see from Fig 7 that the error covariance is not diagonal any more and the coupling between different k-modes cannot be neglected for error estimations (Mondal et al., 2016).

3.3 Numerical simulations

The full complexities of the radiative transfer through the clumpy IGM can only be taken into account through the numerical solution of the radiative equation (4). However, radiative transfer simulations are still computationally extremely challenging and hence the equation is usually solved under reasonable

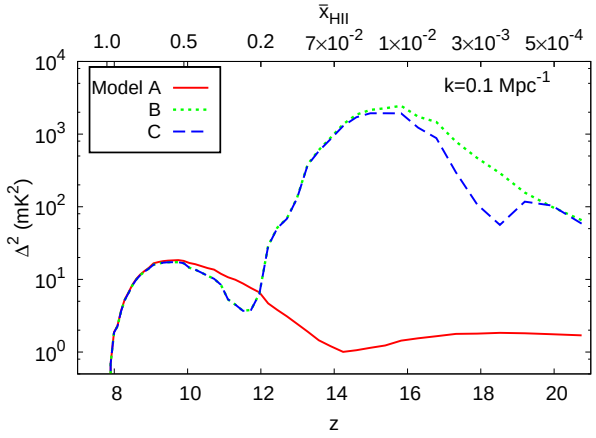

Figure 9: Evolution of 21 cm power spectrum at scale $k = 0.1$ Mpc $^{-1}$ for models A (solid red), B (dotted green) and C (dashed blue), respectively. See Ghara et al. (2015a) for details.

approximations. One such algorithm has been implemented in the radiative transfer code "Conservative Causal Ray-tracing method" (C^2-RAY) which works by tracing rays from all sources and iteratively solving for the time evolution of the ionized hydrogen fraction (Mellema et al., 2006; Iliev et al., 2006b). It turns out that the ionization fields generated by the C^2-RAY have properties which are quite similar to the semi-numerical calculations described in the previous section (Majumdar et al., 2014). Fig 5 shows the 21 cm power spectrum obtained from the C^2-RAY compared with various semi-numerical schemes. The match turns out to be quite reasonable thus showing that one can possibly use the fast semi-numerical models to generate the 21 cm maps.

An alternate, relatively faster, method is to use the density field and haloes from a dark matter only N-body simulation, and post-process with a spherically symmetric one-dimensional radiative transfer algorithm (Thomas and Zaroubi, 2008; Thomas et al., 2009). The main idea is to generate spherically symmetric 21 cm patterns around individual sources (galaxies) and then account for the overlap of such regions suitably. This method has been implemented by Ghara et al. (2015a) whose code not only accounts for ionization of hydrogen and helium, but also the effects of X-ray heating and Lyα radiation. Inclusion of these effects allows one to estimate the spin temperature at different points self-consistently and hence study the effect of fluctuations in T_S. Some sample outputs from the code are shown in Fig 8 for three different models of treating the spin temperature fluctuations. The corresponding evolution of the 21 cm signal fluctuations at a scale $k \sim 0.1$ Mpc^{-1} is shown in Fig 9. If we concentrate on model C where the heating and the Lyα coupling are calculated self-consistently, we find that the evolution shows three distinct "peaks". They arise from different physical processes, i.e., the one at the lowest redshift $z \sim 9$ arises from fluctuations in $x_{\rm HI}$, the second peak at $z \sim 15$ corresponds to fluctuations in the X-ray heating and the one at $z \sim 20$ is from the Lyα coupling fluctuations. Measuring these peak-like features could be quite important in understanding the physical processes at early times. It should however be kept in mind that various line of sight effects may affect the amplitude of these peaks and hence care should be maintained while interpreting the results (Ghara et al., 2015a,c).

4 Future outlook

There has been tremendous progress in modelling the physics of cosmic dawn and reionization in recent times. It is now possible to construct models that are consistent with all available observations related to reionization (Mitra et al., 2015). The prediction of the 21 cm signal is possibly a greater challenge and there are various approaches in modelling this.

The construction of the SKA-low phase 1 will allow us to probe the 21 cm cosmological signal with unprecedented sensitivity. Fig 10 compares the expected sensitivity of SKA1-low with some of the existing facilities. As one can see, the noise variance for the SKA1-low will be almost a order of magnitude better than any of the existing ones, thus allowing us to probe the high-z universe in much more detail.

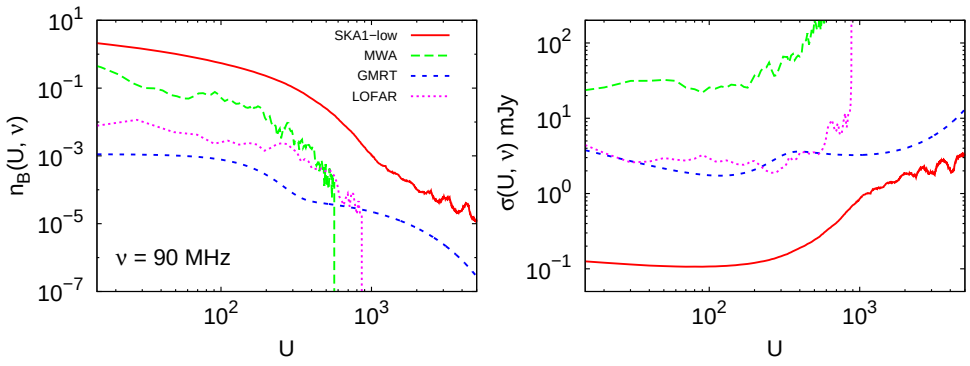

Figure 10: The baseline distributions (left panel) and the corresponding rms noise in visibilities (right panel) for the SKA1-low, MWA, GMRT and LOFAR at frequency 90 MHz. $n_{\rm B}(U, \nu)$ denote the number of antenna pairs having same baseline U at frequency ν. The rms is computed for an observation time of 1000 hours and frequency resolution of 50 kHz. See Ghara et al. (2015b) for details.

Given this advancement, we require equally advanced techniques in modelling the signal so as to interpret the data accurately. Some of the directions in which the models discussed in the article can be improved are as follows:

- Since the physical processes at high redshifts are uncertain, they need to be parametrized by a number of free parameters (and functions). The analytical calculations could be quite helpful in probing the space of these unknown parameters as they are fast. The challenge then would be to improve the analytical models and make them as accurate as possible, most likely by comparing with semi-numerical and radiative transfer simulations. There also remain some conceptual issues with these excursion set based approaches, e.g., violation of photon conservation (Paranjape et al., 2015).

- One important physical process which is still not accounted for satisfactorily is the effect of high density regions or sinks of ionizing photons. Appropriate self-consistent and accurate treatments of these regions are required for analytical, semi-numerical and radiative transfer simulations. This could turn out to be a major challenge for reionization models in the near future (Mesinger et al., 2015; Choudhury et al., 2015; Shukla et al., 2016).

- In addition to the 21 cm experiments, there would be instruments at other wave bands which are likely to come up in the near future probing the high-z universe, e.g., JWST, TMT and so on. The models of galaxy formation as well as HI distribution should be sufficiently broad so as to explain all these observations simultaneously. This would be very important for understanding the EoR.

- The sensitivities of the SKA1-low would not only probe the power spectrum of HI fluctuations, but would also allow us to image the HI distribution. It is thus important to explore the new information one can obtain through these images.

- With the improvement in the noise properties of the instrument, it becomes important to devise advanced statistical estimators which can be used for obtaining the relevant quantities of interest. Thus a better modelling of the system noise coupled with improved reionization models is required in the near future.

References

Barkana, R. and Loeb, A.: 2001, Phys. Rep. **349**, 125

Bharadwaj, S. and Ali, S. S.: 2005, MNRAS **356**, 1519

Bi, H. and Davidsen, A. F.: 1997, ApJ **479**, 523

Bolton, J. S. and Becker, G. D.: 2009, MNRAS **398**, L26

Bond, J. R., Cole, S., Efstathiou, G., and Kaiser, N.: 1991, ApJ **379**, 440

Carilli, C.: 2015, *Advancing Astrophysics with the Square Kilometre Array (AASKA14)* p. 171

Choudhury, T. R.: 2009, *Current Science* **97**, 841

Choudhury, T. R. and Ferrara, A.: 2005, MNRAS **361**, 577

Choudhury, T. R., Haehnelt, M. G., and Regan, J.: 2009, MNRAS **394**, 960

Choudhury, T. R., Padmanabhan, T., and Srianand, R.: 2001a, MNRAS **322**, 561

Choudhury, T. R., Puchwein, E., Haehnelt, M. G., and Bolton, J. S.: 2015, MNRAS **452**, 261

Choudhury, T. R., Srianand, R., and Padmanabhan, T.: 2001b, ApJ **559**, 29

Datta, K. K., Choudhury, T. R., and Bharadwaj, S.: 2007, MNRAS **378**, 119

Davis, M., Efstathiou, G., Frenk, C. S., and White, S. D. M.: 1985, ApJ **292**, 371

Field, G. B.: 1959, ApJ **129**, 536

Furlanetto, S. R., Oh, S. P., and Briggs, F. H.: 2006, Phys. Rep. **433**, 181

Furlanetto, S. R., Zaldarriaga, M., and Hernquist, L.: 2004, ApJ **613**, 1

Geil, P. M. and Wyithe, J. S. B.: 2008, MNRAS **386**, 1683

Ghara, R., Choudhury, T. R., and Datta, K. K.: 2015a, MNRAS **447**, 1806

Ghara, R., Choudhury, T. R., and Datta, K. K.: 2015b, *ArXiv e-prints*

Ghara, R., Datta, K. K., and Choudhury, T. R.: 2015c, MNRAS **453**, 3143

Iliev, I. T., Ciardi, B., Alvarez, M. A., Maselli, A., Ferrara, A., Gnedin, N. Y., Mellema, G., Nakamoto, T., Norman, M. L., Razoumov, A. O., Rijkhorst, E.-J., Ritzerveld, J., Shapiro, P. R., Susa, H., Umemura, M., and Whalen, D. J.: 2006a, MNRAS **371**, 1057

Iliev, I. T., Mellema, G., Pen, U.-L., Merz, H., Shapiro, P. R., and Alvarez, M. A.: 2006b, MNRAS **369**, 1625

Koopmans, L., Pritchard, J., Mellema, G., Aguirre, J., Ahn, K., Barkana, R., van Bemmel, I., Bernardi, G., Bonaldi, A., Briggs, F., de Bruyn, A. G., Chang, T. C., Chapman, E., Chen, X., Ciardi, B., Dayal, P., Ferrara, A., Fialkov, A., Fiore, F., Ichiki, K., Illiev, I. T., Inoue, S., Jelic, V., Jones, M., Lazio, J., Maio, U., Majumdar, S., Mack, K. J., Mesinger, A., Morales, M. F., Parsons, A., Pen, U. L., Santos, M., Schneider, R., Semelin, B., de Souza, R. S., Subrahmanyan, R., Takeuchi, T., Vedantham, H., Wagg, J., Webster, R., Wyithe, S., Datta, K. K., and Trott, C.: 2015, *Advancing Astrophysics with the Square Kilometre Array (AASKA14)* p. 1

Majumdar, S., Bharadwaj, S., and Choudhury, T. R.: 2013, MNRAS **434**, 1978

Majumdar, S., Jensen, H., Mellema, G., Chapman, E., Abdalla, F. B., Lee, K.-Y., Iliev, I. T., Dixon, K. L., Datta, K. K., Ciardi, B., Fernandez, E. R., Jelić, V., Koopmans, L. V. E., and Zaroubi, S.: 2016, MNRAS **456**, 2080

Majumdar, S., Mellema, G., Datta, K. K., Jensen, H., Choudhury, T. R., Bharadwaj, S., and Friedrich, M. M.: 2014, MNRAS **443**, 2843

Mellema, G., Iliev, I. T., Alvarez, M. A., and Shapiro, P. R.: 2006, New A **11**, 374

Mellema, G., Koopmans, L. V. E., Abdalla, F. A., Bernardi, G., Ciardi, B., Daiboo, S., de Bruyn, A. G., Datta, K. K., Falcke, H., Ferrara, A., Iliev, I. T., Iocco, F., Jelić, V., Jensen, H., Joseph, R., Labroupoulos, P., Meiksin, A., Mesinger, A., Offringa, A. R., Pandey, V. N., Pritchard, J. R., Santos, M. G., Schwarz, D. J., Semelin, B., Vedantham, H., Yatawatta, S., and Zaroubi, S.: 2013, *Experimental Astronomy* **36**, 235

Mesinger, A., Aykutalp, A., Vanzella, E., Pentericci, L., Ferrara, A., and Dijkstra, M.: 2015, MNRAS **446**, 566

Mesinger, A. and Furlanetto, S.: 2007, ApJ **669**, 663

Mesinger, A., Furlanetto, S., and Cen, R.: 2011, MNRAS **411**, 955

Miralda-Escudé, J., Haehnelt, M., and Rees, M. J.: 2000, ApJ **530**, 1

Mitra, S., Choudhury, T. R., and Ferrara, A.: 2011, MNRAS **413**, 1569

Mitra, S., Choudhury, T. R., and Ferrara, A.: 2012, MNRAS **419**, 1480

Mitra, S., Choudhury, T. R., and Ferrara, A.: 2015, MNRAS **454**, L76

Mondal, R., Bharadwaj, S., and Majumdar, S.: 2016, MNRAS **456**, 1936

Mondal, R., Bharadwaj, S., Majumdar, S., Bera, A., and Acharyya, A.: 2015, MNRAS **449**, L41

Musso, M. and Sheth, R. K.: 2012, MNRAS **423**, L102

Paranjape, A. and Choudhury, T. R.: 2014, MNRAS **442**, 1470

Paranjape, A., Choudhury, T. R., and Padmanabhan, H.: 2015, *ArXiv e-prints*

Paranjape, A. and Sheth, R. K.: 2012, MNRAS **426**, 2789

Press, W. H. and Schechter, P.: 1974, ApJ **187**, 425

Pritchard, J. R. and Loeb, A.: 2012, *Reports on Progress in Physics* **75(8)**, 086901

Sheth, R. K. and Tormen, G.: 1999, MNRAS **308**, 119

Shukla, H., Mellema, G., Iliev, I. T., and Shapiro, P. R.: 2016, MNRAS **458**, 135

Thomas, R. M. and Zaroubi, S.: 2008, MNRAS **384**, 1080

Thomas, R. M., Zaroubi, S., Ciardi, B., Pawlik, A. H., Labropoulos, P., Jelić, V., Bernardi, G., Brentjens, M. A., de Bruyn, A. G., Harker, G. J. A., Koopmans, L. V. E., Mellema, G., Pandey, V. N., Schaye, J., and Yatawatta, S.: 2009, MNRAS **393**, 32

Wouthuysen, S. A.: 1952, AJ **57**, 31

Zahn, O., Lidz, A., McQuinn, M., Dutta, S., Hernquist, L., Zaldarriaga, M., and Furlanetto, S. R.: 2007, ApJ **654**, 12

Line of sight anisotropies in the cosmic dawn and EoR 21-cm power spectrum

Suman Majumdar*[1], Kanan K. Datta[2], Raghunath Ghara[3], Rajesh Mondal[4], T. Roy Choudhury[3], Somnath Bharadwaj[4], and Abhirup Datta[5]

[1]*Department of Physics, Blackett Laboratory, Imperial College, London SW7 2AZ, UK*
[2]*Department of Physics, Presidency University, 86/1 College Street, Kolkata - 700073, India*
[3]*National Centre for Radio Astrophysics, TIFR, Post Bag 3, Ganeshkhind, Pune 411007, India*
[4]*Department of Physics & Centre for Theoretical Studies, Indian Institute of Technology Kharagpur, Kharagpur - 721302, India*
[5]*Centre for Astronomy, Indian Institute of Technology Indore, Indore - 452020, India*

Abstract

The line of sight direction in the redshifted 21-cm signal coming from the cosmic dawn and the epoch of reionization is quite unique in many ways compared to any other cosmological signal. Different unique effects, such as the evolution history of the signal, non-linear peculiar velocities of the matter etc will imprint their signature along the line of sight axis of the observed signal. One of the major goals of the future SKA-LOW radio interferometer is to observe the cosmic dawn and the epoch of reionization through this 21-cm signal. It is thus important to understand how these various effects affect the signal to detect and analyze it properly. For more than one and half decades, various groups in India have been actively trying to understand and quantify the different line of sight effects that are present in this signal through analytical models and simulations. In many ways the importance of this sub-field under 21-cm cosmology have been identified, highlighted and pushed forward by the Indian community. In this article we briefly describe their contribution and implication of these effects in the context of the future surveys of the cosmic dawn and the epoch of reionization that will be conducted by the SKA-LOW.

1 Introduction

The 'Cosmic Dawn' (CD) is the period in the history of our universe when the first sources of light were formed and they gradually warmed up their surrounding intergalactic medium (IGM). This period was followed by the 'Epoch of Reionization' (EoR) when these first and subsequent population of sources produced enough ionizing photons to gradually change the state of most of the hydrogen in our universe from neutral (H Romani) to ionized (H Romanii). These two epochs possibly are the least known periods in the history of our universe. Our present understanding of these epochs is mainly constrained by the observations of the cosmic microwave background radiation (CMBR) (Komatsu et al., 2011; Planck Collaboration, 2015) and the absorption spectra of the high redshift quasars (Becker et al., 2001; Fan et al., 2003; Becker et al., 2015). These indirect observations are rather limited in their ability to answer many fundamental questions regarding these periods; *e.g.* the properties of these first sources of light and how they evolve as reionization progresses, precise duration and timing of the CD and the EoR, the relative contribution in the heating and ionization of the IGM from various types of sources, and the typical size and distribution of the heated and ionized regions. It is being anticipated that the currently ongoing and proposed future radio interferometric surveys of these epochs, through the brightness temperature fluctuations of the redshifted 21-cm signal originating due to the hyperfine transition in the neutral hydrogen, has the potential to answer most these fundamental questions.

*s.majumdar@imperial.ac.uk

The currently ongoing redshifted 21-cm radio interferometric surveys, being conducted using the GMRT[1] (Paciga et al., 2013), LOFAR[2] (Yatawatta et al., 2013; van Haarlem et al., 2013), MWA[3] (Tingay et al., 2013; Bowman et al., 2013; Dillon et al., 2014) and PAPER[4] (Parsons et al., 2014; Jacobs et al., 2015; Ali et al., 2015), are mainly aimed at detecting this signal from the EoR. Most of these instruments are not sensitive enough at high redshifts to detect this signal from the CD. The low frequency aperture array of the upcoming Square Kilometre Array (SKA-LOW[5]) will be a significant step forward in this regard as it will have enough sensitivity over a large range of low frequencies to observe the redshifted 21-cm signal from both the CD and the EoR (Mellema et al., 2013; Koopmans et al., 2015). Also, it is worth mentioning that, while the first generation experiments aim to detect the signal through statistical estimators like variance and power spectrum (due to their limited sensitivity), the SKA-LOW is expected to be sensitive enough (owing to its large collecting area) to make images of fluctuations in H Romani from these epochs (Mellema et al., 2015).

However, as the redshifted 21-cm signal from the CD and the EoR has not been detected till date by any of these first generation telescopes and they so far only managed to provide somewhat weak upper limits on the signal power spectra (Paciga et al., 2013; Ali et al., 2015) at large length scales, so it has been planned that the first phase of the SKA-LOW will survey a large volume of the sky for a relatively shorter observation time to estimate the signal power spectrum at different redshifts, which will possibly constrain some of the main parameters of the signal (Koopmans et al., 2015). The spherically averaged power spectrum which is perceived as the main tool to achieve the first detection of the signal with the first generation instruments and the initial tool for the CD-EoR parameter estimation with the SKA-LOW, provides a high signal to noise ratio (SNR) by averaging the signal in spherical shells in Fourier space, while still preserving many important features of the signal. However, as the CD-EoR 21-cm signal is expected to be highly non-Gaussian in nature (Bharadwaj and Pandey, 2005; Mondal et al., 2015, 2016a,b), thus the power spectrum alone cannot represent all the properties of such a field.

Even when one is dealing with the power spectra of the signal, one has to be aware of the fact that the line of sight (LoS) direction of the redshifted 21-cm signal is unique. As the 21-cm signal originates from a line transition, signal coming from different cosmological distances along the LoS essentially belongs to different epochs and gets redshifted to different wavelengths, characterized by their cosmological redshift z. This implies that the signal present in an actual observational data cube containing a range of frequencies or wavelengths will evolve in time along the frequency or LoS direction. This is popularly known as the light cone effect. Thus while analyzing the three dimensional data one has to take this into account for a proper interpretation of the signal.

Another effect which also affects the signal along the LoS direction is the non-random distortions of the signal caused by the peculiar velocities of the matter particles. The coherent inflows of matter into overdense regions and the outflows of matter from underdense regions will produce an additional red or blueshift in the 21-cm signal on top of the cosmological redshift, changing the contrast of the 21-cm signal, and making it anisotropic along the LoS. It has been first highlighted by Bharadwaj and Ali (2004, 2005) and Ali et al. (2005) that the peculiar velocities will significantly change the amplitude and the shape of the 21-cm power spectrum measured from the observations of the periods before, during and even after the reionization.

Ali et al. (2005) was also first to highlight another source of anisotropy along the LoS of the redshifted 21-cm signal from the CD and the EoR, which is caused due to the Alcock-Paczynski effect (Alcock and Paczynski, 1979). This is the anisotropy due to the non-Euclidean geometry of the space-time. It is important to take into account this effect when one wants to do parameter estimation using the CD-EoR 21-cm power spectrum to quantify the uncertainties of such an analysis caused by the wrong modelling of the background cosmology.

Understanding and quantifying the line of sight anisotropy (caused by several aforementioned reasons) in the CD-EoR 21-cm power spectrum has been one of the long standing important issues in 21-cm cosmology. This will be especially important in the context of the upcoming SKA-LOW observations, which will probably be the first instrument to have enough sensitivity to constrain the model parameters of both the CD and the EoR significantly using the 21-cm power spectrum. The Indian community has

[1]http://www.gmrt.ncra.tifr.res.in
[2]http://www.lofar.org
[3]http://www.haystack.mit.edu/ast/arrays/mwa
[4]http://eor.berkeley.edu
[5]http://www.skatelescope.org

been particularly very active for almost one and half decade in this sub-field under 21-cm cosmology. To be more precise, in the context of the 21-cm cosmology this sub-field was first identified and highlighted by the Indian community through analytical models of the signal power spectrum (Bharadwaj et al., 2001; Bharadwaj and Ali, 2004, 2005; Bharadwaj and Pandey, 2005; Ali et al., 2005; Datta et al., 2007). These analytical predictions were later tested, validated and further pushed forward by the same groups from the Indian community (along with their international collaborators) using various kinds of simulations (Choudhury et al., 2009; Datta et al., 2012; Majumdar et al., 2013; Jensen et al., 2013; Datta et al., 2014; Majumdar et al., 2014; Ghara et al., 2015a,b; Majumdar et al., 2016). In this article we aim to summarize the effects of line of sight anisotropy in the CD-EoR 21-cm power spectrum considering future SKA-LOW observations and the Indian contribution in this subject.

The structure of this article is as follows. In Section 2, we briefly describe different sources that contribute to the LoS anisotropy of the signal. We next describe different methods to quantify the LoS anisotropy present in the power spectra in Section 3. In Sections 4 and 5 we describe how one would be able to quantify and interpret the two major sources of LoS anisotropy in the signal using the simulated expected signal at different era, for several ongoing experiments and as well as for the SKA-LOW. We further discuss several issues that may hinder the detection of the signal as well as the quantification of the anisotropy in it in Section 6. Finally, in Section 7, we summarize our review.

2 Line of sight anisotropies in the redshifted 21-cm signal from the CD and EoR

We briefly describe here the three major LoS anisotropies affecting the redshifted 21-cm signal originating from the cosmic dawn and the EoR.

2.1 Redshift space distortions

The effect of redshift space distortions in the redshifted 21-cm signal from the CD and EoR is one of the fields that has been pioneered and pushed forward by the Indian community for almost over a decade. The fluctuations in the brightness temperature of the redshifted 21-cm radiation essentially trace the H Romani distribution during the CD and the EoR. In a completely neutral IGM the H Romani distribution is expected to follow the underlying matter distribution with a certain amount of bias, at large enough length scales. The coherent inflows of matter into overdense regions and the outflows of matter from underdense regions will produce an additional red or blue shift on top of the cosmological redshift. If we consider a distant observer located along the x axis and use the x component of the peculiar velocity to determine the position of H Romani particles in redshift space

$$s = x + \frac{v_x}{aH(a)}\,, \tag{1}$$

where a and $H(a)$ are the scale factor and Hubble parameter respectively. Thus, in redshift space the apparent locations of the H Romani particles will change according to the above equation, which will effectively change the contrast of the 21-cm signal and will make it anisotropic along the LoS. However, as the first sources of lights were formed and they start converting their surrounding H Romani into H Romanii , the one-to-one correspondence between matter and H Romani no longer holds and the effect of the matter peculiar velocities on the 21-cm signal becomes much more complicated. In the context of the 21-cm signal from the CD and EoR, this effect was first pointed out and quantified in Bharadwaj and Ali (2004) and Bharadwaj and Ali (2005). Their analytical treatment showed that the redshift space distortions changes the shape and amplitude of the signal power spectrum significantly when measured from the recorded visibilities in a radio interferometric observation. It has also been proposed that one can possibly extract the matter power spectrum (Barkana and Loeb, 2005; Shapiro et al., 2013) at these epochs using the redshift space anisotropy present in the 21-cm power spectrum.

2.2 Light cone effect

The other LoS anisotropy that will be present in the observed 21-cm signal is known as the light cone anisotropy. As light takes a finite amount of time to reach from a distant point to an observer, thus

the cosmological 21-cm signal coming from different cosmological redshifts essentially belongs to different distances and thus correspond to different cosmological epochs. In the context of redshifted 21-cm signal, this change in frequency due to cosmological redshift can be represented by

$$\lambda_{\rm obs} = \lambda_{\rm emitted}(1+z)\,. \tag{2}$$

Any radio interferometric observation produces a three dimensional data set containing a range of frequencies. The time evolution of the signal will be present in such a data set as one changes the frequency. Thus while making estimating power spectrum of the signal from such a data one needs take into account this effect for a proper interpretation of the signal. In the context of 21-cm signal this was first considered by Barkana and Loeb (2006) in their analytical estimation of the two point correlation function of the signal. This also makes the shape of the H Romanii regions around extremely bright sources (e.g. quasars) anisotropic along the LoS (Wyithe et al., 2005; Yu, 2005; Majumdar et al., 2011, 2012). If the reionization was dominated by such sources than the effect on power spectrum and correlation functions in such a case has been studied by Sethi and Haiman (2008).

2.3 Alcock-Paczynski effect

The Alcock-Paczynski effect (Alcock and Paczynski 1979, hereafter the AP effect), another anisotropy in the signal along the LoS, is caused due to the non-Euclidean geometry of the space-time. This makes any object, which is intrinsically spherical in shape, to appear elongated along the LoS. At low redshifts (for $z \leq 0.1$) it is not that significant but at high redshifts this causes a significant distortions in the signal, which makes the power spectrum of the 21-cm signal from the CD and the EoR anisotropic along the LoS. The AP effect in the context of 21-cm signal from the EoR was first considered by Ali et al. (2005) in their analysis of the signal through the power spectrum. The proposal of Barkana and Loeb (2005), that one can probably distinguish different sources that contribute to the 21-cm power spectrum by measuring the anisotropy in the power spectrum, has the implicit assumption that the background cosmological model is known to a great degree and hence does not take into account the anisotropies introduced by the geometry (AP effect). Ali et al. (2005) in contrast adopted a framework which allows the high redshift 21-cm signal to be interpreted without reference to a specific background cosmological model and also studied the variation in the anisotropy due to the AP effect depending on different background cosmological models. They further quantify the relative contribution in anisotropy due to the AP effect when compared with the anisotropy due to the redshift space distortions and how they differ in their nature.

3 Methods to quantify the LoS anisotropy in 21-cm signal

We next discuss different possible ways of quantifying any line of sight anisotropy present in the signal through its power spectrum.

3.1 μ-decomposition of the power spectrum

It is convenient to introduce a parameter μ, defined as the cosine of the angle between a specific Fourier mode $\mathbf{k}$ and the LoS. In case of plane parallel redshift space distortions, the redshift space power spectrum then can be expressed as a fourth-order polynomial in μ:

$$P^{\rm s}(k,\mu) = \overline{\delta T_b}^2(z)\left[P_{\mu^0}(k) + \mu^2 P_{\mu^2}(k) + \mu^4 P_{\mu^4}(k)\right]\,, \tag{3}$$

where $\overline{\delta T_b}$ is the average differential brightness temperature of the 21-cm signal at a specific redshift z. In the context of the CD and EoR 21-cm signal this representation of the power spectrum is popular, as one can directly identify each coefficients of the powers of μ with physical quantities contributing to the 21-cm power spectrum under the linear (Bharadwaj et al., 2001; Bharadwaj and Ali, 2004, 2005; Ali et al., 2005; Barkana and Loeb, 2005; Lidz et al., 2008; Majumdar et al., 2013) or quasi-linear (Mao et al., 2012; Jensen et al., 2013; Majumdar et al., 2014, 2016; Ghara et al., 2015a,b) model for the signal (which is valid mainly for the large scale fluctuations in the signal). Following this quasi-linear model one can

express each of these coefficients of μ as:

$$\begin{aligned} P_{\mu^0}(k) &= P_{\rho_{\rm HI},\rho_{\rm HI}}(k) + P_{\eta,\eta}(k) + P_{\rho_{\rm HI},\eta}(k)\,, \\ P_{\mu^2}(k) &= 2\left[P_{\rho_{\rm HI},\rho_{\rm M}}(k) + P_{\rho_{\rm M},\eta}(k)\right]\,, \\ P_{\mu^2}(k) &= P_{\rho_{\rm M},\rho_{\rm M}}(k)\,. \end{aligned} \tag{4}$$

where $\rho_{\rm HI}$ is the neutral hydrogen density, $\rho_{\rm M}$ is the total hydrogen density and $\eta(z,\mathbf{x}) = 1 - T_{CMB}(z)/T_{\rm S}(z,\mathbf{x})$ represents spin temperature fluctuations in the H Romani distribution. The spin temperature ($T_{\rm S}$), which represents the relative population of atoms in two different spin states, can get affected by the Lyman-α pumping and heating during the Cosmic Dawn and the early stages of reionization (Bharadwaj et al., 2001; Bharadwaj and Ali, 2004, 2005; Ali et al., 2005; Ghara et al., 2015a,b). For most part of the reionization, by when the IGM is expected to be significantly heated above the CMB temperature, it can be safely assumed that $T_{\rm S} \gg T_{CMB}$ (unless it is a case of very late heating). In that case, all terms related to η turns out to be zero and it becomes very tempting to conclude that at least at large scales this representation will hold and it would be possible to separate the astrophysics ($P_{\rho_{\rm HI},\rho_{\rm HI}}$ and $P_{\rho_{\rm HI},\rho_{\rm M}}$) from cosmology ($P_{\rho_{\rm M},\rho_{\rm M}}$). However, one has to be aware of the fact that this representation is not in orthonormal basis, thus each of these coefficients are not independent of the other, thus decomposing the power spectrum in this form and identifying the coefficients of the powers of μ with certain physical quantities may lead to erroneous conclusions. It is also important to note that this model do not consider any AP effect to be present in the signal, which will introduce an additional μ^6 term in eq. (3) (Ali et al., 2005).

3.2 Legendre polynomial decomposition of the power spectrum

A different approach to quantify the LoS anisotropy is to instead expand the power spectrum in the orthonormal basis of Legendre polynomials, which is a well known approach in the field of galaxy redshift surveys (Hamilton, 1992, 1998; Cole et al., 1995). In this representation (assuming plane parallel redshift distortions), the power spectrum can be expressed as a sum of the even multipoles of Legendre polynomials:

$$P^{\rm s}(k,\mu) = \sum_{l\ \rm even} \mathcal{P}(\mu) P^{\rm s}_l(k). \tag{5}$$

From an observed or simulated 21-cm power spectrum, one can calculate the angular multipoles $P^{\rm s}_l$ following:

$$P^{\rm s}_l(k) = \frac{2l+1}{4\pi} \int \mathcal{P}(\mu) P^{\rm s}(k) {\rm d}\Omega. \tag{6}$$

The integral is performed over the entire solid angle to take into account all possible orientations of $\mathbf{k}$ with the LoS direction. Each multipole moment estimated through eq. (6) will be independent of the other, as this is a representation in orthonormal basis. In the context of 21-cm signal from the EoR, the effect of redshift space distortions was first quantified in Majumdar et al. (2013) by estimating the quadrupole ($P^{\rm s}_2$) and monopole ($P^{\rm s}_0$) moments of the power spectrum from EoR simulations. If one considers the quasi-linear model of the signal, the first three non-zero angular multipoles of the power spectrum can be expressed as (Majumdar et al., 2014, 2016):

$$P^s_0 = \overline{\delta T_b}^2(z) \left[\frac{1}{5} P_{\rho_{\rm M},\rho_{\rm M}} + P_{\rho_{\rm HI},\rho_{\rm HI}} + P_{\eta,\eta} + 2P_{\eta,\rho_{\rm HI}} + \frac{2}{3} P_{\rho_{\rm HI},\rho_{\rm M}} + \frac{2}{3} P_{\eta,\rho_{\rm M}}\right] \tag{7}$$

$$P^s_2 = 4\,\overline{\delta T_b}^2(z) \left[\frac{1}{7} P_{\rho_{\rm M},\rho_{\rm M}} + \frac{1}{3} P_{\rho_{\rm HI},\rho_{\rm M}} + \frac{1}{3} P_{\eta,\rho_{\rm M}}\right] \tag{8}$$

$$P^s_4 = \frac{8}{35}\,\overline{\delta T_b}^2(z)\, P_{\rho_{\rm M},\rho_{\rm M}} \tag{9}$$

This shows that it might be possible to extract the matter power spectrum by estimating the hexadecapole moment ($P^{\rm s}_4$) of 21-cm power spectrum for sufficiently large length scales. However, at those scales the signal might be severely dominated by the cosmic variance. It further shows that, it is not possible to independently extract $P_{\rho_{\rm HI},\rho_{\rm HI}}$ or $P_{\rho_{\rm HI},\rho_{\rm M}}$, even when $T_{\rm S} \gg T_{CMB}$ (*i.e.* when all η related terms are zero).

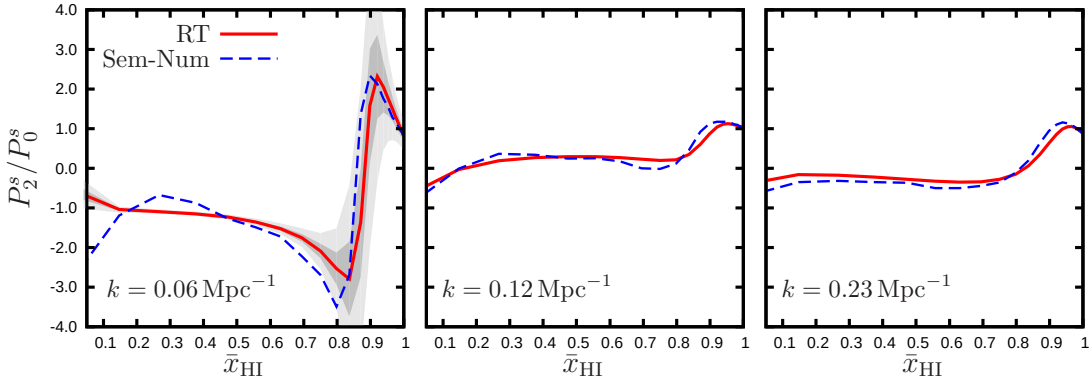

Figure 1: The evolution of the ratio P_2^s/P_0^s with $\bar{x}_{\mathrm{HI}}$ at three representative k values estimated from a set of inside-out simulations of the EoR 21-cm signal (one semi-numerical and the other radiative transfer). The shaded regions in light and dark gray represent uncertainty due to the system noise for 2000 and 5000 hr of observation using a LOFAR like instrument at 150 MHz. Figure taken from Majumdar et al. (2014).

3.3 Other alternative method

A rather simplistic alternative method to quantify the LoS anisotropy in the signal power spectrum is to calculate the anisotropy ratio proposed by Fialkov et al. (2015), which is defined as:

$$r_\mu(k,z) = \frac{\langle P(\mathbf{k},z)_{|\mu_k|>0.5}\rangle}{\langle P(\mathbf{k},z)_{|\mu_k|<0.5}\rangle} - 1\,, \tag{10}$$

where the angular bracket represent average over angles. Ideally, if the signal is isotropic then $r_\mu(k,z)$ should be zero, otherwise it will take positive or negative values. The redshift evolution of this quantity will some way quantify the integrated or angle averaged degree of anisotropy present in the signal at different stages of the CD and the EoR.

4 Quantifying the redshift space distortions in the 21-cm power spectrum

4.1 During the EoR

The anisotropy in the redshifted 21-cm signal from the EoR has been traditionally quantified through the ratio of the spherically averaged power spectrum in redshift space to the same quantity estimated in real space. Predictions for this ratio has been made from analytical models as well as from radiative transfer and semi-numerical simulations of the signal (*e.g.* Lidz et al. 2007; Mesinger et al. 2011; Mao et al. 2012 etc.). However, one very important point to note here that, in reality one would not be able to estimate this ratio, as the signal will always have redshift space distortions present in it, thus it is not possible to estimate the power spectrum of the signal in real space. Instead of estimating this ratio, Majumdar et al. (2013) suggested that one could independently estimate different angular multipole moments of the power spectrum of the signal (following eq. [5] and [6]) directly from the observed visibilities, which is the basic observable in any radio interferometric survey. They further suggested that, the ratio between the first two non-zero even multipole moments of the power spectrum (*i.e.* monopole or P_0^s and quadrupole or P_2^s) can be used as an estimator to quantify any LoS anisotropy present in the signal. It is precisely due to the fact that, if there is no LoS anisotropy in the signal, any higher order multipole moment, other than the monopole moment (which by definition is the spherically averaged power spectrum) will be zero. To quantify the effect of redshift space distortions in the signal Majumdar et al. (2013) used a set of semi-numerical simulations (with a proper implementation of the redshift space distortions in it using actual matter peculiar velocities) of the signal and studied the evolution of the ratio of P_2^s/P_0^s

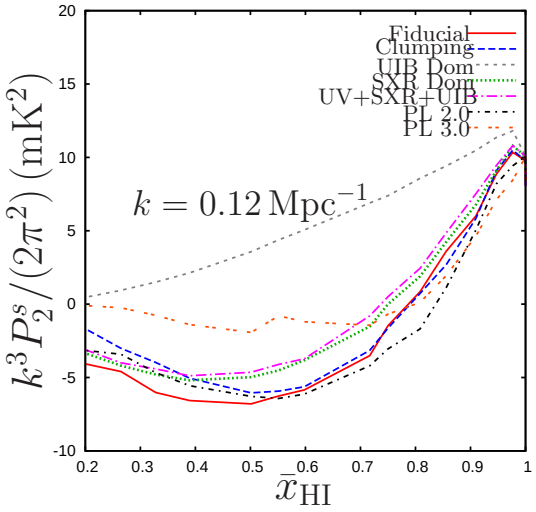

Figure 2: The quadrupole moment of the power spectrum for different reionization scenarios as a function of the global neutral fraction at $k = 0.12$ Mpc^{-1}. Figure taken from Majumdar et al. (2016).

with an evolving global neutral fraction ($\bar{x}_{\rm HI}$) at different length scales observable to the present and future EoR surveys. They observed that at the early stages of the EoR ($1 \gtrsim \bar{x}_{\rm HI} \gtrsim 0.9$), for an inside-out reionization scenario, at large and intermediate length scales ($0.5 \gtrsim k \gtrsim 0.05\,\mathrm{Mpc}^{-1}$), this ratio is positive and gradually goes up from the initial value of around $P_2^s/P_0^s \approx 50/49$ (predicted by the linear model for a completely neutral IGM) to higher values (≈ 3 for $k \approx 0.05\,\mathrm{Mpc}^{-1}$ at $\bar{x}_{\rm HI} \approx 0.9$) as reionization progresses further. Once the early stage of the EoR is over, one observes a sharp transition in this ratio at around $\bar{x}_{\rm HI} \approx 0.9$, where it becomes negative and reaches values as low as ≈ -3 at large length scales. It slowly goes up again with decreasing neutral fraction (for $0.5 \lesssim \bar{x}_{\rm HI} \lesssim 0.9$) and reaches a value of -1 by $\bar{x}_{\rm HI} \approx 0.5$. This ratio remains negative and almost constant ($P_2^s/P_0^s \approx -1$) for the rest of the reionization ($\bar{x}_{\rm HI} \leq 0.5$), until the signal strength goes down and it becomes undetectable. Majumdar et al. (2013) ascribes the sharp peak and dip features of the P_2^s/P_0^s versus $\bar{x}_{\rm HI}$ curve around $\bar{x}_{\rm HI} \approx 0.9$ and negative value of P_2^s/P_0^s for $\bar{x}_{\rm HI} \leq 0.9$ to the inside-out nature of the reionization. The robustness of these results (and associated features in the behaviour of P_2^s/P_0^s) were further confirmed by Majumdar et al. (2014) by estimating the same ratio from a radiative transfer and a set of semi-numerical simulations (Figure 1). They also showed that this ratio would be detectable using LOFAR after 2000 hr of observations. Both of these studies also find that the hexadecapole moment (P_4^s) will be severely dominated by cosmic variance and thus it would be difficult to conclude anything about the matter power spectrum through it.

In a similar study with a radiative transfer simulation, but using the μ-decomposition technique described in Section 3 through eq. (3), Jensen et al. (2013) also found that it is not possible to extract the coefficients of μ^2 and μ^4 terms in the signal power spectrum, *i.e.* not possible to extract $P_{\rho_{\rm HI},\rho_{\rm M}}$ and $P_{\rho_{\rm M},\rho_{\rm M}}$ independently, rather it is possible to extract the sum of the coefficients of μ^2 and μ^4, though it to would be more prone to errors compared to estimating the quadrupole moment (P_2^s) of the power spectrum, as it is a representation in non-orthonormal basis.

4.1.1 Constraining the EoR history using the redshift space anisotropy in the 21-cm signal

The quasi-linear model in eq. (8) suggest that the quadrupole moment (P_2^s) contains matter power spectrum and the cross-power spectrum between the matter and H Romani (when $T_{\rm S} \gg T_{CMB}$, *i.e.* all η related terms are zero). While the matter power spectrum contains the amplitude of the matter density fluctuations (which evolves rather slowly with redshift), the cross-power spectrum $P_{\rho_{\rm HI},\rho_{\rm M}}$ contains the information of the phase difference between the matter and the H Romani field. If the distribution and the properties of the reionization sources change, the topology of the ionization field will also change and one would expect then the phase difference between the matter and the H Romani field to also change,

which it turn should have a signature in the quadrupole moment. To test whether this idea can be used to distinguish between different reionization sources using the nature and amplitude of P_2^s, Majumdar et al. (2016) simulated a collection of reionization scenarios considering various degrees of contribution from different kinds of reionization sources. The reionization scenarios they consider include ionizing photon contribution from the usual UV photon sources hosted by the halos with mass $\gtrsim 10^9\,\mathrm{M}_\odot$, a uniform ionizing background generated by hard X-ray sources, a local uniform ionizing background generated by soft X-ray sources (limited by the mean free path of soft X-ray photons), various combinations of all of these three contributions, reionization driven by quasar like very strong sources located around the most massive halos etc. They find that, for all of their reionization scenarios (except the one dominated by a uniform ionizing background), the quadrupole moment at large length scales ($k = 0.12$ Mpc^{-1}) evolves with $\bar{x}_{\rm HI}$ in a rather robust manner (Figure 2), even though the topology of the 21-cm signal look significantly different in all of those scenarios. They further show that as long as the major ionizing photon sources follow the underlying matter distribution, the phase difference between the matter and the H Romani evolves with $\bar{x}_{\rm HI}$ in almost similar fashion, though the topology of the 21-cm signal can be drastically different. This is why the quadrupole moment (P_2^s) evolves in a robust fashion with $\bar{x}_{\rm HI}$ in all of those scenarios. Building on this idea, they further demonstrate that this robustness of P_2^s can be used to extract the reionization history to a great degree. They show that for an instrument with the sensitivity of the first phase of the SKA-LOW, it will require 100 hr of observation to constrain the reionization history ($\bar{x}_{\rm HI}$ versus z) very precisely, if foregrounds have already been removed to a great degree.

4.2 During the Cosmic Dawn

The 21-cm signal from the Cosmic Dawn and the very early stages of the EoR ($\bar{x}_{\rm HI} \gtrsim 0.95$) are expected to be affected by the spin temperature fluctuations caused by the inhomogeneous X-ray heating and Lyman-α coupling around the early sources of light. In this regime one would not be able to assume $T_{\rm S} \gg T_{CMB}$ and the fluctuations in the quantity $\eta(z, \mathbf{x}) = 1 - T_{CMB}(z)/T_{\rm S}(z, \mathbf{x})$ will contribute to the 21-cm brightness temperature significantly as predicted by Bharadwaj et al. (2001); Bharadwaj and Ali (2004, 2005); Ali et al. (2005) etc. Ghara et al. (2015a) developed and used an one dimensionals radiative transfer simulation to study the effects of spin temperature fluctuations on the 21-cm power spectrum during these stages while implementing the effect of redshift space distortions in the signal using the actual matter peculiar velocities. It was assumed that each of the early sources of light produced in their simulation has two components: i) usual stellar component (modelled using general population synthesis prescriptions) and ii) a mini-quasar component (assumed to have a power-law spectrum). They found some distinct features in the large scale power spectrum in this case when compared to the scenario where inhomogeneities in the gas temperature and the Lyman-α coupling are ignored. They observed three distinct peaks in the large scale spherically averaged power spectrum of the signal when plotted as a function of redshift (left panel of Figure 3). The peak which appears latest in the history is associated with $\sim 50\%$ neutral fraction of the IGM and the H Romani fluctuations have the maximum contribution to the power spectrum at this stage. The second peak is related to the fluctuations in the heating pattern and appears when $\sim 10\%$ of the volume is heated above $T_{\rm CMB}$. The third peak, which corresponds to the earliest stages of the 21-cm history, corresponds to the inhomogeneities in the Lyman-α coupling. Identification of these peaks (two of which were not reported earlier in the literature) would be very important when one would try to parametrize the CD and the EoR using the observed power spectrum and variance of the 21-cm signal from the proposed shallow survey using the first phase of SKA-LOW (Koopmans et al., 2015).

To quantify the effect of redshift space distortions Ghara et al. (2015a) estimated the ratio of the spherically averaged power spectrum in redshift space and in real space. They find that this ratio at large length scales to be not that high as reported by some earlier studies (Majumdar et al., 2013; Jensen et al., 2013), when one includes the effect of spin temperature fluctuations. They associate this disagreement to the fact that they do not include the sources with mass lower than $10^9\,\mathrm{M}_\odot$ and also to the fact that during the CD and the early stages of the EoR the fluctuations in 21-cm are mainly driven by the fluctuations in $T_{\rm S}$, which is mildly correlated to the density field, thus the redshift space distortions do not change the amplitude and shape of the power spectrum drastically here. They have also estimated the μ-decomposed power spectrum (right panel of Figure 3) following eq. (3) to further understand the effect of redshift space distortions on the signal power spectrum. They find that both

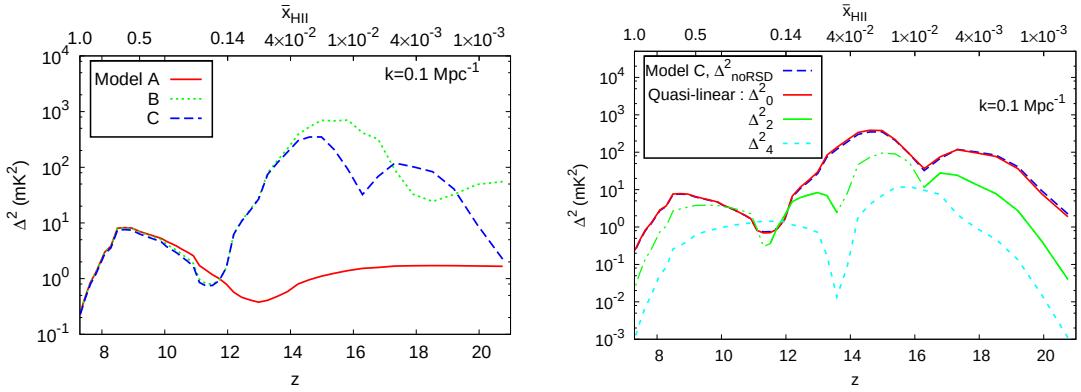

Figure 3: The left panel shows the spherically averaged 21-cm power spectrum at large length scales for three different models of X-ray heating and Lyman-α coupling. Model A: IGM is Lyman-α coupled and highly heated, Model B: IGM is strongly Lyman-α coupled but self consistently heated with X-ray sources, Model C: IGM is self consistently coupled with Lyman-α and heated by X-ray sources. The right panel shows the redshift space μ-decomposed power spectra estimated following eq. (3) for Model C. Figure taken from Ghara et al. (2015a).

the coefficients of μ^2 and μ^4 have non-zero values during this stage, however their amplitude are smaller or comparable but not higher than the coefficient of μ^0 term (which is equivalent to the real space power spectrum) in the power spectrum. In a later work, Ghara et al. (2015b) have computed the anisotropy ratio (top panels of Figure 4) defined by eq. (10) as a function of z at large and intermediate length scales ($k = 0.1$ and $0.5\,\mathrm{Mpc}^{-1}$) for the similar reionization scenarios as in Ghara et al. (2015a) but here they have also included the sources of mass lower than $10^9\,\mathrm{M}_\odot$. It is evident from these figures that the anisotropy due to the redshift space distortions can be significant ($r_\mu \geq 1$) at large and intermediate length scales even during the Cosmic Dawn and the early stages of the EoR when one takes into account the inhomogeneities in the X-ray heating and Lyman-α coupling.

5 Quantifying the light cone effect in the 21-cm power spectrum

5.1 During the EoR

The first numerical investigation of the light cone effect on the 21-cm power spectrum from the EoR was done by Datta et al. (2012). They used a set of radiative transfer simulations of volume $(163\,\mathrm{Mpc})^3$ having three different reionization histories (from rapid to slow) to study the light cone effect. They have quantified the impact of the light cone effect by estimating the relative difference between the spherically averaged power spectrum of the light cone box $[\Delta^2_{\rm LC}(k)]$ and the same estimated from a coeval cube $[\Delta^2_{\rm CC}(k)]$, corresponding to the central redshift of the light cone box, *i.e.* through the quantity $[\Delta^2_{\rm CC}(k) - \Delta^2_{\rm LC}(k)]/\Delta^2_{\rm LC}(k)$ (Figure 5). They observed that the relative change in the power spectrum can be up to $\approx 50\%$ within the k range $\sim 0.1 - 9.0\,\mathrm{Mpc}^{-1}$ and the large scales are affected more compared to the small scales. They find that the light cone power spectrum get enhanced at large scales and suppressed at small scale compared to the coeval box power spectrum at the redshift of the centre of the box. This enhancement and suppression of power happens around a Fourier mode $k_{\rm cross-over}$, which gradually shifts towards the large scales as reionization progresses. Using simple toy models of power spectra, they argue that this behaviour is a signature of the difference in the bubble size distribution in the coeval box and the light cone box. They also observed that the difference in between $\Delta^2_{\rm LC}$ and $\Delta^2_{\rm CC}$ is minimum when reionization is half way through. The line of sight extent of the light cone box influences the difference between $\Delta^2_{\rm LC}$ and $\Delta^2_{\rm CC}$. This difference goes down with the reduction of the LoS extent of the light cone box. It was also noticed that as any radio interferometric observation do not measure the $k_\perp = 0$ mode, thus the DC value of the signal power spectrum cannot be measured, which in turn removes the effect of the evolution of mass averaged neutral fraction ($\bar{x}_{\rm HI}$) (across the LoS) from the observed light cone power spectrum. Datta et al. (2012) have further observed that the change in

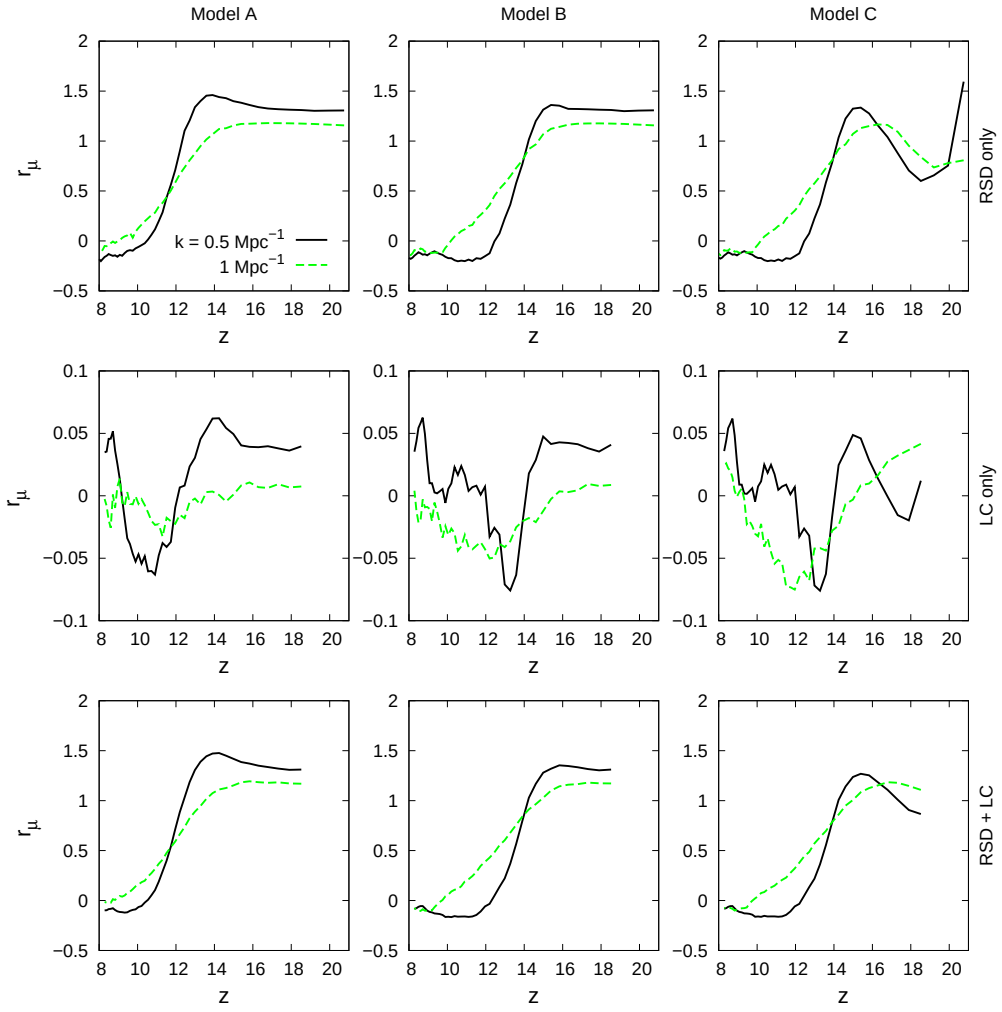

Figure 4: This shows the anisotropy ratio r_μ computed following eq. (10) as a function of redshift for large and intermediate length scales. The models A, B and C are the same as described in Figure 3, the only difference here is that all of them also include sources of mass lower than $10^9\,M_\odot$. The three rows from top to bottom shows the ratio computed when the signal includes only the redshift space distortions, only light cone effect and both redshift space distortions and light cone effect, respectively. Figure taken from Ghara et al. (2015b).

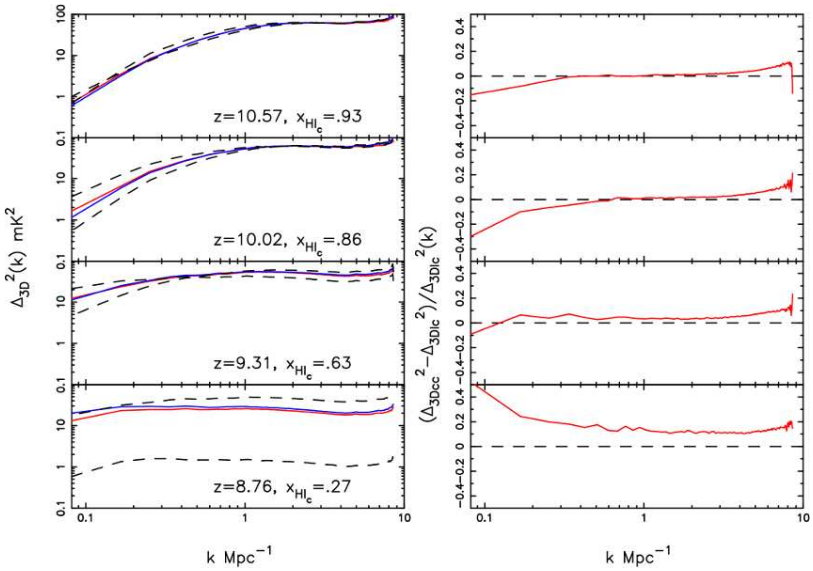

Figure 5: The left panels show the spherically averaged 21-cm power spectrum estimated from the light cone cube (LC:red solid line) and coeval cube at the central redshift (CC:blue solid line) at different stages of the EoR. The dashed lines show the power spectrum from the coeval cubes at redshifts corresponding to the back and the front sides of the light cone box. The right panels show the relative difference in the power spectra between the LC and the CC boxes, estimated at the same stages of the EoR as shown on the left. Figure taken from Datta et al. (2012).

reionization history (whether rapid or slow), does not change the light cone affect on the power spectrum significantly. The light cone effect is more dependent on the mass averaged neutral fraction at the central redshift of the light cone box rather than the total EoR history. These findings of Datta et al. (2012) regarding the light cone effect were later confirmed independently by La Plante et al. (2014) as well.

It is intriguing to ask the question, whether the light cone effect introduces any significant LoS anisotropy to the observed EoR 21-cm power spectrum. If the anisotropy introduced by the light cone effect is significant and also contributes in a similar fashion in the power spectrum as the redshift space anisotropy, then it would be really difficult to distinguish between these two effects from a real observation. Also, several other proposed outcomes using the SKA-LOW observations, which uses the redshift space anisotropy as a tool, such as separating the cosmology from astrophysics (Barkana and Loeb, 2005) or extracting the reionization history (Majumdar et al., 2016), would be difficult to achieve. Datta et al. (2014) have tried to address mainly this issue, *i.e.* whether the light cone effect introduces any significant anisotropy to the signal power spectrum and what could be the best observational strategy to minimize the impact of the light cone effect on the EoR 21-cm power spectrum.

Datta et al. (2014) used a significantly large simulation volume ($[607\,\mathrm{Mpc}]^3$), which is comparable to the field of view of LOFAR, to study the impact of the light cone effect on the signal. The large simulation volume allowed them to study this effect in case of both very rapid as well rather slow reionization histories. They find the impact of the light cone effect on the spherically averaged power spectrum is maximum when the reionization is $\sim 20\%$ and $\sim 80\%$ finished and it is rather small at $\sim 50\%$ reionization. Which, reconfirms the findings of Datta et al. (2012). However, they do not observe any significant LoS anisotropy introduced to the power spectrum due to the light cone effect. They used a toy model to explain this rather surprising finding. They find that, even though the light cone effect makes the H Romanii bubbles larger in an observational data cube towards the side closer to the observer compared to the opposite side of the observational volume along the LoS, it does not necessarily makes the H Romanii bubbles elongated or compressed along the LoS. This systematic change in H Romanii bubble size along the LoS does not make the power spectrum anisotropic as long as the bubbles remain approximately spherical in shape. The power spectrum can only become anisotropic when the shape of the individual H Romanii bubbles distort along the LoS, which can only happen if the

major sources of reionization are extremely strong in terms of their photon emission rate (*e.g.* quasars), which will lead to a relativistic growth of the H Romanii regions. They also studied the power spectrum by including both redshift space distortions and light cone effect to the signal and found that the light cone effect does not change the signatures of the redshift space distortions at any stage of the EoR.

Datta et al. (2014) also identified that there exists an optimal frequency bandwidth along the LoS for the power spectrum estimation, within which the light cone effect can be ignored without loosing the signal to the uncertainties due to the sample variance. They found that for large scales such as $k = 0.16\,\mathrm{Mpc}^{-1}$ this is ~ 11 MHz and for intermediate scales $k = 0.41\,\mathrm{Mpc}^{-1}$ this is ~ 16 MHz, if one allows a change of 10% in the power spectra. These optimal bandwidths may change depending on the reionization history.

5.2 During the Cosmic Dawn

Ghara et al. (2015b) performed the first numerical study on the impact of the light cone effect on the redshifted 21-cm power spectrum from the Cosmic Dawn. They used a set of one dimensional radiative transfer simulations (similar to Ghara et al. 2015a) for the signal, while considering spin temperature fluctuations in the signal due to the inhomogeneous X-ray heating by the first sources and non-uniform Lyman-α coupling. They found that the impact of the light cone effect is more dramatic when one considers both the inhomogeneous X-ray heating and the Lyman-α coupling induced spin temperature fluctuations in the signal, compared to the case when these effects are ignored. It was observed that at large length scales $k \sim 0.05\,\mathrm{Mpc}^{-1}$, light cone effect is more prominent around the peaks and dips of the power spectrum when plotted as a function of redshift (Figure 6). They observed that the large scale signal power spectrum is suppressed around the three distinct peaks (by factors of ≈ 0.7) and enhanced (by factors of ≈ 2) around the dips due to this effect. This enhancement/suppression was found to be higher in a case where one includes sources of mass lower than $10^9\,\mathrm{M}_\odot$ in their reionization prescription. A significant light cone effect was also observed at small length scales ($k \sim 1\,\mathrm{Mpc}^{-1}$), during the Cosmic Dawn.

The reason behind this behaviour is that where ever the power spectrum experiences any non-linear evolution, the light cone effect becomes substantial at those points, as any linear evolution will be mostly cancelled out (Datta et al., 2012). This is possibly why this effect appears to be more prominent around the heating peak and the peak and dip caused due to the inhomogeneous Lyman-α coupling. It was also observed that inclusion or exclusion of light cone effect changes the power spectrum at large scales ($k \sim 0.05\,\mathrm{Mpc}^{-1}$) by -100 to $100\,\mathrm{mK}^2$ and at small scales ($k \geq 0.5\,\mathrm{Mpc}^{-1}$) by -250 to $100\,\mathrm{mK}^2$. These large differences should be in principle detectable by SKA-LOW, due to its higher sensitivity. It was proposed that the power spectrum peaks at large scales during the CD can be used to extract the source properties, X-ray and Lyman-α backgrounds etc (Mesinger et al., 2014). However, while performing such an exercise on an actual observational data set, one needs to take into account the light cone effect as it suppresses those peaks.

Similar to Datta et al. (2014) in the EoR, Ghara et al. (2015b) also did not find any significant LoS anisotropy introduced by the light cone effect in the signal from the CD. They had estimated the anisotropy ratio r_μ for large and intermediate scales (Figure 4) to quantify the LoS anisotropy due to the light cone effect. They found that the LoS anisotropy quantified by this ratio is less than 5% during most of the duration of the CD and the EoR. They had also observed that, the light cone anisotropy do not destroy the anisotropy due to the redshift space distortions present in the signal.

6 Detectability of the line of sight anisotropy signatures

6.1 Foreground avoidance versus foreground removal

One of the major obstacle for the detection of the CD-EoR 21-cm signal is the foreground emission from galactic and extra-galactic point sources, which is expected to be few orders of magnitude larger than the signal itself. These foregrounds are assumed to be spectrally smooth, which implies that they will only affect the lowest k modes parallel to the LoS ($k_\parallel$). However, due to the frequency dependence of an interferometers's response, the foregrounds will propagate into higher k modes. This causes the foregrounds to become confined to a wedge-shaped region in $k_\parallel - k_\perp$ plane, which was first identified

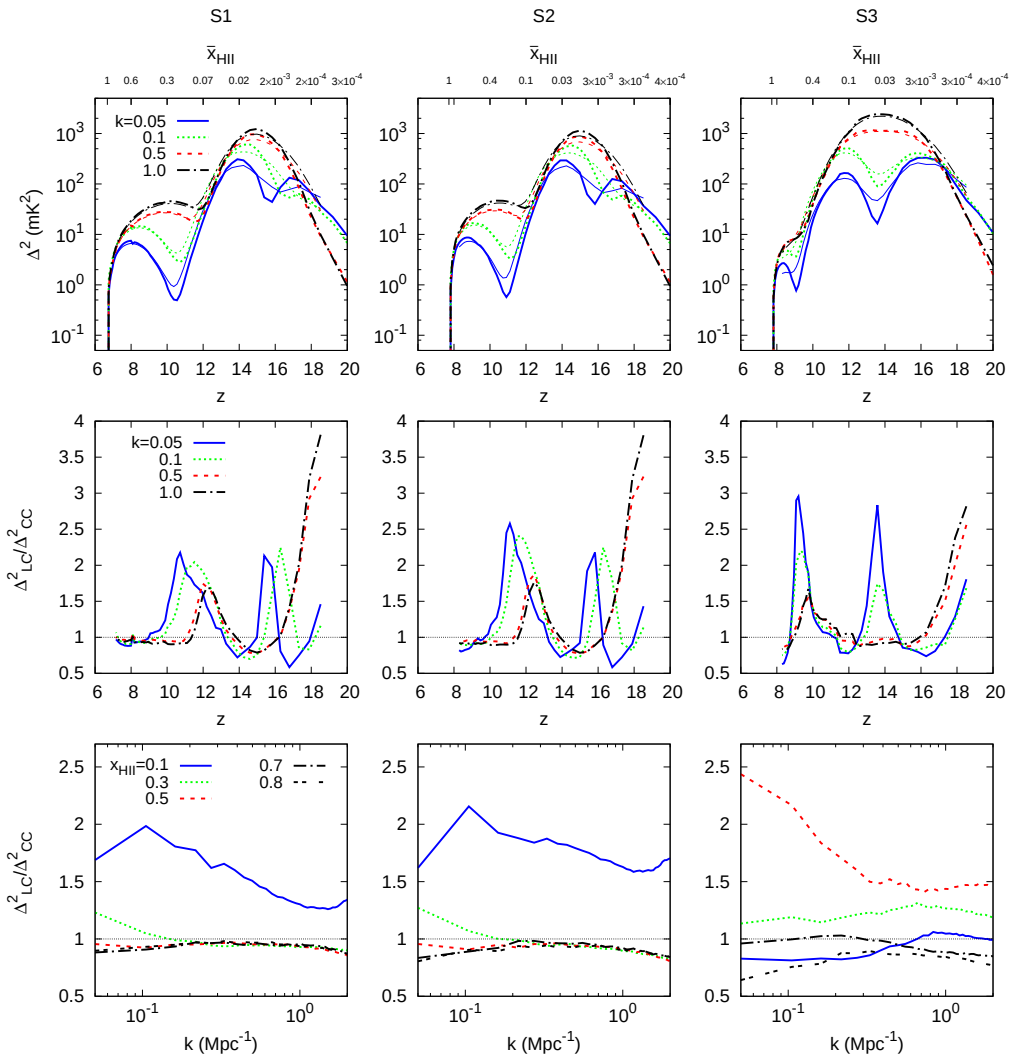

Figure 6: The top panels show evolution of the spherically averaged 21-cm power spectrum with redshift from simulation boxes with (thin line) and without (thick line) light cone effect in them. The middle and the bottom panels show relative change in the power spectrum due to the light cone effect when compared with the coeval power spectra. Three different columns correspond to three different models for reionization sources. Figure taken from Ghara et al. (2015b).

by Datta et al. (2010). One of the ways to deal with the foregrounds is thus to avoid this region where foregrounds will be dominant and restrict the signal power spectrum estimation within the region of the $k_\parallel - k_\perp$ space which is expected to be clean from foregrounds (see *e.g.* Trott et al. 2012; Dillon et al. 2014; Pober et al. 2014 etc). One drawback of this method is that one have to live with the low SNR of the signal power spectrum, after throwing away a large fraction of the data in this way. The other drawback will be that the directional dependence of the power spectrum will be hard to quantify in this method. Detectability of any LoS anisotropy (more precisely the anisotropy due to the redshift space distortions in this context) present in the 21-cm signal power spectrum will depend on the fact that the power spectrum is sampled uniformly over all angles (or μ values) with respect to the LoS. Any sort of biased sampling of the power spectrum in this regard may lead to misinterpretation of signal characteristics and the related characteristics of the CD-EoR parameters. This would be inevitable in this foreground avoidence technique (Pober, 2015). Even when one is interested only in the spherically averaged power spectrum, it has been observed that the biased sampling of the $k_\parallel - k_\perp$ plane will introduce an atrificial but significantly large bias to the estimated power spectrum (Jensen et al., 2016). Thus to quantify the LoS anisotropies in the CD-EoR 21-cm signal using the future SKA-LOW shallow or medium survey (Koopmans et al., 2015), it is very important that we employ a proper foreground subtraction technique rather than using foreground avoidance.

6.2 Uncertainties due to the cosmic variance

Any statistical estimation of the CD-EoR 21-cm power spectrum comes with an intrinsic uncertainty of its own, which arises due to the uncertainties in the signal across its different statistically independent realizations, *i.e.* due to the cosmic variance of the signal. In most of the analysis present in the current literature related to the characterization of the CD-EoR 21-cm signal power spectrum, it has been assumed that the signal has properties similar to a Gaussian random field, which makes its cosmic variance to scale as the square root of the number of independent measurements. This could be a reasonably good assumption during the early phases of reionization, but during the later stages of the EoR, the signal becomes highly non-Gaussian as it gets characterized by the H Romanii regions around the reionization sources (Bharadwaj and Ali, 2005; Bharadwaj and Pandey, 2005). The size and population of these H Romanii regions gradually grow as reionization progresses, making the signal more and more non-Gaussian. A similar picture can be drawn during the early stages of the cosmic dawn as well, when the signal is characterized by the heated regions around the first sources of light. Using a large ensemble of simulated EoR 21-cm signal, Mondal et al. (2015) was the first to study the impact of the non-Gaussianity of this signal on the cosmic variance of its power spectrum estimation. They had shown that for a fixed observational volume it is not possible to obtain an SNR above a certain limit, even when one increases the number of Fourier modes for the estimation of the power spectrum. In a more detailed follow up work, Mondal et al. (2016a) had provided an theoretical framework to interpret the entire error covariance matrix of the signal power spectrum. They identify two sources of contribution in the error covariance. One is the usual variance of Gaussian random field and other is the trispectrum of the signal, which comes due to the fact that the different Fourier modes in the signal are correlated due their inherent non-Gaissianity. They establish the fact that errors in differnt length scales of the EoR 21-cm power spectrum are correlated. In a further follow up on this, Mondal et al. (2016b) studied the evolution of these errors with the evolving IGM neutral fraction. Using the EoR simulations they had established that for any mass averaged neutral fraction $\bar{x}_{\rm HI} \leq 0.8$ the error variance will have a significantly large contribution from the trispectrum of the signal for any Fourier mode $k \geq 0.5\,{\rm Mpc}^{-1}$. This dependence may change depending on the reionization source model and the resulting 21-cm topology. It is important to properly quantify the actual uncertainties present in the power spectrum of the EoR 21-cm signal due to the cosmic variance as that will decide the statistical significance with which the LoS anisotropies in the power spectrum can be quantified.

7 Summary and Future Scopes with the SKA-LOW

In most part of this review, we have been trying to stress on the fact that the understanding of the LoS anisotropy in the redshifted 21-cm is not only important for the current ongoing surveys of the CD-EoR but it will be specifically very crucial for the future SKA-LOW surveys of this era, as the SKA-LOW is

expected to measure this signal with an unprecedented sensitivity in both spatial as well as frequency direction compared to any of its predecessors. In context of the proposed survey strategies for the SKA-LOW (Koopmans et al., 2015), the following issues related to LoS anisotropy in the signal would be particularly important —

- It has been proposed that using the shallow survey (observing $10,000\,\mathrm{deg}^2$ in the sky for 10 hr) with SKA-LOW one would be able constrain different parameters for the CD-EoR 21-cm signal by comparing it with a large ensemble of simulated 21-cm power spectra (Greig et al., 2015). However, as it has been shown in the previous few sections, that a proper accounting of the impact of the redshift space distortion, the light cone effect and the bias in the sampling of the $k_\perp - k_\parallel$ space would be necessary to get a unbiased estimation of these parameters. It would be important to take into account the AP effect as well to account for any anisotropies in the signal due to the non-Euclidean geometry of the space-time. Finally, the effect of the non-Gaussian nature of the signal on it's power spectrum error covariance needs to be taken into account. This will help to quantify the uncertainties in the estimated reionization parameters properly.

- While estimating power spectrum from the observed three dimensional data one should estimate it within an optimal band width to avoid any significant impact due to the light cone effect. The width of this optimal bandwidth needs to be properly examined with a larger variety of reionization sources and reionization histories.

- Accounting for the possible light cone effect would be also important, when one will try to characterize the heating sources during the CD from the peaks of 21-cm power spectrum, as this effect tends to reduce those peaks.

- If the foreground removal works reasonably well, it would be possible to constrain the reionization history from the evolution of the quadrupole moment of the power spectrum estimated from the proposed medium deep survey by the SKA-LOW (observing $1000\,\mathrm{deg}^2$ of the sky for 100 hr).

- Presence of the noise bias and several telescope related anomalies in the observed data may make the quantification of the signal and the LoS anisotropy present in it very difficult. Thus it would be necessary to develop clever estimators of the signal power spectrum, which will inherently remove such bias and anomalies (Datta et al., 2007; Choudhuri et al., 2014, 2016).

References

Alcock, C. and Paczynski, B.: 1979, Nature **281**, 358

Ali, S. S., Bharadwaj, S., and Pandey, B.: 2005, MNRAS **363**, 251

Ali, Z. S., Parsons, A. R., Zheng, H., Pober, J. C., Liu, A., Aguirre, J. E., Bradley, R. F., Bernardi, G., Carilli, C. L., Cheng, C., DeBoer, D. R., Dexter, M. R., Grobbelaar, J., Horrell, J., Jacobs, D. C., Klima, P., MacMahon, D. H. E., Maree, M., Moore, D. F., Razavi, N., Stefan, I. I., Walbrugh, W. P., and Walker, A.: 2015, ApJ **809**, 61

Barkana, R. and Loeb, A.: 2005, ApJ **624**, L65

Barkana, R. and Loeb, A.: 2006, MNRAS **372**, L43

Becker, G. D., Bolton, J. S., Madau, P., Pettini, M., Ryan-Weber, E. V., and Venemans, B. P.: 2015, MNRAS **447**, 3402

Becker, R. H., Fan, X., White, R. L., Strauss, M. A., Narayanan, V. K., Lupton, R. H., Gunn, J. E., Annis, J., Bahcall, N. A., Brinkmann, J., Connolly, A. J., Csabai, I., Czarapata, P. C., Doi, M., Heckman, T. M., Hennessy, G. S., Ivezić, Ž., Knapp, G. R., Lamb, D. Q., McKay, T. A., Munn, J. A., Nash, T., Nichol, R., Pier, J. R., Richards, G. T., Schneider, D. P., Stoughton, C., Szalay, A. S., Thakar, A. R., and York, D. G.: 2001, AJ **122**, 2850

Bharadwaj, S. and Ali, S. S.: 2004, MNRAS **352**, 142

Bharadwaj, S. and Ali, S. S.: 2005, MNRAS **356**, 1519

Bharadwaj, S., Nath, B. B., and Sethi, S. K.: 2001, *Journal of Astrophysics and Astronomy* **22**, 21

Bharadwaj, S. and Pandey, S. K.: 2005, MNRAS **358**, 968

Bowman, J. D., Cairns, I., Kaplan, D. L., Murphy, T., Oberoi, D., Staveley-Smith, L., Arcus, W., Barnes, D. G., Bernardi, G., Briggs, F. H., Brown, S., Bunton, J. D., Burgasser, A. J., Cappallo, R. J., Chatterjee, S., Corey, B. E., Coster, A., Deshpande, A., deSouza, L., Emrich, D., Erickson, P., Goeke, R. F., Gaensler, B. M., Greenhill, L. J., Harvey-Smith, L., Hazelton, B. J., Herne, D., Hewitt, J. N., Johnston-Hollitt, M., Kasper, J. C., Kincaid, B. B., Koenig, R., Kratzenberg, E., Lonsdale, C. J., Lynch, M. J., Matthews, L. D., McWhirter, S. R., Mitchell, D. A., Morales, M. F., Morgan, E. H., Ord, S. M., Pathikulangara, J., Prabu, T., Remillard, R. A., Robishaw, T., Rogers, A. E. E., Roshi, A. A., Salah, J. E., Sault, R. J., Shankar, N. U., Srivani, K. S., Stevens, J. B., Subrahmanyan, R., Tingay, S. J., Wayth, R. B., Waterson, M., Webster, R. L., Whitney, A. R., Williams, A. J., Williams, C. L., and Wyithe, J. S. B.: 2013, PASA **30**, 31

Choudhuri, S., Bharadwaj, S., Ghosh, A., and Ali, S. S.: 2014, MNRAS **445**, 4351

Choudhuri, S., Bharadwaj, S., Roy, N., Ghosh, A., and Ali, S. S.: 2016, MNRAS

Choudhury, T. R., Haehnelt, M. G., and Regan, J.: 2009, MNRAS **394**, 960

Cole, S., Fisher, K. B., and Weinberg, D. H.: 1995, MNRAS **275**, 515

Datta, A., Bowman, J. D., and Carilli, C. L.: 2010, ApJ **724**, 526

Datta, K. K., Choudhury, T. R., and Bharadwaj, S.: 2007, MNRAS **378**, 119

Datta, K. K., Jensen, H., Majumdar, S., Mellema, G., Iliev, I. T., Mao, Y., Shapiro, P. R., and Ahn, K.: 2014, MNRAS **442**, 1491

Datta, K. K., Mellema, G., Mao, Y., Iliev, I. T., Shapiro, P. R., and Ahn, K.: 2012, MNRAS **424**, 1877

Dillon, J. S., Liu, A., Williams, C. L., Hewitt, J. N., Tegmark, M., Morgan, E. H., Levine, A. M., Morales, M. F., Tingay, S. J., Bernardi, G., Bowman, J. D., Briggs, F. H., Cappallo, R. C., Emrich, D., Mitchell, D. A., Oberoi, D., Prabu, T., Wayth, R., and Webster, R. L.: 2014, Phys. Rev. D **89(2)**, 023002

Fan, X., Strauss, M. A., Schneider, D. P., Becker, R. H., White, R. L., Haiman, Z., Gregg, M., Pentericci, L., Grebel, E. K., Narayanan, V. K., Loh, Y.-S., Richards, G. T., Gunn, J. E., Lupton, R. H., Knapp, G. R., Ivezić, Ž., Brandt, W. N., Collinge, M., Hao, L., Harbeck, D., Prada, F., Schaye, J., Strateva, I., Zakamska, N., Anderson, S., Brinkmann, J., Bahcall, N. A., Lamb, D. Q., Okamura, S., Szalay, A., and York, D. G.: 2003, AJ **125**, 1649

Fialkov, A., Barkana, R., and Cohen, A.: 2015, *Physical Review Letters* **114(10)**, 101303

Ghara, R., Choudhury, T. R., and Datta, K. K.: 2015a, MNRAS **447**, 1806

Ghara, R., Datta, K. K., and Choudhury, T. R.: 2015b, MNRAS **453**, 3143

Greig, B., Mesinger, A., and Koopmans, L. V. E.: 2015, *ArXiv e-prints*

Hamilton, A. J. S.: 1992, ApJ **385**, L5

Hamilton, A. J. S.: 1998, in D. Hamilton (ed.), *The Evolving Universe*, Vol. 231 of *Astrophysics and Space Science Library*, p. 185

Jacobs, D. C., Pober, J. C., Parsons, A. R., Aguirre, J. E., Ali, Z. S., Bowman, J., Bradley, R. F., Carilli, C. L., DeBoer, D. R., Dexter, M. R., Gugliucci, N. E., Klima, P., Liu, A., MacMahon, D. H. E., Manley, J. R., Moore, D. F., Stefan, I. I., and Walbrugh, W. P.: 2015, ApJ **801**, 51

Jensen, H., Datta, K. K., Mellema, G., Chapman, E., Abdalla, F. B., Iliev, I. T., Mao, Y., Santos, M. G., Shapiro, P. R., Zaroubi, S., Bernardi, G., Brentjens, M. A., de Bruyn, A. G., Ciardi, B., Harker, G. J. A., Jelić, V., Kazemi, S., Koopmans, L. V. E., Labropoulos, P., Martinez, O., Offringa, A. R., Pandey, V. N., Schaye, J., Thomas, R. M., Veligatla, V., Vedantham, H., and Yatawatta, S.: 2013, MNRAS **435**, 460

Jensen, H., Majumdar, S., Mellema, G., Lidz, A., Iliev, I. T., and Dixon, K. L.: 2016, MNRAS **456**, 66

Komatsu, E., Smith, K. M., Dunkley, J., Bennett, C. L., Gold, B., Hinshaw, G., Jarosik, N., Larson, D., Nolta, M. R., Page, L., Spergel, D. N., Halpern, M., Hill, R. S., Kogut, A., Limon, M., Meyer, S. S., Odegard, N., Tucker, G. S., Weiland, J. L., Wollack, E., and Wright, E. L.: 2011, ApJS **192**, 18

Koopmans, L., Pritchard, J., Mellema, G., Aguirre, J., Ahn, K., Barkana, R., van Bemmel, I., Bernardi, G., Bonaldi, A., Briggs, F., de Bruyn, A. G., Chang, T. C., Chapman, E., Chen, X., Ciardi, B., Dayal, P., Ferrara, A., Fialkov, A., Fiore, F., Ichiki, K., Illiev, I. T., Inoue, S., Jelic, V., Jones, M., Lazio, J., Maio, U., Majumdar, S., Mack, K. J., Mesinger, A., Morales, M. F., Parsons, A., Pen, U. L., Santos, M., Schneider, R., Semelin, B., de Souza, R. S., Subrahmanyan, R., Takeuchi, T., Vedantham, H., Wagg, J., Webster, R., Wyithe, S., Datta, K. K., and Trott, C.: 2015, *Advancing Astrophysics with the Square Kilometre Array (AASKA14)* p. 1

La Plante, P., Battaglia, N., Natarajan, A., Peterson, J. B., Trac, H., Cen, R., and Loeb, A.: 2014, ApJ **789**, 31

Lidz, A., Zahn, O., McQuinn, M., Zaldarriaga, M., Dutta, S., and Hernquist, L.: 2007, ApJ **659**, 865

Lidz, A., Zahn, O., McQuinn, M., Zaldarriaga, M., and Hernquist, L.: 2008, ApJ **680**, 962

Majumdar, S., Bharadwaj, S., and Choudhury, T. R.: 2012, MNRAS **426**, 3178

Majumdar, S., Bharadwaj, S., and Choudhury, T. R.: 2013, MNRAS **434**, 1978

Majumdar, S., Bharadwaj, S., Datta, K. K., and Choudhury, T. R.: 2011, MNRAS **413**, 1409

Majumdar, S., Jensen, H., Mellema, G., Chapman, E., Abdalla, F. B., Lee, K.-Y., Iliev, I. T., Dixon, K. L., Datta, K. K., Ciardi, B., Fernandez, E. R., Jelić, V., Koopmans, L. V. E., and Zaroubi, S.: 2016, MNRAS **456**, 2080

Majumdar, S., Mellema, G., Datta, K. K., Jensen, H., Choudhury, T. R., Bharadwaj, S., and Friedrich, M. M.: 2014, MNRAS **443**, 2843

Mao, Y., Shapiro, P. R., Mellema, G., Iliev, I. T., Koda, J., and Ahn, K.: 2012, MNRAS **422**, 926

Mellema, G., Koopmans, L., Shukla, H., Datta, K. K., Mesinger, A., and Majumdar, S.: 2015, *Advancing Astrophysics with the Square Kilometre Array (AASKA14)* p. 10

Mellema, G., Koopmans, L. V. E., Abdalla, F. A., Bernardi, G., Ciardi, B., Daiboo, S., de Bruyn, A. G., Datta, K. K., Falcke, H., Ferrara, A., Iliev, I. T., Iocco, F., Jelić, V., Jensen, H., Joseph, R., Labroupoulos, P., Meiksin, A., Mesinger, A., Offringa, A. R., Pandey, V. N., Pritchard, J. R., Santos, M. G., Schwarz, D. J., Semelin, B., Vedantham, H., Yatawatta, S., and Zaroubi, S.: 2013, *Experimental Astronomy* **36**, 235

Mesinger, A., Ewall-Wice, A., and Hewitt, J.: 2014, MNRAS **439**, 3262

Mesinger, A., Furlanetto, S., and Cen, R.: 2011, MNRAS **411**, 955

Mondal, R., Bharadwaj, S., and Majumdar, S.: 2016a, MNRAS **456**, 1936

Mondal, R., Bharadwaj, S., and Majumdar, S.: 2016b, *in preparation*

Mondal, R., Bharadwaj, S., Majumdar, S., Bera, A., and Acharyya, A.: 2015, MNRAS **449**, L41

Paciga, G., Albert, J. G., Bandura, K., Chang, T.-C., Gupta, Y., Hirata, C., Odegova, J., Pen, U.-L., Peterson, J. B., Roy, J., Shaw, J. R., Sigurdson, K., and Voytek, T.: 2013, MNRAS **433**, 639

Parsons, A. R., Liu, A., Aguirre, J. E., Ali, Z. S., Bradley, R. F., Carilli, C. L., DeBoer, D. R., Dexter, M. R., Gugliucci, N. E., Jacobs, D. C., Klima, P., MacMahon, D. H. E., Manley, J. R., Moore, D. F., Pober, J. C., Stefan, I. I., and Walbrugh, W. P.: 2014, ApJ **788**, 106

Planck Collaboration: 2015, *ArXiv e-prints*

Pober, J. C.: 2015, MNRAS **447**, 1705

Pober, J. C., Liu, A., Dillon, J. S., Aguirre, J. E., Bowman, J. D., Bradley, R. F., Carilli, C. L., DeBoer, D. R., Hewitt, J. N., Jacobs, D. C., McQuinn, M., Morales, M. F., Parsons, A. R., Tegmark, M., and Werthimer, D. J.: 2014, ApJ **782**, 66

Sethi, S. and Haiman, Z.: 2008, ApJ **673**, 1

Shapiro, P. R., Mao, Y., Iliev, I. T., Mellema, G., Datta, K. K., Ahn, K., and Koda, J.: 2013, *Physical Review Letters* **110(15)**, 151301

Tingay, S. J., Goeke, R., Bowman, J. D., Emrich, D., Ord, S. M., Mitchell, D. A., Morales, M. F., Booler, T., Crosse, B., Wayth, R. B., Lonsdale, C. J., Tremblay, S., Pallot, D., Colegate, T., Wicenec, A., Kudryavtseva, N., Arcus, W., Barnes, D., Bernardi, G., Briggs, F., Burns, S., Bunton, J. D., Cappallo, R. J., Corey, B. E., Deshpande, A., Desouza, L., Gaensler, B. M., Greenhill, L. J., Hall, P. J., Hazelton, B. J., Herne, D., Hewitt, J. N., Johnston-Hollitt, M., Kaplan, D. L., Kasper, J. C., Kincaid, B. B., Koenig, R., Kratzenberg, E., Lynch, M. J., Mckinley, B., Mcwhirter, S. R., Morgan, E., Oberoi, D., Pathikulangara, J., Prabu, T., Remillard, R. A., Rogers, A. E. E., Roshi, A., Salah, J. E., Sault, R. J., Udaya-Shankar, N., Schlagenhaufer, F., Srivani, K. S., Stevens, J., Subrahmanyan, R., Waterson, M., Webster, R. L., Whitney, A. R., Williams, A., Williams, C. L., and Wyithe, J. S. B.: 2013, PASA **30**, 7

Trott, C. M., Wayth, R. B., and Tingay, S. J.: 2012, ApJ **757**, 101

van Haarlem, M. P., Wise, M. W., Gunst, A. W., Heald, G., McKean, J. P., Hessels, J. W. T., de Bruyn, A. G., Nijboer, R., Swinbank, J., Fallows, R., Brentjens, M., Nelles, A., Beck, R., Falcke, H., Fender, R., Hörandel, J., Koopmans, L. V. E., Mann, G., Miley, G., Röttgering, H., Stappers, B. W., Wijers, R. A. M. J., Zaroubi, S., van den Akker, M., Alexov, A., Anderson, J., Anderson, K., van Ardenne, A., Arts, M., Asgekar, A., Avruch, I. M., Batejat, F., Bähren, L., Bell, M. E., Bell, M. R., van Bemmel, I., Bennema, P., Bentum, M. J., Bernardi, G., Best, P., Bîrzan, L., Bonafede, A., Boonstra, A.-J., Braun, R., Bregman, J., Breitling, F., van de Brink, R. H., Broderick, J., Broekema, P. C., Brouw, W. N., Brüggen, M., Butcher, H. R., van Cappellen, W., Ciardi, B., Coenen, T., Conway, J., Coolen, A., Corstanje, A., Damstra, S., Davies, O., Deller, A. T., Dettmar, R.-J., van Diepen, G., Dijkstra, K., Donker, P., Doorduin, A., Dromer, J., Drost, M., van Duin, A., Eislöffel, J., van Enst, J., Ferrari, C., Frieswijk, W., Gankema, H., Garrett, M. A., de Gasperin, F., Gerbers, M., de Geus, E., Grießmeier, J.-M., Grit, T., Gruppen, P., Hamaker, J. P., Hassall, T., Hoeft, M., Holties, H. A., Horneffer, A., van der Horst, A., van Houwelingen, A., Huijgen, A., Iacobelli, M., Intema, H., Jackson, N., Jelic, V., de Jong, A., Juette, E., Kant, D., Karastergiou, A., Koers, A., Kollen, H., Kondratiev, V. I., Kooistra, E., Koopman, Y., Koster, A., Kuniyoshi, M., Kramer, M., Kuper, G., Lambropoulos, P., Law, C., van Leeuwen, J., Lemaitre, J., Loose, M., Maat, P., Macario, G., Markoff, S., Masters, J., McFadden, R. A., McKay-Bukowski, D., Meijering, H., Meulman, H., Mevius, M., Middelberg, E., Millenaar, R., Miller-Jones, J. C. A., Mohan, R. N., Mol, J. D., Morawietz, J., Morganti, R., Mulcahy, D. D., Mulder, E., Munk, H., Nieuwenhuis, L., van Nieuwpoort, R., Noordam, J. E., Norden, M., Noutsos, A., Offringa, A. R., Olofsson, H., Omar, A., Orrú, E., Overeem, R., Paas, H., Pandey-Pommier, M., Pandey, V. N., Pizzo, R., Polatidis, A., Rafferty, D., Rawlings, S., Reich, W., de Reijer, J.-P., Reitsma, J., Renting, G. A., Riemers, P., Rol, E., Romein, J. W., Roosjen, J., Ruiter, M., Scaife, A., van der Schaaf, K., Scheers, B., Schellart, P., Schoenmakers, A., Schoonderbeek, G., Serylak, M., Shulevski, A., Sluman, J., Smirnov, O., Sobey, C., Spreeuw, H., Steinmetz, M., Sterks, C. G. M., Stiepel, H.-J., Stuurwold, K., Tagger, M., Tang, Y., Tasse, C., Thomas, I., Thoudam, S., Toribio, M. C., van der Tol, B., Usov, O., van Veelen, M., van der Veen, A.-J., ter Veen, S., Verbiest, J. P. W., Vermeulen, R., Vermaas, N., Vocks, C., Vogt, C., de Vos, M., van der Wal, E., van Weeren, R., Weggemans, H., Weltevrede, P., White, S., Wijnholds, S. J., Wilhelmsson, T., Wucknitz, O., Yatawatta, S., Zarka, P., Zensus, A., and van Zwieten, J.: 2013, A&A **556**, A2

Wyithe, J. S. B., Loeb, A., and Barnes, D. G.: 2005, ApJ **634**, 715

Yatawatta, S., de Bruyn, A. G., Brentjens, M. A., Labropoulos, P., Pandey, V. N., Kazemi, S., Zaroubi, S., Koopmans, L. V. E., Offringa, A. R., Jelić, V., Martinez Rubi, O., Veligatla, V., Wijnholds, S. J., Brouw, W. N., Bernardi, G., Ciardi, B., Daiboo, S., Harker, G., Mellema, G., Schaye, J., Thomas, R., Vedantham, H., Chapman, E., Abdalla, F. B., Alexov, A., Anderson, J., Avruch, I. M., Batejat, F., Bell, M. E., Bell, M. R., Bentum, M., Best, P., Bonafede, A., Bregman, J., Breitling, F., van de Brink, R. H., Broderick, J. W., Brüggen, M., Conway, J., de Gasperin, F., de Geus, E., Duscha, S., Falcke, H., Fallows, R. A., Ferrari, C., Frieswijk, W., Garrett, M. A., Griessmeier, J. M., Gunst, A. W., Hassall, T. E., Hessels, J. W. T., Hoeft, M., Iacobelli, M., Juette, E., Karastergiou, A., Kondratiev, V. I., Kramer, M., Kuniyoshi, M., Kuper, G., van Leeuwen, J., Maat, P., Mann, G., McKean, J. P., Mevius, M., Mol, J. D., Munk, H., Nijboer, R., Noordam, J. E., Norden, M. J., Orru, E., Paas, H., Pandey-Pommier, M., Pizzo, R., Polatidis, A. G., Reich, W., Röttgering, H. J. A., Sluman, J., Smirnov, O., Stappers, B., Steinmetz, M., Tagger, M., Tang, Y., Tasse, C., ter Veen, S., Vermeulen, R., van Weeren, R. J., Wise, M., Wucknitz, O., and Zarka, P.: 2013, A&A **550**, A136

Yu, Q.: 2005, ApJ **623**, 683

Probing individual sources during reionization and cosmic dawn using SKA HI 21-cm observations

Kanan K. Datta*[1], Raghunath Ghara[2], Suman Majumdar[3], T. Roy Choudhury[2], Somnath Bharadwaj[4], Himadri Roy[1], and Abhirup Datta[5]

[1] *Department of Physics, Presidency University, Kolkata, W.B, India*
[2] *National Centre for Radio Astrophysics, TIFR, Post Bag 3, Ganeshkhind, Pune 411007, India*
[3] *Department of Physics, Blackett Laboratory, Imperial College, London SW7 2AZ, UK*
[4] *Department of Physics & Centre for Theoretical Studies, Indian Institute of Technology Kharagpur, Kharagpur - 721302, India*
[5] *Centre for Astronomy, Indian Institute of Technology Indore, Indore - 452020, India*

Abstract

Detection of individual luminous sources during the reionization epoch and cosmic dawn through their signatures in the HI 21-cm signal is one of the direct approaches for probing the epoch. Here, we summarize our previous works on detecting individual sources during reionization epochs and cosmic dawn in HI 21-cm maps and present a preliminary results on the prospects of detecting such sources using the SKA1-low experiment. We first discuss the expected HI 21-cm signal around luminous sources at different stages of reionization and cosmic dawn. We propose two visibility based estimators for detecting the signal: one based on the matched filtering technique and the other relies on simply combing the signal from different baselines and frequency channels.

We find that that the SKA1-low should be able to detect ionized bubbles of radius $R_b \gtrsim 10$ Mpc with ~ 100 hr of observations at redshift $z \sim 8$ provided that the mean outside neutral fraction $x_{\rm H\ I} \gtrsim 0.5$. We also investigate the possibility of detecting HII regions around known bright QSOs such as around ULASJ1120+0641 discovered by (Mortlock et al., 2011). We find that a 5σ detection is possible with 600 hr of SKA1-low observations if the QSO age and the outside $x_{\rm H\ I}$ are at least $\sim 2 \times 10^7$ Myr and ~ 0.2 respectively.

Finally, we investigate the possibility of detecting the very first X-ray and Ly-alpha sources during the cosmic dawn. We consider the mini-QSOs as a source of X-ray photons. We find that around ~ 1000 hr would be needed to detect those sources individually with the SKA1-low. We also summarize how the SNR changes with various parameters related to the source properties.

1 Introduction

The emergence of first galaxies, quasars in the Universe is one of the significant events in its history. According to the standard scenario, the Ly-α, X-ray, UV photons produced by these first sources percolate through the intergalactic medium (IGM) and completely altered its thermal and ionization state. Unfortunately, we know very little about the nature and properties of these sources.

Recently, tens of extremely bright quasars at redshifts $z \gtrsim 6$ have been detected by various surveys (Fan et al., 2006; Mortlock et al., 2011; Venemans et al., 2015). In addition, hundreds of high redshift galaxies at similar redshifts have been discovered by various techniues (Ouchi et al., 2010; Hu et al., 2010; Kashikawa et al., 2011; Ellis et al., 2013; Bouwens et al., 2015). These sources played an important role during the last phase of the epoch of reionization (EoR). We expect many such sources to exist even at higher redshifts during the initial stages of reionization and cosmic dawn.

It is likely that the UV photons from these sources ionized the neutral Hydrogen atoms around them and create ionized bubbles which are embedded in neutral Hydrogen medium. The Ly-α from the very first luminous sources during the cosmic dawn couple the IGM temperature with HI spin temperature.

*kanan.physics@presiuniv.ac.in

Similarly the X-ray photons from X-ray sources heat up the IGM temperature and therefore raise both the IGM kinetic and the HI spin temperature. The coupling and the heating are initially efficient near the sources. It has been suggested that one can detect the 21-cm signatures around these individual sources using low-frequency telescopes (Datta et al., 2007b, 2008, 2009) which can be helpful in constraining the source properties (Majumdar et al., 2012; Datta et al., 2012). We note that upcoming space telescopes such as the James Webb Space Telescope (JWST)[1] should also be able to detect some of these brightest sources during cosmic dawn and reionization epoch in the optical/infrared band (Zackrisson et al., 2011; De Souza et al., 2013, 2014).

Detection of individual luminous sources during the reionization epoch and cosmic dawn through their signature on the HI 21-cm signal is one of the direct approaches to understand the epoch. Ongoing experiments such as the GMRT, MWA, LOFAR primarily aim to detect the HI 21-cm signal statistically using quantities such as the power spectrum, rms, skewness of the HI 21-cm brightness temperature fluctuations.

We take an alternative approach to undersatnd the reionization epoch and cosmic dawn through detection of HI 21-cm signature of the sources. In this paper, we summarize our previous works on detecting individual sources in HI 21-cm maps and present a preliminary results on the prospects of detecting such sources using the SKA1-low experiment. With an order of magnitude higher sensitivity, better baseline coverage and improved instrument the SKA1-low is expected to detect such objects individually with much less observations time. We first discuss the expected HI 21-cm signal around luminous sources at different stages of reionization and cosmic dawn. then we propose two visibility based estimators for detecting the signal: one based on the matched filtering technique and the other relies on simply combing the signal from different baselines and frequency channels.

The outline of the paper is as follows: In section 2, we discuss the HI 21-cm signal profile around individual sources during the cosmic dawn and reionization epoch. In subsection 2.3 we calculate corresponding visibility signal. Section 3 discusses two estimators which are visibility based for detecting the signal discussed in section 2. We also describe the filter we consider for the first estimator which uses the matched filtering technique. Section 4 discusses the results on the detectability of ionized bubbles, known bright QSOs in the reionization epoch and the first sources during the cosmic dawn using SKA1-low telescope. We summarize the work presented here in section 5.

2 The HI 21-cm signal around individual sources

The first sources are expected to emit in UV, Ly-alpha, X-ray frequencies. In a likely scenario, a fraction of the Ly-α photons from the first generation of stars escape from their host environment and couple the H I spin temperature with the IGM gas kinetic temperature very quickly. At the same time the soft X-ray photons emitting from sources like the mini-QSOs, X-ray binaries, Pop III stars etc. enter into the IGM and heat it up. This causes the HI spin temperature above the background CMB temperature. Subsequently, the UV photons start ionizing HI surrounding the sources and create ionized bubbles which are embedded into HI medium. The Ly-α coupling, X-ray heating, and UV ionization are initially done near the sources and slowly spread over the entire IGM. We expect three distinct differential HI 21-cm brightness temperature (δT_B) profiles around sources at three different stages of the cosmic dawn and reionization. In general, the differential brightness temperature of the HI 21-cm signal can be written as

$$\delta T_b(\vec{\theta},\nu) = 27\ x_{\rm HI}(\mathbf{x},z)[1+\delta_{\rm B}(\mathbf{x},z)]\left(\frac{\Omega_B h^2}{0.023}\right) \times \left(\frac{0.15}{\Omega_m h^2}\frac{1+z}{10}\right)^{1/2}\left[1-\frac{T_{CMB}(z)}{T_{\rm S}(\mathbf{x},z)}\right]\ {\rm mK}, \quad (1)$$

where $\mathbf{x} = r_z\hat{\mathbf{n}}$ and $1+z = 1420\ {\rm MHz}/\nu_{\rm obs}$, r_z is the radial comoving distance to redshift z. $\delta_{\rm B}(z,\mathbf{x})$ and $x_{\rm HI}(z,\mathbf{x})$ denote the density contrast in baryons and neutral hydrogen (HI) fraction respectively at $\mathbf{x}$ at a redshift z. $T_{\rm CMB}(z) = 2.73\times(1+z)$ K is the CMB temperature at a redshift z and T_S is the spin temperature of neutral hydrogen gas. We ignore the line of sight peculiar velocity effects (Bharadwaj

[1] http://jwst.nasa.gov

and Ali, 2004; Barkana and Loeb, 2005) in the above expression, which, we believe do not affect the results presented here..

Below, we briefly discuss the HI 21-cm brightness temperature profile around individual sources expected at different stages of reionization and cosmic dawn.

2.1 Model A: HI 21-cm signal from ionized bubbles during reionization

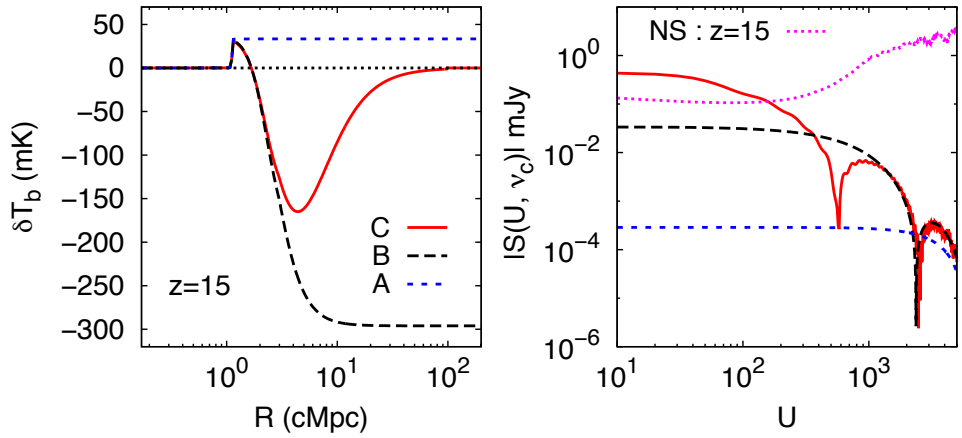

Figure 1: Left panel: The differential brightness temperature profile around an isolated mini-QSO. The source properties are taken to be those corresponding to the fiducial values. The results are shown for all three coupling models A, B, C described in the texts. Right panel: The absolute value of the corresponding visibility amplitude as a function of baseline U. Also shown are rms noise in the visibilities calculated for 1000 h of observation with the SKA1-low with a frequency resolution of 50 kHz. We have fixed $U_{\rm min} = 10$ while calculating the rms noise. The figure is taken from our previous work (Ghara et al., 2015).

In this scenario, we assume that the IGM kinetic temperature is fully coupled with the HI spin temperature and both the temperatures are much higher than the CMB temperature. This is a likely scenario when the Universe is already $\sim 10-20\%$ ionized or after that. Now, we consider a spherical ionized bubble of comoving radius R_b centered at redshift z_c surrounded by uniform IGM with neutral hydrogen fraction $x_{\rm HI}$. We refer this as model A. These kind of ionized bubbles are expected to be common during the later stages of reionization as there are a significant numbers of UV sources which create spherical ionized regions around them. A bubble of comoving radius R_b will be seen as a circular disc in each of the frequency channels that cut through the bubble. At a frequency channel ν, the angular radius of the disc is $\theta_\nu = (R_b/r_\nu)\sqrt{1-(\Delta\nu/\Delta\nu_b)^2}$, where $\Delta\nu = \nu - \nu_c$ is the distance from the bubble's centre $\nu_c = 1420MHz/(1+z_c)$ and $\Delta\nu_b = R_b/r'_\nu$, $\Delta\nu_b$ is the bubble's radius in frequency space. Here, r_ν is the comoving distance corresponding to $z = (1420\,{\rm MHz}/\nu) - 1$ and $r'_\nu = dr_\nu/d\nu$. The specific intensity profile of HI 21-cm signal in this scenario can be written as

$$I_\nu(\vec{\theta}) = \bar{I}_\nu x_{\rm HI}\left[1-\Theta\left(1-\frac{\mid\vec{\theta}-\vec{\theta}_c\mid}{\theta_\nu}\right)\right]\Theta\left(1-\frac{\mid\nu-\nu_c\mid}{\Delta\nu_b}\right) \quad (2)$$

where the radiation from the uniform background HI distribution with neutral Hydrogen fraction $x_{\rm HI}$ can be written as $x_{\rm HI}\ \bar{I}_\nu$ where $\bar{I}_\nu = 2.5\times10^2\,\frac{Jy}{sr}\left(\frac{\Omega_b h^2}{0.02}\right)\left(\frac{0.7}{h}\right)\left(\frac{H_0}{H(z)}\right)$ and $\Theta(x)$ is the Heaviside step function. Note that, here we assume $T_S >> T_{\rm CMB}$, neutral Hydrogen overdensity parameter $\delta_B = 0$. In the Raleigh-Jeans limit the specific intensity $\bar{I}_\nu$ in eq. 2 can be calculated from the differential brightness temperature in eq. 1 using the relation $\bar{I}_\nu = \left(\frac{2K_B}{\lambda^2}\right)\delta T_b(\vec{\theta},\nu)$.

The dashed blue line in the left panel of figure 1 shows the HI differential brightness temperature profile as a function of comoving distance from the source. As mentioned above, we assume $T_s > T_\gamma$

here. The brightness temperature is zero very close to the source because the region is highly ionised and equals to the background HI differential brightness temperature.

2.2 Model B & C: 21-cm signal around sources during cosmic dawn

In model B the Ly-α coupling is assumed to be efficient throughout i.e, the IGM kinetic temperature is completely coupled with the HI spin temperature. Additionally, we assume that there is a X-ray source at the centre of a host DM halo. We refer this as model B. In this model the HI 21-cm signal pattern, in general, can be divided into three prominent regions: (i) the signal is absent inside the central ionized (H II) bubble of the source. (ii) The H II (ionized) region is followed by a region which is neutral and heated by X-rays. In this region, the IGM kinetic temperature $T_K > T_{\rm CMB}$ and thus the HI 21-cm signal is seen in emission. (iii) The third is a strong absorption region which is colder than $T_{\rm CMB}$ as the X-rays photons have not been able to penetrate into this region. At reasonably far from the source the spin temp eventually becomes equal to the background IGM temp.

We consider a third model, referred as model C, which calculates the Ly-alpha coupling, heating, ionisation self-consistently. This is believed to be the case at very early stages of the cosmic dawn. In addition to all three prominent regions described in the model B there will one more prominent region i.e, Beyond the absorption region, the signal gradually approaches to zero as the Ly -α coupling becomes less efficient far away from the source.

Here, we consider only mini-QSOs as a X-ray sources (see (Ghara et al., 2015) for other X-rays sources). The stellar mass for this source model is taken to be $M_\star = 10^7\,M_\odot$. The value of the escape fraction is taken to be $f_{\rm esc} = 0.1$. The X-ray to UV luminosity is fixed as $f_X = 0.05$, while the power law index of the X-ray spectrum of Mini-QSO model is chosen to be $\alpha = 1.5$. It is assumed that the age of the sources is $t_{\rm age} = 20$ Myr. The densities of hydrogen and helium in the IGM are assumed to be uniform and the density contrast δ is set to 0. We denote this model source as our "fiducial" model. We choose the fiducial redshift to be 15 for presenting our results.

The black dashed and the solid red lines in the left panel of the figure 1 show the 21-cm differential brightness temperature δT_b profile around a mini-QSO like source described above for the B and C models respectively.

2.3 Visibilities

The expected visibility signal in each frequency channel is the Fourier transform of the sky intensity pattern and can be approximated as (see (Datta et al., 2007b) for the model A, and the Appendix A of (Ghara et al., 2015)for the B and C models)

$$S^{(i)}(U,\nu) \approx -2m x_{\rm HI}\pi I_{\nu,i}\theta^2_{\nu,i}\left[\frac{J_1(2\pi U\theta_{\nu,i})}{2\pi U\theta_{\nu,i}}\right]\Theta\left(1-\frac{|\nu-\nu_c|}{\Delta\nu_{b,i}}\right). \quad (3)$$

We assume that the source is at the phase centre of the antenna field of view. i denotes various models such as model A, B, C. The integer $m = 1$ for the A and C model and -1 for the B model. The above visibility signal picks up an extra phase factor if the source is not at the centre of the field of view. The right panel of Fig: 1 shows the visibility signal $S^{(i)}(U,\nu)$ as a function of baseline U.

For the model A, the HI 21-cm signal is zero within a circular disc through an ionized bubble of radius $R_{b,1}$. In each channel of frequency ν, the signal has a peak value $|S(0,\nu)| = \pi x_{\rm HI}\bar{I}_{\nu,A}\theta^2_{\nu,A}$. The signal is largely contained within baselines $U \le U_0 = 0.61/\theta_{\nu,A}$ (blue dashed line in the right panel of figure 1), where the Bessel function has its first zero crossing, and the signal is much smaller at larger baselines.

For the B and C model, we find that the emission and absorption bubbles are larger than the H II bubble. We further find that the visibility signal is essentially determined by the emission region in the B model and by the absorbtion region in the C model (black dashed and red solid lines respectively in the right panel of figure 1). The first zero crossings of the visibility signal for the B and C model occur at lower values of U compared to the model A. For example, the first zero crossing appears around $U_0 = 2390$ and 590 for the models B and C respectively, while it appears around $U_0 = 5650$ for the model A. In addition, we find that the amplitude of the visibility signal at small U is the largest (smallest) for C (A). The amplitude of the visibility at small baselines scales roughly as $\bar{I}_{\nu,A}\theta^2_{\nu,i}$, where $\bar{I}_{\nu,i}$ is the signal amplitude in the emission region for the model A and in the absorption region in models B and

C. $\theta_{\nu,i} = R_{\nu,i}/r_\nu$ is the total radial extent of the ionized region for the model A, ionized and emission regions for model B and ionized, emission and absorption regions for models C. Given this scaling, it is easy to see that since the size of the absorption region is much larger than the ionized and emission regions, the visibility amplitude in model C would be the largest. This is further assisted by the fact that the $\bar{I_{\nu,i}}$ itself is very high in the absorption region.

3 Estimators for detecting sources individually

The visibility recorded in radio-interferometric observations can be written as a combination of four separate contributions

$$V(\vec{U},\nu) = S(\vec{U},\nu) + HF(\vec{U},\nu) + N(\vec{U},\nu) + F(\vec{U},\nu) \tag{4}$$

where the baseline $\vec{U} = \mathbf{d}/\lambda$, $\mathbf{d}$ is physical separation between a pair of antennas projected on the plane perpendicular to the line of sight. $S(\vec{U},\nu)$ is the HI signal that we are interested in, $HF(\vec{U},\nu)$ is contribution from fluctuating HI outside the targeted region, $N(\vec{U},\nu)$ is the system noise which is inherent to the measurement and $F(\vec{U},\nu)$ is the contribution from other astrophysical sources referred to as the foregrounds.

It is a major challenge to detect the signal which is expected to be buried in noise and foregrounds both of which are much stronger. It would be relatively simple to detect the signal in a situation where there is only noise and no foregrounds. There are various ways of reducing the rms noise in observations. Below we discuss two ways to minimize the noise contribution in the measurements and maximize the signal to noise ratio.

3.1 Matched filter technique

This technique has been proposed and explored for detecting individual ionized bubbles described in the A type model. Bubble detection is carried out by combining the entire observed visibility signal weighed with the filter. The estimator $\hat{E}$ is defined as (Datta et al., 2007b)

$$\hat{E} = \left[\sum_{a,b} S_f^*(\vec{U}_a,\nu_b)\hat{V}(\vec{U}_a,\nu_b)\right] / \left[\sum_{a,b} 1\right] \tag{5}$$

where the sum is over all frequency channels and baselines. The expectation value $\langle E\rangle$ is non-zero only if an ionized bubble is present. $S_f(\vec{U}_a,\nu_b)$ is a filter which has been constructed to detect the particular ionized bubble.

The system noise (NS), HI fluctuations (HF) and the foregrounds (FG) all contribute to the variance of the estimator

$$\langle(\Delta\hat{E})^2\rangle = \left\langle(\Delta\hat{E})^2\right\rangle_{\rm NS} + \left\langle(\Delta\hat{E})^2\right\rangle_{\rm HF} + \left\langle(\Delta\hat{E})^2\right\rangle_{\rm FG} . \tag{6}$$

Because of our choice of the matched filter, the contribution from the residuals after foreground subtraction $\left\langle(\Delta\hat{E})^2\right\rangle_{\rm FG}$ is predicted to be smaller than the signal (Datta et al., 2007b), Datta 2012) and we do not consider it in the subsequent analysis. The contribution $\left\langle(\Delta\hat{E})^2\right\rangle_{\rm HF}$ which arises from the HI fluctuations outside the target bubble imposes a fundamental restriction on bubble detection. It is not possible to detect an ionized bubbles for which $\langle E\rangle \leq \sqrt{\left\langle(\Delta\hat{E})^2\right\rangle_{\rm HF}}$. Bubble detection is meaningful only in situations where the contribution from HI fluctuations is considerably smaller than the expected signal. Once this condition is satisfied, it is the SNR defined as

$$SNR = \langle E\rangle / \sqrt{\left\langle(\Delta\hat{E})^2\right\rangle_{\rm NS}} \tag{7}$$

It is possible to analytically estimate $\langle \hat{E} \rangle$ and $\langle (\Delta \hat{E})^2 \rangle_{\rm NS}$ in the continuum limit (Datta et al., 2007b). We have

$$\langle \hat{E} \rangle = \int d^2U \int d\nu \, \rho_N(\vec{U},\nu) \; {S_f}^*(\vec{U},\nu) S(\vec{U},\nu) \, , \tag{8}$$

and

$$\langle (\Delta \hat{E})^2 \rangle_{\rm NS} = \sigma^2 \int d^2U \int d\nu \, \rho_N(\vec{U},\nu) \;\; \mid S_f(\vec{U},\nu) \mid^2 \; . \tag{9}$$

$\rho_N(\vec{U},\nu)$ is the normalized baseline distribution function defined so that $\int d^2U \int d\nu \rho_N(\vec{U},\nu) = 1$. For a given observation, $d^2U \, d\nu \, \rho_N(\vec{U},\nu)$ is the fraction of visibilities in the interval $d^2U \, d\nu$ of baselines and frequency channels. Further, we expect $\rho_N(\vec{U},\nu) \propto \nu^{-2}$ for an uniform distribution of the antenna separations $\mathbf{d}$.

The term σ in eq. (9) is the rms. noise expected in an image made using the radio-interferometric observation being analyzed. Assuming observations at two polarizations, we have

$$\sigma = \frac{k_B T_{sys}}{A_{eff} \sqrt{N_b t_{obs} B}} \tag{10}$$

where k_B is the Boltzmann constant, T_{sys} the system temperature, A_{eff} the effective collecting area of an individual antenna in the array, N_b the number of baselines, t_{obs} the total observing time and B the observing bandwidth.

3.2 Filter

In order to detect an ionized bubble whose expected signal is $S(\vec{U},\nu)$ we use the matched filter $S_f(\vec{U},\nu)$ defined as

$$\begin{aligned} S_f(\vec{U},\nu) = & \left(\frac{\nu}{\nu_c} \right)^2 \Big[S(\vec{U},\nu) - \\ & \Theta \left(1 - 2 \frac{\mid \nu - \nu_c \mid}{B'} \right) \frac{1}{B'} \int_{\nu_c - B'/2}^{\nu_c + B'/2} S(\vec{U},\nu') \, d\nu' \Big] \, . \end{aligned} \tag{11}$$

Note that the filter is constructed using the signal that we are trying to detect. The term $(\nu/\nu_c)^2$ accounts the frequency dependent U distribution for a given array. The function Θ is the Heaviside step function. The second term in the square brackets serves to remove the foregrounds within the frequency range $\nu_c - B'/2$ to $\nu_c + B'/2$. Here $B' = 4 \, \Delta\nu_b$ is the frequency width that we use to estimate and subtract out a frequency independent foreground contribution. This, we have seen in Paper I, is adequate to remove the foregrounds such that the residuals are considerably smaller than the signal. Further we have assumed that B' is smaller than the total observational bandwidth B. The filter $S_f(\vec{U},\nu)$ depends on $[R_b, z_c, \vec{\theta}_c]$ the comoving radius, redshift and angular position of the target bubble that we are trying to detect.

3.3 Combining visibilities

The success of the matched filter method depends on ability to find a suitable filter. The signal to noise ration (SNR) is maximum in a situation when the filter matches perfectly with the signal. Prior knowledge about the signal and its dependence on various parameters is necessary in order to find an appropriate filter. The HI 21-cm signal around the sources during the cosmic dawn depends on various parameters such as the number of Ly-α, X-ray, UV photons available, X-ray spectral index, background IGM kinetic temperature, source age, UV escape fraction, IGM overdensity etc. Dependence of the HI 21-cm signal around cosmic dawn sources on so many unknown parameters makes it difficult to choose an appropriate filter for the B and C type model. We, therefore, do not attempt to apply the matched filter technique to the B, C type models. Instead, we simply add the visibility signal from all baselines

and frequency channels to enhance the SNR. The estimator is defined as (see (Ghara et al., 2015) for details)

$$\hat{E}_2 = \left[\sum_{a,b} \hat{V}(\vec{U}_a, \nu_b)\right] / \left[\sum_{a,b} 1\right] \tag{12}$$

Note that the above estimator is a special case of the matched filter estimator i.e, $S_f(\vec{U}, \nu) = 1$ for all baselines and frequency channels. The SNR can be written as,

$$\mathrm{SNR} = \frac{1}{\sigma_N} \frac{\int d^2U \int d\nu \; \rho_N(\vec{U}, \nu) \; S(\vec{U}, \nu)}{\int d^2U \int d\nu \; \rho_N(\vec{U}, \nu)}, \tag{13}$$

where

$$\sigma_N = \frac{\sqrt{2} \; k_B T_{\mathrm{sys}}}{A_{\mathrm{eff}} \; \sqrt{t_{\mathrm{obs}} \; B_\nu \; N_{\mathrm{ant}}(N_{\mathrm{ant}} - 1)/2}}. \tag{14}$$

The quantity B_ν denotes the bandwidth of the observations, and is simply the frequency resolution $\Delta\nu_c$ times the number of frequency channels. Note that the above definition (13) of the SNR implies that we weight the visibility signal $S(\vec{U}, \nu)$ at individual baselines by the number $n_{\mathrm{B}}(U, \nu)$ of baselines. Since $n_{\mathrm{B}}(U, \nu) \propto \sigma^{-2}(U, \nu)$, we have simply weighed the visibilities according to inverse of the noise error.

4 Results

4.1 Prospects of detecting ionized bubbles (H II regions) during reionization

In this section, we discuss the possibility of detecting individual ionized bubbles using the matched filter technique. We implement this technique only for the model A. Figure 2 shows the SNR as a function of comoving radius R_b (Mpc) of ionized bubble for the matched filter technique. Ionized bubbles are assumed to be embedded in uniform IGM with neutral Hydrogen fraction $x_{\mathrm{HI}} \approx 0.5$. The upper green line of the figure 2 shows results for the SKA1-low for a total 100 hr of observations at frequency 165 MHz corresponding to redshift $z = 7.6$. For a comparison we show results for LOFAR (red line) for the same observation time. Here, we assume that the SKA1-low baseline distribution is same as LOFAR. We find more than 4σ is possible for the SKA1-low for the entire range of bubble sizes we consider. It is possible to detect ionized bubbles of radii $R_b = 20$ and 30 Mpc with SNR$>$ 15 and 30 with SKA1-low 100 hr observations. We also find that the SNR is around 10 times higher for the SKA1-low compared to LOFAR.

4.2 Prospects of detecting bright QSOs

We estimate the possibility of detecting the H II bubble around a quasar using the SKA1-low medium or deep HI 21-cm survey. For this analysis we assume that the quasar under consideration has a spectroscopically confirmed redshift from infrared surveys (similar to the case of (Mortlock et al., 2011)), and its location and the luminosity (an extrapolation from the measured spectra) are known. We also assume that the H II bubble is embedded in uniform IGM with the mean neutral fraction $x_{\mathrm{H\,I}}$. We estimate the total observation time required for the SKA1-low to detect such an H II region around a high redshift quasar using HI 21-cm observations. We investigate the minimum background $x_{\mathrm{H\,I}}$ and the quasar age required for a statistically significant detection of the H II bubble. We consider the matched filtering technique described above and introduced in (Datta et al., 2007b) for our analysis. We assume that the quasar under consideration is emitting with a constant ionizing photon luminosity throughout its age and, therefore, growing in size following the model of (Yu, 2005) (here we consider it to be same as the (Mortlock et al., 2011) quasar ULASJ1120+0641 i.e. $\dot{N}_\gamma = 1.3 \times 10^{57}\,\mathrm{sec}^{-1}$). We consider the apparent anisotropy in the quasar H II regions shape arising due to the finite light travel time (Yu, 2005) and include that as the matched filter parameter in our targeted search (Majumdar et al., 2011, 2012). The apparent radii of the ionized bubble for different QSO age and the outside $x_{\mathrm{H\,I}}$ are shown in figure 3. We assume that the quasar is located at redshift $z = 8$.

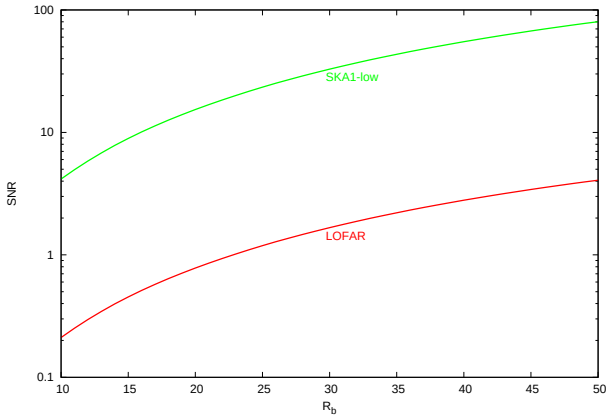

Figure 2: This shows the SNR as a function of comoving radius R_b (Mpc) of ionized bubble using the matched filter technique for the model A. Ionized bubbles are assumed to be embedded in uniform IGM with neutral Hydrogen fraction $x_{\rm HI} \approx 0.5$. The upper and lower lines show results for the SKA1-low and LOFAR respectively for a total 100 hr of observations at frequency 165 MHz corresponding to redshift $z = 7.6$. Here, we assume that the shape of SKA1-low baseline distribution is same as LOFAR.

For the SKA1-low interferometer we assume[2] $A_{eff}/T_{sys} \approx 500\,{\rm m^2\,K^{-1}}$ at $110 - 160$ MHz with frequency resolution of $\Delta\nu = 0.1$ MHz, number of antennas 512 and a total bandwidth of 32 MHz, which yields a value of $C^x = 3.904$ Jy in the following expression of R.M.S. of noise (Datta et al., 2007b) contribution in a single baseline

$$\sqrt{\langle \hat{N}^2 \rangle} = C^x \left(\frac{\Delta\nu}{1{\rm MHz}}\right)^{-1/2} \left(\frac{\Delta t}{1sec}\right)^{-1/2} . \quad (15)$$

Using this expression of noise and following the method described in (Majumdar et al., 2012) we estimate the minimum observation time required for a 3σ and 5σ detection of the H II bubble using the SKA1-low. Note that we do not assume the HIfluctuations outside the targeted bubble due to galaxy generated H II regions and density fluctuations (Datta et al., 2008, 2012; Majumdar et al., 2012). Figure 4 shows our estimates for SKA1-low. Four different shades of black from dark to light represent 100, 200, 400 and 600 hr of observations respectively. We find that at least 3σ detection is possible with 100 hr of observations if the QSO age and the mean $x_{\rm H\ I}$ outside the QSO H II region are higher than 10^7 Myr and 0.7 respectively. If the mean $x_{\rm H\ I}$ outside the QSO H II region are ~ 0.4, 0.3 and 0.2, then the total observations time required are 200, 400 and 600 hr respectively when the QSO age is $\sim 10^7$ Myr. A 5σ detection is possible if the QSO age and the outside $x_{\rm H\ I}$ are at least $\sim 2 \times 10^7$ Myr and ~ 0.2 respectively.

4.3 Prospects of detecting sources during cosmic dawn

Different panels of Figure 5 show the SNR as a function of various parameters related to the source properties (e.g., stellar mass, escape fraction of ionizing photons, X-ray to UV luminosity ratio, and age of the source and the overdensity of the surrounding IGM) for the SKA1-low. Recall that the fiducial value of the parameters are $M_* = 10^7 M_\odot$, $\delta = 0$, $f_{\rm esc} = 0.1$, $f_X = 0.05$, $\alpha = 1.5$, $t_{\rm age} = 20$ Myr. While showing the dependence of the SNR on a particular parameter, we have fixed all the other parameters to their fiducial values. The characteristics of the observations are chosen such that the total observational time is 1000 hours, while the bandwidth is 16 MHz.

[2]https://www.skatelescope.org/wp-content/uploads/2012/07/SKA-TEL-SKO-DD-001-1

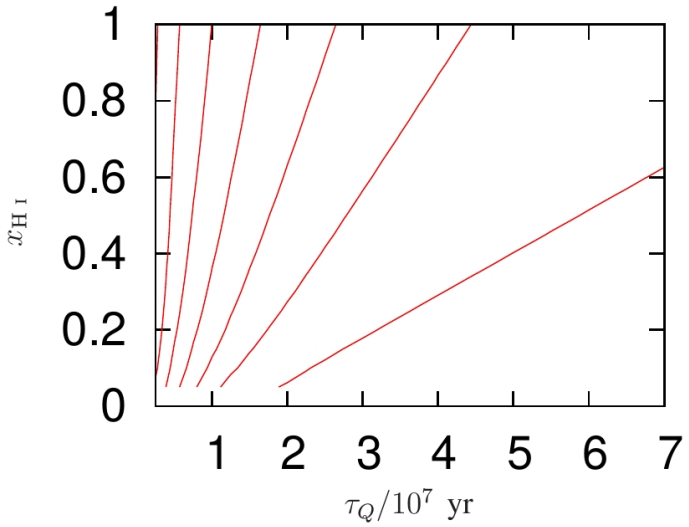

Figure 3: This shows the apparent comoving size of the H II bubble around a quasar with the ionizing photon emission rate $\dot{N}_\gamma = 1.3 \times 10^{57}\,\mathrm{sec}^{-1}$, same as ULASJ1120+0641 (Mortlock et al., 2011). Different contours from right to left represent 40, 35, 30, 25, 20, 15 and 10 Mpc.

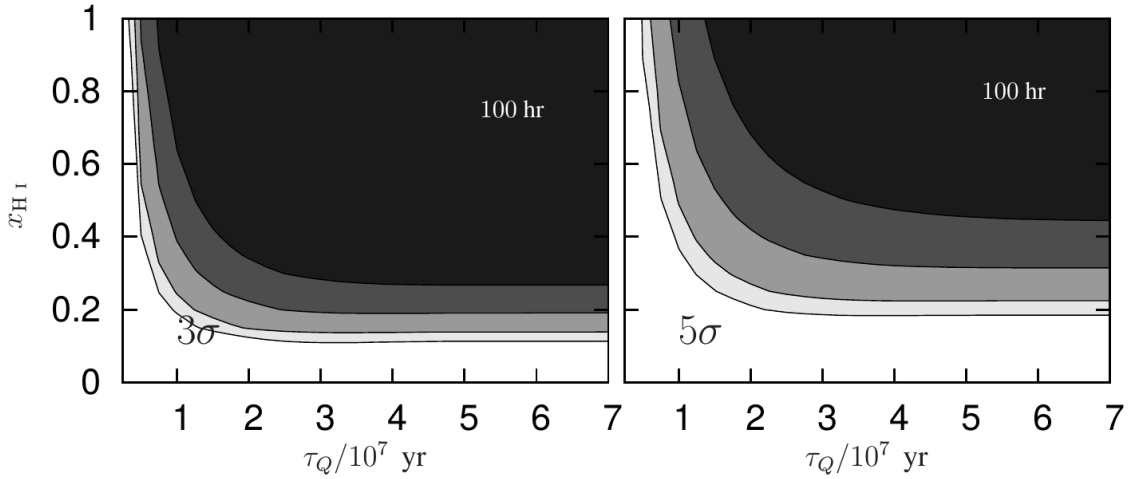

Figure 4: This shows the estimates of minimum observation time required for 3σ and 5σ (left and right panels respectively) detection of the H II bubble around the quasar ULASJ1120+0641 discovered by (Mortlock et al., 2011) using SKA1-low. Different shades of black from dark to light represent 100, 200, 400 and 600 hr of observations respectively.

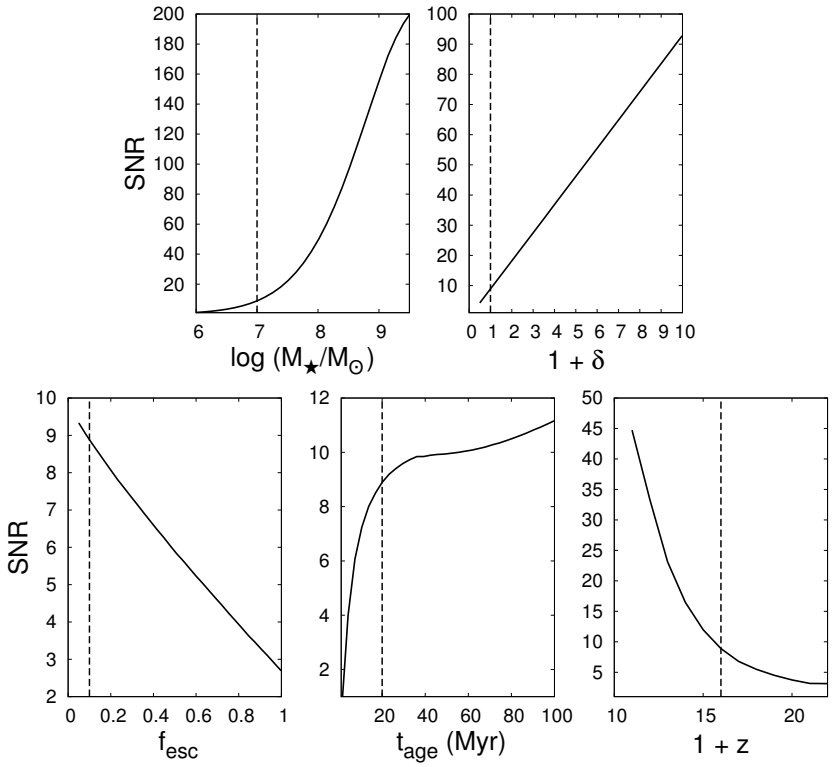

Figure 5: The SNR as a function of different model parameters for the source model mini-QSO and coupling model C. While calculating the dependence of the SNR on a particular parameter, we have fixed the other parameters to their fiducial values. The fiducial value for each parameter is denoted by the vertical dashed line in the corresponding panel. The SNR is calculated using eq. 13 for 1000 hr of observations with SKA1-low with a bandwidth of 16 MHz. See (Ghara et al., 2015) for details.

The SNR increases with the stellar mass (top left panel) as the strength of the 21-cm signal increases and thus the visibility amplitude increases. On the other hand, the radius of both the ionised and heated bubbles increase with the mass of the source, which result in faster decrease of the visibility with the baseline. Although the visibility signal is much stronger at smaller baselines for large stellar mass sources, the very small baselines $U_{min} < 8$ are not available for SKA1-low baseline distribution at redshift 15. This slows the growth of the SNR for the extremely high mass $M_* > 10^9 M_\odot$

sources. From the bottom left panel, we find that the SNR decreases with increase of escape fraction. This is because of the amount of Ly-α photons, produced due to the recombination of the absorbed photons in the ISM, is proportional to $1 - f_{\rm esc}$ and thus the Ly-α coupling becomes less effective as $f_{\rm esc}$ increases. This leads to a smaller absorption region and thus a smaller amplitude of the 21-cm signal. The size of the 21-cm signal region increases with the age of the source as the photons are able to propagate longer distance and thus the visibility amplitude at lower baselines as well as the SNR increase with the age of the source, as shown in the bottom middle panel of Figure 5 . The strength of the signal increase with the increase of the overdensity $(1 + \delta)$, as δT_b is proportional to the overdensity . Thus the SNR increase almost linearly with $(1 + \delta)$, as shown in the top right panel. The SNR is found to be weakly dependent on the two X-ray parameters f_X and α and we dont show them here.

5 Discussion and conclusions

Detection of individual luminous sources during the reionization epoch and cosmic dawn through their signature on the HI 21-cm signal is one of the direct approaches to understand the epoch. Ongoing experiments such as the GMRT, MWA, LOFAR primarily aim to detect the HI 21-cm signal statistically using quantities such as the power spectrum, rms, skewness of the HI 21-cm brightness temperature fluctuations. Although, it has been proposed that these experiments should be able to detect individual ionized bubbles around reionization sources using optimum detection methods such as the matched filter technique (Datta et al., 2007b, 2008, 2009; Majumdar et al., 2011, 2012; Datta et al., 2012). With an order of magnitude higher sensitivity, better baseline coverage and improved instrument the SKA1-low is expected to detect such objects with much less observations time.

In this work, we summarize our previous works on this issue and present some preliminary results on the prospects of detecting individual sources during reionization and cosmic dawn using SKA1-low HI 21-cm maps. While calculating the HI 21-cm signal around individual sources we consider three scenarions: (i) In the first scenario named model A, we assume that the IGM kinetic temperature is fully coupled with the HI spin temperature and both the temperatures are much higher than the CMB temperature. This is a likely scenario when the Universe is already $\sim 10-20\%$ ionized or after that. The central source creates a spherical ionized bubble which is embedded in a uniform neutral (or partially neutral) medium. (ii) The second scenario named model B, the IGM kinetic temperature is completely coupled with the HI spin temperature. Additionally, we assume that there is a X-ray source at the centre of a host DM halo and calculate the IGM kinetic temperature and the HI spin temperature profile self-consistently. (iii) In the third model named model C, we calculate the Ly-alpha coupling, heating, ionisation self-consistently. This is believed to be the case at very early stages of the cosmic dawn. We discuss various features in the differential brightness temperature profile around the central source in these three models. Subsequently, we calculate, analytically, the visibility signal for such HI 21-cm signal and study its various properties.

We propose two visibility based methods for detecting such signal around individual sources: one based on the matched filter formalism and the other relies on combining signal from all baselines and frequency channels. We apply the first method to the model A i.e, to spherical ionized bubble model at the reionization epoch. We find that the SKA1-low should be able to detect ionized bubbles of radius $R_b \gtrsim 10$ Mpc with ~ 100 hr of observations at redshift $z \sim 8$ provided that the mean outside neutral fraction $x_{\rm H\,I} \gtrsim 0.5$. Higher observation time would be required for lower neutral fraction. We also investigate the possibility of detecting HII regions around known bright QSOs such as around ULASJ1120+0641 discovered by (Mortlock et al., 2011). We find that a 5σ detection is possible with 600 hr of SKA1-low observations if the QSO age and the outside $x_{\rm H\,I}$ are at least $\sim 2 \times 10^7$ Myr and ~ 0.2 respectively.

Finally, we investigate the possibility of detecting the very first X-ray and Ly-alpha sources in model B and C during the cosmic dawn. We consider the mini-QSOs as a source of X-ray photons. We find that

around ~ 1000 hr would be needed to detect those sources individually with SKA1-low. We also study how the SNR changes with various parameters related to the source properties such as the stellar mass, escape fraction of ionizing photons, X-ray to UV luminosity ratio, age of the source and the overdensity of the surrounding IGM.

Finally, we emphasise that the work we present and discuss here should be treated as a preliminary one. Further work needs to be done to understand the signal properties in detail. Detail investigation is also necessary to understand the impact of the foreground subtraction, calibration, ionospheric turbulence, RFI mitigation effects etc. We plan to adress some of these issues in future.

References

Barkana, R., & Loeb, A. 2005, ApJL, 624, L65

Bharadwaj, S., & Ali, S. S. 2004, MNRAS, 352, 142

Bouwens R. J., et al., 2015, ApJ, 803, 34

Datta, K. K., Choudhury, T. R., & Bharadwaj, S. 2007, MNRAS, 378, 119

Datta, K. K., Bharadwaj, S., & Choudhury, T. R. 2007, MNRAS, 382, 809

Datta, K. K., Majumdar, S., Bharadwaj, S., & Choudhury, T. R., 2008,MNRAS, 391, 1900

Datta, K. K., Bharadwaj, S., & Choudhury, T. R. 2009, MNRAS, 399, L132

Datta, K. K., Friedrich, M. M., Mellema, G., Iliev, I. T., & Shapiro, P. R. 2012, MNRAS, 424, 762

De Souza R. S., Ishida E. E. O., Johnson J. L., Whalen D. J., Mesinger A., 2013, MNRAS, 436, 1555

De Souza R. S., Ishida E. E. O., Whalen D. J., Johnson J. L., Ferrara A., 2014, MNRAS, 442, 1640

Ellis R. S., et al., 2013, ApJ, 763, L7

Fan X., et al., 2006, AJ, 132, 117

Ghara, R., Choudhury, T. R., & Datta, K. K. 2015, arXiv:1511.07448

Hu E. M., Cowie L. L., Barger A. J., Capak P., Kakazu Y., Trouille L., 2010, ApJ, 725, 394

Kashikawa N., et al., 2011, ApJ, 734, 119

Majumdar, S., Bharadwaj, S., Datta, K., K., & Choudhury, T. R. 2011, MNRAS, 413, 1409

Majumdar, S., Bharadwaj, S., & Choudhury, T. R. 2012, MNRAS, 426, 3178

Mortlock, D., J., et al. 2011, Nature, 474, 7353

Ouchi M., et al., 2010, ApJ, 723, 869

Venemans B. P., et al., 2015, ApJ, 801, L11

Yu, Q. & Lu, Y. 2005, ApJ, 620, 31

Yu, Q. 2005, ApJ, 623, 683

Zackrisson E., Rydberg C.-E., Schaerer D., Ostlin G., Tuli M., 2011, ApJ, 740, 13

Visibility based angular power spectrum estimator for redshifted 21 cm experiments

Sk. Saiyad Ali*[1], Somnath Bharadwaj[2], Samir Choudhuri[2], Abhik Ghosh[3], and Nirupam Roy[2]

[1] *Department of Physics,Jadavpur University, Kolkata 700032, India*
[2] *Department of Physics, & Centre for Theoretical Studies, IIT Kharagpur, Pin 721 302, India*
[3] *Kapteyn Astronomical Institute, PO Box 800, 9700 AV Groningen, The Netherlands*

Abstract

We briefly review the Tapered Gridded Estimator (TGE) to quantify the angular power spectrum C_ℓ of the sky signal directly from the visibilities measured in radio interferometric observations. The TGE uses the visibilities after gridding in the uv plane. This also enables us to taper the sky response and thereby suppresses the sidelobe-response of the telescope's primary beam and reduces the contribution from the residual point sources located at the periphery of the telescope's main lobe. This is an useful ingredient in wide-field foreground removal for detecting the cosmological 21-cm signal. Further, the estimator is devised in such a way that it computes the noise bias internally and subtract accurately its contribution to extract desire signal for providing an unbiased estimation of C_ℓ. We have used the TGE to the worked example of 150 MHz GMRT observations to show that it is possible to considerably reduce the oscillations in the multi-frequency angular power spectrum of the sky signal by suppressing the sidelobe response of the primary beam. We validate our theoretical formalism of the TGE using simulations at 150 MHz for GMRT and LOFAR. Further, we demonstrate, using 150 MHz GMRT simulation, that the TGE successfully recovers the C_ℓ of the input model of diffuse Galactic synchrotron emission from the residual visibility data over the entire ℓ range by reducing the contribution from the residual point sources located at the periphery of the beam. We propose the TGE as an effective novel tool to observationally quantify both foregrounds and the cosmological 21-cm signal.

Key words: methods: statistical, data analysis - techniques: interferometric- cosmology: diffuse radiation

1 Introduction

Observations of the redshifted 21-cm radiation from the large scale distribution of neutral hydrogen (HI) is one of the most promising probes to study the high redshift Universe (recent reviews: Morales & Wyithe 2010; Mellema et al. 2013). Although, one of the key challenges in a statistical detection of the 21-cm signal comes from the contamination by the Galactic and extra-galactic foregrounds which are orders of magnitude higher compared to the relatively weak 21-cm signal (Ali, Bharadwaj & Chengalur 2008; Bernardi et al. 2009; Ghosh et al. 2012). Several methods of foreground removal and foreground avoidance have been proposed in the literature for detecting the Epoch of Reionization (EoR) 21-cm signal (Chapman et al. 2014, references therein). In general, foreground avoidance method is based on the assumption that the foregrounds are smooth in frequency and therefore it will mostly occupy a limited space in the Fourier domain $(k_\perp, k_\parallel)$ labeled as the foreground "wedge". The HI power spectrum can be estimated from the uncontaminated modes above the wedge region termed as the "EoR window" where the HI signal is dominant over the foregrounds. On the other hand, foreground removal methods tries to build up a physical model of the foregrounds and subtracts it form the calibrated data where the residuals have contribution from only the 21-cm signal and noise.

*saiyad@phy.jdvu.ac.in

In radio interferometric observations, the quantity measured is the complex visibility. The measurement is done directly in Fourier space which makes interferometers ideal instruments to quantify the power spectrum of the sky signal. The visibility based power spectrum estimators also have the added advantage that they avoid possible imaging artifacts due to the dirty beam, etc (Trott et al. 2011). A visibility based estimator, namely the "Bare Estimator", has been successfully employed to study the power spectrum of the HI in the interstellar medium (ISM) of several nearby galaxies (eg. Begum et al. 2006; Dutta et al. 2009) and used for measuring the angular power spectrum of the sky signal using GMRT data in the context of HI observations (Ali, Bharadwaj & Chengalur 2008; Ghosh et al. 2011a). The Bare Estimator directly uses pairwise correlations of the measured visibilities by avoiding the self correlation that is responsible for the noise bias. The Bare Estimator is very precise, but computationally very expensive for large data volumes, as it scales with the square of the visibility number. Moreover, accurate determination and possible subtraction of any additive noise bias is an important issue for any estimator. For example, the image based estimator (Seljak 1997; Bernardi et al. 2009; Iacobelli et al. 2013) for C_ℓ and the visibility based estimator (Liu & Tegmark, 2012) for $P(k_\perp, k_\parallel)$ rely on modelling the noise properties of the data and subtracting out the expected noise bias. However, the actual noise in the observations could have baseline, frequency and time dependent variations which are very difficult to model, and there is always a possibility of residual noise bias contaminating the 21-cm signal. We note that, in a recent study, Paciga et al. (2011) have avoided the noise bias by cross-correlating observations made on different days assuming noise are independent in different days.

In general, all the different foreground removal techniques use the smooth spectral behaviour of the various foreground components. In our earlier works, Ghosh et al. (2011a,b) have found that residual point sources located away from the phase center introduce oscillations along frequency direction in the measured multi-frequency angular power spectrum $C_\ell(\Delta\nu)$ or MAPS (Datta, Roy Choudhury & Bharadwaj, 2007). The oscillations are more rapid if the distance of the source from the phase center increases, and also with increasing baseline. This oscillatory patterns pose a serious obstacle for foreground removal. Equivalently, the dominant contribution to the width of the "foreground wedge" (below which most of the foregrounds are localized) in a 2D cylindrical power spectrum arises from the sources located near the horizon of the field of view (Thyagarajan et al. 2013). Using GMRT data Ghosh et al. (2011b, 2012) have shown that it is possible to reduce the oscillations by tapering the primary beam (PB) of the antenna elements. It has been recently demonstrated from both simulated and observed data for MWA that removal of the wide-field foregrounds (particularly point sources) is crucial to accurately measure the 21 cm power spectrum (Pober et al. 2016). In our recent paper (Choudhuri et al., 2016a), based on 150 MHz GMRT simulation, we have shown that it is possible to suppress the point source contributions from the outer parts of the main lobe of the primary beam by tapering the sky response to measure the C_ℓ of the sky signal.

In this article, we focus on the TGE which uses the measured visibilities after gridding on a rectangular grid in the uv plane to quantify the angular power spectrum (C_ℓ) of the sky signal. The estimator can self-consistently compute the noise bias and accurately subtract it to provide an unbiased estimation of C_ℓ's. We note that the TGE has a lower precision as compared to the Bare Estimator, but takes less computation time which is mostly proportional to the data volume (Choudhuri et al. 2014). This is relevant to the current and next generation radio interferometers which are expected to produce considerably large volumes of visibility data in observations spanning many frequency channels and large observing times. We have used the TGE for 150 MHz GMRT observation to show that it is possible to considerably reduce the oscillations in the multi-frequency angular power spectrum of the sky signal by suppressing the contribution from the outer region. As a test-bed for the estimator, we consider a situation where the point sources have been identified and subtracted out perfectly so that the residual visibilities are dominated by the Galactic synchrotron radiation. To validate the estimator we investigated how well the TGE is able to recover the angular power spectrum of the input model which was used to simulate the Galactic synchrotron emission for the Giant Metrewave Radio Telescope (GMRT)[1] and the Low Frequency Array (LOFAR, var Haarlem et al. (2013)) at 150 MHz. Further, we use simulated 150 MHz GMRT data which includes point sources and diffuse Galactic synchrotron radiation to validate that it is possible to suppress the contribution from the residual point sources, in the outer parts of the primary beam and in the the sidelobes, in estimating the C_ℓ of the diffuse radiation.

A brief outline of the paper follows. In Section 2 we present briefly the TGE as an effective tool to

[1] http://www.gmrt.ncra.tifr.res.in

observationally quantify both foregrounds and the cosmological 21-cm signal. In Section 3 we validate our theoretical analysis using simulations at 150 MHz for GMRT and LOFAR. In this Section we have also applied the TGE for 150 MHz GMRT observation to see how tapering of the primary beam works to reduce the oscillations in the multi-frequency angular power spectrum of the sky signal. We present summary and conclusions in Section 4.

2 The Tapered Gridded Estimator

In this section, we briefly review the formalism for Tapered Gridded Estimator (TGE) which is used to estimate the angular power spectrum from the measured visibility data. Choudhuri et al. (2014) presents a detailed discussion of this estimator, and we only present a brief outline here. The measured visibilities are a sum of two components namely the sky signal and the system noise

$$\mathcal{V}(\mathbf{U},\nu) = \mathcal{S}(\mathbf{U},\nu) + \mathcal{N}(\mathbf{U},\nu)\,. \tag{1}$$

We assume that the signal and the noise are both uncorrelated Gaussian random variables with zero mean. The measured visibilities record the Fourier transform of the product of the primary beam pattern $\mathcal{A}(\vec{\theta},\nu)$ and $\delta I(\vec{\theta},\,\nu)$, the angular fluctuation in the specific intensity of the sky signal. The TGE allows us to taper the sky response of the antenna elements and thereby suppresses the contribution coming from the outer part of the primary beam and the sidelobes. We implement the tapering by multiplying the field of view with a frequency independent window function, $\mathcal{W}(\theta)$. Equivalently, in the Fourier domain we convolve the measured visibilities with $\tilde{w}(\mathbf{U})$, the Fourier transform of $\mathcal{W}(\theta)$. The convolved visibilities are evaluated on a rectangular grid in uv space using

$$\mathcal{V}_{cg} = \sum_i \tilde{w}(\mathbf{U}_g - \mathbf{U}_i)\,\mathcal{V}_i \tag{2}$$

where $\mathbf{U}_g$ refers to the different grid points and $\mathcal{V}_i$ refers to the measured visibilities at baseline $\mathbf{U}_i$. We note that the gridding process considerably reduces the data volume and the computation time required to estimate the power spectrum (Choudhuri et al., 2014). It may be noted that tapering the sky response is effective only if the window function $\tilde{w}(\mathbf{U}_g - \mathbf{U}_i)$ in eq. (2) is densely sampled by the uv distribution. The results of this article, shown later, indeed justify this assumption for the GMRT which is limited by the patchy uv coverage.

The convolved visibilities of the sky signal gives us an estimate of the product of the intensity fluctuations $\delta I(\vec{\theta},\nu)$ and a modified primary beam pattern $\mathcal{A}_W(\vec{\theta},\nu) = \mathcal{W}(\theta)\,\mathcal{A}(\vec{\theta},\nu)$. We model the modified primary beam pattern as a Gaussian $\mathcal{A}_{\mathcal{W}}(\theta) = e^{-\theta^2/\theta_1^2}$ with $\theta_1 = f(1+f^2)^{-1/2}\theta_0$. Here, $\theta_0 = 0.6 \times \theta_{FWHM}$ and θ_{FWHM} is the Full Width Half Maxima of the true primary beam pattern of the telescope.

The correlation of the gridded visibilities $\langle \mathcal{V}_{cg}\mathcal{V}^*_{cg}\rangle$ provides a direct measurement of the angular power spectrum C_{ℓ_g}. We define the estimator at a grid point g as,

$$\hat{E}_g = \frac{(\mathcal{V}_{cg}\mathcal{V}^*_{cg} - \sum_i \mid \tilde{w}(\mathbf{U}_g - \mathbf{U}_i) \mid^2 \mid \mathcal{V}_i \mid^2)}{(\mid K_{1g} \mid^2 V_1 - K_{2gg}V_0)}\,. \tag{3}$$

where, $V_0 = \frac{\pi\theta_0^2}{2}\left(\frac{\partial B}{\partial T}\right)^2$, $V_1 = \frac{\pi\theta_1^2}{2}\left(\frac{\partial B}{\partial T}\right)^2$, $K_{1g} = \sum_i \tilde{w}(\mathbf{U}_g - \mathbf{U}_i)$, $K_{2gg'} = \sum_i \tilde{w}(\mathbf{U}_g - \mathbf{U}_i)\tilde{w}^*(\mathbf{U}_{g'} - \mathbf{U}_i)$
Now, the expectation values of the individual term in the numerator can be written as,

$$\langle \mathcal{V}_{cg}\mathcal{V}^*_{cg}\rangle = \mid K_{1g} \mid^2 V_1 C_{\ell_g} + 2\sigma_n^2 K_{2gg} \tag{4}$$

and

$$\begin{aligned}\sum_i \mid \tilde{w}(\mathbf{U}_g - \mathbf{U}_i) \mid^2 \langle \mid \mathcal{V}_i \mid^2 \rangle &= V_0 \sum_i \mid \tilde{w}(\mathbf{U}_g - \mathbf{U}_i) \mid^2 C_{\ell_i} + 2\sigma_n^2 K_{2gg} \\ &\simeq V_0 C_{\ell_g} K_{2gg} + 2\sigma_n^2 K_{2gg}\end{aligned} \tag{5}$$

We see that the expectation of $\hat{E}_g$ gives an unbiased estimate of the angular power spectrum C_ℓ avoiding the positive noise bias caused by the system noise. The details of the noise variance calculation

for this estimator can be found in Choudhuri et al. (2014). The sky coverage of the modified primary beam $\mathcal{A}_{\mathcal{W}}(\theta)$ falls with a decrease in f. This explains the bahaviour of the cosmic variance contribution which increases as f is reduced. We further see that the system noise contribution also increases as f is reduced. This can be attributed to the term $V_1 = \frac{\pi\theta_1^2}{2}$ which appears in eq. (3). This effectively increases the system noise contribution relative to C_ℓ as f is reduced.

3 Results

At the beginning of this section, we highlight the effect of tapering in measuring the sky signal at 150 MHz GMRT observations through multi-frequency angular power spectrum $C_\ell(\Delta\nu)$. Later, we will come back to validate the estimator defined in Section 2 using simulations at 150 MHz. The measured $C_\ell(\Delta\nu)$, for a fixed ℓ, from the sky signal which is dominated by foregrounds, is expected to vary smoothly with $\Delta\nu$ and remain nearly constant over the observational bandwidth. But, the estimated $C_\ell(\Delta\nu)$ from GMRT 150 MHz observations has a oscillating component with larger amplitudes as a function of of $\Delta\nu$ (Ali, Bharadwaj & Chengalur, 2008). These oscillations could arise from bright continuum sources located at large angular separations from the phase center. The emission from the bright sources can leak through the frequency dependent sidelobe of the primary beam. We investigate whether tapering the sky response of the primary beam actually mitigates the oscillations in the estimated MAPS from the observed GMRT data reported in earlier work at 150 MHz (Ali, Bharadwaj & Chengalur 2008, FIELD IV of the paper, Ghosh et al. 2012). For this purpose, we introduce the dimensionless decorrelation function $\kappa_\ell(\Delta\nu) = C_\ell(\Delta\nu)/C_\ell(0)$ which has the maximum value $\kappa_\ell(\Delta\nu) = 1$ at $\Delta\nu = 0$, and is in the range $\mid \kappa_\ell(\Delta\nu) \mid \leq 1$ for other values of $\Delta\nu$. We use $\kappa_\ell(\Delta\nu)$ to quantify the $\Delta\nu$ dependence of $C_\ell(\Delta\nu)$ at a fixed value of ℓ. Figure 1 shows $\kappa_\ell(\Delta\nu)$ with and without the tapering for the sky signal. We have considered f = 0.6 and 0.8 which respectively correspond to a tapered sky response with FWHM 2.3° and 3.04° as compared to the untapered PB which has a FWHM of 3.8° at 150 MHz. The oscillatory pattern is distinctly visible when the tapering is not applied. We observe for most values of ℓ, the oscillations are considerably reduced and are nearly absent when tapering is applied. We do not, however, notice any particular qualitative trend between decrease of oscillations and f values. The tapering, which has been implemented through a convolution, is expected to be most effective in a situation where the uv plane is densely sampled by the baseline distribution. Though, in this analysis our results are limited by the patchy uv coverage of the GMRT data. This also possibly explains why some small oscillations persist even after tapering is applied.

Further, as a test bed for the estimator defined in Section 2, we consider simulated visibilities due to the diffuse synchrotron emission which is modelled as Gaussian random filed with a fixed power law index. The details of the simulation have been presented in our earlier paper (Choudhuri et al. 2014). In that paper, to validate the estimator, we investigated how well the TGE is able to recover the angular power spectrum of the input model C_ℓ^M (eq. 14, Choudhuri et al. 2014) which was used to simulate the Galactic synchrotron emission at 150 MHz. Figure 2 shows the estimated C_ℓ of the diffuse Galactic synchrotron radiation from the simulated GMRT and LOFAR data with $f = 0.8$. We choose a weight scheme ($w_g = \mid K_{1g} \mid^2$) such that it assigns a larger weight to grid points which have a denser visibility sampling relative to the grid points with sparser sampling. This is expected to minimize the system noise contribution. We used 20 realizations to calculate the mean and the variance of the estimated C_ℓ. We notice that for both GMRT and LOFAR, the estimated C_ℓ lies roughly within the 1σ of the input model of the angular power spectrum C_ℓ^M. For GMRT, however, the estimated C_ℓ values all appear to be somewhat in excess of C_ℓ^M indicating that we have an overestimate of the angular power spectrum relative to C_ℓ^M. We note that the Tapered Gridded Estimator is expected to give an unbiased estimate of C_ℓ provided we have an uniform and sufficiently dense baseline distribution. On the other hand, the GMRT has a relatively patchy uv coverage and we think the overestimate is a consequence of GMRT's patchy uv coverage, and is not inherent to the TGE. In comparison, we find the estimated C_ℓ values are in better agreement with C_ℓ^M for the LOFAR simulation (Right panel, Figure 2). We think this is due to the uniform and denser uv coverage of LOFAR as compared to the GMRT. We would also like to highlight that the analytic predictions of error estimates are in good agreement with the rms fluctuation estimated from the 20 simulated realizations.

As noted earlier bright point sources located far away from the phase centre of the telescope can leak through the sidelobe of the primary beam and this can limit our ability for a detection of the faint

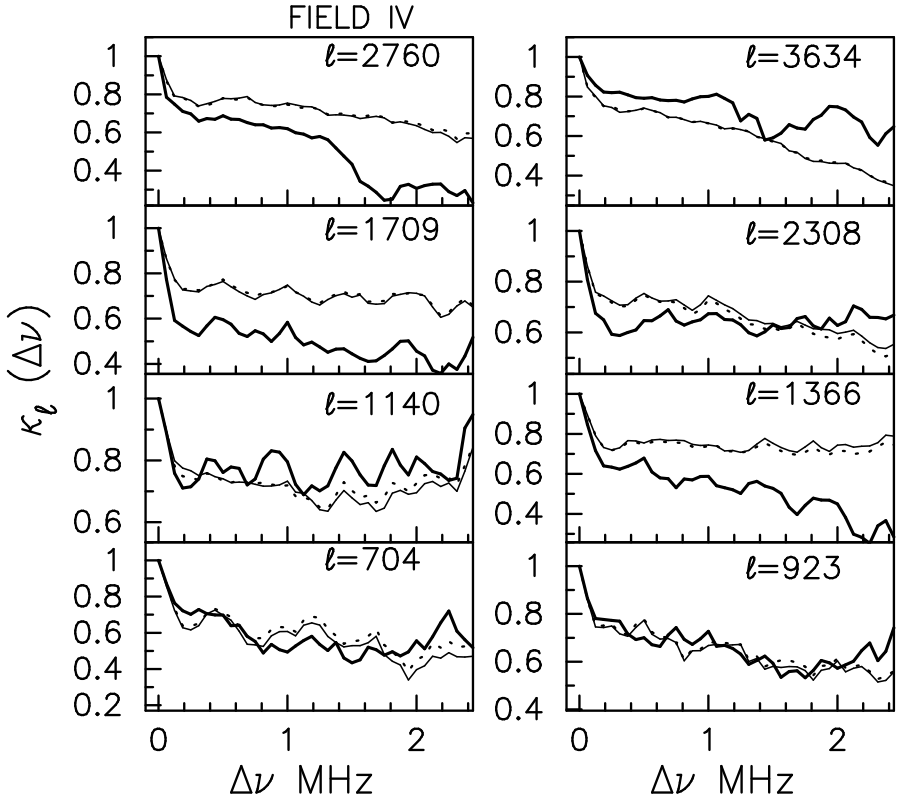

Figure 1: This figure shows the measured $\kappa_\ell(\Delta\nu)$ as a function of $\Delta\nu$ for the different ℓ values as shown in each panel, for FIELD IV (Ghosh et al. 2012). The thick solid, thin solid and dotted curves show results for no tapering, and tapering with f = 0.8 and 0.6 respectively.

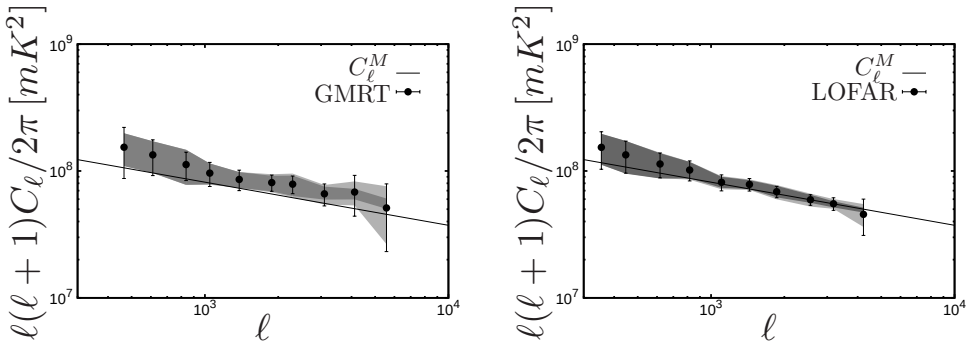

Figure 2: This shows C_ℓ multiplied with $\ell(\ell+1)/2\pi$, plotted as a function of ℓ. The left-hand (right-hand) panel shows the results for GMRT (LOFAR) with $f = 0.8$ and weight $w_g =\mid K_{1g} \mid^2$. The solid line shows the input model (eq. 14, Choudhuri et al. 2014) used for the simulations, and the points show the values estimated by the Tapered Gridded Estimator (eq. 3). The light shaded region shows the 1σ variation measured from 20 realizations of the simulations. The dark shaded region shows the cosmic variance which has been calculated by setting the system noise $\sigma_n = 0$ in the simulation, and the error bars display the 1σ error bars which was predicted analytically using eq. 42, Choudhuri et al. 2014.

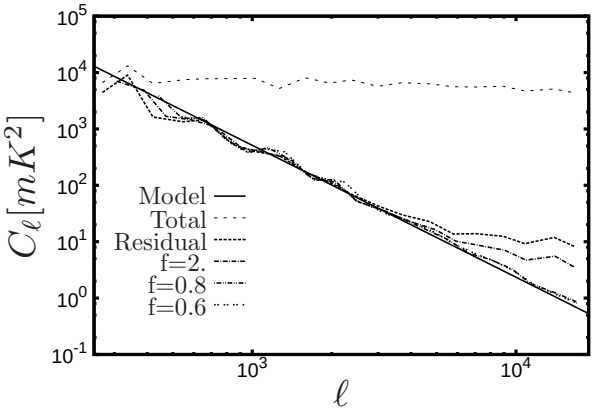

Figure 3: This figure shows the estimated angular power spectrum C_ℓ of total (diffuse Galactic synchrotron and the point sources) and the residual data (after point source subtraction). The flat nature of the total power spectrum arises due to the discrete points sources (Poisson) considered in our simulation. It also shows the estimated C_ℓ from the residual data using the TGE for the different values of f as shown in the figure. The figure is included here from Choudhuri et al. 2016a.

cosmological 21-cm signal. To suppress their contribution using TGE, we have set up a simulation where we add point sources out side of the main lobe of the PB and subtract sources only from the inside of the PB (see for details, Choudhuri et al. 2016b). Hence, the residual data after source subtraction has possible effect of the emission leaking through the sidelobes of the PB. The details of the simulation and data analysis, including point source subtraction are presented in Choudhuri et al. (2016b).

Next, we apply the TGE to the residual data after subtracting the model point sources from the initial visibility data to measure the angular power spectrum C_ℓ of the underlying diffuse emission. Figure 3 shows the C_ℓ of the total (the diffuse Galactic synchrotron emission and point sources) and also the residual data where the point sources are subtracted from the main lobe of the PB. We find that the estimated total power spectrum is almost flat at all angular scales. This is due to the Poisson distribution of point sources which dominates the C_ℓ at all angular multipoles (ℓ's). We do not include the clustering component of the point sources in our simulation. We also show the estimated C_ℓ from the residual visibility data using TGE with different f values $2.0, 0.8$ and 0.6 (Figure 3). We notice that in the absence of tapering we are able to recover the angular power spectrum of the diffuse synchrotron radiation at the low angular multipoles (large angular scales) $\ell < 3 \times 10^3$. The residual point source contribution is nearly independent of ℓ and has a value $C_\ell \approx 10$ mK^2 which dominates the estimated C_ℓ at the large angular multipoles (small angular scales) $\ell \geq 10^4$. The point source contribution comes down by a factor of more than 2 if we use the TGE with $f = 2.0$. We are now able to recover the angular power spectrum of the diffuse synchrotron radiation to larger ℓ values ($\ell < 5 \times 10^3$) as compared to the situation without tapering. The point source contribution, however, still dominates at larger ℓ values. We find that the point source contribution to C_ℓ is suppressed by more than a factor of 10 if we use TGE with $f = 0.8$ or 0.6. We are able to recover the angular power spectrum of the diffuse synchrotron radiation over the entire ℓ range using either value of f. The fact that there is no noticeable change in C_ℓ if the value of f is reduced from 0.8 to 0.6 indicates that a tapered sky response with $f = 0.8$ is adequate to detect the angular power spectrum of the diffuse synchrotron radiation over the entire ℓ range of our interest here.

4 Summary and conclusions

In this article we have briefly reviewed the TGE which quantifies the angular power spectrum of the sky brightness temperature. It suppresses the contribution from outside of the main lobe of primary beam by multiplying the sky with a frequency independent window function. Also, it uses the visibility data after gridding on a rectangular grid in the uv plane to reduce the computation time. Another advantage

of this estimator is that it internally calculate the noise bias and subtract this out to get an unbiased estimate of the power spectrum of the sky signal.

We have carried out different simulations to validate the TGE. In the first situation, we have simulated the diffuse Galactic synchrotron radiation which is modelled as a homogeneous and isotropic Gaussian random field with a power law angular power spectrum. In Figure 2, we find that the TGE is able to recover the input model C_ℓ^M to a high level of precision for LOFAR where the baselines have a uniform uv coverage. For the GMRT, which has a patchy uv coverage, the C_ℓ estimated from the TGE is largely within the 1σ errors from the input model C_ℓ^M. There is, however, indication that the angular power spectrum is overestimated to some extent. The overestimate is a consequence of GMRT's patchy uv coverage and is not inherent to the estimator which is unbiased by construction. It is possible to use simulations to quantify this overestimate and correct for this in a real observation. It is also interesting to point out that the TGE works well when the uv coverage (baseline distribution) is dense and uniform. This will be one of the key advantage with SKA-I, which will have a much denser baseline sampling compared to the current generation radio interferometers, in measuring the diffuse angular power spectrum of the synchrotron emission or the 21-cm signal at the low radio frequencies.

In the second situation, we include point sources along with the diffuse Galactic synchrotron radiation to study the effect of tapering on unsubtracted point sources to recover the angular power spectrum of the diffuse synchrotron radiation from the residual data. We find, using simulated data, that the TGE very effectively suppresses the contribution of the residual point sources located at the periphery of the telescope's field of view and recover the angular power spectrum of the diffuse synchrotron radiation at all angular scales of our interest (Figure 3). It is, hence, not necessary to image a very large region to model and subtract point sources even from the outer region in order to recover the power spectrum of the diffuse emission.

In our earlier publication (Ghosh et al., 2012), we have applied the TGE for 150 MHz GMRT observation to show that it is possible to considerably reduce the oscillations in the multi-frequency angular power spectrum of the sky signal by suppressing the sidelobe response of the primary antenna elements (Figure 1). The oscillations in $\kappa_\ell(\Delta\nu)$ are considerably reduced and are nearly absent when tapering is applied for most values of ℓ. A small oscillatory pattern persists even after the tapering is applied. This, however, does not pose a problem for foreground removal as the $C_\ell(\Delta\nu)$, after tapering, is well fitted by a low order polynomial, and the foregrounds were successfully removed (Ghosh et al., 2011b) from the measured angular power spectrum at 610 MHz.

We note that earlier studies on GMRT 150 MHz observations (Ali, Bharadwaj & Chengalur, 2008; Paciga et al., 2011) have found that, for EoR studies, the bright compact sources are the most dominating foreground component at the angular scales ($\leq 4^\circ$). It is difficult to model and subtract the point sources at the periphery of the telescope's field of view. Because of the incomplete sampling of the visibility data, bright point sources affect the interferometric observations significantly and pose a severe problem for detecting and measuring the redshited 21-cm signal from the EoR. The difficulties include the fact that the antenna response is highly frequency dependent near the nulls of the primary beam, and the calibration differs from that of the phase center due to ionospheric fluctuations. The accurate and precise subtraction of bright point sources from the wide-field dataset are needed as a primary step for measurement of the weak ($\sim 20-30$ mK) and structured EoR signal. The wide-field foreground removal is highly relevant issue for different ongoing EoR experiments and the next generation telescope, with innovative designs, Square Kilometer Arrayupcoming Square Kilometre Array[2] (SKA) for measuring the EoR signal. In this article we briefly demonstrate, using simulated data, that the TGE very effectively tackles the wide-field foreground removal issue by suppressing the contribution of the residual point sources located at the periphery of the telescope's field of view using tapering, and is able to successfully recover the input sky model from residual data. As a first step the knowledge gained by exploring the low frequency foregrounds will help us to constrain the astrophysics of the foreground emission such as the fundamental properties of turbulence of the ISM, Galactic magnetic field, synchrotron emitting medium and the intervening Faraday structure.

We have found that the TGE works very well in a situation where the baselines have a nearly uniform and dense uv coverage, it leads to an overestimate of C_ℓ if we have a sparse uv coverage (Figure 2). The improved method of TGE (Bharadwaj et al. 2016, in prep.) will be unbiased for both patchy and uniform uv coverage to estimate the C_ℓ of the sky signal. It is important to generalize the TGE to estimate the

[2]https://www.skatelescope.org

multi-frequency angular power spectrum $C_\ell(\nu_1, \nu_2)$ or equivalently the three dimensional power spectrum $P(k_\parallel, k_\perp)$ from the data to better characterize the foreground emission and the 21-cm signal (Bharadwaj et al. 2016, in prep.).

References

Ali S. S., Bharadwaj S.,& Chengalur J. N., 2008, MNRAS, 385, 2166A

Bernardi, G., de Bruyn, A. G., Brentjens, M. A., et al. 2009, A & A, 500, 965

Begum, A., Chengalur, J. N., & Bhardwaj, S. 2006, MNRAS, 372, L33

Bharadwaj S. & others, MNRAS, 2016, in Preparation

Chapman, E., Zaroubi, S., Abdalla, F., et al. 2014, arXiv:1408.4695

Choudhuri, S., Bharadwaj, S., Ghosh, A., & Ali, S. S., 2014, MNRAS, 445, 4351

Choudhuri, S., Bharadwaj, S., Roy, N., Ghosh, A., & Ali, S. S., 2016a, submitted to MNRAS

Choudhuri, S., Roy, N., Bharadwaj, S., Ali, S. S., Ghosh, A., & Dutta, P. 2016b, ready to submit MNRAS

Datta K. K., Roy Choudhury, T.,& Bharadwaj. S, 2007, MNRAS, 378, 119

Dutta P., Begum A., Bharadwaj S., & Chengalur J. N. 2009, MNRAS, 398, 887

Ghosh, A., Bharadwaj, S., Ali, S. S., & Chengalur, J. N. 2011a, MNRAS, 411, 2426

Ghosh, A., Bharadwaj, S., Ali, S. S., & Chengalur, J. N. 2011b, MNRAS, 418, 2584

Ghosh, A., et al. 2012, MNRAS, 426, 3295

Iacobelli, M., Haverkorn, M., Orrú, E., et al. 2013, A & A, 558, A72

Liu, A., & Tegmark, M. 2012, MNRAS, 419, 3491

Mellema, G., et al. 2013, Experimental Astronomy, 36, 235

Morales, M. F., & Wyithe, J. S. B. 2010, ARAA, 48, 127

Paciga G. et al., 2011, MNRAS, 413, 1174

Pober, J. C., Hazelton, B. J.,Beardsley, A. P., et al. 2016, arXiv:1601.06177

Seljak, U., 1997, Ap.J, 482, 6

Thyagarajan, N., Udaya Shankar, N., Subrahmanyan, R., et al. 2013, Ap.J, 776, 6

Trott, C. M., Wayth, R. B., Macquart, J.-P. R., & Tingay, S. J. 2011, Ap.J, 731, 81

van Haarlem, M. P., Wise, M. W., Gunst, A. W., et al. 2013, A & A, 556, A2

Primordial non-Gaussianity from 21-cm emission from the epoch of reionization

Pravabati Chingangbam*[1], Akanksha Kapahtia[1,2], Vidhya Ganesan[1,2], Shiv Sethi[3], L. Sriramkumar[4], and Girish Kulkarni[5]

[1] *Indian Institute of Astrophysics, Koramangala II Block, Bangalore 560 034, India*
[2] *Indian Institute of Science, Bangalore 560 012, India*
[3] *Raman Research Institute, Bangalore 560 080, India*
[4] *Department of Physics, Indian Institute of Technology Madras, Chennai 600036, India*
[5] *Institute of Astronomy and Kavli Institute of Cosmology, University of Cambridge, Madingley Road, Cambridge CB3 0HA, UK*

Abstract

We present an outline for using Minkowski Functionals to probe and constrain primordial non-Gaussianity manifest in 21-cm differential brightness temperature. We discuss how to calculate Minkowski Functionals for two-dimensional slices of simulated differential brightness temperature. We plan to apply this to future data from SKA.

1 Introduction

The detailed understanding of the epoch of reionization remains a challenging issue in modern cosmology. Cosmoic microwave background (CMB) observations suggest that the universe got reionized at $z \simeq 9$ (Planck Collaboration et al., 2015c). However, these observations are not able to provide tomography of the duration of the epoch. The best way to study this epoch in detail is to detect neutral hydrogen (HI) from this era. The baryonic component of the Universe after the epoch of recombination was mostly in the form of HI. It is possible to detect the redshifted 21-cm radiation from HI from pre-reionization and the reionization era of the universe. In addition to the complications of the reionization physics (see e.g. (Furlanetto et al., 2006)), this emission has spatial fluctuations imprinted from the primordial density perturbations. Locked in the nature of these emissions are clues about the physics of the primordial Universe - the amplitude, shape and statistical nature of primordial fluctuations; global matter densities and expansion rate; and physical details of the evolution of structure formation.

Inflation has proved to be a rather efficient paradigm to generate the primordial perturbations. Even amongst the simplest of slow roll scenarios involving a single canonical scalar field, there exist a plethora of inflationary models that remain consistent with the data, both at the level of power spectra (in this context, see, for instance, Refs. (Martin et al., 2014b,a; Planck Collaboration et al., 2015b)) and at the level of non-Gaussianities (Planck Collaboration et al., 2015a). These slow roll models lead to nearly scale invariant primordial spectra and rather small values of the non-Gaussianity parameter $f_{\rm NL}$ that characterizes the primordial scalar bi-spectrum (they typically result in $f_{\rm NL} \simeq 10^{-2}$, of the order of the first slow roll parameter). The strongest constraints on $f_{\rm NL}$ until now have been arrived at from the CMB data, which suggest that the primordial perturbations are consistent with a Gaussian distribution (Planck Collaboration et al., 2015a). However, the uncertainities in $f_{\rm NL}$ have turned out to be large, with $\sigma_{f_{\rm NL}} \sim 5$–$40$ depending on the shape of the primordial bi-spectrum that is considered. Further measurements of CMB polarization are expected to improve the constraints on $f_{\rm NL}$ only marginally. Whereas, $\Delta f_{\rm NL} \sim 1$ would be required in order to significantly tighten the constraints on inflationary models.

*prava@iiap.res.in

The 21-cm data can potentially be used to constrain cosmology (McQuinn et al., 2006; Furlanetto et al., 2006; Mao et al., 2008; Muñoz et al., 2015), in the same way that temperature and polarization fluctuations of the CMB have been used. The constraints from CMB were limited essentially because of the fact that being a two-dimensional surface, the modes are limited. In contrast, mapping the three-dimensional distribution of neutral Hydrogen will provide a much larger number of modes (Muñoz et al., 2015). Moreover, it will be able to probe scales that are much smaller than what is accessible to the CMB.

The detection of 21-cm signal is experimentally extremely challenging. The ongoing radio interferometers MWA, LOFAR, and PAPER might need up to 1000 hrs of integration to reduce the noise to levels needed to detect the signal. This is further complicated by the fact that Galatic and extra-Galactic forgrounds dominate the signal by many orders of magnitude. However, rapid technological advances in recent decades and superior understanding of the nature of the HI signal from the epoch of reionization makes this problem tractable and might enable statistical detection of the signal in the near future (e.g. (Zaroubi, 2013)).

The upcoming radio interferometer Square Kilometer Array (SKA) will improve upon the ongoing experiements on multiple fronts. SKA will have more collecting area, superior angular resolution, and unprecedented frequency coverage. The SKA might enable direct detection of the 21 cm signal in the redshift range $6 < z < 30$, corresponding to the frequency range $200\,\mathrm{MHz} > \nu > 50\,\mathrm{MHz}$. Hence it provides the best hope for potential use of 21 cm signal for tightening cosmological contraints, complementary to the CMB and large scale structure.

In the light of the limit on the constraint on primordial non-Gaussianity, and consequently inflationary models, from CMB data, the measurements of the fluctuations in the distribution of neutral Hydrogen using the 21-cm line offers the exciting window of opportunity to obtain much more stringent constraint on $f_{\rm NL}$. It has been argued in (Cooray, 2006) that 21-cm anisotropies can potentially measure the local form primordial non-Gaussianity parameter $f_{\rm NL}$ if it is ≥ 0.1. This is one order of magnitude improvement over the constraint of $f_{\rm NL} \geq 3$ from CMB experiments.

In order to realize this possibility one needs to design statistics which efficiently capture the non-Gaussian deviations. Some of the methods that have been discussed in the literature are the bispectrum of the brightness temperature (Cooray, 2006; Muñoz et al., 2015), scale dependent bias in the power spectrum of ionized hydrogen (Joudaki et al., 2011), and the power spectrum and other clustering properties (Lidz et al., 2013; Mao et al., 2013).

One of the tools that are frequently used to study the statistical properties of random fields in cosmology are what are known as Minkowski Functionals. In this work we focus our attention on Minkowski Functionals in two dimensions (Tomita, 1986; Coles, 1988; Gott et al., 1990; Winitzki and Kosowsky, 1998). The two-dimensional MFs have been very effectively used to search for deviations from Gaussian statistics of the primordial density perturbations as manifest in the CMB temperature fluctuations (Komatsu et al., 2011; Planck Collaboration et al., 2015a) and polarization (Ganesan et al., 2015; Planck Collaboration et al., 2015a). They are good at picking out spurious sources of non-Gaussianities, such as foreground contamination (Chingangbam and Park, 2013), since they contain all orders of n-point functions and not restricted to specific forms. In the context of 21-cm emissions, the genus, which is one of the Minkowski Functionals was used to study different reionization models and history in (Wang et al., 2015; Lee et al., 2008; Hong et al., 2014). MFs in three dimensions have also been used for similar purpose in (Yos). In this article our goal is to use two-dimensional Minkowski Functionals to analyze primordial non-Gaussianity in 21-cm signal anisotropies.

In section II we describe the brightness temperature field, primordial non-Gaussianity and the simulation of the 21-cm brightness temperature for Gaussian and non-Gaussian primordial perturbations. In section III we give a brief description of Minkowski Functionals. In section IV we describe the relevance of Minkowski Functionals for the 21-cm brightness temperature and how to compute them numerically. We end with concluding remarks in section V.

2 Brightness temperature simulation and primordial non-Gaussianity

Let us denote the offset of the 21-cm brightness temperature, T_b, from the CMB temperature, T_{CMB}, at some redshift z by $\delta T_b(z, \nu)$ For an observed frequency ν, and along a line of sight, $\delta T_b(z, \nu)$ can be

written as (Furlanetto, 2006; Mesinger et al., 2011),

$$\begin{aligned}\delta T_b(\mathbf{x}, z, \nu) &\simeq 27 x_{HI}\,(1+\delta_m(\mathbf{x}, z)\left(\frac{H}{dv_r/dr + H}\right)\\ &\times\left(1-\frac{T_{\rm CMB}}{T_S}\right)\left(\frac{1+z}{10}\,\frac{0.15}{\Omega_m h^2}\right)^{1/2}\\ &\times\left(\frac{\Omega_b h^2}{0.023}\right)\ \text{in mK},\end{aligned} \tag{1}$$

where x_{HI} is the fraction of neutral Hydrogen, δ_m is the evolved matter density contrast, $H(z)$ is the Hubble parameter, dv_r/dr is the gradient of the line of sight comoving velocity, and T_s is the gas spin temperature. The redshift z is related to the 21-cm frequency $\nu_0 = 1420\,\text{MHz}$ by $z = \nu_0/\nu - 1$. The spatial fluctuation of $\delta T_b(z)$ comes from the fluctuation of δ_m. During the post-heating regime, for redshifts lower than roughly 20, $T_s > T_{CMB}$ and at lower redshifts the term T_{CMB}/T_S can be ignored.

2.1 Primordial non-Gaussianity

The primordial scalar three-point function or the scalar bi-spectrum $\mathcal{B}_{\mathcal{R}}(\boldsymbol{k}_1, \boldsymbol{k}_2, \boldsymbol{k}_3)$ is defined as

$$\langle \mathcal{R}_{\boldsymbol{k}_1}\,\mathcal{R}_{\boldsymbol{k}_2}\,\mathcal{R}_{\boldsymbol{k}_3}\rangle = (2\,\pi)^3\;\mathcal{B}_{\mathcal{R}}(\boldsymbol{k}_1, \boldsymbol{k}_2, \boldsymbol{k}_3)\,\delta^{(3)}(\boldsymbol{k}_1 + \boldsymbol{k}_2 + \boldsymbol{k}_3), \tag{2}$$

where $\mathcal{R}_{\boldsymbol{k}}$ represents the Fourier modes of the curvature perturbation. The shape of the primordial scalar bi-spectrum depends on the mechanism that generates the non-Gaussianities in the early universe. The generated shapes are broadly classified as local, equilateral and orthogonal. While comparing with the data, each of these shapes is characterized by a corresponding non-Gaussianity parameter $f_{\rm NL}$, which is essentially a suitable dimensionless ratio of the bi-spectrum to the power spectrum. For instance, the local form of the primordial scalar bi-spectrum is expressed in terms of the corresponding non-Gaussianity parameter $f_{\rm NL}^{\rm loc}$ and the scalar power spectrum $\mathcal{P}_{\mathcal{R}}(\boldsymbol{k})$ as follows (Komatsu, 2010):

$$\begin{aligned}\mathcal{B}_{\mathcal{R}}(\boldsymbol{k}_1, \boldsymbol{k}_2, \boldsymbol{k}_3) &= -\frac{3}{10}\,\frac{1}{\sqrt{2\,\pi}}\,\frac{f_{\rm NL}^{\rm loc}}{k_1^3\,k_2^3\,k_3^3}\\ &\times\Big[k_1^3\,\mathcal{P}_{\mathcal{R}}(k_2)\,\mathcal{P}_{\mathcal{R}}(k_3)\\ &+ \text{two permutations}\Big].\end{aligned} \tag{3}$$

It should be noted that the most stringent constraints from the CMB data have been arrived at on the local shape of the bi-spectrum. These constraints correspond to $f_{\rm NL}^{\rm loc} = 0.8 \pm 5.0$ (Planck Collaboration et al., 2015a) which is, evidently, consistent with a Gaussian primordial distribution.

At the linear order, the curvature perturbation is related to the Bardeen potential Φ in the matter dominated epoch through the relation $\mathcal{R} = -5\,\Phi/3$. The bi-spectrum of the Bardeen potential can be defined in terms of the corresponding Fourier modes as follows:

$$\langle \Phi_{\boldsymbol{k}_1}\,\Phi_{\boldsymbol{k}_2}\,\Phi_{\boldsymbol{k}_3}\rangle = (2\,\pi)^3\;\mathcal{B}_{\Phi}(\boldsymbol{k}_1, \boldsymbol{k}_2, \boldsymbol{k}_3)\,\delta^{(3)}(\boldsymbol{k}_1 + \boldsymbol{k}_2 + \boldsymbol{k}_3). \tag{4}$$

Upon utilizing the expression (3) for the primordial bi-spectrum, we can express the local form of the bi-spectrum $\mathcal{B}_{\Phi}(\boldsymbol{k}_1, \boldsymbol{k}_2, \boldsymbol{k}_3)$ as

$$\begin{aligned}\mathcal{B}_{\Phi}(\boldsymbol{k}_1, \boldsymbol{k}_2, \boldsymbol{k}_3) &= \frac{1}{2}\,\frac{1}{\sqrt{2\,\pi}}\,\frac{f_{\rm NL}^{\rm loc}}{k_1^3\,k_2^3\,k_3^3}\\ &\times\Big[k_1^3\,\mathcal{P}_{\Phi}(k_2)\,\mathcal{P}_{\Phi}(k_3)\\ &+ \text{two permutations}\Big],\end{aligned} \tag{5}$$

where $\mathcal{P}_{\Phi}(\boldsymbol{k})$ denotes the power spectrum associated with the Bardeen potential.

2.2 Simulations of 21-cm temperature

We use the publicly available semi-analytic code `21cmFAST` (Mesinger et al., 2011) to make simulations of the 21-cm brightness temperature. This code implements the following steps. First it generates Gaussian random initial conditions for the dark matter density and velocity field at some initial redshift, for a given simulation box size and number of particles. Then first order perturbation theory is used to obtain the evolved large scale density, $\delta_m(\vec{x}, z)$, and velocity density fields, upto the desired redshift. Next the ionization field, x_{HI}, at the desired redshift is generated. To do this it is assumed that the number of ionizing photons is proportional to the collapsed halo fraction in the evolved density field computed from the extended Press-Schechter formalism. The spin temperature is separately computed. Then, from the ionization fraction, evolved density field, evolved peculiar velocity field and the spin temperature, the differential brightness temperature is computed.

For our analysis we have made a few simulations with ΛCDM parameter values from the PLANCK 2015 data(Planck Collaboration et al., 2015c), at redshift values $z = 20, 15, 10$, with simulation box size to be $200h^{-1}$Mpc with a resolution of 900 cells. We have input ionization fraction values $x_{HI} = 0.65$.

To make simulations of non-Gaussian δT_b we need to implement the primordial non-Gaussian initial conditions discussed in the previous subsection. For this we need to modify the initial conditions subroutine of the `21cmFAST` code. We plan to implement this in the near future.

3 Minkowski functionals in two dimensions

Minkowski Functionals (MFs) are defined as follows. Consider a random field defined on d-dimensions and choose a particular value of the field, usually referred to as *threshold value*. Then one can consider the set of all points where the field has values higher than or equal to the threshold. This set is called the *excursion set* (Adler, 1981). There is a one-parameter family of excursion sets indexed by the threshold parameter. The morphological properties of the excursion sets changes systematically as we vary the threshold value and this systematic behaviour can reveal the statistical nature of the field. The morphological properties of the excursions sets can be quantified in terms of geometrical and topological quantities namely, the MFs. In two dimensions, which is our focus here, there are three MFs (Tomita, 1986; Winitzki and Kosowsky, 1998). The first, denoted by V_0, is the *area fraction* which is the ratio of the area of the excursion set to the total area for which the field is defined. The second, denoted by V_1, is the total length of iso-temperature contours or boundaries of the excursion set, usually referred to as the *contour length*. The third, denoted by V_2, is the *genus* which is the difference between the numbers of hot spots and cold spots.

Let f denote a generic random field, σ_0 its rms and let $u \equiv f/\sigma_0$. Let ν be the threshold value chosen from the range of u. Then, the MFs are defined mathematically as follows:

$$V_0(\nu) \equiv \int \mathrm{d}a, \quad V_1(\nu) \equiv \int_C \mathrm{d}l, \quad V_2(\nu) \equiv \frac{1}{2\pi} \int_C K \, \mathrm{d}l, \tag{6}$$

where $\mathrm{d}a$ is the area element of the excursion set, C denotes contours that form the boundaries of the excursion sets, $\mathrm{d}l$ is the line element on C and K is the curvature of the contours. Eqs.(6) reduce to simple analytic functions of ν for special random fields. For the special case of a Gaussian random field the MFs are given by,

$$V_k(\nu) = A_k \, H_{k-1}(\nu) \, e^{-\nu^2/2}, \quad k = 0, 1, 2, \tag{7}$$

where $H_k(\nu)$ is the k-th Hermite polynomial and the amplitudes are

$$A_0 = \frac{1}{\sqrt{2\pi}}, \quad A_1 = \frac{1}{8} \frac{\sigma_1}{\sqrt{2}\sigma_0}, \quad A_2 = \frac{1}{(2\pi)^{3/2}} \left(\frac{\sigma_1}{\sqrt{2}\sigma_0} \right)^2, \tag{8}$$

where σ_1 is the rms of the gradient of the field. The cosmological information is encoded in the amplitudes via the variances σ_0, σ_1. Fig. (1) shows the shapes of the MFs for a Gaussian field.

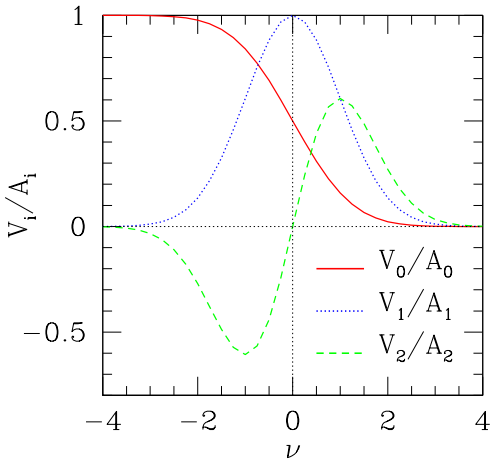

Figure 1: Plots showing the shapes of the three Minkowski Functionals for a Gaussian field in two dimensions. The amplitudes have been scaled out.

4 Minkowski functionals for two-dimensional δT_b on redshift slices

In the context of the CMB, the random fields of interest are the temperature fluctuations, ΔT, E, B modes and the total polarization intensity, P. For primordial Gaussian fluctuations ΔT, E, B are expected to be Gaussian, while P has Rayleigh form of the probability distribution function. The analysis then consists of numerical calculations of the MFs for these fields that are observed in experiments and comparing them with the expected Gaussian form.

In the case of the brightness temperature field the situation is quite different from the CMB. δT_b will inherit its statistical properties from δ_m, which in turn inherits it from the primordial density fluctuations and the gravitation evolution that it goes through. On sufficiently large scales one would expect δ_m to evolve linearly and hence exhibit the nature of the primordial fluctuations. However on small scales its gravitational evolution becomes highly non-linear and hence its statistical behaviour becomes dominated by the non-Gaussian nature induced by the gravitational evolution. A thorough theoretical understanding of the interplay between the manifestation of the nature of the primordial fluctuations, gravitational evolution and the relevant scales is essential before we analyze observations of the brightness temperature. It is also essential to understand the complications that will be introduced by other sorces of non-Gaussianities and how to disentangle them. MFs will be very valuable in such investigations. Our approach here is to make simulations of the 21-cm field with Gaussian and non-Gaussian primordial initial conditions and calculate MFs.

In the top panel of Fig. (2) we show a sample slice of the simulated δT_b field produced using `21cmFAST`, at redshift $z = 20$ and $x_{HI} = 0.65$. The middle and lower panels show excursion sets of δT_b for field threshold values 20 and 50 mK respectively. The excursion will then be used for calculation of MFs.

4.1 Numerical method for calculation of MFs for two-dimensional δT_b on redshift slices

For a given random field, in the absence of any prior knowledge of its statistical properties, the MFs have to be calculated numerically. For the field of view relevant for experiments such as the SKA, the flat sky approximation should be sufficient for analysing the observed sky patch. In this case the MFs can be calculated in a geometrical way by identifying excursion set regions and calculating the boundary length and curvature.

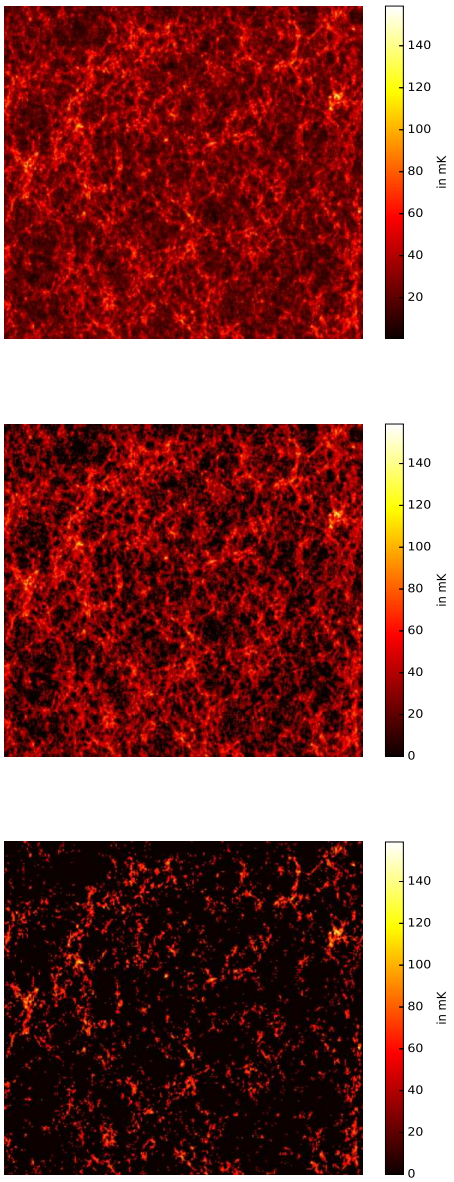

Figure 2: *Top*: A slice from the δT_b simulation at redshift $z = 20$ with $x_{HI} = 0.65$. *Middle*: The excursion set for δT_b for threshold value 20 mK. The black regions are the excluded excluded. *Bottom*: Same as middle panel but for threshold value 50.

It is also straightforward to employ the methods of calculation used for the CMB which are implemented on the surface of a sphere using equal area pixels and the publicly available code `HEALPIX` (Górski et al., 2005). A simple outline of the algorithm can be as follows. The three dimensional δT_b data is converted into two-dimensional slices, each of which corresponds to a patch on the surface of a sphere. We can choose one of the coordinates of the grid, say z, as the line of sight direction from us. Then we obtain two-dimensional x, y slices for each z value. From the value of the redshift at which δT_b is obtained the comoving distance of the $z = 0$ slice from us can be calculated. Then the comoving distance for each slice can be calculated by adding z to it. Approximating that each x, y slice is part of a spherical surface, we find the spherical coordinates θ, ϕ value for each x, y cell. Next we transfer each θ, ϕ to a `HEALPIX` pixel by using the `ang2pix` subroutine. Thus we get a patch of sky carrying δT_b data for each x, y slice. Note that we are ignoring the curvature of the redshift slices. This is okay for small simulation box sizes or sufficiently small field of views.

5 Discussions

21-cm observations promise to provide us access to unprecedented volume of cosmological data - from a period when the age of the Universe was a mere hundreth of its current age. From the point of view of cosmology this is very exciting because it will provide new test of the standard model of cosmology that is complementary to the existing ones, and simultaneously improve the constraints on cosmological parameters. For primordial non-Gaussianity the prospect is an order of magnitude improvement on constraints on the non-Gaussianity parameters. MFs are good at identifying spurious sources of non-Gaussianities since they are sensitive to all orders of n-point functions and not tailored for specific forms. Hence, they promise to be very useful tools to characterize primordial, as well as secondary, non-Gaussianity and to characterize different reionization models. We plan to carry out this study in the near future. Since they are defined directly in field space their computation and analysis of other contaminants to the field of interest is relatively easier than other statistics such as the bispectrum that are defined in Fourier space. Much of the technology that have been developed for using them in the context of the CMB can be extended to the 21-cm observations.

Acknowledgment

The computation required for this work was carried out on the Hydra cluster at the Indian Institute of Astrophysics. We acknowledge use of the `21cmFAST` code (Mesinger et al., 2011). P.C. would like to thank Yougang Wang for useful discussions.

References

Adler, R. J.: 1981, *The Geometry of Random Fields*

Chingangbam, P. and Park, C.: 2013, J. Cosmology Astropart. Phys. **2**, 031

Coles, P.: 1988, MNRAS **234**, 509

Cooray, A.: 2006, *Physical Review Letters* **97(26)**, 261301

Furlanetto, S. R.: 2006, MNRAS **371**, 867

Furlanetto, S. R., Oh, S. P., and Briggs, F. H.: 2006, Phys. Rep. **433**, 181

Ganesan, V., Chingangbam, P., Yogendran, K. P., and Park, C.: 2015, J. Cosmology Astropart. Phys. **2**, 028

Górski, K. M., Hivon, E., Banday, A. J., Wandelt, B. D., Hansen, F. K., Reinecke, M., and Bartelmann, M.: 2005, ApJ **622**, 759

Gott, III, J. R., Park, C., Juszkiewicz, R., Bies, W. E., Bennett, D. P., Bouchet, F. R., and Stebbins, A.: 1990, ApJ **352**, 1

Hong, S. E., Ahn, K., Park, C., Kim, J., Iliev, I. T., and Mellema, G.: 2014, *Journal of Korean Astronomical Society* **47**, 49

Joudaki, S., Doré, O., Ferramacho, L., Kaplinghat, M., and Santos, M. G.: 2011, *Physical Review Letters* **107(13)**, 131304

Komatsu, E.: 2010, *Classical and Quantum Gravity* **27(12)**, 124010

Komatsu, E., Smith, K. M., Dunkley, J., Bennett, C. L., Gold, B., Hinshaw, G., Jarosik, N., Larson, D., Nolta, M. R., Page, L., Spergel, D. N., Halpern, M., Hill, R. S., Kogut, A., Limon, M., Meyer, S. S., Odegard, N., Tucker, G. S., Weiland, J. L., Wollack, E., and Wright, E. L.: 2011, ApJS **192**, 18

Lee, K.-G., Cen, R., Gott, III, J. R., and Trac, H.: 2008, ApJ **675**, 8

Lidz, A., Baxter, E. J., Adshead, P., and Dodelson, S.: 2013, Phys. Rev. D **88(2)**, 023534

Mao, Y., D'Aloisio, A., Zhang, J., and Shapiro, P. R.: 2013, Phys. Rev. D **88(8)**, 081303

Mao, Y., Tegmark, M., McQuinn, M., Zaldarriaga, M., and Zahn, O.: 2008, Phys. Rev. D **78(2)**, 023529

Martin, J., Ringeval, C., Trotta, R., and Vennin, V.: 2014a, J. Cosmology Astropart. Phys. **3**, 039

Martin, J., Ringeval, C., and Vennin, V.: 2014b, *Physics of the Dark Universe* **5**, 75

McQuinn, M., Zahn, O., Zaldarriaga, M., Hernquist, L., and Furlanetto, S. R.: 2006, ApJ **653**, 815

Mesinger, A., Furlanetto, S., and Cen, R.: 2011, MNRAS **411**, 955

Muñoz, J. B., Ali-Haïmoud, Y., and Kamionkowski, M.: 2015, Phys. Rev. D **92(8)**, 083508

Planck Collaboration, Ade, P. A. R., Aghanim, N., Arnaud, M., Arroja, F., Ashdown, M., Aumont, J., Baccigalupi, C., Ballardini, M., Banday, A. J., and et al.: 2015a, *ArXiv e-prints*

Planck Collaboration, Ade, P. A. R., Aghanim, N., Arnaud, M., Arroja, F., Ashdown, M., Aumont, J., Baccigalupi, C., Ballardini, M., Banday, A. J., and et al.: 2015b, *ArXiv e-prints*

Planck Collaboration, Ade, P. A. R., Aghanim, N., Arnaud, M., Ashdown, M., Aumont, J., Baccigalupi, C., Banday, A. J., Barreiro, R. B., Bartlett, J. G., and et al.: 2015c, *ArXiv e-prints*

Tomita, H.: 1986, *Progress of Theoretical Physics* **76**, 952

Wang, Y., Park, C., Xu, Y., Chen, X., and Kim, J.: 2015, ApJ **814**, 6

Winitzki, S. and Kosowsky, A.: 1998, New A **3**, 75

Zaroubi, S.: 2013, in T. Wiklind, B. Mobasher, and V. Bromm (eds.), *The First Galaxies*, Vol. 396 of *Astrophysics and Space Science Library*, p. 45